EPFL

Thèse n° 9970

From coating flow patterns to porous body wake dynamics via multiscale models

Présentée le 20 mai 2022

Faculté des sciences et techniques de l'ingénieur
Laboratoire de mécanique des fluides et instabilités
Programme doctoral en mécanique

pour l'obtention du grade de Docteur ès Sciences

par

Pier Giuseppe LEDDA

Acceptée sur proposition du jury

Prof. C. Ancey, président du jury
Prof. F. Gallaire, directeur de thèse
Prof. J. Magnaudet, rapporteur
Prof. S. Bagheri, rapporteur
Prof. P. M. Reis, rapporteur

École polytechnique fédérale de Lausanne

2022

An expert is a person who has found out
by his own painful experience all the mistakes
that one can make in a very narrow field.
Niels Bohr

When I heard the learn'd astronomer,
When the proofs, the figures, were ranged in columns before me,
When I was shown the charts and diagrams, to add, divide, and measure them,
When I sitting heard the astronomer where he lectured with much applause in the lecture-room,
How soon unaccountable I became tired and sick,
Till rising and gliding out I wander'd off by myself,
In the mystical moist night-air, and from time to time,
Look'd up in perfect silence at the stars.
Walt Whitman, *When I heard the learn'd astronomer*

To my family,
to Laura,
to my friends.

Acknowledgements

No man is an island, even if the undersigned comes from an island. The work presented in this thesis is a result of a journey that would not have been possible without the helping hand and the guidance of several people. To be honest, to properly acknowledge every person from whom I learned something and helped me during this period is a monumental task. When I was writing this part, I realized that trying to compress human relations in a few sentences is extremely reductive. What matters is the time spent together.

I first start by acknowledging Professors Pedro M. Reis, Jacques Magnaudet and Shervin Bagheri that kindly accepted to read this thesis and discuss my work. Thank you Prof. Christophe Ancey for accepting to be the president of the jury and for the beautiful course on similarity solutions. Thank you François for giving me the opportunity to go through this journey, the time you dedicated me, your endless patience, intellectual integrity and immense knowledge, your precious suggestions. I will always remember and try to apply your positive attitude even in the most difficult moments. I am proud of having achieved this result guided by such an incredible person like you. A particular acknowledgment goes to Simone who, despite the distance, always guided and helped me in this labyrinth called PhD. I will never forget your teachings and always keep inside me the discussion when you asked me if I wanted to go to Lausanne. I hope that one day I will have the opportunity to have a tour as a passenger in your boat, maybe in Bosa. This thesis would not have been possible without the guidance of several "senior researchers" at different steps of this journey. Thank you Lorenzo for taking care of me when I arrived as a master student and for helping me in my initial difficult steps. It is difficult to express my gratitude to Gaétan; thank you for your voracity toward knowledge and our endless discussions. Thank you Giuseppe for being a guide and a friend during the last part of this journey. Thank you for showing me how to be a gentleman in every situation. Thank you Francesco for the nice discussions and for helping me in understanding what I really want for my future and how to approach it. A special thank goes to Matteo, with whom I shared the same apartment for three years. Thank you for having helped me when I was lost and for all the time spent together, for the trip in Seattle, for your visit in Bosa.

I would like to acknowledge the collaborators which contributed to this thesis. A first thank goes to Gioele and Gaétan, who helped me during the first steps in the world of the Rayleigh-Taylor instability and created an amazing experimental apparatus, respectively. Thank you P-T and Etienne for having shared your incredible experimental knowledge. Thank you Professors Benoit Scheid and Matthieu Wyart for the precious suggestions in the draperies work. Thank you Louis Martin-Monier and Prof. Fabien Sorin for the nice collaboration based on your

amazing experiments. Thank you Matteo for having introduced me to the world of differential geometry. Thank you Giuseppe for our endless discussions on homogenization. I would also like to thank Edouard for his patience in explaining to me sensitivity and lagrangian concepts. Thank you Simone for giving me the opportunity to supervise the master thesis of outstanding students: Matteo C., Filippo and Giovanni. I have learned a lot from these experiences. I would also like to thank the people that I met around the world. To be honest, I am terrible in names; I will be very short for this reason. Thank you Benoit for giving me the opportunity to participate to the conference your organized, and for showing me your beautiful lab in Bruxelles. Your passion toward research is something inspiring. Thank you Camille and Gaétan for having hosted me during the week in Princeton and the time spent with the Complex Fluids Group. Thank you P-T and Etienne for showing me your experiments and the work in your lab. Thank you Professors G. Querzoli and M.G. Badas for the visit in Cagliari, for showing me the lab and the beautiful experimental apparatus reproducing the heart.

I have to acknowledge people in and outside LFMI in Lausanne who enriched this journey, despite the external boundary conditions which made things more difficult. I am sorry if I forget someone, but as I said, what matters is the time spent together. A special thank goes to Petra, for always having taken care of me without any reserve. I would like to first acknowledge the officemates of the big office, Eunok, Isha, Giacomo and Alessandro. Life has been much easier thanks to you. Thank you Ludo, Hervé, Martin, for always have been around in the experimental rooms. Thank you Mathias, Simon, Vlado, Shahab, Y-M, Jesus for being part of this journey in different moments. I thank all friends from FLEXLAB, ECPS and EMSI. I wish Kevin and Simeon a beautiful PhD. Thank you Bertil for the funny moments together and for your incredible cider. I would like to thank my friends I knew in Pisa; when we meet and talk, it seems to be still in 2015. Thank you Marco, Mattia, Dimitri and Antonio. I wish you all the best for your future.

I would like to finally thank the people that supported and guided me in the journey of my life. Thank you Davide and Marco C. for having been present in each moment of my life since we met twenty years ago, for the beautiful moments we shared, we share and will share. Thank you Jonny, Gianmarco P., Marta and Francesca for the time we spent together, I enjoyed every moment. The list becomes long; thank you Peppe, Marco M., Enrico, Salvatore, Pippo, Peppone, Carlos, Raymond, Marco S., Tore S., Mauro, Cristiana, Nanni, Dario ... Thank you to my grandmothers with whom I shared beautiful moments and for all things they taught me. I would like to thank my parents and my brother Fulvio for their unconditional support of all my choices and for always listening to me, even in my worst moments. Every time that I come back home I feel as if I never left, ten years ago. Finally, thank you Laura for your outstanding patience with me, for your incredible curiosity for the world around us, for giving me the energy and attitude to approach this journey since the first day we met, and for being close to me even when we were far.

Lausanne, May 3, 2022 P. G. L.

Abstract

Multiscale phenomena are involved in countless problems in fluid mechanics. Coating flows are known to exhibit a broad variety of patterns, such as wine tears in a glass and dripping of fresh paint applied on a wall. Coating flows are typically modeled under the assumption that the thickness of the fluid layer is much smaller than the characteristic length of the free-surface deformations, i.e. there is a *separation of scales* between the *microscopic* variations of the velocity and pressure field along the thin layer and the *macroscopic* modulations of the free-surface. A different multiscale phenomenon of undeniable interest in the fluid dynamics community is the flow around and through porous objects. Dandelion seeds are transported by the wind thanks to a hairy structure, called pappus, known to present larger values of the aerodynamic drag and a more stable wake compared to an impervious disk in the same flow conditions.

This thesis investigates the pattern formation of several coating flows and the wake dynamics past diverse permeable bodies via multiscale models. We initially consider the flow of a thin viscous film underneath an inclined planar substrate. We show the emergence of free-surface structures modulated along the direction transversal to the main flow, called rivulets. These rivulets result from a pure equilibrium between hydrostatic gravity and surface tension effects, and may destabilize with the formation of traveling drops. We determine via a linear stability analysis the critical values of the inclination angle and film thickness beyond which rivulets destabilize. We numerically study the linear and non-linear response with respect to a harmonic forcing in the inlet flow rate, determining the diverse lenses' patterns emerging on a steady rivulet. The dripping problem is deepened by considering a single drop deposited on a very thin film. Very slight inclinations with respect to the horizontal, of the order of degrees, lead to the formation of a rivulet in the wake of a shrinking drop. Subsequently, we investigate the role of these instabilities in karst draperies formation, by coupling the hydrodynamic model with the deposition of calcium carbonate on the substrate. We implement an algorithm which retrieves the asymptotic properties of the two-dimensional linear impulse response from numerical simulations. The analysis shows the predominance of streamwise structures, reminiscent of draperies, growing on the substrate. The role of modifications of the substrate is then investigated in the cases of dewetting of very thin polymer films, in the context of production of optical metasurfaces, and in the case of three-dimensional spreading of a mass of fluid.

The last part of the thesis is devoted to the modifications of wake flows instabilities past bluff bodies when composed of a permeable microstructure, with a focus on the case of a porous

sphere and a cylindrical circular membrane. We develop an inverse procedure to optimize and retrieve the microstructure based on flow objectives. The analysis is concluded by studying the path instability of a freely-falling permeable disk. A complex series of bifurcations occurs but, as the ratio between voids and solid structure increases, all wake and path instabilities are damped.

Keywords: multiscale, pattern formation, hydrodynamic instability, Rayleigh-Taylor, thin-films, homogenization, porous, membrane, optimization, free-fall

Resumé

Les phénomènes multi-échelles sont impliqués dans d'innombrables problèmes en mécanique des fluides. Les films de liquides visqueux sont connus pour présenter une grande variété de motifs, comme les larmes de vin dans un verre et l'égouttement de peinture sur un mur. Ces écoulements de lubrification sont généralement modélisés en supposant que l'épaisseur de la couche de fluide est bien plus petite que la longueur caractéristique des déformations de la surface libre, c'est-à-dire qu'il y a une *séparation d'échelles* entre les variations *microscopiques* de vitesse et de pression le long de l'épaisseur et les modulations *macroscopiques*. Un autre phénomène multi-échelle d'indéniable intérêt pour la communauté de la dynamique des fluides est l'écoulement autour et au travers des objets poreux. Les graines de pissenlit sont transportées par le vent grâce à une structure composée de poils, appelée pappus, connue pour présenter des valeurs plus importantes de trainée aérodynamique ainsi qu'un sillage plus stable par rapport à un disque imperméable dans les mêmes conditions d'écoulement.

Cette thèse étudie la formation de motifs de plusieurs écoulements de films minces et la dynamique du sillage de divers corps poreux via des modèles multi-échelles. Nous considérons d'abord l'écoulement d'un film mince et visqueux sous un substrat plan et incliné. Nous montrons l'émergence de structures de surface libre modulées le long de la direction transversale à l'écoulement principal, appelées rivulets. Ces rivulets résultent d'un équilibre entre la gravité hydrostatique et la tension de surface, et peuvent ensuite se déstabiliser, donnant lieu à la formation de gouttes. Nous déterminons par une analyse de stabilité linéaire les valeurs critiques de l'inclination et de l'épaisseur au dessus desquelles les rivulets se déstabilisent. Nous étudions numériquement la réponse linéaire et non linéaire par rapport à un forçage harmonique du débit d'entrée, en déterminant la croissance des gouttes sur un rivulet stable. Le problème de l'égouttement est approfondi en considérant une goutte déposée sur un film très mince. De très légères inclinaisons, de l'ordre de quelques degrés, conduisent à la formation d'un rivulet dans le sillage d'une goutte rétrécissant en parallèle. Ensuite, nous étudions ces instabilités dans le contexte des formations karstiques, en couplant le modèle hydrodynamique avec le dépôt de carbonate de calcium sur le substrat. Nous implémentons un algorithme qui détermine les propriétés asymptotiques de la réponse impulsionnelle linéaire bidimensionnelle à partir de simulations numériques. L'analyse montre la prédominance des structures alignées dans la direction de l'écoulement, et qui se développent sur le substrat. Le rôle du substrat est enfin étudié dans les cas de mouillage de films polymères très fins, dans le contexte de la production de métasurfaces optiques, puis dans le cas de l'écoulement

tridimensionnel d'une masse de fluide sur un substrat courbe.
La dernière partie de la thèse est consacrée aux instabilités des écoulements de sillage de corps non-profilés lorsqu'ils sont composés d'une microstructure poreuse. Nous développons une procédure pour optimiser et retrouver la microstructure en fonction des objectifs fixés à l'écoulement macroscopique. L'analyse se termine par l'étude de l'instabilité de la trajectoire d'un disque poreux en chute libre. Une succession complexe de bifurcations se produit, mais, lorsque la fraction de vide augmente, toutes les instabilités sont amorties.

Mots clés : multi-échelle, formation de motifs, instabilité hydrodynamique, Rayleigh-Taylor, écoulement de film mince, homogénéisation, milieux poreux, membranes, optimisation, chute libre

Riassunto

In meccanica dei fluidi, i fenomeni multiscala sono presenti in innumerevoli problemi. È noto che film di liquidi viscosi presentano un'ampia varietà di motivi, come le lacrime di vino sulle pareti di in un bicchiere e la colatura di vernice fresca applicata su un muro. Questi flussi sono tipicamente modellizzati assumendo che lo spessore dello strato di fluido sia molto più piccolo della lunghezza caratteristica delle deformazioni della superficie libera. In altri termini, si afferma la presenza di una *separazione di scale* tra le variazioni *microscopiche* del campo di velocità e pressione lungo lo spessore e le modulazioni *macroscopiche*. Un altro fenomeno multiscala di innegabile interesse nella comunità fluidodinamica è il flusso intorno e attraverso oggetti porosi. I semi di dente di leone sono trasportati dal vento grazie a una struttura composta di peli, chiamata pappo, nota per presentare valori maggiori della resistenza aerodinamica e una scia più stabile rispetto a un disco impervio nelle stesse condizioni di flusso.

La presente tesi studia la formazione di motivi in diversi flussi di film fluidi e la dinamica di scia di diversi corpi permeabili, attraverso modelli multiscala. Il primo caso considerato è il flusso di un sottile film viscoso sotto un substrato piano inclinato. I rivoli, strutture della superficie libera modulate lungo la direzione trasversale al flusso principale, dominano la dinamica. Tali rivoli sono dati da un puro equilibrio tra pressione idrostatica e tensione superficiale, e possono destabilizzarsi con la formazione di gocce. Tramite un'analisi di stabilità lineare, vengono determinati i valori critici dell'angolo di inclinazione e dello spessore del film al di sopra dei quali i rivoli si destabilizzano. La risposta lineare e non lineare rispetto a una forzante armonica nella portata d'ingresso determina i diversi motivi di gocce che emergono su un rivolo. Il problema della crescita e caduta delle gocce viene approfondito considerando una singola goccia depositata su un film molto sottile. Lievissime inclinazioni rispetto all'orizzontale, dell'ordine dei gradi, portano alla formazione di un rivolo nella scia di una goccia. Successivamente, il ruolo di queste instabilità nelle formazioni calcaree viene investigato accoppiando il modello idrodinamico con la deposizione di carbonato di calcio sul substrato. Viene implementato un algoritmo che recupera le proprietà asintotiche della risposta impulsiva lineare e bidimensionale dalle simulazioni numeriche. L'analisi mostra la predominanza di formazioni allineate col flusso, che crescono sul substrato. Il ruolo delle variazioni del substrato viene indagato nei casi del fenomeno di *dewetting* di film polimerici molto sottili, nel contesto della produzione di metasuperfici, e nel caso della propagazione tridimensionale di una massa fluida.

L'ultima parte della tesi è dedicata alle instabilità dei flussi di scia di corpi tozzi composti

da una microstruttura permeabile. Viene sviluppata una procedura inversa per ottimizzare e recuperare la microstruttura basata su obiettivi di flusso. L'analisi si conclude studiando l'instabilità della traiettoria di un disco permeabile in caduta libera. Si verifica una complessa serie di biforcazioni ma, con l'aumento del rapporto tra vuoti e struttura solida, tutte le instabilità vengono smorzate.

Parole chiave: multiscala, formazione di motivi, instabilità idrodinamica, Rayleigh-Taylor, flussi di film sottili, omogeneizzazione, mezzi porosi, membrane, ottimizzazione, caduta libera

Contents

1 Introduction

1.1 Multiscale approaches in fluid mechanics: a brief overview

Multiscale phenomena are ubiquitous in fluid mechanics. Let us think about the variety of events occurring in our climate system, a source of inspiration in this regard (figure 1.1). From drop formation in clouds and rain which refresh Mediterranean summers to cold weather fronts which ruin our holiday plannings and tropical cyclones, to name a very few, the extremely rich dynamics of climate spans an incredibly vast range of length scales. While resolving all the spatial and time scales remains a monumental task, global climate models typically are based on (analytical or non-analytical) representations of the effect of the unresolved processes on the resolved-scale processes (Flato et al., 2014). The boundary layer is another multiscale phenomenon thoroughly investigated in fluid dynamics. For large inertia of the flow, viscous effects are confined in a region of very small thickness, in the vicinity of solid walls (Schlichting and Kestin, 1961). By exploiting the *separation of scales*, one can define a problem in the absence of viscous effects far from the wall, and "reconnect" (i.e. *match*) it with the microscopic solution inside the boundary layer. The boundary layer solution is then used, for example, to evaluate the wall viscous drag which affects the macroscopic flow. The concept of upscaling the flow at a certain, unresolved, microscale to keep the effect at the resolved macroscale is a key ingredient in this thesis.

Coating flows are involved in countless environmental, chemical, and engineering processes. The plethora of observed coating patterns motivated a great deal of studies aimed at understanding the underlying physical mechanisms. Such patterns are identified as the physical origin for several geological structures such as stalactictes (Short et al., 2005b; Camporeale and Ridolfi, 2012) and flutings (Camporeale, 2015; Bertagni and Camporeale, 2017) observed in limestone caves (figure 1.2(a,b)) and indeed originate from a multiscale process. Karst features, which can be of the order of meters, result from the flow of very thin layers of water, of the order of 10 μm, on the cave walls. The chemical mechanism behind the growth of speleothems is the precipitation of calcium carbonate dissolved in water which flows on the cave walls, which occurs for centuries. Due to the higher partial pressure of CO_2 in the soil and rock compared

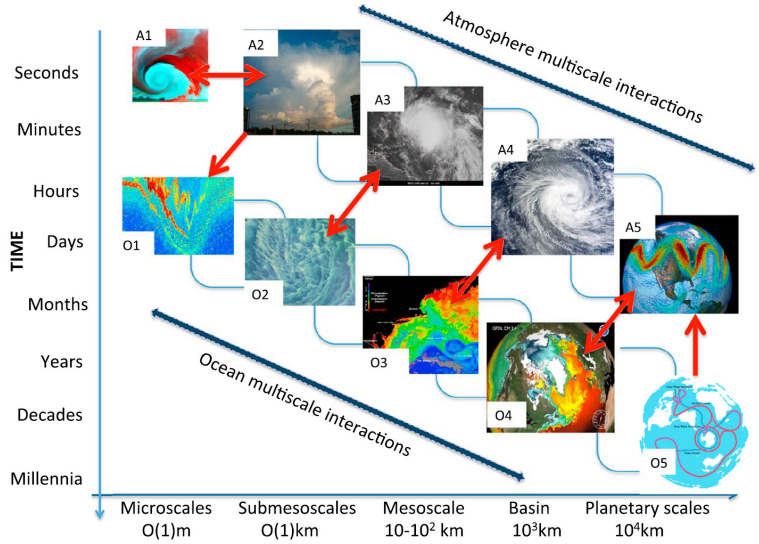

Figure 1.1: Diagram illustrating multiscale processes and scale interaction mechanisms in the atmosphere and ocean, reproduced from Stammer et al. (2018).

to the atmosphere, flowing water enriches in carbon dioxide. The pH of the solution is lowered and the quantity of calcium carbonate that can be dissolved in water increases (Short et al., 2005a,b). Once the water enriched in CO_2 flows through an opening on the walls of a cave, the CO_2 outgases from the solution since the concentration in the air is lower than in the water. As a result, the solution is supersaturated and calcium carbonate minerals deposit on the surface (Buhmann and Dreybrodt, 1985). The role of hydrodynamics in the speleothem formation increased in interest in the last two decades. Short et al. (2005a) showed that the stalactite shape is self-similar and results from the coupling of hydrodynamics and the deposition process. In Camporeale and Ridolfi (2012) the problem of the origin of crenulations on stalactites was tackled in the context of falling film theory, indicating that the pattern is mainly dictated by a hydrodynamic instability (Vesipa et al., 2015). The emergence of draperies structures in limestone caves is also driven by falling liquid film instabilities (Bertagni and Camporeale, 2017). In particular, these mechanisms can be traced back to a positive feedback between the deposition process and the tendency of the flowing thin layer of water underneath the cave walls, heavier than the air, to re-arrange into drops, when the substrate is horizontal, or into rivulets (modulations of the free-surface transversal to the main flow direction) when the substrate is inclined (Rayleigh-Taylor instability). This re-organization of the fluid layer enhances the formation of karst structures. However, the interaction between coating flows and growth or dissolution is not limited to limestone caves. Similar stalactites and flutings are observed due to solidification and melting of water (Camporeale, 2015), while physical or chemical erosion leads to scallops (Meakin and Jamtveit, 2010) or linear karren (Bertagni and Camporeale, 2021) patterns.

The flow of the thin water layers on these features is a multiscale process itself. In this case, the separation of scales is due to the thickness of the film much smaller than the characteristic

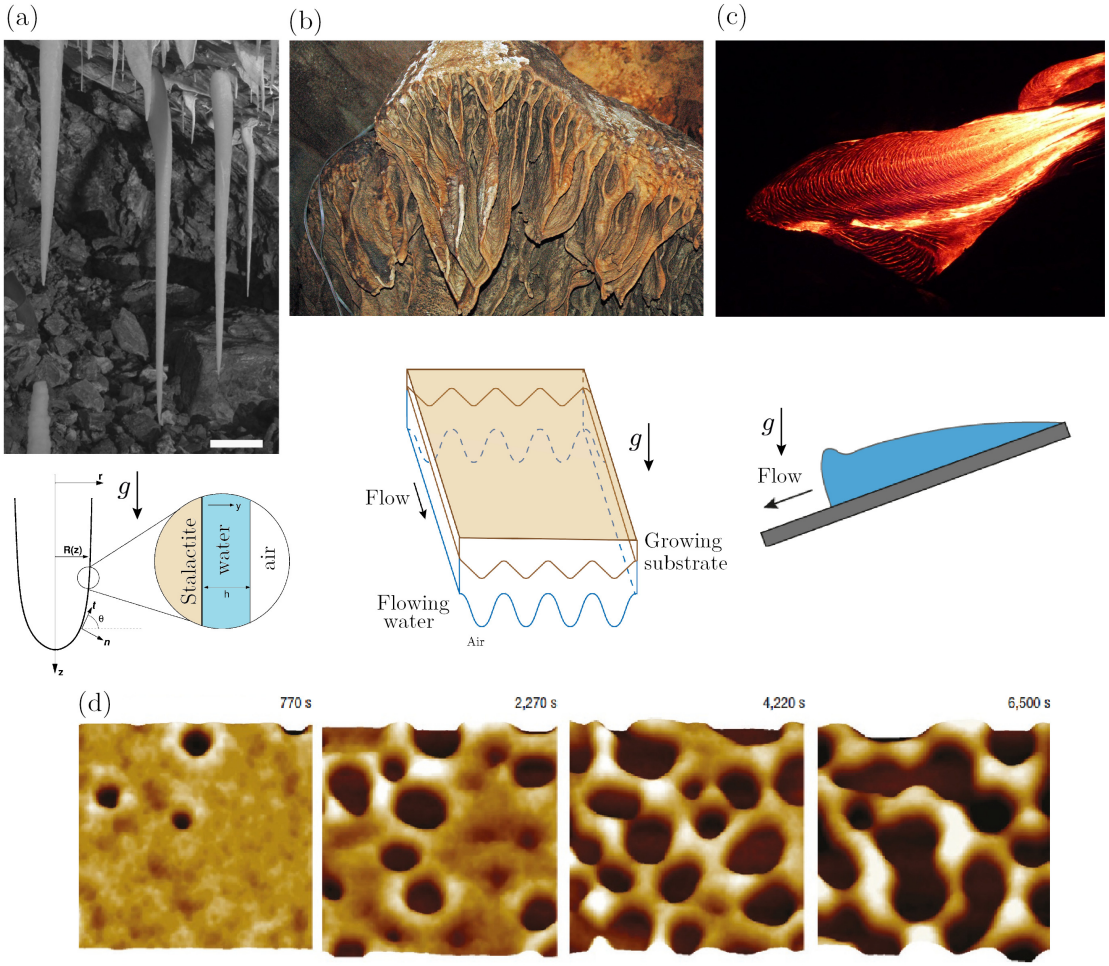

Figure 1.2: (a) Stalactite and thin film configuration during the growth of the stalactite. reproduced from Short et al. (2005b). (b) Travertine draperies (Crystal Onyx Cave, near Cave City, Kentucky, USA) by James St. John (https://wordpress.org/openverse/photos/d6995bba-b451-4bc2-a17a-20bc4cbf148f) and sketch of the physical configuration during growth of the substrate. (c) Spreading of lava (https://wordpress.org/openverse/photos/5f48b0ef-2072-4d50-857f-162d1aa5099a), together with a sketch of the two-dimensional spreading process. (d) Spinoidal dewetting of a 3.9 nm thin polymer film, reproduced from Becker et al. (2003).

length of the modulations of the free surface[1] of the thin liquid film itself. Exhibiting a broad variety of flow behaviors, first systematic analyses of coating flows were performed in the pioneering works of P.L. Kapitza and S.P. Kapitza, in inertia-driven flows (Kapitza, 1948; Kapitza and Kapitza, 1965; Kalliadasis et al., 2011). Intriguing patterns in coating flows may emerge due to other physical mechanisms as Marangoni effects (Oron, 2000; Hosoi and Bush, 2001; Rubio et al., 2013; Sterman-Cohen and Oron, 2020), contact-line driven instabilities (Huppert, 1982a; Spaid and Homsy, 1996; Lin et al., 2012; Xue and Stone, 2021), or the Rayleigh-Taylor

[1] The free surface is the interface between the liquid film and the surrounding fluid, e.g. air. In the following, we will omit the adjective liquid.

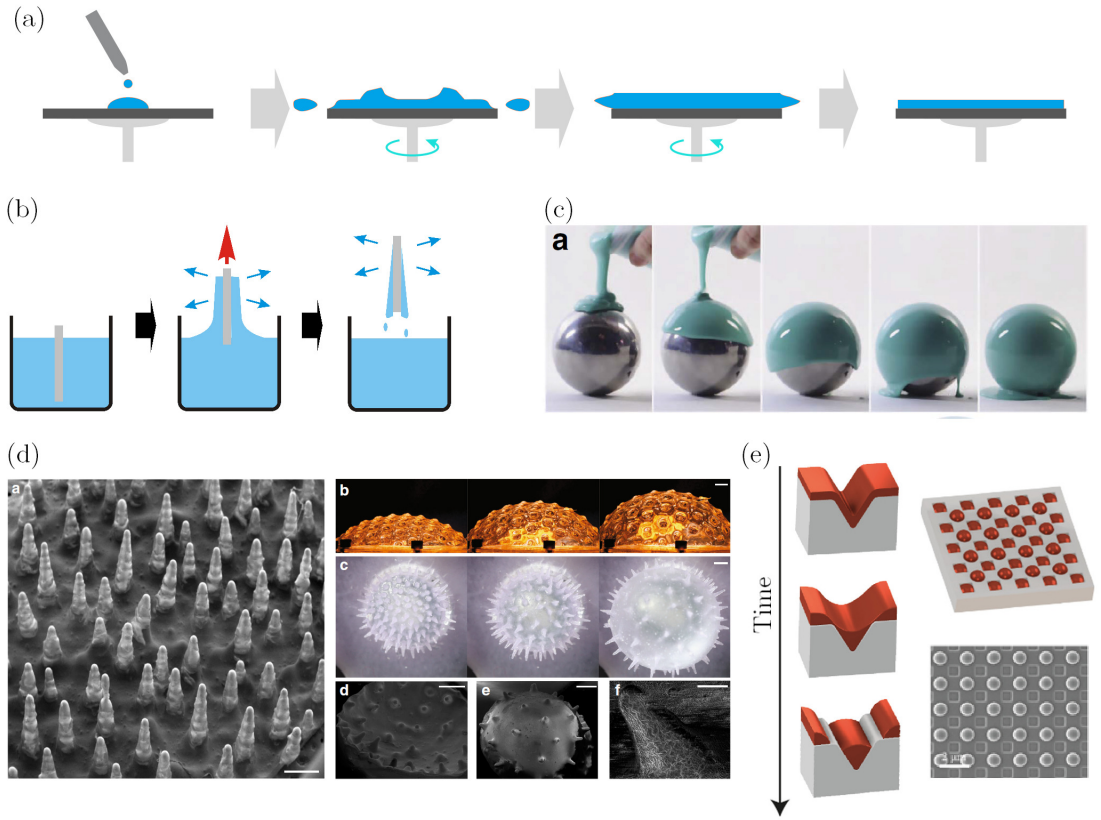

Figure 1.3: (a) Spin coating. (b) Dip coating. (c) Fabrication of slender elastic shells by the coating of curved surfaces, extracted from Lee et al. (2016). (d) Fabrication of soft patterned materials via thin film instabilities, extracted from Marthelot et al. (2018). (e) Schematic of the dewetting process of ultra-thin films induced by patterned substrates (on the left) and resulting three-dimensional drop patterns (on the right).

instability (Gallaire and Brun, 2017). Gravity currents are flows driven by gravity differences typically imputed to the presence of one phase heavier than the other, often a gas or air, which spreads on a substrate (figure 1.2(c)). These flows are ubiquitous in environmental and geophysical fluid dynamics. Typical examples include oil spreading on the sea (Hoult, 1972), lava (Balmforth et al., 2000) and pyroclastic flows due to a volcano eruption, dust storms, avalanches (Simpson, 1982; Huppert, 1986; Balmforth and Kerswell, 2005; Huppert, 2006), slurry and sheet flows (Ancey, 2007), to name a few.

Depending on the interactions between the film, substrate, and surrounding environment, thin films with sufficient mobility may also dewet either through spontaneous amplification of surface perturbations (spinodal dewetting, figure 1.2(d)) or through nucleation and growth of holes. The ruptured holes grow due to an imbalance in the component of surface tension tangential to the substrate at the contact line and often the growing holes (or the rims of the growing holes) coalesce, resulting in cellular structures and threads that disintegrate into droplets (De Gennes et al., 2004; Reiter, 1992; Xie et al., 1998). A huge effort in the

understanding of dewetting phenomena has been focused on the dynamics of very thin films with thickness less than the millimeter scale (Redon et al., 1991; Reiter, 1992; Brochard-Wyart and De Gennes, 1992; Bischof et al., 1996; Xie et al., 1998; Sferrazza et al., 1998; Herminghaus et al., 1998).

Typical engineering and chemical applications involve fabrication processes through several techniques (Weinstein and Ruschak, 2004), such as spin coating (Scriven, 1988; Schwartz and Roy, 2004) and dip coating (figures 1.3(a,b), which finds its theoretical foundations in the pioneering work of Landau and Levich (1942). Recent developments (Lee et al., 2016) showed that coating-assisted fabrication has revealed itself as a rapid and efficient way to obtain prototypes of curved spherical shells, with the process illustrated in figure 1.3(c). Soft patterned materials can be shaped by exploiting thin film instabilities (Marthelot et al., 2018), e.g. by rotation of a substrate combined with the solidification process of a polymer which leads to elongated drops structures, see figure 1.3(d). The potential of dewetting has been investigated as an efficient self-assembly process with several technologically relevant applications, such as water harvesting (Thickett et al., 2011), the fabrication of water-stable photodetectors (Chakrabarty et al., 2020), or peptide self-assembly (Bhandaru et al., 2021). Recent works have also highlighted the possibility of exploiting the resulting dewetted patterns for their tailored scattering properties (Gupta et al., 2019). Resorting to high-index dielectric glasses has relevance in nanophotonics (Gupta et al., 2019), where the control of the nanoresonator geometry allows for wide engineering of scattering and resonant properties. Several approaches to induce order through pattern-directed dewetting have been proposed, either based on chemical (Lu et al., 2002; Meyer and Braun, 2000) or topographic modulation (Bhandaru et al., 2014; Roy and Mukherjee, 2012; Kargupta and Sharma, 2001, 2002) of the substrate. By combining engineered substrates with functional materials, dewetting triggered by thermal annealing has emerged as a viable alternative (Thompson, 2012; Verma and Sharma, 2011; Seemann et al., 2005; Le Bris et al., 2014), as illustrated in figure 1.3(e).

Typical mathematical approaches to model coating flows are based on the assumption of *thin* film. But, "thin" with respect to what? As already introduced, the microscopic length is the thickness of the liquid film itself while the macroscopic one is the characteristic wavelength of the free surface deformations. *Lubrication* models, valid in the absence of inertia of the flow, stem from the idea of investigating the film thickness dynamics (figure 1.4) while the local values of velocity and pressure inside the thin film are slaved by the thickness evolution itself (Oron et al., 1997; Kalliadasis et al., 2011). The first step in the derivation of a lubrication model consists in a boundary layer approximation (Kalliadasis et al., 2011) that exploits the separation of scales and recognizes a fast variation along the thickness direction and slow variations along the directions tangential to the substrate, which is typically embodied in the *separation of scales parameter*

$$\varepsilon = \frac{\ell}{L}, \tag{1.1}$$

which quantifies the ratio between the microscopic (ℓ) and macroscopic (L) characteristic length of the considered problem. The second step is based on an asymptotic expansion

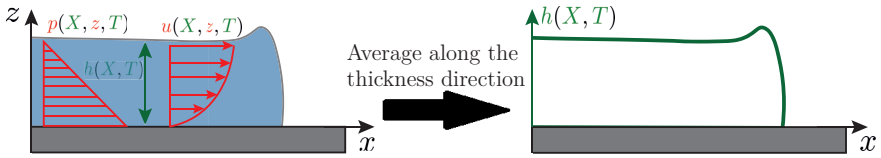

Figure 1.4: Principle of the lubrication model. The velocity and pressure fields are characterized by a semiparabolic and linear, respectively, fast variation along the z direction, and a slow variation along the x direction slaved by the film thickness. Upon integration of the velocity field along the z direction, one obtains a problem for the slowly-varying film thickness dynamics. The problem is thus reduced to one unknown, the thickness of the thin film.

of the velocity and pressure fields at different orders in ε, from which one determines the velocity and pressure profiles as a function of the thickness of the thin layer. Upon integration along the thickness direction, an evolution equation for the thickness of the thin layer is obtained. A classical example is the spreading of a very thin liquid film on a flat horizontal substrate, reported in figure 1.4 (Smith, 1969). Under the assumption of fast variations along to the thickness direction z and zero pressure and tangential stress at the free surface, one can simplify the two-dimensional Stokes equations by keeping the pressure term and the z derivatives:

$$\partial_{zz} u = \partial_x p, \quad \partial_z p = -\rho g, \quad u|_{z=0} = 0, \quad \partial_z u|_{z=h(x,t)} = 0, \quad p|_{z=h(x,t)} = 0, \tag{1.2}$$

By integrating the continuity equation, one obtains the following equation:

$$\partial_t h(x,t) + \partial_x \left(\int_0^{h(x,t)} u \mathrm{d}y \right) = 0, \tag{1.3}$$

which, after evaluation of the pressure and velocity fields, reads:

$$\partial_t h(x,t) + \frac{\rho g}{3\mu} \partial_x \left(h(x,t)^3 \partial_x h(x,t) \right) = 0, \tag{1.4}$$

where ρ and μ are the density and viscosity of the fluid in the thin layer, respectively. The average effect of the linear hydrostatic pressure gradient and semiparabolic velocity z profiles are embedded in the lubrication model through the term $h^3 \partial_x h$. Therefore, the upscaling process for the lubrication model, which projects the effect of the small scale (velocity and pressure fields along the film thickness) on the large scales (the modulations of the free surface), is based on a multiple scales expansion in ε, followed by an averaging step. The only remaining unknown is the film thickness, making this equation suitable for analytical developments.

The flow of a liquid phase through a body containing interconnected voids is frequently encountered in engineering applications as well as in nature. The characteristic size of the pores is typically much smaller than the macroscopic size of the porous medium itself. In most cases, the focus is on the global, macroscopic, behavior of the flow through the porous

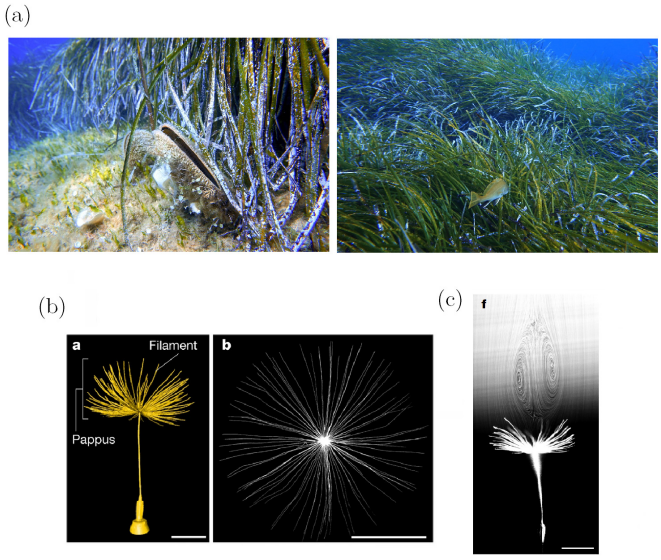

Figure 1.5: (a) The seagrass Posidonia oceanica (left: https://wordpress.org/openverse/image/d6ec0be4-8718-4148-93a7-ddd359a04fa5; right: https://search.openverse.engineering/image/0a42ae71-1775-4b9c-97bf-bf5250c44eef). (b) The pappus structure, reproduced from Cummins et al. (2018). (c) Detail of the recirculation region past a dandelion in hovering flight, reproduced from Cummins et al. (2018).

body, neglecting the details of the flow at the microscopic scale. Typically, the flow around and through the porous object presents flow structures of length scale much larger than the microstructure characteristic scale. There are several industrial applications concerning flows through permeable structures with a plethora of microscopic properties and pore sizes, ranging from millimeters for particle filtration to nanometers for desalination (Fritzmann et al., 2007; Elimelech and Phillip, 2011; Matin et al., 2011) and wastewater recovery (Shannon et al., 2008; Rahardianto et al., 2010). At larger scales, the flow around permeable bluff bodies, as parachutes and nets, is gaining increasing interest (Cummins et al., 2018; Labbé and Duprat, 2019). Fog water harvesting systems, particularly employed in arid climates (Olivier, 2004; Labbé and Duprat, 2019), are built using either nets (Park et al., 2013) or harps (Shi et al., 2018; Labbé and Duprat, 2019). Aquatic vegetation plays an essential role in marine ecosystems. Ensembles of plants, so-called canopies, deform in *honami* or *monami* shapes (figure 1.5(a)); in other words, they damp waves and therefore stabilize the seabed, among several other biological functions (Finnigan, 2000; Nepf, 2012; Brunet, 2020). It is not surprising that canopy flows have received growing attention over the past decades (Nepf, 1999; de Langre, 2008). Owing to the separation of scales between the size of a single plant compared to the typical extent of a canopy, the latter is often considered as a porous structure (Battiato and Rubol, 2014; Zampogna et al., 2016). Canopies strongly modify turbulent flows inducing hydrodynamic instabilities, coherent structures (Hamed et al., 2020; Sharma and García-Mayoral, 2020; Endrikat et al., 2021; Liu et al., 2021) and fluid-structure interactions (Wong et al., 2020). Additionally, several minute insects such as the thrips (*Thysanoptera*) use hairy appendages

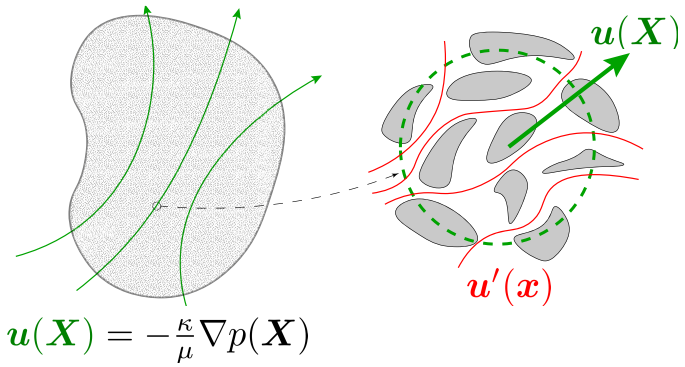

Figure 1.6: Principle of the Darcy law for the flow through a porous medium. The fast-varying flow field at the microscopic scale $\boldsymbol{x}$ (red streamlines) is upscaled by considering the average drag exerted by the pores in an elementary volume. At the macroscopic scale $\boldsymbol{X}$, the pore geometry is filtered out and replaced by the permeability κ, which relates the macroscopic velocity field (green streamlines) with the macroscopic pressure gradient.

for feeding and locomotion (Wu et al., 1975). These filaments-made wings have convenient lift to weight and lift to drag ratios with respect to an impervious wing (Sunada et al., 2002) and can be modeled as porous structures composed of arrays of cylinders (Cummins et al., 2017). In a similar fashion, the seeds of the *tragopon pratensis* (Casseau et al., 2015) are transported by the wind thanks to a particular umbrella-like extension called *pappus*, which can be seen as the equivalent of a parachute. Also in this case, the flow pattern past these seeds advected by wind gust can be explained using the model of a porous disk, with a Reynolds number based on the pappus diameter $Re \sim 10^2$ (figure 1.5(c)). In opposition to the impervious case, characterized by an unsteady wake at these values of the Reynolds number, the flow past these porous structures is steady (Cummins et al., 2018), see figure 1.5(d). Owls are renowned for their silent flight, which stems from the microscopic permeable structure of the hair composing the wings (Wagner et al., 2017; Jaworski and Peake, 2020). Within the vascular system of plants, permeable microstructures called sieve plates are crucial for sap translocation (Jensen et al., 2016).

The separation of scales allows one to define a continuum model in which the macroscopic effect of the microscopic flow through the pores is described through an average drag which affects the macroscopic, averaged, velocity and pressure fields (figure 1.6), see e.g. Whitaker (1986) for the volume averaging method. The most celebrated result, which stems from the experimental works of Darcy in the 19th century (Darcy, 1856), is the linear relation between the pressure gradient and the average velocity through the porous medium:

$$\boldsymbol{u} = -\frac{\kappa}{\mu}\nabla p, \tag{1.5}$$

where κ is the so-called *permeability*, which indeed describes the average drag effects at the microscale. Note that, in the absence of macroscopic viscous effects, the pressure drop in a certain distance L represents the macroscopic drag exerted by the microscopic solid structures.

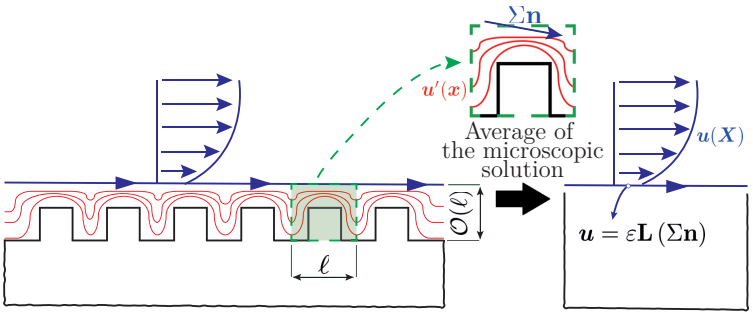

Figure 1.7: Multiscale homogenization technique applied to the flow over a microstructured substrate. The microscopic solution, characterized by fast spatial variations, (red streamlines) can be retrieved by a microscopic problem forced by the macroscopic stress at a certain distance of the order of the microscopic length scale, in a periodic repetition. Through an averaging step, a slip boundary condition for the macroscopic, slowly-varying, velocity field (blue streamlines and profile) is retrieved, which faithfully reproduces the microscopic viscous effects. This macroscopic velocity field is intended as the average of the fast-varying microscopic field, in the periodic repetition.

The permeability has the dimensions of the square of a length; since it results from the average solution of the microscopic problem in a domain of characteristic size ℓ, one can express the permeability as $\kappa = \text{const} \times \ell^2$. In non-dimensional form, $Da = \kappa / L^2 = \text{const} \times \varepsilon^2$, where Da is the Darcy number and ε is, again, the separation of scales parameter.

A formal approach to the study of the flow through porous media is based on *homogenization technique*. Homogenization has been applied successfully to a plethora of problems in fluid mechanics (Mei and Vernescu, 2010), such as the flow through porous media (Zampogna and Bottaro, 2016), the interface problem between a porous structure and a free fluid region (Lācis and Bagheri, 2017), the flow on a microstructured wall (Zampogna et al., 2019b), and the flow through a microstructured permeable membrane (Zampogna and Gallaire, 2020). An asymptotic expansion allows one to obtain a microscopic problem forced by the macroscopic variables, e.g. the pressure or the stress. In the absence of inertia, the linearity of the microscopic problem leads to a generic solution linear with the macroscopic forcing. In figure 1.7 we illustrate the idea for the case of the flow in the vicinity of a microstructured wall, following Zampogna et al. (2019b). In analogy with the lubrication problem, the separation of scales parameter between the characteristic length of the elementary cell and the length of the wall allows for a multiple scales expansion. However, homogenization distinguishes between fast (microscopic) and slow (macroscopic) variations along all spatial directions. The separation of scales allows one to consider a microscopic and periodic elementary cell. Thanks to the linearity of the equations pertaining at these small scales, the microscopic solution $(\boldsymbol{u}', p')$ can be written in terms of the macroscopic stress which forces the microscopic flow at its far boundaries. Upon solution of these problems, its average is employed in a slip condition on the velocity to be imposed at the wall:

$$\boldsymbol{u} = \varepsilon \mathbf{L}(\Sigma \mathbf{n}), \tag{1.6}$$

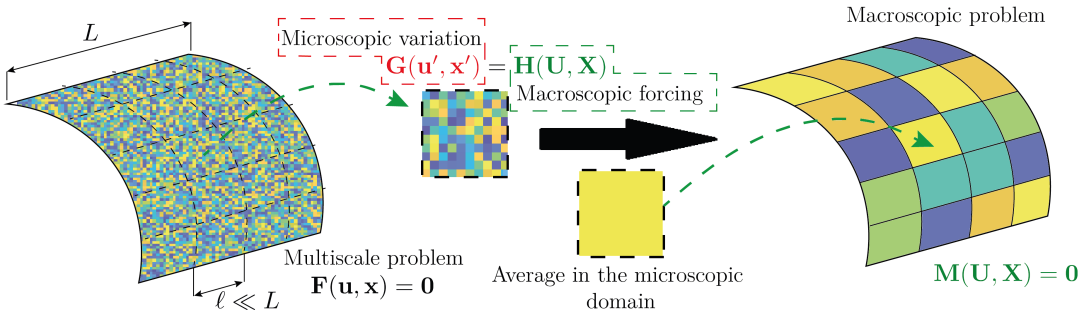

Figure 1.8: Generic features of a multiscale approach when different spatial scales $\mathbf{x} = \mathbf{x}' + \varepsilon\mathbf{X}$ are involved. The separation of scales $\varepsilon = \ell/L \ll 1$ allows one to define, from the initial multiscale problem $\mathbf{F}(\mathbf{u},\mathbf{x}) = \mathbf{0}$, a microscopic problem in the fast-varying variables $(\mathbf{u}',\mathbf{x}')$ forced by the slowly-varying macroscopic variables $(\mathbf{U},\mathbf{X})$. The average of the microscopic solution is then employed in the macroscopic, slowly-varying, problem.

where $\mathbf{L}$ is the slip tensor, Σ is the macroscopic stress at the wall and $\mathbf{n}$ is the normal to the wall. Once again, the macroscopic solution takes into account the microscopic flow but "smoothens" the variations occurring at the microscopic scale.

The above-described models share some characteristics, summarized in figure 1.8:

- the flow presents a separation of scales;
- the microscopic flow features can be expressed as functions of some macroscopic forcing, e.g. the free surface deformations for the lubrication model, the pressure gradient for a bulk porous medium, or the macroscopic stress far from a microstructured wall, at a distance much larger than the microscopic length;
- the microscopic flow is averaged along the fast-varying directions;
- the result is a macroscopic equation or boundary condition;
- only the "long-wave" (i.e. the macroscopic scale) features of the flow are retained, neglecting all the variations occurring at the microscopic scale (the film thickness for the lubrication model, the pore size in the porous model);
- the averaged macroscopic effects are thus the object of the investigation.

This thesis, financed by the Swiss National Science Foundation under grant 200021_178971 and whose outline is reported in figure 1.9, exploits multiscale approaches to systematically study the macroscopic behavior of different flows. In Part I, we study, through a lubrication model, the pattern formation for the flow of a thin film under an inclined planar substrate. Part II investigates the effect of modulations or large variations of the substrate for different coating patterns, i.e. substrate growth due to a deposition law, dewetting at the nanoscale,

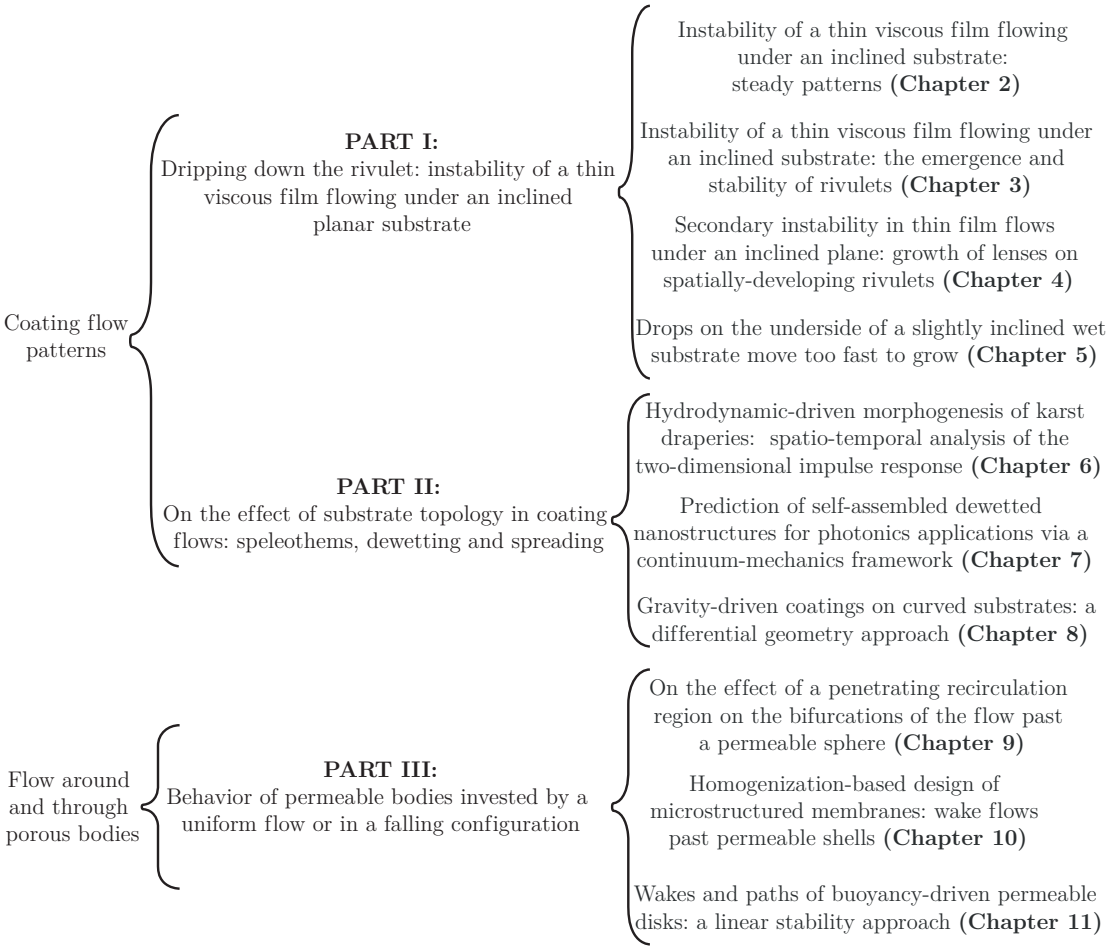

Figure 1.9: Outline of this thesis.

and non-uniform spreading. Part III is devoted to the study of the flow past a porous sphere, a permeable cylindrical shell invested by a uniform flow and the instability of a freely falling permeable disk. In the following sections, we present the analytical tools and detailed motivations underlying the structure of this thesis.

1.2 Linear stability analysis: a brief overview

Amidst the theoretical approaches employed in this work, linear stability analysis is the crucial tool exploited throughout the thesis. In this section, we illustrate some essential concepts of linear stability theory, which will help in the understanding of the patterns investigated in this thesis.

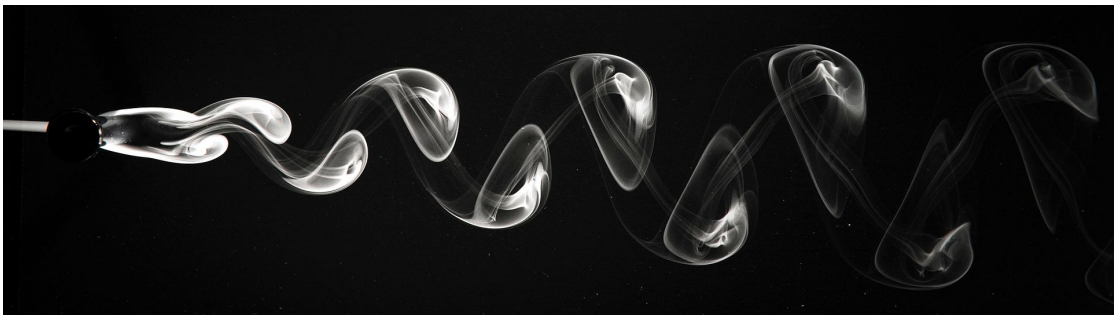

Figure 1.10: Experimental visualization of the vortex shedding past a circular cylinder. Photograph by Jürgen Wagner (https://commons.wikimedia.org/wiki/File:Karmansche_Wirbelstr_kleine_Re.JPG).

1.2.1 Bifurcations and pattern formation

Eye-catching regular patterns are ubiquitous in our experience; examples include the beautiful columnar jointings of the Giant's Causeway in Northern Ireland, karst structures observed in limestone caves all around the world, our fingerprints, and the viscous coiling occurring when we drop honey on bread. The pioneering works of Thompson (1942) and Turing (1952) paved the way to a great deal of pattern formation and morphogenesis studies. One of the most celebrated examples of pattern formation in fluid dynamics is the von Karman vortex street past bluff bodies (figure 1.10). The steady flow past a circular cylinder undergoes an instability that leads to a two-dimensional oscillatory flow characterized by the alternate shedding of vortices (Williamson, 1996). Other relevant patterns (figure 1.11) include (a) the Rayleigh-Plateau instability of a jet due to the action of surface tension, which results in the formation of droplets, (b) the Kelvin-Helmholtz instability that occurs in the presence of two streams of different velocity, (c) the Rayleigh-Taylor instability that occurs whenever a heavier fluid lies above a lighter fluid, (d) wine tears due to surface tension gradients (Marangoni effects), and (f) capillary ridge (or fingering) instabilities.

Hydrodynamic instability theory showed undeniable potential in the understanding of the conditions (i.e. the *thresholds*) which lead the so-called *base flow* to destabilize and a different pattern to emerge. Anticipating the developments of the following sections, a fundamental concept to be introduced is the *dispersion relation*, which relates the behavior in space and time of a growing/damped perturbation (Huerre and Monkewitz, 1990)

$$D(k,\omega) = 0, \tag{1.7}$$

when the perturbation is assumed in normal form both in space and time

$$q' \propto \exp\left(\mathrm{i}(kx - \omega t)\right). \tag{1.8}$$

We identify the wavenumber of the perturbation k and its growth rate $\sigma = -\mathrm{Im}(\omega)$, while $\mathrm{Re}(\omega)$ is the frequency of oscillation. Through the dispersion relation, we thus relate the

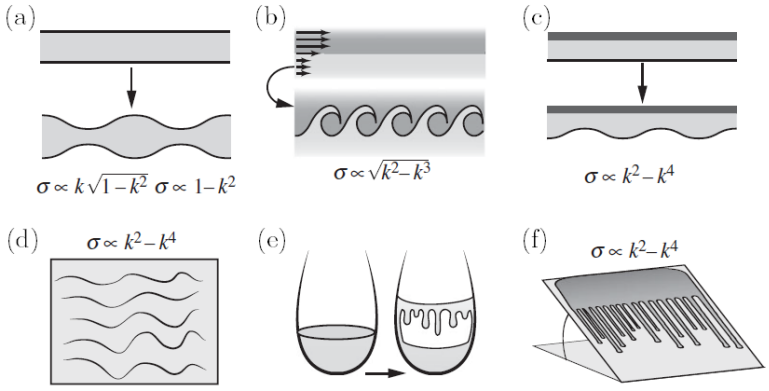

Figure 1.11: Sketch of different instabilities, reproduced from Gallaire and Brun (2017). (a) Plateau-Rayleigh instability, (b) Kelvin-Helmholtz instability, (c) Rayleigh-Taylor instability in a thin layer, (d) Kapitza waves, (e) wine tears and (f) capillary ridge instability.

growth rate to the wavenumber of the perturbation. The linear instability is characterized by a dispersion relation, as shown in figure 1.11. For such a normal mode perturbation in space and time, the dispersion relation identifies a continuum of unstable modes which depend on the wavenumber. This concept, which stems from local stability analysis, is deepened in the next section.

1.2.2 Local stability analysis

Local stability analysis deals with perturbations expanded in modal form in time and along one or more spatial directions. We introduce a coordinate system (x, y, z). We assume that the baseflow $\mathbf{Q}$ is invariant along the x direction and solution of a steady problem, i.e. $\mathbf{Q}(y, z)$. If the flow is also unidirectional, it is said to be *parallel*. Local stability approaches are typically employed for parallel flows (Briggs, 1964; Bers, 1975; Huerre and Monkewitz, 1990), but not limited to them (Pier, 2008). The flow decomposition reads:

$$\mathbf{q} = \mathbf{Q}(y, z) + \epsilon \hat{\mathbf{q}}(y, z) \exp\left(i(kx - \omega t)\right), \tag{1.9}$$

where ϵ is a small parameter, not related to the previously discussed separation of scales parameter. The flow equations in the generic form

$$\partial_t \mathbf{q} + \mathbf{N}(\mathbf{q}) = \mathbf{0} \tag{1.10}$$

are expanded in orders of ϵ, with the decomposition (1.9). At order $\mathcal{O}(1)$, one recovers the baseflow equations:

$$\mathbf{N}(\mathbf{Q}(y, z)) = \mathbf{0}, \tag{1.11}$$

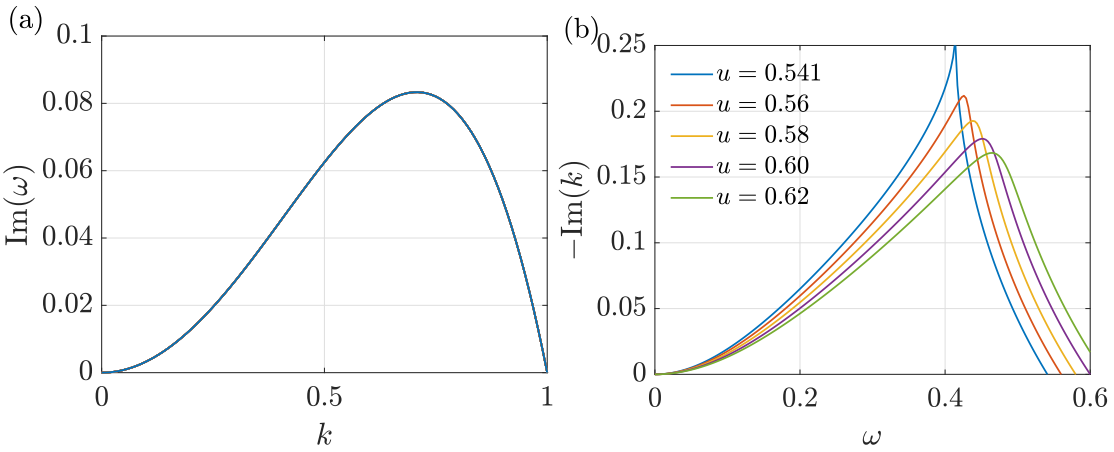

Figure 1.12: (a) Temporal and (b) spatial growth rates resulting from the temporal and spatial stability analysis of the dispersion relation (1.13). The temporal growth rate does not depend on u.

while at order $\mathcal{O}(\epsilon)$ one finds the dispersion relation:

$$-\mathrm{i}\omega\hat{\mathbf{q}}(y,z) + \mathbf{L}((\mathbf{Q}(y,z),k)\hat{\mathbf{q}}(y,z) = \mathbf{0}, \tag{1.12}$$

where $\mathbf{L}$ stems from the linearization of $\mathbf{N}$. The resulting eigenvalue problem (1.12) can be solved by (i) assigning the value of $k \in \mathbb{R}$ and looking for $\omega \in \mathbb{C}$, so-called *temporal* stability analysis or by (ii) assigning $\omega \in \mathbb{R}$ and looking for $k \in \mathbb{C}$, so-called *spatial* stability analysis (Huerre and Monkewitz, 1990). In an experimental situation, the first case consists in feeding the flow with a spatial forcing (e.g. a slightly sinusoidal wall for the spreading of a fluid on a substrate) and looking at the temporal evolution at fixed locations. The second case instead consists in a temporal, harmonic, forcing of the flow (e.g. a time-dependent oscillation of the flat substrate for the spreading problem) which results in a spatial amplification downstream.

To give a practical example, we consider the stability of a flat film (i.e. the baseflow thickness reads $H = 1$) under an inclined planar substrate. In this case, the dispersion relation is analytical and reads, in non-dimensional form (Fermigier et al., 1992; Brun et al., 2015):

$$\omega = uk + \frac{\mathrm{i}}{3}(k^2 - k^4). \tag{1.13}$$

The resulting (a) temporal and (b) spatial growth rates are reported in figure 1.12. The temporal growth rate does not depend on u and presents a *maximum* and a *cut-off* wavenumber, i.e. the wavenumber beyond which perturbations are damped. The spatial growth rate curves instead change with u. We initially consider the case $u = 0.62$. We observe zero growth rate for $\omega = 0$ and a cut-off at high frequencies. As u decreases, the maximum growth rate increases and becomes sharper. For $u \approx 0.541$, the dispersion relation shows an almost vertical vertical tangent at the maximum, i.e. $\partial_\omega k \to \infty$. For $u < 0.54$, the spatial problem is ill-posed. Physically, this means that the flow does not synchronize to the forced frequency

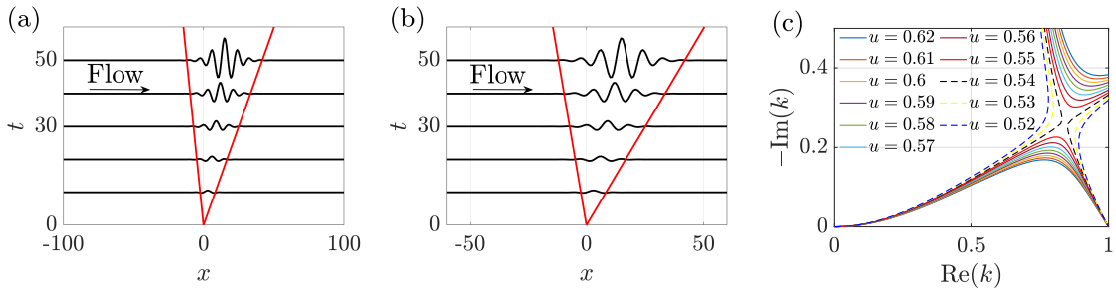

Figure 1.13: (a,b) One-dimensional flat film response to an initial impulse located at $x = 0$ resulting from the dispersion relation (1.13), for (a) $u = 0.62$ (convectively unstable case) and (b) $u = 0.3$ (absolutely unstable case). (c) Isocontours of zero temporal growth rate $\mathrm{Im}(\omega) = 0$ in the complex k plane, for the dispersion relation (1.13).

but instead presents its own intrinsic oscillatory behavior (Huerre and Monkewitz, 1990). The transition to this state is called *convective-absolute transition*. Convective flows are typically also called *noise amplifiers*, since the response to a perturbation depends on the frequency of the perturbation itself, i.e. the flow presents an *extrinsic* dynamics. Absolutely unstable flows are called *oscillators*, since they present their *intrinsic* frequency, independently of the nature of the small perturbation. While at a first sight the temporal and spatial stability problems may seem unrelated, they can be unified by considering the *spatiotemporal* stability analysis, presented in the next section.

1.2.2.1 Spatiotemporal stability analysis

The temporal and spatial stability analyses are generalized by considering complex values both for k and ω, so-called spatiotemporal stability analysis (Huerre and Monkewitz, 1990). As depicted in figure 1.13(a,b), the flow is said convectively unstable if the growing perturbation is advected downstream from the initial impulse location, while it is said to be absolutely unstable when the growing perturbation instead propagates also upstream of the initial location (Brun et al., 2015). The absolute-convective transition can be found by determining the saddle points of the complex dispersion with zero temporal growth rate (Briggs, 1964; Bers, 1975; Huerre and Monkewitz, 1990):

$$\frac{\mathrm{d}\omega}{\mathrm{d}k} = 0, \quad \mathrm{Im}(\omega) = 0. \tag{1.14}$$

For $\mathrm{Im}(\omega) > 0$, the flow is absolutely unstable, and vice versa. Figure 1.13(c) shows the isocontours $\mathrm{Im}(\omega) = 0$ for different values of u of the dispersion relation (1.13). For $u \approx 0.541$, $\mathrm{Im}(\omega) = 0$ at the saddle point. Note that this value of u corresponds to the one that shows an almost vertical tangent in the spatial dispersion relation (figure 1.12(b)).

The complete spatiotemporal response of a given flow to external perturbations is characterized through the large-time asymptotic behavior of the linear impulse response, the so-called Green function (Huerre and Monkewitz, 1990). The Green function is the most synthetic

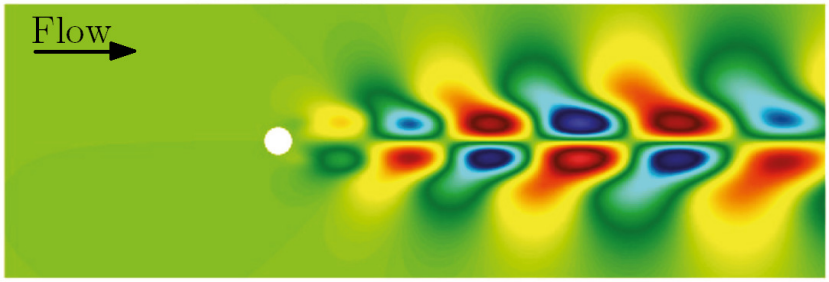

Figure 1.14: Streamwise component of the real part of the velocity field, for the unstable mode of the steady flow past a circular cylinder at $Re = 50$. Extracted from Xu et al. (2018).

and complete way to describe the nature of a forced linear system, since the response to any generic forcing is given by the convolution between the Green function and the forcing itself. Adopting the general format of a two-dimensional spatial normal mode expansion in x and y, the large-time asymptotic response can be retrieved by the determination of the saddle points of the spatio-temporal growth rate, at each ray $(x/t, y/t)$ in the complex planes of the spatial wavenumbers which define the response (Briggs, 1964; Bers, 1975; Huerre and Monkewitz, 1990; Carriere and Monkewitz, 1999; Juniper, 2007; Brun et al., 2015). In the two-dimensional case and for $t \to \infty$, the Green function asymptotically reads:

$$\tilde{g}(x, y, t) \sim \hat{g} \exp[\mathrm{i}\left(k_x x + k_y y - \omega t\right)]/t, \quad t \to \infty \tag{1.15}$$

where the streamwise wavenumber k_x, the spanwise wavenumber k_y and the complex frequency ω are varying in space and time, via their dependence on so-called rays x/t and y/t. At large times, the dominating contribution with group velocity $(x/t, y/t)$ is thus given by:

$$\frac{\partial \omega''}{\partial k_x} = \frac{\partial \omega''}{\partial k_y} = 0, \tag{1.16}$$

where $\omega'' = \omega - k_x x/t - k_y y/t$. The resulting values of k_x, k_y and ω'' for each ray $(x/t, y/t)$ allow one to reconstruct the linearized dynamics of the wavepacket. We refer to Chapter 6 for a detailed discussion.

Up to now, we focused on parallel flows. In the following, we describe the class of instability which affects non-parallel baseflows, e.g. the steady flow past a circular cylinder.

1.2.3 Global stability analysis

Local stability analysis stems from the idea that the baseflow is invariant at least in one direction, along which one expands the perturbation in modal form. Instead, we now consider a steady baseflow $\mathbf{Q}(x, y, z)$. In the context of global stability analysis, the following decomposition is considered (Huerre and Monkewitz, 1990; Chomaz, 2005; Theofilis, 2011):

$$\mathbf{q}(x, y, z, t) = \mathbf{Q}(x, y, z) + \epsilon \hat{\mathbf{q}}(x, y, z) \exp(\sigma t), \tag{1.17}$$

where $\mathrm{Re}(\sigma)$ is the growth rate and $\mathrm{Im}(\sigma)$ is the frequency of the self-sustained oscillation.

In a similar fashion to the local stability analysis, the non-linear problem

$$\partial_t \mathbf{q} + \mathbf{N}(\mathbf{q}) = \mathbf{0} \tag{1.18}$$

is expanded in powers of ϵ, resulting in the baseflow problem

$$\mathbf{N}(\mathbf{Q}(x,y,z)) = \mathbf{0} \tag{1.19}$$

and in the eigenvalue problem for the perturbation

$$\sigma\hat{\mathbf{q}}(x,y,z) + \mathbf{L}(\mathbf{Q}(x,y,z))\hat{\mathbf{q}}(x,y,z) = 0. \tag{1.20}$$

If there exists an eigenvalue with $\mathrm{Re}(\sigma) > 0$, the associated eigenvector $\hat{\mathbf{q}}(x,y,z)$ grows exponentially in time. In figure 1.14 we report the real part of the streamwise component of the velocity field for the unstable mode of the steady and symmetric flow past a circular cylinder, at $Re = 50$. The spatial distribution is antisymmetric with respect to the axis $y = 0$ and oscillating along the x direction, thus highlighting the presence of a pattern of vortices that travel downstream. This spatial variation has to be combined with the temporal growth and oscillation so as to obtain the self-sustained linear perturbation dynamics. With this analysis, one identifies instabilities characterized by their intrinsic frequency, i.e. oscillators.

The sequence of bifurcations that a flow may encounter can therefore be approached in the context of bifurcation theory and linear stability analysis (cfr. Theofilis, 2011 for a review). Global stability analysis is now largely employed and its reliability in the prediction of instability thresholds and shedding frequencies close to the threshold (Barkley, 2006) is now well assessed, spanning different length scales, from microfluidics systems (Bongarzone et al., 2021) to industrial applications such as wind and hydraulic turbines (Iungo et al., 2013; Viola et al., 2014; Pasche et al., 2017). For large amplitude of the growing perturbation, the exponential growth is modified by the presence of non-linear effects which typically lead to a saturation of the response (Chomaz, 2005).

1.2.4 Link between global and local stability analysis

In this section, we provide a link between local and global stability analysis, under the assumption of *weakly non-parallel flow*. Weakly non-parallel flows are characterized, at each streamwise location, by a spatial scale of the instability much smaller than the one of the variations of the baseflow along the streamwise direction. The local dispersion relation thus depends on the considered streamwise location, i.e. $D(k,\omega;X) = 0$, where X is the slowly-varying streamwise coordinate. A suitable ansatz for the perturbation is the Werner-Kramers-Brillouin (WKB) asymptotic approximation (Crighton and Gaster, 1976; Gaster et al., 1985; Monkewitz

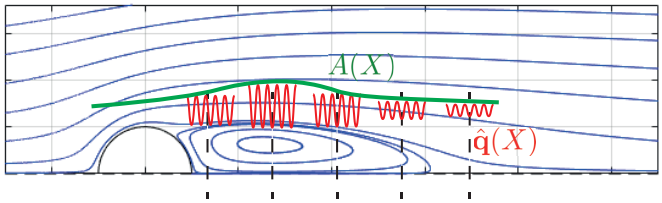

Figure 1.15: Application of the weakly non-parallel approach to the wake past a circular cylinder (only the upper half on the domain is shown). At each streamwise location, one solves the local stability problem retrieving the asymptotic properties (k,ω) and the eigenvector $\hat{\mathbf{q}}$. The slices of the local stability analysis are smoothly reconnected by an envelope function A.

et al., 1993; Pier et al., 2001; Pier, 2003a, 2011):

$$\mathbf{q}' = A(X;\omega)\,\hat{\mathbf{q}}(X;\omega)\exp\left(\frac{\mathrm{i}}{\varsigma}\int_0^X k\left(x';\omega\right)\mathrm{d}x' - \mathrm{i}\omega t\right), \tag{1.21}$$

where A is the slowly-varying amplitude that smoothly connects the eigenvectors at each streamwise slice, and $\varsigma \ll 1$ is a measure of the weak non-parallelism.

Within this framework, the global instability results from the interactions of the local behavior of stable, convective, or absolutely unstable regions. In a globally stable flow, there may be regions in which perturbations are amplified but advected downstream. Another possibility for a globally stable flow is the presence of regions of absolute instability, but the upstream-propagating perturbations are damped because of the presence of stable regions upstream. From this point of view, the relative size and strength of the stable, convectively and absolutely unstable regions play a role. The global behavior of a flow can therefore be seen as a competition between production and transport of perturbations of the baseflow. A necessary condition for global instability is the presence of a sufficiently large region of absolute instability (Huerre and Monkewitz, 1990). This analysis has been applied with success both for globally unstable (Monkewitz et al., 1993) and stable (Viola et al., 2016) flows. For globally stable flows, a weakly non-parallel ansatz is suitable for the study of the spatial response with respect to a time-periodic forcing of frequency ω. At each streamwise location, one solves the local spatial stability problem and then the different slices are reconnected through the slowly varying amplitude A (Huerre and Monkewitz, 1990).

In this section, we introduced some crucial concepts which will be employed throughout the thesis. In the following, we exploit the multiscale and stability tools to introduce the different flows explored in this thesis.

1.3 Coating flows

Part I and Part II exploit the lubrication approximation to study the thin film dynamics for different configurations. We initially derive the lubrication model and then describe the

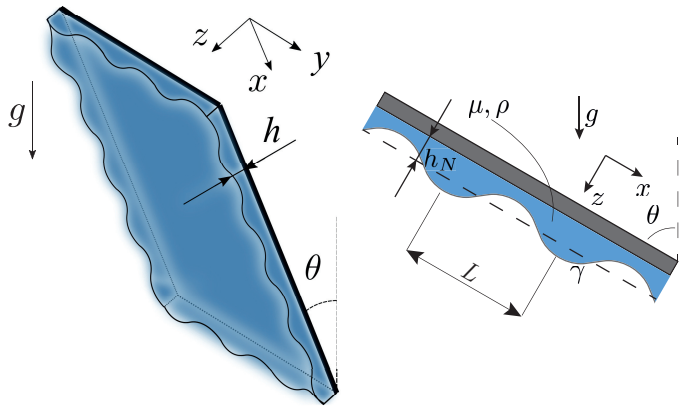

Figure 1.16: Three-dimensional flow of a thin film under an inclined planar substrate, with a two-dimensional sketch with revelant quantities.

coating flow patterns investigated in this thesis.

1.3.1 Multiscale approach: lubrication model

We consider the flow of a thin film below an inclined planar substrate, subject to gravity and surface tension (figure 1.16). A reference frame $(\bar{x},\bar{y},\bar{z})$ is introduced, where $\bar{x}$ is aligned with the main stream direction, $\bar{y}$ is perpendicular to the streamwise direction and lies on the substrate (*spanwise* direction) and $\bar{z}$ is orthogonal to the substrate and is the direction along which the film thickness is measured. A thin viscous liquid layer of velocity $(\bar{u},\bar{v},\bar{w})$ and thickness $\bar{h}(\bar{x},\bar{y},\bar{t})$ along $\mathbf{e}_z$ is flowing on the substrate. The fluid of density ρ is subject to gravity g that is, with the tilting of the substrate, along $\mathbf{g} = (g\cos(\theta),0,g\sin(\theta))$. The fluid has a surface tension γ and is initially assumed to never dewet the substrate. We consider dimensional quantities.

The procedure is analogous to the one outlined in Oron et al. (1997) and Kalliadasis et al. (2011), with a slightly different non-dimensionalization. The Navier-Stokes equations, together with the continuity equation, read:

$$\partial_{\bar{x}}\bar{u}+\partial_{\bar{y}}\bar{v}+\partial_{\bar{z}}\bar{w}=0, \tag{1.22}$$

$$\rho\left(\partial_{\bar{t}}\bar{u}+\bar{u}\partial_{\bar{x}}\bar{u}+\bar{v}\partial_{\bar{y}}\bar{u}+\bar{w}\partial_{\bar{z}}\bar{u}\right)=-\partial_{\bar{x}}\bar{p}+\mu\left(\partial_{\bar{x}\bar{x}}\bar{u}+\partial_{\bar{y}\bar{y}}\bar{u}+\partial_{\bar{z}\bar{z}}\bar{u}\right)+\rho g\cos(\theta), \tag{1.23}$$

$$\rho\left(\partial_{\bar{t}}\bar{v}+\bar{u}\partial_{\bar{x}}\bar{v}+\bar{v}\partial_{\bar{y}}\bar{v}+\bar{w}\partial_{\bar{z}}\bar{v}\right)=-\partial_{\bar{y}}\bar{p}+\mu\left(\partial_{\bar{x}\bar{x}}\bar{v}+\partial_{\bar{y}\bar{y}}\bar{v}+\partial_{\bar{z}\bar{z}}\bar{v}\right), \tag{1.24}$$

$$\rho\left(\partial_{\bar{t}}\bar{w}+\bar{u}\partial_{\bar{x}}\bar{w}+\bar{v}\partial_{\bar{y}}\bar{w}+\bar{w}\partial_{\bar{z}}\bar{w}\right)=-\partial_{\bar{z}}\bar{p}+\mu\left(\partial_{\bar{x}\bar{x}}\bar{w}+\partial_{\bar{y}\bar{y}}\bar{w}+\partial_{\bar{z}\bar{z}}\bar{w}\right)+\rho g\sin(\theta). \tag{1.25}$$

At the contact between the solid substrate and the fluid, the no-slip condition $\bar{\boldsymbol{u}}=\mathbf{0}$ is imposed, while at the free interface $\bar{z}=\bar{h}$, we impose the kinematic condition and the stress balance:

$$\partial_{\bar{t}}\bar{h}=\bar{w}-\bar{u}\partial_{\bar{x}}\bar{h}-\bar{v}\partial_{\bar{y}}\bar{h},\quad (\bar{p}_\infty-\bar{p})\mathbf{n}+\mathbf{P}\cdot\mathbf{n}=\gamma\bar{\kappa}\mathbf{n} \tag{1.26}$$

where $\mathbf{P}$ is the deviatoric stress tensor $\mathbf{P} = \mu(\nabla\bar{\boldsymbol{u}} + (\nabla\bar{\boldsymbol{u}})^T)$, $\mathbf{n}$ is the unity vector normal to the surface

$$\mathbf{n} = \frac{\left[-\partial_{\bar{x}}\bar{h}, -\partial_{\bar{y}}\bar{h}, 1\right]}{\sqrt{1 + (\partial_{\bar{x}}\bar{h})^2 + (\partial_{\bar{y}}\bar{h})^2}}, \tag{1.27}$$

and $\bar{\kappa}$ is the mean curvature of the interface. The equations are non-dimensionalized by employing the characteristic film thickness h_N and the characteristic drainage velocity $U = \rho g h_N^2/\mu$. The separation of scales parameter reads $\varepsilon = h_N/L \ll 1$, where L is the characteristic wavelength of the free surface deformations. The multiscale approach is based on the following expansion of the non-dimensional spatial variables:

$$X = \varepsilon x, \quad Y = \varepsilon y, \quad T = \varepsilon t. \tag{1.28}$$

The continuity equation, upon non-dimensionalization and introduction of the separation of scales parameters, reads:

$$\varepsilon\partial_X u + \varepsilon\partial_Y v + \partial_z w = 0 \tag{1.29}$$

The balance in the continuity equations leads to a velocity in the normal-to-the-substrate direction of order $w \sim \mathcal{O}(\varepsilon)$. The non-dimensional Stokes equations read:

$$\varepsilon Re\,(\partial_t u + u\partial_X u + v\partial_Y u + w\partial_z u) = -\varepsilon\partial_X p + \left(\varepsilon^2\partial_{XX}u + \varepsilon^2\partial_{YY}u + \partial_{zz}u\right) + \cos(\theta), \tag{1.30}$$

$$\varepsilon Re\,(\partial_t v + u\partial_X v + v\partial_Y v + w\partial_z v) = -\varepsilon\partial_Y p + \left(\varepsilon^2\partial_{XX}v + \varepsilon^2\partial_{YY}v + \partial_{zz}v\right), \tag{1.31}$$

$$\varepsilon^2 Re\,(\partial_t w + u\partial_X w + v\partial_Y w + w\partial_z w) = -\partial_z p + \left(\varepsilon^3\partial_{XX}w + \varepsilon^3\partial_{YY}w + \varepsilon\partial_{zz}w\right) + \sin(\theta). \tag{1.32}$$

Assuming that, at most, $Re = \mathcal{O}(\varepsilon)$, the LHS of the previous equations is of order $\mathcal{O}(\varepsilon^2)$ and thus neglected. Up to order $\mathcal{O}(\varepsilon)$, the boundary conditions at $z = h$ read:

$$p = p_\infty - \varepsilon^2\frac{1}{Bo}\kappa + \mathcal{O}(\varepsilon^2), \quad \partial_z u = \mathcal{O}(\varepsilon^2), \quad \partial_z v = \mathcal{O}(\varepsilon^2), \quad \partial_T h = w - u\partial_X h - v\partial_Y h. \tag{1.33}$$

where $Bo = \frac{\rho g h_N^2}{\gamma}$ is the Bond number. Exploiting the *least degeneracy principle* (Van Dyke, 1975), we keep the curvature term by assuming that $Bo = \mathcal{O}(\varepsilon^{-2})$. We then perform an asymptotic expansion in the pertinent variables:

$$u = u_0 + \varepsilon u_1 + \mathcal{O}(\varepsilon^2), \quad v = v_0 + \varepsilon v_1 + \mathcal{O}(\varepsilon^2), \tag{1.34}$$

$$w = w_0 + \varepsilon w_1 + \mathcal{O}(\varepsilon^2), \quad p = p_0 + \varepsilon p_1 + \mathcal{O}(\varepsilon^2), \tag{1.35}$$

At order $\mathcal{O}(1)$, the following velocity and pressure profiles are obtained:

$$u_0 = -\cos(\theta)\left(\frac{z}{2} - h\right)z, \quad v_0 = 0, \quad w_0 = -\cos(\theta)\partial_X h\frac{z^2}{2}, \quad p_0 = \sin(\theta)(z-h) - \frac{\varepsilon^2}{Bo}\kappa + p_\infty. \tag{1.36}$$

We thus obtain at leading order:

$$[\partial_T h]_0 = w_0 - u_0\partial_X h - v_0\partial_Y h = -\cos(\theta)h^2\partial_X h. \tag{1.37}$$

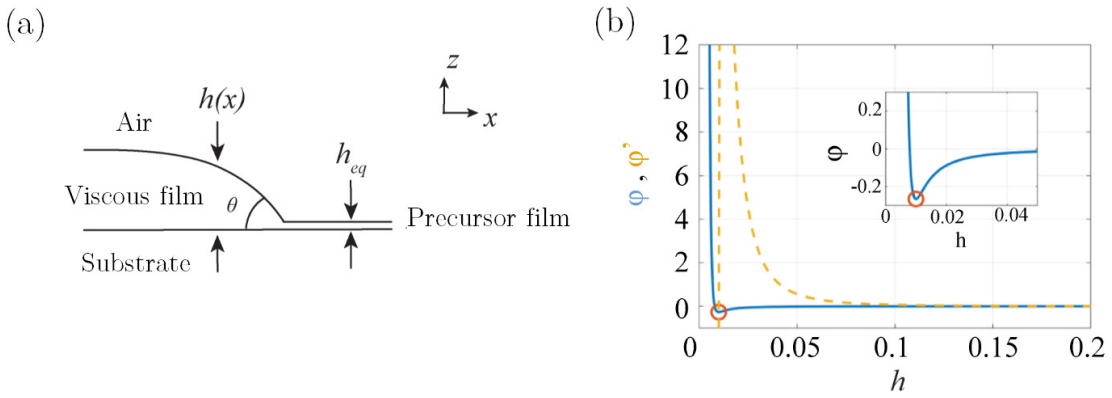

Figure 1.17: (a) Two-dimensional sketch for a thin film with apparent contact angle given by the disjoining pressure equilibrium. (b) Lennard-Jones potential as a function of the film thickness. In the inset: zoom in the vicinity of the minimum of the potential.

The system of equations, at order $\mathcal{O}(\varepsilon)$, reduces to:

$$\partial_X p_0 = \partial_{zz} u_1, \quad \partial_Y p_0 = \partial_{zz} v_1, \quad \partial_X u_1 + \partial_Y v_1 + \partial_z w_1 = 0, \tag{1.38}$$

$$\partial_z u_1 = 0 \text{ at } z = h, \quad \partial_z v_1 = 0 \text{ at } z = h, \quad [u_1, v_1, w_1] = [0,0,0], \text{ at } z = 0. \tag{1.39}$$

$$\tag{1.40}$$

The integration on z twice in $[0, h]$ for the x, y momentum equations gives the plane velocity profiles:

$$u_1 = \partial_X p_0 \left(\frac{z}{2} - h\right) z, \quad v_1 = \partial_Y p_0 \left(\frac{z}{2} - h\right) z. \tag{1.41}$$

We thus integrate the continuity equation along the z direction, and substitute $w_1(h)$ in the kinematic boundary condition:

$$[\partial_T h]_1 = -\left(\partial_X \left(h^3 \left(\sin(\theta)\partial_X h + \varepsilon^2 \frac{1}{Bo}\partial_X \kappa\right)\right) + \partial_Y \left(h^3 \left(\sin\theta \partial_Y h + \varepsilon^2 \frac{1}{Bo}\partial_Y \kappa\right)\right)\right). \tag{1.42}$$

$$\tag{1.43}$$

We substitute the expression for $\frac{\partial h}{\partial T} = \left[\frac{\partial h}{\partial T}\right]_0 + \varepsilon \left[\frac{\partial h}{\partial T}\right]_1$. Following Kalliadasis et al. (2011), the parameter ε can be scaled out, leading to:

$$\frac{\partial h}{\partial t} + \frac{1}{3}\nabla \cdot \left(h^3 \left(\sin\theta \nabla h + \frac{1}{Bo}\nabla \kappa + \cos\theta \mathbf{e}_x\right)\right) = 0, \tag{1.44}$$

where ∇ operates in the (x, y) plane. In dimensional form, the lubrication model reads:

$$\frac{\partial \bar{h}}{\partial \bar{t}} + \frac{1}{3\mu}\nabla \cdot \left(\bar{h}^3 \left(\rho g \sin\theta \nabla \bar{h} + \gamma \nabla \bar{\kappa} + \rho g \cos\theta \mathbf{e}_x\right)\right) = 0. \tag{1.45}$$

When wetting and dewetting phenomena are considered, the effect of long-range and short-

range intermolecular interactions is included via a disjoining pressure term in the lubrication model. In the case of a thin film of thickness $< 1\,\mu$m on a horizontal substrate, the Bond number is very small and the dominant balance is given by surface tension effects and disjoining pressure:

$$\frac{\partial \bar{h}}{\partial \bar{t}} + \frac{1}{3\mu}\nabla\cdot\left(\bar{h}^3\left(\gamma\nabla\bar{\kappa} - \nabla\Pi\right)\right) = 0, \tag{1.46}$$

where Π is the disjoining pressure (Kim et al., 1999). The disjoining pressure is obtained from a suitable potential which describes the intermolecular interactions. We employ the Lennard-Jones potential (Seemann et al., 2001; Mitlin, 1993; Sharma and Khanna, 1998):

$$\varphi(\bar{h}) = \frac{B}{\bar{h}^8} - \frac{A}{12\pi\bar{h}^2}, \tag{1.47}$$

where A is the Hamaker constant and B is the Born coefficient of the system (substrate-film-surrounding fluid), which model, respectively, the long-range and short-range interactions. In the case of dewetting, the long-range interactions are attractive, while the short-range ones are repulsive. This combination defines a minimum value of the potential for an equilibrium thickness $h_{\text{eq}} = (48\pi B/A)^{1/6}$. The previously introduced Lennard-Jones potential is linked to the disjoining pressure, Π, through

$$\Pi = -\frac{\partial\varphi}{\partial\bar{h}} = \frac{8B}{\bar{h}^9} - \frac{A}{6\pi\bar{h}^3}. \tag{1.48}$$

A positive Hamaker constant induces destabilizing pressure gradients for films larger than the equilibrium thickness, h_{eq}. When a region of the film reaches the precursor film thickness, h_{eq}, the local equilibrium at the interface between the precursor film and the thicker regions defines an apparent contact angle, θ (see figure 1.17), given by (Seemann et al., 2001; Sharma, 1993)

$$1 + \tan^2\theta = \left[\frac{\varphi\left(h_{\text{eq}}\right)}{\gamma} + 1\right]^{-2}. \tag{1.49}$$

Considering solely angles between 0° to 90°, equation (1.49) provides a bijective relationship between the contact angle and the precursor film h_{eq}.

1.3.2 The effect of substrate topology on coating flows

Substrate variations are known to modify flow patterns. While in the previous section we outlined the model for a flat substrate, relevant variations of the flow patterns may emerge due to the presence of modulations of the substrate. We first consider a case in which the substrate modulations perturb the picture of the flow below a planar substrate. The first case is suitable to understand the origin of draperies structures in limestone caves (Bertagni and Camporeale, 2017). The coupling between the hydrodynamic model and the deposition of karst draperies is therefore introduced. We then consider a second limiting case, in which the characteristic length of the modulations of the substrate is very large compared to the film thickness.

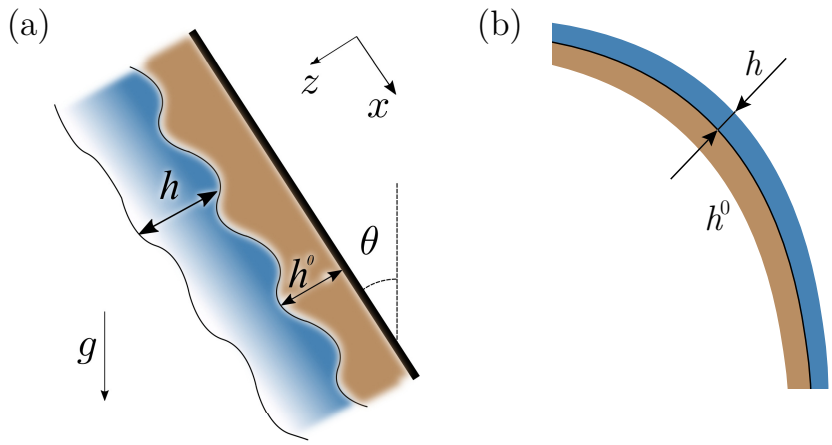

Figure 1.18: (a) Sketch of the substrate and liquid film variables for the model with small substrate variations. (b) Sketch of the substrate and thin film thickness for the model with large substrate variations.

1.3.2.1 Extension of the lubrication model to small substrate variations

We consider a thin film, of thickness $\bar{h}$, flowing under an inclined substrate with substrate variations $\bar{h}^0$ with respect to a planar reference (figure 1.18(a)). While the Stokes equations still hold in the bulk domain, the homogenous Dirichlet boundary condition at the wall now has to be imposed at $\bar{z} = \bar{h}^0$ and the free surface is now located at $\bar{z} = \bar{h} + \bar{h}^0$. Following the same multiscale procedure for the planar case, one obtains, in non-dimensional form, the following tangential velocity and pressure profiles at different orders:

$$u_0 = -\cos(\theta)\left(\frac{z}{2} - h - h^0\right)(z - h^0), \quad v_0 = 0, \quad p_0 = \sin(\theta)(z - h - h^0) - \frac{\varepsilon^2}{Bo}\kappa + p_\infty, \tag{1.50}$$

$$u_1 = \partial_X p_0 \left(\frac{z}{2} - h - h^0\right)(z - h^0), \quad v_1 = \partial_Y p_0 \left(\frac{z}{2} - h - h^0\right)(z - h^0), \tag{1.51}$$

where κ is the curvature of the free surface, located at $z = h + h^0$. The integration of the continuity equation in the domain $(h^0, h + h^0)$ leads to the following lubrication model

$$\frac{\partial h}{\partial t} + \frac{1}{3}\nabla \cdot \left(h^3 \left(\sin\theta \nabla(h + h^0) + \frac{1}{Bo}\nabla\kappa + \cos\theta \mathbf{e}_x\right)\right) = 0, \tag{1.52}$$

which reads, in dimensional form:

$$\frac{\partial \bar{h}}{\partial \bar{t}} + \frac{1}{3\mu}\nabla \cdot \left(\bar{h}^3 \left(\rho g \sin\theta \nabla(\bar{h} + \bar{h}^0) + \gamma \nabla\bar{\kappa} + \rho g \cos\theta \mathbf{e}_x\right)\right) = 0. \tag{1.53}$$

The presence of substrate variations does not influence the advection of perturbations downstream (embodied in the term $\rho g \cos\theta \bar{h}^3 \mathbf{e}_x$), while the hydrostatic pressure gradients and the curvature term are modified.

1.3.2.2 Draperies morphogenesis

Karst structures observed in limestone caves result from the deposition of calcium carbonate ($CaCO_3$) contained in the thin layer of water flowing on the cave walls. As water flows, the quantity of dissolved calcium and carbon dioxide increases. The partial pressure of CO_2 is larger than in the surrounding environment, thus leading to a series of chemical reactions in which CO_2 outgases from the solution (Romanov et al., 2008; Dreybrodt, 1999; Kaufmann, 2003; Kaufmann and Dreybrodt, 2007). Denoting with $k_{\pm}$ the reaction rate constants (whose inverse define a time scale), the slowest reactions involve the coupling between calcium carbonate and CO_2

$$\begin{aligned} &CO_2 + H_2O \overset{k_{\pm 1}}{\rightleftharpoons} H^+ + HCO_3^-, \\ &CO_2 + OH^- \rightleftharpoons HCO_3^-, \end{aligned} \tag{1.54}$$

while the other chemical reactions are much faster so that they can be considered equilibrated in the time scale of these reactions (Short et al., 2005b). Therefore, for each molecule of calcium carbonate deposited on the cave wall, one molecule of carbon dioxide is released in the surrounding environment. The typical time scales related to these reactions are of the order of 10 s, much greater than the typical time scale of the diffusion process for the considered thicknesses of the thin layer, i.e. 0.1s (Balestra, 2018). Therefore, one can safely assume a constant concentration of calcium carbonate along the thin layer of fluid. Short et al. (2005b) studied the advection-diffusion-deposition process in the thin layer, leading to the following deposition law for the substrate, which accounts for the flux of CO_2 outgasing from the solution (and thus the flux of $CaCo_3$ depositing on the cave walls):

$$\frac{\partial \bar{h}^0}{\partial \bar{t}} = \bar{C}\bar{h}, \tag{1.55}$$

where $\bar{C}$ is the chemistry-dependent constant. We refer to Short et al. (2005b) for a detailed description, together with the chemical reactions. The chemistry dependent constant is of the order of $\bar{C} \sim 10^{-7} s^{-1}$ (Camporeale, 2015). Considering the time scale of the Rayleigh-Taylor instability for a horizontal substrate, $\tau_{\mathrm{RT}} = \frac{\nu \ell_c^2}{h_N^3 g}$, the deposition constant in the dimensionless time scale is of the order $C \sim 10^{-4}$. The growth of karst draperies in limestone caves (figure 1.2(b)) is thus studied in the context of the Rayleigh-Taylor instability. Bertagni and Camporeale (2017) showed the predominance of these structures via the thin film equation, combining a two-dimensional linear stability analysis and a weakly non-linear approach: the growth rate of perturbations from a flat condition is slightly larger for streamwise aligned structures as long as the inertia of the flow is neglected.

1.3.2.3 The effect of large substrate variations on coating flows

The model for small substrate variations relies on the employment of the same cartesian coordinate system of the flat substrate case. When the substrate presents large variations of inclination and curvature, the model previously described cannot be employed. For classical

substrates such as cylinders (Balestra et al., 2018a) and spheres (Lee et al., 2016; Balestra et al., 2018b), the lubrication problem can be suitably solved in cylindrical and spherical coordinates, respectively. A lubrication model for generic substrate geometries was developed in Roy et al. (2002) by considering a generic orthogonal local coordinate system. Introducing the film thickness $\bar{h}$ measured along the direction normal to the substrate at each point,the authors obtained a coordinate-free expression of the lubrication equation:

$$\begin{aligned}(1-\bar{\mathcal{K}}\bar{h}+\bar{\mathcal{G}}\bar{h}^2)\frac{\partial \bar{h}}{\partial \bar{t}}+\frac{\gamma}{3\mu}\bar{\nabla}\cdot\left[\bar{h}^3\left(\bar{\nabla}\bar{\bar{\kappa}}-\frac{1}{2}\bar{h}(2\bar{\mathcal{K}}\mathbb{I}-\bar{\mathbb{K}})\cdot\bar{\nabla}\bar{\mathcal{K}}\right)\right] \\ +\frac{\rho g}{3\mu}\bar{\nabla}\cdot\left[\bar{h}^3\left(\bar{\boldsymbol{g}}_t-\bar{h}\left(\bar{\mathcal{K}}\mathbb{I}+\frac{1}{2}\bar{\mathbb{K}}\right)\cdot\bar{\boldsymbol{g}}_t+\bar{\mathrm{g}}_3\bar{\nabla}\bar{h}\right)\right]=0,\end{aligned} \tag{1.56}$$

where the vector $\bar{\boldsymbol{g}}_t$ is given by the gravity component tangent to the substrate, $\bar{\mathrm{g}}_3$ is the local gravity component normal to the substrate, $\bar{\mathbb{K}}$ is the curvature tensor, $\bar{\mathcal{K}}$ and $\bar{\mathcal{G}}$ are the local mean and gaussian curvatures of the substrate, respectively, and $\bar{\bar{\kappa}}$ is the mean curvature of the free surface. An analogous coordinate-free expression in the presence of inertia was derived in Howell (2003). Thiffeault and Kamhawi (2006) obtained the same lubrication model as Roy et al. (2002) by exploiting classical differential geometry to derive the equations in the natural, local (*general*) coordinates system (see figure 1.18(b)), which is not necessarily orthogonal (Deserno, 2004; Irgens, 2019).

1.3.3 Coating flow patterns

Here, we introduce some relevant coating flow patterns which result from the intertwining between gravity, surface tension, and dewetting phenomena.

1.3.3.1 Rayleigh-Taylor instability

A horizontal flat interface separating a heavier fluid and a lighter fluid in two semi-infinite regions will deform with time if the overlaying fluid is the heaviest one (Rayleigh, 1882; Taylor, 1950). Adding surface tension stabilizes the small-scale disturbances of the interface, but large-scale disturbances are always unstable (Chandrasekhar, 2013). The instability is driven by a competition between gravity, which pulls the heavy fluid down and surface tension that tends to restore a flat interface and pushes it back. This instability is of prime concern when coating surfaces, e.g. with paint or lubricants as coating irregularities or detachment of droplets may appear. As such, many studies have focused on means of controlling or suppressing the growth of pendant drops. This can be achieved, for example, by surface tension gradients arising from a temperature difference across the thin film or from the evaporation of the solvent in a multicomponent liquid (Burgess et al., 2001; Weidner et al., 2007; Alexeev and Oron, 2007; Bestehorn and Merkt, 2006). The Rayleigh-Taylor instability can also be controlled by high-frequency vibrations of the substrate (Lapuerta et al., 2001; Sterman-Cohen et al., 2017) or by the application of an electric field (Barannyk et al., 2012; Cimpeanu et al., 2014).

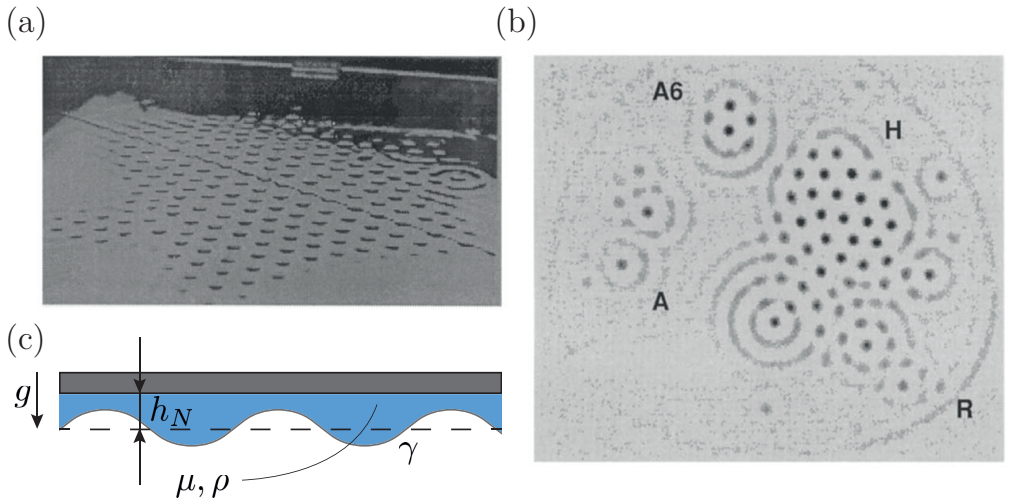

Figure 1.19: (a) Array of pendant drops observed from above across a thick glass plate and (b) pattern visualization from above with dye. Reproduced from Limat et al. (1992). (c) Sketch of the problem of the Rayleigh-Taylor instability of a thin film underneath a horizontal planar substrate, with relevant quantities.

When the film is located underneath a substrate, its thickness is limited by gravity to typically a few millimeters, and the flow is thus strongly confined which enhances viscous dissipation (figure 1.19). In this case, the lubrication model given by equation (1.45). We study the stability of the two-dimensional flat film with respect to perturbations in modal form in space and time (figure 1.19(c)):

$$\bar{h}(\bar{x},\bar{y},\bar{t}) = h_N + \epsilon\eta \exp\left(\mathrm{i}\left(k\bar{x} - \omega\bar{t}\right)\right). \tag{1.57}$$

Substituting this decomposition in the non-linear equation, at order $\mathcal{O}(\epsilon)$ one obtains the dispersion relation (Limat et al., 1992)

$$\omega = \mathrm{i}\frac{\rho g h_N^3}{3\mu}\left(k^2 - \ell_c^2 k^4\right), \tag{1.58}$$

already introduced in Section (equation (1.13)) as toy model, specified to $u = 0$. There is a range of unstable wavelengths, bounded by the capillary length ($k_{cut} = 1/\ell_c$). The maximum growth rate is attained at $k_{max} = 1/\sqrt{2}\ell_c$. The lenses may saturate for small enough initial thickness (Marthelot et al., 2018), or algebraically grow (Yiantsios and Higgins, 1989; Lister et al., 2010), eventually resulting in dripping droplets. In the three-dimensional case, the interest lies in the emerging pattern of drops. In the absence of boundaries, hexagonal patterns of drops invade the domain (figure 1.19(b)). These drops may again fall or saturate, but also translate and collide, with eventual merging (Lister et al., 2010). Spontaneous sliding of the droplets across the planar surface of the substrate can occur (Glasner, 2007) due to a symmetry-breaking instability (Dietze et al., 2018).

If the substrate is inclined of an angle θ with respect to the vertical, the dispersion relation

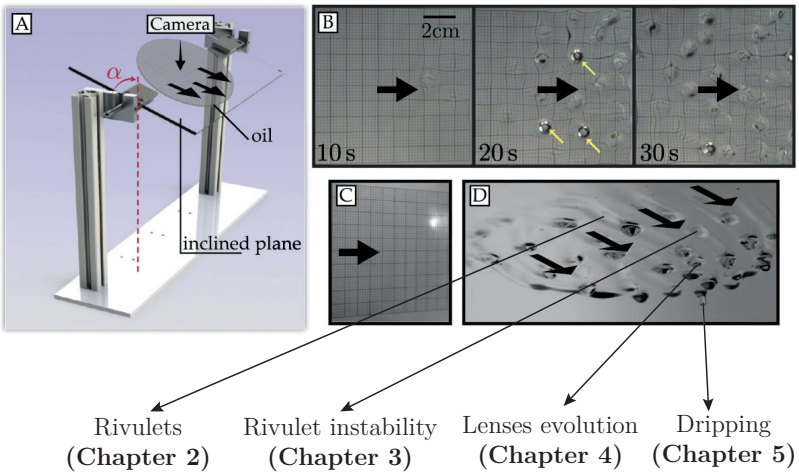

Figure 1.20: Experimental apparatus and drop formation, reproduced from Brun et al. (2015), together with a reference to the different problems explored in **Part I**.

reads (Brun et al., 2015):

$$\omega = \frac{\rho g h_N^2}{\mu}\cos\theta k + \mathrm{i}\frac{\rho g h_N^3}{3\mu}\left(k^2\sin\theta - \ell_c^2 k^4\right), \tag{1.59}$$

as anticipated in equation (1.13). The difference with the horizontal case resides in the presence of a real part of ω, which represents the downstream advection of perturbations due to the gravity component tangent to the substrate, while the growth rate is slightly modified by the presence of the factor $\sin\theta$ in front of the k^2 term, which represents the gravity component projected along the direction normal to the substrate. As already mentioned, equation (1.59) is analogous to (1.13). The latter is obtained by non-dimensionalizing the thickness using h_N and the spatial variables with $\ell_c/\sqrt{\sin\theta} = \ell_c^*$, and $u = \cot\theta\ell_c^*/h_N = \cot\theta\tilde{\ell}_c^*$. Therefore, the flow is convectively unstable when $u > 0.541$, and vice versa. In the absolutely unstable case, Brun et al. (2015) observed a large amount of dripping droplets while in the convectively unstable case much less dripping events. These observations can be related to the balance between the advection and growth of perturbations for different values of the thickness and inclination angle. The model was refined introducing inertial and viscous extensional stresses (Scheid et al., 2016; Kofman et al., 2018). These authors showed that the occurrence of the absolute instability does not predict the dripping satisfactorily. A further numerical study by Rohlfs et al. (2017) showed the existence of two-dimensional stationary traveling waves, invariant along the direction perpendicular to the flow.

In the three-dimensional case, a strong modulation of the thickness along the direction perpendicular to the flow (*spanwise* direction) is identified as *rivulet* formation. The presence of a predominant rivulet pattern when the inertia of the fluid is negligible was experimentally observed by Charogiannis et al. (2018). Similar rivulet patterns were observed by Rietz et al. (2017), in an experimental set-up where gravity was replaced by centrifugal acceleration. **Ow-**

Figure 1.21: Rivulets, lenses, and dripping thanks to a spatially and temporally forced film. We directly observe the interface lightened from the side. The typical distance between rivulets is 15mm.

ing to the intrinsic three-dimensionality of the emerging pattern, two-dimensional analyses fail to predict the thin film dynamics and the bifurcations of the free surface patterns. The route to dripping is summarized in figure 1.20. An initial film is deposited on a flat glass plate, which is then rotated along a horizontal axis at a fixed angle θ. The initially flat film destabilizes and rivulet structures emerge. Slightly downstream, these rivulets destabilize along the streamwise direction and, after some distance, arrays of drop-like structures, called lenses, emerge. These lenses may ultimately drip. Forcing both spatially (with a sinusoidal forcing at the inlet) and temporally (e.g. by creating an oscillating flow rate) can select much more regular patterns as illustrated in figure 1.21: the spatial forcing selects regular streamwise structures (rivulets) on which lay temporally forced lenses. Although these lenses have almost a constant velocity, the merging of two lenses leads to a dramatic dripping as we can observe in the bottom right corner of the picture. **Starting from these observations, Part I is devoted to the study of the three-dimensional free surface patterns of a thin film flowing under an inclined substrate, with a perspective on the dripping phenomenon. Chapter 2 is devoted to the analysis of the steady rivulet patterns through experiments, linear stability analysis and numerical simulations. Chapter 3 investigates the destabilization toward the formation of drops traveling on the rivulets through a linear stability analysis compared with experimental measurements. Chapter 4 then studies the lenses patterns emerging on the rivulets and the eventual dripping through linear stability analysis and numerical simulations. Chapter 5 eventually deepens the dripping problem by considering a simplified configuration of a drop on a very thin film, through a combination of experiments, numerical simulations and theoretical developments. In Part II, Chapter 6 studies the two-dimensional spatiotemporal impulse response of the flow when the thin film dynamics under an inclined plane is coupled with the deposition process.**

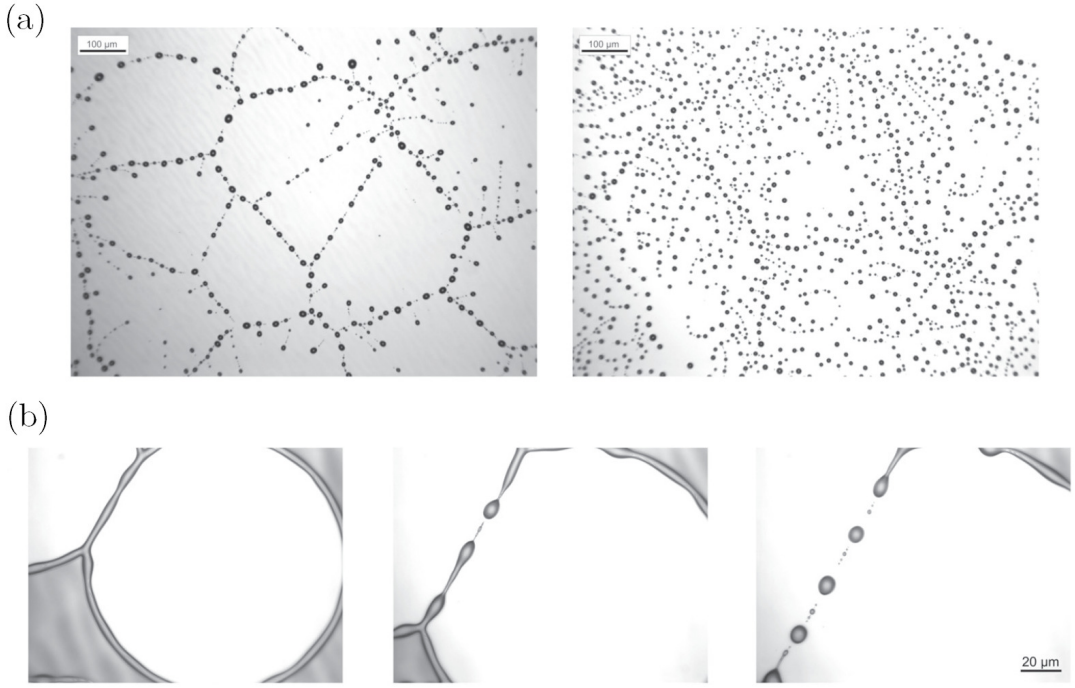

Figure 1.22: (a) Stationary droplet patterns emerging from a uniform film of thickness 110 nm after dewetting for two different polymers. (b) Detail of the disintegration in droplets of a rim composing a cellular structure. Extracted from Peschka et al. (2019).

1.3.3.2 Dewetting

The previously-introduced spinoidal dewetting, i.e. dewetting induced by the amplification of surface perturbations, typically occurs for very thin films < 10 nm, while for thicker films nucleation and growth of holes can be observed (Bischof et al., 1996; Xie et al., 1998). The initial breaking of the film in holes, either induced by spinoidal dewetting or nucleation, is followed by the growth of polygonal networks of straight liquid rims, who then evolve to droplet arrays through the Rayleigh-Plateau instability (figure 1.22).

In this case, the lubrication model given by equation (1.46) and the disjoing pressure $\Pi = -\frac{\partial \varphi}{\partial \bar{h}} = \frac{8B}{\bar{h}^9} - \frac{A}{6\pi\bar{h}^3}$ determines the flow behavior. When $\partial_{\bar{h}}\Pi > 0$, the substrate-film-bulk fluid system reduces its energy by dewetting, i.e. by thinning in some regions and thickening in others. Vice versa, spreading (wetting) occurs (Derjaguin and Churaev, 1974; Kim et al., 1999). Linear stability analysis allows one to predict the initial wavelength of the spinoidal instability (Wyart and Daillant, 1990; Xie et al., 1998). We consider a normal mode expansion around the flat film solution:

$$\bar{h}(\bar{x},\bar{t}) = h_i + \epsilon\eta \exp\left(\mathrm{i}(k\bar{x} - \omega\bar{t})\right). \tag{1.60}$$

Upon simplification of the exponential term and the (constant) eigenvector η, we obtain the

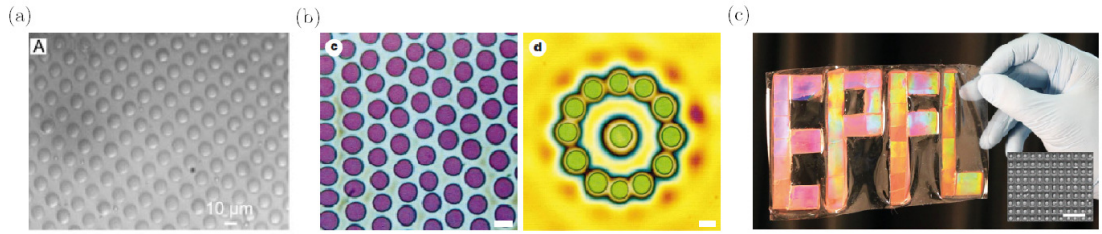

Figure 1.23: (a) Ordered arrays of droplets formed by condensation of water on a gold substrated cooled below the dew point, reproduced from Lu et al. (2002). (b) Optical micrographs of polystyrene films which have been exposed to an electric field, reproduced from Schaeffer et al. (2000). (c) Ordered patterns induced by dewetting of an optical glass on a prepatterned substrate and large-scale picture of an EPFL logo-shaped metasurface, reproduced from Gupta et al. (2019).

dispersion relation:

$$\omega = \frac{\mathrm{i}h_i^3}{3\mu}\left(k^2\left(\frac{A}{2\pi h_i^4} - \frac{72B}{h_i^{10}}\right) - \gamma k^4\right). \tag{1.61}$$

The dispersion relation is formally analogous to the Rayleigh-Taylor instability case. Far from the equiibrium thickness, the term related to short-range interactions is much smaller than the Van der Waals term, and thus the dispersion relation can be approximated as follows:

$$\omega = \frac{\mathrm{i}h_i^3}{3\mu}\left(k^2\left(\frac{A}{2\pi h_i^4}\right) - \gamma k^4\right). \tag{1.62}$$

when $A < 0$ the growth rate is always negative, while for $A > 0$ a range of unstable wavelengths is identified, with a cut-off at $k = k_c = \sqrt{A/(2\pi h_i^4 \gamma)}$. The maximum of the growth rate is attained at $k = (1/\sqrt{2})k_c$.

Dewetting threatens the integrity of thin films, typically yielding semi-ordered tessellation patterns. This has often been an undesirable phenomenon, jeopardizing the film morphology with little practical use. Nevertheless, a few research endeavors have investigated the potential of dewetting as an efficient self-assembly process. Several approaches have been proposed based on selective wetting (Lu et al., 2002; Meyer and Braun, 2000) or spatially-patterned electric fields (Morariu et al., 2003; Schaeffer et al., 2000), leading to ordered arrays of droplets, see figure 1.23. These investigations have demonstrated interesting possibilities but remained limited in terms of materials, scalability, geometry or resolution. Patterned substrates allow for improved control of the rearrangement mechanism and higher complexity in the final microstructures. This is particularly relevant in nanophotonics, where changes in feature size to as little as 10 nm can strongly impact the resonant behavior and the resulting optical properties. The flow of viscous films on patterned substrates has been theoretically investigated via the competition between template-induced reflow and spinoidal dewetting through linear analysis (Gupta et al., 2019), which fails to predict the complete dewetting dynamics (Volodin

and Kondyurin, 2008a,b).

In Part II, Chapter 7 presents a lubrication model to describe the re-arrangement process of a dewetting thin film on a templated substrate approximated through a small substrate variations model (Section 1.3.2.1).

1.3.3.3 Spreading patterns

Gravity currents are flows driven by gravity differences due to the presence of one phase heavier than the other that spreads on a substrate. The analysis of spreading requires as a first step the knowledge of the position, velocity and thickness of the advancing front. One of the first systematic analyses on gravity currents can be found in Benjamin (1968), in which the author presented a theoretical analysis on the spreading of an inviscid fluid on a plane substrate with a constant velocity U_F. The thickness was seen to scale with the square of the front velocity, $h_F \sim U_F^2$. A crucial step forward was performed by Hoult (1972), which formally solved the equations of the spreading of oil under a free surface with a *long-wave* approximation, such as the well-known shallow water or Saint-Venant equations for large-inertia flows (Vreugdenhil, 1994). If the inertia of the flow is negligible, the lubrication approximation can be employed. In the latter case, the dominant balance to describe the *viscous* gravity current is given by viscosity and buoyancy. With the aim of comparing their results with those of Keulegan (1957), Huppert and Simpson (1980) focused on the two-dimensional spreading on a horizontal substrate. By combining a lubrication approximation with the volume conservation, the authors determined that the spreading front position and thickness scale as $x_F \propto t^{1/5}$ and $h_F \propto t^{-1/5}$, respectively, for a viscous gravity current, recovering the result of Smith (1969) (figure 1.24(a)). However, not all currents emerge from the release of an initial amount of fluid, but they can be continuously fed (Didden and Maxworthy, 1982). An analysis focused on a two-dimensional viscous gravity current with a constant flow rate of the form t^γ was conducted in Huppert (1982b), in which the author derived a similarity solution for the thickness and front position, which read $x_F \propto t^{(3\gamma+1)/5}$ and $h_F \propto t^{(2\gamma-1)/5}$, respectively.

When the substrate is inclined (figure 1.24(b)), a gravity component parallel to the substrate is introduced. The thickness is not constant in space, but its distribution far from the front can be recovered by solving the flow equations, considering only the drainage along the in-plane directions of the substrate, referred here as *drainage* solution (Huppert, 1982a). Retaining only the tangential gravity term, the lubrication model for a two-dimensional thin film flowing on an inclined planar substrate, completed by the mass conservation when an initial mass of fluid is released, read:

$$\frac{\partial \bar{h}}{\partial \bar{t}} + \frac{1}{3\mu}\partial_{\bar{x}}\left(\bar{h}^3 \rho g \cos\theta\right) = 0, \quad \int_0^{x_F(t)} \bar{h}(\bar{x},\bar{t})\mathrm{d}\bar{x} = A. \tag{1.63}$$

Equation (1.63) admits a solution in self-similar form $\bar{h} = (\mu/(\rho g \cos\theta))\bar{x}^{1/2}\bar{t}^{-1/2}$, which does not depend on the mass conservation (Jeffreys, 1930; Huppert, 1982a). Employing the drainage

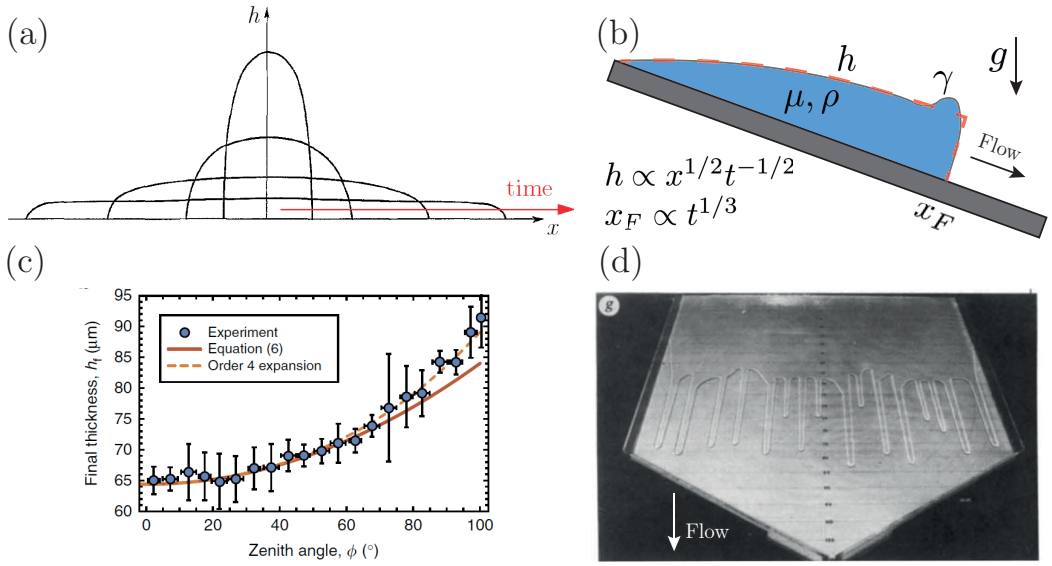

Figure 1.24: (a) Propagation of a viscous gravity current on a flat horizontal substrate, reproduced from Smith (1969). (b) Spreading on an inclined substrate with the expression of the drainage solution (red dashed line) and front position x_F. (c) Drainage thickness distribution along a sphere, from Lee et al. (2016). (d) Propagation of a three-dimensional gravity current on an inclined substrate. The instability leads to the formation of elongated fingers along the streamwise direction. reproduced from Huppert (1982a).

solution, the mass conservation gives the front position:

$$\bar{x}_F = \left(9A^2\rho g\cos\theta/4\mu\right)^{1/3}\bar{t}^{1/3}. \tag{1.64}$$

The lubrication leading order solution presents a discontinuity at the front, as long as surface tension and hydrostatic pressure gradients in the normal-to-the-substrate direction are neglected. The mathematical derivation may be more involved when the substrate is curved, e.g. in the case of the release of an initial volume of fluid on a cone (Acheson, 1990), a cylinder or a sphere (Takagi and Huppert, 2010; Lee et al., 2016; Balestra et al., 2019). Takagi and Huppert (2010) studied the drainage and spreading on a cylinder and a sphere, in the vicinity of the pole. The authors showed that the drainage thickness scales as $h \sim t^{-1/2}$ both for the cylinder and the sphere; the spreading front angle ϑ_F, measured from the pole, instead scales as $\vartheta_F \sim t^{1/2}$ for the cylinder and as $\vartheta_F \sim t^{1/4}$ for the sphere. More refined drainage solutions were obtained through an asymptotic expansion in the vicinity of the pole by Balestra et al. (2019) and Lee et al. (2016) for the cylinder and the sphere (figure 1.24(c)), respectively.

The knowledge of the spreading front velocity is a crucial step to study the destabilization of the advancing front of the fluid, which leads to the formation of fingers aligned with the flow direction, as shown in figure 1.24(d) (Huppert, 1982a; Silvi and Dussan, 1985; Troian et al., 1989a,b; Kondic and Diez, 2001; Diez and Kondic, 2001). **In Part II, Chapter 8 studies the three-dimensional drainage and spreading on generic substrates modeled through the**

model with large substrate variations of Section 1.3.2.3.

1.4 Flows around and through permeable bluff bodies

1.4.1 Multiscale approach: homogenization technique

Owing to the intrinsic separation of scales involving flows around and through porous bodies, multiscale approaches are largely employed to model the flow through porous media. We recall the Darcy law for a generic porous medium (Darcy, 1856):

$$\nabla \bar{p} = -\mu \boldsymbol{\kappa}^{-1} \bar{\boldsymbol{u}}. \tag{1.65}$$

The permeability tensor $\boldsymbol{\kappa}$ is a property of the porous medium which represents the ability of the fluid to pass through. The permeability is related to the fraction of voids (porosity) in the volume but also the shape of the pores. Several laws have been proposed to relate these two quantities, e.g. the Ergun equation (Ergun, 1952; Macdonald et al., 1979) for a packed bed of particles. To overcome the limit of creeping flow through the pores, Forchheimer (1901) introduced a quadratic term in the Darcy Law to account for inertial effects in the porous medium:

$$\nabla \bar{p} = -\mu \boldsymbol{\kappa}^{-1} \bar{\boldsymbol{u}} - \mathbf{C}|\bar{\boldsymbol{u}}|\bar{\boldsymbol{u}}, \tag{1.66}$$

where $\mathbf{C}$ is a tensor that depends both on the geometry and flow conditions. In the creeping flow regime, Brinkman (1949) proposed a slightly different equation to consider the interface effects between the porous medium and the free-fluid region, imposing the equilibrium of forces acting on a volume element of fluid and taking account for the damping force, in the absence of inertia:

$$\nabla \bar{p} = -\mu \boldsymbol{\kappa}^{-1} \bar{\boldsymbol{u}} + \mu_{eff} \nabla^2 \bar{\boldsymbol{u}}, \tag{1.67}$$

where μ_{eff} is the effective viscosity, which differs in general from the fluid viscosity. The Brinkman correction to the Darcy Law presents a diffusive term that allows the velocity to be continuous at the interface and recover the viscous effects which penetrate inside the porous medium in the so-called Brinkman layer. Beavers and Joseph (1967) performed a series of experiment in a channel with a bottom porous bed, determining the velocity at the interface separating the free fluid and the porous medium:

$$\frac{\mathrm{d}\bar{u}_t^{out}}{\mathrm{d}n} = \frac{\alpha_{BJ}}{\sqrt{\kappa}}(\bar{u}_t^{out} - \bar{u}_t^{in}). \tag{1.68}$$

Neale and Nader (1974) matched the experiments of Beavers and Joseph (1967) using the Brinkman equation, imposing the velocity and stresses continuity, so-called Brinkman conditions. The thickness of the Brinkman layer is of the order $\delta_{BrL} \sim \sqrt{\kappa}$.

These milestones in the description of the flow through porous media have been mostly obtained from ad-hoc cases and empirical approaches. Homogenization provides relevant

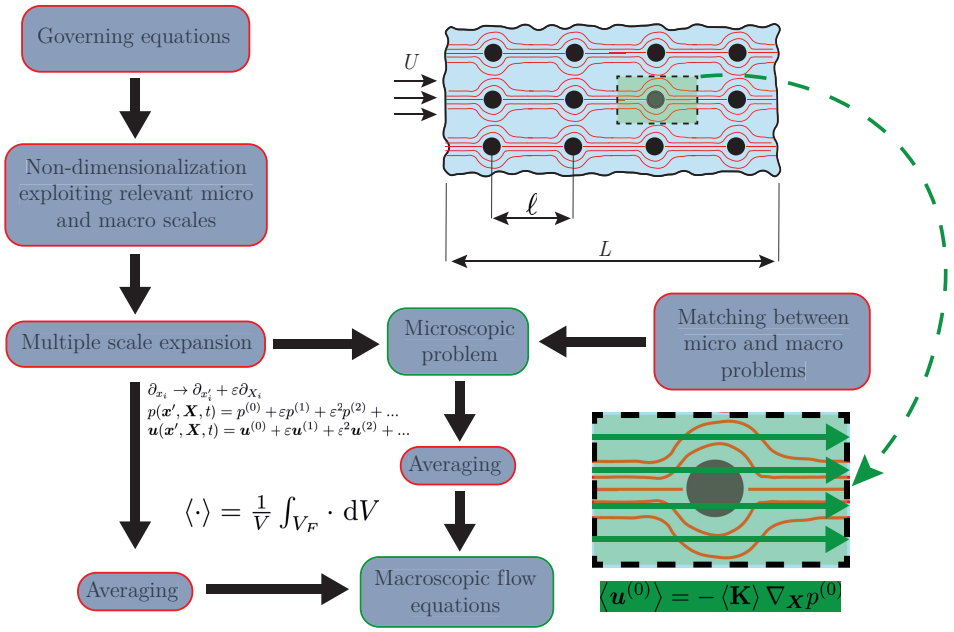

Figure 1.25: Flow chart illustrating the process of homogenization technique, together with sketches showing the macroscopic and microscopic problems and reduction to an average velocity through the microscopic domain.

insights into modeling of multiscale fluid-structure interactions, extending the classical Darcy model to treat inertia within the pores (Zampogna and Bottaro, 2016; Zampogna et al., 2016) and handling with interfaces between porous and free-fluid regions (Lācis and Bagheri, 2017; Lācis et al., 2017; Lācis et al., 2020). In Zampogna and Gallaire (2020) homogenization revealed itself a suitable tool to describe flows around microstructured permeable surfaces or membranes, opening the path to a more formal approach in the characterization and design of membranes and filters. Homogenization techniques have the great advantage to give a direct and immediate link with the micro-structure composing the porous medium, making them suitable for optimization approaches (Schulze and Sesterhenn, 2013).

Homogenization allows one to obtain a macroscopic description of the flow through the porous medium via a multiscale expansion followed by an averaging step. In figure 1.25 the main steps of the homogenization technique are reported, together with sketches showing the macroscopic and microscopic problems and the reduction to an average velocity through the microscopic domain. Following Zampogna and Bottaro (2016), the Darcy law for a porous medium without boundaries is here derived. The Navier Stokes equations are non-dimensionalized by assuming that the macroscopic pressure gradient is balanced by the microscopic viscous term $O\left(\frac{P}{L}\right) \sim O\left(\frac{\mu U}{\ell^2}\right)$:

$$\nabla \cdot \boldsymbol{u} = 0, \quad Re\,(\partial_t \boldsymbol{u} + \boldsymbol{u}\nabla\boldsymbol{u}) = -\frac{1}{\varepsilon}\nabla p + \nabla^2 \boldsymbol{u}, \tag{1.69}$$

where $\varepsilon = \ell / L$ is the separation of scales parameter. The first step of the multiscale technique

is the introduction of fast (microscopic) and slow (macroscopic) variations along all spatial directions, i.e. $x = \boldsymbol{x}' + \varepsilon \boldsymbol{X}$:

$$\partial_{x_i} \rightarrow \partial_{x_i'} + \varepsilon \partial_{X_i}. \tag{1.70}$$

We thus perform an asymptotic expansion in the pertinent variables:

$$p(\boldsymbol{x}', \boldsymbol{X}, t) = p^{(0)} + \varepsilon p^{(1)} + \varepsilon^2 p^{(2)} + ..., \quad \boldsymbol{u}(\boldsymbol{x}', \boldsymbol{X}, t) = \boldsymbol{u}^{(0)} + \varepsilon \boldsymbol{u}^{(1)} + \varepsilon^2 \boldsymbol{u}^{(2)} + ... \tag{1.71}$$

Upon introduction of this decomposition in equation (1.69), at $\mathcal{O}(1)$ we obtain, in components:

$$\nabla_{\boldsymbol{x}'} \cdot \boldsymbol{u}^{(0)} = 0, \quad \nabla_{\boldsymbol{x}'} p^{(0)} = 0, \tag{1.72}$$

which implies that the leading-order pressure does not vary at the microscale, $p^{(0)} = p^{(0)}(\boldsymbol{X}, t)$. The problem at order $\mathcal{O}(\varepsilon)$ reads:

$$\nabla_{\boldsymbol{X}} \cdot \boldsymbol{u}^{(0)} + \nabla_{\boldsymbol{x}'} \cdot \boldsymbol{u}^{(1)} = 0, \quad Re\left(\partial_t \boldsymbol{u}^{(0)} + \boldsymbol{u}^{(0)} \nabla_{\boldsymbol{x}'} \boldsymbol{u}^{(0)}\right) = -\nabla_{\boldsymbol{x}'} p^{(1)} - \nabla_{\boldsymbol{X}} p^{(0)} + \nabla^2_{\boldsymbol{x}'} \boldsymbol{u}^{(0)}. \tag{1.73}$$

The LHS is negligible if, at most, $Re = \mathcal{O}(\varepsilon)$. In this case, the formal solution reads (Mei and Vernescu, 2010):

$$\boldsymbol{u}^{(0)} = -\mathbf{K} \nabla_{\boldsymbol{X}} p^{(0)}, \quad p^{(1)} = -\boldsymbol{Q} \nabla_{\boldsymbol{X}} p^{(0)} + p_0^{(1)}(\boldsymbol{X}, t) \tag{1.74}$$

where $\mathbf{K}$ is a tensor, $\boldsymbol{Q}$ is a vector and $p_0^{(1)}$ is an integration constant. The coefficients $\mathbf{K}$ and $\boldsymbol{Q}$ thus satisfy the following microscopic problems, written in components for the sake of clarity:

$$\partial_{x_j'} K_{ij} = 0, \quad -\partial_{x_j'} \partial A_j + \partial_{x_j' x_j'} K_{ij} = -\delta_{ij}, \tag{1.75}$$

which are forced Stokes problem with the unknowns K_{ij} and A_j for $i, j = 1, 2, 3$ (12 equations and 12 unknowns). These equations are solved in a periodic repetition of the microstructure composing the porous medium. We therefore impose periodic boundary conditions at the external boundaries of the microscopic domain and $K_{ij} = 0$ on solid walls. An additional constraint to impose the uniqueness the solution is $\langle A_j \rangle = 0$ (Zampogna and Bottaro, 2016), where we introduced the volume average in the microscopic domain $\langle \cdot \rangle$:

$$\langle \cdot \rangle = \frac{1}{V} \int_{V_F} \cdot \, \mathrm{d}V \tag{1.76}$$

Applying volume average on (1.74) and the continuity equation, one obtains, respectively:

$$\left\langle \boldsymbol{u}^{(0)} \right\rangle = -\langle \mathbf{K} \rangle \nabla_{\boldsymbol{X}} p^{(0)}, \quad \nabla_{\boldsymbol{X}} \cdot \left\langle \boldsymbol{u}^{(0)} \right\rangle = 0. \tag{1.77}$$

Coming back to dimensional variables and omitting the average symbol, the problem reads

$$\bar{\boldsymbol{u}} = -\frac{\boldsymbol{\kappa}}{\mu} \nabla \bar{p}, \quad \nabla \cdot \bar{\boldsymbol{u}} = 0. \tag{1.78}$$

which is the Darcy law, imposed on the slowly-varying, macroscopic, spatial scale. In analogy with the previous cases, the macroscopic effect of the flow, obtained through averaging

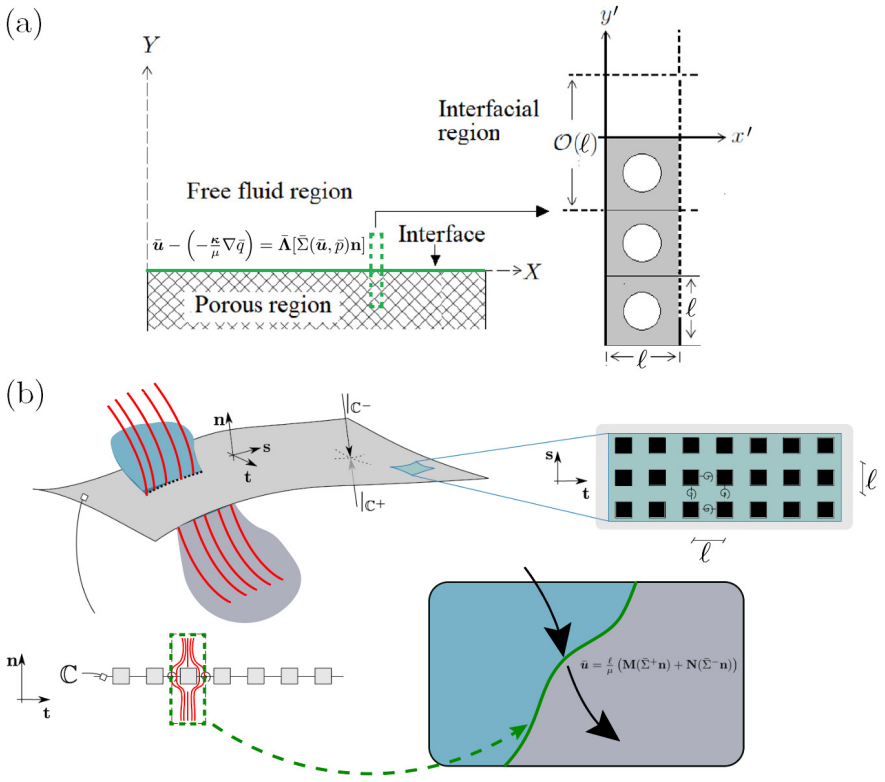

Figure 1.26: Macroscopic and microscopic description for the flow (a) at the interface between a porous medium and a free-fluid region (reproduced from Naqvi and Bottaro (2021)) and (b) through a microstructured membrane ("thin" porous medium).

of the microscopic quantities, results from microscopic problems forced by slowly-varying macroscopic variables.

In analogy with the averaging technique, one can extend this analysis by considering inertial terms in the equation, leading to the Darcy-Forchheimer equation (Mei and Vernescu, 2010). When the interface between a porous medium and a free-fluid region is considered, a similar analysis is carried out (Lācis and Bagheri, 2017; Lācis et al., 2020; Naqvi and Bottaro, 2021), see figure 1.26(a). By solving the microscopic problems and applying the averaging technique in a region which contains both the microscopic structure and the free-fluid region, the Darcy law is recovered inside the porous medium, while the interface conditions read:

$$\bar{\boldsymbol{u}} - \left(-\frac{\boldsymbol{\kappa}}{\mu}\nabla\bar{q}\right) = \bar{\boldsymbol{\Lambda}}[\bar{\boldsymbol{\Sigma}}(\bar{\boldsymbol{u}},\bar{p})\mathbf{n}], \quad \bar{q} = -[\bar{\boldsymbol{\Sigma}}(\overline{\mathbf{u}},\bar{p})\mathbf{n}]\cdot\mathbf{n} \tag{1.79}$$

where $(\bar{\boldsymbol{u}},\bar{p})$ denote the velocity and pressure field outside of the porous medium, q denotes the pressure inside the porous medium (governed by the Darcy law), $\bar{\boldsymbol{\Lambda}}$ is the so-called slip tensor and $\bar{\boldsymbol{\Sigma}}(\bar{\boldsymbol{u}},\bar{p}) = -\bar{p}\mathbb{I}+\mu\left(\nabla\bar{\boldsymbol{u}}+\nabla\bar{\boldsymbol{u}}^T\right)$ is the stress tensor. The slip tensor is obtained through the average solution of microscopic linear problems analogous to (1.75) in the vicinity of the interface of the porous medium. The boundary condition ensures the continuity of stresses

along the interface and a jump in the tangential velocity. This jump stems from the viscous effects that penetrate inside the porous medium, in a similar fashion to the viscous term in the Brinkman formulation. Viscous effects are thus recovered thanks to a slip condition on the tangential velocity.

Similar derivations can be employed for different microstructured surfaces, e.g. the flow around and through a "thin" porous structure, i.e. a membrane (figure 1.26(b)). In this case, the flow through the membrane is described by the continuity of the velocity and a stress boundary condition to be imposed on the, infinitely thin, surface of the membrane (Zampogna and Gallaire, 2020):

$$\bar{\boldsymbol{u}} = \frac{\ell}{\mu}\left(\mathbf{M}(\bar{\Sigma}^{+}\mathbf{n}) + \mathbf{N}(\bar{\Sigma}^{-}\mathbf{n})\right), \tag{1.80}$$

i.e. the velocity, continous across the membrane, is a linear combination of the upstream ($^{+}$) and downstream ($^{-}$) to the membrane stresses through the tensors **M** and **N**, which are computed from linear problems analogous to (1.75).

1.4.2 Wake flows past solid bluff bodies

Owing to the large range of applications, flows past bluff bodies have been the object of substantial interest in the field of hydrodynamic instability. The uniform flow past a circular cylinder has been the testing ground for research on bluff body aerodynamics for decades. The flow is steady for low values of the Reynolds number and is characterized by a recirculation region which increases its dimensions as the Reynolds number increases. The steadiness of the wake is broken at a critical Reynolds number of 46.7 (Jackson, 1987; Provansal et al., 1987), beyond which the flow undergoes an instability that leads to a two-dimensional oscillatory flow characterized by the alternate shedding of vortices, i.e. the renowned von Kármán vortex street (Williamson, 1996). At larger Reynolds numbers $Re \approx 192$, the two-dimensional wake becomes unstable and three-dimensional structures develop, whose characteristic trace is still the two-dimensional alternate shedding of vortices (Barkley and Henderson, 1996). The flow past a two-dimensional, infinitely thin, flat plate shows a similar pattern evolution, with a critical Reynolds Number for the onset of the vortex shedding of $Re_{cr} = 31.6$ (see Thompson et al. (2014)).

Axisymmetric wakes result from the flow past disk and spheres, among many others. Figure 1.27(a) shows some typical wake patterns observed for the flow past a disk and a sphere, at different Reynolds numbers. In both cases, the steady and axisymmetric toroidal recirculation region becomes larger as the Reynolds number increases, and a first stationary bifurcation with azimuthal wavenumber $m = 1$ occurs. The mode consists in a shift of the wake along one direction (Taneda, 1956; Johnson and Patel, 1999; Natarajan and Acrivos, 1993; Shenoy and Kleinstreuer, 2008), e.g. see figure 1.27(a), cases **a** and **a**$'$, for the sphere. At larger Reynolds numbers, the bifurcations depend on the considered body but, eventually, a helicoidal mode

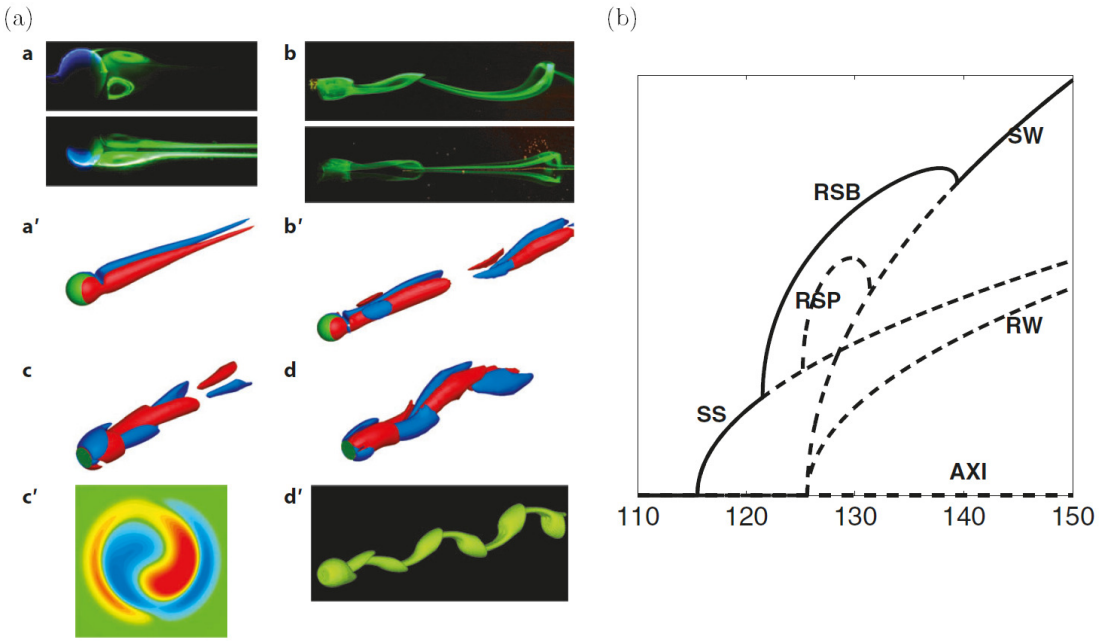

Figure 1.27: (a) Modes in the wake of a sphere (**a**,**a**′,**b**,**b**′) and an infinitely thin disk (**c**,**c**′,**d**,**d**′), illustrated with streamwise vorticity isosurfaces (**a**′,**b**′,**c**,**d**), streamwise vorticity contours in a cross-plane (**c**′), and experimental (**a**,**b**) and numerical (**d**′) dye lines. Experiments with a sphere from of A. Przadka and S. Goujon-Durand, reproduced from Ern et al. (2012). (b) Bifurcation diagram as a function of the Reynolds number for the wake past a circular disk. reproduced from Fabre et al. (2008).

characterized by a periodic shedding of coherent structures dominates the flow dynamics (Natarajan and Acrivos, 1993). The complex series of bifurcations of the disk obtained through slow manifold theory and normal forms by Fabre et al. (2008) is reported in figure 1.27(b). The solid (resp. dashed) lines represent stable (resp. unstable) branches. The steady and axisymmetric branch becomes unstable for $Re > 116.7$, and a stable branch (SS) characterized by the steady shift of the wake emerges (Natarajan and Acrivos, 1993; Meliga et al., 2009). At $Re = 121$, a Hopf bifurcation occurs and the mode (RSB) exhibits vortical structures of opposite signs twisted around each other (figure 1.27(a), cases **c** and **c**′). A third branch (SW) originates from the axisymmetric one at $Re = 125$ and is stable for $Re > 140$, whose wake presents alternate vortical structures of the same magnitude (figure 1.27(a), cases **d** and **d**′). A similar, but more intricate, series of bifurcations is observed for the sphere. The first, steady, bifurcation of the sphere wake occurs at $Re = 212.6$ (Natarajan and Acrivos, 1993; Meliga et al., 2009). The steady and axisymmetric wake undergoes a second instability at $Re = 280.7$ (Meliga et al., 2009). The unsteady bifurcation of the steady non-axisymmetric, bifurcated, wake (so-called *secondary* instability) occurs at $Re = 271.8$ (Citro et al., 2017), beyond which an alternate shedding of hairpin vortices takes place (Gumowski et al., 2008) (figure 1.27(a), cases **b** and **b**′).

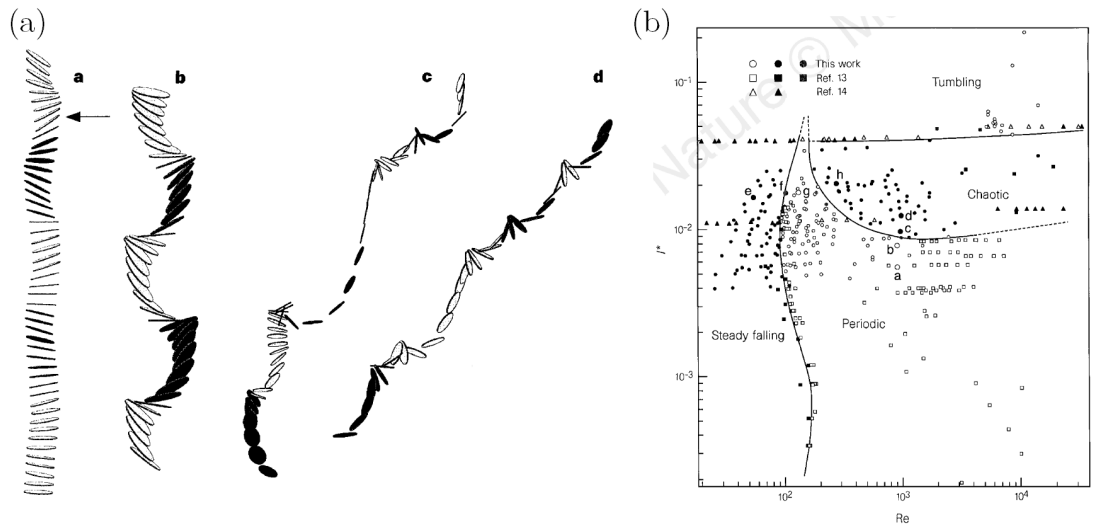

Figure 1.28: (a) Trajectories of falling disks, obtained by imaging from the side using a video camera. **a**. Steady falling. **b**. Periodic motion. **c**. Chaotic motion. **d**. Tumbling motion. (b) Bifurcation diagram as a function of the Reynolds number Re and the inertia of the body I^*. reproduced from Field et al. (1997).

Up to now, we considered the flow past fixed objects. The occurrence of bifurcations resulting from fluid-solid interactions on a freely-falling object is a relevant problem in fluid dynamics, with applications spanning from meteorology, ecology, and insect flight to engineering applications (see Ern et al. (2012) for a review). Intriguing falling paths result from the coupling between aerodynamic forces and the inertia of the considered body. A classical example is the free-fall of paper sheets, which typically may show a steady descent, or a fluttering, or a tumbling motion, faithfully reproduced by ODE models which include aerodynamic interactions (Belmonte et al., 1998; Pesavento and Wang, 2004; Andersen et al., 2005). The stability analysis of a two-dimensional falling plate was analyzed in two companion papers by Fabre et al. (2011) (with a quasi-static approach) and Assemat et al. (2012) (with the full coupling between aerodynamics and equations of motion). For large ratios between the density of the solid and the one of the surrounding fluid, the mode is very similar to the classical von Karman vortex street observed for fixed bluff bodies, and the vertical and angular velocity eigenmodes are asymptotically small. Additional modes associated with a very slow dynamics become unstable with a threshold similar to the one of the von Karman vortex street when thicker plates are considered, in agreement with Fabre et al. (2011). This ultimately would lead to a superposition of a fast oscillation due to the vortex shedding overposed to a slow oscillation due to the inertia of the body. A similar result is obtained for very small density ratios; the intermediate case instead showed more intricate eigenmodes with a strong fluid-structure interaction. Among axisymmetric bodies, the disk exhibits a plethora of possible falling trajectories, such as periodic, tumbling and chaotic motion (Willmarth et al., 1964; Field et al., 1997), depending on the moment of inertia of the disk and the Reynolds number (see figure 1.28). More recently, Fernandes et al. (2007) developed an ODE model to describe the

quasi-planar zigzag motion of an axisymmetric body, and Auguste et al. (2013) performed a numerical campaign to understand the different falling paths, varying the disk inertia and the Reynolds number. In the latter work, a significant effect of the disk thickness on the resulting falling trajectories was observed. The authors identified several planar and non-planar paths in the parameters space. The emergence of these trajectories was rationalized in Tchoufag et al. (2014) via a linear stability analysis on the steady and axisymmetric, vertical, falling state, with respect to azimuthal perturbations. The authors reconstructed different bifurcations and identified the threshold beyond which the steady vertical trajectory is unstable, with a very good agreement with the results of Auguste et al. (2013).

While the flow instabilities and the fluid-structure interactions of falling solid bodies have been widely investigated in the literature, similar analyses for porous bodies are still lacking. Part III is devoted to the modifications of the marginal stability thresholds for different permeable bluff bodies.

1.4.3 Flows past permeable structures

Inspired by nature and motivated by engineering applications, the flows through porous bodies received growing interest over the years. At the beginning of the last century, based on the concept that the permeability modifies the flow around a solid object, Prandtl (1904) designed a passive blowing system to control the flow past a circular cylinder. Subsequently, Castro (1971) studied experimentally the flow around perforated flat plates observing two different flow behaviors: a configuration in which the von Karman vortex street dominates the wake, and another in which the vortex shedding is inhibited due to the air bleeding from the holes. Furthermore, in some cases, the mean flow is characterized by the presence of a detached recirculation bubble. He also observed that the transition between these two states, i.e. with attached or detached recirculation region, is quite sudden. Successively, the turbulent wake past a nominally two-dimensional porous cylinder has been investigated (Zong and Nepf, 2012), identifying two wake regions: a steady wake region that extends for several cylinder diameters behind the body and a region further downstream associated with the vortex shedding. Increasing the porosity, and thus the permeability, the vortex street formation moves further downstream. More recently, the problem of the flow around porous disks has been approached experimentally (Strong et al., 2019) and numerically (Cummins et al., 2017) . In the first case, Strong et al. (2019) showed that the drag rescaled with the one of an impervious disk is almost constant when sufficiently low permeability is considered, in the inertialess regime. The authors observed a sudden drag decrease for large permeability; same values of porosity can realize different values of the permeability, depending on the voids' characteristic length. For non-negligible values of the Reynolds number, by increasing the disk permeability three different flow regimes have been recognized (Cummins et al., 2017): (i) an effectively impervious regime, which is characterized by the presence of a toroidal vortex recirculation region located close to the disk, is observed at low permeability; (ii) subsequently a transition regime in which the recirculation region shortens and moves downstream for

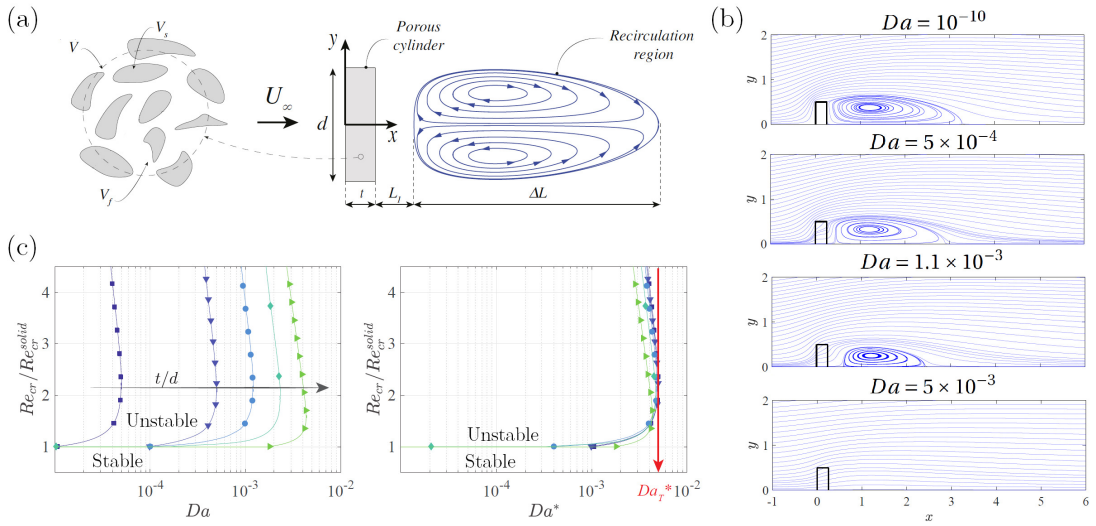

Figure 1.29: (a) Sketch of the flow configuration studied in Ledda et al. (2018) together with a zoom on a representative elementary volume. (b) Steady flow streamlines for the flow past a permeable rectangle with thickness-to-height ratio of 0.25, at Re = 30, for increasing Darcy number $Da = \kappa/L^2$. Because of symmetry, only the streamlines in the region $y > 0$ are reported. (c) Effect of the thickness-to-height ratio t/d on the critical value of the Reynolds number for the onset of the von Karman vortex street . On the left: neutral stability curves in the $Da - Re_{cr}$ plane. On the right: neutral stability curves using a modified $Da^* = Da \cdot (t/d)^{-1} = \kappa/(td)$. The considered cases are: $t/d = 0.01$ ■, $t/d = 0.1$ ▼, $t/d = 0.25$ •, $t/d = 0.5$ ⧫, $t/d = 1.0$ ►.

intermediate permeability; (iii) a high permeability regime where the recirculation region is no more present.

In two papers not included in this thesis, the author studied the wake flow past permeable bodies through a Brinkman model (1.67) in which the convective term was retained (Ochoa-Tapia and Whitaker, 1995; Breugem, 2004). Ledda et al. (2018) investigated the effect of the permeability on the wake patterns of two-dimensional porous rectangular cylinders at low to moderate Reynolds numbers in the framework of local and global stability analyses. Different aspect ratios of the cylinder were considered, varying the thickness-to-height ratios, t/d, from 0.01 (flat plate) to 1.0 (square cylinder), see figure 1.29(a). The results show that the permeability of the bodies has a strong effect in modifying the characteristics of the wakes and the associated flow instabilities. In particular, the fluid flows through the porous bodies and, thus, as the permeability is progressively increased, the recirculation region, initially attached to the rear part of the bodies, at first detaches from the body and, eventually, disappears even in the near wakes (figure 1.29(b)). Global stability analyses lead to the identification of critical values of the permeability above which any linear instability is prevented. As reported in figure 1.29(c), a different scaling of the non-dimensional permeability allows identifying a general threshold for all considered configurations that ensures the suppression of vortex shedding. It has been here observed that the marginal stability curve in the Darcy-Reynolds

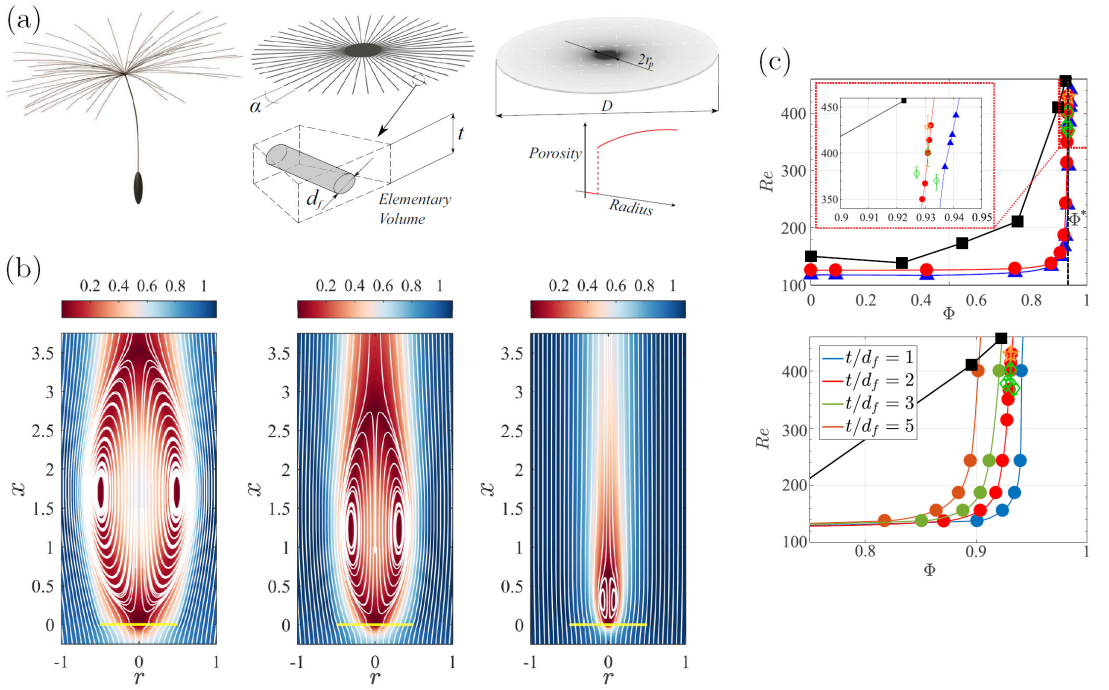

Figure 1.30: Results from Ledda et al. (2019). (a) On the left: sketch of a dandelion pappus. Center: simplified discrete model of a pappus. On the right: continuous porous disk considered to model the flow past a pappus, where porosity and permeability are functions of the disk radius. (b) Steady and axisymmetric solution of the flow equations for increasing mean porosity Φ, at $Re = 400$. The isocontours represent the velocity magnitude. (c) Top figure: marginal stability curves for the steady (▲) and unsteady (•) bifurcations for $t/d_f = 2$, with a comparison with the results of Cummins et al. (2018) for porous disks (■), freely falling dandelions pappi for $n_f = 95, 100, 106$ (◇) and the critical Reynolds number for the dandelion pappus (⋆). The vertical line depicts the threshold of mean porosity for unconditional stability Φ^* and the inset zooms in the threshold region. Bottom figure: effect of the disk thickness on the marginal stability curve of the unsteady bifurcation.

numbers plane well correlates with one iso-level of the length of the recirculation region. Interestingly, the flow can be unstable even without a recirculation region if a sufficiently elongated region exists with a wake defect larger than 95%. This behavior has been readily explained by investigating the local stability properties of the baseflow and by identifying the region of absolute instability in the wake. This analysis showed that when the velocity on the symmetry axis is less than the 5% of the free-stream velocity the baseflow can sustain locally absolutely unstable perturbations.

Ledda et al. (2019) studied the stability of the steady and axisymmetric flow of a variable-permeability permeable disk with respect to azimuthal perturbations. The work was inspired by the flight of dandelion seeds. The problem was approached through the approximation of an anisotropic and non-homogenous rigid porous disk for the pappus (figure 1.30(a)), combined with the linear stability analysis. The non-uniform distribution of permeability

qualitatively modifies the wake compared to the case of constant permeability. The wake is indeed characterized by a toroidal recirculation which slightly moves downstream as the mean porosity Φ of the object is increased while it becomes progressively smaller until it disappears (figure 1.30(b)). The results show the presence of a mean porosity threshold, which depends on the thickness of the disk, beyond which the flow is always characterized by a separated, steady and axisymmetric recirculating vortex ring. The threshold is in agreement with the experimentally observed values of porosity, as shown in figure 1.30(c).

Permeability variations therefore induce modifications of the wake and its bifurcations. An increase of permeability, kept constant inside the body, leads to a detachment and shrinking of the recirculation region, until disappearing. In the case of the two-dimensional permeable rectangle, the onset of the von Karman street is delayed and quenched for large enough permeabilities. When another thin object is considered, i.e. a porous disk, the bifurcations behavior remains qualitatively similar, even if permeability variations along the radius induce modifications of the recirculation region. However, for thick porous objects, the wake, and thus its stability properties, may behave differently, as observed for a porous sphere at low Reynolds numbers, characterized by an upstream displacement of the recirculation region, which may also penetrate inside the body (Yu et al., 2012). Moreover, the modifications induced by variable distributions of permeability suggest that the latter can be employed in optimization procedures, in the perspective of passive flow control (see e.g. Schulze and Sesterhenn, 2013). Owing to the direct and immediate link with the micro-structure composing the porous medium, homogenized approaches have great potential in retrieving a real, full-scale, configuration which satisfies the desired objectives. **With the aim of understanding the flow bifurcations in the presence of different behaviors of the recirculation region, Chapter 9 studies the steady and axisymmetric flow past a permeable sphere and its bifurcations via a homogenized model with interface conditions between the porous body and the free-fluid region (Lācis and Bagheri, 2017). A preliminary analysis to retrieve the full-scale structure is carried out. These concepts are developed in Chapter 10, where the optimization of the flow past a permeable cylindrical membrane, modeled as a thin membrane (Zampogna and Gallaire, 2020), is performed via gradient-based optimization, exploiting the macroscale interface condition and microscopic problems to retrieve the full-scale structure based on the identified macroscopic properties, constant or variable in the medium. Chapter 11 further extends the analysis by exploiting the homogenized model for thin membranes to study the fluid-structure interaction of a falling or rising thin permeable disk.**

Part I

Dripping down the rivulet: instability of a thin viscous film flowing under an inclined planar substrate

2 Instability of a thin viscous film flowing under an inclined substrate: steady patterns

Remark This chapter is largely inspired by the publications of the same name

G. Lerisson[1], P. G. Ledda[1], G. Balestra[2], F. Gallaire[1]
[1]Laboratory of Fluid Mechanics and Instabilities, École Polytechnique Fédérale de Lausanne, Lausanne, CH-1015, Switzerland
[2]iPrint Institute, University of Applied Sciences and Arts of Western Switzerland, Fribourg, CH-1700, Switzerland

Journal of Fluid Mechanics, **898**, A6 (2020)
Journal of Fluid Mechanics, **926**, E1 (2021)

Authors'contributions Following a preliminary experiment by G.B., G.L. and F.G. conceived the project. P.G.L. performed, together with G.L., the stability analysis until Section 2.5.1. P.G.L. carried out the theoretical, numerical and experimental analyses from Section 2.5.2. All authors actively participated to the theoretical developments, analysis and interpretation of the results. P.G.L. wrote the manuscript with G.L., with input from the coauthors, guided by F.G..

The flow of a thin film coating the underside of an inclined substrate is studied. We measure experimentally spatial growth rates and compare them to the linear stability analysis of a flat film modeled by the lubrication equation. When forced by a stationary localized perturbation, a front develops that we predict with the group velocity of the unstable wave packet. We compare our experimental measurements with numerical solutions of the non-linear lubrication equation with complete curvature. Streamwise structures dominate and saturate after some distance. We recover their profile with a 1D lubrication equation suitably modified to ensure an invariant profile along the streamwise direction and compare them with the solution of a purely two-dimensional pendent drop, showing overall a very good agreement. Finally, those different profiles agree also with a 2D simulation of the Stokes equations.

2.1 Introduction

We refer to Section 1.3.3.1 for a general introduction about the Rayleigh-Taylor instability.

To date, experiments are mostly transient in nature since a finite volume of fluid was released (Fermigier et al., 1992; Brun et al., 2015), with the noticeable exceptions of Rietz et al. (2017), in which the wall normal gravity component is replaced by a centrifugal acceleration, and Charogiannis et al. (2018). The difference between transient release dynamics and alimented flows appears to be significant. For the classical Rayleigh-Taylor instability under a flat ceiling, permanent-fed experiments through a porous supply have been mostly done in a horizontal annular geometry, which effectively mimics a one-dimensional substrate (Limat et al., 1992; Abdelall et al., 2006). This latter configuration gives rise to a particularly rich and complex dynamics of interacting dripping drops or continuous columns (Pirat et al., 2004; Brunet et al., 2007), and may even lead to massive dripping within corrugated sheets (Yoshikawa et al., 2019).

We thus propose a new experimental set-up, combining a permanent liquid supply to a tilted and flat coated surface, in contrast to recent studies on cylindrical and spherical substrates displaying a stabilizing effect on the film thanks to drainage-induced thinning and stretching (Balestra et al., 2018a,b). In order to overcome the limitation of a transient experiment, we impose a constant flow rate so that the flow can reach a steady state or an asymptotic behavior. The Reynolds number of our flow is as small as possible, using very viscous oils, as simple non-inertial models already incur complex non-linearities. The experiment allows us to explore a wide range of parameters, i.e. all angles from vertical to horizontal and large variations of the film thickness. In this experiment we can observe a whole variety of patterns, from almost unperturbed flat films to heavy rains of oil droplets (Lerisson et al., 2019). In particular, we study the stability of the flat film solution, and identify a range of parameters within which the film destabilizes into long rivulet structures.

In this chapter, we study the steady patterns emerging from natural and external forcing, describing the behavior of such a thin film continuously flowing under an inclined flat substrate with a combination of experiments, numerical simulations and linear stability theory. The experimental set-up is first described In Section 2.2 together with the measurement techniques, which are illustrated by a first spatially forced film, as well as the necessary scalings. Section 2.3 is devoted to a theoretical spatial stability analysis, which is compared to experimental measurements. Section 2.4 is devoted to the measurements of a freely flowing film together with numerical simulations. Again, the results are compared to the predictions of a local linear stability analysis. We finally discuss the nature of fully nonlinear static rivulet solutions, which naturally emerge in these steady patterns. We show that they have the shape of purely two-dimensional (2D) pendent drops, known to adopt the shape of an Elastica. In this chapter, we only focus on steady flows; the dynamics and transients that lead to those patterns are not investigated.

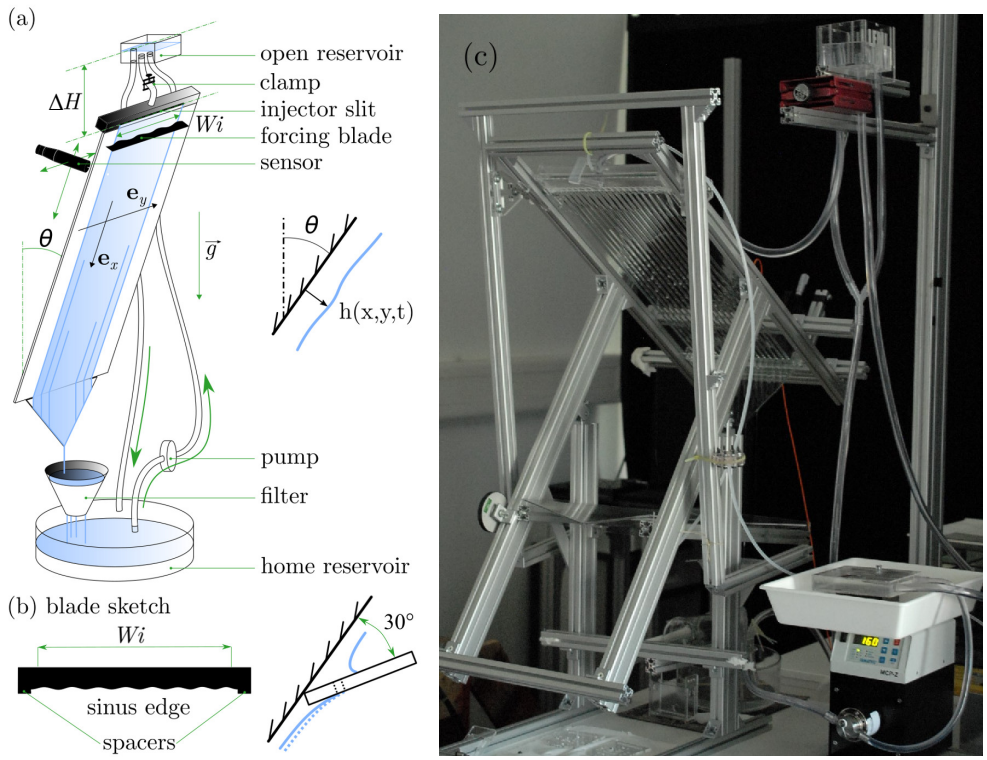

Figure 2.1: (a) Sketch of the experimental apparatus, (b) details of the forcing blade used to perturb the film and (c) picture of the experimental apparatus. Rivulets can be oberved under the glass plate.

2.2 Methods

2.2.1 Experimental apparatus

The experiment (figure 2.1) consists in injecting a Newtonian fluid on the underside of an inclined flat substrate with a constant flow rate. The substrate is a glass plate (dimensions 600x300mm) attached to an orientable structure, forming an angle θ with the vertical axis. In the present study, θ is varied from 20° to 55°. The fluid is silicon oil (Bluestar Silicons 47V1000) of measured viscosity $\mu = 1089\,\text{mPa.s}$, density $\rho = 974\,\text{kg.m}^{-3}$, kinematic viscosity $\nu = \mu/\rho = 1.12\,10^{-3}\,\text{m}^2\text{.s}^{-1}$ and surface tension $\gamma = 21\,\text{mN.m}^{-1}$. The fluid is injected through a horizontal slit-shaped inlet from a closed reservoir fully filled with oil and connected to an open reservoir. The open reservoir, placed above the inlet, is constantly filled and the height of the liquid is kept constant with an overflow. The oil flowing down the substrate is collected in a home reservoir and loops back during the experiment. The flow rate is set by varying the height difference ΔH between the closed reservoir and the open reservoir, giving an upper bound of $1.7\,10^{-3}\text{kg.s}^{-1}$ (corresponding to a film of equivalent thickness $h_N = 1.5\,\text{mm}$) and down to arbitrary low flux values. The flow rate is measured by weighting the oil leaving the substrate (for 3 minutes). Before any experiment, the substrate is pre-wetted to ensure a zero

contact angle (total wetting). All the experimental results presented here are measured on stationary films, i.e. the thickness reaches a stationary state. A forcing blade, consisting of a laser-cut rectangle with a sinusoidal long edge (sketched figure 2.1(b)), can be placed just below the inlet. The blade does not occlude the flow and is spaced from the glass by lateral spacers. An acute angle (about 30°) is introduced between the blade and the glass. The liquid fully fills the created gap underneath the blade and slightly spreads spanwise. The blade is always larger than the initial inlet and the lateral spreading remains in the sinusoidal part. The modified width W_i^* is measured systematically, resulting in a new equivalent thickness h_N. The sinus has a peak-to-peak amplitude of 0.5 mm and the spacers of 1 mm which should be projected with the acute angle, giving a perturbation of amplitude $\approx 250\,\mu$m The blade acts as a new initial condition and is taken as a new inlet reference for the flow.

We measure the film thickness $\bar{h}$ with a confocal chromatic sensor (STIL CCS) located on the upper (dry) side of the substrate. The sensor gives a point thickness measurement at an acquisition rate of 500 Hz. The sensor is attached to a 2-axis linear stage and we perform horizontal scans of length $\bar{L}_s = 200$ mm in the $\bar{y}$ direction (4 seconds per scan). The sensor performs two scans back and forth and returns to its initial position; we thus obtain the thickness profile twice. We compute the difference between these two measurements and remove errors by discarding values with a difference greater than $50\,\mu$m and values where the variation between successive points is larger than $500\,\mu$m. We map the whole substrate every 10, 30 or 50 mm in the $\bar{x}$ direction. The optical measurement cannot access film thickness distributions with a surface steepness higher than 40 degrees, following the STIL CCS specifications.

In addition, we set up another acquisition method based on the absorption of a colored liquid. The same silicon oil is mixed with Sudan Black B that has a peak of absorption at 595 nm. A flat screen of light covers the whole glass plate. A camera (Nikon D850 with a Nikon 50mm lens) is then attached to the structure at 85 cm from the glass plate, giving a resolution of 7.6 px.mm^{-1}. The luminance measured by each pixel is related to the thickness with the Beer-Lambert's law (Limat et al., 1992) :

$$\bar{h}(\bar{x},\bar{y},\bar{t}) = \frac{1}{C_L}\log\left(\frac{I_0(\bar{x},\bar{y})}{I(\bar{x},\bar{y},\bar{t})}\right), \tag{2.1}$$

where I_0 is the initial luminance measured without any liquid, I the luminance at time t, and C_L a constant value that is determined with a calibration procedure that consists in measuring the luminance through a known wedge.

Finally, we can enhance optically film perturbations and identify phases and patterns. The visualization technique is based on the distortion of a regular grid through the transparent liquid film. The grid has been fixed to a square light screen, placed behind the glass plate. In order to reduce the parallax effect, we placed the camera at a distance of 5 m from the plate.

2.2.2 Scalings

The reduced capillary length is given by a balance between surface tension and gravity projected perpendicularly to the substrate. In order to conveniently scale the in-plane $(\hat{x}, \hat{y})$ length scales, we define the reduced capillary length ℓ_c^*:

$$\ell_c^* = \frac{\ell_c}{\sqrt{\sin\theta}}, \tag{2.2}$$

where $\ell_c = \sqrt{\gamma/\rho g} = 1.49$mm is the capillary length. With the angle variation, it gives a range for the reduced capillary length of 1.85mm $< \ell_c^* <$ 2.54mm. For a given volumic flow rate q, we can define the Nusselt flat film thickness h_N, used to define the wall-normal $(\bar{z})$ length-scale:

$$h_N = \left(\frac{3\nu q}{\bar{W}_i g \cos\theta}\right)^{\frac{1}{3}}, \tag{2.3}$$

which is the constant thickness of an equivalent flat viscous film of width $\bar{W}_i$, assuming a half plane Poiseuille flow in the $\mathbf{e}_x$ direction and no flow in the $\mathbf{e}_y$ and $\mathbf{e}_z$ direction. In this study, h_N is varied from 0.5mm to 1.5 mm.

2.3 Forced dynamics

For a certain range of θ and h_N, the flat film is convectively unstable (Brun et al., 2015); perturbations grow and are advected downstream. We first study the film response to a spatially periodic forcing.

2.3.1 Experimental results

We place a horizontal blade with a sinusoidal-shaped edge against the substrate. The height of the liquid film is imposed by the distance separating the blade and the substrate. The blade is located just below the inlet (at $x = 0$) and imposes an inlet condition with dimensionless horizontal wave vector k_f and corresponding wavelength λ_f in the y direction, with $k_f = 2\pi/\lambda_f$. We design a set of blades for a range of spacings that goes from 5 cm to 1 cm, leading to a variation of the horizontal wave vector $0.32 < k_f < 1.44$ for an inclination angle $\theta = 20°$, and $0.15 < k_f < 0.75$ for $\theta = 39°$.

Figure 2.2 shows a typical measurement of the entire film thickness h by absorption, with $h_N = 1515\,\mu$m and $\theta = 39°$. The film is flowing in the positive x direction. The sinusoidal shape of the forcing propagates downwards, forming mainly streamwise phase lines. The amplitude of the response grows with x between $x = 0$ and $x = 50$ in a self-preserving manner. Between $x = 50$ and $x = 200$, the amplitude reaches a plateau and the shape is no longer sinusoidal. Beyond $x = 200$, the shapes start to develop streamwise oscillations. These oscillations are unsteady and their occurrence is not studied here. The flow rate and inclination angle chosen

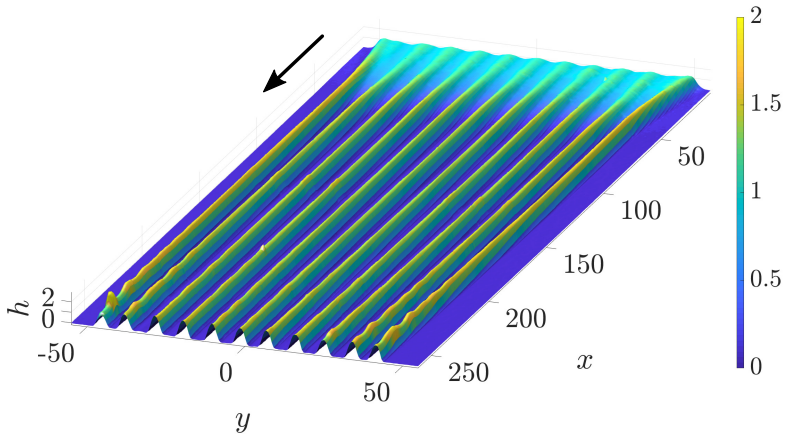

Figure 2.2: Film thickness for $\theta = 39°$ and $h_N = 1515\,\mu$m ($u = 1.5$), forcing at the optimal wavelength $\lambda_f = 8.90$. The thickness is measured with the absorption method and normalized by the flat film thickness h_N.

for this particular case of figure 2.2 are larger than the ones considered in the rest of the study, in which the responses are always stationary.

We first focus on the spatial growth phase. We follow the evolution of the thickness for several position x between $x = 19.7$ and $x = 118$ for different wavelengths and a fixed flow rate. We observe three regimes.

Case (a) of figure 2.3 shows the forcing propagating downstream with decreasing amplitude, until vanishing around $x = 50$. The film is then flat except on its lateral sides where thickness perturbations with respect to a flat condition propagate and grow. In cases (b,c), the forcing propagates in the domain with an amplitude that slightly increases in the streamwise direction. On the lateral sides, the signal is deformed and this deformation propagates inward. In case (c), the profile never follows the forced wavelength but follows $\lambda_f/2$; similarly, the obtained pattern is deformed when penetrating away from the lateral sides.

2.3.2 Linear stability

We compare these experimental results to the linear prediction obtained from the dispersion relation of the linearized thin film equation. The non-linear thin film equation is based on the assumption that the orthogonal derivatives ($\bar{z}$) are much larger than the in-plane ($\bar{x}, \bar{y}$) derivatives. We define the characteristic time scale τ :

$$\tau = \frac{\nu \ell_c^2}{h_N^3 g \sin^2\theta}. \tag{2.4}$$

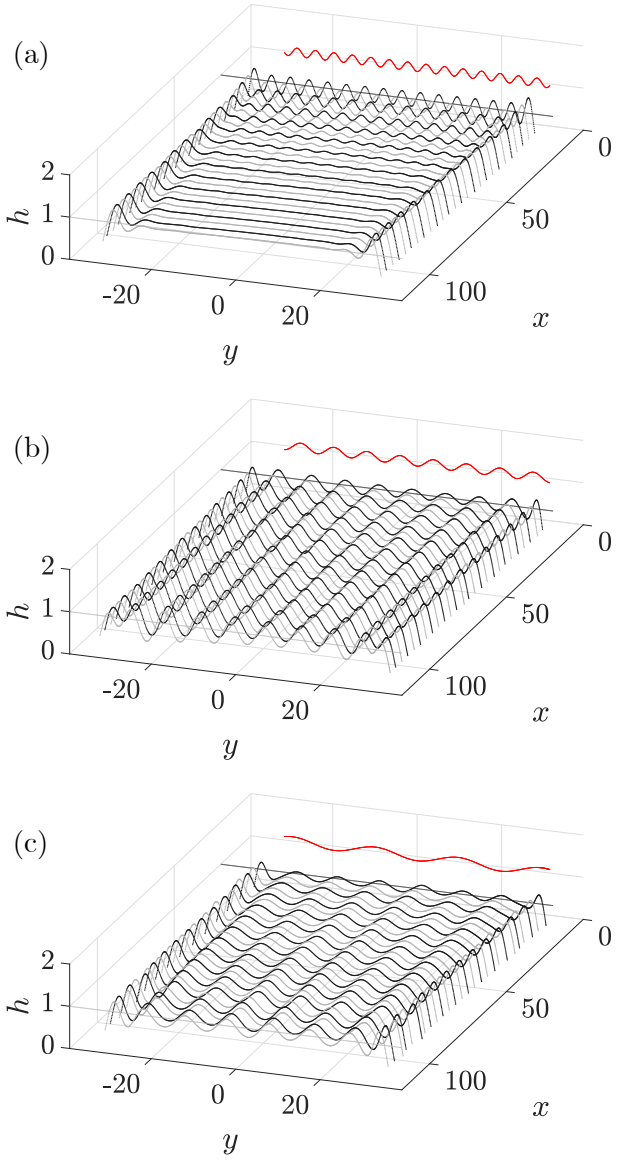

Figure 2.3: Evolution of the film thickness for $\theta = 20°$ and $h_N = 560\,\mu$m ($u = 12.5$) and forced wavelengths : (a) $\lambda_f = 4.37$, (b) $\lambda_f = 7.87$, and (c) $\lambda_f = 19.67$. The thickness is measured using the CCS scanning every 10 mm (in dimensionless form $\delta_x = 10\text{mm}/\ell_c^* = 3.9$). The red line shows the imposed inlet thickness at $x = 0$.

Spatial direction $\bar{x}$ and $\bar{y}$ are non-dimensionalized by ℓ_c^*, thickness $\bar{h}$ by h_N and time $\bar{t}$ by τ:

$$x = \bar{x}/\ell_c^*, \quad y = \bar{y}/\ell_c^*, \quad h = \bar{h}/h_N, \quad t = \bar{t}/\tau. \tag{2.5}$$

Following previous works (Ruschak, 1978; Wilson, 1982; Kheshgi et al., 1992; Weinstein and Ruschak, 2004), the full curvature term is retained. In non-dimensional form, the equation reads:

$$\partial_t h + \tilde{\ell_c}^* \cot(\theta) h^2 \partial_x h + \frac{1}{3}\nabla\cdot(h^3(\nabla h + \nabla\kappa)) = 0, \tag{2.6}$$

where ∇ operates in the (x, y) plane, $\tilde{\ell_c}^* = \ell_c^*/h_N$ and κ is the mean curvature:

$$\kappa = \frac{\partial_{xx}h\left(1+\left(\frac{1}{\ell_c^*}\partial_y h\right)^2\right) + \partial_{yy}h\left(1+\left(\frac{1}{\ell_c^*}\partial_x h\right)^2\right) - 2\left(\frac{1}{\ell_c^*}\right)^2\partial_{xy}h\partial_x h\partial_y h}{\left(1+\left(\frac{1}{\ell_c^*}\partial_x h\right)^2+\left(\frac{1}{\ell_c^*}\partial_y h\right)^2\right)^{3/2}}. \tag{2.7}$$

In the following, we focus on the emergence of steady states in response to a stationary forcing. We thus assume no time variations and we consider a stationary perturbation with respect to the flat film condition. Introducing $h = 1 + \epsilon h'$ with a steady perturbation $h' \propto \mathrm{e}^{i\mathbf{k}\cdot\mathbf{x}}$ where $\mathbf{k} = (k_x, k_y)$, equation (2.6) is linearized to obtain the dispersion relation :

$$\frac{i}{3}(|\mathbf{k}|^2 - |\mathbf{k}|^4) + \underbrace{\cot\theta\tilde{\ell_c}^*}_{u} k_x = 0 \tag{2.8}$$

where u is the coefficient of a linear phase advection which corresponds to the surface film velocity that advects the linear perturbations downstream, and is the only parameter which appears in the linearized dynamics.

We neglect the lateral side and assume the forcing and the response to be homogeneous and purely in the spanwise direction i.e. $\mathrm{Im}(k_y) = 0$ and $k_y = k_f$. For each forcing wavelength $2\pi/k_y$, we thus obtain the corresponding spatial growth rate $k_x(k_y)$ by solving the equation :

$$(k_y^2 - k_y^4) + (k_x^4 + k_x^2 + 2k_x^2k_y^2) - 3iuk_x = 0. \tag{2.9}$$

which is a fourth-order polynomial in k_x which can be solved for as a function of k_y. Among all the four roots of the complex polynomial, we discard solutions which have $\mathrm{Re}(k_x) \neq 0$ i.e. solutions that oscillate along the streamwise direction. There is only one branch that corresponds to a purely growing downstream amplified spatial wave ($\mathrm{Re}(k_x) = 0$). The maximum growth rate is not attained exactly at $k_y = 1/\sqrt{2}$, as for the temporal growth rate Brun et al. (2015) but it deviates by no more than 0.2% for the considered cases in this study (see figure 2.14 in appendix 2.7.1). In such convective situation where we have $u > c_{g0}$ with $u = 12.5$ (figure 2.3) and the absolute group velocity $c_{g0} = 0.54$ (Brun et al., 2015), the streamwise growth of spanwise wavenumbers strongly resembles their temporal growth, a property alike Gaster transformation (Gaster, 1962), though not directly related to it.

Experimentally, we measure the spatial growth rate and compare it to $\mathrm{Im}(k_x)$ by measuring the amplitude $A(x)$ defined by :

$$A(x) = \sqrt{\int_{\bar{y}=0.2\hat{L}_s}^{\bar{y}=0.8\hat{L}_s} \left(\bar{h} - h_N\right)^2 \mathrm{d}\bar{y}}, \tag{2.10}$$

along the x direction. Results corresponding to the three cases presented in figure 2.3 are plotted in figure 2.4(a,b,c) (black crosses) in log scale as a function of x along with the theoretical prediction (red lines) normalized by the first measurement. Case (a) shows an exponentially decreasing amplitude up to $x = 40$ before saturating to a lower noisy value. The decrease is well captured by the linear prediction (2.9). Case (b) shows an exponentially increasing amplitude all over the x measurement range which is well predicted by the theory. In case (c) the amplitude is also following an exponential increase but at a rate that is much faster than the prediction for the corresponding wavelength; we also plot the growth predicted for the super-harmonic wavelength ($\lambda = \lambda_f/2$) that almost perfectly matches the experimental measurement.

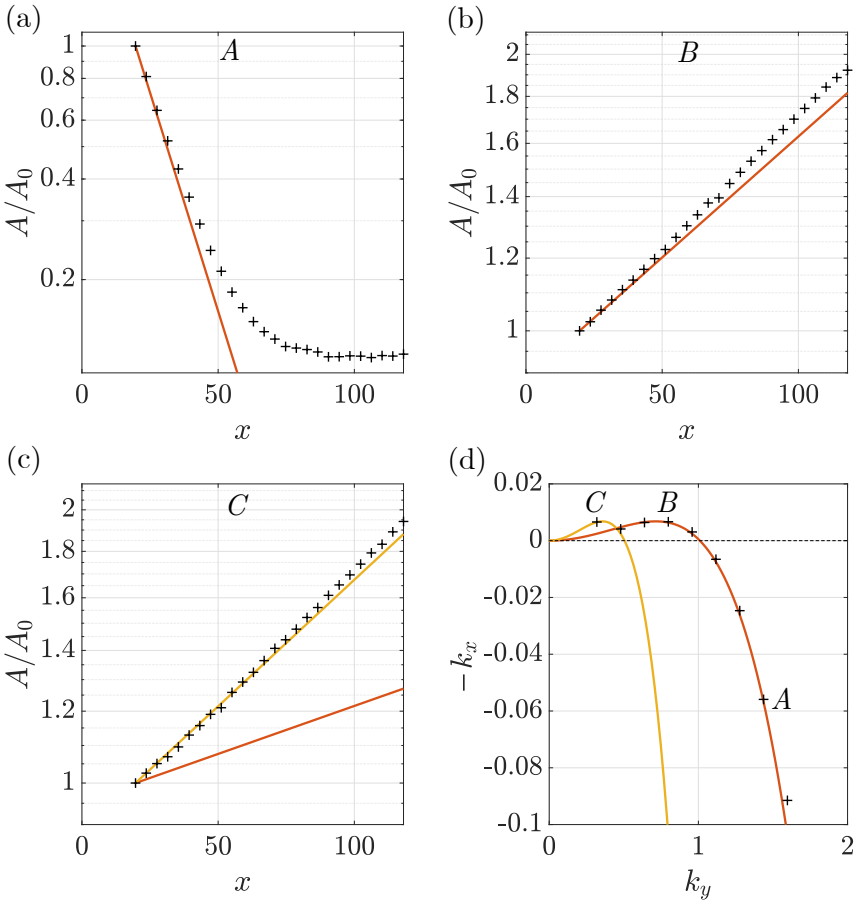

Figure 2.4: (d) Theoretical (red curve) and experimental (black crosses) spatial growth rates as a function of the forcing wavelength k_y; the yellow curve is the theoretical prediction for the harmonic ($2k_y$). (a),(b) and (c) Experimental amplitudes (crosses) and theoretical prediction (red lines) for the three cases presented in figure 2.3. The yellow line in (c) is the prediction for the harmonic $2k_y$. The corresponding measurements are reported as points A, B and C on (d).

The measurements are summarized in figure 2.4(d) where we plot the growth rates for $0 < k_y < 2$. The predicted growth rate (red line, solution of equation (2.9)) is in excellent agreement with the experimental data (crosses). In addition, we plot in yellow the solution of equation (2.9)

for $k_y = 2k_f$. The measured points labeled A, B and C corresponds to the full measurements shown in (a), (b) and (c).

The linear dispersion relation shows a cut-off wavenumber at $k_y = 1$, corresponding to a dimensional wavelength of $2\pi\ell_c^*$. So when we increase the angle θ, the range of unstable wavelength decreases. The spatial growth rate k_x is a decreasing function of u which depends on the two parameters, h_N and θ. Increasing θ (toward a more horizontal substrate) leads to a decrease of u and an increase of k_x. If the forced wavelength is unstable, its amplitude grows and saturates close to the inlet. Similarly, increasing h_N leads to a decrease of u and an increase of k_x, while the dimensional velocity of the flat film surface is however increased. This comes from the time scale that is inversely proportional to h_N^3: while perturbations are advected faster with an increase of h_N (that would lead to a smaller spatial growth rate), they are amplified even more (resulting in the spatial growth rate eventually to increase).

2.4 Natural dynamics

Even without the inlet device shown in figure 2.1(b), thickness perturbations with respect to the flat film grow from the sides and may invade the entire domain (as shown in figure 2.5(a,c,e)). Far from the sides, the film thickness is constant for all x in (a) and (c). In case (e), the perturbation invades the entire film. The side perturbations penetrate inside while also being advected downstream. In case (b), (d) and (f), we perturb the film by placing a small cylinder (of diameter 2 mm) in the middle of the film and close to the inlet. The perturbation is stationary and propagates both downstream and in the spanwise direction. The perturbation amplitude grows with the streamwise direction and high amplitude variations cannot be captured in (f).

In this context of highly advected perturbations, we look for the steady front of the region invaded by the perturbation.

2.4.1 "Spatio-spatial" stability analysis

Instead of focusing on the spatio-temporal growth and propagation of this wavepacket in two dimensions of space, we assume steady patterns and only consider a "spatio-spatial" wavepacket growth. The classical absolute/convective calculation can be generalized to the streamwise spatial growth of spanwise spatially periodic disturbances. In this analogy, x plays the role of time and k_x that of the complex frequency while k_y is the complex spatial wavenumber; the dispersion relation (2.9) now takes into account for complex wavenumbers, $D(k_x, k_y, u) = 0$.

We can make an analogy with a spatio-temporal analysis, where the front is defined by a particular ray $x/t = v$ for which the perturbation is marginally stable, as $t \to \infty$ (Huerre and Monkewitz, 1990; Van Saarloos, 2003; King et al., 2016). In this approach, the front is the

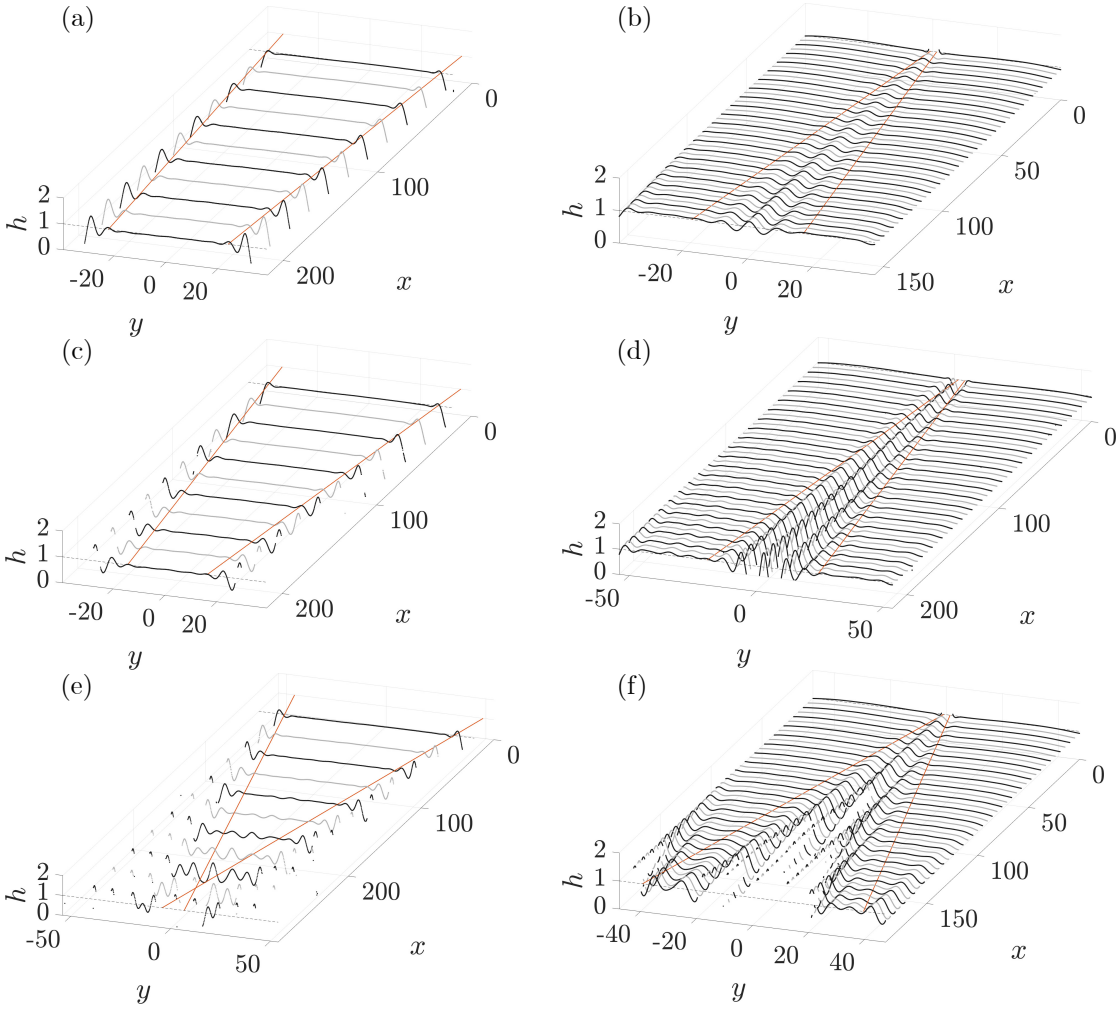

Figure 2.5: Evolution of the film thickness without forcing in case of : (a) $h_N = 678\mu$m, $\theta = 20°$ ($u = 10.3$), (c) $h_N = 1142\mu$m, $\theta = 20°$ ($u = 6.1$), (e) $h_N = 726\mu$m, $\theta = 40°$ ($u = 3.0$), and with a stationary localized forcing in case of : (b) $h_N = 1334\mu$m, $\theta = 20°$ ($u = 5.2$), (d) $h_N = 390\mu$m, $\theta = 40°$ ($u = 5.7$), (f) $h_N = 1357\mu$m, $\theta = 30°$ ($u = 2.7$). The red lines are the theoretical predictions for the front propagation computed with the help of equation (2.9).

velocity, i.e. the amount of space per unit of time, at which the perturbation spreads in the domain while being advected. Here, we look for the front angle $y/x = \tan(\phi)$, i.e. the amount of spanwise space per unit of streamwise space, separating the perturbed domain from the region where the perturbation does not propagate, as $x \to \infty$.

We then numerically determine the angle ϕ for which $\frac{\partial \mathrm{Im}(k_x)}{\partial \mathrm{Im}(k_y)} = \tan(\phi)$, imposing $\frac{\partial \mathrm{Re}(k_x)}{\partial \mathrm{Im}(k_y)} = 0$. It consists in the extraction of the relevant roots from a complex 4-th order polynomial, which is performed using the built-in Matlab function *fsolve* for a two variables system. For a given u, we increase y/x and plot $\mathrm{Im}(k_x) - y/x\mathrm{Im}(k_y)$, tracking the saddle points in the complex k_y plane until we find the ones that have a zero spatial growth rate $\mathrm{Im}(k_x) = 0$ and a non-zero $\mathrm{Re}(k_y)$. According to Barlow et al. (2017) and Huerre and Monkewitz (1990), we verified that

the maximum growth rate in the spatial dispersion i.e. $\frac{\partial \mathrm{Im}(k_x)}{\partial \mathrm{Re}(k_y)} = 0$ is a contributing saddle point and identified its locus as y/x is varied, which implies that it contributes to the asymptotic behavior of the solution. The results are shown in appendix 2.7.1 (figure 2.13) where the dependency of the front angle ϕ on the velocity u is given in blue.

In figure 2.5(a,c,e), we assume the system to be dominantly perturbed by the lateral side of the film, at the worst position i.e. at the inlet, and that this perturbation excites all wavelengths. We thus define two front lines (drawn in red) that follow the front propagation angle ϕ and which start from the inlet sides. All the considered perturbation waves that are able to go within those two front lines are stable, while all the perturbation waves that propagate outside are unstable. Those front lines thus separate the region where the side perturbations have invaded the domain (outside the lines) from the region where they have not (within the lines).

In figure 2.5(b,d,f), we perturb the system and therefore draw the red front lines starting from the edge of the perturbing cylinder. Similarly, the front lines separate an inner region where the perturbation spreads from an outer region where it cannot invade.

In the first two cases (a) and (c), the lines well predict the limit of penetration for the perturbations. This validates our hypothesis that the perturbation is mostly composed of spanwise waves that are mostly excited by the side boundary condition.

Moreover, the unstable waves have a vanishing growth rate close to the front lines which qualitatively explains the vanishing amplitude of the perturbation approaching the front. Similarly, at a fixed x position and varying the y position, the wavelength is not constant, which is qualitatively expected from the front velocity criterion that is different for each wavelength. From the calculation, fast propagating waves have a larger wavelength than slow propagating ones, which is what we qualitatively observe.

In the last case (e), the lines cross before the x end of the experiment and the film is fully invaded downstream. We also see perturbations growing above the lines. The presence of imperfections within the inlet slit is evidenced here thanks to large growth rates for this set of parameters, i.e. at large angle θ and high initial thickness h_N. This faults the assumption of a system solely perturbed on the sides of the inlet.

In the forced cases (b), (d) and (f), the agreement between the observed front and the prediction is good. Note that the perturbation coming from the sides enters downstream in the measured region in case (f).

2.4.2 Non-linear simulations

In this section, we perform numerical simulations of the thin film equation with complete curvature (2.6). Numerical simulation are performed with the finite element software COMSOL. In COMSOL, the equation is solved for a thickness h and a curvature κ. In the numerical method, we use a time marching technique and an additional term is added to equation (2.6)

in order to account for the outlet condition, imposed using a sponge method and resulting in the following equation to be numerically solved:

$$\partial_t h + \frac{1}{3}\nabla\cdot(h^3(u\mathbf{e}_x + \nabla h + \nabla\kappa)) = -\mathrm{Sp}(x)h. \tag{2.11}$$

The function $\mathrm{Sp}(x)$ is a mask function for the sponge method that relaxes the thickness to 0 (Högberg and Henningson, 1998):

$$\mathrm{Sp}(x) = \frac{1+\tanh(x-6L_x/7)}{2}. \tag{2.12}$$

This avoids reflection effects from the outlet.

The domain is a rectangle of dimension $L_x \times L_y$ with Dirichlet boundary conditions. On the lateral boundaries and on the outlet, the thickness h and the curvature κ are set to zero. Before the outlet, 10% of the domain is damped by a sponge method. The inlet imposes a jet function $J(y)$ (Monkewitz and Sohn, 1988) that reproduces the experimental inlet conditions:

$$J(y) = \frac{1}{1+\left(\exp\left(\frac{2|y|}{W_i}\right)^2 - 1\right)^{N_j}}, \tag{2.13}$$

of parameters $N_j = 20$ and width $W_i = \bar{W}_i/\ell_c^*$. The inlet curvature imposed is computed from the inlet thickness distribution, setting the streamwise curvature to zero. The initial condition for the thickness follows the jet function on the y direction:

$$h(x,y,t=0) = J(y)(1-\mathrm{Sp}(x)), \tag{2.14}$$

and the initial curvature is computed from the initial thickness.

The triangular mesh is created in COMSOL with the largest element smaller than $\tilde{\ell_c}^*$. We use cubic elements for the thickness and the curvature, and the time solver uses a fully implicit method. A simulation consists in a time-stepping of the equations until a stationary solution is obtained. A typical simulation lasts $T_f = 1000\tau$.

In figure 2.6, we plot transverse profiles (along the y direction of the thickness h at three x positions obtained numerically (blue curves) and experimentally (black dots) for three couples (h_N, θ). Figures 2.6(a) and (b) share the same angle θ while figures 2.6(b,c) share the same h_N (i.e. the same flow rate). In all figures and simulations, the film thickness is stationary, even though the liquid is flowing downstream.

Figures 2.6(a) and (b) are similar and the numerical prediction is in remarkably good agreement (the only fitting parameter being the inlet jet width that fits the experimental inlet). The thickness goes to zero on lateral boundaries and equals 1 in the center. The film span decreases with increasing x. A perturbation grows equally from the sides with an oscillatory shape and spreads with increasing x. The perturbation grows and penetrates inside the film

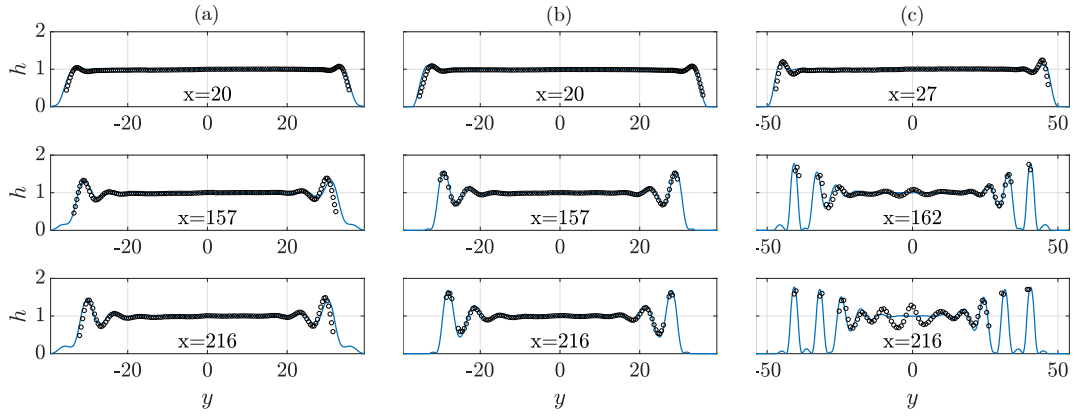

Figure 2.6: Comparison of experiment (black circles) and numeric (blue lines) for (a) $h_N = 1142\,\mu$m $\theta = 20°$ (u=6.1), (b) $h_N = 678\,\mu$m $\theta = 20°$ (u=10.3), (c) $h_N = 726\,\mu$m $\theta = 40°$ (u=3.0).

with increasing x.

In figures 2.6(c), the agreement is good on the sides. The sensor is unable to measure steep films but the lateral peaks are well predicted by the simulation. However, the central part of the film, which remained flat in the other cases, is now perturbed. This perturbation is not captured by the simulation as there are no variations at the inlet (except at the sides) while, in the experiment, the inlet generates noise at the center.

At $x = 216$, the sensor is unable to measure steep films, but the lateral peaks captured are well predicted by the numerical simulation. The experiment is supposed to be in total wetting condition (zero contact angle) since the substrate is pre-wetted, avoiding any contact line dynamic as in the simulated equation. The lateral sides of the film are free to move and relax to very thin film thicknesses where the temporal evolutions are very small (scaling with h^3), and the validity of this side dynamics is confirmed by the good agreement.

As seen before, side perturbations penetrate inside the film with increasing x and have, in figure 2.6(c), invaded all the film downstream. The non-linear simulations capture the peak positions contrarily to the linear prediction that only captures the front position. The peak amplitudes are also captured and we observe that they saturate, which cannot be described by a linear theory.

It is remarkable to note the validity of the thin film equation with complete curvature in cases where the assumptions implied by this equation are not obviously satisfied, for instance in presence of order one slopes (Krechetnikov, 2010).

Increasing h_N or θ leads to an increase of the peak numbers and their penetration. However, we do not observe strong variations of the maximum peak amplitude when varying the parameters. The next section will focus on the saturated amplitude and the associated streamwise structures.

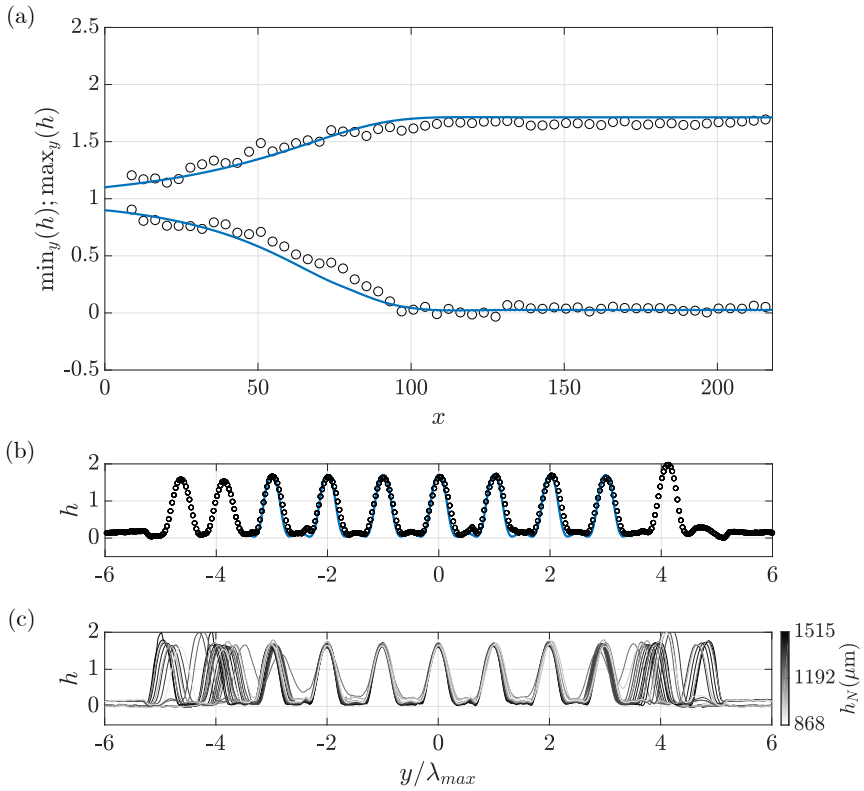

Figure 2.7: (a,b) Comparison of an experimental cut (black circles) of parameters $\theta = 39°$, $h_N = 1515\,\mu$m, forced at the dominant wavelength λ_{max} and the same parameters numerical simulation (blue line). (a) shows a projection of the maximal and minimal thickness over y, along x and (b) is a transverse cut at $x = 156$. (c) compares 20 transverse measurement cuts at $x = 156$ and $x = 187$ for a range of h_N and two differents angle ($\theta = 26°, 39°$). The y axis is non-dimensionalized by the dominant wavelength. The darkness of each curve is proportional to h_N.

2.5 Non-linear saturated rivulet solutions

Downstream, as shown in the full profile figure 2.2, the system exhibits long structures called rivulets.

2.5.1 Non-linear structures

To study these structures, we look at the most unstable forcing, i.e. at the wavelength at which the growth rate is maximum. We plot in figure 2.7 a comparison between numerical and experimental results. We measure in (a), the maximal and minimal values of the thickness along x. Again, we note a good agreement between experiments and simulations. The amplitude increases as the structures penetrate downstream to reach a saturated value at large x. We choose a streamwise position where the structures are saturated and do not vary with x ($x = 200$). We compare these saturated rivulets with the simulation (figure 2.7(b)) and find

a good agreement. We then vary the parameters (θ, h_N). The measurements are plotted in figure 2.7(c) for ten different equivalent film thicknesses h_N and two angles θ (a total of 20 cuts). As the linearly most unstable wavelength λ_{max} depends on the angle, the abscissa is non-dimensionalized by λ_{max}. Except for the sides, all the curves collapse to a similar profile, which suggests the existence of two-dimensional, steady and attracting, rivulet shapes.

2.5.2 Range of possible rivulets

In contrast to section 2.3, we now consider the case of a high amplitude forcing. We use a comb-like blade, with constant spacing, placed at the inlet. The comb teeth (figure 2.8(a)), of width $\bar{l}_t = 2\,\text{mm}$, are parallel to the glass plate and cover the inlet injection slit. The teeth are placed $\bar{l}_{dt} = 5\,\text{mm}$ downstream of the inlet and present a thickness of $\bar{t}_t = 1\,\text{mm}$. The comb occludes the inlet in correspondence of the teeth and covers the latter as it is welled up by capillarity. We focus on the observed spanwise peak-to-peak distance L_{obs} of the obtained periodic structures. We fix $\theta = 55°$, and $h_N = 0.4\,l_c = 594\,\mu\text{m}$ and look at a regular grid through the thin film. The resulting distorted pattern clearly captures the presence of rivulets. We define $K_{obs} = 2\pi/L_{obs}$; in figure 2.8(a) a typical pattern is visualized, for a forcing of $k_f = 0.41$. We identify the presence of peaks, following the yellow lines; in this case the observed spacing is half the forced one (super-harmonic). Figure 2.8(b) shows K_{obs} as a function of the forced wavenumber. The three solid lines correspond to the cases $K_{obs} = 2\,k_f$ (super-harmonic, orange line), $K_{obs} = k_f$ (fundamental harmonic, red line), $K_{obs} = k_f/2$ (sub-harmonic, blue line); the experimental results are reported with black dots. The spacing is the same as the forced one, for $k_f = 0.47, 0.55, 0.71, 0.76, 0.78$. In the case $k_f = 0.95, 1.19$ the periodic structures length is twice the forced one (sub-harmonic). We note a transition from $K_{obs} = 2\,k_f$ to $K_{obs} = k_f$ for $0.41 < k_f < 0.47$, and to $K_{obs} = k_f/2$ for $0.78 < k_f < 0.95$. In figure 2.8(c) we plot the three dispersion relations for the fundamental harmonic, sub-harmonic and super-harmonic. The fundamental harmonic dispersion relation intersects the super-harmonic at $k_f^{(1)} = 1/\sqrt{5} \simeq 0.45$, and the sub-harmonic at $k_f^{(2)} = 2/\sqrt{5} \simeq 0.89$. The grey-shaded areas in figure 2.8 (b-c) identify the region in which the fundamental harmonic has a greater growth rate, $(k_f^{(1)} < k_f < k_f^{(2)})$. In this region we experimentally observe $K_{obs} = k_f$. The film selects the most unstable harmonic among the unstable ones. Even in presence of a high amplitude forcing, the linear theory well predicts the resulting pattern. In particular, there is a narrow range of possible rivulets, of periodic length $\sqrt{5}\pi < L_y < 2\sqrt{5}\pi$. In the following, we focus on the wavelength that has the maximum growth rate in the linear dispersion relation, i.e. $L_y = 2\pi\sqrt{2} \simeq 8.89$.

2.5.3 The optimal rivulet

In Section 2.5.1, the simulations indicate the emergence of a rivulet state which is invariant both in time and along the streamwise direction. Exploiting the time invariance, the steady version of the general thin film equation (2.6) could be solved but it remains an elliptic non-linear PDE in (x, y). Under the assumption $\frac{\partial}{\partial x} \ll \frac{\partial}{\partial y}$, this equation can be further parabolized

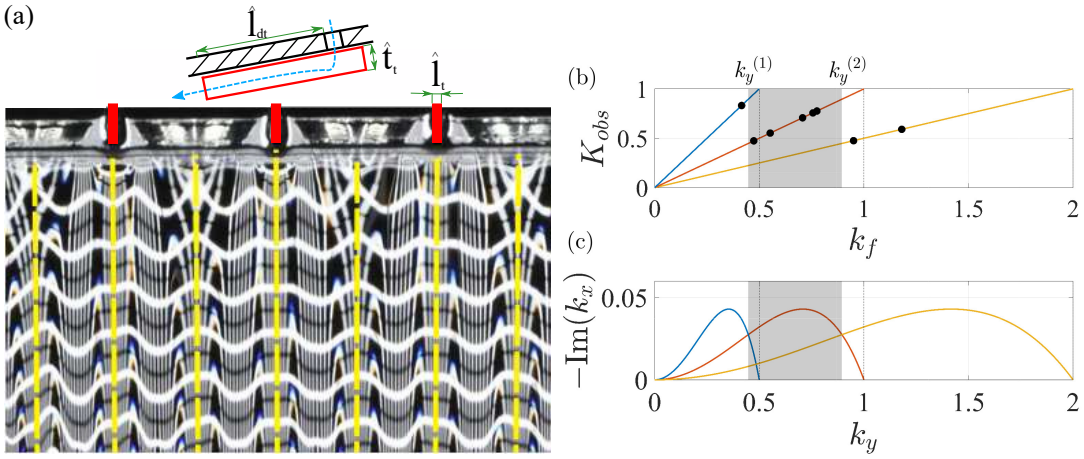

Figure 2.8: (a) Detail of the comb-like blade and rivulets visualization using the distortion technique, for $\theta = 55°$, $h_N = 0.4\, l_c = 594\,\mu$m, $k_f = 0.41$ ($u = 1.9$). The forcing comb is placed over the inlet (red lines on the top of the figure); the white lines represent the film thickness. The dashed yellow lines have been added in post-processing to highlight the rivulets peaks. In this case, we have $K_{obs} = 2\,k_f$ (b) K_{obs} as a function of the forcing wavenumber k_f; the black dots are the experimental results. (c) Linear dispersion relations for the fundamental harmonic, super-harmonic and sub-harmonic. In both figures, the solid lines are respectively $K_{obs} = 2\,k_f$ (super-harmonic, orange line), $K_{obs} = k_f$ (fundamental harmonic, red line), $K_{obs} = k_f/2$ (sub-harmonic, blue line); the grey shaded area is the region in which the fundamental harmonic has the highest growth rate.

and marched downstream in x to yield the fully developed x and t invariant rivulet profile. Alternatively, we preferred to exploit directly the streamwise x-invariance observed sufficiently downstream and solve the naturally parabolic time evolution towards the steady rivulet profile. However, the resulting one-dimensional problem in y satisfies the conservation of mass in the cross-section; on the other hand, in the initial two-dimensional problem the flow rate, and not the mass, is conserved, for each transversal section. We refer to the first case as *closed flow condition*, and to the second as *open flow condition*. Here, the concepts of open and closed flow conditions slightly differ from the definitions given in Kalliadasis et al. (2011), in which they relate to the streamwise boundaries, since, in our case, the flow is perpendicular to the wavy profile. In order to impose the open flow condition in the one-dimensional problem in y, we start from the Stokes equations in (y,z), complemented by the boundary conditions. We impose the constraint on the tranverse flow rate (in the x direction) by introducing a parameter $\sigma(t)$ in the continuity equation, i.e. $\frac{\partial u_y}{\partial y} + \frac{\partial u_z}{\partial z} = \sigma$, relaxing the hypothesis of mass conservation in the cross-section. The derivation of the thin film equation follows the classical one and leads to the following equation to be numerically solved:

$$\partial_t h + \frac{1}{3}\partial_y \left[h^3 \left(\partial_y \kappa + \partial_y h \right) \right] = \sigma h, \tag{2.15}$$

with periodic boundary conditions at the border of the domain $y \in [0, 2\pi\sqrt{2}]$; the curvature can be expressed as $\kappa = \partial_{yy}h/(1+((1/\tilde{\ell}_c^*)\partial_y h)^2)^{3/2}$.

We consider the non-dimensionalized Nusselt streamwise velocity profile (Kalliadasis et al., 2011) at each spanwise location:

$$u_N(y,z,t) = \cot(\theta)\tilde{\ell}_c^* \frac{1}{2} z(2h(y,t)-z). \tag{2.16}$$

The flow rate can be expressed as:

$$q(t) = \int_0^{2\pi\sqrt{2}} \left\{ \int_0^{h(y)} u_N(y,z,t)\mathrm{d}z \right\} \mathrm{d}y. \tag{2.17}$$

Starting from a flat film (i.e. $h(y,t=0)=1$), the initial flow rate is $q_i = (1/3)2\pi\sqrt{2}\cot(\theta)\tilde{\ell}_c^*$. At each time t the flow rate is required to stay constant and equal to its initial value q_i; this condition can be achieved by imposing the correct value of σ at each time t. In the equation $q(t) = q_i$ the term $\cot(\theta)\tilde{\ell}_c^*$ simplifies and so the flow rate constraint (2.15) is independent on the angle θ and $\tilde{\ell}_c^*$. The resulting problem completed by (2.15) does not depend on the linear advection velocity u, but only on $\tilde{\ell}_c^*$.

The numerical implementation is based on a Fourier spectral method for the spatial derivatives, and on a second-order Crank-Nicolson scheme, implemented in the built-in MATLAB routine *ode23t*, for the time integration. At each time step the value of σ is obtained iteratively imposing the condition on the flow rate. The numerical simulation is stopped at $t = t^*$, when the L^2 norm of the difference between two successive time steps $\| \delta h \|_{L^2} = 1/\delta t \| h(t+\delta t) - h(t) \|_{L^2}$ is less than a fixed tolerance $\epsilon = 10^{-6}$. During the simulation σ is always smaller than 10^{-2} and approaches 10^{-6} when the simulation is stopped. In figure 2.9(a) we see the evolution of the maximum and minimum thickness of the rivulet profile, for $\tilde{\ell}_c^* = 1$ (red lines). The maximum thickness over the domain reaches a constant value $\max_y(h) = 1.71$. The minimum thickness is decreasing and decays with the law $\min_y(h) \sim t^{-1/2}$ (black dotted line in figure 2.9(a), as already observed in Yiantsios and Higgins (1989). In fig 2.9(b) the rivulet profiles for different models are reported. The red solid line indicates the model defined above. We can distinguish between two regions: a side lobe, characterized by a very low thickness, and a central lobe, in which the maximum thickness is localized. The limit of these regions is defined by the position y_{min} of the minimum thickness; this position is slowly moving. The evolution of the central lobe reveals that in a large region near the maximum thickness the profile reaches a saturated state, while near the minimum thickness the shape is slowly evolving. The comparison with the two-dimensional (x,y) simulations of the lubrication equation (black circles) shows a very good agreement between the two models, in particular in terms of maximum thickness and central lobe profile. We define the equivalent Nusselt thickness $\bar{h}_N$ of the rivulet profile as the mean of the thickness accross the width of the rivulet ($\bar{h}_N = (1/L_y)\int_0^{L_y} h\mathrm{d}y$), when $t = t^*$. The equivalent Nusselt thickness of our computed so-

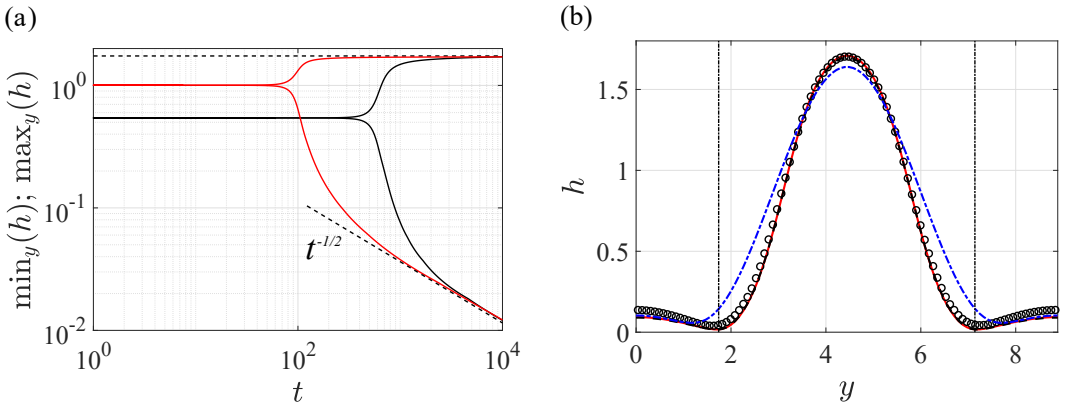

Figure 2.9: (a) Evolution of the maximum and the minimum thickness for the one-dimensional model, open flow condition (red lines) and closed flow condition with $h(y, t = 0) = 0.54$ (black lines). The dashed lines are the long-time behavior of the maximum and minimum thickness. (b) Rivulets profile for different models: one-dimensional open flow model (red solid line), closed flow model with initial condition $h(y, t = 0) = 0.54$ (black dashed line), two-dimensional thin film equation (black circles), and one-dimensional open flow model with linearized curvature (blue dashed line). The vertical black dotted lines identify the minimum thickness locations, that separate the side lobes region and the central lobe. $\tilde{\ell}_c^* = 1$.

lution is $\bar{h}_N = 0.54$. In figure 2.9 (a-b) we show the case of closed flow condition (obtained imposing $\sigma = 0$ in equation (2.15), with the fictitious initial thickness $h(y, t = 0) = 0.54$ (black lines). The comparison reveals that the long-time behavior of the maximum and minimum thickness of the two models is the same, and the profiles are perfectly matching.

The hypothesis of the existence of a saturated state in the streamwise direction is confirmed by our one-dimensional analysis, which agrees with the two-dimensional simulations and consequently with the experimental profiles.

The agreement between the open and closed flow models is related to the evolution of the rivulet profile at long times. The flow rate can be seen as the sum of two contributions, one given by the side lobes region and the other by the central lobe. At long times the relative evolution of the thickness in the central lobe is negligible, in particular in the regions in which the thickness is high. Conversely the side lobe regions are draining. From a more physical point of view, we expect the film to continue thining until intermolecular forces arise ($\approx$ 100nm), which can either lead to de-wetting (as in thermocapillary or Marangoni instability (Scheid, 2013)) or to more complex phenomena (Boos and Thess, 1999; Craster and Matar, 2009). The physics at the molecular scale is out of the scope of this work. The flow rate is related to the cube of the thickness; the contribution of the side lobes region and near y_{min} ($h \sim 10^{-1}$) is negligible compared to the contribution near the maximum height ($h \sim 1$). When the central lobe has saturated, the overall flow rate evolution becomes extremely small. Consequently, $\sigma \simeq 0$, and the mass is eventually also conserved. This leads to a good agreement between open and closed flow conditions with appropriate parameters, $h(y, t = 0) = 0.54$.

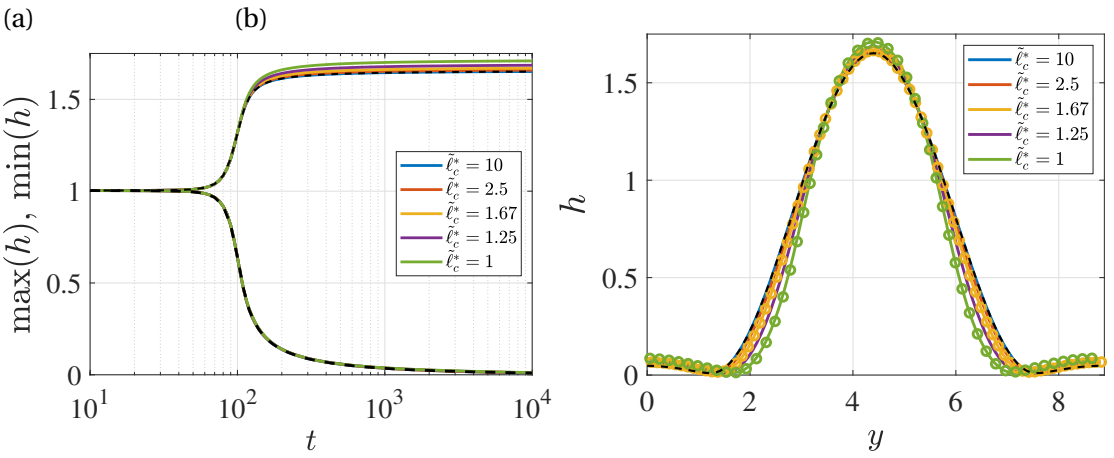

Figure 2.10: (a) Evolution of the maximum and minimum thickness and (b) corresponding rivulet profiles for the open flow model for different $\tilde{\ell}_c^*$. The circles denote the non-dimensionalized profiles of the 2D Stokes simulations with initial thickness that ensures the correct flow rate. The black dashed lines denote the model with linearized curvature, i.e. $\tilde{\ell}_c^* \to \infty$.

The analysis is repeated for different values of $\tilde{\ell}_c^*$. Figure 2.10 shows (a) the evolution in time and (b) the resulting rivulet profiles at $t = 10000$. The rivulet profile depends on $\tilde{\ell}_c^*$ and tends to an attracting profile as $\tilde{\ell}_c^* \to \infty$ (i.e. the thickness goes to zero). The present study can be repeated in the case of linearized curvature, i.e. $\kappa = \frac{\partial^2 h}{\partial y^2}$, which is reported in figure 2.9(b) (blue dashed line) and 2.10 (black dashed lines), for the one-dimensional open flow case. The profiles for different values of $\tilde{\ell}_c^* \to \infty$ indeed collapse to the linearized curvature case, and already for $\tilde{\ell}_c^* = 10$ we do not observe appreciable differences. The model with linearized curvature shows a different profile, and in particular the maximum thickness is underestimated. The use of linearized curvature may lead to a non-correct evaluation of the equivalent Nusselt thickness and the flow rate. In conclusion, there is a family of rivulet profiles which depend weakly on $\tilde{\ell}_c^*$ and tend to the linearized curvature case as $\tilde{\ell}_c^*$ increases.

2.5.4 The two-dimensional static pendent drop

In this section we analyze the static equilibrium of a two-dimensional pendent drop. We consider a two-dimensional thin liquid film on the underside of a wall; we define a coordinate system $(\bar{y}, \bar{z})$, where $\bar{z}$ is the normal direction to the substrate. We introduce a curvilinear abscissa $\bar{s}$ on the interface, and the angle ψ between the interface and the substrate.

The pressure drop at the interface is given by the Laplace law:

$$\bar{p} = \bar{p}_0 - \gamma \frac{\mathrm{d}\psi}{\mathrm{d}\bar{s}} \quad \text{at } \bar{z} = \bar{h}(\bar{s}), \tag{2.18}$$

where γ is the surface tension, and $\bar{p}_0$ the exterior pressure. The normal to the substrate

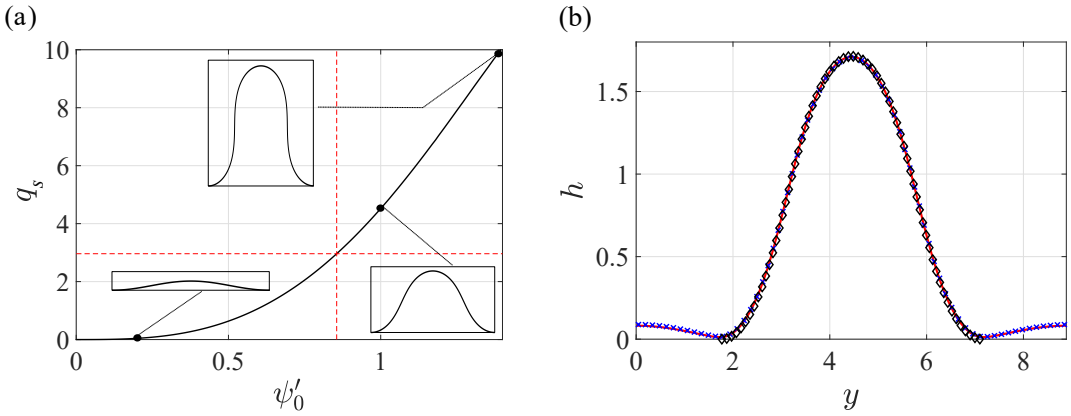

Figure 2.11: (a) Evolution of the equivalent flow rate $q_s = q/\cot(\theta)\tilde{l}_c^*$ with the initial curvature, for different two-dimensional pendent drops, using the pendulum equation; the red dashed lines identify the flow rate and the initial curvature for the rivulet profile. (b) Rivulet profile for the one-dimensional open-flow model (red line), pendulum equation (black diamonds), and Stokes equations (blue crosses). $\tilde{\ell}_c^* = 1$.

component of the momentum equation reads:

$$\frac{\partial \bar{p}}{\partial \bar{z}} = -\rho g \sin(\theta)\bar{z}. \tag{2.19}$$

We derive with respect to $\bar{s}$ the equation (2.18) and we substitute the pressure gradient in equation (2.19) :

$$\gamma \frac{\mathrm{d}^2\psi}{\mathrm{d}\bar{s}^2} = -\rho g \sin(\theta)\frac{\mathrm{d}\bar{z}}{\mathrm{d}\bar{s}} \quad \text{at } \bar{z} = \bar{h}(\bar{s}), \tag{2.20}$$

Using the geometrical relation $\frac{\mathrm{d}\bar{h}}{\mathrm{d}\bar{s}} = \sin(\psi)$, the equation in dimensional forms reads:

$$\frac{\mathrm{d}^2\psi}{\mathrm{d}\bar{s}^2} = -\frac{1}{\ell_c^{*2}}\sin(\psi). \tag{2.21}$$

We non-dimensionalize $\bar{s}$ with respect to the reduced capillary length ℓ_c^* and recover the pendulum equation:

$$\frac{\mathrm{d}^2\psi}{\mathrm{d}s^2} = -\sin(\psi). \tag{2.22}$$

As first pointed out by Maxwell (1875), there is an analogy between the shape of the interface of a pendent drop and the large deformations of a compressed elastic rod (the 'elastica'). Both phenomena are described by the pendulum equation (Duprat and Stone, 2015; Zaccaria et al., 2011; Roman et al., 2020).

We compare the central lobe of the rivulet profile with a two-dimensional pendent drop in total wetting conditions, i.e. $\psi(0) = 0$ and $h(0) = 0$. The thickness and the corresponding spanwise location are recovered integrating $\mathrm{d}h/\mathrm{d}s = -\tilde{\ell}_c^* \sin\psi$ and $\frac{\mathrm{d}y}{\mathrm{d}s} = \cos(\psi)$. The last boundary

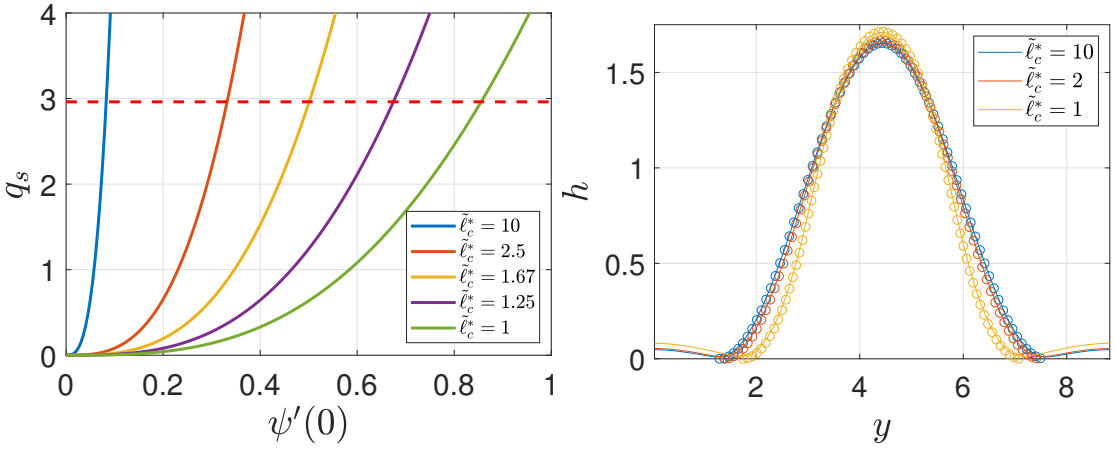

Figure 2.12: Results of the elastica procedure for different $\tilde{\ell}_c^*$. On the left: flow rate q_s as a function of the initial curvature $\psi'(0)$. The red dashed line denotes the rivulet flow rate to be imposed. On the right: comparison of the open flow model (solid lines) with the elastica one (circles).

condition is relative to the initial curvature of the profile: $\frac{d\psi}{ds}(0) = \psi_0'$. The simulation is stopped when a second zero of the thickness $h(s^*) = 0$ is reached; the width ΔL_y between the two zeros is the lateral size of the pendent drop. We initially consider the case $\tilde{\ell}_c^* = 1$. We obtain a family of profiles depending on ψ_0'. Each profile has a different maximum height and width ΔL_y, and thus in equivalent flow rate $q_s = q/\cot(\theta)\tilde{l}_c^*$ (that can be evaluated using equation (2.16),(2.17)). According to figure 2.11(a), the flow rate monotonically increases with the initial curvature: for each value of ψ_0', there is a unique value of the flow rate. Increasing ψ_0' leads to an increase of the maximum thickness and a decrease of ΔL_y. We choose the initial curvature to obtain the correct rivulet flow rate (i.e. $q_s = (1/3)2\pi\sqrt{2} \simeq 2.96$). In this way ,we neglect the flow rate in the side lobes regions. The value of the initial curvature that ensures the correct flow rate is $\psi_0' = 0.86$. In figure 2.11(b) the solution (black diamonds) is compared with the solution of the one-dimensional open flow thin film equation (red solid line, already shown in figure 2.9(b)). The pendulum equation result agrees with the rivulet profile; the maximum height is $\max_y(h) = 1.713$, the first minimum thickness is located at $y_{min} = 1.77$ and $\Delta L_y = 5.346$, close to the thin film equation values ($h_{max} = 1.7096$, $y_{min} = 1.74$, $\Delta L_y = 5.405$). In the thin film equation results, the side lobes regions are draining; the minimum location is moving and ΔL_y is slowly getting closer to the value identified with the pendent drop analogy.

As a final point, we compare the results with a direct numerical simulation of the $2D$ Stokes equation in the (y,z) plane. Using the built-in COMSOL Multiphysics moving mesh solver for the Stokes equations, we study the evolution in the (y,z) plane of a static two-dimensional pendent drop on the underside of a flat wall. The domain is a rectangular box of lateral size $L_y = 2\pi\sqrt{2}$, in which periodic conditions are imposed on the sides. On the upper boundary we apply a no-slip condition, while on the lower one the free-interface conditions. Moreover, the lower boundary is free to deform and move according to the interface deformation. The initial condition is given by the initial mesh, which vertical size is equal to $h(x, t = 0) =$

$\bar{h}_N(1 + A\cos(2\pi y/L_y))$, where $A = 10^{-3}$; $\bar{h}_N = 0.54$ is the equivalent Nusselt thickness that gives the correct flow rate at long times. The results (blue crosses in figure 2.11(b)) agree with the previous models.

The same analysis is repeated for different values of $\tilde{\ell}_c^*$, reported in figure 2.12. The value of the initial curvature ψ_0' that matches the flow rate depends on $\tilde{\ell}_c^*$. The resulting profiles show slight differences and perfectly agree with the central lobe profiles of the open flow model of the previous section. While the side lobes region is characterized by a slowly decreasing small thickness, the central lobe saturates. The shape of the central lobe is governed by the statics of the interface, and in particular by the equilibrium of hydrostatic pressure and capillary effects, described by the pendulum equation. This balance perfectly predicts the rivulet profile.

2.6 Conclusion and discussion

We have built a novel experiment of a continuously flowing viscous film below an inclined flat substrate. We first verified the validity of the simplest thin film equation with a quantitative comparison with experimental thickness profiles obtained with a forcing at the inlet. We measured the perturbation penetration based on a calculation of the front angle, using a standard method (spatial theory) with a novel approach (two-dimensional "spatio-spatial" theory). We found a good agreement with our experiment meaning that the front velocity is dictated by the linear behavior (Van Saarloos, 2003). This front calculation was similar to previous temporal studies of the front velocity below a horizontal substrate (Limat et al., 1992) and of absolute to convective transition below a tilted substrate (Brun et al., 2015). In our case, we exploited the steadiness of the experimental film response to compute a time-independent linear response.

The flow was modeled by a thin film equation, with a low Reynolds number and a curvature term that is not simplified. Numerical simulations showed a good agreement with our experiment. In this equation, short waves were linearly inherently damped by surface tension and non-linear structures quickly saturate when the film becomes thinner. The most unsteady structures are spanwise invariant, as they have an oscillating phase when advected downstream. However, those spanwise structures are non-linearly damped by the system which selects streamwise structures, i.e. stationary rivulets. We observed that the linear wavelength selection mechanism still applies when the film is strongly forced with a non-sinusoidal function. The selected wavelength is chosen among the spatial period of the forcing and its multiples. This selection implies a narrow range of possible rivulets, centered around the most unstable linear wavelength. Within this range we studied the rivulet that has the same period as the most unstable linear wave. We showed that the rivulet profile can be recovered with a flow rate-preserving (open flow condition), one dimensional lubrication equation in the spanwise direction accounting for the full curvature. We managed to obtain exactly the same profile without the open flow condition but with an appropriate initial condition that matches the correct final flow rate (*closed flow condition*). We compared the obtained central rivulet

profile with a 2D pendent drop in total wetting and obtain a perfect agreement. The rivulet shape results from a perfect balance between gravity and surface tension of a two-dimensional drop. We then compare the different models with a 2D DNS of a Stokes flow in a periodic domain and find a good agreement.

In conclusion, we found a wide range of parameters for which rivulets are quasi-saturated and steady while the flat film is linearly convectively unstable. In this case, the thin film is unlikely to drip even though the flat film is linearly unstable. In the whole scenario of dripping of an overhanging liquid, these results suggest that a thin film would not immediately go from a flat state to a dripping state, but rather go by an intermediate state. In a certain range of parameters, the final state would be rivulets that are exactly two-dimensional pendent drops. The dripping might be linked to the secondary instability i.e. the stability of the rivulet itself, more than to the stability of the flat film. In this process, we saw that the dripping could be stabilized by rivulets, but, dripping might also be enhanced by rivulets, which could act as a catalyst.

2.7 Appendix

2.7.1 Spatio-temporal theory

The purpose of this appendix is to show the close link between the "spatio-spatial" dispersion relation $k_x(k_y)$ properties and those of the temporal dispersion relation $\omega(k)$.

We begin by comparing the spatial growth rate $-\mathrm{Im}(k_x(k_y))$ to its temporal approximation $\mathrm{Im}(\omega(k_y))/u$ in figure 2.14(a). For high values of u (the one considered in the present study), the spatial growth rate is very well predicted by the temporal growth rate of a wave advected at the velocity u. We observe a small shift of the dominant wavenumber that we plot as a function of u in figure 2.14(b); the temporal approximation for the dominant wavenumber is valid in our range of u.

In a spatio-temporal theory, we compute the maximum velocity c_{g0} at which an unstable wavepacket can propagate, and similarly to the temporal growth rate prediction, we will assume this wavepacket to be advected at velocity u. Due to the isotropy of the dispersion relation, except within the purely non-dispersive uk_x advection part, the prediction obtained in one dimension of space immediately translates to 2D, i.e. an initially isotropic wavepacket grows with a circular edge invading the flat film at a front velocity of $(u\cos(\alpha)+c_{g0})\mathbf{e}_\alpha$ in any $\mathbf{e}_\alpha$ direction. With the ansatz $h' \propto \mathrm{e}^{(\mathbf{kx}-\omega t)}$ in equation (2.6) , the spatio-temporal dispersion relation reads :

$$\omega(\mathbf{k}) = \frac{i}{3}(|\mathbf{k}|^2 - |\mathbf{k}|^4) + \underbrace{\cot\theta\,\tilde{\ell_c}^*}_{u} k_x. \tag{2.23}$$

We assume ω and k to be complex :

$$\omega_r = \frac{1}{3} k_r \left(k_i (4k_r^2 - 2) - 4k_i^3 + 3u \right), \tag{2.24}$$

$$\omega_i = \frac{1}{3} \left(-k_i^4 + k_i^2 (6k_r^2 - 1) + k_r^2 - k_r^4 \right). \tag{2.25}$$

We then look for a real group velocity $c_g = \frac{\partial \omega_i}{\partial k_i}$, imposing $\frac{\partial \omega_i}{\partial k_r} = 0$ which implies if $k_r \neq 0$:

$$k_r = \sqrt{\frac{6k_i^2 + 1}{2}}, \tag{2.26}$$

and then :

$$c_g = \frac{1}{3}(32k_i^3 + 4k_i). \tag{2.27}$$

In order to determine the fastest velocity at which a perturbation can invade the domain i.e. the front velocity c_{g0}, we look for the velocity on rays where the spatio-temporal growth rate is equal to zero i.e. (Van Saarloos, 2003; King et al., 2016) :

$$\omega_i|_{c_g} = \omega_i - c_{g0} k_i = 0, \tag{2.28}$$

$$c_{g0} = \frac{1}{3} \frac{\sqrt{34 + 14\sqrt{7}}}{\sqrt{27}} \approx 0.54. \tag{2.29}$$

This calculation was done in (Duprat et al., 2007; Brun et al., 2015) and was applied in (Limat et al., 1992) to compute the front velocity of the perturbation in the horizontal case $\theta = \pi/2$.

In the present study, we can focus on a perturbation composed of waves that have their wavevectors (and their group velocity) along the spanwise y direction, $\mathbf{k} = (0, k_y)$ and $\mathbf{c_g} = c_g \mathbf{e_y}$. The fastest group velocity c_{g0} and the downstream advection u are now orthogonal and we define the front angle as :

$$\phi = \arctan \frac{c_{g0}}{u}. \tag{2.30}$$

The resulting ϕ obtained with the spatio-temporal theory is plotted in figure 2.13 along with the front angle computed from the "spatio-spatial" theory used in the study.

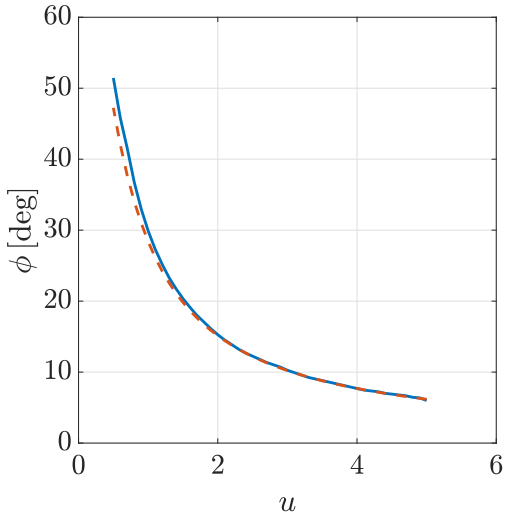

Figure 2.13: Prediction of the front angle ϕ as a function of u according to the "spatio-spatial" theory described in the body of the text (blue curve) and the spatio-temporal theory (dashed red curve).

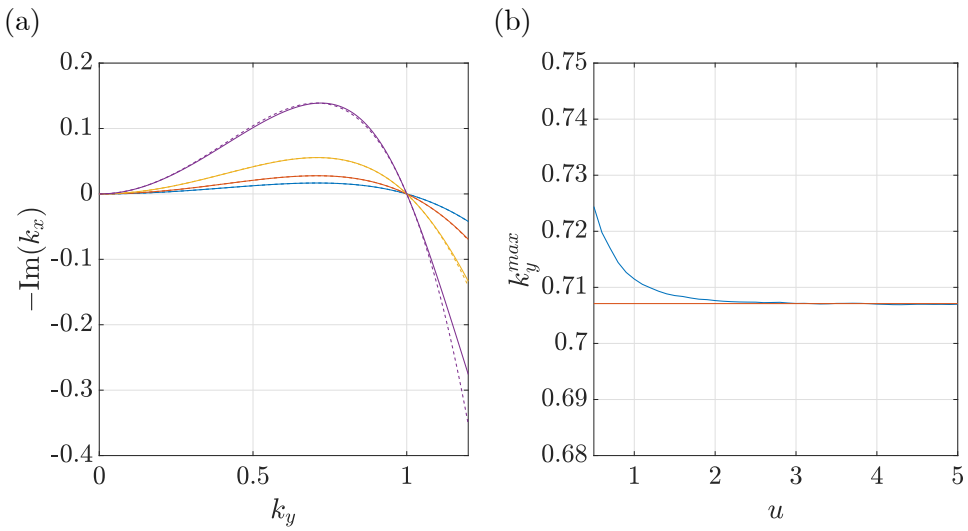

Figure 2.14: (a) Comparison of spatial growth rate to rescaled temporal growth rate $\omega/(3u)$ for different u (from curve with highest to lowest growth rate, $u = 0.6; 1.5; 3; 5$). (b) Comparison as a function of u of the dominant wavenumber $\mathrm{Re}(k_y)$ from the spatial theory (blue) and the temporal theory (red).

3 Instability of a thin viscous film flowing under an inclined substrate: the emergence and stability of rivulets

Remark This chapter is largely inspired by the publications of the same name

P. G. Ledda[1], G. Lerisson[1], G. Balestra[2], F. Gallaire [1]
[1]Laboratory of Fluid Mechanics and Instabilities, École Polytechnique Fédérale de Lausanne, Lausanne, CH-1015, Switzerland
[2]iPrint Institute, University of Applied Sciences and Arts of Western Switzerland, Fribourg, CH-1700, Switzerland

Journal of Fluid Mechanics, **904** , A23 (2020)
Journal of Fluid Mechanics, **926**, E2 (2021)

Authors'contributions G.L. and F.G. conceived the project. P.G.L. performed the theoretical analyses and actively discussed the implications and limitations with coauthors. P.G.L. performed all numerical analyses. P.G.L. also performed the experimental measurements of the rivulet secondary instability. P.G.L. wrote the manuscript with input from the coauthors, guided by F.G..

We study the pattern formation of a thin film flowing under an inclined planar substrate. The phenomenon is studied in the context of the Rayleigh-Taylor instability using the lubrication equation. Inspired by experimental observations, we numerically study the thin film response to a streamwise-invariant sinusoidal initial condition. The numerical response shows the emergence of predominant streamwise-aligned structures, modulated along the direction perpendicular to the flow, called rivulets. Oscillations of the thickness profile along the streamwise direction do not grow significantly when the inclination is very large or the liquid layer very thin. However, for small inclinations or thick films, streamwise perturbations grow on rivulets. A secondary stability analysis of one-dimensional and steady rivulets reveals a strong stabilization mechanism for large inclinations or very thin films. The theoretical results are compared with experimental measurements of the streamwise oscillations of the rivulet profile, showing a good agreement. The emergence of rivulets is investigated by studying the impulse response. Both the experimental observation and the numerical simulation show a marked anisotropy favoring streamwise-aligned structures. A weakly non-linear model is proposed to rationalize the leveling of all but streamwise-aligned structures.

3.1 Introduction

We refer to Section 1.3.3.1 for a general introduction about the Rayleigh-Taylor instability.

In Chapter 2, an experimental set-up able to continuously feed an inclined planar substrate with fluid was presented. Using a very viscous fluid such that inertial effects are negligible, the natural emergence of elongated, streamwise-oriented, steady patterns was observed. A detailed analysis of the appearance of these so-called rivulets was then performed, both when a spanwise periodic forcing is imposed at the inlet and when the rivulets emerge naturally from the lateral boundaries of the experiment. The forced dynamics revealed that there is a narrow range of attainable spacings of rivulets. The non-linear simulations agreed with the thickness measured in experiments, observing steady and streamwise-invariant rivulet states, periodic along the spanwise direction. The one-dimensional and saturated rivulet profile was recovered by simple static arguments, i.e. the equilibrium between capillary effects and hydrostatic pressure gradient (Roman et al., 2020; Zaccaria et al., 2011; Duprat and Stone, 2015). The correct shape was obtained imposing the local flow rate along the direction transverse to the rivulet profile.

In this chapter, we aim at rationalizing the observations of steady rivulet patterns by investigating the *intrinsic* rivulets selection and their stability. The chapter is organized as follows. We first introduce an experimental visualization for the evolution of the film when the inlet is steadily forced along the spanwise direction. A numerical study for an initial condition that mimics these experimental conditions, namely a regular pattern of sinusoidal perturbations in the spanwise direction, is performed. Periodic boundary conditions in all in-plane directions are imposed. The experimental and numerical results are then rationalized by a secondary stability analysis. We perturb the one-dimensional rivulet profile along the streamwise direction with a normal mode expansion and obtain a dispersion relation characterizing the secondary growth of lenses. We thus present a comparison of the secondary stability study with experimental measurements of the spatial amplification of disturbances over steady rivulets. The last section is devoted to the study of the emergence of rivulets from a flat film when the film is impulsively perturbed. We introduce a qualitative experimental visualization when the film is excited by a localized perturbation in the thickness, the results of which are numerically reproduced. A weakly non-linear model is eventually proposed to rationalize these observations.

3.2 Observations of the secondary stability and instability of rivulets

3.2.1 Experimental observations

In this section, we briefly present selected results from Chapter 2, in the presence and absence of the spanwise inlet forcing devices. Figure 3.1(a) shows a film thickness distribution obtained using an absorption technique. The inlet spanwise thickness profile is amplified, and streamwise-saturated and steady rivulets are observed downstream. The saturated rivulets

(a) (b)

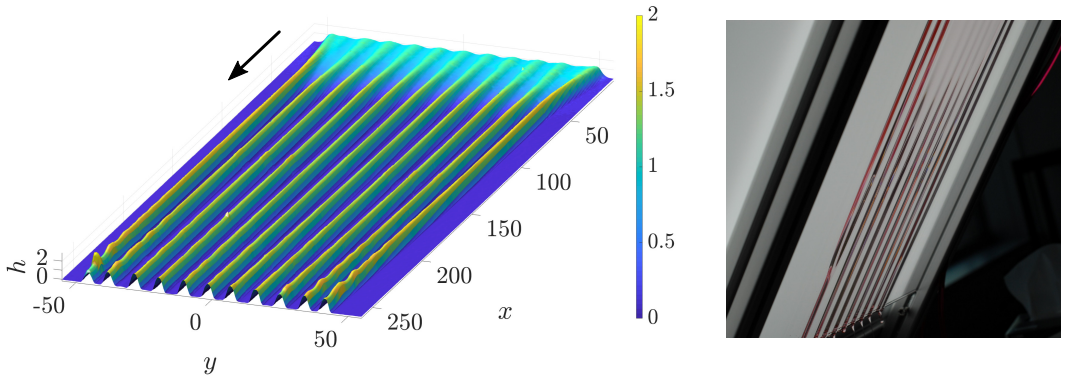

Figure 3.1: (a) Film thickness for $\theta = 39°$ and $h_N = 1515\,\mu$m ($u = 1.5$), steady inlet forcing with the sinusoidal blade at the wavelength $\bar{L}_f = 2\pi\sqrt{2}\ell_c/\sqrt{\sin\theta}$. The thickness is measured with the absorption method and normalized by the flat film thickness h_N. The in-plane distances are normalized by the reduced capillary length $\ell_c/\sqrt{\sin\theta}$. (b) Typical rivulet pattern in the absence of the inlet forcing devices, $\theta = 20°$.

are periodic along the spanwise direction. There is a narrow range of attainable spacings, when the inlet is forced, around the value $\bar{L}_r = 2\pi\sqrt{2}\ell_c^*$ (value shown in figure 3.1(a)), i.e. the most amplified wavelength in the dispersion relation of the flat film. Interestingly, even in the absence of the spanwise inlet forcing devices, the predominant spacing of the emerging rivulet structures is $\bar{L}_r$ (see figure 3.1(b)).

However, far downstream in figure 3.1(a), oscillations appear on the rivulet profiles. These oscillations are amplified and rivulets carrying traveling lenses are observed, for these values of angle and flow rate.

3.2.2 Numerical observations

The aim of this section is to numerically study the emerging patterns for an initial condition that mimics the experimental conditions described in the previous section.

We consider a gravity-driven thin film of viscous Newtonian fluid flowing under a planar substrate inclined with respect to the vertical with an angle θ. We introduce the following adimensionalization:

$$x = \bar{x}/\ell_c^*;\ y = \bar{y}/\ell_c^*;\ z = \bar{z}/h_N;\ t = \bar{t}/\tau, \tag{3.1}$$

where $\tau = \nu\ell_c^2/h_N^3\sin^2(\theta)g$ is the characteristic time scale of the Rayleigh-Taylor instability. The numerical model for the evolution of the film thickness h is the lubrication equation in which the complete expression of the curvature is retained (Ruschak, 1978; Wilson, 1982;

Weinstein and Ruschak, 2004):

$$\partial_t h + u h^2 \partial_x h + \frac{1}{3}\nabla \cdot \left[h^3 \nabla h + h^3 \nabla \kappa \right] = 0, \tag{3.2}$$

where ∇ operates in the (x, y) directions, $u = \cot(\theta)\tilde{\ell}_c^*$ and $\tilde{\ell}_c^* = \ell_c^* / h_N$. The linear advection velocity u corresponds to the surface film velocity at which linear interface thickness perturbations with respect to a flat condition are advected downstream (Brun et al., 2015). In physical quantities, an increase of the parameter u implies a decrease of the flow rate (since u is inversely proportional to h_N) or θ. The curvature κ reads:

$$\kappa = \frac{\partial_{xx} h \left(1 + \left(\frac{1}{\tilde{\ell}_c^*}\partial_y h\right)^2\right) + \partial_{yy} h \left(1 + \left(\frac{1}{\tilde{\ell}_c^*}\partial_x h\right)^2\right) - 2\left(\frac{1}{\tilde{\ell}_c^*}\right)^2 \partial_{xy} h \partial_x h \partial_y h}{\left(1 + \left(\frac{1}{\tilde{\ell}_c^*}\partial_x h\right)^2 + \left(\frac{1}{\tilde{\ell}_c^*}\partial_y h\right)^2\right)^{3/2}}. \tag{3.3}$$

The two-dimensional equation is implemented in COMSOL Multiphysics. We use the built-in Finite Elements Method solver, exploiting cubic elements with Lagrangian shape functions and a fully implicit time solver. The largest mesh element size is half of the reduced capillary length $\tilde{\ell}_c^*$. The domain size is $L_x \times L_y$, where $L_x = 231$ and $L_y = 106$, leading to approximately 50000 elements. A convergence analysis was performed, showing that convergence is achieved for this characteristic size of the elements. The equations are solved for the variables (h, κ). For all the considered cases, periodic boundary conditions are used.

Experimentally, in the absence of spanwise inlet perturbation devices, the rivulet spacing is the one dictated by the most amplified mode in the flat film dispersion relation, i.e. $L_r = 2\pi\sqrt{2}$. We numerically study the non-linear time evolution when a streamwise-invariant sinusoidal initial condition is considered. We choose as initial condition a sinus of wavelength $L_r = 2\pi\sqrt{2}$:

$$h(x, y, t = 0) = \bar{h}_N \left(1 + \mathrm{A}\cos\left(\frac{2\pi y}{L_r}\right)\right), \tag{3.4}$$

where $\mathrm{A} = 10^{-2}$, and $\bar{h}_N = 0.54$ is the initial value of the thickness that gives, for a pure streamwise saturated structure, the same local flow rate in the streamwise direction as a flat film of thickness $h = 1$ in the case $\tilde{\ell}_c^* = 1$.

We introduce the moving reference frame at the linear advection velocity u ($\xi = x - ut, y$). Figure 3.2 shows the evolution of the thickness with time for $\tilde{\ell}_c^* = 1$ and (a) $u = 5.45$ and (b) $u = 1.5$. For visualization purposes, we focus in the region $\xi \in [-8\pi\sqrt{2}, 8\pi\sqrt{2}]$ and $y \in [-6\pi\sqrt{2}, 6\pi\sqrt{2}]$. In both cases, the streamwise invariant initial condition is amplified and reaches, at $t = 800$, a saturated state in the streamwise direction. For (a) $u = 5.45$, we do not observe any further evolution of the pattern for $t > 800$. For (b) $u = 1.5$, at $t = 800$ the rivulet profiles saturate. For $t > 800$, however, streamwise thickness perturbations grow, and at $t = 1200$ the flow is characterized by lenses traveling on the rivulets.

The streamwise-invariant sinusoidal initial condition is amplified leading to a rivulet pattern

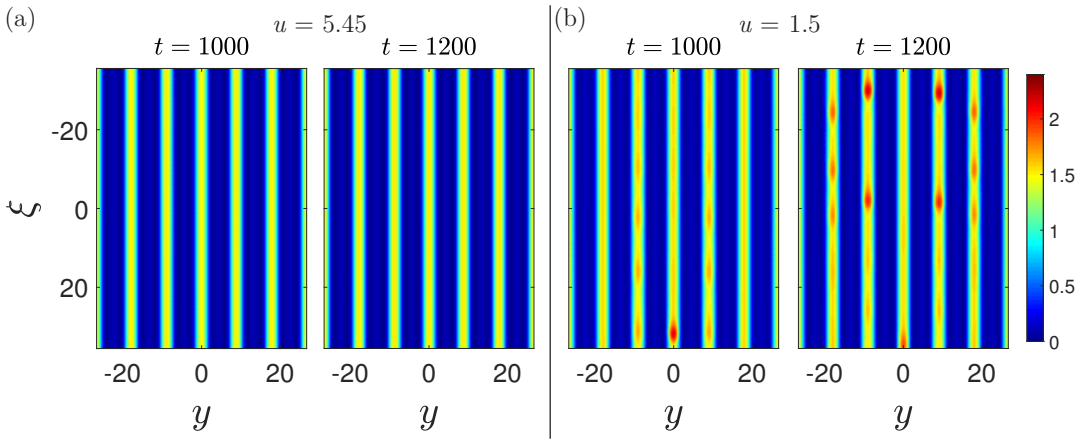

Figure 3.2: Non-linear response in the case of a streamwise-invariant sinusoidal initial condition, for $\tilde{\ell}_c^* = 1$ and (a) $u = 5.45$ and (b) $u = 1.5$. From left to right: $t = 1000$, $t = 1200$. Results are reported in the moving reference frame at the linear advection velocity ($\xi = x - ut, y$).

saturated in space and time, periodic along the spanwise direction. The experimental observations of predominant spanwise-periodic rivulet patterns and the occurrence of lenses on the rivulets are confirmed by the non-linear simulations with periodic boundary conditions. In the following, we aim at rationalizing the emergence of predominant rivulets structures and their destabilization.

3.3 Secondary stability analysis of rivulets

In Section 3.2.1 it was experimentally shown that rivulet structures grow in the domain and saturate to a steady and spanwise-periodic state, invariant along the streamwise direction. However, for low values of u and/or $\tilde{\ell}_c^*$, and at large distances from the inlet, the rivulet profile undergoes an instability and traveling lenses emerge on the rivulet structures, as shown in figure 3.1(a). The saturation of the rivulet structures and the occurrence of lenses were also observed in the non-linear numerical simulation of figure 3.2. No lateral interactions between rivulets are observed as the lenses grow. Here, we study the robustness of the saturated rivulet pattern via a secondary stability analysis. We first introduce the steady, streamwise-invariant and spanwise-periodic rivulet profile $H_r(y)$, and then we focus on its *local* stability properties when perturbed along the streamwise direction x. The validity of the local stability analysis is limited to the regions where steady and one-dimensional rivulets are observed.

3.3.1 Baseflow

In this section, we define the saturated rivulet profile $H_r(y)$, serving as baseflow for the local stability analysis. The numerical baseflow is the large-time solution ($t = 10000$) of the one-dimensional model presented in Section 2.5.3. The profile, of periodic wavelength L_r, is given

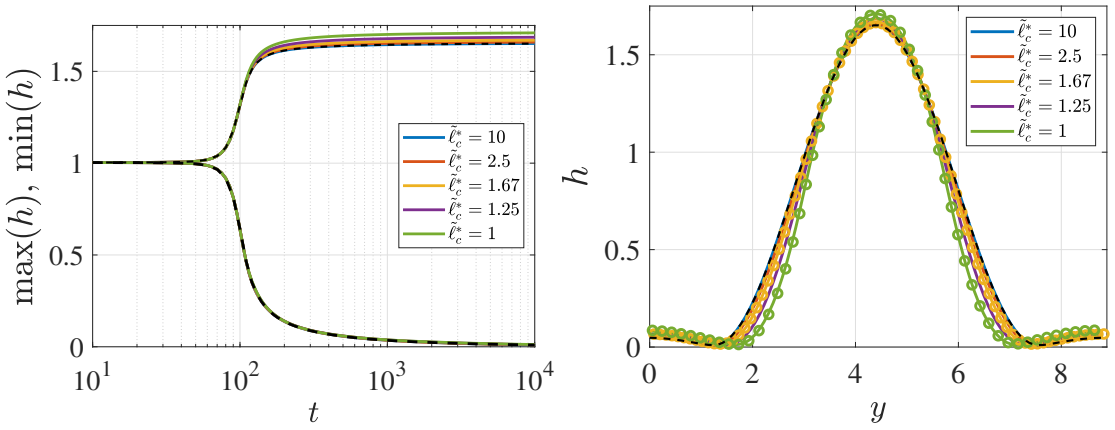

Figure 3.3: Evolution of the maximum and minimum thickness (on the left) and corresponding rivulet profiles (on the right) for the open flow model for different $\tilde{\ell}_c^*$ of Section 2.5.3. The circles denote the non-dimensionalized profiles of the 2D Stokes simulations with initial thickness that ensures the correct flow rate. The black dashed lines denote the model with linearized curvature, i.e. $\tilde{\ell}_c^* \to \infty$.

by a one-dimensional model in which the flow rate in the streamwise direction coincides with the one of a flat film of thickness $h = 1$, leading to a mean value $\bar{h}_N < 1$, which depends on $\tilde{\ell}_c^*$, of the thickness of the rivulet. The numerical procedure revealed that the rivulet profile is slowly saturating to a steady state $H_r(y)$. In figure 3.3, we report some numerical periodic profiles for different values of $\tilde{\ell}_c^*$ and $t = 10000$ (solid line), used for the stability analysis. The rivulet is characterized by a central lobe of large thickness that saturates to a steady profile described by the pendulum equation (red circles in figure 3.3), while the side lobes (of very low thickness) are slowly draining with a power-law $t^{-1/2}$ (Lister et al., 2010). It is remarkable that, with the considered adimensionalization, the profiles are independent of u while still depend on $\tilde{\ell}_c^*$. The numerical profile 3.3 will be used as baseflow $H_r(y)$ for the stability analysis.

3.3.2 Dispersion relation

Following the classical approach of the local stability analysis, we consider as a base state the single, spanwise-periodic and steady rivulet $H_r(y)$ described in the previous Section 3.3.1. The quasi-steadiness of the rivulet profile allows us to neglect the slow evolution of the side lobes at long times and thus to consider a normal mode expansion in time and along the direction in which the base state is invariant, i.e. the streamwise direction x (Schmid et al., 2002). The spanwise periodicity governing the base state $H_r(y)$ is also enforced on the perturbation. The following normal mode decomposition is therefore used:

$$h(x,y,t) = H_r(y) + \varepsilon\tilde{\eta}(x,y,t) = H_r(y) + \varepsilon\eta(y)e^{\mathrm{i}(k_x x - \omega t)}, \quad \varepsilon \ll 1, \tag{3.5}$$

where $\tilde{\eta}$ is the thickness perturbation with respect to the baseflow profile $H_r(y)$. By considering the two-dimensional non-linear equation equation (3.2) and introducing the normal mode

decomposition equation (3.5), one obtains, up to $\mathcal{O}(\varepsilon)$:

$$\varepsilon\partial_t\tilde{\eta}+\varepsilon u H_r^2\partial_x\tilde{\eta}+\frac{1}{3}\partial_y\left[H_r^3\left(\frac{\mathrm{d}H_r}{\mathrm{d}y}+\frac{\mathrm{d}\kappa_{(0)}}{\mathrm{d}y}\right)+\varepsilon H_r^3\partial_y\tilde{\eta}\right.$$
$$\left.+\varepsilon H_r^3\partial_y\tilde{\kappa}_{(1)}+3\varepsilon H_r^2\left(\frac{\mathrm{d}\kappa_{(0)}}{\mathrm{d}y}+\frac{\mathrm{d}H_r}{\mathrm{d}y}\right)\tilde{\eta}\right]+\frac{\varepsilon}{3}\partial_x\left[H_r^3(\partial_x\tilde{\kappa}_{(1)}+\partial_x\tilde{\eta})\right]=0, \quad (3.6)$$

where $\kappa_{(0)}$ is the baseflow curvature, i.e. equation (3.3) evaluated for the baseflow $H_r(y)$, $\kappa_{(0)}=\frac{\mathrm{d}^2H_r}{\mathrm{d}y^2}/(1+(\frac{\mathrm{d}H_r}{\mathrm{d}y})^2)^{3/2}$. Furthermore, $\tilde{\kappa}_{(1)}$ is the first order term of the curvature, i.e. the Jacobian of the curvature evaluated in the baseflow and applied to $\tilde{\eta}$ ($\tilde{\kappa}_{(1)}=[\partial_{\tilde{\eta}}\kappa(H_r)]\tilde{\eta}$). Deriving this expression with respect to x and y, we obtain $\partial_x\tilde{\kappa}_{(1)}=\mathrm{i}k_x\kappa_{(1)}(y)\exp(\mathrm{i}(k_xx-\omega t))$ and $\partial_y\tilde{\kappa}_{(1)}=\frac{\mathrm{d}\kappa_{(1)}}{\mathrm{d}y}(y)\exp(\mathrm{i}(k_xx-\omega t))$.

At $\mathcal{O}(1)$ the baseflow equation is recovered, while at $\mathcal{O}(\varepsilon)$ one obtains the following evolution equation for the perturbation:

$$-\mathrm{i}\omega\eta+\mathrm{i}k_xuH_r^2\eta+\frac{1}{3}\frac{\mathrm{d}}{\mathrm{d}y}\left[3H_r^2\left(\frac{\mathrm{d}H_r}{\mathrm{d}y}+\frac{\mathrm{d}\kappa_{(0)}}{\mathrm{d}y}\right)\eta\right.$$
$$\left.+H_r^3\left(\frac{\mathrm{d}\kappa_{(1)}}{\mathrm{d}y}+\frac{\mathrm{d}\eta}{\mathrm{d}y}\right)\right]-\frac{1}{3}k_x^2\left[H_r^3\left(\kappa_{(1)}+\eta\right)\right]=0, \quad (3.7)$$

which is the dispersion relation $D_r(\omega,k_x)=0$. The baseflow $H_r(y)$ can be perturbed (i) imposing the streamwise wavenumber $k_x\in\mathbb{R}$ and looking at the temporal evolution through the complex frequency $\omega\in\mathbb{C}$ (*temporal stability analysis*) or (ii) imposing a temporal forcing of real frequency ω and looking at the spatial amplification of the perturbation, embodied by the complex spatial wavenumber $k_x\in\mathbb{C}$ (*spatial stability analysis*).

The numerical implementation of equation (3.7) is performed in MATLAB by a spectral collocation Fourier method. Once discretized, the eigenfunction problem (3.7) becomes an eigenvalue problem. The temporal and spatial stability analyses are respectively solved using the built-in MATLAB functions *eig* and *polyeig*. Numerical convergence is achieved for 100 collocations points. A preparatory analysis on the numerical rivulet profile $H_r(y)$ used as baseflow for the stability analysis revealed a variation of the eigenvalues of the order of the numerical discretization, as long as $t>5000$.

3.3.3 Effect of the linear advection velocity

In this section, we study the effect of the linear advection velocity u on the stability properties of the one-dimensional rivulet profile $H_r(y)$, with fixed $\tilde{\ell}_c^*=1$.

3.3.3.1 Temporal stability analysis

We report the results for the temporal stability analysis. Positive (resp. negatives) values of the temporal growth rate $\mathrm{Im}(\omega)=\omega_i$ denote unstable (resp. stable) wavenumbers. A preliminary

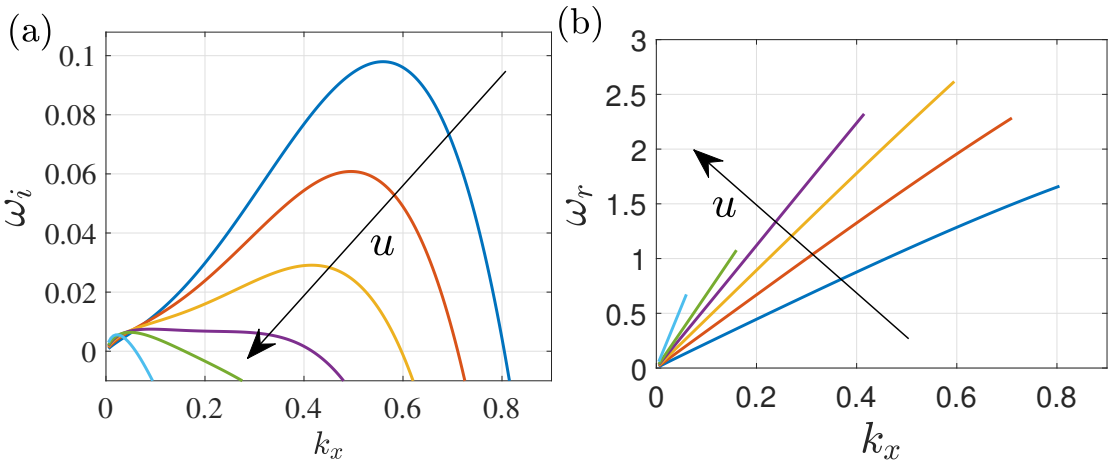

Figure 3.4: (a) Temporal growth rate ω_i and (b) real frequency ω_r as functions of the streamwise wavenumber k_x, from the temporal stability analysis, for $u = 1$ (blue line), $u = 1.5$ (red line), $u = 2$ (yellow line), $u = 2.5$ (purple line), $u = 3$ (green line), $u = 5$ (light blue line).

analysis on the spectrum revealed that all the eigenvalues have negative ω_i for all k_x, except one that is analyzed in the following.

In figure 3.4(a) we report the variation of ω_i with k_x, for different values of u. The dispersion relations are characterized by a local maximum associated with the *dominant* wavenumber, and by a value of the wavenumber beyond which the temporal growth rate is negative (the *cut-off* wavenumber), i.e. perturbations with wavenumber larger than the cut-off are damped. Rivulets are strongly stabilized as the value of u increases. For $u = 1$ the growth rate ω_i presents its maximum value at a dominant wavenumber close to $k_x = 0.56$, while the cut-off wavenumber $k_x^{cut} = 0.8$. An increase of u quickly quenches large wavenumbers. Both the dominant growth rate and the cut-off wavenumber decrease. At $u = 5$, $k_x^{cut} \sim 10^{-2}$, with $\max(\omega_i) \sim 10^{-3}$. For these values of u, the unstable wavelengths are of the order of one hundred reduced capillary lengths. The real frequency $\mathrm{Re}(\omega) = \omega_r$ increases slightly less than linearly with k_x (figure 3.4(b)). The resulting phase velocities ω_r / k_x increase as u increases.

In figure 3.5(a) we show the real (dashed-dotted line) and imaginary (dashed line) parts of the mode $\eta(y)$ for the dominant wavenumber $k_x = 0.5$, normalized by the maximum modulus $\max(|\eta|)$, for $u = 1.5$. The mode is non-zero only in the steady central lobe region. For the same value of u, in figure 3.5(b) we report a three-dimensional plot of the linear combination of the baseflow $H_r(y)$ (extended in the x direction along which it is invariant) with the mode at the dominant wavenumber (normalized by the maximum modulus), i.e. $h(x, y) = H_r(y) + \mathrm{ARe}\left(\eta(y) \exp(\mathrm{i}k_x x)\right)$, with $\mathrm{A} = 0.25$ an arbitrary amplitude for visualization purposes. The resulting pattern is characterized by rivulets that carry lenses. The temporal dependence of the mode, which is not represented in figure 3.5(b), is characterized by a growing amplitude $\exp(\omega_i t)$ and by an oscillating behavior $\exp(\mathrm{i}\omega_r t)$. The presence of a non-zero real part of ω (figure 3.4(b)) implies that the perturbations are oscillating in time at fixed locations. This effect is related to the advection as lenses are traveling along the streamwise

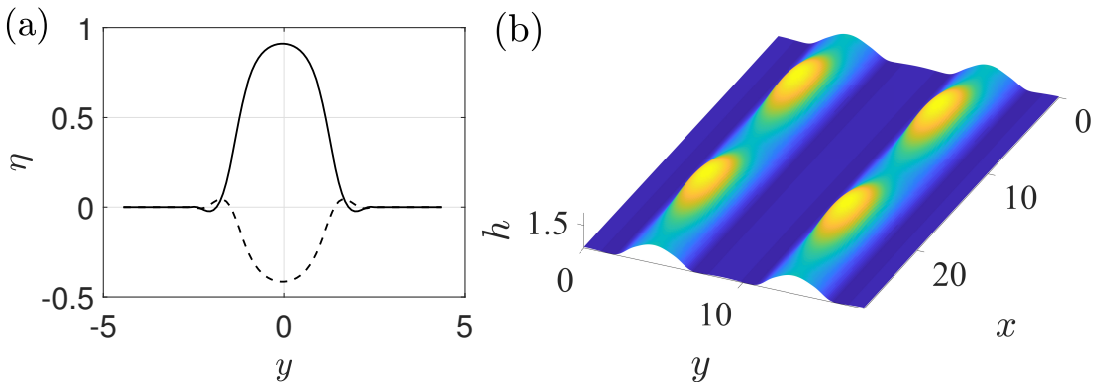

Figure 3.5: Temporal stability analysis, $u = 1.5$. (a) Real (solid line) and imaginary (dashed line) parts of the eigenvector $\eta(y)$, for the dominant wavenumber $k_x = 0.5$, normalized by the maximum modulus. (b) Linear combination of the baseflow $H_r(y)$ (extended in the x direction along which it is invariant) with the mode at the dominant wavenumber (normalized with the maximum modulus), i.e. $h(x,y) = H_r(y) + A\mathrm{Re}\left(\eta(y)\exp(\mathrm{i}k_x x)\right)$. $A = 0.25$ is an arbitrary amplitude for visualization purposes.

direction.

The stability analysis reveals the occurrence of a secondary instability of the saturated and one-dimensional rivulets, which is located in the steady central lobe and leads to a pattern characterized by lenses that travel on the rivulets. Nevertheless, an increase in the advection u induces a very strong stabilization and only very large wavelengths remain slightly unstable. The stabilization is related to the advection term. In particular, perturbations in regions of different thickness experience different advection velocities, proportional to uH_r^2 (Kalliadasis et al., 2011). Regions of higher thickness travel faster than regions of lower thickness, leading to a steepening of the interface profile and eventually to a capillary leveling of perturbations. This steepening-leveling mechanism is all the more pronounced as u is large. Small wavelengths, which present high interface gradients, are progressively stabilized with u, leading to a cut-off wavelength of the order of $10^2\ell_c^*$ at $u = 5$. In the numerical simulation of figure 3.2(a) the resulting pattern does not show any appreciable streamwise perturbations since the cut-off wavelength ($L_c = 2\pi/k_x^{cut} \approx 2\times 10^2$) is of the order of the maximum acceptable wavelength fitting in the domain.

3.3.3.2 Spatial stability analysis

We study the spatial stability properties of the rivulet baseflow $H_r(y)$ introduced in Section 3.3.1. The saturated rivulet profile is perturbed with a temporal harmonic perturbation of real frequency $\omega = \omega_r$ and we look for the spatial evolution of the perturbation, in terms of spatial growth rate $-\mathrm{Im}(k_x)$ and streamwise wavenumber $\mathrm{Re}(k_x)$ through the dispersion relation $D_r(k_x,\omega)$ (equation (3.7)). Positive values of the spatial growth rate denote unstable configu-

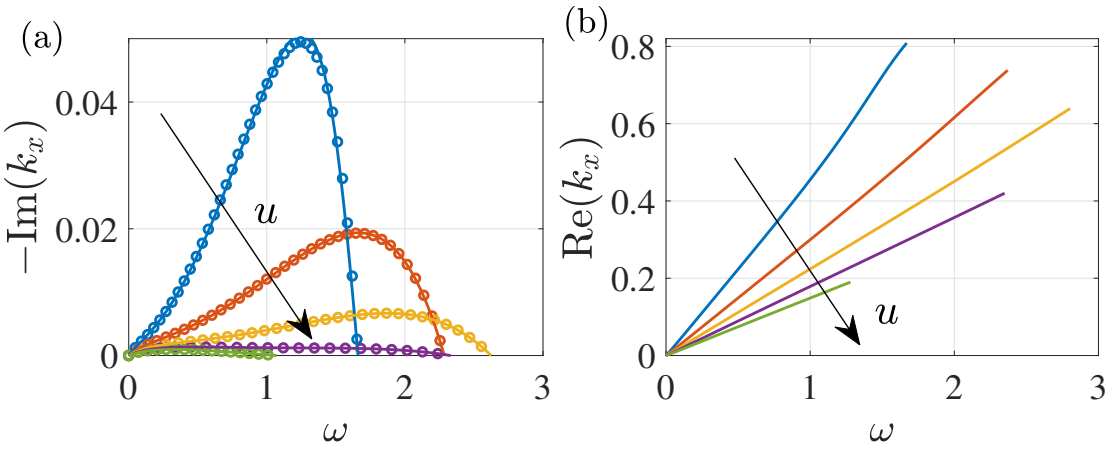

Figure 3.6: (a) Spatial growth rate and (b) streamwise wavenumber as functions of ω, from the spatial stability analysis, for $u = 1$ (blue line), $u = 1.5$ (orange line), $u = 2$ (yellow line), $u = 2.5$ (purple line), $u = 3$ (green line). The circles identify the values of the spatial growth rate obtained by the Gaster transformation.

rations associated with downstream propagating waves (Huerre and Rossi, 1998; Schmid et al., 2002; Gallaire and Brun, 2017). The spectrum is characterized by only one unstable mode associated with downstream propagating waves, which is described in the following.

In figure 3.6(a) we report the spatial growth rate $-\mathrm{Im}(k_x)$ as a function of ω. The spatial growth rate presents a behavior similar to the temporal growth rate of Section 3.3.3.1, i.e. characterized by a maximum (*dominant*) value and a cut-off frequency beyond which perturbations are damped. The dominant value of $-\mathrm{Im}(k_x)$ strongly decreases with u, while its associated dominant frequency presents a non-monotonous behavior. The same non-monotonous behavior is observed in the cut-off frequency. The streamwise wavenumber $\mathrm{Re}(k_x)$ (figure 3.6(b)) shows, with a good approximation, a linear dependence with ω. For fixed ω, the value of $\mathrm{Re}(k_x)$ decreases with u.

The results of the spatial stability analysis are compared with those of the temporal stability analysis, suitably rescaled by the Gaster transformation (Gaster, 1962), valid for strongly convectively unstable systems (see Appendix 3.7.1 for details). Within this approximation, from the temporal stability analysis of Section 3.3.3.1 (labeled with (T)) we retrieve the spatial stability analysis properties (labeled with (S)) through the relations:

$$\omega_r(S) = \omega_r(T), \quad \mathrm{Re}(k_x(S)) = \mathrm{Re}(k_x(T)), \quad \mathrm{Im}(k_x(S)) = -\frac{\omega_i(T)}{\frac{\partial \omega_r}{\partial k_x}(T)}, \tag{3.8}$$

The results of the Gaster transformation equation (3.8) (circles) are in good agreement with the spatial stability analysis results in figure 3.6(a), for $u > 1$. In Appendix 3.7.1 we report the results for $u < 1$, where the Gaster transformation prediction deviates from the spatial stability analysis results.

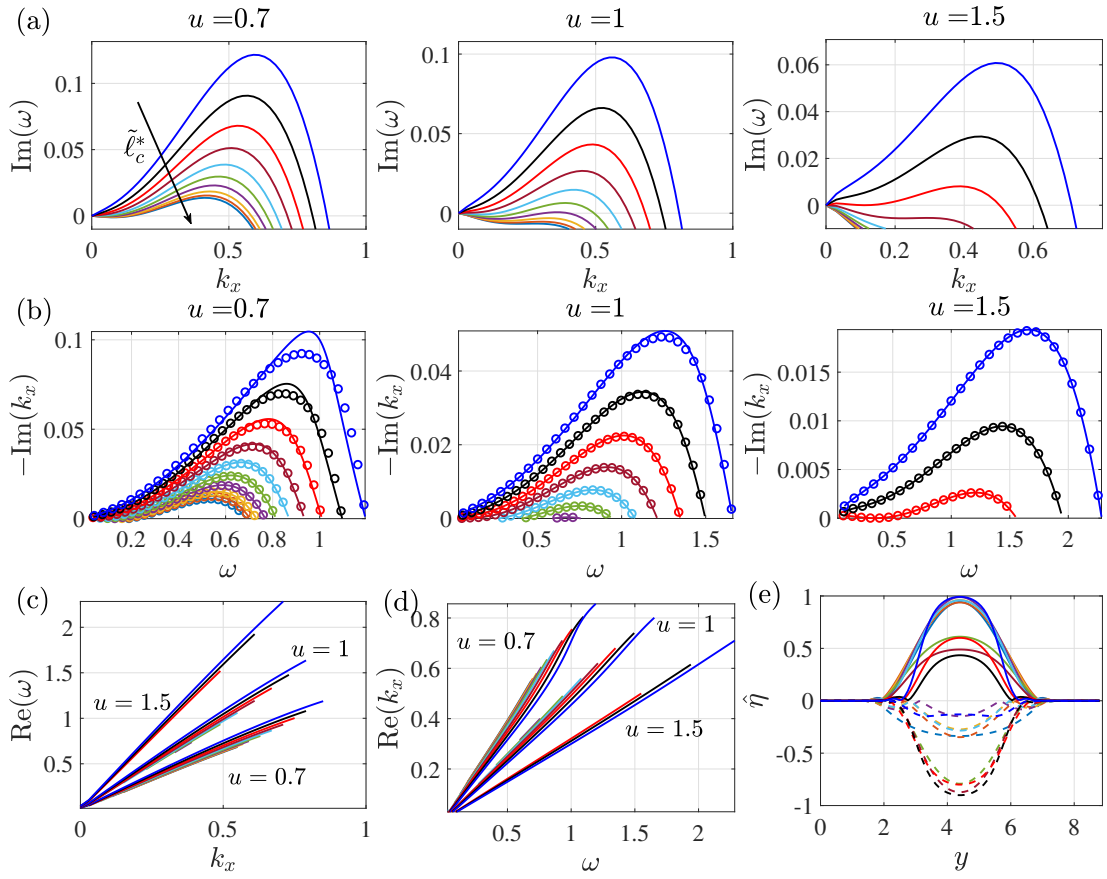

Figure 3.7: Results of the linear stability analysis for varying $\tilde{\ell}_c^*$. (a) Temporal stability analysis: temporal growth rate as a function of k_x. (b): Spatial growth rate from the spatial stability analysis (lines) and from the Gaster transformation (circles) as a function of ω. (c) Real part of the complex frequency from the temporal approach as a function of k_x. (d) Variation of $\mathrm{Re}(k_x)$ with ω, for the spatial approach. (e) Most unstable mode for $u = 0.7$ and varying $\tilde{\ell}_c^*$, real (solid lines) and imaginary (dashed lines) parts, for the temporal approach. The different colours correspond to $\tilde{\ell}_c^* = 1$ (blue), $\tilde{\ell}_c^* = 1.1$ (black), $\tilde{\ell}_c^* = 1.25$ (red), $\tilde{\ell}_c^* = 1.43$ (maroon), $\tilde{\ell}_c^* = 1.67$ (cyan), $\tilde{\ell}_c^* = 2$ (green), $\tilde{\ell}_c^* = 2.5$ (purple), $\tilde{\ell}_c^* = 3.33$ (yellow), $\tilde{\ell}_c^* = 5$ (orange), $\tilde{\ell}_c^* = 10$ (light blue).

3.3.4 Effect of $\tilde{\ell}_c^*$

We complete the analysis by reporting in figure 3.7 the results of the linear temporal and spatial stability analyses for different values of $\tilde{\ell}_c^*$. The temporal stability analysis (i.e. $k_x \in \mathbb{R}$ is fixed and one looks for $\omega \in \mathbb{C}$) shows a reduction of the temporal growth rate $\mathrm{Im}(\omega)$ as $\tilde{\ell}_c^*$ increases. This reduction yields to the complete quenching of the secondary instability for sufficiently large u and $\tilde{\ell}_c^*$. Similarly, the spatial stability analysis (i.e. $\omega \in \mathbb{R}$ is fixed and one looks for $k_x \in \mathbb{C}$) shows an analogous reduction of the spatial growth rate $-\mathrm{Im}(k_x)$ with $\tilde{\ell}_c^*$. In contrast, $\mathrm{Re}(\omega)$ in the temporal approach and $\mathrm{Re}(k_x)$ in the spatial one do not vary significantly with increasing $\tilde{\ell}_c^*$.

An increase of $\tilde{\ell}_c^*$, with fixed advection u, leads to a decrease of the film thickness and thus

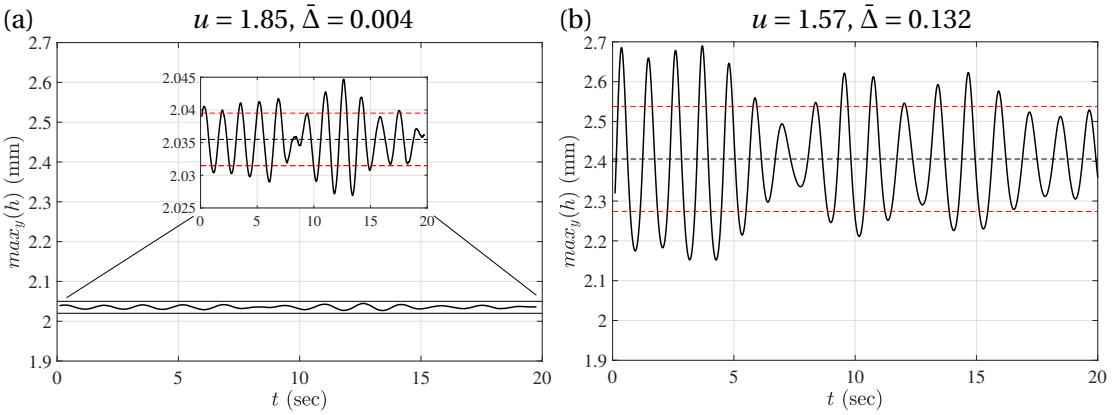

Figure 3.8: Registered maximum height $\bar{h}_{max}(t)$ of the rivulet, for (a) $\theta = 40°$ and $h_N = 1190\,\mu$m , (b) $\theta = 40°$ and $h_N = 1418\,\mu$m. The black dashed line denotes $\hat{\bar{h}}$, and the red dashed lines $\hat{\bar{h}} \pm \bar{\Delta}$.

of the hydro-static pressure gradients due to the gravity component normal to the substrate. As a consequence, the growth rates are reduced and the flow is thus stabilized. However, the quantities Re(ω) and Re(k_x) are directly related to the advection of perturbations, which is dominated by u.

In the following, we experimentally investigate the link between the spatial stability analysis and the observable dynamics.

3.4 Experimental measurements of the rivulet secondary instability

3.4.1 Methods

As described in Section 3.2.1, steady rivulets invade the experiment and saturate along the streamwise direction (figure 3.1). At a certain distance from the inlet, streamwise oscillations on the rivulet profiles grow and evolve in traveling lenses. We investigate the dependence of the overall dynamics and the amplitude of lenses with the parameters, by exploring different angles $40° < \theta < 80°$ and thicknesses in the range $0.12 < h_N/\ell_c < 1$.Note that $u = \frac{\cot(\theta)\ell_c}{\sqrt{\sin\theta}h_N}$, i.e. high values of the linear advection velocity correspond to low values of the flow rate or θ. We modify the inlet condition using the spanwise comb-like blade with the optimal spacing predicted by the flat film linear dispersion relation, i.e. $\bar{L}_r = 2\pi\sqrt{2}\ell_c^*$. The requirement of a reasonably small and constant error in a large range of the flow parameters, exempted from a case-dependent calibration procedure, makes the STIL-CCS confocal chromatic sensor a suitable candidate. The latter is placed at the end of the plate to measure the variation of the amplitude of lenses oscillations as a function of θ and h_N/ℓ_c.

The procedure is the following. We place the comb in position, and we wait the time necessary for rivulets to invade the whole domain. We then measure the central rivulet maximum

thickness $\bar{h}_{max}(t)$ for 20 periods. This leads to a registration time T that goes from 20 to 2000 seconds, depending on the angle. Once the data are registered, the flow rate is increased. We wait the time necessary to advect all the transient effects away from the glass plate; it varies from one minute, for $\theta = 40°$, to one hour, for $\theta = 80°$. Assuming the saturated rivulet profile (figure 3.3), we transform the point measurement of the maximum thickness in an estimate of the integral flux (i.e. h_N) by introducing the average thickness $\hat{\bar{h}}$ as follows:

$$\hat{\bar{h}} = \left(\frac{3}{T} \int_0^T \frac{\bar{h}_{max}^3(t)}{3} dt \right)^{1/3}, \quad h_N \approx \hat{\bar{h}}/1.71, \tag{3.9}$$

being $\bar{h}_{max} \approx 1.71 h_N$ for a steady and saturated one-dimensional rivulet with $\tilde{\ell}_c^* = 1$. The deviation $\bar{\Delta}$ from the average thickness value is computed as:

$$\bar{\Delta} = \sqrt{\frac{1}{T} \int_0^T \left(\bar{h}_{max}(t) - \hat{\bar{h}} \right)^2 \mathrm{d}t}, \tag{3.10}$$

which is adimensionalized using the capillary length, i.e. $\Delta = \bar{\Delta}/\ell_c$. Two typical measurements are reported in figure 3.8.

3.4.2 Results

In figure 3.9 we report the deviation Δ as a function of h_N/ℓ_c, for different angles θ. At low values of h_N/ℓ_c, Δ is constant at a *plateau* value around $\Delta \sim 10^{-3}$. The plateau corresponds to the resolution of the optical sensor and is of order $1\,\mu$m. At higher values of h_N/ℓ_c, Δ increases with h_N/ℓ_c. We measure an increase of Δ of two decades.

The amplitude of the oscillations at the end of the plate is compared with the theoretical findings of the spatial stability analysis. The spatial amplification at a distance x of a temporal perturbation Δ_0 on a fully-developed rivulet profile reads:

$$\Delta/\Delta_0 = \exp(-\mathrm{Im}(k_x)x). \tag{3.11}$$

We assume that the observable disturbances are the inlet ones as they are amplified on the largest distance, i.e. $x = L$. The perturbation amplitude Δ_0 originates from background noise that is below the sensitivity of our measurement sensor ($\sim 1\mu$m). We assume that the noise triggers the dominant mode described in Sections 3.3.3.1 and 3.3.3.2,and that Δ_0 is constant for a fixed angle. Note that the dominant spatial growth rate changes with h_N/ℓ_c since the value of u is varied.

In figure 3.9 the red lines denote the theoretical values of Δ for an inlet perturbation amplitude Δ_0 chosen as the saturation value of the optical sensor, varying slightly from one set of experiments to the other. The theoretical amplification follows the same trend as the experimental one. We also include errorbars, which reflect the relative tolerance in the measurement of

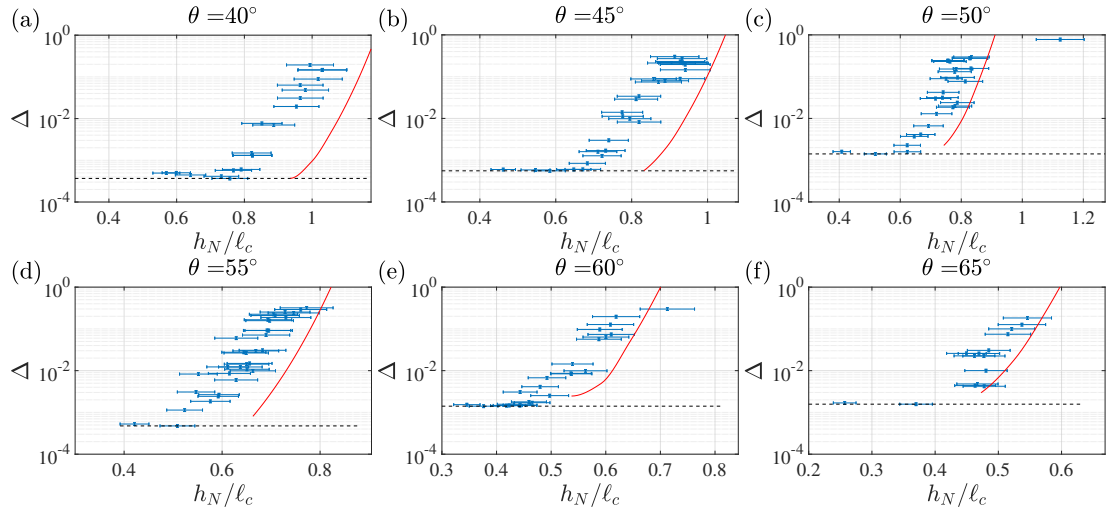

Figure 3.9: Values of Δ (blue dots) as a function of h_N/ℓ_c, for different values of θ. The black horizontal line denotes the plateau value due to the resolution of the optical sensor. The red lines denote the amplification estimated using the spatial stability analysis and the size of the plate, i.e. $\Delta = \Delta_0 \exp(-\mathrm{Im}(k_x)\, L)$, with initial amplitude the saturation value of the optical sensor.

Δ and h_N/ℓ_c of 15%. This relates to the experimental error due to the undersampling in the identification of the position of the maximum thickness of the rivulet, since the resolution in the spanwise location is ≈ 1 mm, while the rivulet thickness varies from $h = 1.5$ to $h = 1.7$ in a region of ≈ 1.5 mm extension. Besides, the relation (3.9) is an approximation, since $1.65 < \max(h) < 1.71$ as $\tilde{\ell}_c^*$ varies, which gives a supplementary uncertainty of $\approx 4\%$ on $\max(h)$ and therefore on h_N. The measurement is not a direct measure of the spatial growth rate, but of the variation of the spatial growth rate with the parameters. The variation of the deviation with the parameters well agrees with the linear prediction.

In figure 3.10 the experimental measurements of Δ (colored dots) are summarized and reported together with the spatial amplification Δ/Δ_0 and the marginal stability curve from the spatial stability analysis (red dashed lines). The experimental values of Δ and h_N/ℓ_c are mean values in the 15% uncertainty region mentioned earlier. At low values of h_N/ℓ_c the experimental values of Δ are below the resolution of the optical sensor. As h_N/ℓ_c increases, Δ emerges from the measurement resolution and we observe an increase of two orders of magnitudes in the considered range of parameters. This strong increase can be correlated to the theoretical marginal stability and amplification curves. A good agreement is observed between the theoretical onset of the instability (red solid line) and the trend of the experimental amplification with θ and h_N/ℓ_c(colored dots). The experimental amplification is of the order of the resolution of the optical sensor below the threshold identified by the marginal stability curve, while beyond this threshold we observe very large values of the experimental amplification. Also the trends of the theoretical amplification (blue dashed lines) well follow the experimental amplification.

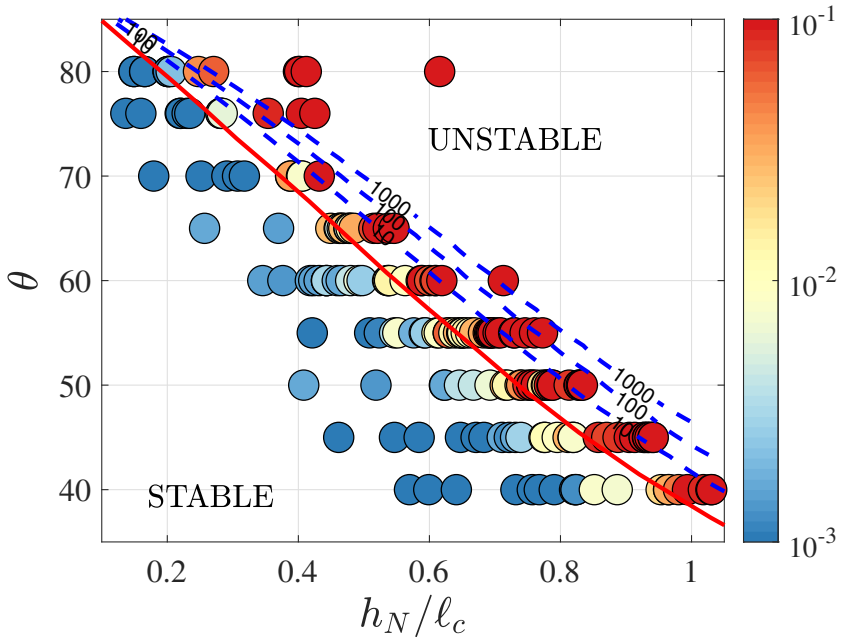

Figure 3.10: Results of the analysis in the $(\theta, h_N/\ell_c)$ plane: experimental measurements of Δ (coloured dots) and inlet disturbance amplification $\Delta/\Delta_0 = \exp(-\mathrm{Im}(k_x)L)$ evaluated by the spatial stability analysis. The red solid line denotes the iso-contour $\mathrm{Im}(\omega) = 0$, which identifies the marginal stability threshold.

Low values of the flow rate (h_N/ℓ_c) or θ imply high values of u and $\tilde{\ell}_c^*$. When high values of u and $\tilde{\ell}_c^*$ are considered, the occurrence of a steady and saturated rivulet pattern is observed (figure 3.11(a)). For low enough values of u and $\tilde{\ell}_c^*$, a state characterized by lenses which travel on rivulets is observed (figure 3.11(b)), as shown in (Lerisson et al., 2019). Small variations of angle and flow rate lead to dramatic effects on the overall pattern dynamics. A change in the inclination of the plate of 10 degrees, e.g. from $\theta = 60°$ to $\theta = 50°$ at $h_N/\ell_c = 0.55$, is enough to pass from a state characterized by large amplitude lenses to a rivulet pattern.

In the route to dripping, the formation of lenses can be interpreted as a secondary instability of steady and streamwise-saturated rivulets; we identified the existence of a theoretical threshold below which rivulets are stable. While Chapter 4 will be completely dedicated to the linear and non-linear formation of lenses, in the next section we aim at giving an insight into the physical origin of rivulets, so as to have a clear picture of the first phase in the route to dripping.

3.5 Linear and non-linear impulse response: breaking of isotropy and emergence of rivulets

In the previous sections, we numerically and experimentally studied the stability of steady and streamwise-saturated rivulet structures with respect to streamwise perturbations, and the link with the growth of traveling lenses. As observed in figure 3.1, the instability of rivulets and

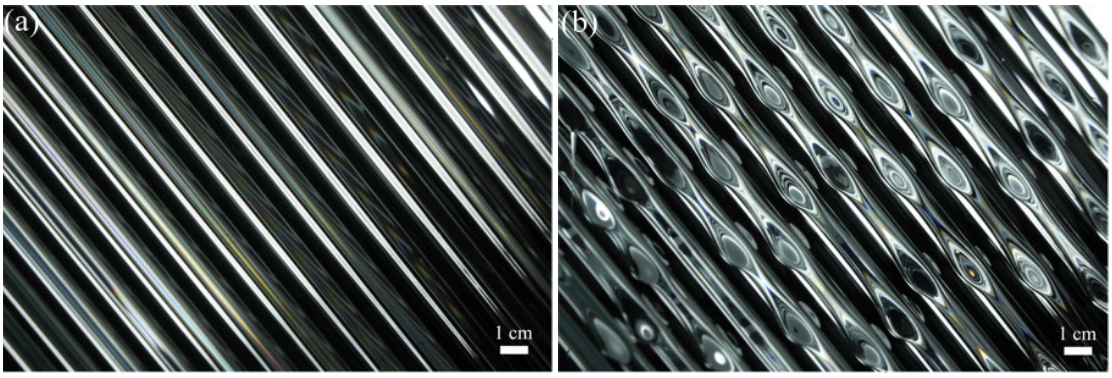

Figure 3.11: Representative patterns at $\theta = 45°$ for (a) $h_N = 623\,\mu$m, i.e. $h_N/\ell_c = 0.42$ and $u = 2.83$, characterized by rivulets, and for (b) $h_N = 1352\,\mu$m, i.e. $h_N/\ell_c = 0.92$ and $u = 1.29$, characterized by rivulets which carry lenses.

the consequent emergence of lenses is preceded by the formation of rivulet structures that invade the whole domain. Hereafter, we aim at giving a physical insight into the predominance of rivulet structures by studying the response of the flat film to an impulsive perturbation localized in space and time, i.e. the impulse response.

3.5.1 Experimental observation

In this section, we introduce a qualitative visualization of the evolution of a localized perturbation in the film thickness. The experimental apparatus is set without any inlet perturbation devices. When high inclination angles and low flow rates are considered (i.e. high values of u), we experimentally observe a large region characterized by a uniform flat film where thickness perturbations from the lateral boundaries of the experiment do not penetrate. In this region, we trigger the destabilization with a thickness perturbation by blowing a puff of air with a syringe. The whole field is then projected on a screen via the shadowgraph technique and captured with a camera.

In figure 3.12 we show the evolution of the perturbation with time. The initially localized perturbation is advected away in the streamwise direction with a constant velocity and spreads in the domain. The perturbation phase lines are concentric circles in the upstream part of the response. Nevertheless, the isotropy disappears in the downstream part. The shadowgraph reveals that the phase lines tend to be parallel to the streamwise direction, the effect becoming more and more evident as the time increases.

The presence of phase lines aligned with the streamwise directions suggests the existence of a wavefront characterized by streamwise structures, i.e. rivulets, when the flat film is perturbed using an impulse thickness perturbation. The selection of a streamwise wavefront is not related to the boundaries of the thin film in the experiment, i.e. the rivulets selection is *intrinsic*.

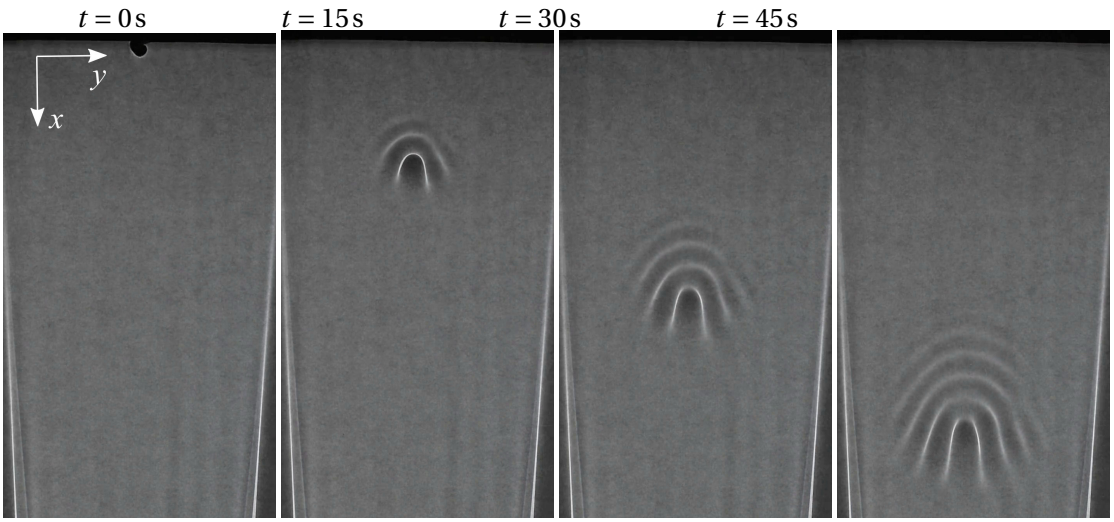

Figure 3.12: Shadowgraph visualization of an experimental impulse response, for $\theta = 20°$ and $h_N = 1292\,\mu m$, i.e. $u = 5.45$. Time increases going to the right and each snapshot is separated by 15 s.

3.5.2 Numerical observation

Inspired by this experimental observation, in this section we numerically simulate the impulse response, via equation (3.2), for $u = 5.45$ and $\tilde{\ell}_c^* = 1$, in a double-periodic domain. The initial condition is taken in the form:

$$h(x,y,0) = 1 + \mathrm{A}\exp\left(-\frac{x^2+y^2}{2}\right), \tag{3.12}$$

where $A = 10^{-2}$. In figure 3.13 we plot the time evolution of the response in the moving reference frame ($\xi = x - ut, y$), from $t = 0$ to $t = 90$. In the moving reference frame, the response progressively invades the domain from the initial impulse location. At $t = 30$, we observe circular phase lines. At $t = 60$ the response loses its isotropy in the downstream part. At $t = 90$ streamwise structures are dominant in the downstream front of the response and they are also observable upstream.

In the moving reference frame, the response spreads from the initial impulse location, meaning that in the fixed reference frame, the response is advected downstream at the linear advection velocity u. The numerical evolution qualitatively agrees with the experimental observation of Section 3.5.1. We first observe the evolution of the impulse response into an isotropic pattern. At large times, the response mostly evolves toward streamwise structures. However, the complicated form of the non-linear equation (3.2), including non-linear advection, hydrostatic pressure distribution and capillary effects, does not allow one to identify the physical mechanisms that lead to the emergence of streamwise structures observed in figures 3.12 and 3.13. Chapter 2 furthermore showed that the rivulet propagation and growth is well described by the linear stability analysis of the flat film even at large amplitudes of the thickness perturbation,

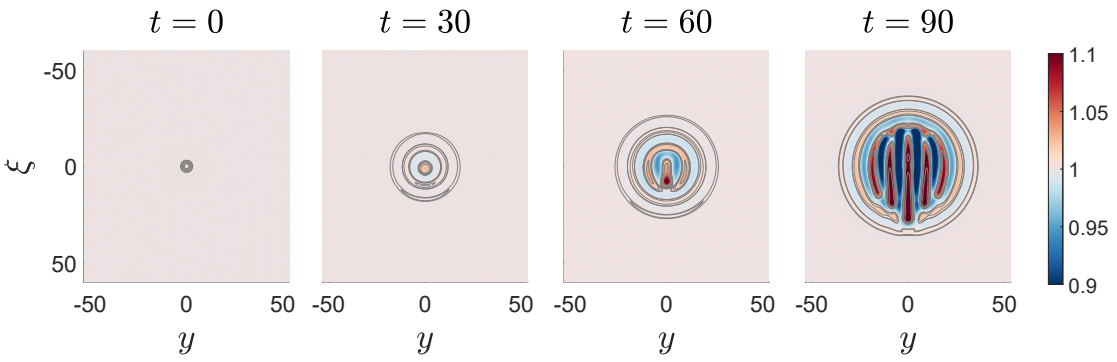

Figure 3.13: Impulse response, $u = 5.45$ and $\tilde{\ell}_c^* = 1$. The time increases from left to right and the time step is 30. Results are reported in the moving reference frame at the linear advection velocity ($\xi = x - ut, y$).

beyond the expected validity of the linear theory. Hereafter, we study the *origin* of the selection of rivulet structures by the linear and weakly non-linear dynamics.

3.5.3 Linear response

Upon introduction of the decomposition $h = 1 + \varepsilon\eta$ ($\varepsilon \ll 1$) in equation (3.2), the linearized equation at $\mathcal{O}(\varepsilon)$ for the evolution of the thickness perturbation η with respect to the flat film reads:

$$\partial_t \eta + u\partial_x \eta + \frac{1}{3}\left[\nabla^2\eta + \nabla^4\eta\right] = 0. \tag{3.13}$$

The dispersion relation is recovered introducing the normal mode decomposition $\eta \propto \exp[\mathrm{i}(\mathbf{k}\cdot\mathbf{x} - \omega t)]$, with $\mathbf{k} = \left(k_x, k_y\right)$, where k_x and k_y denote respectively the streamwise and spanwise wavenumbers:

$$\omega = uk_x + \frac{\mathrm{i}}{3}\left(k^2 - k^4\right), \tag{3.14}$$

where $k = \sqrt{k_x^2 + k_y^2}$. The dispersion relation $D(\omega, k_x, k_y) = 0$ is characterized by an isotropic temporal growth rate ω_i, as shown in figure 3.14(a). The temporal frequency ω_r is linear in k_x and does not depend on k_y.

The initial condition for the numerical simulation is the thickness perturbation $\eta(x, y, 0) = \mathrm{A}\exp(-x^2/2 - y^2/2)$, where $\mathrm{A} = 10^{-2}$. The linear numerical simulation results for $u = 5.45$, in the moving reference frame ($\xi = x - ut, y$), are presented in figure 3.14(b). As time increases, the perturbation spreads in concentric circles from the initial impulse location. Similarly to the non-linear simulation of figure 3.13, the response is advected away at the linear advection velocity u, in the fixed reference frame. The results can be rationalized considering the dispersion relation of equation (3.13). The wavepacket is non-dispersive since ω_r is linear in k_x. This means that there is no distortion of the wavepacket. Since the growth is isotropic, concentric circles invade the domain and at the same time are advected downstream with

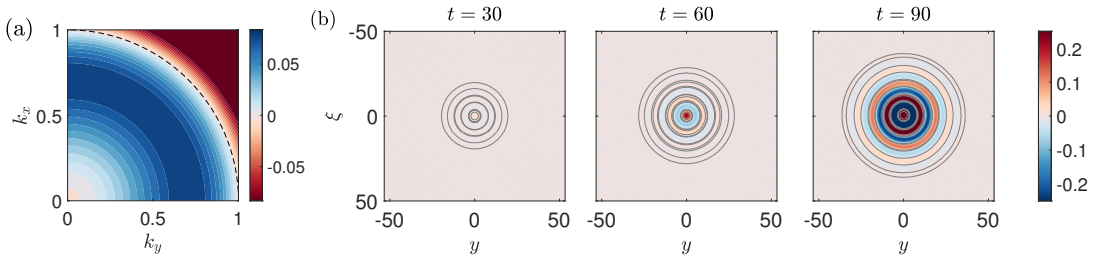

Figure 3.14: (a) Temporal growth rate ω_i as a function of k_x and k_y. (b) Linear impulse response, $u = 5.45$. The vertical and horizontal axis are respectively the streamwise and spanwise directions. From left to right: $t = 30$, $t = 60$, $t = 90$. Results are reported in the moving reference frame at the linear advection velocity ($\xi = x - ut, y$).

constant velocity $\omega_r / k_x = u$. Higher values of u imply faster advection velocities. In the moving reference frame (ξ, y), the equation (3.13) reads:

$$\partial_t \eta + \frac{1}{3}\left[\nabla^2_{\xi y}\eta + \nabla^4_{\xi y}\eta\right] = 0, \tag{3.15}$$

where $\nabla_{\xi y}$ operates in the reference frame (ξ, y). In this reference frame, the response spreads in perfectly isotropic concentric circles without being advected away. The linear dynamics agrees well with the early-times evolution of the non-linear simulation shown in figure 3.13, when the amplitude of the perturbations is still very small. However, since the linearized dynamics is not able to capture the anisotropy of the pattern observed in the non-linear simulation, we propose next a weakly non-linear study.

3.5.4 Weakly non-linear response: the Nepomnyashchy equation

We consider a weakly non-linear model for the flow of a thin film on the underside of an inclined planar substrate. Following Kalliadasis et al. (2011), the derivation is based on a multiple scale approach combined with an asymptotic expansion. Under the assumption of small interfacial disturbances and $u = \mathcal{O}(1)$, the weakly non-linear dynamics for a thickness perturbation η with respect to the flat film reads:

$$\partial_t \eta + 2u\eta\partial_\xi \eta + \frac{1}{3}\left[\nabla^2_{\xi y}\eta + \nabla^4_{\xi y}\eta\right] = 0, \tag{3.16}$$

where $\nabla_{\xi y}$ operates in moving the reference frame (ξ, y). The equation is formally analogous to the Nepomnyashchy equation (Kalliadasis et al., 2011). We consider the evolution of the thickness perturbation η starting from a Gaussian impulse $\eta(\xi, y, 0) = \mathrm{A}\exp(-\xi^2/2 - y^2/2)$ ($\mathrm{A} = 10^{-2}$), in analogy with the linear simulation.

In figure 3.15(a) we report the thickness perturbation evolution. The initial localized perturbation spreads in the domain and is always centered in the vicinity of the initial impulse position, because of the moving reference frame. At $t = 30$ the perturbation has spread isotropically

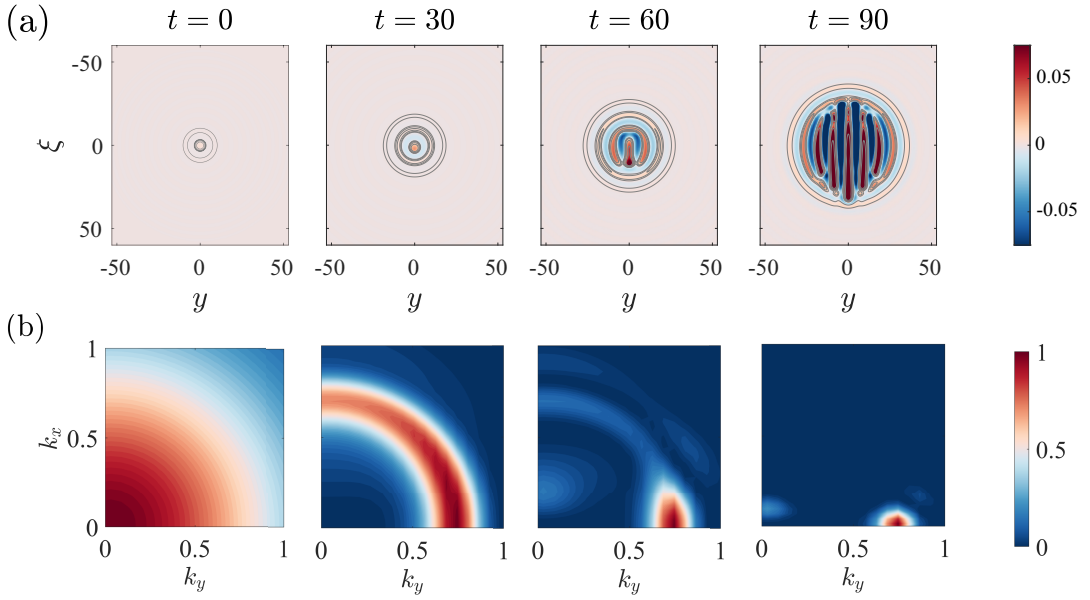

Figure 3.15: $u = 5.45$. (a) Impulse response in the moving reference frame ($\xi = x - ut, y$) from the weakly non-linear model and (b) its two-dimensional Fourier energy spectrum. From left to right: $t = 0$, $t = 30$, $t = 60$, $t = 90$.

in the domain. Nevertheless, at $t = 60$, streamwise structures arise. At $t = 90$, the streamwise structures have invaded most of the perturbation region.

In figure 3.15(b) we show the two-dimensional Fourier energy spectrum of η, normalized by its maximum value. Since we are considering a real signal, the Fourier spectrum is symmetric with respect to the k_x and k_y axes. We thus report only the values in the first quadrant ($k_x > 0, k_y > 0$). At $t = 0$, we observe the Fourier spectrum of a Gaussian impulse, which is a Gaussian centered around ($k_x = 0, k_y = 0$), i.e. the initial spectrum is isotropic. At $t = 30$ the energy is located in a region around $\sqrt{k_x^2 + k_y^2} = 1/\sqrt{2}$. As time progressively increases, the energy concentrates towards ($k_x = 0, k_y = 1/\sqrt{2}$).

Initially, the response is characterized by an isotropic pattern, reminiscent of the linear growth that is experienced in the first stages of the perturbation growth. As the amplitude becomes sufficiently large, the spectrum shows that the energy is focusing on the axis $k_x = 0$, i.e. streamwise structures are selected. The emergence of streamwise structures agrees well with the results of the fully non-linear simulation and with the experimental observation. Moreover, the spectrum is localized around $k_y = 1/\sqrt{2}$, the most amplified wavelength predicted by the flat film dispersion relation (equation (3.14)), and rivulet structures are growing exponentially. Thus, the dynamics of pure streamwise structures stays linear, even in the weakly non-linear regime.

The origin of the selection of rivulet structures is identified in the weakly non-linear advection term $2u\eta\partial_\xi\eta$, which acts in an indirect manner to favor rivulet structures while damping all

other orientations. The weakly non-linear model of equation (3.16) is formally analogous to the linear model of equation (3.15), except for the weakly non-linear advection term. It should be noticed that this term influences the dynamics of streamwise-inhomogeneous structures only, on which it is seen to have a damping effect. The non-linear advection term embodies the difference in the perturbation advection velocity in regions of different thickness and is known to create wave steepening (Babchin et al., 1983). The emerging steep gradients are damped by surface tension effects, leveling therefore the non-streamwise structures. In conclusion, the most unstable solution in the weakly non-linear regime is the one in which the capillary damping is reduced the most, as the term $2u\eta\partial_\xi\eta$, responsible for wave steepening, vanishes.

When only streamwise structures are present, the advection term disappears and the weakly non-linear model is formally analogous to the linear equation in the moving reference frame equation (3.15). Consequently, the response of streamwise structures is linear up to second order in the perturbation.

In conclusion, the weakly non-linear dynamics gives an insight into the origin of the emergence of rivulet structures: the latter are the only ones screened from the action of the difference in the advection. The dynamics of pure streamwise structures remains linear even in the weakly non-linear regime, thus explaining the agreement between the linear prediction and the experimental measurements at large amplitudes observed in Chapter 2. At late times, rivulets eventually invade the perturbation region. In the case of steady inlet forcing (figure 3.1) rivulets invade the whole domain and steady and streamwise saturated rivulet structures emerge downstream, as a result of the weakly non-linear dynamics. As seen in the previous sections, rivulets may eventually destabilize through a secondary instability, resulting in traveling lenses. In both the emergence and the stability of rivulets, the differences in advection in regions of different thickness is crucial.

3.6 Conclusions

We studied the selection and stability of rivulet structures in a thin film flowing under an inclined planar substrate. When the inlet is steadily forced along the spanwise direction, predominant rivulet structures were experimentally observed, which may destabilize at some distance from the inlet through the development of traveling lenses. Inspired by this experimental observation, we performed a non-linear simulation with periodic boundary conditions, starting from an initial condition that mimicked the experimental forcing. The response to a streamwise-invariant sinusoidal initial condition confirmed the emergence of a persistent pattern of saturated rivulets, which may destabilize.

We then focused on the study of the mechanisms that may explain the behaviors observed in the experiment and numerical simulations, by studying the secondary stability of one-dimensional and saturated rivulets when perturbed in the streamwise direction. As the relative importance of advection increases, short wavelengths are progressively stabilized and only very large wavelengths remain slightly unstable. We relate their stabilization to the different

advection of thickness perturbations on the rivulet profile. An increase in the advection results in steeper gradients for the same perturbation wavelength. Capillary forces counteract the wave steepening and eventually damp the perturbation, for high enough values of the advection. A decrease of the ratio between the characteristic film thickness and the reduced capillary length leads to a reduction of the growth rates of the instability, until stabilization of all wavelengths. This strong stabilization mechanism is related to the reduction of the hydrostatic pressure gradients due to the gravity component normal to the substrate, as the ratio is decreased. We compared the theoretical results for the marginal stability and spatial amplification of disturbances of the inlet flow rate with extensive experimental measurements of oscillations on rivulets, and confirmed the observation of a steady and saturated rivulet state when high values of u and $\tilde{\ell}_c^*$ are considered.

Finally, we gave an insight into the early-stages selection of streamwise-aligned structures by studying the evolution of a localized impulse in the flat film. The experimental response showed that the wavefront selects mostly streamwise structures. The numerical impulse response also showed an initial isotropic growth followed by the selection of predominant rivulet structures. The numerical results were rationalized using a weakly non-linear model, which showed the same selection of rivulets. The strength of the weakly non-linear model was to identify one source of non-linearity as the selection mechanism of streamwise structures, i.e. the weakly non-linear advection. The latter is known to create wave steepening, counteracted by capillary terms. The evolution leads to leveling of all but streamwise structures. We concluded that the departure from a flat film towards streamwise structures is the solution in which the wave steepening and capillary damping effects are reduced the most. As a consequence, the selection of streamwise structures is due to the difference in the advection of perturbations in regions of different thickness, which acts to level all but pure streamwise perturbations (rivulets), while the dynamics of the latter remains linear even in the weakly non-linear regime.

Our work aimed at laying rigorous foundations in the study of coating flows on the underside of planar substrates, interpreting the route to dripping as a destabilization of the flat film towards rivulets followed by a secondary instability. Nevertheless, several open questions are left. In complement to the spatio-temporal impulse response studied in this work, the response to a permanent in time but localized in space defect was considered briefly in Chapter 2. However, a more detailed study to properly quantify the evolution of the response, e.g. in terms of asymptotic properties of the linear response, still needs to be performed.

Despite the predominance of streamwise-oriented structures, for some conditions, lenses appear on rivulets. While in this work a first analysis was performed in terms of spatial growth, a complete analysis of the precise evolution of perturbations along the streamwise direction remains to be pursued. In particular, a weakly non-parallel approach combined with a global resolvent technique could be suitable in this case. Furthermore, although the rivulet configuration shown in figure 3.11(b) may seem regular, we sometimes observe catastrophic events: lenses can merge in the streamwise direction, and eventually drip. While this work and

the one in Chapter 2 were focused on the emergence and stability of steady structures, further investigations focused on the dynamics of the traveling lenses are crucial to understand the route to dripping.

3.7 Appendix

3.7.1 Absolute-convective transition of the saturated rivulet profile.

The purpose of this Appendix is to verify the application of the Gaster transformation used in Section 3.3.3.2, for the case $\tilde{\ell}_c^* = 1$. The Gaster transformation is applied in the context of strongly convectively unstable systems.

To verify the convective nature of the instability of the one-dimensional and steady rivulet profile, we evaluate the value of u at which the absolute-convective transition occurs. We thus apply the Briggs-Bers criterion (Briggs, 1964; Bers, 1975; Huerre and Monkewitz, 1990; Schmid et al., 2002) to the dispersion relation $D_r(\omega, k_x) = 0$, equation (3.7). We look for the saddle points in the complex k_x plane $\frac{\partial \omega}{\partial k_x} = 0$ and evaluate the imaginary part of ω at the saddle point $\mathrm{Im}(\omega_0)$. The absolute-convective transition occurs when $\mathrm{Im}(\omega_0) = 0$. A spectral code is implemented in MATLAB, and saddle points are searched for with the built-in function *fsolve*. We identified a single saddle point in the complex-k_x plane. The absolute-convective transition occurs at $u_0 = 0.56$ (figure 3.16), which is much lower than the values of u used throughout this work. Interestingly, the convective-absolute transition for the flat film takes place at $u_0 = 0.54$ (Brun et al., 2015), very close to the saturated rivulet value, for $\tilde{\ell}_c^* = 1$.

In figure 3.17 we report the comparison between the spatial stability analysis and the Gaster transformation, for $u < 1$. As u approaches the value for the absolute-convective transition, the prediction of the Gaster transformation deviates from the spatial stability analysis results.

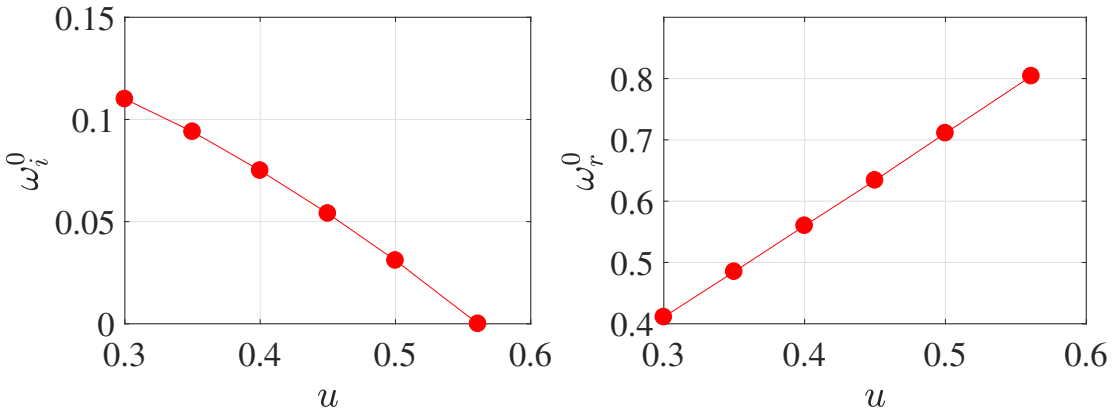

Figure 3.16: (a) Imaginary and (b) real parts of the complex frequency ω_0 for the absolute-convective stability analysis. The absolute-convective transition occurs at $u_0 = 0.56$.

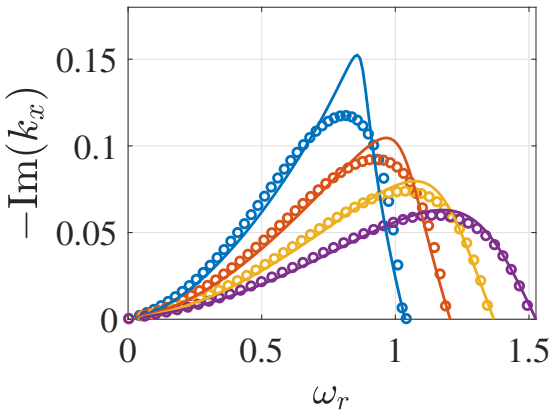

Figure 3.17: Spatial growth rate given by the spatial stability analysis (solid lines) and by the Gaster transformation (circles), for $u = 0.6$ (blue), $u = 0.7$ (orange), $u = 0.8$ (yellow), $u = 0.9$ (purple).

4 Secondary instability in thin film flows under an inclined plane: growth of lenses on spatially-developing rivulets

Remark This chapter is largely inspired by the publication of the same name

P. G. Ledda, F. Gallaire
Laboratory of Fluid Mechanics and Instabilities, École Polytechnique Fédérale de Lausanne, Lausanne, CH-1015, Switzerland

Proceedings of the Royal Society A, **477**:20210291 (2021)

Authors'contributions P.G.L. and F.G. conceived the project. P.G.L. performed the theoretical developments and actively discussed with F.G. at each step. P.G.L. performed all the numerical analyses. P.G.L. wrote the manuscript with F.G..

The response of a thin film flowing under an inclined plane, modeled using the lubrication equation, is studied. The flow at the inlet is perturbed by the superimposition of a spanwise-periodic steady modulation and a decoupled temporally-periodic but spatially-homogeneous perturbation. As the consequence of the spanwise inlet forcing, so-called rivulets grow downstream and eventually reach a streamwise-invariant state, modulated along the direction perpendicular to the flow. The linearized dynamics in the presence of a time-harmonic inlet forcing shows the emergence of a time-periodic flow characterized by drop-like structures (so-called lenses) that travel on the rivulet. The spatial evolution is rationalized by a weakly non-parallel stability analysis. The occurrence of the lenses, their spacing and thickness profile, is controlled by the inclination angle, flow rate, and the frequency and amplitude of the time-harmonic inlet forcing. The faithfulness of the linear analyses is verified by non-linear simulations. The results of the linear simulations with inlet forcing are combined with the computations of non-linear traveling lenses solutions in a double-periodic domain to obtain an estimate of the dripping length, for a large range of conditions.

4.1 Introduction

We refer to Section 1.3.3.1 for a general introduction about the Rayleigh-Taylor instability.

Chapter 2 compared experiments with theoretical and numerical findings, showing that, for some conditions of inclination angle and flow rate, a steady pattern of rivulets was reached. After some distance from the inlet, these rivulets were characterized by a central lobe of very large thickness and side lobes of very small thickness. The central lobe is a streamwise-invariant profile well described by a two-dimensional pendent drop shape, similar to the results of Pitts (1973), but with a flow rate constraint rather than a volume one. Subsequently, in Chapter 3, we performed a secondary stability analysis of these streamwise-saturated states, highlighting a strong stabilization mechanism as the plate was inclined or the flow rate reduced. For small inclinations and large flow rates, traveling lenses grew on the rivulets (see figure 4.1(a)), whose initial growth was well described by the linear stability analysis. The non-linear behavior of such lenses was studied by Indeikina et al. (1997), where the authors experimentally investigated the dripping from a rivulet and described the traveling lenses solution by matched asymptotic expansions, using a lubrication equation with the linearized expression of the curvature. They interpreted the blow-up of the numerical solution of the lubrication equation as the initial stage of dripping.

As confirmed by Chapter 3, the streamwise-invariant rivulet profiles behaved as noise amplifiers in a certain region of the parameter space. In such conditions, the flow instability depends on the imposed temporal forcing at the inlet (Garnaud et al., 2013; Boujo et al., 2013; Boujo and Gallaire, 2015; Shukla and Gallaire, 2020).

In this chapter, the complex interface patterns governing the thin film dynamics, with the development of growing lenses on the top of spatially developing rivulets, are investigated by focusing on the secondary instability of one single and spanwise-periodic rivulet, with a perspective on the dripping phenomenon. The chapter is organized as follows. In Section 4.2 the lubrication model and the numerical implementation are presented. Subsequently, Section 4.3 is devoted to the analysis of the steady rivulet emerging when a slightly modulated constant thickness is imposed at the inlet, which will serve as a base state for the secondary stability analysis conducted in Section 4.4, where the linearized dynamics of lenses around the steady baseflow solution when the inlet is forced via a harmonic forcing is studied. In Section 4.4.3, the observed patterns are rationalized via a weakly non-parallel (WKBJ) local stability analysis. Subsequently, the non-linear response to harmonic inlet forcing is studied, and eventually the non-linear periodic traveling lens solutions in periodic domains of various lengths is investigated. This allows us, in Section 4.7, to unify the results of the previous sections to give an estimate of the dripping length for a large range of inclination angle and flow rate.

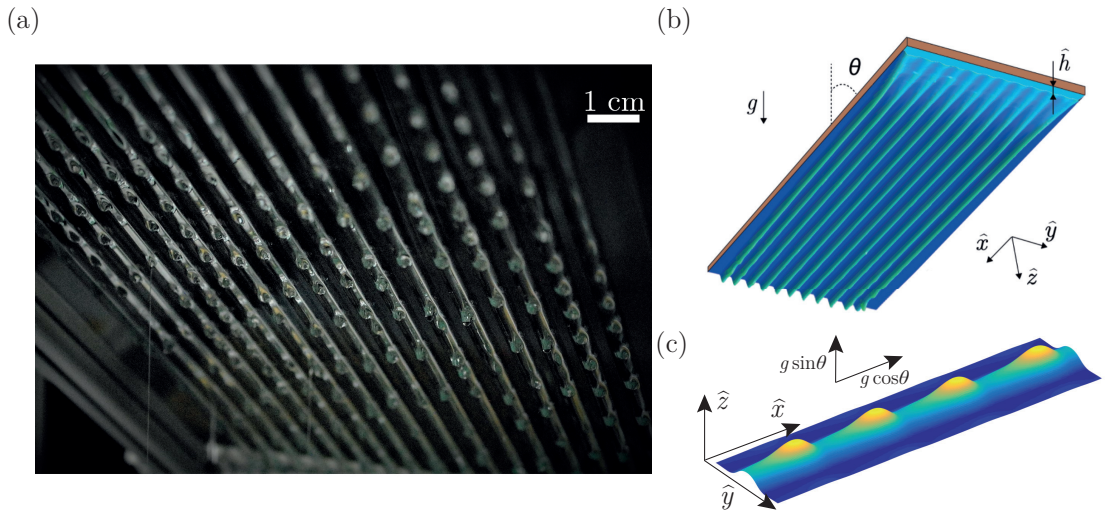

Figure 4.1: (a) Experimental photo of rivulets that carry lenses below an inclined planar substrate. The fluid is silicon oil, of viscosity $\mu \approx 1\,\mathrm{Pa\,s}$ and density $\rho \approx 970\,\mathrm{kg/m^3}$. The inclination angle with respect to the vertical is 45° and the film thickness is $\approx 1\,\mathrm{mm}$. The red line indicates the maximum thickness location and the green dashed line the maximum thickness of the rivulet upstream of the instability. (b) Sketch of the flow configuration, with rivulets that invade the domain and lenses of small amplitude observed downstream. (c) Sketch of a single rivulet that is carrying lenses.

4.2 Governing equation and numerical method

In this section, the governing equation for a thin film coating the underside of an inclined plane and its numerical implementation are introduced. We consider a thin film of thickness $\bar{h}$, of a viscous fluid flowing under a planar substrate, inclined with respect to the vertical direction of an angle θ. The streamwise and spanwise directions are denoted $(\bar{x}, \bar{y})$ (see figure 4.1). The streamwise component of the gravity g reads $g_x = g\cos(\theta)$, while there is no projection along the spanwise direction. The fluid properties are the viscosity μ, the density ρ, and the surface tension coefficient γ. The capillary length $\ell_c = \sqrt{\gamma/(\rho g)}$ and the characteristic film thickness h_N are introduced. The characteristic time scale of the Rayleigh-Taylor instability reads

$$\tau = \frac{\nu \ell_c^2}{h_N^3 g \sin^2\theta}. \tag{4.1}$$

Spatial directions $\bar{x}$ and $\bar{y}$ are non-dimensionalized by the reduced capillary length $\ell_c^* = \ell_c/\sqrt{\sin\theta}$, thickness $\bar{h}$ by h_N and time by τ:

$$x = \bar{x}/\ell_c^*, \quad y = \bar{y}/\ell_c^*, \quad h = \bar{h}/h_N, \quad t = \bar{t}/\tau. \tag{4.2}$$

The modelization of the flow of a thin film is based on the separation of scales between the normal and tangential to the substrate length scales (Kalliadasis et al., 2011). Different levels of

approximation are employed to describe the flow, depending on the considered regime. A set of boundary layer equations holds for thin film flows mostly governed by gravity and surface tension (Chang, 1994). When the inertia of the flow is small, the boundary layer equations are further simplified, leading to a single evolution equation for the thickness, called Benney equation (Benney, 1966; Oron et al., 1997; Scheid et al., 2005). Pumir et al. (1983) numerically observed a blow-up of the solution at large Reynolds numbers. To further extend these models at larger Reynolds numbers, more refined methods have been proposed (Ruyer-Quil and Manneville, 2000; Scheid et al., 2016). However, in this work we consider the situation in which the Reynolds number is very small and inertial effects can be neglected. Despite this assumption, a plethora of patterns is observed, since these simple non-inertial models already incur complex non-linearities. For negligible inertia, the Benney equation is accurate and widely employed (Oron et al., 1997). The thin film model with the complete expression of the curvature κ (Ruschak, 1978; Wilson, 1982; Kheshgi et al., 1992; Weinstein and Ruschak, 2004) is thus considered, together with the above-defined non-dimensionalization:

$$\partial_t h + \tilde{\ell_c}^* \cot(\theta) h^2 \partial_x h + \frac{1}{3}\nabla\cdot(h^3(\nabla h + \nabla\kappa)) = 0, \tag{4.3}$$

where ∇ operates in the (x,y) plane, $\tilde{\ell_c}^* = \ell_c^*/h_N$ and κ is the mean curvature:

$$\kappa = \frac{\partial_{xx}h\left(1+\left(\frac{1}{\tilde{\ell}_c^*}\partial_y h\right)^2\right) + \partial_{yy}h\left(1+\left(\frac{1}{\tilde{\ell}_c^*}\partial_x h\right)^2\right) - 2\left(\frac{1}{\tilde{\ell}_c^*}\right)^2 \partial_{xy}h\partial_x h\partial_y h}{\left(1+\left(\frac{1}{\tilde{\ell}_c^*}\partial_x h\right)^2 + \left(\frac{1}{\tilde{\ell}_c^*}\partial_y h\right)^2\right)^{3/2}}. \tag{4.4}$$

The linear advection velocity $u = \tilde{\ell_c}^* \cot(\theta)$ is introduced, which is the velocity of advection of thickness perturbations of a flat film (Brun et al., 2015). In this work, we perform our analytical and numerical analyses for the case $\tilde{\ell}_c^* = 1$ and study the effect of u. This choice stems from our aim to put a maximum emphasis on the non-linear curvature effects, which ensure an unstable behavior of the flow in a large range of u.

A configuration in which the flow is continuously fed at the inlet is considered. Spanwise-periodic rivulet structures emerge and invade the domain, with a natural spacing $L_y = 2\pi\sqrt{2}$. In this work, we numerically investigate the evolution of one spanwise-periodic rivulet, of natural spanwise periodicity L_y, when the inlet is temporally forced. A rectangular domain of streamwise length L_x and spanwise length $L_y = 2\pi\sqrt{2}$ is considered, with inlet and outlet conditions along the streamwise direction and periodic boundary conditions imposed along the spanwise direction. The inlet condition is a flat film perturbed by a cosine along the spanwise direction (of amplitude A and wavelength L_y) and by a time-periodic forcing $\tilde{f}$ (of amplitude ε), imposed by a Dirichlet boundary condition of the form:

$$h(x=0,y) = 1 + \mathrm{A}\cos(y/\sqrt{2}) + \varepsilon\tilde{f}(y,t). \tag{4.5}$$

The outlet condition is imposed by employing a Sponge method, similarly to Chapter 2,

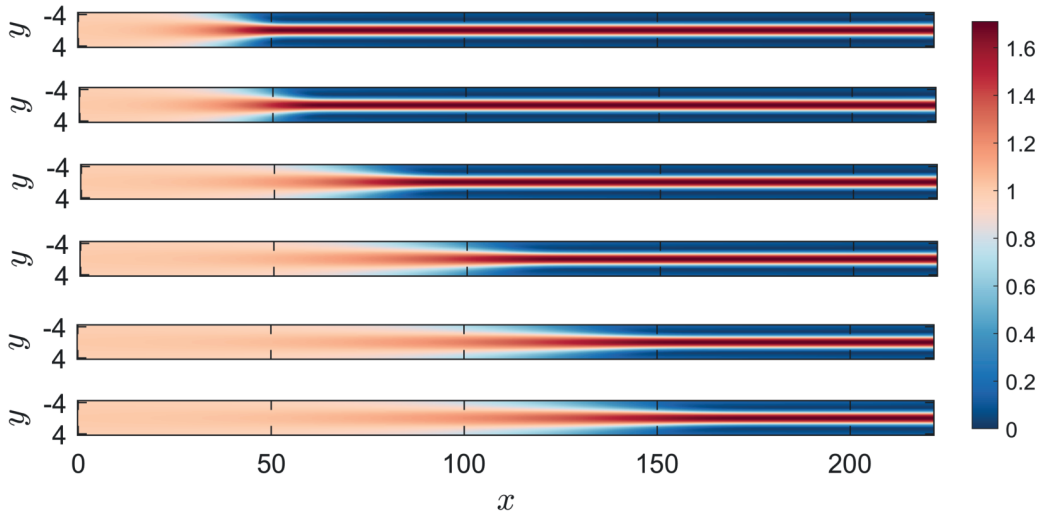

Figure 4.2: Two-dimensional visualization of the steady baseflow $H(x,y)$. From the top to the bottom: $u = 0.85$, $u = 1$, $u = 1.5$, $u = 2$, $u = 2.5$, $u = 2.75$.

resulting in the following equation to be numerically solved in the whole domain:

$$\partial_t h + \tilde{\ell_c}^* \cot(\theta) h^2 \partial_x h + \frac{1}{3}\nabla\cdot(h^3(\nabla h + \nabla\kappa)) = -\mathrm{Sp}(x)(h-1), \tag{4.6}$$

where $\mathrm{Sp}(x) = \frac{1}{2}(1+\tanh(x-6L_x/7))$ is the Mask function of the Sponge method (Högberg and Henningson, 1998) that ensures the relaxation of the thickness to $h = 1$ and avoids reflections from the outlet.

Equations (4.4,4.6) are numerically implemented in the finite-element solver COMSOL Multiphysics, employing third-order Lagrange shape functions. Both the steady and unsteady solver are employed, exploiting respectively the built-in Newton-Rapson algorithm and a second-order Backward Differentiation Formula. The Newton algorithm is initialized using the large-time solution ($t = 1000$) of the unsteady equation for a value of $u = 5$, in which no unsteady instabilities are numerically and experimentally observed owing to the large value of u. The previous solution is taken as initial guess for successive and smaller values of u. In the following, the Sponge region is excluded from the results, leading to a domain of effective length $L_x = 225$, unless stated differently. Numerical convergence is achieved with a characteristic size of the elements equal to half of the reduced capillary length, already validated in Chapters 2 and 3. Furthermore, the presented results are not influenced by the imposed spanwise periodic length, both for the steady and unsteady simulations.

4.3 The steady baseflow

The present section is devoted to the study of the steady solution $h = H(x,y)$ of the flow equation (4.6), $\varepsilon = 0$, when inlet and outlet conditions in a spanwise-periodic box of span L_y

are considered. In equation (4.5), $A = A^* = 10^{-2}$ is assumed. In figure 4.2 the thickness profile in the (x, y) plane, for decreasing values of u, is reported. In all cases, the thickness profile evolves from a flat condition at the inlet, slightly perturbed with a cosine, to a streamwise-invariant rivulet state. The more u decreases, the further downstream the streamwise-invariant rivulet state emerges.

In figure 2, (a) the variation of the minimum and maximum thickness with x (solid lines) and (b) the resulting spanwise profiles at different streamwise locations are reported. In panel (a), the maximum and the minimum thickness saturate respectively to $\sim 10^{-2}$ and ≈ 1.71. The presence of a streamwise saturation allows one to define a *healing* length L_h for the saturated rivulet profile, defined as the streamwise location beyond which $\frac{\mathrm{d}}{\mathrm{d}x}\max(H) < 10^{-4}$, marked by an asterisk in figure 4.3(a). The healing length always increases with u and has a linear dependence for $u > 0.75$. In panel (a), the dashed line denotes the streamwise amplification predicted by the steady dispersion relation of the flat film, briefly summarized as follows. Introducing in equation (4.3) the ansatz $h = 1 + \varepsilon\eta$, $\varepsilon \ll 1$, with $\eta \propto \exp\left(\mathrm{i}(k_x x + k_y y\right)$, the equation at $\mathcal{O}(\varepsilon)$ leads to the following dispersion relation:

$$\left(k_y^2 - k_y^4\right) + \left(k_x^4 + k_x^2 + 2k_x^2 k_y^2\right) = 3iuk_x, \tag{4.7}$$

where k_x and k_y are respectively the streamwise and spanwise wavenumbers. The estimated amplification then reads $\max_y(H) = 1 + \mathrm{A}\exp(\kappa x)$, where $\kappa = -\min(\mathrm{Im}(k_x))$ is the spatial growth rate (i.e. the opposite of the imaginary part of k_x) in the steady dispersion relation (4.7), for $k_y = 1/\sqrt{2}$. The linear rivulet amplification well approximates the non-linear simulations results, for small values of the perturbation $\eta = H - 1$. The rivulet (panel (b)) evolves from a slightly perturbed cosine to the saturated rivulet profile.

So far, the steady solution of the flow equation (4.3) was studied for $A = A^*$. Owing to the good agreement between the non-linear simulation and the linear rivulet amplification for low amplitudes $\max_y(H) - 1 \lessapprox 0.2$, these results are generalized to different values of A. When the amplitude is smaller than the studied case, i.e. $A < A^*$, the resulting mode is analogous to a cosine and the initial part is thus approximated as

$$H(x, y) = 1 + \mathrm{A}\exp(\kappa x)\cos(\frac{y}{\sqrt{2}}), \tag{4.8}$$

which is then connected, at some coordinate $x = x^* = \frac{1}{\kappa}\log\left(\frac{A^*}{A}\right)$, to the solution for $A = A^*$ reported in figure 4.2. In contrast, for $A^* < A < 0.2$, the solution is assumed to start at the coordinate $x = x_0$, where the reference solution $H(x, y)$ initiated with A^* attains A, i.e. $H(x_0, 0) = A$. It thus consists of a variation of the origin of the x axis.

The steady simulations of equation (4.3) show that the rivulet evolves along the streamwise direction reaching a streamwise-saturated state. The latter is independent of u and is characterized by a central lobe of large thickness and side lobes of low thickness. While in Chapter 3 the attention was focused on the analysis of the evolution of unsteady perturbations of

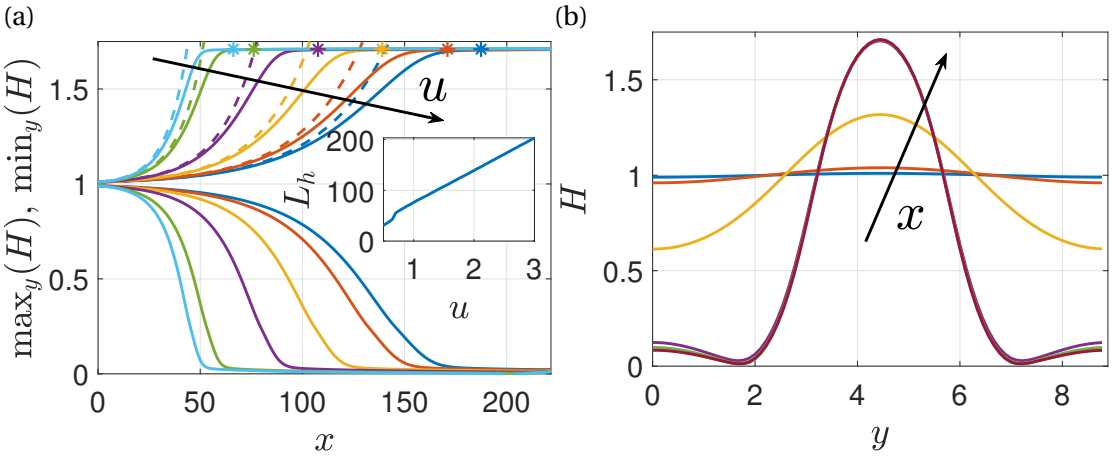

Figure 4.3: (a) Evolution with x of the maximum and minimum values of the steady baseflow $H(x,y)$, for $u = 0.85$ (cyan), $u = 1$ (green), $u = 1.5$ (purple), $u = 2$ (yellow), $u = 2.5$ (orange), $u = 2.75$ (blue). The stars denote the healing length for each value of u. In the inset: healing length as a function of u. (b) $u = 2$. Evolution of the profile at different streamwise locations $x = 0$ (blue), $x = 25$ (orange), $x = 50$ (yellow), $x = 100$ (purple), $x = 150$ (green), $x = 200$ (cyan), $x = 220$ (maroon).

the streamwise-invariant rivulet profile, hereafter the streamwise evolution of the base flow starting at the inlet is included by studying the evolution of unsteady perturbations with respect to the two-dimensional steady baseflow $H(x,y)$.

4.4 Secondary stability analysis: linear response to harmonic inlet forcing

4.4.1 Linearized dynamics around the baseflow solution

In this section, the equation describing the linearized dynamics of a thickness perturbation with respect to the steady baseflow $H(x,y)$ defined in the previous section is introduced. The following decomposition is considered:

$$h(x,y,t) = H(x,y) + \varepsilon\tilde{\eta}(x,y,t), \quad \varepsilon \ll 1, \tag{4.9}$$

where $\tilde{\eta}$ is the *perturbation* with respect to the baseflow $H(x,y)$. The decomposition (4.9) is next introduced in the flow equation (4.6), leading to the baseflow equation at leading order (i.e. the steady version of equation (4.3)) and the following equation at order ε:

$$\partial_t\tilde{\eta} + \frac{1}{3}\nabla\cdot\left(H^3\left(\nabla\tilde{\eta} + \nabla\tilde{\kappa}_{(1)}\right) + 3H^2\left(\nabla H + \nabla\kappa_{(0)} + u\right)\tilde{\eta}\right) = -\mathrm{Sp}(x)\tilde{\eta} \tag{4.10}$$

where the baseflow curvature $\kappa_{(0)}$ is given by equation (4.4) with $\tilde{\ell}_c^* = 1$, while the first order $\tilde{\kappa}_{(1)}$ curvatures is expressed in terms of the x and y components of the normal vector at order

ε and reads, upon assumption of $\tilde{\ell}_c^* = 1$:

$$\tilde{\kappa}_{(1)} = \nabla \cdot \tilde{\mathbf{n}}_{(1)}, \;\; \tilde{\mathbf{n}}_{(1)} = \frac{[\partial_x \tilde{\eta}(1+\partial_y H^2) - \partial_y H \partial_y \tilde{\eta} \partial_x H, \partial_y \tilde{\eta}(1+\partial_x H^2) - \partial_y H \partial_x \tilde{\eta} \partial_x H]}{(1+\partial_x H^2 + \partial_y H^2)^{3/2}}, \quad (4.11)$$

and the inlet condition now reads:

$$\tilde{\eta} = \tilde{f}(y) = f(y)\exp(\mathrm{i}\omega t) \quad (4.12)$$

In analogy to the non-linear equation (4.6), the numerical implementation of (4.10) is performed in COMSOL Multiphysics.

The linearized equation (4.10) is the starting point for our analysis. In the following, the dynamics of thickness perturbations with respect to the steady baseflow $H(x,y)$, when the inlet is temporally forced via a harmonic forcing, is studied. As it is well known from the literature, the linear response of the base state for an external harmonic forcing is only well defined if the baseflow is globally stable with respect to perturbations, i.e. there is no intrinsic oscillatory behavior of the flow (Schmid et al., 2002; Shukla and Gallaire, 2020). In Appendix 4.9.1, the global stability analysis is reported, revealing that the instability occurs for $u < u_0$, $u_0 = 0.56$. In the following, values of u larger than the global instability threshold, i.e. $u > u_0$, are considered, thus focusing on the regime in which the flow is said to be convectively unstable and behaves as a noise amplifier.

4.4.2 Global linear analysis

In this section, we study the secondary instability of the spatially-developing and steady baseflow $H(x,y)$ subject to a harmonic inlet forcing $\tilde{f}$ of frequency ω, i.e. $\tilde{f} = f(y)\exp(\mathrm{i}\omega t)$. The equation for the linearized dynamics (4.10) together with the following ansatz for the perturbation $\tilde{\eta}$ are considered:

$$\tilde{\eta}(x,y,t) = \eta(x,y)\exp(\mathrm{i}\omega t) \quad (4.13)$$

Substituting this expression in equation (4.10) and simplifying the exponential term, one obtains:

$$\mathrm{i}\omega\eta + \frac{1}{3}\nabla\cdot\left(H^3\left(\nabla\eta + \nabla\kappa_{(1)}\right) + 3H^2\left(\nabla H + \nabla\kappa_{(0)} + u\right)\eta\right) = -\mathrm{Sp}(x)\eta, \quad (4.14)$$

with the Dirichlet boundary condition $\eta(x=0,y) = f(y)$ at the inlet. The inlet forcing is first given by

$$f(y) = \frac{1}{\sqrt{L_y}}, \quad (4.15)$$

so that $\int_{\Gamma_i} |f|^2 \mathrm{d}y = 1$. This forcing can be experimentally reproduced, as it consists of a time-harmonic variation of the flow rate at the inlet, thus making this numerical study suitable for further experimental validations.

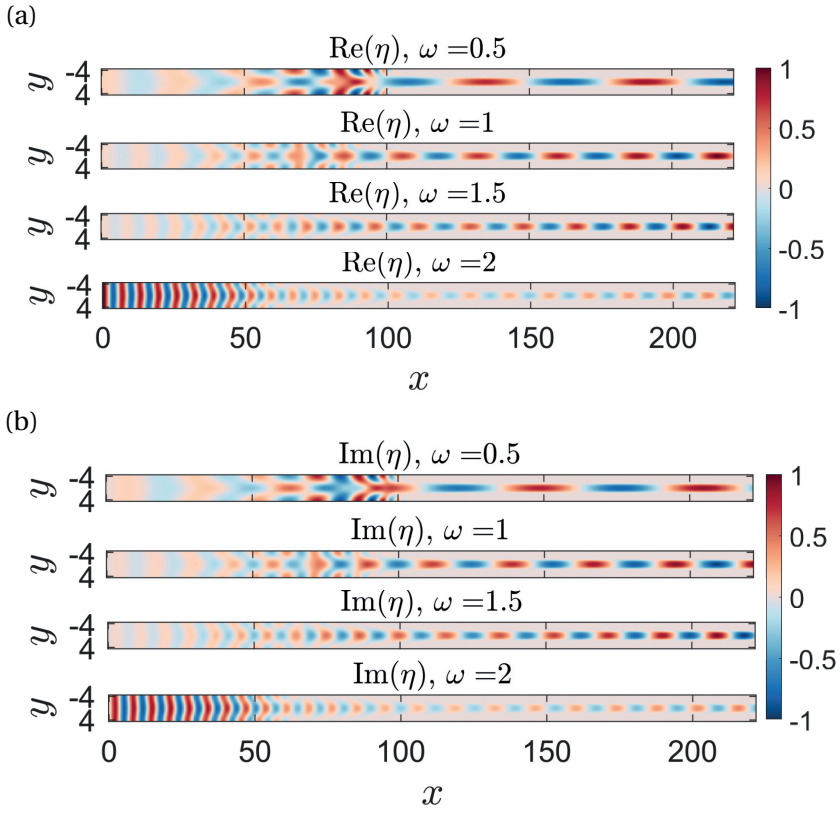

Figure 4.4: Global linear response, (a) real and (b) imaginary parts. Quantities are rescaled with the maximum absolute value, $u = 2$.

Equation (4.14), together with the boundary condition (4.15) at the inlet and periodic ones on the lateral sides, is a linear problem of the form $i\omega\mathbf{I}\eta + \mathbf{L}\eta = \mathbf{B}f$, where $\mathbf{L}$ and $\mathbf{B}$ are respectively the linearized operator and the so-called prolongation operator, which maps the boundary forcing inside the domain. The numerical implementation is performed in COMSOL Multiphysics, in analogy to the baseflow computation.

Figure 4.4 shows the response η, for $u = 2$ and for different values of the forcing frequency ω. Close to the inlet, the perturbation strongly resembles a wavy oscillation, without any appreciable dependence on the y direction. In the streamwise-invariant rivulet region, drop-like structures, so-called *lenses*, are observed. The streamwise wavelength of the lenses decreases as ω increases. Coincidently, the transition region between wavy oscillations and lenses is moved slightly upstream. In this region, an intricate pattern is observed, with strong perturbations on the lateral sides that are then damped downstream. Concerning the streamwise amplification of the perturbation, a variety of behaviors is observed. For $\omega = 0.5$, the peak in the amplitude is located at $x \approx 100$, while for $\omega = 1$ and $\omega = 1.5$ it moves to the outlet. For $\omega = 2$, a strong damping of the so far growing oscillations is observed for $x > 50$, followed by a progressive and modest increase of the amplitude of the lenses.

In figure 4.5(a), the evolution of the real part of the perturbation at the centerline, i.e. $y = 0$,

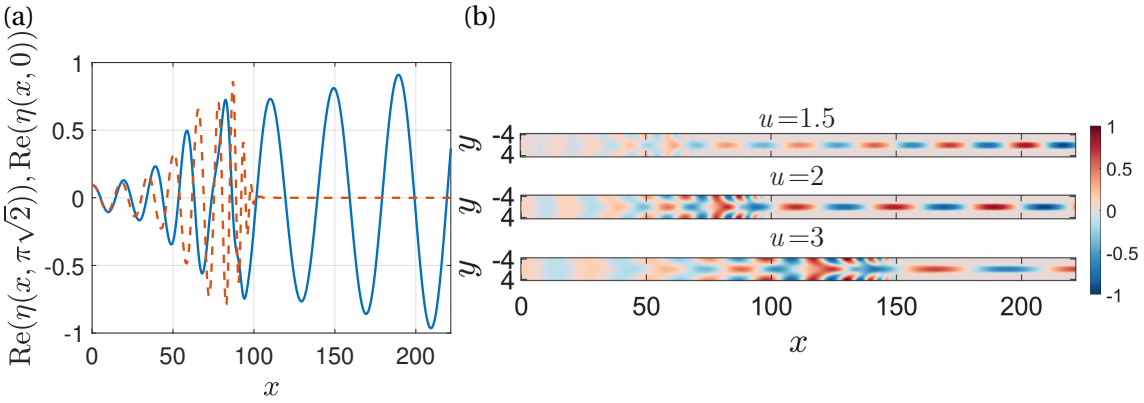

Figure 4.5: Real part of the global linear response, for $\omega = 0.7$, (a) at the centerline (solid) and on the lateral boundary (dashed), for $u = 2$, and (b) from the top to the bottom, $u = 1.5$, $u = 2$, $u = 3$.

(solid line) and on the lateral side, i.e. $y = \pi\sqrt{2}$, (dashed line) is reported, for $\omega = 0.7$ and $u = 2$. Interestingly, at $x \approx 75$, close to the healing length L_h, the streamwise oscillations are not purely sinusoidal as they become further downstream, but a more intricate profile is observed, both at the centerline and on the lateral side.

Figure 4.5(b) presents the pattern for fixed forcing frequency $\omega = 0.7$ and for three different values of u. As u increases, the transition region is shifted downstream and lenses with increasing streamwise extension are observed.

We now turn to a quantitative analysis of the linear response. A long-established way of measuring the amplification of the response for a forcing frequency ω is the gain $G(\omega)$, defined as the ratio between the amplitude of the output response and the amplitude of the input forcing (Schmid et al., 2002; Viola et al., 2016; Shukla and Gallaire, 2020). The gain is defined as follows:

$$G^2(\omega) = \frac{\int_\Omega |\eta|^2 \mathrm{d}x\mathrm{d}y}{\int_{\Gamma_i} |f|^2 \mathrm{d}y}, \tag{4.16}$$

where Ω denotes the whole domain and Γ_i the inlet boundary. Note that, according to the definition of f given in equation (4.15), the denominator of equation (4.16) is equal to one.

In figure 4.6(a) the gain $G(\omega)$, for different values of u, is reported. The gain curves are characterized by a maximum (*optimal*) value, associated with an optimal frequency. The optimal gain and frequency respectively increase and decrease as u decreases. From $u = 3$ to $u = 1$, the gain increases of two orders of magnitude, from 10^2 to 10^4, and the optimal frequency decreases from $\omega_{\mathrm{opt}} = 1.6$ to $\omega_{\mathrm{opt}} = 0.8$.

Since in some cases the maximum response is attained at the outlet, the effect of the streamwise length L_x of the domain on the gain is reported in figure 4.6(b), for $u = 2$. For a fixed frequency ω, the gain increases with the streamwise length. However, the optimal frequency only slightly varies with the streamwise length, from a value of $\omega_{\mathrm{opt}} = 1.24$ for $L_x = 125$ to

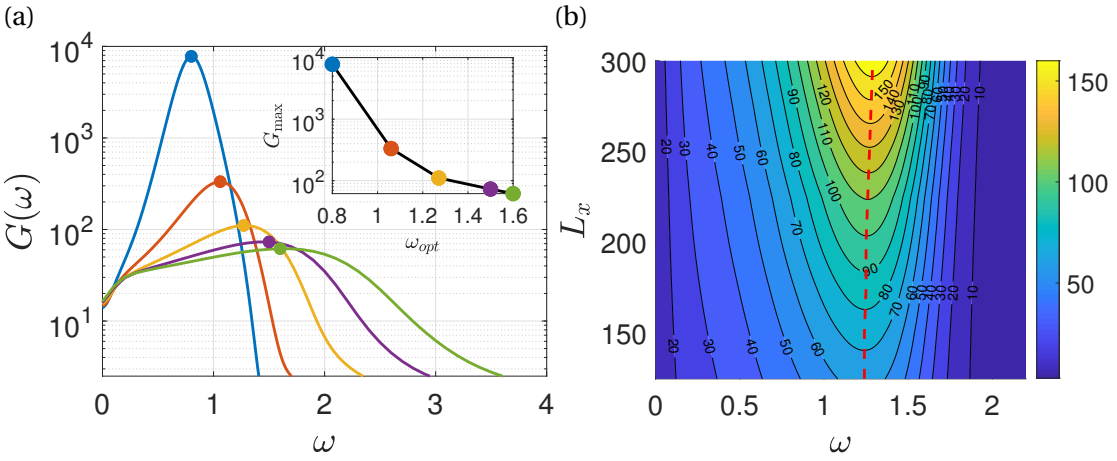

Figure 4.6: (a) Variation of the Gain $G(\omega)$ with ω and for $u = 1$ (blue), $u = 1.5$ (orange), $u = 2$ (yellow), $u = 2.5$ (purple), $u = 3$ (green). In the inset: maximum value and optimal frequency for different values of u. (b) Iso-contours of the Gain as a function of ω and the streamwise length of the domain L_x, $u = 2$.

$\omega_{\text{opt}} = 1.29$ for $L_x = 300$.

The analysis of the linear response shows that, in the presence of a harmonic inlet forcing, a secondary instability occurs on the spatially-developing rivulet and perturbations evolve downstream into traveling lenses. The occurrence of such lenses is controlled by different parameters. The first one is the linear advection velocity u, which is a combination of inclination angle and flow rate. An increase of u leads to lenses of larger spacing and smaller amplitude. The harmonic inlet forcing frequency ω modifies both the spacing and the amplitude of the lenses.

An optimal frequency that most amplifies the lenses is identified. The weak dependence of the optimal frequency with the streamwise length of the domain indicates that the transition region from flat film to saturated rivulet is crucial for the evolution and amplification of the inlet forcing.

Finally, figures 4.4 and 4.5(a) show an intricate evolution of the oscillations, in particular close to the transition region between wavy oscillations and lenses. This observation suggests that there may be different spatial modes that interact as the perturbation is advected downstream.

In the following, the structure of the linear response is investigated by a weakly non-parallel local stability analysis.

4.4.3 Weakly non-parallel stability analysis (WKBJ)

In a parallel convectively unstable flow, the spatial stability branches fully describe the response to harmonic forcing of frequency ω (Huerre and Rossi, 1998). Within this framework,

the perturbation with respect to the streamwise-invariant baseflow reads $\tilde{\eta} \propto \exp(\mathrm{i}(k_x x - \omega t))$, where k_x is the complex streamwise wavenumber, resulting from the polynomial eigenvalue problem associated with the dispersion relation (Schmid et al., 2002). The imaginary and real parts of k_x respectively describe the amplification in space and the spatial frequency.

The weak non-parallelism of the baseflow $H(x,y)$ is included by employing the WKBJ formalism introduced by Gaster et al. (Gaster et al., 1985). A fast and slow streamwise scales are introduced, respectively denoted as x and $X = \sigma x$, where σ is a measure of the weak non-parallelism of the baseflow. The following ansatz for the perturbation $\tilde{\eta}$ is considered:

$$\tilde{\eta}(x,t) = \mathcal{A}(X)\eta(X,y)\exp\left[\mathrm{i}\left(\frac{1}{\sigma}\int_0^X k_x(X')\,\mathrm{d}X' - \omega t\right)\right] \tag{4.17}$$

where η is the local eigenvalue and $\mathcal{A}(X)$ is the envelope function which smoothly connects the progressive slices of the spatial stability analysis. An asymptotic expansion in σ is performed on the linearized equation (4.10). At order $\mathcal{O}(1)$ the following eigenfunction problem is obtained:

$$-\mathrm{i}\omega\eta + (\mathrm{i}k_x)uH^2\eta + \frac{1}{3}\frac{\mathrm{d}}{\mathrm{d}y}[3H^2(\partial_y H + \partial_y\kappa_{(0)})\eta + \\ + H^3(\frac{\mathrm{d}\kappa_{(1)}}{\mathrm{d}y} + \frac{\mathrm{d}\eta}{\mathrm{d}y})] - \frac{1}{3}k_x^2[H^3(\kappa_{(1)} + \eta)] = 0, \tag{4.18}$$

which is formally analogous to the streamwise-invariant dispersion relation derived in Chapter 3, and it can be written in the form $\mathrm{i}\omega\mathbf{I}\eta = \mathbf{L}\eta$. At each streamwise cross-section, the eigenmode is normalized imposing $\int_0^{L_y}\hat{\eta}^H\hat{\eta}\mathrm{d}y = 1$, where $(\cdot)^H$ denotes the transconjugate.

At order $\mathcal{O}(\sigma)$, a compatibility condition is imposed, resulting in the following amplitude equation:

$$M(X)\frac{\mathrm{d}\mathcal{A}}{\mathrm{d}X} + N(X)\mathcal{A} = 0 \rightarrow \mathcal{A}(X) = \mathcal{A}(0)\exp\left(-\int_0^X \frac{N(X)}{M(X)}\mathrm{d}X'\right). \tag{4.19}$$

The gain is expressed as follows:

$$G^2(\omega, L_x) = \frac{\int_0^{L_x}\mathcal{A}^H(x')\mathcal{A}(x')\int_0^{L_y}(\eta^H(x',y)\cdot\eta(x',y))\,\mathrm{d}y\left(e^{\int_0^{x'}-2\mathrm{Im}(k_x)\mathrm{d}x''}\right)\mathrm{d}x'}{\int_0^{L_y}\eta^H(0,y)\cdot\eta(0,y)\mathrm{d}y}. \tag{4.20}$$

Since at each cross section $\int_0^{L_y}\eta^H\eta\mathrm{d}y = 1$, the total gain simplifies to:

$$G^2(\omega, L_x) = \int_0^{L_x}\mathcal{A}^H(x')\mathcal{A}(x')\left(e^{\int_0^{x'}-2\mathrm{Im}(k_x)\mathrm{d}x''}\right)\mathrm{d}x'. \tag{4.21}$$

The procedure is as follows. At each streamwise location x, we solve for the dispersion relation (4.18), thus obtaining the streamwise wavenumber and the corresponding eigenvector. Then, the coefficients of equation (4.19) are evaluated and the amplitude is obtained by integration

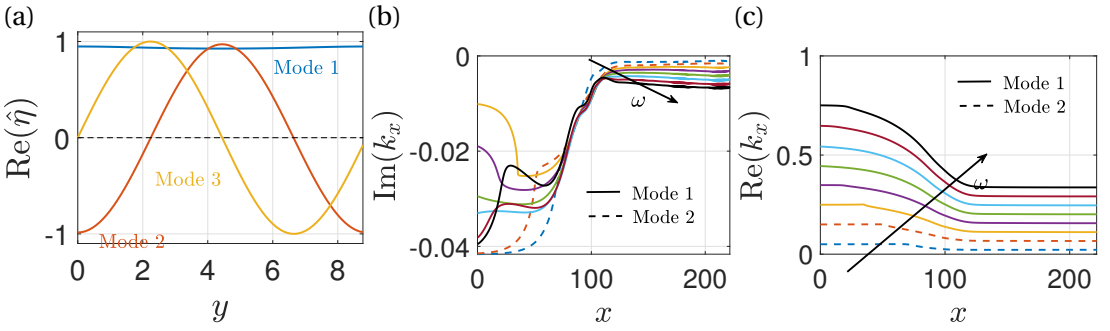

Figure 4.7: (a) Real part of the three unstable modes at the inlet, for $\omega = 0.5$. (b,c) Imaginary (b) and real (c) parts of the streamwise wavenumber, from the spatial stability analysis, for the downstream unstable mode. The solid and dashed lines respectively denote Modes 1 and 2 at the inlet. The colors identify $\omega = 0.1$ (dashed blue), $\omega = 0.3$ (dashed orange), $\omega = 0.5$ (yellow), $\omega = 0.7$ (purple), $\omega = 0.9$ (green), $\omega = 1.1$ (cyan), $\omega = 1.3$ (maroon), $\omega = 1.5$ (black). The value of the linear advection velocity is $u = 2$.

of the ODE.

The baseflow $H(x, y)$ is the steady solution of equation (4.6) outlined in Section 4.3. The baseflow is then imported in MATLAB for the resolution of the eigenvalue problem (4.18), at each of the considered 500 streamwise locations in the range $0 < x < 225$. No appreciable variations of the results are observed with a larger number of sections along the streamwise direction. The numerical discretization of the eigenfunction problem is performed using a Fourier pseudospectral collocation method. A preparatory analysis shows that numerical convergence is already achieved with 80 collocation points along the spanwise direction. The adjoint eigenvalue problem, needed for the amplitude equation, is numerically solved by using the discrete adjoint (Schmid et al., 2002) that, for an identity weight matrix, reduces to the transpose conjugate $\mathbf{L}^\dagger = \mathbf{L}^H$. The derivatives of the baseflow, streamwise wavenumber and eigenvectors, required for the amplitude equation (4.19), are evaluated using second-order finite differences. The numerical integration of equation (4.19) is performed with the built-in MATLAB function *trapz*.

The results of the above-described analysis are now presented. In the context of spatial stability analysis, negative values of the imaginary part of k_x denote unstable configurations associated with downstream propagating waves (Huerre and Rossi, 1998; Schmid et al., 2002; Gallaire and Brun, 2017). A preliminary analysis at the inlet shows that the spectrum is characterized by three unstable modes associated with downstream propagating waves. The three different modes are tracked along the streamwise direction by using the result in the previous section as the initial guess for the calculation at the successive one. Two of the modes are symmetric with respect to the axis $y = 0$, while the other one is antisymmetric. Figure 4.7(a) shows the real part of the three modes at the inlet section. We denote as *flat* or *Mode 1* the mode that is almost invariant along the spanwise direction, *cosine* or *Mode 2* the mode analogous to a cosine, and *sine* or *Mode 3* the antisymmetric mode.

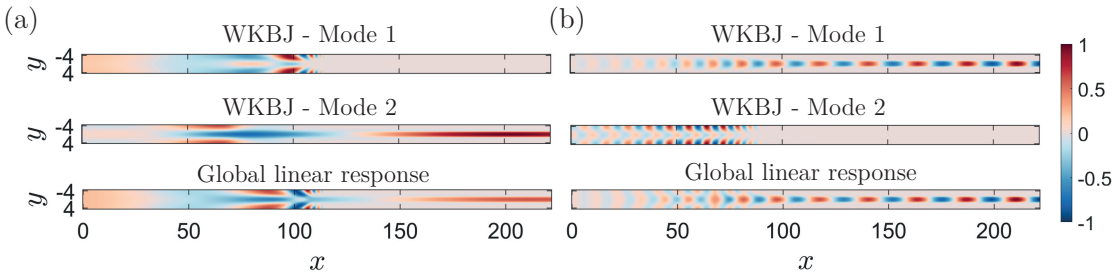

Figure 4.8: $u = 2$ and (a) $\omega = 0.1$, (b) $\omega = 1.2$. Comparison of the real part of the global linear response (on the bottom) with the WKBJ real part of Mode 1 (top) and Mode 2 (center).

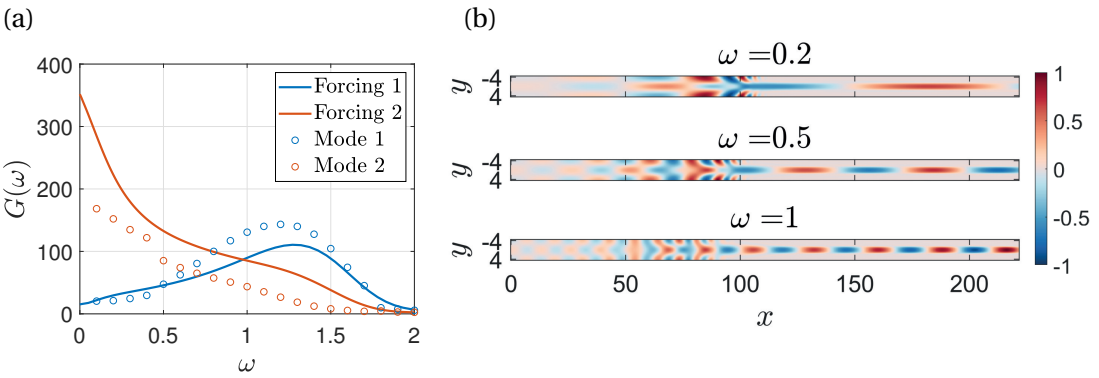

Figure 4.9: $u = 2$. (a) Gain resulting from the global linear approach, flat (Forcing 1, blue solid line) and cosine (Forcing 2, orange solid line) inlet forcings. The dots are the values of the gain obtained from the WKBJ analysis, flat (Mode 1, blue circles) and cosine (Mode 2, orange circles) inlet modes. (b) Real part of the global linear response with the harmonic cosine forcing at the inlet (Forcing 2). Eigenvectors are rescaled with the maximum absolute value.

We focus on the symmetric modes, while the antisymmetric one is reported in Appendix 4.9.2 as it is not relevant for the dynamics due to the chosen inlet forcing of Section 4.4.2. For $\omega = 0.1, 0.3$ the unstable lenses mode in the streanwise-invariant rivulet region originates from Mode 2, while for $\omega > 0.5$ it stems from Mode 1 (see figure 4.7(a)). Figure 4.7(b,c) shows the streamwise evolution of k_x for different values of the forcing frequency, and $u = 2$. Only the cases that evolve downstream to the unstable mode are reported. The imaginary and real parts of k_x respectively increase and decrease with x, reaching downstream a constant value. An increase of ω, in the considered range, shows a decrease of the real part of k_x.

The amplitude equation (4.19) allows one to connect the different streamwise slices of the modes, whose results for the real part are reported in figure 4.8, compared to the global linear response of Section 4.4.2. In panel (a), Mode 1 is amplified until $x \approx 100$, where it presents large values on the sides and is damped downstream. Mode 2 evolves into lenses of extremely large spatial period. In panel (b), Mode 1 survives downstream with smaller lenses, while Mode 2 is damped at $x \approx 100$. The pattern of the global linear response is very similar to the superposition of the modes obtained with the WKBJ approach.

We then move to a quantitative comparison of the gain between the global linear analysis and the WKBJ approach. In figure 4.9(a), the gain of Modes 1 and 2 are compared with the ones from the global linear analysis with inlet forcing (i) the spanwise-invariant oscillation of the thickness (described in Section 4.4.2) (Forcing 1) and (ii) a cosine along the spanwise direction oscillating in time, in analogy to Mode 2 (Forcing 2). The typical linear response to the Forcing 2 is reported in figure 4.9(b). The gain curve of the Forcing 2 is characterized by a large value of the static gain (i.e. at $\omega = 0$) and $G(\omega)$ decreases with ω. The two gain curves of the global linear response are analogous to those of the WKBJ approach.

The WKBJ analysis reveals that the linear response to harmonic inlet forcing (Section 4.4.2) can be interpreted as the superposition of two symmetric modes and only one of these two survives downstream, and is localized in the central lobe of the rivulet. As the rivulet profile saturates, the thickness on the sides is of order 10^{-2}, thus quenching the instability because of the very thin layers of fluid involved in this region. The real part of k_x is decreasing downstream, and thus the perturbation presents larger wavelengths than upstream. This is due to larger advection velocities (proportional to uH^2) on the central part of the rivulet, compared to regions close to the inlet with lower maximum thickness. The comparison of the global linear analyses with the inlet forcings that reproduce the spatial modes confirms the good agreement in terms of gain and validates the interpretation of the linear response as the interaction of these two modes.

Finally, at very low values of the forcing frequency, the wavelengths of the resulting unstable mode are of the order of the variations of the baseflow, thus violating the hypothesis of slowly-evolving baseflow compared to the perturbation. However, a good agreement is observed also in this case.

In this section, we aimed at interpreting the secondary instability observed in the global linear response of Section 4.4.2 by a local stability analysis combined with a WKBJ approach. However, the previous analyses were focused on the linear response. The range of validity of the previous analyses is assessed by investigating the non-linear dynamics. Henceforth, the non-linear response to the inlet forcing described in Section 4.4.2 is studied.

4.5 Non-linear response to inlet harmonic forcing

In this section, the non-linear response to harmonic inlet forcing is studied. The non-linear equation (4.6) is thus considered and the evolution of the response with initial condition the steady baseflow $H(x, y)$ described in Section 4.3 is studied. The Dirichlet boundary condition at the inlet reads:

$$h(x = 0, y, t) = 1 + \mathrm{A}^* \cos(y/\sqrt{2}) + \varepsilon \sin(\omega t), \tag{4.22}$$

where ε and ω are respectively the amplitude and the frequency of the harmonic inlet forcing.

Figure 4.10 shows the resulting pattern at $t = 125$, for $\omega = 1.25$ and $u = 2$. For $\varepsilon = 10^{-4}$, 10^{-3}, the

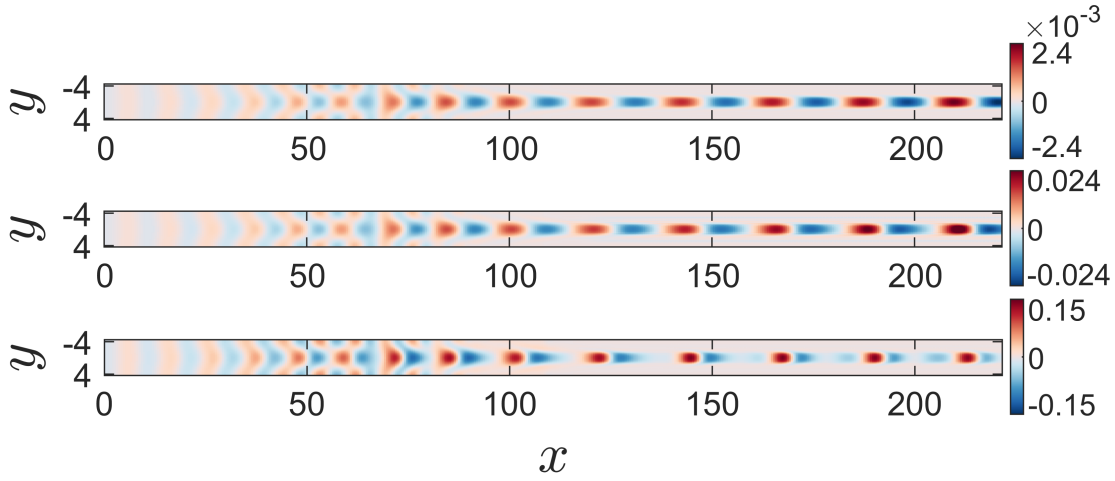

Figure 4.10: Non-linear response to harmonic forcing at $t = 125$, for $\omega = 1.25$ and $u = 2$, in terms of perturbation $\eta = h - H$. From the top to the bottom: $\varepsilon = 10^{-4}$, $\varepsilon = 10^{-3}$, $\varepsilon = 10^{-2}$.

results show lenses analogous to those of the global linear response, and the amplitude of the response is proportionally increasing with the forcing one. However, already at $\varepsilon = 10^{-2}$, the pattern significantly differs from the previously described linear response, and the amplitude of the response does not follow a linear increase with the forcing amplitude. In figure 4.11(a) the centerline and side profile for $\varepsilon = 10^{-2}$ is reported. At the centerline, profiles similar to those reported in Kofman et al. (2018) and Rohlfs et al. (2017) are observed.

As a quantitative comparison with the linear analysis, the non-linear gain is introduced:

$$G^2_{\mathrm{NL}}(\omega, u) = \frac{\overline{\int_\Omega (h-H)^2 \mathrm{d}\Omega}}{\overline{\int_\Gamma (\varepsilon \sin(\omega t))^2 \mathrm{d}\Gamma}}, \tag{4.23}$$

where the overline denotes time averaging. In figure 4.11(b), the comparison between the non-linear gain and the linear one reveals a very good agreement for $\varepsilon = 10^{-4}, 10^{-3}$. For $\varepsilon = 10^{-2}$ the maximum gain is lower, although the curve resembles the global linear one.

The non-linear simulations confirm the results of the linear analyses when the amplitude of the harmonic forcing is sufficiently small. At larger values of the amplitude of the harmonic forcing, the non-linear effects become predominant and strongly non-linear lenses are observed, with centerline profiles reminiscent of previous analyses (Rohlfs et al., 2017; Kofman et al., 2018). A strong saturation mechanism of the amplitudes is observed. In a perspective of flow control, the amplitude of the harmonic inlet forcing thus plays a key role, together with the forcing frequency. For large enough values of the amplitude, a pattern of almost periodic traveling lenses. The amplitude of these lenses slowly evolves downstream when u is sufficiently large.

In this section, the different patterns of lenses emerging from the inlet and the effect of u, frequency and initial amplitude of the harmonic perturbation was characterized. In the following, the late stage of the process of growth and the structure of these lenses in the rivulet

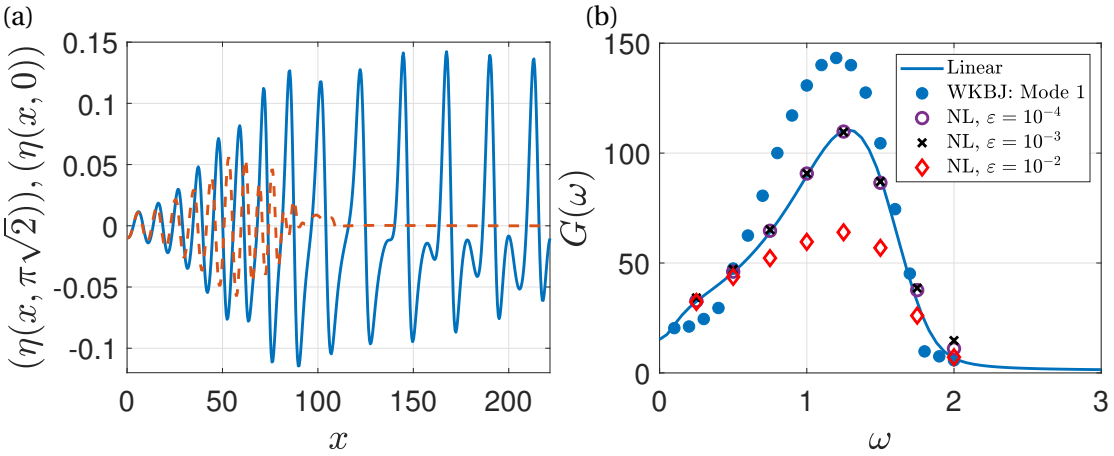

Figure 4.11: (a) . Perturbation $\eta = h - H$ from the non-linear simulations, at the centerline (solid) and on the lateral boundary (dashed), $\varepsilon = 10^{-2}$, for $u = 2$, $\omega = 1.25$ and $t = 125$. (b) Total gain from the WKBJ approach for Mode 1, the global linear analysis and the non-linear simulations for different values of the inlet amplitude.

region are investigated. Since a parametric study considering the streamwise evolution with inlet and outlet conditions would involve a large number of parameters (ω, u, ε) and require extremely long domains, we first study the evolution of non-linear structures, starting from a rivulet, in a periodic domain of variable streamwise length.

4.6 Non-linear evolution of traveling lenses in a periodic domain

The present section is devoted to the study of the non-linear evolution of lenses in a periodic domain of respectively streamwise and spanwise size L_p and $L_y = 2\pi\sqrt{2}$. Equation (4.3) is solved with periodic boundary conditions and the following initial condition:

$$h(x,y,0) = H_r(y) + \varsigma \mathrm{Re}\left(\check{\eta}\exp\left(\mathrm{i}k_x x\right)\right), \quad \varsigma = 10^{-2}. \tag{4.24}$$

$H_r(y)$ is the streamwise-invariant rivulet profile, extended along the streamwise direction, at $t = 400$, obtained from equation (4.3) imposing $\partial_x = 0$, and $\check{\eta}$ is the linear mode obtained from the linear stability analysis of $H_r(y)$. The initial condition for the evaluation of $H_r(y)$ is $h = 0.54$, which is the thickness required to have the same flow rate of the simulations with inlet and outlet conditions, in the streamwise-invariant rivulet region. The simulations, in analogy with the previous non-linear ones, are performed in COMSOL Multiphysics.

The influence of u and the streamwise wavenumber of the periodic domain $k_x = 2\pi/L_p$ on the results is now described. Figure 4.12 shows the thickness profile, at large times, for $k_x = 0.3$ and two different values of u. The large-time solution is characterized by a rivulet carrying a lens, whose profile is similar to an axisymmetric drop. Similar results are obtained increasing u and varying k_x, as in figure 4.13, which shows a lens traveling on the rivulet, for $k_x = 0.5$.

(a) (b)

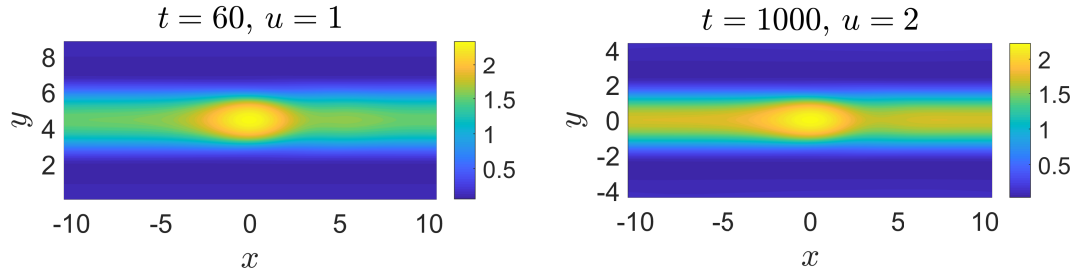

Figure 4.12: Thickness profile for the non-linear simulation with periodic domain, $k_x = 0.3$. (a) $u = 1$ and $t = 60$, (b) $u = 2$ and $t = 1000$. The x and y scales are the same so as to show the correct aspect ratio of the lens.

(a) (b)

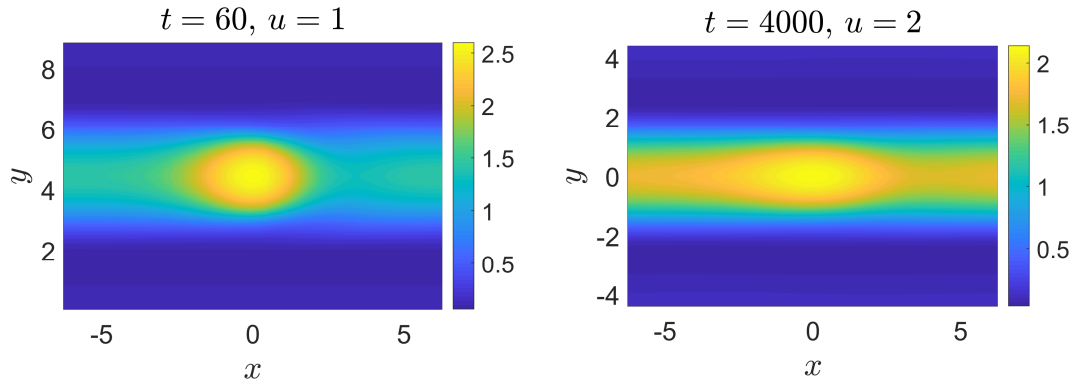

Figure 4.13: Thickness profile for the non-linear simulation with periodic domain, $k_x = 0.5$. (a) $u = 1$ and $t = 60$, (b) $u = 2$ and $t = 4000$. The x and y scales are the same so as to show the correct aspect ratio of the lens.

For visualization purposes, the maximum thickness has been repositioned at the center of the domain, since the lens is traveling. In Pier et al. (2001), the non-linear response for a fixed k_x gives the non-linear complex dispersion relation between the frequency ω_{NL} and k_x, the streamwise wavenumber itself, for a saturated traveling wave. We extend this idea to the case of a non-saturated response by considering a time-dependent dispersion relation, in which the non-constant and non-linear frequency reads:

$$\omega_{\mathrm{NL}}(t, k_x) = \frac{\mathrm{d}X_{\max}}{\mathrm{d}t} k_x, \tag{4.25}$$

where $X_{\max}$ is the maximum thickness location.

The time evolution shows that the maximum value of the thickness $\max(h)$ always increases as the lens travels (figure 4.14(a)). A final and rapid blow-up of the solution is always observed, in which the values of the time derivative of the maximum thickness take very large values.

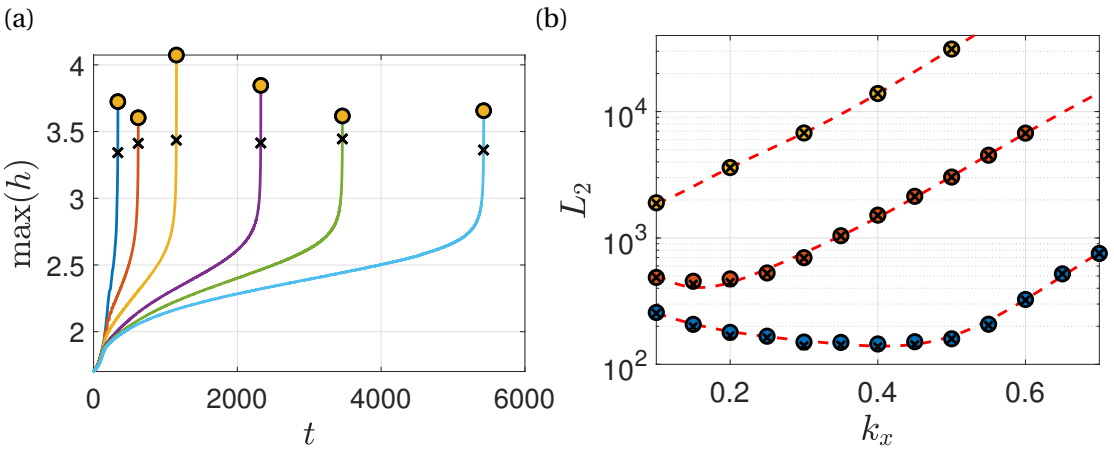

Figure 4.14: (a) Evolution of the maximum thickness with x for $u = 2$, $k_x = 0.1$ (blue), $k_x = 0.2$ (orange), $k_x = 0.3$ (yellow), $k_x = 0.4$ (purple), $k_x = 0.45$ (green), $k_x = 0.5$ (cyan). (b) Distance for the blow-up of the solution (dots) and at which $\frac{\mathrm{d}}{\mathrm{d}t}\max(h) > 0.1$ occurs (crosses), for the non-linear simulations in the periodic domain, $u = 1$ (blue), $u = 1.5$ (orange), $u = 2$ (yellow).

The spatial evolution is deduced by following the maximum value of the thickness that travels in the periodic domain. In figure 4.14(b) we report the distance L_2 for the blow-up of the solution (dots) and at which $\frac{\mathrm{d}}{\mathrm{d}t}\max(h) > 0.1$ (marked by crosses in figure 4.14(a)) occurs, as a function of k_x. The distance for the blow-up of the solution strongly increases with u. For $u = 1$ and $u = 1.5$ the behavior of L_2 is non-monotonous with ω, while L_2 increases with ω, for $u = 2$.

The blow-up of the solution is interpreted as the manifestation of the onset of the dripping process, according to Kofman et al. (2018) and Indeikina et al. (1997). Both the final simulation distance and the one beyond which $\frac{\mathrm{d}}{\mathrm{d}t}\max(h) > 0.1$ are considered, without appreciable differences. Therefore, a first estimate of the order of magnitude of the dripping distance is given using the results of figure 4.14.

In this section, a first estimate of the order of magnitude of the dripping distance is given. This estimate can be improved considering the streamwise-transient evolution of perturbations at low amplitudes studied in Sections 4.4.2 and 4.4.3.

4.7 An estimate of the dripping length

In the previous section, the non-linear structures emerging from a fully-developed rivulet profile, in a periodic domain of variable streamwise length was studied. However, when inlet and outlet conditions are considered, the growth of perturbations in the region where the rivulet evolves is crucial, as observed in Section 4.4.2. If the amplitude of the inlet forcing is small enough, the growth of perturbations between the inlet and the saturated rivulet profile follows the linearized dynamics described in Section 4.4.2. Therefore, in the spirit of Pier (2003b), the growth of lenses is composed of (i) an initial linear growth described

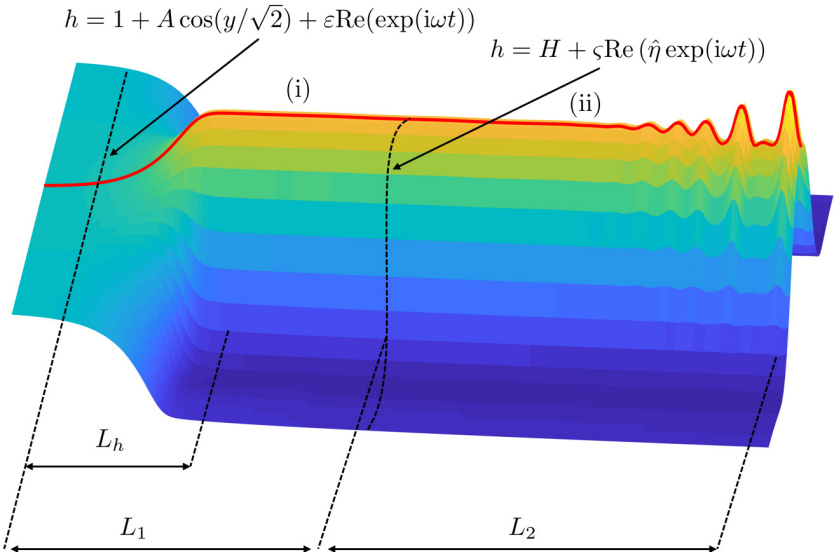

Figure 4.15: Sketch of the configuration considered for the estimate of the dripping length.

by the linearized dynamics and (ii) by a non-linear growth described by the evolution in the periodic domain of the previous section. We consider a harmonic inlet perturbation of frequency ω and amplitude ε, for the steady baseflow $H(x,y)$ described in Section 4.3, i.e $h(x=0,y,t) = 1 + \mathrm{A}^* \cos(y/\sqrt{2}) + \varepsilon\mathrm{Re}(\exp(\mathrm{i}\omega t))$.

The transition between stages (i) and (ii) is defined where the maximum value of the thickness perturbation $h-H$ is $\max(h-H) = \varsigma$, where $\varsigma \ll 1$, assumed to be $\varsigma = 10^{-2}$ (see figure 4.15) according to the simulations of the previous section. In pratice, the distance needed to pass from stage (i) to (ii), identified as $L_1(\omega,\varepsilon,u)$, is obtained from the global linear analysis with inlet and outlet conditions (Section 4.4.2) as the coordinate $x = L_1$ at which $\sqrt{L_y}\varepsilon\max(|\eta|) = \varsigma$ (since the inlet condition is given by equation (4.15)). In figure 4.16(a) the variation of L_1 with the forcing frequency ω and for different values of ε, for $u = 1$, is reported. L_1 is non-monotonous with ω, whilst it always decreases with ε.

The dripping distance L_{drip} is thus given by $L_{\mathrm{drip}}(\omega,\varepsilon,u) = L_1(\omega,\varepsilon,u) + L_2(\omega,u)$, where $L_2(\omega,u)$ is obtained from the simulations with double-periodic domain of Section 4.6 as follows. Since the simulations with inlet and outlet conditions were conducted with an imposed temporal frequency rather than a streamwise spatial forcing, the results of the simulations with periodic domain cannot be directly applied. At each time step, and for each simulation with $k_x = \mathrm{const}$, the instantaneous and non-linear temporal frequency is evaluated using the definition of non-linear phase speed $\omega_{\mathrm{NL}}(t,k_x) = \frac{\mathrm{d}X_{\max}}{\mathrm{d}t}k_x$, where $X_{\max}$ is the maximum thickness location. The results for $u = 1$ is reported in figure 4.16(b). To evaluate $L_2(\omega,u)$, the iso-contour $\omega_{\mathrm{NL}} = \omega$ is thus followed in time, crossing the values of k_x until we reach the dripping threshold for a time $t = T$. Equation (4.25) is integrated to obtain the dripping distance $L_2(\omega,u)$:

$$L_2 = \int_0^T \frac{\omega}{k_x}\mathrm{d}t. \tag{4.26}$$

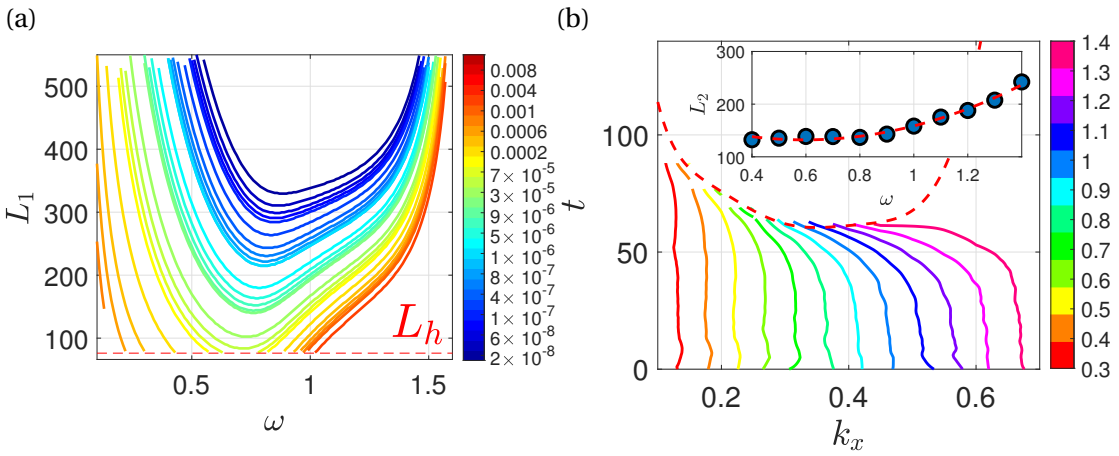

Figure 4.16: $u = 1$. (a) Variation of L_1 with ω; different colours denote different values of ε according to the colorbar. The red dashed line denotes the healing length L_h. (b) Variation of the non-linear frequency $\omega_{\mathrm{NL}} = \frac{\mathrm{d}X_{\max}}{\mathrm{d}t} k_x$ with time; different colours denote different values of k_x according to the colorbar. The red dashed line denotes the dripping threshold. In the inset: variation of L_2 with ω resulting from the integration in time for fixed ω.

The numerical implementation is performed in MATLAB. The non-linear frequency is evaluated with second order finite differences and a time step of $\Delta t = 0.05$, for different k_x whose step is $\Delta k_x = 0.025$. The integral is performed along the iso-level ω_{NL} =const using the built-in MATLAB function *trapz*. The variation of L_2 with ω (for $u = 1$) is reported in the inset of figure 4.16(b). An increase of L_2 with ω is observed, in the considered parameters range.

Note that the decomposition into L_1 and L_2 only holds if L_1 is larger than the healing length for the fully developed rivulet profile L_h, as the results of Section 4.6 imply as initial condition a fully developed rivulet and thus cannot be applied, if it has not been attained. Figure 4.17(a) shows the results of the prediction (solid line) compared to the non-linear simulations of equation (4.3) with inlet and outlet conditions (dots) with a domain size of $L_x = 900$, whose thickness distribution at the first dripping onset is reported in panel (b). The non-linear simulation is stopped when the critical value of $\frac{\mathrm{d}}{\mathrm{d}t}\max(h) > 0.1$ is reached for the first time. The prediction fairly agrees with the non-linear simulations results, with a relative error of $\approx 10\%$. The agreement is reasonably good also when u is varied, as reported in the inset of figure 4.17(a).

In this section, a method to estimate the dripping length by exploiting the results of the global linear analysis and the non-linear simulations in doubly-periodic domain was outlined, for the steady baseflow described in Section 4.3. As reported in figure 4.17(b), the non-linear response exhibits non-negligible variations along the streamwise direction at the dripping location, breaking the assumption of traveling and periodic lenses. However, the prediction fairly agrees with the simulations, thus giving a reasonable estimate of the dripping distance as a function of the parameters (ω, ε, u). The proposed approach gives a fairly accurate prediction and is suitable for a parametric study, in opposition to the non-linear simulations with inlet

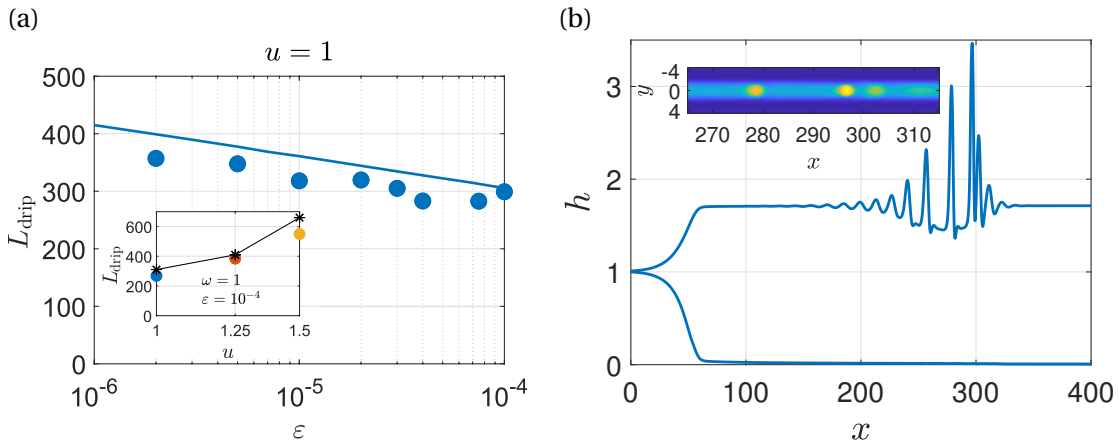

Figure 4.17: (a) Dripping length L_{drip} as a function of ε, prediction (solid line) and results of the non-linear simulation (dots), for $\omega = 1$ (blue) and $u = 1$. In the inset: dripping length as a function of u, for $\varepsilon = 10^{-4}$ and $\omega = 1$. (b) Maximum and minimum thickness at $t = 150$, for $\varepsilon = 7.5 \times 10^{-5}$ and $\omega = 1$. In the inset: thickness distribution close to the dripping region.

and outlet conditions, which do not appear as suitable for describing a complete map of the dripping length in the parameters space.

4.8 Conclusion and discussion

In this work, the secondary instability of a thin film flowing under an inclined plane when the inlet is temporally forced was studied. Inspired by the experimental results of Chapter 2, we considered the steady solution of the flow equation, for fixed $\tilde{\ell}_c^* = 1$ and with inlet and outlet conditions, in a spanwise-periodic domain of size $L_y = 2\pi\sqrt{2}$, i.e. the natural spacing of rivulets. The steady baseflow was characterized by a streamwise-invariant state emerging downstream, at a distance found to be linear with u.

The linear response was then studied, with the inlet forced with a harmonic forcing consisting of an oscillation of the thickness around the steady constant value. Thickness perturbations evolved into lenses traveling on the rivulet, whose spacing was found to decrease with the forcing frequency. An increase of the linear advection velocity led to lenses of larger spacing and smaller amplitudes, while the forcing frequency was seen to modify both the spacing and the amplitude of such lenses. The gain curves showed a maximum, associated with an optimal frequency decreasing with u, which did not vary significantly with the streamwise length of the domain.

The linear response was rationalized via a weakly non-parallel (WKBJ) spatial stability analysis. The linear dynamics was interpreted as the superposition of two linearly unstable modes, one damped and the other one amplified downstream. The gain curves of the linear response were well reproduced by the weakly non-parallel analysis.

For low amplitudes of the forcing, the non-linear response to harmonic forcing showed patterns similar to the linear ones. Associated with an increase of the non-linear effects, lower values of the gain were observed, without relevant changes of the optimal frequency. Trains of almost periodic lenses, slowly evolving downstream, were observed. The non-linear structures were then characterized by studying the evolution in doubly-periodic domains of variable streamwise length, where the blow-up of the solution was interpreted as the initial stage of dripping. A dripping distance was defined by combining the results of the linear response with the non-linear evolution in a doubly-periodic domain, giving an estimate in fair agreement with the non-linear simulations.

Our work provides a description of three-dimensional patterns of a thin film flowing under an inclined plane when the inlet is temporally forced, thus disclosing the existence of regular arrays of traveling lenses on the rivulets. We show the possibility to exploit the flow rate, inclination angle, and the frequency and amplitude of the time-harmonic inlet forcing so as to obtain lenses with different spacings and shapes. These considerations may find further development in manufacturing processes of complex structures by means of curing processes of coatings below surfaces (Marthelot et al., 2018). Besides, we proposed a method to estimate the dripping distance of a rivulet, both for spatially-periodic structures and when the evolution from the inlet is considered.

This work may be extended in several ways to refine the presented results. First, the case of a rivulet with natural spacing $L_y = 2\pi\sqrt{2}$ was investigated, in which the temporal inlet forcing was small enough so that the dynamics was considered as a perturbation of the steady and spanwise-periodic rivulet. Further developments may include spanwise-periodic rivulets with wavelength differing from the natural one, briefly presented in Chapter 2. Another extension is the analysis for different values of $\tilde{\ell}_c^*$ to better characterize the response in the whole parameter space. Last, a lubrication-type approximation to describe the dynamics of lenses was employed. Albeit suitable to describe the first stage of the dripping process, the lubrication model cannot describe the later stages of dripping. Further studies may include the analysis of the process leading to a dripping drop detaching from the rivulet.

4.9 Appendix

4.9.1 Global stability analysis

In this section, we present the results of the global stability analysis of the steady baseflow presented in Section 3. Starting from the linearized equation (4.2), we consider the following ansatz:

$$\tilde{\eta}(x, y, t) = \eta(x, y) \exp(\lambda t), \tag{4.27}$$

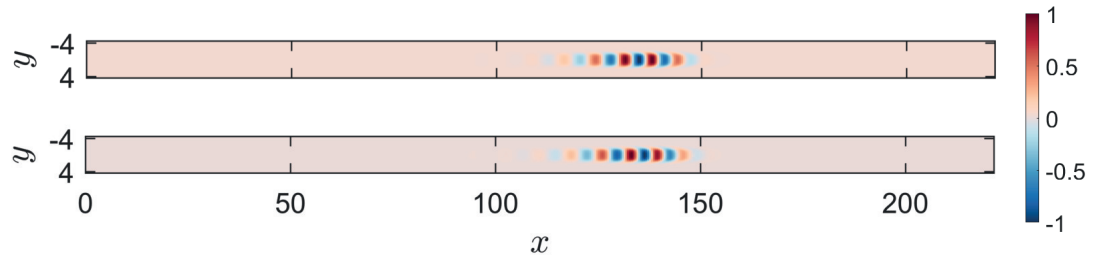

Figure 4.18: Real (on the top) and imaginary (on the bottom) parts of the marginally stable global mode at $u = 0.56$. Eigenvectors are normalized with the maximum absolute value.

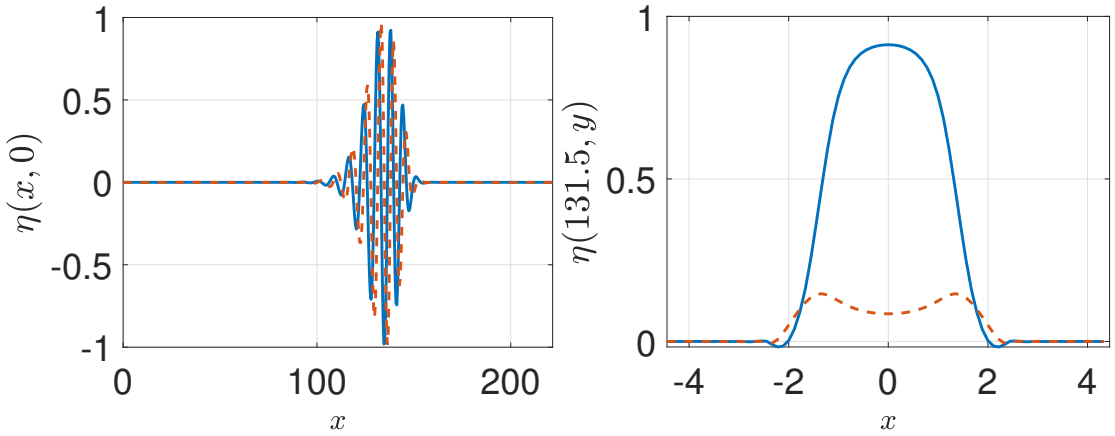

Figure 4.19: Real (solid line) and imaginary (dashed line) parts of the marginally stable global mode at $u = 0.56$. On the left: section at $y = 0$. On the right: section at $x = 131.5$. Eigenvectors are normalized with the maximum absolute value.

where λ is the complex growth rate and $\eta(x,y)$ is the associated eigenvector. We then substitute this ansatz in equation (4.2), leading to the following eigenfunction problem:

$$\lambda\eta + \frac{1}{3}\nabla\cdot\left(H^3\left(\nabla\eta + \nabla\kappa_{(1)}\right) + 3H^2\left(\nabla H + \nabla\kappa_{(0)} + u\right)\eta\right) = -\mathrm{Sp}(x)\eta. \tag{4.28}$$

Positive (resp. negative) values of the real part of λ denote unstable (resp. stable) configurations. Once discretized, the eigenfunction problem becomes an eigenvalue problem. We exploit the built-in eigenvalue solver in COMSOL Multiphysics, based on the ARPACK Library. The steady baseflow $H(x,y)$ is marginally stable at the value of the linear advection velocity $u_0 = 0.56$, below which it is unstable. The mode (see figures (4.18,4.19)), of frequency $\mathrm{Im}(\lambda) = 0.82$, is located in the streamwise-saturated rivulet region, and shows a pattern of alternate lenses. These results are in very good agreement with the analysis performed in Chapter 3, in which the absolute to convective transition of the instability for the one-dimensional rivulet profile was found at the same value of u_0, with the same frequency. For $u > u_0$, we expect the baseflow $H(x,y)$ behaving as a noise amplifier (Huerre and Monkewitz, 1990).

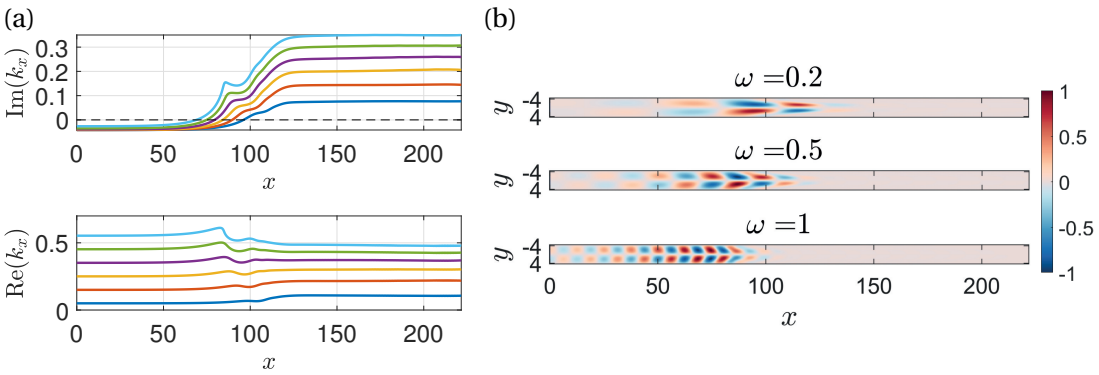

Figure 4.20: $u = 2$. (a) Variation with x of the imaginary (top) and real (bottom) parts of the streamwise wavenumber of the antisymmetric mode (3) of the WKBJ analysis. $\omega = 0.1$ (blue), $\omega = 0.3$ (orange), $\omega = 0.5$ (yellow), $\omega = 0.7$ (purple), $\omega = 0.9$ (green), $\omega = 1.1$ (cyan). (b) Real part of Mode 3 of the WKBJ approach.

4.9.2 Antisymmetric sine mode from the WKBJ approach

Here, we describe the antisymmetric mode. In figure 4.20 we show the results for $u = 2$. In all the reported cases, the imaginary part of k_x is initially negative (corresponding to downstream exponential amplification) and increases with x, reaching positive values downstream (corresponding to spatially decaying downstream propagating perturbations). The real part of k_x does not show significant variations with x. The response resulting from the WKBJ approach is reported in figure 4.20(b), in the (x, y) plane. The spanwise-sinusoidal oscillation is amplified downstream, until $x \approx 100$, beyond which it is rapidly damped.

The antisymmetric mode is localized on the sides of the domain and is amplified in the region $0 < x < 100$. However, owing to the very small thickness in the streamwise-invariant rivulet region, the side lobes of the saturated rivulet profile cannot sustain the instability, and the mode is damped as the streamwise-invariant state forms.

5 Drops on the Underside of a Slightly Inclined Wet Substrate Move Too Fast to Grow

Remark This chapter is largely inspired by the publication of the same name

E. Jambon-Puillet[1], P. G. Ledda[2], F. Gallaire[2], P-T Brun[1]
[1]Department of Chemical and Biological Engineering, Princeton University,Princeton, New-Jersey 08540, USA
[2]Laboratory of Fluid Mechanics and Instabilities, École Polytechnique Fédérale de Lausanne, Lausanne, CH-1015, Switzerland

Physical Review Letters, **127**, 044503 (2021)

Authors'contributions P.G.L. performed the numerical simulations and participated in the collective effort to develop the theoretical framework. P.G.L. participated in the collective writing of the paper, starting from the first draft and successive versions of E. J-P.

Pendant drops suspended on the underside of a wet substrate are known to accumulate fluid from the surrounding thin liquid film, a process that often results in dripping. The growth of such drops is hastened by their ability to translate over an otherwise uniform horizontal film. Here we show that this scenario is surprisingly reversed when the substrate is slightly tilted (≈ 2 deg); drops become too fast to grow and shrink over the course of their motion. Combining experiments and numerical simulations, we rationalize the transition between the conventional growth regime and the previously unknown decay regime we report. Using an analytical treatment of the Landau-Levich meniscus that connects the drop to the film, we quantitatively predict the drop dynamics in the two flow regimes and the value of the critical inclination angle where the transition between them occurs.

5.1 Introduction

We refer to Section 1.3.3.1 for a general introduction about the Rayleigh-Taylor instability.

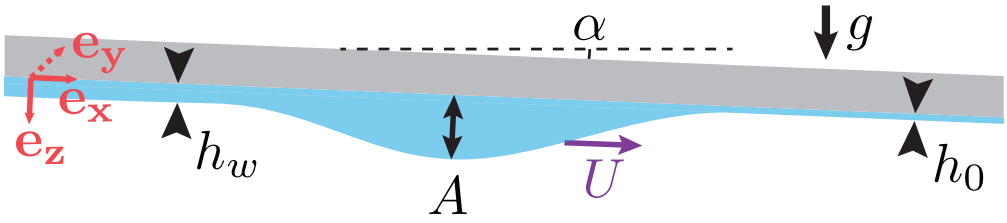

Figure 5.1: Schematic of a pendant drop of amplitude A sliding with velocity U under a substrate pre-wetted with a film of thickness h_0 and inclined by an angle α.

In Chapter 4, we proposed a method to estimate the dripping length by exploiting numerical results. Yet, our understanding of fully formed pendant drops and their transition to dripping remains sparse (Lister et al., 2010) owing to the difficulties of modeling the fully non-linear long-term dynamics. In this Chapter, we focus on a single pendant drop (see figure 5.1), a problem that remains analytically tractable while retaining a rich physics. Pendant drops under uniformly coated films are capable of steady translation, even in the theoretical limit of a perfectly horizontal substrate (Lister et al., 2010). Over the course of their trajectory, these drops accumulate more fluid from the surrounding thin film than if they were stationary (Lister et al., 2010), thereby reaching the critical size leading to dripping (Marthelot et al., 2018) faster than immobile drops. Here, using experiments, numerical simulations and theory, we show that increasing the drop velocity by slightly tilting the substrate surprisingly prevents dripping. Past a critical inclination, the film left by the drop in its wake is thicker than the one absorbed by the drop in its front. This negative balance depletes the volume of fluid in the drop, which shrinks, thereby avoiding dripping. Through an analysis of the Landau-Levich meniscus at the edge of the drop, we unveil the physics at play in these drops that are too fast to grow and predict analytically their dynamics and the transition between the two aforementioned flow regimes.

5.2 Experimental and numerical results

Our experiment is schematized in figure 5.1. Silicone oil (density $\rho = 971$ kg/m^3, surface tension $\gamma = 20.3$ mN/m, viscosity $\mu = 1.13$ Pa.s) is spin-coated on a flat glass substrate to produce a film of uniform thickness h_0 (measured by weighting the sample). The substrate is then flipped and mounted onto a rotating arm while a droplet is applied on the film with a micropipette. The resulting pendant drop has an initial amplitude $\bar{A}_0 \sim \ell_c$ where $\ell_c = \sqrt{\gamma/(\rho g)}$ denotes the capillary length and g denotes the acceleration of gravity. The substrate is then tilted by an angle α and the dynamics is recorded (see Section 5.5.1 for details). Note that the initial coating is sufficiently thin to not destabilize via the Rayleigh-Taylor instability over the course of our experiment (Fermigier et al., 1992). The film thickness is therefore assumed to be uniform and constant far from the drop.

Figure 5.2(a) shows a chronophotography of an experiment performed with a nearly horizontal

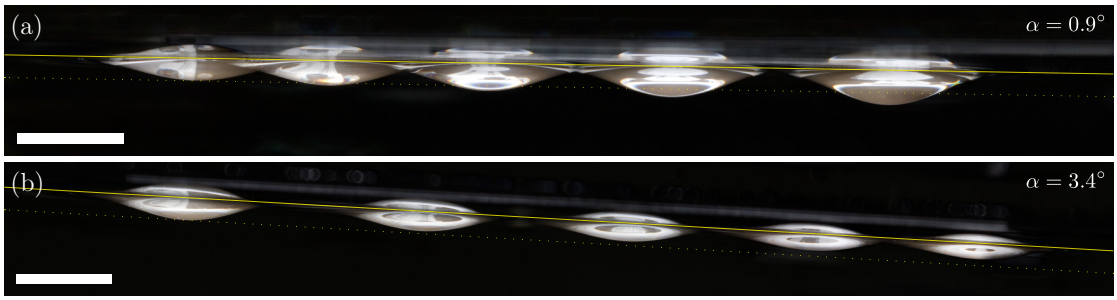

Figure 5.2: Chronophotographies of two experiments at low (a) and high (b) inclination angles with $h_0 \approx 89$ μm (scale bars are 5 mm). The interval between pictures is 9 and 3.75 min, respectively. The pictures include the reflexion of the drop on the substrate. The solid lines indicate the position of the substrate. The dotted lines mark the initial amplitudes of the drops $\bar{A}_0 = \{1.03, 1.16\}$ mm.

substrate ($\alpha = 0.9°$). As evident from the figure, the drop translates by several times its diameter over the course of the experiment while both the drop speed $\bar{U}$ and amplitude $\bar{A}$ increase. In figure 5.2(b), we show an experiment nearly identical to (a), except for that the inclination angle is slightly higher ($\alpha = 3.4°$). As expected, the drop initially moves faster. However, unlike the lower inclination case, it progressively shrinks and decelerates. In figure 5.3 we plot the amplitude $\bar{A}(\bar{t})$ and position $\bar{x}(\bar{t})$ of drops sliding over films of similar thickness ($h_0 \approx 89$ μm) but with different inclination angles α. While the drop accelerates and grows for the three smallest angles, the situation is reversed for the two largest angles. The inclination $\alpha_c \approx 2°$ appears to be the critical angle, α_c, where the drop amplitude and speed are constant ($\bar{U} \approx 2.3$ mm/min). Modifying the film thickness changes the value of α_c, as well as the timescale of the experiment. Increasing the drop initial amplitude $\bar{A}_0$ appears to speed-up the dynamics but does not change its outcome (see Section 5.5.2) .

We turn to numerical simulations to rationalize these two flow regimes. Owing to the dimensions of the problem we use the lubrication approximation to describe the evolution of the position of the interface $\bar{h}(\bar{x}, \bar{y}, \bar{t})$ (Yiantsios and Higgins, 1989) but retain the full fledged expression of the curvature $\bar{\kappa}$ (Wilson, 1982). Note that, in this case, we employ a slightly different adimensionalization from the one employed in the previous chapters, since it is more suitable to describe the almost-horizontal substrate configurations considered here. In the Cartesian frame aligned with the substrate (see figure 5.1), we obtain the following dimensionless thin-film equation after rescaling $\bar{x}$ and $\bar{y}$ using $\ell_c/\sqrt{\cos\alpha}$, h using the coating thickness far from the drop h_0, and t using $\tau = \mu\gamma/\left(h_0^3\rho^2 g^2 \cos^2\alpha\right)$:

$$\begin{aligned} \partial_t h + \widetilde{\alpha} h^2 \partial_x h + (1/3)\nabla\cdot\left[h^3\left(\nabla h + \nabla\kappa\right)\right] = 0, \\ \kappa = \nabla\cdot\left[\nabla h \Big/ \sqrt{1 + \left(h_0\sqrt{\cos\alpha}/\ell_c\right)^2 (\partial_x h)^2 + \left(h_0\sqrt{\cos\alpha}/\ell_c\right)^2 \left(\partial_y h\right)^2}\right], \end{aligned} \tag{5.1}$$

where a bar indicates rescaled variable. Note that the inclination of the substrate is captured

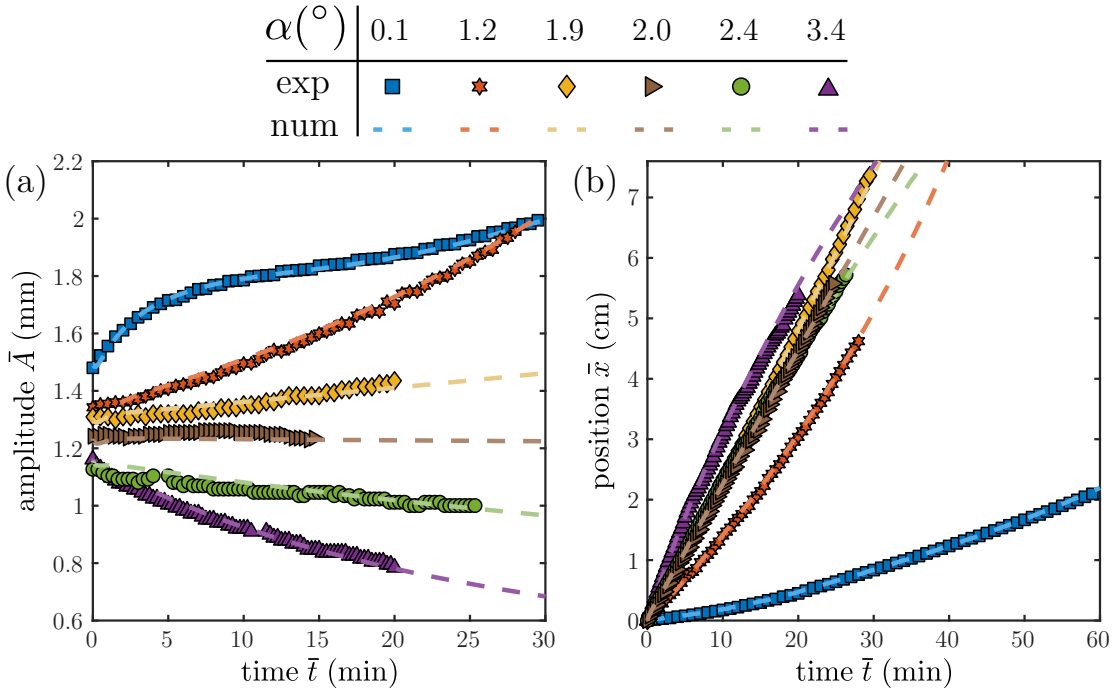

Figure 5.3: Shown is the amplitude $\bar{A}(\bar{t})$ (a) and position $\bar{x}(\bar{t})$ (b) of drops sliding under a film of thickness $h_0 \approx 89$ μm at different inclination angles α (see legend). Markers indicate experiments and dashed lines indicate numerical simulations.

by $\widetilde{\alpha} = \frac{\ell_c \tan\alpha}{h_0\sqrt{\cos\alpha}} \approx \frac{\ell_c \alpha}{h_0}$.

We solve equation (5.1) with the finite element software COMSOL on a rectangular domain with periodic boundary conditions and the initial condition $h(x,y,0) = 1 + \bar{h}_d(x,y)/h_0$. Here, $\bar{h}_d(x,y)/\ell_c$ is the dimensionless profile of a static pendant drop obtained by integrating the Young-Laplace equation numerically (see Section 5.5.1 for numerical details). In figure 5.3 we show the evolution of the drop amplitude $\bar{A}(\bar{t})$ and position $\bar{x}(\bar{t})$ obtained numerically with the parameters corresponding to the aforementioned experiments within their uncertainty ($\Delta h_0 = 7$ μm, $\Delta\alpha = 0.15°$). The agreement between experiments and numerics is favorable thereby validating our simulations.

Leveraging our simulations we investigate the physics setting the value of the critical angle α_c. In figure 5.4(a) we plot side-by-side the log of the dimensionless film thickness $\bar{h}(x,y)/h_0$ for two drops, each of which corresponds to a given flow regime. The two situations only differ in the value of the dimensionless inclination angle $\widetilde{\alpha}$. Yet, their respective wakes are qualitatively different. In particular, the wake thickness $\bar{h}_w$ appears to be mostly greater than h_0 for large inclinations and lower than h_0 for small inclinations. This sizable difference plays a key role in defining the flow regimes. Along its trajectory, a drop indeed absorbs the uniform film laying at its front and releases liquid in its wake. The contribution from the Rayleigh-Taylor instability being negligible, the change in volume of the drop is $\partial_{\bar{x}}\bar{V} \approx \int_{-R}^{R}\left(h_0 - \bar{h}_w(\bar{y})\right)\mathrm{d}\bar{y}$ with R the

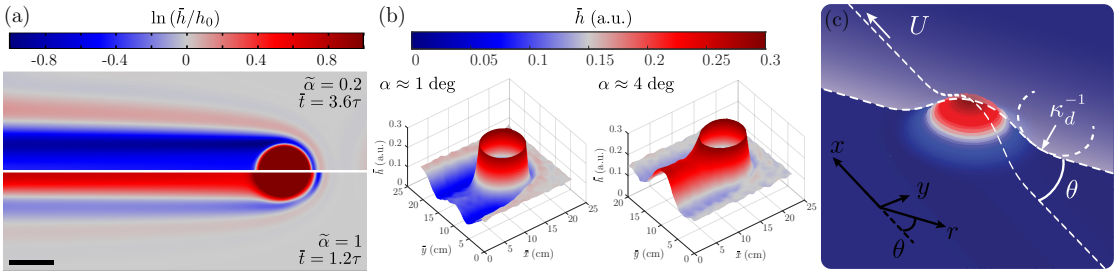

Figure 5.4: (a) Thickness map for two simulations with identical initial drops ($A_0/\ell_c = 1.05$, $h_0/\ell_c = 0.04$) but different inclination angles $\tilde{\alpha}$ (position $x = 37.4\ell_c$). Scale bar $5\ell_c$. (b) Thickness profiles inferred from experiments conducted with dyed oil at low and high inclination angles ($A_0/\ell_c \approx 0.8$, $h_0 \approx 85\ \mu$m). (c) Three dimensional schematics of the drop introducing the polar coordinates $\{r, \theta\}$, and curvature κ_d.

drop radius. The drop shrinks if $\partial_{\bar{x}}\bar{V} < 0$, i.e. if the average thickness left in the wake is less than h_0 as seen for the greater values of the inclination. The structure of the wake is thus key for rationalizing the transition between the two flow regimes. This numerical observation is confirmed in experiments: as evident from figure 5.4(b) the wake is thinner than h_0 for $\alpha < \alpha_c$ and thicker for $\alpha > \alpha_c$ (see details in Section 5.5.2).

5.3 Analytical treatment of the Landau-Levich meniscus and drop to rivulet transition

We model the variation in thickness across the wake using an approach analogous to that used in Landau-Levich and Bretherton problems. We treat our problem in the polar coordinate system centered on the drop apex (see figure 5.4(c)). Focusing on the matching region between the drop and the film, we expect the radial curvature to vary rapidly and dominate the pressure gradient (Lister et al., 2010). Consequently, we neglect the advection and gravity terms in the meniscus such that equation (5.1) reduces to a radial Landau-Levich equation (see Section 5.5.3). Therefore, we treat the wake as a collection of two-dimensional radial Landau-Levich films, where the projected speed $\bar{U}\cos(\theta)$ is the effective deposition speed. In this framework, we obtain (Cantat, 2013)

$$\bar{h}_w(\theta) \approx 1.34\bar{\kappa}_d^{-1}\cos(\theta)^{2/3}\,\mathrm{Ca}^{2/3}. \tag{5.2}$$

Here $\bar{\kappa}_d$ is the curvature at the edge of the drop, which is assumed to remain close to that of a static pendant drop $\bar{\kappa}_d \approx 0.28\bar{A}/\ell_c^2$ (see Section 5.5.3), and $\mathrm{Ca} = \mu\bar{U}/\gamma$ is the capillary number of the problem. Note that the drop speed $\bar{U}(\bar{t})$ and amplitude $\bar{A}(\bar{t})$ are a priori unknown and depend on the drop initial profile, the film thickness and the inclination of the substrate. Varying the dimensionless parameters of the problem ($\bar{A}_0/\ell_c$, h_0/ℓ_c and $\tilde{\alpha}$) we generate a large data set of simulations to assess the validity of our model.

In figure 5.5(a) we plot the wake profile in the transverse direction $\bar{h}_w(\bar{y})$ for a given drop

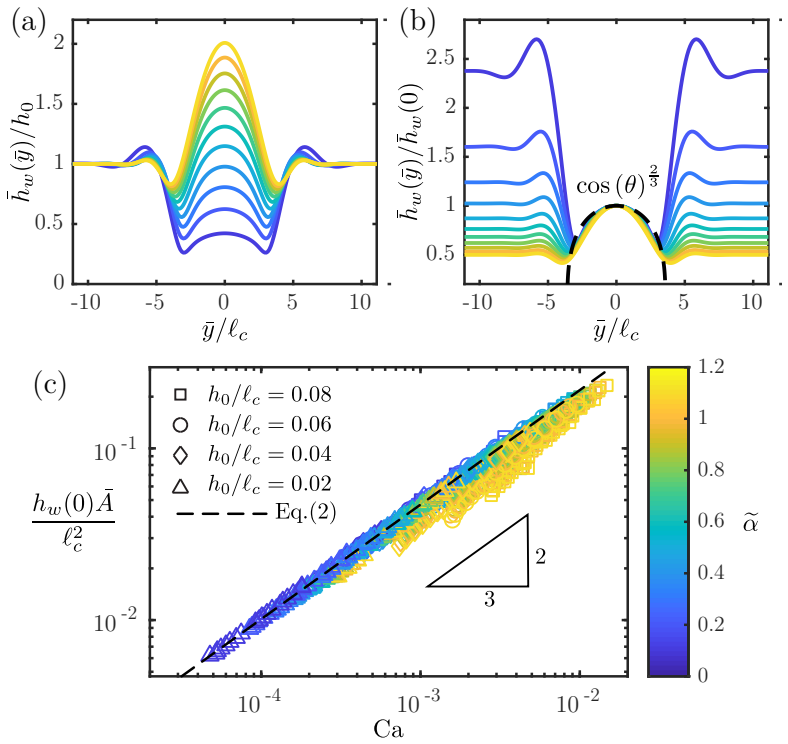

Figure 5.5: (a) Wake profile $\bar{h}_w(y)/h_0$ taken $\approx 6\ell_c$ behind a drop for different inclination angles $\widetilde{\alpha}$ [color coded see (c)], $\bar{A}_0/\ell_c = 1.4$ and $h_0/\ell_c = 0.04$. (b) Same data rescaled by the central thickness $\bar{h}_w(0)$. The black dashed line derives from equation (5.2): $\bar{h}_w(\bar{y})/\bar{h}(0) = \cos(\theta)^{2/3} = \cos(\arcsin(\bar{y}/R))^{2/3}$. (c) Dimensionless thickness in the center of the wake $\bar{h}_w(0)\bar{A}/\ell_c^2$ as a function of the capillary number Ca for our 176 simulations. The color codes $\widetilde{\alpha}$, the symbols code h_0/ℓ_c and the black dashed line corresponds to equation (5.2): $y = 1.34/0.28\,x^{2/3}$.

and film at different inclinations angles (the wake is quasi-invariant in the $\bar{x}$ direction, see figure 5.4(a)). We first focus on the angular dependence by rescaling the data by $\bar{h}_w(\bar{y}=0)$. As shown in figure 5.5(b), the profiles collapse in the central region of the wake defined as $-R < \bar{y} < R$ with R the drop radius. The resulting master curve matches our theoretical prediction $\bar{h}_w(\theta)/\bar{h}_w(0) = \cos(\theta)^{2/3}$ with no fitting parameter (see equation (5.2)). We then compare our prediction for $\bar{h}_w(0)$ to data from all our simulations in figure 5.5(c). Note that each simulation provides multiple data points as $\bar{A}$ and $\bar{U}$ are both function of time and thus vary over the course of a simulation. The resulting collapse and overall favorable agreement with equation (5.2) confirms the validity of our approach. Note that the agreement becomes less favorable when $\widetilde{\alpha}$ and h_0/ℓ_c increase, a result consistent with the approximations made in our model (negligible advection in the meniscus and static pendant drop shape, see Section 5.5.3).

Using equation (5.2), we evaluate the amount of liquid deposited in the wake $\int_{-R}^{R} \bar{h}_w(\bar{y})\mathrm{d}\bar{y} =$

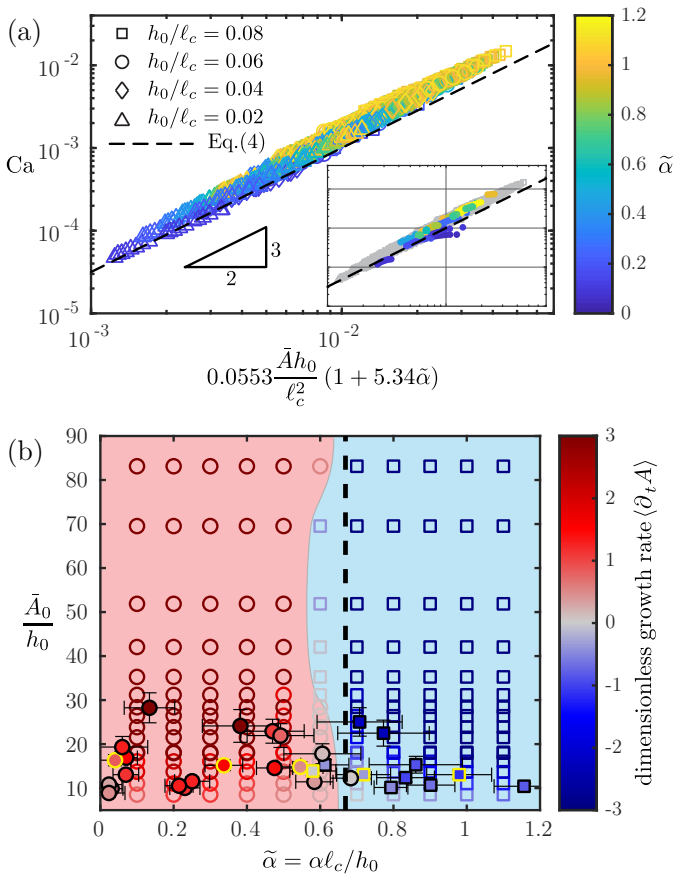

Figure 5.6: (a) Drop dimensionless speed Ca compared to our theory (equation (5.4)). Our 176 simulations are shown, the color codes $\tilde{\alpha}$, the symbols code h_0/ℓ_c and the black dashed line is our prediction $y = x^{3/2}$. Inset: Same plot including experimental data ($0.03 < h_0/\ell_c < 0.1$). The numerics are drawn in light grey for clarity. (b) State diagram for the drop growth-decay. Symbols are colored according to the dimensionless growth rate averaged over the experiment/simulation $\langle\partial_t A\rangle$, circles represent growth ($\langle\partial_t A\rangle > 0$) while squares represent decay ($\langle\partial_t A\rangle < 0$). Experimental results are shown as filled symbols while numerical results are open symbols. The experiments of figure 5.3 are circled in yellow. The background color is a guide to the eye and the dashed black line is our theory $\tilde{\alpha}_c \approx 0.67$.

$R\bar{h}_w(0)\int_{-\pi/2}^{\pi/2}\cos(\theta)^{5/3}\,\mathrm{d}\theta$ and obtain the drop growth rate

$$\partial_{\bar{x}}\bar{V} \approx R\left(2h_0 - 7.91\ell_c^2\mathrm{Ca}^{2/3}/\bar{A}\right). \tag{5.3}$$

Next, we derive an expression for Ca in order to close the problem.

To obtain the drop speed, we perform a force balance on the drop (Aussillous and Quéré, 2002). The force driving the motion of the drop derives from the change in gravitational energy $E_p = \rho g \bar{V}\bar{z}_c$, with $\bar{z}_c$ the altitude of the drop center of mass. Defining $\bar{F}_g = -\partial_{\bar{x}}E_p$ we find $\bar{F}_g \approx \rho g\bar{V}\alpha + 2\rho g\bar{z}_c R h_0 - 7.91\gamma R\bar{z}_c\mathrm{Ca}^{2/3}/\bar{A}$. While the first term in the expression of $\bar{t}_g$ is

conventional, the other two terms originate from the change of volume of the drop $\partial_{\bar{x}}\bar{V}$ in equation (5.3). The motion of the drop is resisted by viscous stresses in the film. The flow being significant only around the drop and the meniscus being the thinnest part of that region, we anticipate the meniscus to be the main source of dissipation. The corresponding viscous force per unit length is $\bar{f}_v(\theta) = 4.94\gamma\,(\mathrm{Ca}\cos\theta)^{2/3}$ (Cantat, 2013). Integrating along the drop contour, the total friction force is $\bar{\mathbf{F}}_v = \int_{-\pi/2}^{\pi/2} \bar{f}_v(\theta)\left(\cos\theta\mathbf{e}_x + \sin\theta\mathbf{e}_y\right) R\mathrm{d}\theta \approx 8.31\gamma R\mathrm{Ca}^{2/3}\mathbf{e}_x$. Assuming that the drop shape remains close to that of a static pendant drop we have $\bar{z}_c \approx 0.29\bar{A}$, $R \approx 3.58\ell_c$ and $V \approx 0.89\bar{A}R^2$ (see Section 5.5.3 for the derivation of all the prefactors). Balancing $\bar{F}_g$ and $\bar{F}_v = \bar{\mathbf{F}}_v \cdot \mathbf{e}_x$, we obtain:

$$\mathrm{Ca}^{2/3} = 0.0553\frac{\bar{A}h_0}{\ell_c^2}\left(1 + 5.34\widetilde{\alpha}\right). \tag{5.4}$$

In figure 5.6(a) we compare the drop speed obtained in simulations with equation (5.4) and find favorable agreement without any fitting parameter. Likewise, we show in the inset of figure 5.6(a) equation (5.4) also captures our experiments. Note that, the agreement becomes less favorable when $\widetilde{\alpha}$ and h_0/ℓ_c increase, as expected from the deterioration of our model assumptions (static pendant drop shape and negligible advection in the meniscus, see Section 5.5.3).

We now leverage our results and combine equation (5.3) and equation (5.4) to derive the drop growth rate $\partial_x V$ and subsequently integrate this expression over time to obtain the drop dimensionless amplitude

$$\frac{A(t)}{A_0} = \left(1 - \frac{1}{2}\mathrm{f}(\widetilde{\alpha})A_0^{1/2}t\right)^{-2} \tag{5.5}$$

with $\mathrm{f}(\widetilde{\alpha}) = (0.0065 - 0.0097\widetilde{\alpha})(1 + 5.34\widetilde{\alpha})^{3/2}$ (see Section 5.5.3). In figure S5(a) we show that equation (5.5) compares favorably with experiments without fitting parameters. The value of critical inclination is obtained solving for the root of f, yielding $\widetilde{\alpha}_c \approx 0.67$. In figure 5.6(b) we show the combined experimental and numerical state diagram for the drop dynamics, where the two flow regimes are apparent. As predicted by our model, the transition occurs at a roughly constant critical angle $\widetilde{\alpha}_c \approx 0.6$ in good agreement with our estimate.

5.4 Conclusion

In summary, using experiments and numerical simulations, we have revealed a transition from growth to decay for pendant drops sliding under slightly inclined pre-wet substrates. This transition, which occurs at a surprisingly low angle, is governed by the amount of fluid left in the wake of the drop. As the inclination angle increases, the drop becomes too fast to grow and its volume is slowly depleted. We have rationalized this complex non-linear problem with an analytically tractable Landau-Levich model that accurately predicts the drop dynamics in the two regimes, in spite of the approximations introduced in its derivation. Note that

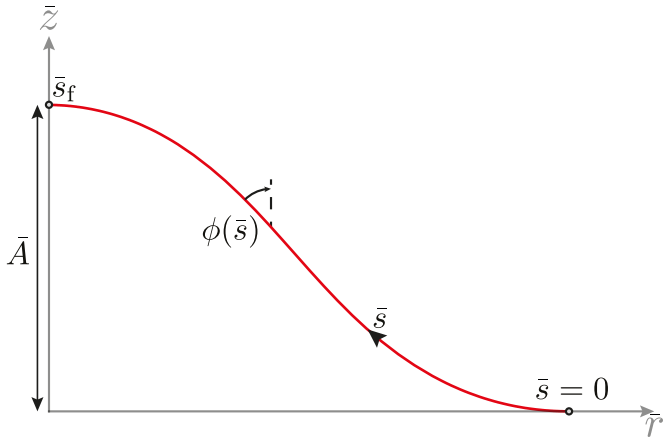

Figure 5.7: Schematic of a pendant drop defining the coordinates used for the numerical integration.

on longer time scales the Rayleigh-Taylor instability will eventually influence the dynamics of drops that do not drip. Although this situation is beyond the scope of the present study, preliminary results indicate that the wake forms lenses that are later absorbed by the drop (see Section 5.5.2). Yet, no dripping is observed which suggests that the critical angle we have introduced remains accurate. As such, our results could find application in dripping prevention for drops directly deposited on substrates, e.g. in coating and printing technologies (Kumar, 2015). Additionally, our results could be extended to control and transport pendant drops via carefully crafted substrate topography. Finally, our analysis could be generalized to model the dynamics of sliding liquid plugs in pre-wetted channels (Bico and Quéré, 2002) and sliding liquid bridges between pre-wetted substrates (Reyssat, 2014; Balestra, 2018).

5.5 Supplemental Material

5.5.1 Methods

Experiments. Silicone oil v1000 (Gelest DMS-T31) dyed in black was used in our experiments. The oil-dye viscosity $\mu = 1.13$ Pa.s was measured in a rheometer (Anton Paar MCR 301) and its surface tension $\gamma = 20.3$ mN/m with the pendant drop method, both at room temperature $T = 21°$C. To prepare the uniform coating h_0, the edges of a rectangular flat, float glass plate (130x90x1.8 mm) were first covered with tape over a width of ≈ 1 cm. Oil was then spin-coated (Laurell WS-650Mz-23NPPB) on the plate and the tape subsequently pealed to remove the edge bead that forms during spin-coating. The plate was then weighted to determine the film thickness $h_0 = m/(\rho S)$ with m the film mass, $\rho = 971$ kg/m^3 the oil density, and S the surface area not covered by the tape (measured with a camera). The experimental uncertainties on the weight measurement translate to a thickness uncertainty $\Delta h_0 \approx \pm 7$ μm. The film thickness

was determined for each experiment but most of them were done with similar spin-coating settings leading films thicknesses fluctuating around $h_0 \approx \{55, 89, 110\}$ μm.

The coated plate was then attached upside-down with a magnet to an arm mounted on a rotation stage which has been pre-leveled with a bubble level. Using a micropipette, a drop of oil was injected on the upside-down plate. Since a significant portion of the injected oil dripped along the upside-down pipette tip, the injected volume was difficult to control precisely (~ 50 μL) leading to drops with various initial amplitudes $0.5 < \bar{A}_0/\ell_c < 1.46$. The arm was then rotated to the desired angle α. The rotation stage being precise, the uncertainty on the angle α is mostly determined by the leveling step. To gauge it, we recorded the motion of a drop at 'zero' angle for each set of experiments. Although there was a residual tilt in both the x and y directions, we were able to fit the drop dynamics with the numerics only tilted in one direction. The fitted value of $|\alpha_0| = 0.1 - 0.3°$ was then used to correct the zero angle for the following experiments of the set and sets the angle uncertainty $\Delta\alpha \approx \pm 0.15°$.

The drop dynamics was recorded from the side and the bottom with two synchronized cameras. The field of view and resolution were of the order of {6.5 cm, 10 μm/pix} for the side view and {10 cm, 16 μm/pix} for the bottom view. The duration of an experiment varying between 20 min and 5h, the time interval between pictures was adjusted accordingly between 15s and 4 min. The drop amplitude was measured from the side view while the drop position was measured from the bottom view since drops at low angles can move out of plane of the side view. For the experiments shown in figure 4b, a much higher concentration of dye was used to visualize the wake. The thickness profiles were then extracted from experimental images using Beer-Lambert's law, i.e. $h(x,y) \sim \ln(I(x,y)/I_0(x,y))$ with I the pixel intensity of the image including the drop and its wake and I_0 a reference pixel intensity correcting the non-uniform illumination (obtained from an image with no drop). All image analysis was performed with ImageJ and/or Matlab. The data presented in the main text for both the wake profile (figure 4b) and the drop velocity (inset figure 6a) were denoised with cubic smoothing splines.

Simulations. Finite element simulations were performed with the finite-element solver COMSOL Multiphysics. The simulations solve the dimensional version of equation (1), in its conservation form, using the values for our silicone oil to allow an easier comparison with experiments. To supply the initial condition $\bar{h}(\bar{x},\bar{y},0) = h_0 + \bar{h}_d(\bar{x},\bar{y})$ with $\bar{h}_d(\bar{x},\bar{y})$ a static pendant drop profile, we solved numerically the Young-Laplace equation with the appropriate boundary conditions (Marthelot et al., 2018) using Mathematica (shooting method):

$$\begin{aligned}
&\frac{\mathrm{d}^2\psi(\bar{s})}{\mathrm{d}\bar{s}^2} = \frac{-\cos\psi(\bar{s})}{\ell_c^2} + \frac{\mathrm{d}}{\mathrm{d}\bar{s}}\left[\frac{\cos\psi(\bar{s})}{\bar{r}(\bar{s})}\right] \\
&\frac{\mathrm{d}\bar{h}_d(\bar{s})}{\mathrm{d}\bar{s}} = \cos\psi(\bar{s}), \quad \frac{\mathrm{d}\bar{r}(\bar{s})}{\mathrm{d}\bar{s}} = \sin\psi(\bar{s}), \\
&\bar{h}_d(0) = 0, \quad \psi(0) = -\pi/2, \\
&\bar{r}(\bar{s}_\mathrm{f}) = 0, \quad \phi(\bar{s}_\mathrm{f}) = -\pi/2, \quad \bar{h}_d(\bar{s}_\mathrm{f}) = \bar{A}.
\end{aligned} \tag{5.6}$$

Here, $\{\bar{r}(\bar{s}), \bar{h}_d(\bar{s})\}$ are the (cylindrical) coordinates of the drop surface, $\psi(\bar{s})$ is the local angle that the tangent makes with the vertical and $\bar{s}$ is the arc-length as defined in figure 5.7. The value of $\bar{s}_f$ is a priori unknowns and is determined by the additional boundary condition and each profile can be uniquely defined by its amplitude $\bar{A}$. The drops shapes are then imported in the FEM solver to be used for the initial condition.

We use rectangular domains with periodic boundary conditions using a square mesh with quadratic Lagrange elements for $\bar{h}$ and for $\bar{\kappa}$ (resolved separately) of size $0.125\ell_c$ or smaller. The simulations shown in figure 4-6 have a width $\bar{L}_y \approx 22.2\ell_c$ and length $\bar{L}_x \approx 53.3\ell_c$, and were stopped after 10τ or at the onset of dripping ($\bar{A} > 2.2\ell_c$) or when the drop gets too close to the boundary of our simulation domain (distance of the drop maximum to the boundary smaller than $8\ell_c$). The wake profiles $\bar{h}_w(\bar{y})$ were measured between $4.7\ell_c$ and $7\ell_c$ behind the drop center depending on the length of the Landau-Levich region (estimated by looking for $\partial_{\bar{x}}\bar{\kappa}|_{\bar{y}=0} = \text{const}$). As we only focus on quasi-steady moving drop, we discarded the transient initiation of the drop motion (where the drop grows due to the Rayleigh-Taylor instability, see figure 5.9) and only present data after the drop has moved by one diameter ($\bar{x} > 7\ell_c$), when the wake is fully formed. In total 176 simulations are shown in figure 4-6 performed with the combination of parameters: $h_0 = \{30, 60, 90, 120\}$ μm, $\alpha = \{0.1, 0.2, 0.3, 0.4, 0.5, 0.6, 0.7, 0.8, 0.9, 1.0, 1.1\}h_0/\ell_c$ with $\ell_c = 1.485$ mm, and four drops profiles $\bar{h}_d(\bar{x}, \bar{y})$ with initial amplitudes $\bar{A}_0/\ell_c = \{0.61, 1.0, 1.4, 1.7\}$. The dimensionless values displayed in the main text are therefore relevant to experiments.

5.5.2 Additional experimental and numerical results

Experiments at different film thicknesses. The influence of the initial film thickness h_0 is shown in figure 5.8(a) where we plot the time evolution of the drop amplitude $\bar{A}$ for different values of α and h_0. As shown, the quantitative behavior is similar, the timescale on which the growth occurs and the critical angle α_c for the transition are however different. The drop under a quasi-horizontal substrate with $h_0 \approx 55$ μm dripped in 115 min while the one with $h_0 \approx 115$ μm dripped in 45 min, despite being initially 25% smaller. The critical angles vary between $1 \lesssim \alpha_c\,(^\circ) \lesssim 3$. The same data are plotted in figure 5.8(b) but with the time rescaled by $\tau = \mu\gamma/\left(h_0^3\rho^2 g^2 \cos^2\alpha\right)$, the amplitude rescaled by $\bar{A}_0$ and the color now coding $\tilde{\alpha}$. As shown this rescaling captures the change of thickness h_0 for drops of similar initial amplitudes and the critical dimensionless angle is now of the order of $\tilde{\alpha} \approx 0.6$ for all thicknesses. The blue circles, do not collapse probably due to the substantially larger initial drop size in this experiment which accelerates the dynamics.

Influence of the Rayleigh-Taylor instability. For very low inclination angles, we observe in the experiments an initially rapid growth that slows down before increasing again (see figure 3(a) or figure 5.8). This initial growth and apparent saturation resemble the growth of a motionless drop due to the Rayleigh-Taylor instability. Since drops are always mobile in our experiments,

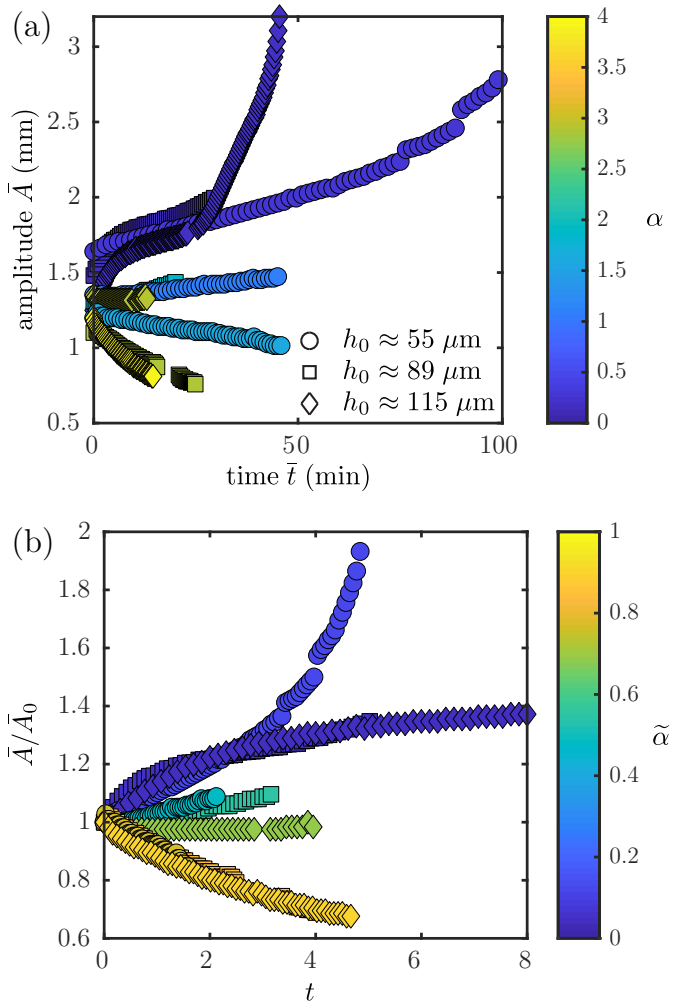

Figure 5.8: (a) Amplitude as a function of time for experimental drops sliding under films of different thicknesses h_0 (see legend) at different inclination angles α (color coded). (b) Same data with $\bar{A}$ rescaled by $\bar{A}_0$, time by τ and the color now coding $\widetilde{\alpha}$.

we simulate a motionless one with $\widetilde{\alpha} = 0$ and compare it to a drop moving at low inclination angle in figure 5.9. As shown, the initial growth is identical for the two drops until $\bar{t} \approx 0.5\tau$, the time required for the drop to move by $\bar{x} \approx \ell_c$. Before, the drop sucks the thin film around it and forms a collar just like an immobile Rayleigh-Taylor drop (Lister et al., 2010). The very beginning of the motion is therefore impacted by the non-linear Rayleigh-Taylor dynamics in addition to the dynamic described in this article.

Late time dynamics. Our experiments and simulations only explore the drop dynamics on a domain of roughly $50\ell_c$ (or 15 drop sizes) and we observe growth until dripping below α_c and shrinking above it. At late time, our model suggests this shrinking to go on until complete

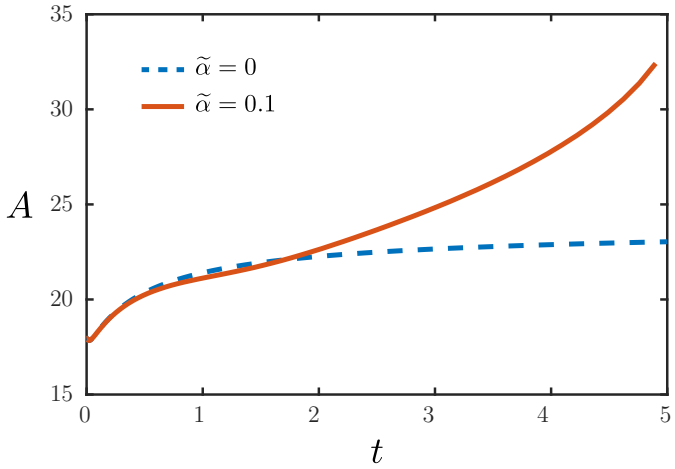

Figure 5.9: Dimensionless amplitude A as a function of dimensionless time t for two simulated drops, one immobile that grows through the Rayleigh-Taylor instability (dashed, $\widetilde{\alpha} = 0$) and the other mobile at very low inclination angle (solid, $\widetilde{\alpha} = 0.1$), film thickness $h_0/\ell_c = 0.06$.

disappearance of the drop as $A \sim t^{-2}$ [equation (5.15)]. However, the assumption of time scale separation between the Rayleigh-Taylor growth mechanism and the shrinking due to the sliding will eventually break down. Our experimental setup being only 13 cm long, we performed an additional simulation on a much longer domain with a slightly coarser mesh to investigate the long time behavior at high angles ($\bar{L}_x \approx 220\ell_c$, $\bar{A}_0/\ell_c = 1.0$, $h_0/\ell_c = 0.06$, mesh size $0.2\ell_c$). The dynamics turned out to be quite complex. The drop slows down and shrinks as expected, but in the meantime the wake grows due to Rayleigh-Taylor instability and eventually forms small lenses. These lenses then ride the drop wake and eventually catch the drop. However, the volume of these lenses being small and stemming from the drop, the coalescence events barely increase the main drop amplitude. It thus seems unlikely that the drop ends up dripping.

5.5.3 Theory

Justification for the 2D Landau-Levich model. We assume as Lister et al. (2010) that the drop moves quasi-steadily at the dimensionless speed U and therefore look for traveling wave solutions of equation (1) of the form $h(x,y,t) = h(x-Ut,y)$ such that $\partial_t h = -U\partial_x h$. Equation (1) thus becomes:

$$\nabla\cdot\left[h^3\left(\nabla h + \nabla\kappa\right)\right] = 3\left(U - \widetilde{\alpha}h^2\right)\partial_x h. \tag{5.7}$$

Now focusing on the annular matching region between the drop and the thin film [$r \approx R$ in polar coordinates $\{r,\theta\}$, see figure 4(c)], we expect small slopes so that we can linearize the curvature $\kappa \approx \nabla^2 h$ which has to vary rapidly to match the drop edge to the thin film. The

curvature gradient term dominates the gravitational term (i.e. $\nabla h \ll \nabla^3 h$) and except at the drop side ($\theta = \pm\pi/2$), the azimuthal variations of the curvatures are negligible compared to the radial ones. At leading order, equation (5.7) therefore becomes (Lister et al., 2010):

$$\frac{\mathrm{d}}{\mathrm{d}r}\left[h^3\frac{\mathrm{d}^3 h}{\mathrm{d}r^3}\right] = 3\left(U - \widetilde{\alpha}h^2\right)\cos\theta\frac{\mathrm{d}h}{\mathrm{d}r}. \tag{5.8}$$

For small angles, i.e. $\widetilde{\alpha} \ll U/h^2$, the advection term is negligible and we recover the formulation of Lister et al. (2010) that yields the Landau-Levich equation after integrating equation (5.8) once. Since $h \sim 1$ in the matching region this condition is equivalent to $\widetilde{\alpha} \ll U = \mathrm{Ca}\,(\ell_c/h_0)^3\cos(\alpha)^{-3/2}$ which is of order 10 in our parameter range.

Pendant drop properties. A small slope solution of the Young-Laplace equation which is valid for small static pendant drops writes (Lister et al., 2010):

$$\frac{\bar{h}_d^*(\bar{r}/\ell_c)}{\bar{A}} = \frac{\mathrm{J}_0(R/\ell_c) - \mathrm{J}_0(\bar{r}/\ell_c)}{\mathrm{J}_0(R/\ell_c) - 1}, \tag{5.9}$$

with $\bar{A}$ the previously defined drop height, J_0 the Bessel function of the first kind of order 0 and $R \approx 3.8317\ell_c$ the drop radius defined by $\mathrm{J}_0'(R/\ell_c) = 0$. Using this approximate solution, we can estimate analytically the numerical prefactors used in the model:

$$\begin{aligned} V &= 2\pi\int_0^R \bar{r}\,\bar{h}_d^*(\bar{r})\mathrm{d}\bar{r} = \frac{\pi\mathrm{J}_0(R/\ell_c)}{\mathrm{J}_0(R/\ell_c)-1}\bar{A}R^2 \approx 0.90201\,\bar{A}R^2, \\ \bar{\kappa}_d &= \left.\frac{\mathrm{d}^2\bar{h}_d^*}{\mathrm{d}\bar{r}^2}\right|_{\bar{r}=R} = \frac{\mathrm{J}_0(R/\ell_c)}{\mathrm{J}_0(R/\ell_c)-1}\bar{A} \approx 0.28712\,\bar{A}, \\ \bar{z}_c &= \frac{1}{2}\frac{\int_0^R \bar{r}\,\bar{h}_d^*(\bar{r})^2\mathrm{d}\bar{r}}{\int_0^R \bar{r}\,\bar{h}_d^*(\bar{r})\mathrm{d}\bar{r}} = \frac{\mathrm{J}_0(R/\ell_c)}{\mathrm{J}_0(R/\ell_c)-1}\bar{A} \approx 0.28712\,\bar{A}. \end{aligned} \tag{5.10}$$

We further checked these prefactors numerically on the exact pendant drop profiles h_d obtained by solving equation (5.6). As shown in figure 5.10, except for the drop radius R, these prefactors remain quite accurate even for larger drops. In our model, we use the values fitted

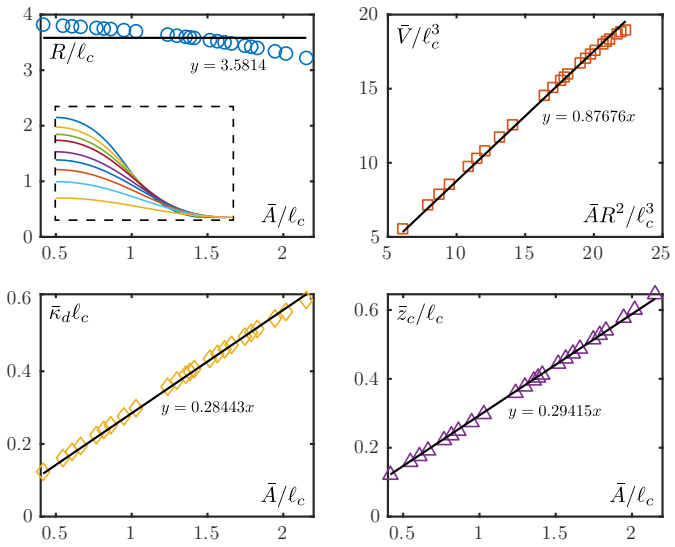

Figure 5.10: Properties of pendant drops $\bar{h}_d$ obtained by numerically solving equation (5.6) (representative profiles are shown in inset). The black lines are best fits.

on the exact profiles and get the following prefactors c_i:

$$
\begin{aligned}
\bar{h}_w(\theta) &= c_h \frac{\ell_c^2}{\bar{A}} (\cos(\theta)\mathrm{Ca})^{2/3} \\
c_h &= 0.6430 \cdot 3^{2/3} \left(\frac{\bar{\kappa}_d \ell_c^2}{\bar{A}}\right)^{-1} \approx 4.7029 \\
\frac{\partial \bar{V}}{\partial \bar{x}} &\approx \int_{-R}^{R} \left(h_0 - \bar{h}_w(\bar{y})\right) \mathrm{d}\bar{y} \approx 2Rh_0 - c_v \mathrm{Ca}^{2/3} R \frac{\ell_c^2}{\bar{A}} \\
c_v &= c_h \int_{-\pi/2}^{\pi/2} \cos^{5/3}(\theta)\, \mathrm{d}\theta \approx 7.9131 \\
\bar{\mathbf{F}}_v &= c_F \gamma R \mathrm{Ca}^{2/3} \mathbf{e}_x \\
c_F &= 4.94 \int_{-\pi/2}^{\pi/2} \cos^{5/3}(\theta)\, \mathrm{d}\theta \approx 8.3121 \\
\mathrm{Ca}^{2/3} &= c_1 \frac{\bar{A}h_0}{\ell_c^2} (1 + c_2 \widetilde{\alpha}) \\
c_1 &= \frac{2\bar{z}_c/\bar{A}}{c_F - (\bar{z}_c/\bar{A}) c_v} \approx 0.055285 \\
c_2 &= \frac{1}{2} \left(\frac{R}{\ell_c}\right) \left(\frac{V}{\bar{A}R^2}\right) \left(\frac{\bar{z}_c}{\bar{A}}\right)^{-1} \approx 5.3386.
\end{aligned}
\tag{5.11}
$$

We note that we recover the velocity and film thickness prediction of Lister et al. (2010) obtained for $\widetilde{\alpha} = 0$ by asymptotically matching the Landau-Levich film to a small slope pendant drop. Our prefactors are however slightly different since they get $c_1' \approx 0.028794$ and $c_v' \approx 7.8350$

after conversion to our notation.

Drop amplitude prediction. By combining equations (3)(4) of the main text we can get a prediction for the drop volume and thus amplitude as a function of time:

$$\frac{\partial \bar{V}}{\partial \bar{t}} = \bar{U}\frac{\partial \bar{V}}{\partial \bar{x}} \approx \bar{U} R h_0 \left[2 - c_v c_1 \left(1 + c_2 \widetilde{\alpha}\right)\right]. \tag{5.12}$$

From equation (5.12) we extract the criterion for the growth to decay transition $\widetilde{\alpha}_c = 2/(c_1 c_2 c_v) - 1/c_2 \approx 0.66902$. Then using $\bar{U} = \gamma \mathrm{Ca}/\mu$ and replacing again Ca with equation (4) we get

$$\frac{\partial \bar{V}}{\partial \bar{t}} \approx \frac{\gamma}{\mu} c_1^{3/2} \frac{\left(\bar{A} h_0\right)^{3/2}}{\ell_c^3} \left(1 + c_2 \widetilde{\alpha}\right)^{3/2} R h_0 \left[2 - c_v c_1 \left(1 + c_2 \widetilde{\alpha}\right)\right], \tag{5.13}$$

which turns into a first order ODE for $A(t)$ after using $\bar{V}(\bar{t}) \approx 0.87676 \bar{A}(\bar{t}) R^2$ and $R \approx 3.5814 \ell_c$. Once made dimensionless by rescaling time with τ and amplitude with h_0 and assuming small slopes such that $\cos\alpha \approx 1$ it reads:

$$\begin{aligned} \frac{\partial A}{\partial t} &\approx \mathrm{f}(\widetilde{\alpha}) A^{3/2}, \\ \mathrm{f}(\widetilde{\alpha}) &= \left(\frac{\bar{A} R^2}{V}\right)\left(\frac{\ell_c}{R}\right) c_1^{3/2} \left(1 + c_2 \widetilde{\alpha}\right)^{3/2} \left[2 - c_v c_1 \left(1 + c_2 \widetilde{\alpha}\right)\right] \\ &\approx (0.0064682 - 0.0096682 \widetilde{\alpha})(1 + 5.3386 \widetilde{\alpha})^{3/2}. \end{aligned} \tag{5.14}$$

Solving equation (5.14) finally yields the prediction for the amplitude as a function of time

$$A(t) \approx \frac{A_0}{\left(1 - \frac{1}{2} \mathrm{f}(\widetilde{\alpha}) A_0^{1/2} \bar{t}\right)^2}. \tag{5.15}$$

We compare equation (5.15) to the experiment presented in figure 3 in figure 5.11(a). Despite all the assumptions of the model, the agreement is good except at the beginning of the motion at very low inclination angles due to the Rayleigh-Taylor growth (see figure 5.9). Using equation (5.14), we construct a theoretical initial growth rate map shown in figure 5.11(b) akin to the phase diagram shown in figure 5(b). We recover the independence of the critical angle $\widetilde{\alpha}_c$ with respect to the drop amplitude as well as the steep increase in growth or decay rate as A_0/h_0 increases.

Limitations of the model. In addition to the fact that the advection term stops being negligible in equation (5.8) for larger values of $\widetilde{\alpha}\,(h_0/\ell_c)^3\,\mathrm{Ca}^{-1}$, our Landau-Levich analysis has a few other limitations. First as shown in figure 5(b), our model only predicts the central part of the wake and not the reconnection to the thin film (for $|\bar{y}| > R$). Using the data of figure 5(b), we

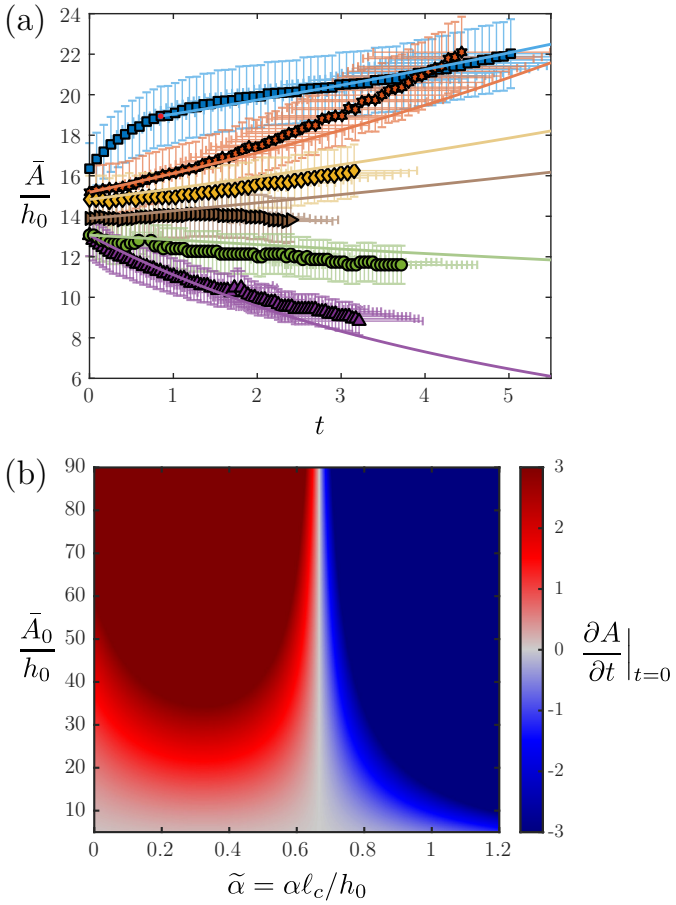

Figure 5.11: (a) Dimensionless amplitude as a function of the dimensionless time for the drops of figure 3 compared to our theory (solid lines) equation (5.15). For the lowest inclination angle, the model was compared to experiment after the transient Rayleigh-Taylor growth (see figure 5.9), i.e. using the red circle as initial condition. (b) Initial drop dimensionless growth rate map as a function of the dimensionless initial amplitude and $\widetilde{\alpha}$.

computed the exact volume change $\partial_{\bar{x}} \bar{V} = \int_{-\infty}^{\infty} \left(h_0 - \bar{h}_w(\bar{y})\right) \mathrm{d}\bar{y}$ and the approximate volume change, neglecting the reconnection region $\partial_{\bar{x}} \bar{V} \approx \int_{-R}^{R} \left(h_0 - \bar{h}_w(\bar{y})\right) \mathrm{d}\bar{y}$. As shown in figure 5.12 where both are plotted and compared to our prediction, the difference is small confirming that the reconnection region is negligible.

Then the pendant drop shapes used for the numerical coefficients (see figure 5.10) are strictly valid for $\alpha = 0$ and $h_0 = 0$. As we increase the angle, we expect the drop shape to vary and even become asymmetric (along x). figure 5.13 shows the horizontal evolution of the curvature $\bar{\kappa}(\bar{x}, 0)$ as the inclination angle $\widetilde{\alpha}$ increases. At low inclination angles, the drop edge curvature to which the Landau-Levich film must connect is close to the one of a static pendant drop $\bar{\kappa}_d$ at both the front and the back of the drop. However, as the angle increases the drop shape starts to distort and the edge curvature changes.

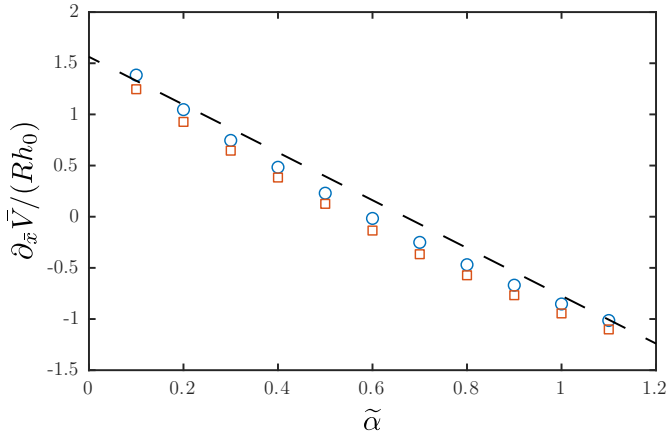

Figure 5.12: Change of drop volume $\partial_{\bar{x}}\bar{V}$ normalized by Rh_0 for the simulated wakes of figure 5(a). Blue circles include the whole data set including the reconnection to the thin film, i.e. $\int_{-\infty}^{\infty}\left(h_0-\bar{h}_w(\bar{y})\right)\mathrm{d}\bar{y}$, while orange squares only include the central part of the wake, $\int_{-R}^{R}\left(h_0-\bar{h}_w(\bar{y})\right)\mathrm{d}\bar{y}$. The dashed line is our model [see equation (5.12)].

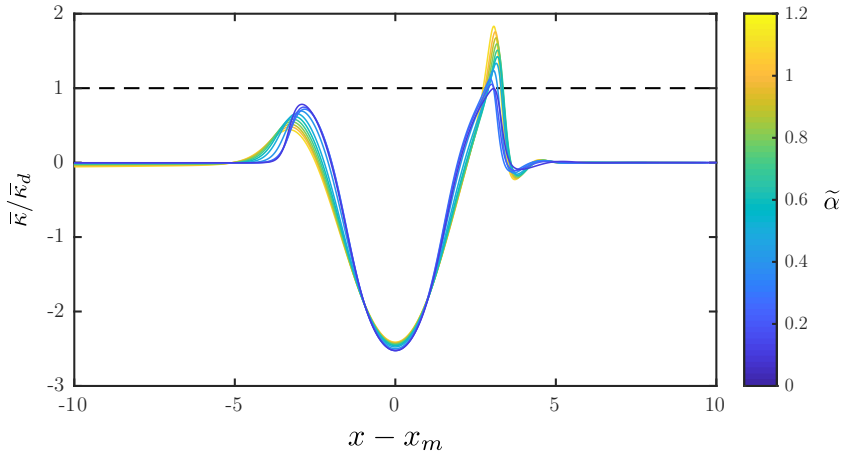

Figure 5.13: Curvature profiles $\bar{\kappa}$ in the flow direction x rescaled by the theoretical value in our model $\bar{\kappa}_d = 0.2844\,A/\ell_c^2$ for a drop of initial size $\bar{A}_0/\ell_c = 1.4$ on a film of thickness $h_0/\ell_c = 0.04$ at different inclination angles $\widetilde{\alpha}$ (color coded). All the profiles corresponds to the last time step of each simulation and were shifted horizontally by x_m, the position of the drop maximum.

Finally, by using the prefactor 4.94 in the friction force $\bar{f}_v(\theta)$, we implicitly assumed that the drop front and back curvatures were identical (Cantat, 2013). As shown in figure 5.13 the front-back curvature difference also increases with $\widetilde{\alpha}$. This should gradually decrease the value of the prefactor of $\bar{f}_v(\theta)$ thereby reducing the friction (Cantat, 2013), thus possibly explaining why the data is slightly above our prediction at high $\widetilde{\alpha}$.

Part II

On the effect of substrate topology in coating flows: speleothems, dewetting and spreading

6 Hydrodynamic-driven morphogenesis of karst draperies: spatio-temporal analysis of the two-dimensional impulse response

Remark This chapter is largely inspired by the publications of the same name

P. G. Ledda[1], G. Balestra[2], G. Lerisson[1], B. Scheid[3], M. Wyart[4], F. Gallaire[1]
[1]Laboratory of Fluid Mechanics and Instabilities, École Polytechnique Fédérale de Lausanne, Lausanne, CH-1015, Switzerland
[2]iPrint Institute, University of Applied Sciences and Arts of Western Switzerland, Fribourg, CH-1700, Switzerland
[3]TIPs, Université Libre de Bruxelles, Avenue F.D. Roosevelt 50, 1050 Bruxelles, Belgium
[4]Physics of Complex Systems Laboratory, École Polytechnique Fédérale de Lausanne, Lausanne, CH-1015, Switzerland

Journal of Fluid Mechanics **910**, A53 (2021)
Journal of Fluid Mechanics **926**, E3 (2021)

Author contributions P.G.L. and F.G. conceived the project. P.G.L. performed all numerical simulations and analyses. P.G.L. wrote the manuscript with input from the coauthors.

We study the role of hydrodynamic instabilities in the morphogenesis of some typical karst draperies structures encountered in limestone caves. The problem is tackled using the long-wave approximation for the fluid film that flows under an inclined substrate, in the presence of substrate variations that grow according to a deposition law. We numerically study the linear and non-linear evolution of a localized initial perturbation both in the fluid film and on the substrate, i.e. the Green function. A novel approach for the spatio-temporal analysis of two-dimensional signals resulting from linear simulations is introduced, based on the concepts of the Riesz transform and the monogenic signal, the multi-dimensional complex continuation of a real signal. This method allows for a deeper understanding of the pattern formation. The linear evolution of an initial localized perturbation in the presence of deposition is studied.

The deposition linearly selects substrate structures aligned along the streamwise direction, as the spatio-temporal response is advected away. Furthermore, the growth of the initial defect produces a quasi-steady region also characterized by streamwise structures both on the substrate and the fluid film, which is in good agreement with the Green function for a steady defect on the substrate, in the absence of deposition.

6.1 Introduction

The astonishing beauty of geological patterns has fascinated humanity for centuries (Hill et al., 1997). We refer to Section 1.1 for an overview of some geological patterns observed in limestone caves. The role of hydrodynamics in the speleothem formation increased in interest in the last two decades. The emergence of draperies structures in limestone caves was shown to be driven by the Rayleigh-Taylor instability, when the substrate is not horizontal (Bertagni and Camporeale, 2017). We refer to Section 1.3.3.1 for a general introduction about the Rayleigh-Taylor instability.

Bertagni and Camporeale (2017) studied the morphogenesis of draperies structures in limestone caves using the thin film equation, combining a two-dimensional linear stability analysis and a weakly non-linear approach to show the emergence of streamwise structures (i.e. rivulets in the fluid film, draperies on the substrate, see figure 6.1(a)). The growth rate of perturbations from a flat condition is slightly larger for streamwise aligned structures as the inertia of the flow is neglected. However, a complete characterization of the two-dimensional spatio-temporal dynamics and a description of the key mechanisms and the physics underlying the selection of streamwise structures on the substrate remain to be assessed. We will highlight in this work that a small coupling of the hydrodynamic effects with the deposition effect is already sufficient to induce a significant anisotropy in the spatio-temporal response, while it has only a minute effect in the temporal dispersion relation.

The response of a given flow to external perturbations can be characterized through the large-time asymptotic behavior of the linear impulse response, the Green function. The Green function is the most synthetic and complete way to describe the nature of a forced linear system, since the response to any generic forcing is given by the convolution between the Green function and the forcing itself. The impulse can be localized only in space (*steady* analysis) or both in space and time (*spatio-temporal* analysis). Considering the steady case, for a thin film flowing over an inclined planar substrate, the linear Green function enables the reconstruction of the response which emerges from the presence of localized defects (Kalliadasis et al., 2000; Hayes et al., 2000; Decré and Baret, 2003). Interestingly, the resulting Green function for a steady defect is characterized by a decaying behavior as the distance from the defect location increases.

In unstable flows, the spatio-temporal Green function analysis is usually analytically tackled within the context of the *saddle points* approach, in which the large-time asymptotic properties of the response can be retrieved by the research of the saddle points of the spatio-temporal

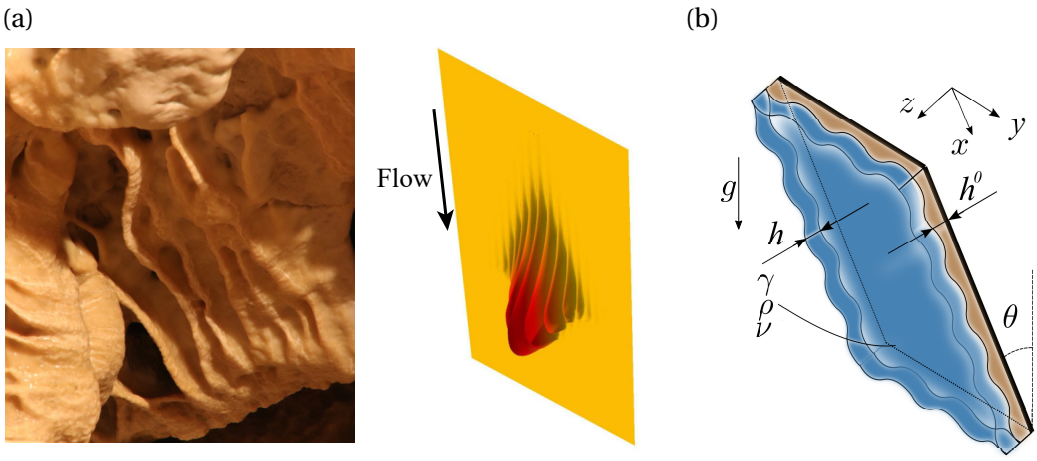

Figure 6.1: (a) Draperies observed in the Vallorbe caves, Switzerland (on the left), and sketch (on the right). (b) Description of the considered problem with the fluid film and substrate thickesses indicated.

growth rate in the complex planes of the spatial wavenumbers which define the response (Briggs, 1964; Bers, 1975; Huerre and Monkewitz, 1990; Carriere and Monkewitz, 1999; Juniper, 2007; Brun et al., 2015).

Alternatively, it has been demonstrated that a numerical approach based on the post-processing of the numerical linear impulse response can well describe the long-time behavior of the impulse response (Brancher and Chomaz, 1997; Delbende et al., 1998; Delbende and Chomaz, 1998; Gallaire and Chomaz, 2003; Mowlavi et al., 2016; Lerisson, 2017; Arratia et al., 2018). The procedure consists of a demodulation of the signal along one direction using the Hilbert transform, which leads to the complex analytic continuation of the real response, the analytic signal. As we detail in this study, the multi-dimensional counterpart of the analytic signal is the monogenic signal (Unser et al., 2009), which finds many applications in image analysis processes and is based on the application of the Riesz transform, the multi-dimensional generalization of the Hilbert transform.

In this Chapter, we propose a numerical method for the analysis of the long-time asymptotic two-dimensional linear impulse response, with the aim of shedding light on the linear physical mechanisms which may lead to the selection of draperies structures on the substrate. The chapter is organized as follows. In Section 6.2, the equations for the evolution of a thin film in the presence of substrate variations are defined. To introduce the numerical procedure for the analysis of the linear response in the presence of a deposition process, we first validate the algorithm against the results of the linear response in the absence of the deposition process and on a flat substrate, since in this circumstance the problem can be solved analytically. We define the theoretical framework of the linear impulse response and we derive the analytical solution for the thin film in the absence of substrate variations. We characterize the response, whose results will be used throughout the work as a comparison with the response in the presence of the deposition process. Subsequently, in Section 6.4 we present the post-processing algorithm

for the analysis of the spatio-temporal impulse response in two dimensions, which we validate using the theoretical results of the previous part. We exploit the validated numerical algorithm in Section 6.5, where we focus on the linear impulse response of a thin film in the presence of a deposition process. The numerical solution of the linearized flow equations is analyzed through the post-processing algorithm. An additional analytical tool for the validation and interpretation of the results is given in Section 6.6, focused on the study of the response in the presence of a steady defect without deposition processes. We compare the numerical results with an analytical approach for the evaluation of the steady Green function within the framework of spatial stability analysis. To verify the faithfulness of the results of the performed linear analyses, non-linear simulations in the presence of the deposition process are reported in Section 6.7.

6.2 Thin film model

We study the dynamics of a thin film of a viscous fluid flowing under a plane inclined with respect to the vertical of an angle θ, in the presence of substrate variations (figure 6.1(b)). The fluid properties are the kinematic viscosity ν, the density ρ and the surface tension coefficient γ. We denote respectively the fluid film thickness and substrate variation thickness as $\bar{h}$ and $\bar{h}^0$. Thus, the distance of the fluid interface from the reference flat substrate is $\bar{h}+\bar{h}^0$. A coordinate system $(\bar{x},\bar{y})$ is defined, where $\bar{x}$ and $\bar{y}$ are respectively the streamwise and spanwise directions. We introduce the initial flat film (Nusselt) thickness h_N and the reduced capillary length ℓ_c^*:

$$\ell_c^* = \frac{\ell_c}{\sqrt{\sin(\theta)}}, \tag{6.1}$$

where $\ell_c = \sqrt{\gamma/(\rho g)}$ is the capillary length. The following non-dimensionalizations are defined:

$$x = \bar{x}/\ell_c^*;\ y = \bar{y}/\ell_c^*;\ h = \bar{h}/h_N;\ t = \bar{t}/\tau_{\mathrm{RT}}, \tag{6.2}$$

where $\tau_{\mathrm{RT}} = \nu\ell_c^2/h_N^3\sin^2(\theta)g$ is the characteristic time scale of the Rayleigh-Taylor instability.

The problem of the lubrication model in the presence of substrate variations has been widely studied in the literature, in the context of the long-wave approximation (Tseluiko et al., 2013) or more involved models based on the introduction of inertia and viscous extensional effects (D'Alessio et al., 2010; Heining and Aksel, 2009). In this work, we consider the model used in Bertagni and Camporeale (2017), for the inertialess case, in which the complete curvature is retained (Weinstein and Ruschak, 2004; Wilson, 1982). The non-dimensional equation for the evolution of the thickness in the presence of substrate variations reads:

$$\partial_t h + uh^2\partial_x h + \frac{1}{3}\nabla\cdot\left[\chi h^3\nabla(h+h^0) + h^3\nabla\kappa\right] = 0, \tag{6.3}$$

where ∇ operates in the (x, y) plane and $u = \cot(\theta)\ell_c^*/h_N$ is the linear advection velocity (Brun et al., 2015). The constant χ is set to $\chi = 1$ for the flow under an inclined substrate, which is analyzed throughout the work, except in the Appendix 6.9.1, where we report the validation of the numerical procedure against a benchmark case in the literature for the flow over an inclined flat substrate ($\chi = -1$). The curvature of the free surface ($h + h^0$), in non-dimensional form, reads:

$$\kappa = \nabla \cdot \left(\frac{\nabla \left(h + h^0 \right)}{\sqrt{1 + \left(\frac{h_N}{\ell_c^*} \right)^2 |\nabla (h + h^0)|^2}} \right). \tag{6.4}$$

In this work, we focus on the substrate growth by precipitation of calcium carbonate in cave walls. The mathematical formulation of the problem involves different chemical reactions and diffusion processes that occur in the fluid layer (Buhmann and Dreybrodt, 1985). Following the derivation of Short et al. (2005b), to which we refer for details, the flux of calcium carbonate depositing on the substrate, i.e. the variation in time of the substrate thickness, can be written as follows:

$$\partial_{\bar{t}} \bar{h}^0 = \bar{C} \bar{h}, \tag{6.5}$$

where $\bar{C}$ is the chemistry-dependent constant, of the order of $\bar{C} \sim 10^{-7} s^{-1}$ (Camporeale, 2015). Considering the time scale τ_{RT}, the deposition constant in the dimensionless time scale is of the order $C \sim 10^{-4}$. Introducing the non-dimensionalization of equation (6.2), the nondimensional equation for the deposition reads:

$$\partial_t h^0 = \check{C} h, \tag{6.6}$$

where $\check{C} = C/\sin^2(\theta)$. Equations (6.3) and (6.6) define the system for the dynamics of a thin film flowing under ($\chi = 1$) an inclined plane in the presence of substrate variations due to the deposition of calcium carbonate.

The equations are linearized around the baseflow solution $[H, H^0]^T = [1, \check{C}t]^T$ introducing the following decomposition:

$$h = 1 + \varepsilon \eta, \quad h^0 = \check{C} t + \varepsilon \eta^0, \tag{6.7}$$

where $\varepsilon \ll 1$ and $[\eta, \eta^0]$ is the *perturbation* with respect to the baseflow solution. Keeping $O(\varepsilon)$ terms in equations (6.3), (6.6), the following system of equations is obtained:

$$\partial_t \eta + u \partial_x \eta + \frac{1}{3} \left[\chi \nabla^2 (\eta + \eta^0) + \nabla^4 (\eta + \eta^0) \right] = 0, \tag{6.8a}$$

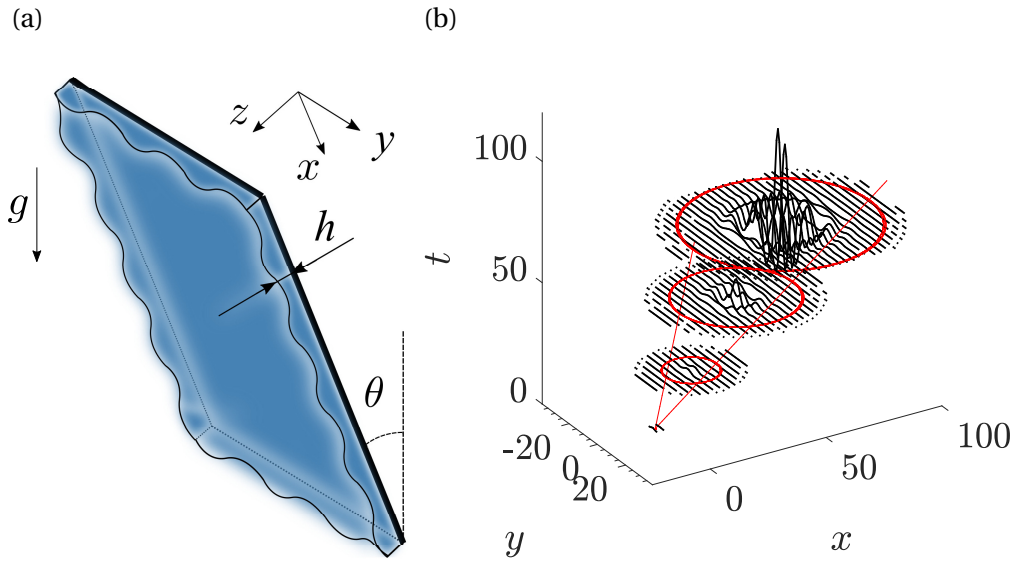

Figure 6.2: (a) Sketch of the flow and substrate configurations adopted in Section 6.3. (b) Sketch of the impulse reponse in a spatio-temporal diagram.

$$\partial_t \eta^0 = \check{C}\eta, \tag{6.8b}$$

which describes the linearized dynamics of the *perturbation* $[\eta, \eta^0]$ around the constant flat film solution $H = 1$ (equation (6.8a)), in the presence of a linear in time substrate growth H^0 due to the deposition law (equation (6.8)(b)), i.e. $[H, H^0]^T = [1, \check{C}t]^T$. Equations (6.8) are the starting point for the analysis of the speleothems morphogenesis, in a linearized dynamics context. The parameters which influence the linearized dynamics are the linear advection velocity u and the deposition constant C, while h_N/ℓ_c^* enters only in the fully non-linear dynamics.

The numerical implementation of the linearized equations (6.8) is based on a Fourier pseudo-spectral scheme implemented in MATLAB. Henceforth, we consider a rectangular domain of size 1000×1000, with a number of collocation points $N_x = N_y = 1001$ and periodic boundary conditions. In Appendix 6.9.1 we report the numerical procedure and the validation against the benchmark case of the response of a thin film flowing over an inclined flat substrate to a steady localized defect (Decré and Baret, 2003; Kalliadasis et al., 2000; Hayes et al., 2000).

6.3 Linear response in the absence of substrate variations

6.3.1 Dispersion relation

In this section, we study the linear response in the absence of substrate variations (figure 6.2). We therefore impose $\eta^0 = 0$ in equation (6.8a), leading to the following equation for the linearized dynamics of the perturbation:

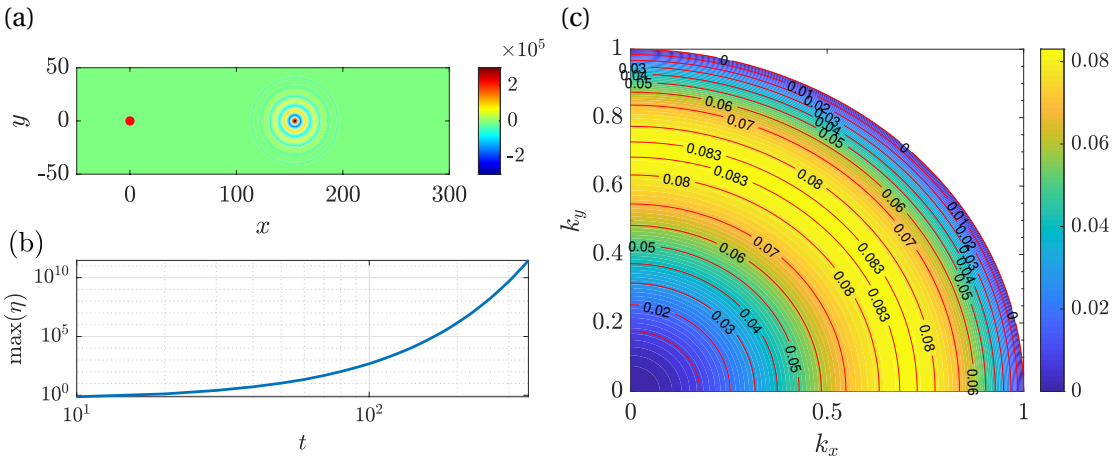

Figure 6.3: Two-dimensional linear impulse response in the absence of substrate variations, for $u = 0.77$. (a) Response in the physical space at $t = 200$. (b) Temporal evolution of the maximum value of the response. (c) Temporal growth rate, as a function of k_x and k_y. The red dot denotes the initial impulse location.

$$\partial_t \eta + u\partial_x \eta + \frac{1}{3}\left[\nabla^2 \eta + \nabla^4 \eta\right] = 0. \tag{6.9}$$

We introduce the ansatz $\eta \sim \exp[\mathrm{i}\left(k_x x + k_y y - \omega t\right)]$, where k_x and k_y are real and ω is complex, within the temporal approach. Introducing $k = \sqrt{k_x^2 + k_y^2}$, the following polynomial dispersion relation is obtained:

$$\omega = u k_x + \frac{\mathrm{i}}{3}\left(k^2 - k^4\right), \tag{6.10}$$

which relates the behavior in space and time of the perturbation. In the absence of deposition process, the temporal growth rate $\mathrm{Im}(\omega)$ does not depend on u, which influences only the advection of perturbations. The response in the absence of deposition is characterized by concentric circles (see figure 6.3(a)) that propagate from a center that is advected away with the linear advection velocity u. The maximum value of the thickness increases exponentially with time (see figure 6.3(b)). In the following, we rescale the fluid thickness using the maximum value, knowing that the growth in amplitude is exponential. The iso-values of the temporal growth rate are concentric circles propagating from $(k_x, k_y) = 0$, (see figure 6.3(c)), i.e. the growth rate is isotropic. The growth rate increases for small wavenumbers, reaches a maximum at $k = 1/\sqrt{2}$, then decreases and becomes negative for $k > 1$, the cut-off wavenumber. Therefore, the linearized dynamics does not show any preferential direction for the growth of perturbations, which are advected away.

6.3.2 Large time behavior of the impulse response

In this section, we analytically study the linear impulse large-time response. So as to better characterize the response observed in figure 6.3(a) and understand the structure when the

deposition process will be introduced, together with the differences with the case in the absence of substrate variations, we present the theoretical tools to describe the impulse response of a linear system, the Green function $\tilde{g}$. The method is a generalization of the classical one-dimensional approach (Brevdo, 1991; Carriere and Monkewitz, 1999; Juniper, 2007). For $t \to \infty$, the Green function asymptotically reads:

$$\tilde{g}(x,y,t) \sim \hat{g} \exp[\mathrm{i}\left(k_x x + k_y y - \omega t\right)]/t, \quad t \to \infty \tag{6.11}$$

where the streamwise wavenumber k_x, the spanwise wavenumber k_y and the complex frequency ω are varying in space and time, via their dependence on so called rays x/t and y/t. The evaluation of the asymptotic properties along the rays (x/t = const, y/t = const) for $t \to \infty$ is performed using the method of the steepest descent in the complex k_x and k_y planes. At large times, the dominating contribution with group velocity $(x/t, y/t)$ is given by the following saddle points in the complex k_x and k_y planes:

$$\frac{\partial \omega''}{\partial k_x} = \frac{\partial \omega''}{\partial k_y} = 0, \tag{6.12}$$

where $\omega'' = \omega - k_x x/t - k_y y/t$. The resulting values of k_x, k_y and ω'' for each ray $(x/t, y/t)$ allow to reconstruct the linearized dynamics of the wavepacket.

The evaluation of the saddle points is performed in MATLAB, by using the built-in function *fsolve* that solves simultaneously for the saddle points in the two complex planes k_x and k_y using the dispersion relation equation (6.10). The initialization is based on the solution of the one-dimensional case documented in Brun et al. (2015) for $(x/t, y/t) = (0,0)$, which corresponds to the maximum temporal growth rate in the dispersion relation and is a contributing saddle point according to Barlow et al. (2017). The solution at different $(x/t, y/t)$ is obtained using as initial guess the previously calculated value.

The asymptotic properties for $u = 0.77$ are reported in figure 6.4. We report only positive values of y/t, since ω'', ω and k_x are symmetric with respect the axis $y/t = 0$, while k_y is antisymmetric. The iso-contours of the spatio-temporal growth rate $\sigma = \mathrm{Im}(\omega'')$ (figure 6.4(a)) are concentric circles that propagate from a center at $(x/t = u, y/t = 0)$. The maximum value $\sigma = 1/12$ is located at the center and coincides with the maximum of the dispersion relation equation (6.10). Increasing the distance from the center, the values of σ decrease. At a distance from the center of ≈ 0.54, the spatio-temporal growth rate is zero, and becomes negative at larger distances. The full description of the asymptotic properties is completed with the results in figure 6.4(b-f). The real part of the complex frequency $\mathrm{Re}(\omega)$ (figure 6.4(b)) is characterized by positive values in the upstream part of the wavepacket and by negative values in the downstream part. The transition region where $\mathrm{Re}(\omega) = 0$ is located at $x/t = u$, and the transition becomes more abrupt whilst decreasing y/t, with a discontinuity at $y/t = 0$. This discontinuity can be observed also in the real parts of the streamwise (figure 6.4(d)) and spanwise (figure 6.4(f)) wavenumbers, while the corresponding imaginary parts (figure

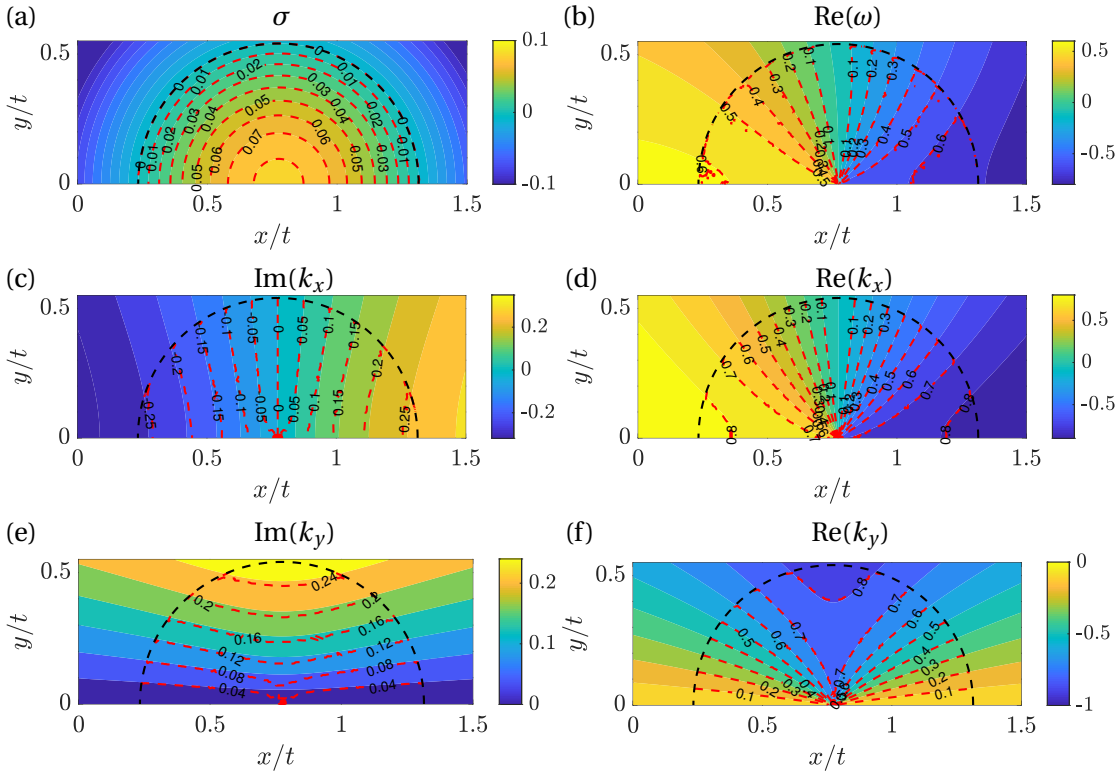

Figure 6.4: Long-time asymptotic properties of the two-dimensional linear impulse response in the absence of deposition, for $u = 0.77$, as functions of x/t and y/t. The colored iso-contour plots represent the analytical results of Section 6.3.2. (a) spatio-temporal growth rate. (b) Real part of the complex frequency. (c) Imaginary part of the streamwise wavenumber. (d) Real part of the streamwise wavenumber. (e) Imaginary part of the spanwise wavenumber. (f) Real part of the spanwise wavenumber. The black dashed line identifies the region $\sigma = 0$. The red dashed lines denote the results of the post-processing algorithm described in Section 6.4.

6.4(c,e)) are zero.

According to the spatio-temporal analysis approach (Van Saarloos, 2003), the front is defined by the region where $\sigma = 0$. In the one-dimensional case the front is defined only by a value of x/t, while in two-dimensions by couples $(x/t, y/t)$. From the analysis, it results that the front of the wave-packet is a circle of radius ≈ 0.54 centered around $(x/t = u, y/t = 0)$. This value agrees with the absolute-convective instability transition predicted by Brun et al. (2015) for the one-dimensional case. Since the center of the wavepacket is located at $x/t = u$, and the front is a circle of radius 0.54 (independent of u), the first case in which the spatio-temporal growth rate is non-negative at $x/t = 0$ is when $u = 0.54$. As the linear advection velocity decreases, the unstable region invades negative values of x/t, i.e. upstream of the initial impulse position, and the flow is said to be absolutely unstable (Huerre and Monkewitz, 1990).

The above-performed analytical spatio-temporal analysis could be in principle performed also in the presence of the deposition process. Nevertheless, the possible presence of multiple

saddle points to be identified and the discrimination of upstream and downstream propagating branches related to the different saddle points makes the problem arduous to tackle theoretically. We therefore propose a numerical approach, which presents some originalities and interesting perspectives. The analytical results of this section will be used to validate the numerical algorithm and as a reference point when restoring the coupling with the deposition process.

6.4 Numerical approach based on the monogenic signal

6.4.1 The Riesz transform and the monogenic signal

In this section, we introduce the mathematical tools necessary for the spatio-temporal analysis of the impulse response from the linear simulations. Numerical analyses of the linear impulse response have been already performed in literature (Delbende et al., 1998; Delbende and Chomaz, 1998; Gallaire and Chomaz, 2003), where the asymptotic properties along one single direction were studied. The study of the asymptotic properties of a one-dimensional wavepacket is based on the introduction of the analytic signal (Delbende et al., 1998), which is the complex continuation of a real signal. The analytic signal is derived using the *Hilbert transform*, which corresponds to a phase shift of $-90°$ and $+90°$ respectively to the positive and negative Fourier components of a function $g(x)$, i.e. the Hilbert transformed signal reads:

$$\mathcal{H}g(x) = H_x \star g(x), \tag{6.13}$$

where H_x is a Heaviside filter characterized by the Fourier transform $\hat{H}_x(k_x) = -\mathrm{i}\,\mathrm{sgn}(k_x)$, and the symbol $\star$ denotes the convolution operator. In the Fourier domain, the convolution becomes a product, such that the Fourier tranform of the Hilbert transformed signal reads $\hat{\mathcal{H}}g = -\mathrm{i}\,\mathrm{sgn}(k_x)\hat{g}(k_x)$, where $\hat{g}$ is the Fourier transformed signal. The analytic signal gives access to the envelope and the phase of the wavepacket; indeed, as an alternative to its representation as the two components function $\mathbf{g}_a(x) = \big(g(x), \mathcal{H}g(x)\big)$, the complex function $g_a(x) = g(x) + \mathrm{i}\mathcal{H}g(x)$ can be defined. The analytic signal g_a is said to be the complex continuation of the real signal and can be rewritten in terms of amplitude and phase $g_a(x) = A\exp(\mathrm{i}\xi)$, where A is the instantaneous amplitude (i.e., the envelope) and ξ the phase of the complex signal. As explained in detail in the Section 6.4.2, the knowledge of the envelope of the wavepacket is necessary to analyze the spatial and temporal growth rates, while the phase gives access to the spatial and temporal frequencies.

Our work aims to generalize the approach of Delbende et al. (1998) to the two-dimensional case, in the presence of two spatial propagation directions. We introduce the *monogenic* signal, the multi-dimensional generalization of the analytic signal (Unser et al., 2009). In literature, there are several attempts to generalize the analytic signal in two-dimensions (Bulow and Sommer, 2001; Felsberg and Sommer, 2001; Hahn, 2003). In this work, we use the definition given by Unser et al. (2009), based on the multi-dimensional generalization of the Hilbert

transform, the *Riesz transform* (Stein and Weiss, 2016). In the two-dimensional case, in analogy to the Hilbert transform, the Riesz operator transforms the scalar signal $g(x,y)$ to the vector signal $\mathbf{g}_R(x,y)$ that reads

$$\mathbf{g}_{\mathrm{R}}(x,y) = \begin{pmatrix} g_{\mathrm{R1}}(x,y) \\ g_{\mathrm{R2}}(x,y) \end{pmatrix} = \begin{pmatrix} H_x * g(x,y) \\ H_y * g(x,y) \end{pmatrix}, \tag{6.14}$$

where $*$ denotes the convolution operator in two dimensions. The functions H_x and H_y are two Heaviside filters characterized respectively by the Fourier transforms $\hat{H}_x(k_x,k_y) = -\mathrm{i}k_x/k$ and $\hat{H}_y(k_x,k_y) = -\mathrm{i}k_y/k$, and they are the generalization of the one dimensional Heaviside filter to two spatial directions. In analogy to the Hilbert transformed signal, we consider a definition of the Riesz transformed signal that combines the two components in one scalar signal (Unser et al., 2009) :

$$\mathcal{R}g(x,y) = g_{\mathrm{R1}}(x,y) + \mathrm{i}g_{\mathrm{R2}}(x,y), \tag{6.15}$$

which in the Fourier domain reads:

$$\hat{\mathcal{R}}g(k_x,k_y) = \frac{\left(-\mathrm{i}k_x + k_y\right)}{k}\hat{g}(k_x,k_y), \tag{6.16}$$

where $\hat{g}$ is the two-dimensional Fourier transform of the signal. Note that at $k_x = k_y = 0$ the Fourier transform of the Riesz transformed signal is singular and the regularization assumes zero value at the origin. We then introduce the monogenic signal as the three-components function:

$$\mathbf{g}_m(x,y) = (g(x,y), \mathrm{Re}(\mathcal{R}g(x,y)), \mathrm{Im}(\mathcal{R}g(x,y))) = \left(g, g_{R1}, g_{R2}\right) \tag{6.17}$$

According to Unser et al. (2009), the relation between the Riesz and the Hilbert transforms along the (x,y) directions can be seen as the equivalent between the definition of gradient and partial derivatives. The quantity $r = \sqrt{g_{R1}^2 + g_{R2}^2} = |\mathcal{R}g|$ identifies the maximum response of the directional Hilbert operator

$$\max_{\psi}\left\{\mathcal{H}_\psi g\right\} = \max_{\psi}\left\{\mathrm{Re}\left(e^{-\mathrm{i}\psi}\mathcal{R}g\right)\right\} \tag{6.18}$$

along the direction d_ψ given by the angle $\psi = \mathrm{atan}(g_{R2}/g_{R1})$. The instantaneous amplitude (i.e. the envelope of the signal) is given by

$$\mathrm{A} = \sqrt{g^2 + g_{R1}^2 + g_{R2}^2}, \tag{6.19}$$

and the phase by

$$\xi = \mathrm{atan}(\sqrt{g_{R1}^2 + g_{R2}^2}/g). \tag{6.20}$$

This decomposition allows us to write the monogenic signal along d_ψ in the form

$$\tilde{g}(x,y,t) = \mathrm{A}\exp(\mathrm{i}\xi). \tag{6.21}$$

The amplitude A represents the envelope of the signal and ξ the phase along the direction d_ψ. Note that equation (6.21) is valid only when amplitude and phase of the signal can be demodulated (Delbende et al., 1998). This is valid when the variations of the envelope occur at a scale much larger than that governing the oscillations. The representation in equation (6.21) is the two-dimensional equivalent of the analytic signal (Delbende et al., 1998) and identifies in $\tilde{g}$ the complex continuation of the two-dimensional real signal g.

6.4.2 Large time asymptotic properties

In this section, we derive the asymptotic properties of the wavepacket by following the same procedure outlined in Delbende et al. (1998). According to Section 6.3.2, the complex Green Function reads:

$$\tilde{g} \sim \exp[\mathrm{i}\left(k_x x + k_y y - \omega t\right)]/t, \tag{6.22}$$

where the asymptotic properties k_x, k_y and ω depend on x/t and y/t.

The linear simulations of the impulse response give as a result the real signal $g(x,y)$. We thus recover the complex Green function by the analytic continuation of g, i.e. the monogenic signal $\tilde{g}$:

$$\tilde{g} \sim \exp[\mathrm{i}\left(k_x x + k_y y - \omega t\right)]/t = \mathrm{A}\exp(\mathrm{i}\xi), \tag{6.23}$$

where $\mathrm{A} = |\tilde{g}|$ and $\xi = \arg(\tilde{g})$. Thus, by exploiting the last expression, we can use the monogenic signal $\tilde{g}$ to evaluate the asymptotic properties of the wavepacket. The spatio-temporal growth rate

$$\sigma = \mathrm{Im}(\omega'') = \mathrm{Im}(\omega) - \mathrm{Im}(k_x)x/t - \mathrm{Im}(k_y)y/t = \mathrm{Im}(\omega) - \mathrm{Im}(k_x)v_x - \mathrm{Im}(k_y)v_y, \tag{6.24}$$

which represents the growth of a perturbation along a ray of group velocities $(x/t, y/t) = (v_x, v_y)$, is obtained by applying the logarithm operator to the absolute value of equation (6.23)

$$|\tilde{g}| \sim \exp(\sigma t)/t = \mathrm{A} \quad \rightarrow \quad \sigma t - \ln(t) \sim \ln(A) \tag{6.25}$$

and thus by evaluating the derivative with respect to time of the resulting expression, for $(x/t = \mathrm{const}, y/t = \mathrm{const})$:

$$\sigma(x = v_x t, y = v_y t) \sim \frac{\mathrm{d}}{\mathrm{d}t}\ln(A(x = v_x t, y = v_y t, t)) + \frac{1}{t}. \tag{6.26}$$

The definition of the spatio-temporal growth rate equation (6.24) allows us to evaluate the imaginary part of the streamwise and spanwise wavenumbers at each ray $(x/t, y/t) = (v_x, v_y)$ (see Appendix 6.9.2 for details):

$$\mathrm{Im}(k_x(x = v_x t, y = v_y t)) = -\partial_{v_x}\sigma, \tag{6.27}$$

$$\mathrm{Im}(k_y(x = v_x t, y = v_y t)) = -\partial_{v_y}\sigma. \tag{6.28}$$

The real parts of the spatial wavenumbers are retrieved by considering equation (6.23) and exploiting the definition of phase:

$$\mathrm{Re}(k_x(x = v_x t, y = v_y t)) \sim \partial_x \xi(x = v_x t, y = v_y t), \tag{6.29}$$

$$\mathrm{Re}(k_y(x = v_x t, y = v_y t)) \sim \partial_y \xi(x = v_x t, y = v_y t). \tag{6.30}$$

Alternatively, still exploiting the logarithm of equation (6.23), a direct evaluation of the real and imaginary parts of the spatial wavenumbers from the complex monogenic signal can be performed:

$$k_x \sim -\mathrm{i}\partial_x \ln(\tilde{g}(x = v_x t, y = v_y t)), \tag{6.31}$$

$$k_y \sim -\mathrm{i}\partial_y \ln(\tilde{g}(x = v_x t, y = v_y t)). \tag{6.32}$$

In this work, we adopted this technique to evaluate the streamwise and spanwise wavenumbers. The temporal growth rate is obtained from the knowledge of the spatio-temporal growth rate and the imaginary part of the wavenumbers:

$$\mathrm{Im}(\omega) = \sigma + \mathrm{Im}(k_x)\, x/t + \mathrm{Im}(k_y)\, y/t. \tag{6.33}$$

The real part of the complex frequency is, by definition, the temporal derivative of the phase ξ:

$$\mathrm{Re}(\omega)(x/t, y/t, t) \sim -\partial_t \xi(x/t, y/t, t). \tag{6.34}$$

Note that in this case the derivative with respect to the time is evaluated in a relatively short time interval, without following the rays $x/t = v_x$ and $y/t = v_y$ (Delbende et al., 1998). Moreover, the sign of the spatial frequencies cannot be recovered from the analysis, since we are post-processing a real signal. In the following, we will consider positive values for the real parts of the complex frequency and spatial wavenumbers.

6.4.3 Numerical procedure and validation

The analytical developments derived in the previous sections aim at describing the asymptotic behavior for $t \to \infty$ using numerical simulations at finite times. Besides, equation (6.21) assumes that the amplitude and the phase of the signal subject to the Riesz transform can be demodulated, i.e. that a separation of scales between the variations of the envelope and the oscillations subsists. In this section, we verify the numerical procedure and the validity of the assumptions using as a test case the analytical solution described in Section 6.3.2. The post-processing algorithm is validated against the theoretical results of the impulse response in the absence of substrate variations. The numerical implementation is based on MATLAB. The linear response is computed using equation (6.9) subjected to the a Gaussian initial condition that mimics the Delta function behavior:

$$\eta(x, y, 0) = \eta^0(x, y, 0) = \exp[-(x^2 + y^2)/2\varsigma^2]. \tag{6.35}$$

with $\varsigma = 1$; no appreciable changes in the response have been observed for $\varsigma < 1$.

The numerical steps for the post-processing are the following. We apply the two-dimensional Fourier transform to the linear response at different times via the built-in MATLAB function *fft2*. We obtain the Riesz transformed signal by equation (6.16) . The inverse Fourier transform is applied (via the built-in MATLAB function *ifft2*) and we build the monogenic signal in the physical space, for different times, according to equation (6.21). We evaluate the spatio-temporal growth rate by equation (6.24), using the monogenic signals evaluated at different times. We then obtain the streamwise and spanwise wavenumbers by a finite difference expression of equation (6.31-6.32), and then the temporal growth rate by a finite difference approximation of equation (6.33). Finally, the real part of the complex frequency is recovered from equation (6.34) using the computed monogenic signals at different times.

We evaluate the derivatives using first-order finite differences. A convergence analysis has been performed on the number of collocation points and the order of the finite differences for the derivatives, and we observed the convergence of the results already for a domain of $L_x = L_y = 1000$ and $N_x = N_y = 1001$. The odd number of points is necessary to have also the zero frequency $k_x = k_y = 0$, where the transfer function of the Riesz transform is singular and has to be regularized imposing the zero value. The results are averaged at different times (Lerisson, 2017). We consider a time step of $\Delta t = 15$ for the evaluation of the spatio-temporal growth rate, from $t = 200$ to $t = 350$. At each time, the real part of the complex frequency is evaluated using a time step of $\delta t = 0.01$ (Delbende et al., 1998).

In figure 6.4 we also report a comparison of the post-processing algorithm (red dashed lines) against the results of the saddle points analysis (colored iso-contours). The results agree with those obtained from the saddle points approach. The spatio-temporal growth rate (figure 6.4(a)) is well described by the numerical post-processing, and the front of the wavepacket is well captured. The other variables well agree with the analytical solution. Figure 6.5 shows the results for the temporal properties and the streamwise wavenumber as functions of x/t, at $y/t = 0$. The comparison reveals a good agreement, except in the center of the wavepacket where the analytical solution is discontinuous. The difference can be imputed to a transient effect at the center of the wavepacket, which is reduced as time increases. Note that the analytical solution of Section 6.3.2 is rigorously valid as $t \to \infty$. Nevertheless, in the numerical simulations, there is a practical limit in the final time related to the numerical noise. The maximum ratio between the smaller and greater values in the simulations is limited to 16 decades, for the *double* precision (Trefethen and Bau III, 1997). Therefore, we cannot go beyond the final time above defined, i.e. $t = 350$. Despite the presence of a discontinuity in the center of the wavepacket, the numerical procedure well captures the structure of the solution. Concerning the spatio-temporal growth rate, the maximum error from the theoretical value is around $\Delta = 2 \times 10^{-3}$, which means a percentual error of 2.5%. The edges of the wavepacket well agree with the analytical solution. We conclude that our post-processing algorithm is able to capture the spatial structure of the asymptotic properties, making it suitable for the study of the impulse response in the presence of the deposition process.

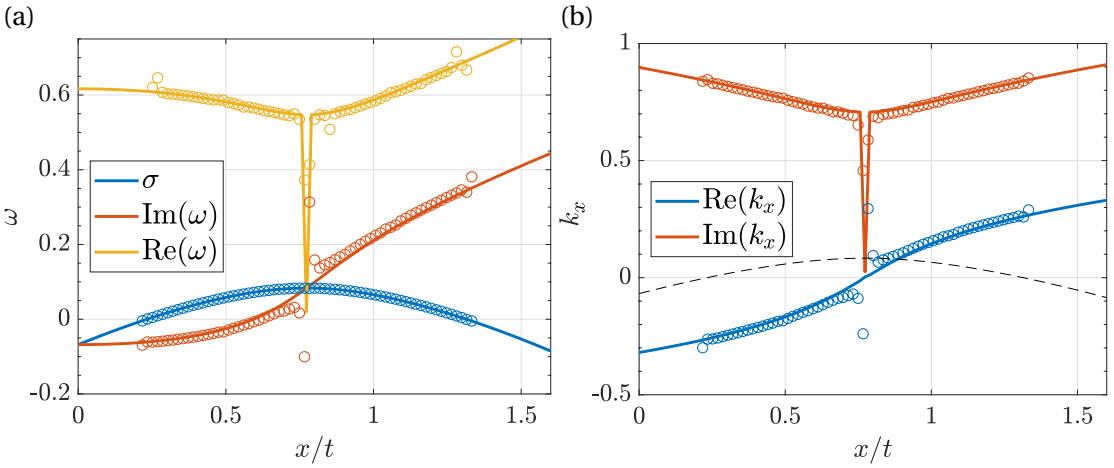

Figure 6.5: Comparison of the long-time asymptotic properties of the two-dimensional linear impulse response in the absence of deposition ($u = 0.77$) as functions of x/t, for $y/t = 0$. The solid lines and the dots denote respectively the analytical (Section 6.3.2) and numerical approaches (Section 6.4). (a) spatio-temporal growth rate, imaginary and absolute value of the real part of the complex frequency. (b) Imaginary and absolute value of the real part of the streamwise wavenumber. The black dashed line denotes the values of σ.

6.5 Linear response in the presence of the deposition process

6.5.1 Dispersion relation

In this section, we briefly study the temporal stability properties in the presence of the deposition process. Following the linear stability analysis approach, we assume the normal mode expansion

$$[\eta, \eta^0]^T = [\eta, \eta^0]^T \exp[\mathrm{i}\left(k_x x + k_y y - \omega t\right)]. \tag{6.36}$$

It is worth to underline that this decomposition for the substrate thickness assumes that the temporal growth due to the presence of the flat film is much slower than the one related to the Rayleigh-Taylor instability. The deposition constant C. describes the growth in the absence of patterns in the fluid film. The characteristic time scale of this process has to be large enough so as to the variations of the baseflow are negligible as the instability occurs. Under these conditions, a separation of scales between the speleothem growth and the Rayleigh-Taylor instability subsists. Since C is already non-dimensionalized with the characteristic time scale of the Rayleigh-Taylor instability, we restrict ourselves to the case $C < 10^{-3}$. In these conditions, we can safely assume the ansatz equation (6.36).

We introduce the normal mode decomposition in the equations for the linearized dynamics equation (6.8), leading to the dispersion relation which relates the complex frequency ω to the wavenumbers (k_x, k_y) for the coupled hydrodynamic-deposition problem:

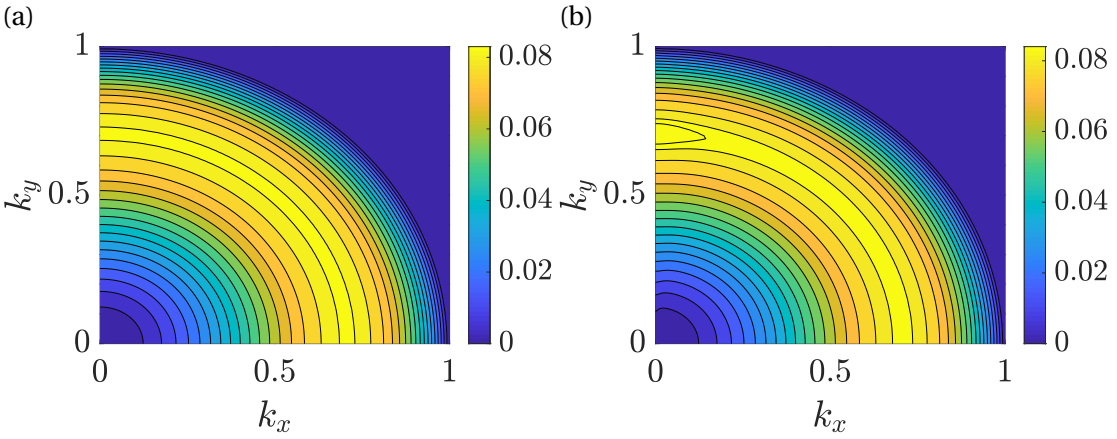

Figure 6.6: Temporal growth rate Im(ω) from the dispersion relation with deposition (equation (6.37)) as a function of (k_x, k_y), for (a) $C = 10^{-5}$, (b) $C = 10^{-3}$.

$$\omega = \frac{\omega^H}{2} \pm \sqrt{\left(\frac{\omega^H}{2}\right)^2 - \frac{\check{C}}{3}\left(k^2 - k^4\right)}, \tag{6.37}$$

where ω^H is the complex frequency in the absence of substrate variations, equation (6.10).

The dispersion relation equation (6.37) is the analogous of the one reported in Bertagni and Camporeale (2017) in the absence of inertial effects. Two branches of the dispersion relation are identified. One branch is always damped while the other one tends to the hydrodynamic case as C goes to zero. The dynamics is governed by two non-dimensional parameters, the linear advection velocity u and the deposition constant C. A preliminary analysis of the influence on the dispersion relation for a large range of u did not show any appreciable effect on the temporal growth rate of perturbations, for fixed deposition constants $10^{-10} < C < 10^{-3}$. For computational reasons, it is not convenient to consider extremely large values of u, as large as those that can be found in limestone caves ($\ell_c/h_N \sim 270$, $u \sim 10^2$), since the advection of perturbations will require the use of irrealistic extremely large computational domains for the numerical simulations, while the physics of the traveling wavepacket would not change significantly. For these reasons, we focus on the case $u = 0.77$ and $\theta = 55°$, and we study the effect of the deposition constant C.

In figure 6.6 we report the temporal growth rate Im(ω) as a function of (k_x, k_y), for different values of the deposition constant. For $C = 10^{-5}$, the temporal growth rate is analogous to the case without deposition, and no appreciable anisotropies are observed. At very high values of the deposition constant, $C = 10^{-3}$, the iso-values are concentric circles in most of the (k_x, k_y) plane, but there is a small region located close to $k_x = 0$ where the growth rate is slightly higher (the difference is of order 10^{-3}). The isotropy is broken, and spanwise structures (*rivulets*) experience a slightly larger growth than the streamwise structures (*waves*), as already pointed out in Bertagni and Camporeale (2017).

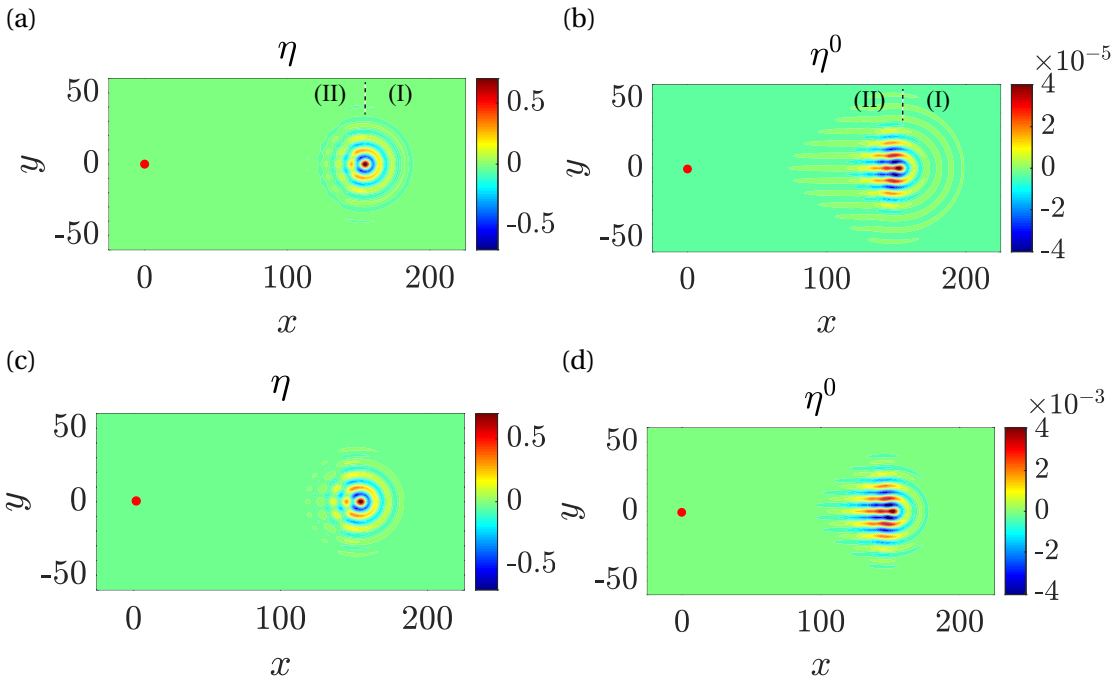

Figure 6.7: Linear impulse response (equation (6.8)), for $u = 0.77$, at $t = 200$. (a-b) $C = 10^{-5}$, (a) fluid film and (b) substrate thickness. (c-d) $C = 10^{-3}$, (c) fluid film and (d) substrate thickness. Results are rescaled with the maximum fluid thickness for visualization purposes. The red dots denote the initial impulse location.

Nevertheless, the small anisotropy in the dispersion relation may be not sufficient to completely characterize a linear selection of streamwise structures in the deposition process that should arise also for low values of the deposition constant, in the range defined by Camporeale (2015). Moreover, the complex form of the dispersion relation does not highlight how the deposition process influences the spatio-temporal growth of perturbations, and thus it does not shed light on the physics underlying the phenomenon. We therefore focus on the response of the system to a localized initial perturbation, i.e. the Green function.

6.5.2 Numerical impulse response

In this section, we focus on the spatio-temporal analysis of the linear impulse response, both on the substrate and in the fluid film, in the presence of the deposition process (equation (6.8)). We consider two representative values of the deposition constant which cover the physical range indicated by Camporeale (2015), $C = 10^{-5}$ and $C = 10^{-3}$. Figure 6.7 shows the linear impulse response in terms of fluid and substrate thickness, at $t = 200$. We recall that in Section 6.3 we observed that the fluid thickness response in the absence of substrate variations was characterized by concentric circles. The fluid film thickness (figure 6.7(a,c)) is characterized by a quite similar structure, albeit some differences can be highlighted. While in the downstream part (I) we observe circular iso-values for η, the pattern in the upstream part

(II) is more intricate.

The substrate thickness (figure 6.7(b,d)) presents similar peculiarities. The iso-values in the downstream part are circular, while in the upstream part streamwise aligned structures are present. The region in which streamwise structures dominate roughly corresponds to the region upstream of the maximum film thickness. These structures grow as higher values of the deposition constant are considered. As a consequence, we observe a more perturbed pattern in the fluid film.

The isotropy breaking in the fluid film is related to the presence of deposited streamwise structures in the upstream part of the wavepacket. While in the downstream part the hydrodynamics dominate the pattern with an isotropic structure reminiscent of the case without deposition (Section 6.3), observed also in the substrate thickness, in the upstream part we observe an interaction between the hydrodynamics and the deposition process.

As the impulse travels, it leaves behind a substrate pattern characterized by predominant streamwise structures. From a physical point of view, this may be explained by the fact that waves are structures that are advected away with the flow, while rivulets are not. Furthermore, it has to be remembered that the deposition law is linear with the film thickness (see equation (6.6)). The growth of substrate disturbances is overposed with the classical growth in the presence of a flat film, i.e. the substrate thickness is always increasing, but this is not obvious for the perturbation η^0. Since waves are traveling structures (i.e., they are oscillating at fixed locations), the linearized deposition law is sequentially increasing and decreasing the substrate perturbation with respect to the linear growth in time, then leading to a much smaller effect on the deposition process. On the contrary, rivulets are not traveling structures. The substrate perturbation always increases or decreases, since there is no advection of the fluid structures along the spanwise direction. As a consequence of the passage of the wavepacket, predominant streamwise structures are deposited on the substrate.

6.5.3 Large time behavior of the impulse response

In this section we apply the post-processing algorithm, introduced in Section 6.4, to the two cases of figure 6.7. According to the decomposition of equation (6.36), the analysis of the asymptotic properties can be applied to both variables. The difference in the patterns observed in figure 6.7 are related to the different eigenvectors $[\hat{\eta}, \hat{\eta}^0]$. In the following, we consider the fluid thickness for the evaluation of the asymptotic properties. However, the observed physical results are not affected by this choice.

In figure 6.8(a) we report the spatio-temporal growth rate obtained from the post-processing algorithm, for $C = 10^{-5}$. The spatio-temporal growth rate is greater than zero in a region downstream of the initial impulse position (III). The unstable region spreads in the $(x/t, y/t)$ plane within a region roughly defined by a front angle $\phi \simeq 36.5°$. In the downstream part of the wavepacket (I), we observe circular iso-values of the spatio-temporal growth rate, which

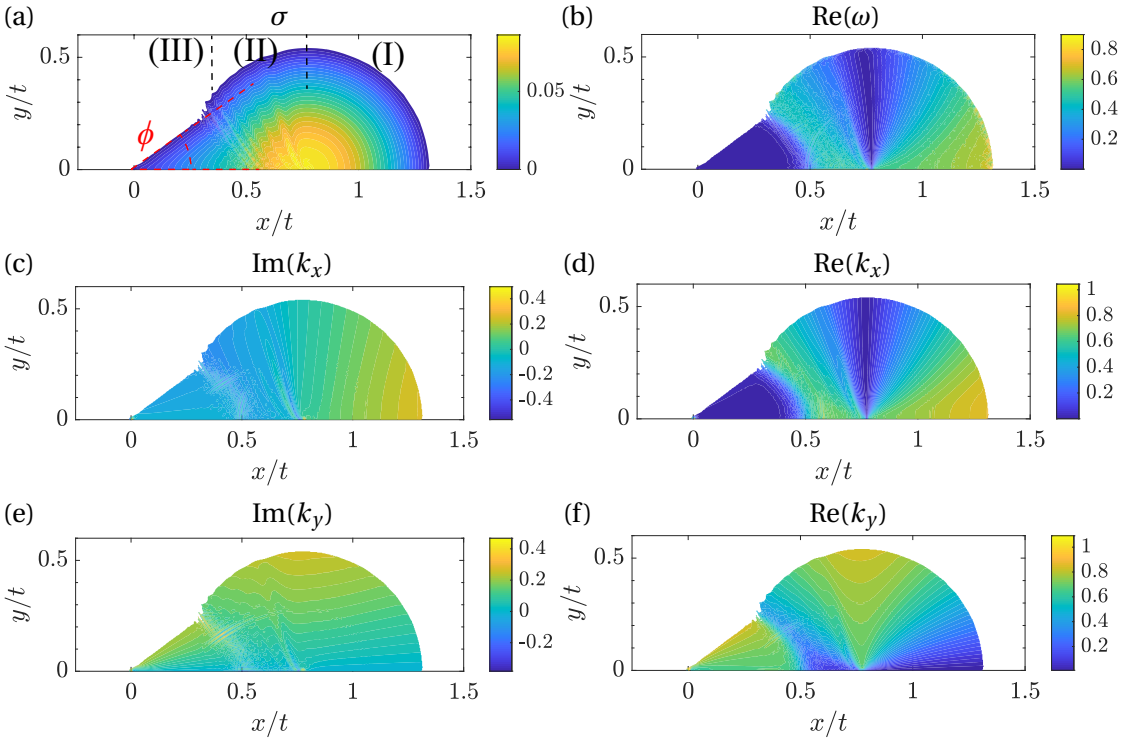

Figure 6.8: Asymptotic properties from the post process algorithm (Section 6.4), for $u = 0.77$ and $C = 10^{-5}$. (a) spatio-temporal growth rate. (b) Real part of the complex frequency. (c) Imaginary part of the streamwise wavenumber. (d) Real part of the streamwise wavenumber. (e) Imaginary part of the spanwise wavenumber. (f) Real part of the spanwise wavenumber.

decreases moving away from the value of $(x/t = u, y/t = 0)$. The two regions interact in the region just upstream of the maximum spatio-temporal growth rate position (II). The real part of the complex frequency (figure 6.8(b)) presents the same structure of the spatio-temporal growth rate. In the region downstream of the initial impulse location, both the real and imaginary parts of the complex frequency are close to zero.

A complete characterization of the asymptotic behavior of the impulse response requires also the evaluation of the spatial asymptotic properties k_x and k_y, which are reported in figure 6.8(c-f). Downstream of the initial impulse location, all the spatial properties iso-values are approximately rays that propagate from the initial impulse position. Interestingly, the real part of the streamwise wavenumber is very small, i.e. $\mathrm{Re}(k_x) \sim 10^{-2}$. Moreover, at $y/t = 0$, $\mathrm{Re}(k_y) \simeq 1/\sqrt{2}$, while in the absence of deposition it was zero except in the singular point at the center of the wavepacket.

The same behavior is found in the case $C = 10^{-3}$ (reported in Appendix 6.9.3), but the front downstream of the initial impulse position is more curved. Moreover, the region in which the two patterns interact is displaced downstream.

The present analysis reveals that there are three regions in the spatio-temporal impulse

response. The region (I) is characterized by asymptotic properties whose distribution is very similar to the case in the absence of substrate variations, studied in Sec 6.3.2. In the region (III), streamwise structures dominate. Since in the region just downstream of the initial impulse location, the complex growth rate is close to zero, the pattern is almost steady. Moreover, the analysis of the spatial asymptotic properties reveals that streamwise aligned structures dominate, since $\mathrm{Re}(k_x) \sim 10^{-2}$ and $\mathrm{Re}(k_y) \sim 1/\sqrt{2}$. The other spatial asymptotic properties are almost constant for $y/x = \text{const}$ since the iso-values are rays that propagate from the initial impulse position. In region (II), the two regions (I) and (III) interact, and it is best observed in the fluid film response (figure 6.7), where the substrate presents non-negligible values of the thickness compared to the fluid film. In this region, due to the high values of the fluid film thickness, we observe a strong deposition and an increase in the substrate thickness.

We therefore identified two linear mechanisms that could lead to the emergence of draperies structures on the substrate. First, the advection of oscillating perturbations along the streamwise direction promotes the deposition of drapery-like structures rather than wave patterns on the substrate (*ripples*). This interpretation confirms the observation of slightly higher growth rates for spanwise perturbations in the two-dimensional dispersion relation of Bertagni and Camporeale (2017). This first mechanism strongly enhances the growth of draperies structures in the region just upstream of the maximum thickness, which is advected away with time. The second mechanism was highlighted thanks to the post-processing algorithm, which shows the presence of another region in which the perturbation grows, absent in the case without substrate variations of Section 6.3.2. The presence of the initial defect that grows without being advected, creates a quasi-steady region characterized by streamwise structures both in the fluid film and on the substrate. The second mechanism appears to be dominant in the regions in which the isotropic response has been advected away. In the following, we investigate the hydrodynamic origin of this second source of anisotropy.

6.6 Linear response in the presence of a steady defect without deposition process

6.6.1 Numerical response and large-time asymptotics

In this section, we provide an additional analytical insight to better understand the physical mechanisms underlying the response in the presence of the deposition process. We consider the linear response of the thin film (equation (6.8)) in the presence of a steady defect (i.e. $C = 0$) of the form:

$$\eta^0(x, y, t) = \exp[-x^2/2 - y^2/2], \tag{6.38}$$

together with the initial condition for the fluid thickness $\eta(x, y, 0) = 0$.

The wavepacket (figure 6.9), in the downstream part (I), is characterized by the isotropic

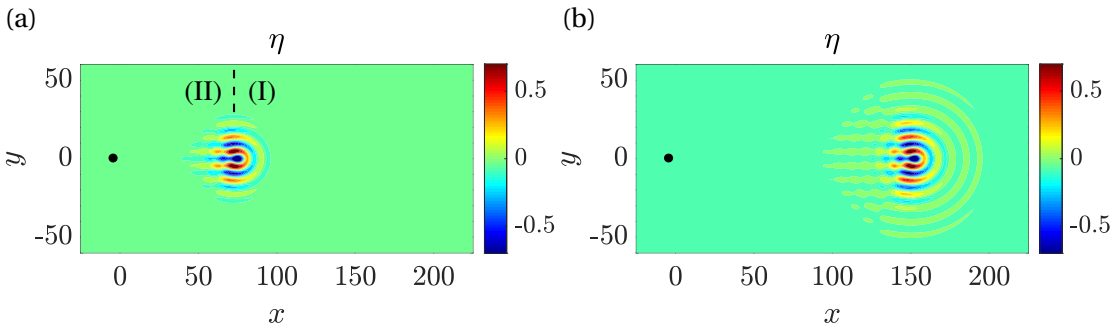

Figure 6.9: Linear fluid film response equation (6.8) (rescaled with the maximum value) in the presence of a steady defect (i.e. $C = 0$) located at $(x = 0, y = 0)$, for $u = 0.77$, (a) $t = 100$, (b) $t = 200$. The black dots denote the steady defect location.

structure typical of the temporal response (figure 6.3,6.7), as described in detail in Section 6.3.2. Nevertheless, in the upstream part (II) we observe streamwise structures more pronounced than in the case of the impulse response in presence of deposition (described in Section 6.3.2), since the initial condition differs from a steady defect as it is characterized by an impulse both in the fluid film and on the substrate.

The asymptotic properties (figure 6.10) resulting from the post-processing algorithm present a spatial structure analogous to the case in the presence of deposition reported in figure 6.8. In the region (III), downstream of the initial impulse location, the iso-values are rays that propagate from $(x/t, y/t) = (0, 0)$. Both real and imaginary parts of the complex frequency are zero in the region downstream of the steady defect, and the real part of the streamwise wavenumber is of order 10^{-2}.

The steady defect analysis confirms that the structure of the wavepacket is mainly driven by hydrodynamic effects. Moreover, the region downstream of the obstacle is steady because $\omega = 0$ and originates from the presence of the steady defect. Since the asymptotic properties are rays that propagate from the center, the properties of the steady pattern are constant at fixed y/x. This invariance suggests that the response can be evaluated in the context of a steady pattern asymptotic analysis.

6.6.2 The two-dimensional steady Green function

In this section, we analytically derive the Green function for a steady defect. The approach is based on the spatio-temporal analysis introduced in Section 6.3.2, but we focus on the growth in space of a steady wavepacket. We can thus make an analogy to the classical one-dimensional analysis (Van Saarloos, 2003): the (x, y) directions play the role of space and time.

Following Hayes et al. (2000), we introduce the total free surface elevation $\eta_t = \eta + \eta^0$. We seek

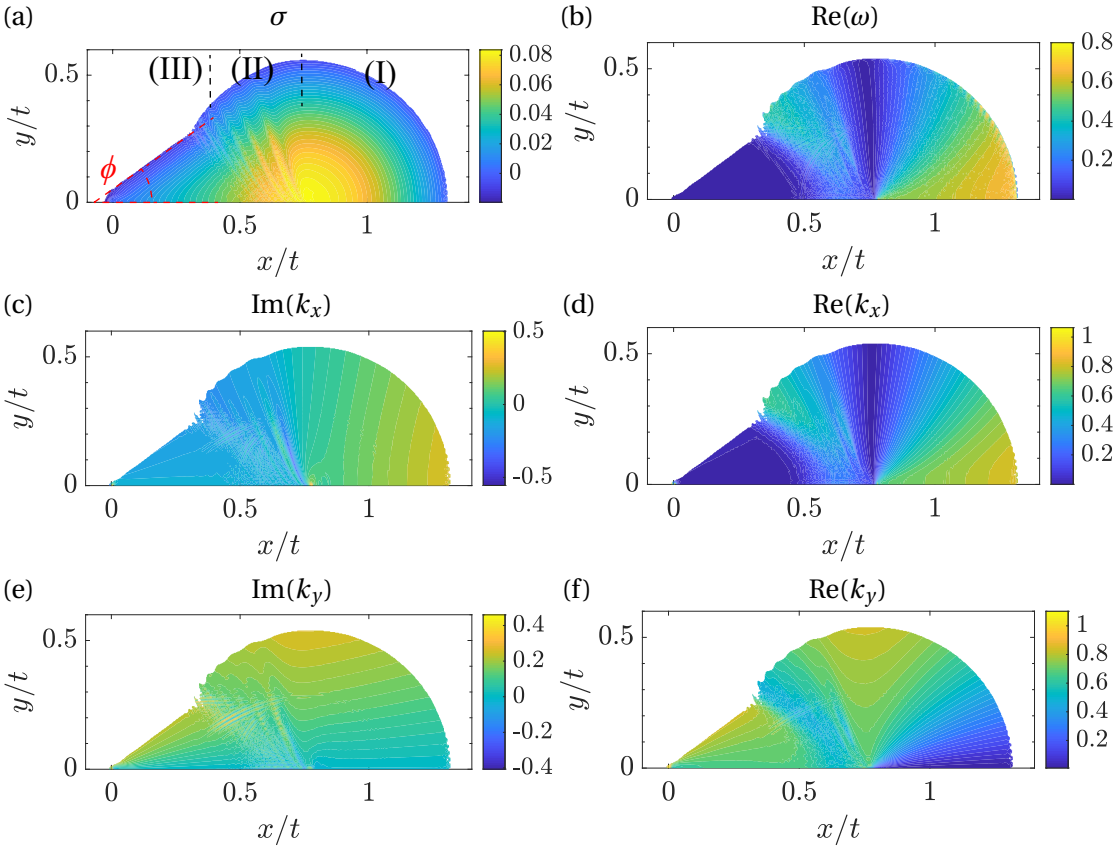

Figure 6.10: Long-time asymptotic properties from the post process algorithm (Section 6.4) of the two-dimensional linear response to steady defect in the absence of deposition, for $u = 0.77$. (a) spatio-temporal growth rate. (b) Real part of the complex frequency. (c) Imaginary part of the streamwise wavenumber. (d) Real part of the streamwise wavenumber. (e) Imaginary part of the spanwise wavenumber. (f) Real part of the spanwise wavenumber.

for the solution of the following problem:

$$u\partial_x \eta_t + \frac{1}{3}\left[\nabla^2(\eta_t) + \nabla^4(\eta_t)\right] = -u\partial_x \eta^0 = f(x,y). \tag{6.39}$$

The impulse is located in the position $y/x = 0$, i.e. the Green function $\tilde{g}_s(x,y)$ solves the steady problem:

$$u\partial_x \eta_t + \frac{1}{3}\left[\nabla^2(\eta_t) + \nabla^4(\eta_t)\right] = \delta(x)\delta(y). \tag{6.40}$$

The solution in the presence of a localized defect η_t is found using the property of the Green function, i.e. $\eta_t = \tilde{g}_s * f$, where $*$ is the convolution operator. Since we consider the response to a steady localized defect $f(x,y) = \partial_x[\delta(x)\delta(y)]$. Using the properties of the Delta function and integrating by parts, we obtain that the solution reads:

$$\eta_t = u\partial_x \tilde{g}_s(x,y) \tag{6.41}$$

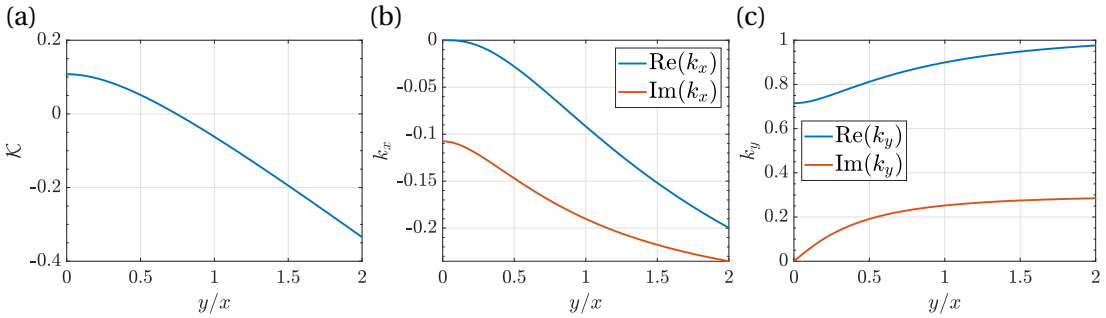

Figure 6.11: Analytical asymptotic properties for the steady two-dimensional Green function. (a) Spatio-spatial growth rate as a function of y/x. (b) Streamwise wavenumber and (c) spanwise wavenumber resulting from the analytical steady response, as functions of y/x.

The solution $\tilde{g}_s$ is found using the same approach of the spatio-temporal stability analysis, where now we have the direction $x \to \infty$. The Green function for steady defect can be expressed as:

$$\tilde{g}_s(x,y) \sim \hat{g}\exp(k_x x + k_y y)/\sqrt{x} \sim \hat{g}\exp(k'_x x)/\sqrt{x}, \tag{6.42}$$

where $k'_x = k_x + k_y(y/x)$. The solution reads:

$$\eta_t = u\partial_x \tilde{g}_s(x,y) \sim \mathrm{i}uk_x \exp[\mathrm{i}(k_x x + k_y y)]/\sqrt{x}, \tag{6.43}$$

i.e. the asymptotic properties of the total elevation η_t wavepacket are the same as those of the Green function for $x \to \infty$.

The spatio-spatial analysis is implemented similarly to the spatio-temporal stability analysis outlined in Section 6.3.2. We look for the steady (i.e. $\omega = 0$) dispersion relation (equation (6.10)) saddle points of $k'_x = k_x + k_y(y/x)$ in the complex k_y plane, varying y/x. The resulting asymptotic properties define the response for each y/x. The method is numerically implemented in MATLAB; we solve for the saddle point using the built-in function *fsolve*. The initial guess is given by the maximum in the steady dispersion relation equation (6.10) for $y/x = 0$, which is a contributing saddle point according to Barlow et al. (2017).

In figure 6.11 we report the spatial asymptotic properties as functions of y/x. The spatio-spatial growth rate $\mathcal{K} = -\mathrm{Im}(k'_x)$ (figure 6.11(a)) is initially positive and decreases with y/x. Beyond the critical value of $y/x = 0.74$ it becomes negative. Both the real and imaginary parts of the streamwise wavenumber (figure 6.11(b)) are negative and decrease with y/x, in opposition to the real and imaginary parts of the spanwise wavenumber (figure 6.11(c)), which are positive and increase with y/x.

The unstable region in the (x, y) plane is located where the spatio-spatial growth rate is positive. At low values of y/x, i.e. close to $y = 0$, we observe a positive spatio-spatial growth rate, i.e. perturbations are growing (remember that one writes $\eta_t \sim \exp[\mathrm{i}(k_x x + k_y y)]$). When $\mathcal{K} = 0$ we define the value of y/x beyond which perturbations are damped, that is $y/x = 0.74$. This value

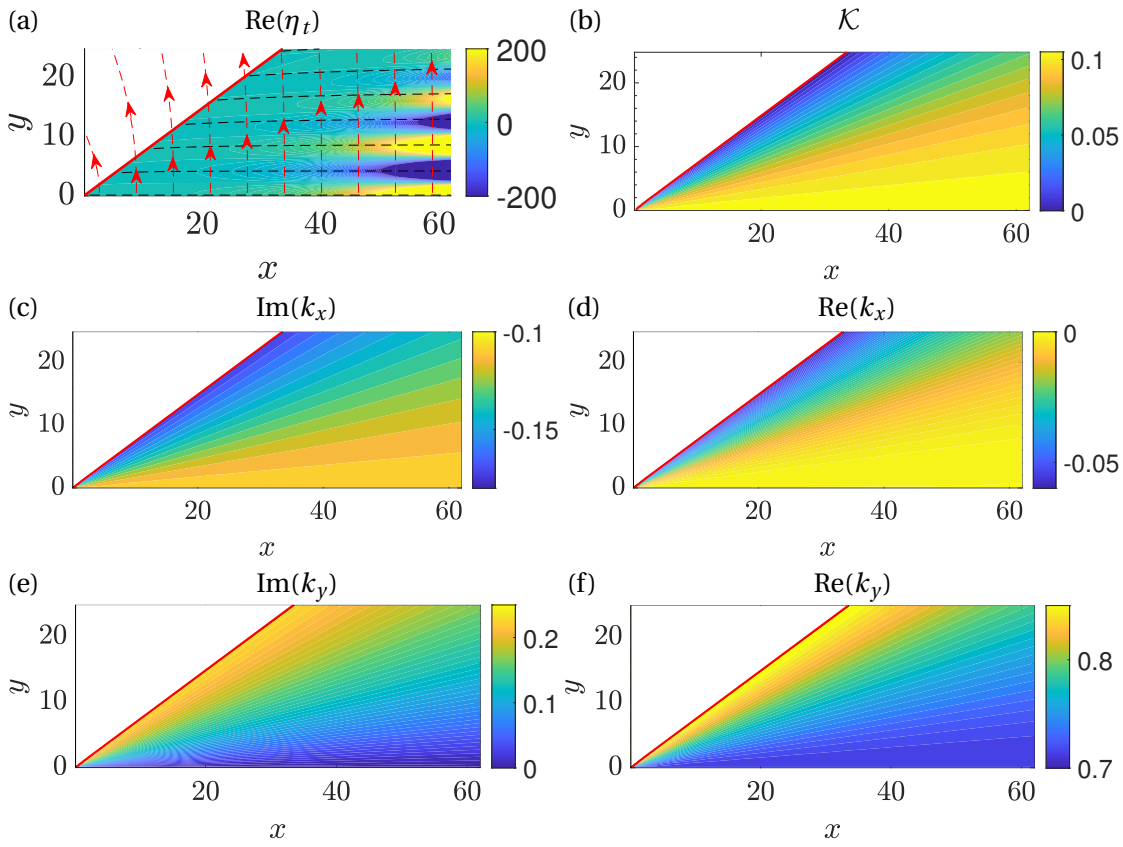

Figure 6.12: Results of the spatio-spatial analysis in the (x, y) plane. (a) Real part of the total free surface elevation η_t obtained from the asymptotic properties. The red and black dashed line denote respectively the streamlines of the wavevector $\mathbf{k} = (\mathrm{Re}(k_x), \mathrm{Re}(k_y))$ and the wavefronts. (b) Spatio-spatial growth rate, (c) imaginary and (d) real parts of the streamwise wavenumber, (e) imaginary and (f) real parts of the spanwise wavenumber. The red line denotes the value of y/x for which $\mathcal{K} = 0$.

of y/x defines a ray in the (x, y) plane, that corresponds to an angle with respect to the x axis of $\phi \simeq 36.5°$, in agreement with the front observed in figures 6.8 and 6.10.

These results can be easily visualized in figure 6.12, in which we report the real part of the total free surface elevation and the asymptotic properties in the (x, y) plane, in a similar fashion to the previous plots for the spatio-temporal response. The total free surface elevation is characterized by predominant streamwise structures. The steady Green function is growing moving away from the obstacle, in strong contrast to the case of the flow over an incline, in which it is decaying (Decré and Baret, 2003; Kalliadasis et al., 2000; Hayes et al., 2000). The streamlines of the wavevector $\mathbf{k} = (\mathrm{Re}(k_x), \mathrm{Re}(k_y))$ (red dashed lines in figure 6.12(a)) are parallel to the y direction at $y = 0$ and slightly bend upstream with y. This slight variation is related to the negative value of the real part of the streamwise wavenumber. The bending of the wavevector streamlines implies that the wavefronts (black dashed lines in figure 6.12(a)), orthogonal to the wavevector directions, tend to slightly diverge from the center going downstream.

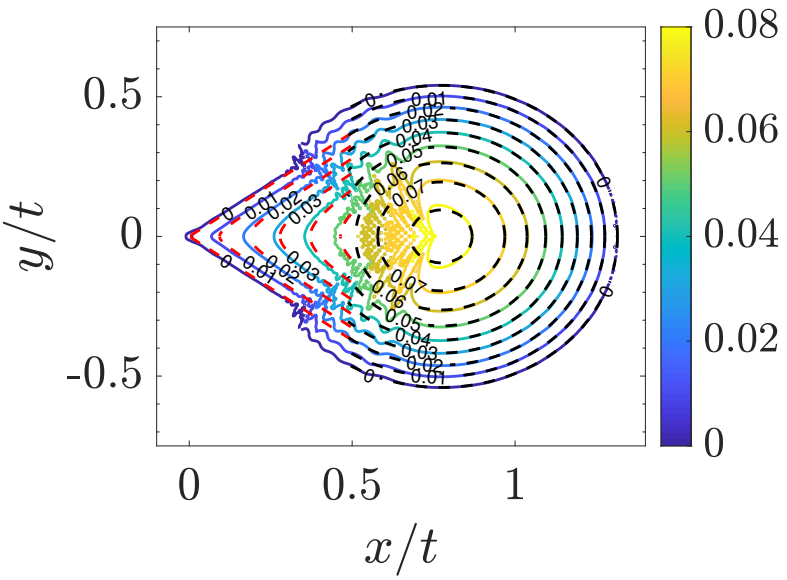

Figure 6.13: Linear response to a steady defect: spatio-temporal growth rate from the post process algorithm of Section 6.4 (colored iso-contours) and from the saddle points approach of Section 6.3.2 (black iso-contours) and spatio-spatial growth rate (changed of sign) from the analytical steady approach of Section 6.6.2 (red iso-contours).

We now consider the spatio-temporal response observed in Section 6.6.1. In the steady regions, the spatio-temporal growth rate (Section 6.3.2) $\sigma = \mathrm{Im}(\omega) - \mathrm{Im}(k_x)x/t - \mathrm{Im}(k_y)y/t = \mathrm{Im}(\omega) + \mathcal{K}x/t$ coincides with the spatio-spatial growth rate rescaled with x/t, i.e. $\sigma = \mathcal{K}x/t$, since $\omega = 0$. In figure 6.13 we show the spatio-temporal growth rate obtained from the numerical simulation compared with analytical values of σ and $\mathcal{K}x/t$ respectively obtained from the spatio-temporal (Section 6.3.2) and spatio-spatial approaches, for $t = 350$. The comparison shows a good agreement between spatio-spatial theory and numerical post-processing in the region downstream of the steady defect. Moreover, the numerical spatio-temporal response well agrees with the spatio-temporal results, in the region downstream of $x/t = u$.

We report in figure 6.14 a comparison of the spatial asymptotic properties, at $y/t = 0$. Also in this case, the results are in good agreement; the values of $\mathrm{Re}(k_y)$ are converging to the analytic values as x increases. The small difference in the values can be imputed to the fact that we are considering not large enough values of x close to the obstacle. The saddle point analysis is rigorously valid for $x \to \infty$, and in this case the steady response is present in the range $0 < x < 175$ for the considered time ($t = 350$), which explains the small difference.

Our analysis shows that the temporal response to a steady defect is characterized by the presence of the steady and unsteady contributions which interact. The steady contribution, which originates from the presence of the steady defect, is not advected away and spreads in the domain as the streamwise coordinate increases. The presence of an initial perturbation gives rise also to a temporal response that is advected away. If enough time is waited, eventually the temporal response is no more present in the field and only the steady response survives,

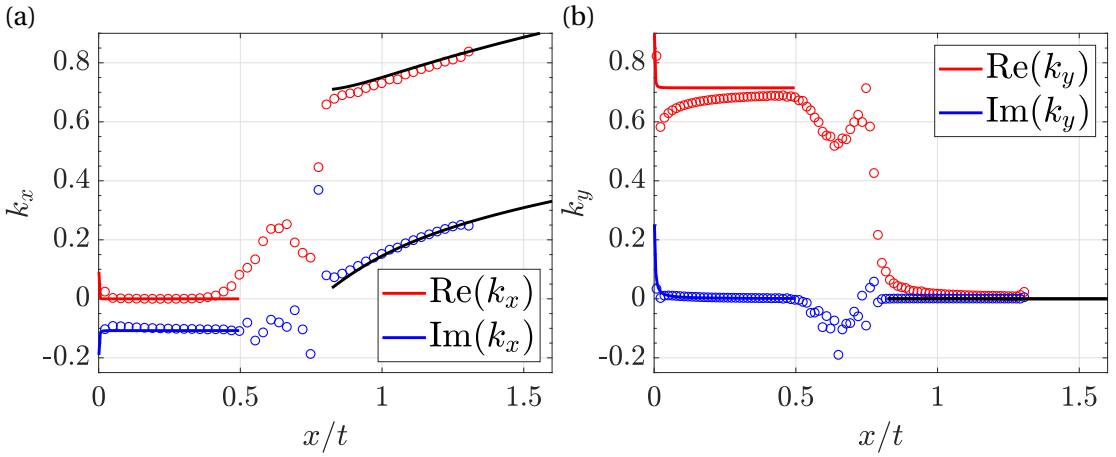

Figure 6.14: Comparison of streamwise (a) and spanwise (b) wavenumbers obtained from the post process algorithm of Section 6.4 (dots), the analytical approach (colored solid lines) for the response to a steady defect of Section 6.6.2, and the analytical results of the spatio-temporal analysis of Section 6.3.2 (black solid lines), on the ray $y/t = 0$.

which is characterized by streamwise aligned structures.

We then conclude that the emergence of streamwise structures both on the fluid film and on the substrate in the region just downstream of the initial impulse location is related to the presence of defects on the substrate and it has a linear hydrodynamic origin. This mechanism is predominant in the regions in which the temporal response has been advected away. In the context of morphogenesis of draperies, we thus argue that the response in the presence of the deposition process contains as fundamental ingredients two hydrodynamic effects, one related to the isotropic unsteady response in the absence of substrate variations, and the other one related to the steady response in the presence of a localized defect in the substrate. The deposition process couples these two different hydrodynamic mechanisms, giving rise to predominant draperies structures on the substrate.

6.7 Non-linear response

The linear response in the presence of the deposition process is compared to non-linear simulations of equations (6.3) and (6.6), for the case $C = 10^{-3}$. The system of equations (6.3), (6.6) is subjected to the initial conditions

$$h = 1 + \mathrm{S}\exp[-x^2/2 - y^2/2], \tag{6.44a}$$

$$h^0 = \mathrm{S}\exp[-x^2/2 - y^2/2], \tag{6.44b}$$

where $\mathrm{S} = 10^{-2}$.

The non-linear simulations are performed using the finite-element software COMSOL Mul-

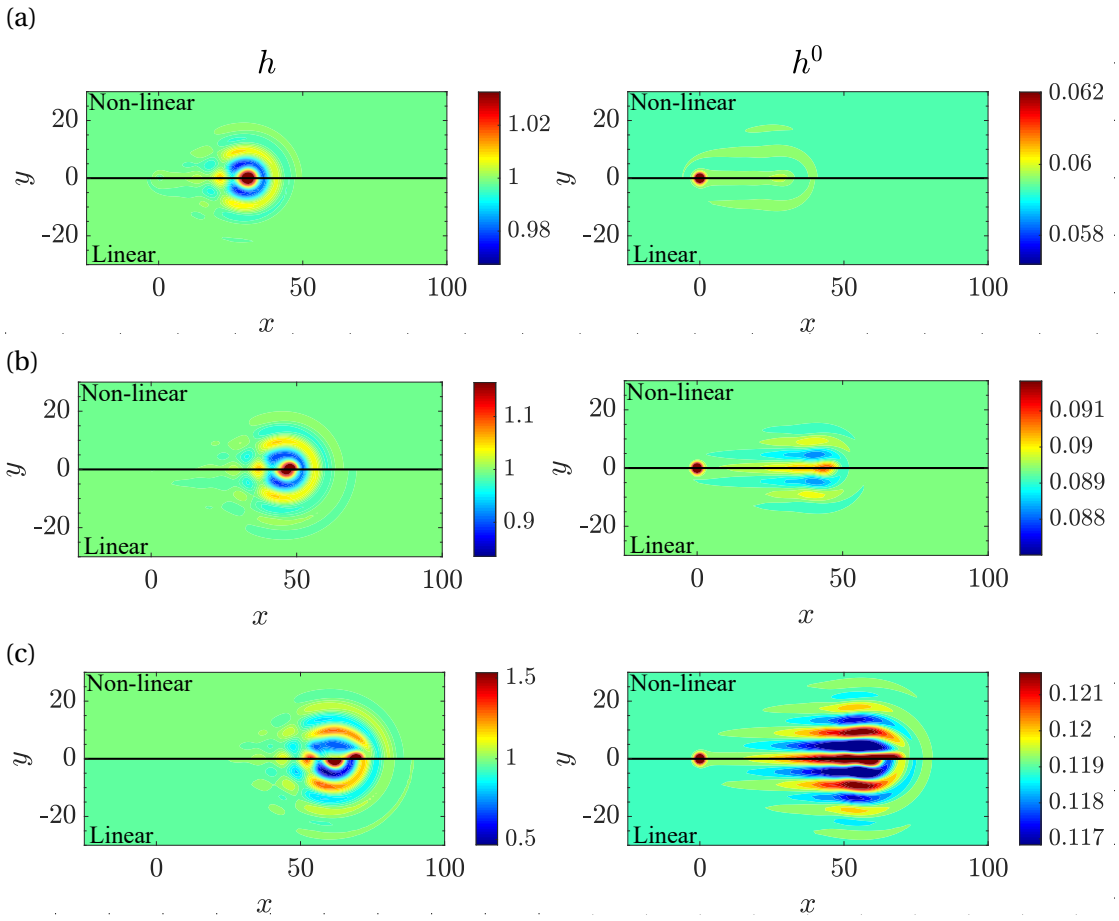

Figure 6.15: Non-linear impulse response of equations (6.3) and (6.6) for $u = 0.77$, $h_N/\ell_c^* = 1$, and $C = 10^{-3}$, at (a) $t = 40$, (b) $t = 60$, (c) $t = 80$. On the left: fluid thickness response. On the right: substrate thickness response. The colobars are centered around the values $h = 1$ and $h^0 = \check{C}t$.

tiphysics. The flow equations are solved in a rectangular domain with periodic boundary conditions, for the variables (h, κ, h^0) using third-order finite elements; the time-marching is obtained by a second-order backward differentiation formula. We consider a domain of size $L_x = 310$ and $L_y = 180$ with periodic boundary conditions and largest mesh element of characteristic size ℓ_c^* in the region, leading to a mesh of approximately 56000 elements. A preliminary analysis shows that the numerical convergence is already achieved with this characteristic size of the elements.

In figure 6.15 we show the results at three different times, for the fluid and substrate thickness. As a comparison, on the bottom, the results for $h = 1 + S\eta$ of the linear simulation of Section 6.5.2 are reported. The non-linear patterns are very similar to the corresponding linear ones, even if some differences can be highlighted. As time increases, the fluid film increases and the perturbation spreads in concentric circles from the maximum thickness location. Streamwise structures are selected in the downstream part of the response close to the maximum value

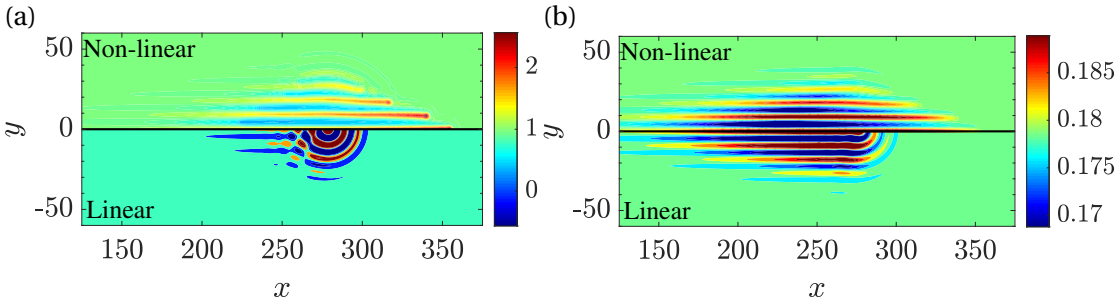

Figure 6.16: Non-linear impulse response of equations (6.3) and (6.6) for $u = 2.31$, $h_N/\ell_c^* = 1$, and $C = 10^{-3}$, at $t = 120$. (a) fluid thickness response. (b) substrate thickness response. The colobars are centered around the values $h = 1$ and $h^0 = \check{C}t$.

position, while in the linear simulation the pattern is isotropic in this region. The dominance of streamwise structures in the downstream part is enhanced as u increases (figure 6.16).

The upstream part shows the same intricate pattern observed in the linear simulations. The substrate thickness presents a defect at the origin, which slowly grows in time. Downstream of the defect at the origin, growing streamwise structures on the substrate emerge and propagate in the domain, with a front well described by a constant angle.

Under the light of the results of the previous linear analyses, we are able now to distinguish the different physical mechanisms underlying the selection of streamwise structures. The selection of streamwise structures both in the fluid film and on the substrate in the downstream part of the initial impulse location is due to the steady defect mechanism of Section 6.6.2, while in the region upstream the maximum thickness draperies are purely selected by the deposition law. Besides, rivulets emerge also in the downstream part of the wavepacket. This selection is absent in the linearized dynamics and is due to non-linear effects. The downstream part of the wavepacket is progressively invaded by rivulets with time, thus enhancing the deposition of streamwise structures on the substrate. Thanks to the linear analyses, we conclude that the linear effects are predominant in the upstream part of the wavepacket such that, after all, the selection of streamwise structures occurs for all the values of the linear advection velocity. The deposition of streamwise structures in the downstream part is largely dictated by the non-linear selection of rivulets in the fluid film, whose dominance is enhanced with u.

In figure 6.16, we observe that the visible perturbation in the non-linear simulation spreads in a larger region compared to the linear simulation. This implies that the linear front given by the iso-level $\sigma = 0$ changes in the non-linear regime. We thus focus on the structure of the non-linear front with time. The analysis performed with the post-process algorithm could be in principle applied to the results of the non-linear simulations. However, non-linearities generate large wavelengths, altering the band structure of the spectrum of the perturbation observed in the linear simulations. As a consequence, it is no more possible to recover the envelope of the response (Melville, 1983; Delbende and Chomaz, 1998).

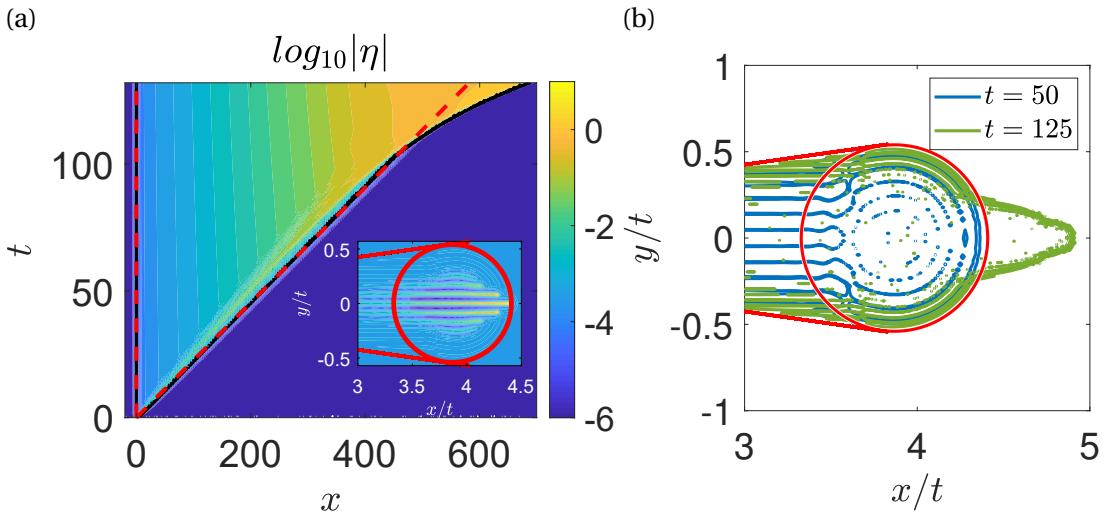

Figure 6.17: (a) Iso-levels of $|\eta|$ as a function of x and t, for $y = 0$. The red dashed lines denote the linear front, while the black line the iso-level that well approximates the front at small times. In the inset: thickness profile for $t = 108$. (b) Iso-level of $|\eta|$ approximating the non-linear front, for $t = 50$ (blue line) and $t = 125$ (green line). The red circle denotes the linear front given by the response in the absence of substrate variations, and the red lines the front given by the steady defect analysis. $u = 3.85$, $h_N/\ell_c^* = 1$, and $C = 10^{-3}$.

Despite this, following Delbende and Chomaz (1998), it is possible to obtain information about the front by following the iso-levels of the absolute value of the response $|\eta|$. We consider the centerline profile (i.e. $y/t = 0$) and we extend the linear fronts (red dashed lines) in the non-linear regime by following the corresponding iso-level of $|\eta|$ (figure 6.17(a)). We assume that this iso-level is a good approximation of the non-linear front. The non-linear front follows the linear one until $t \approx 108$, beyond which it bends and the perturbation spreads in a larger region. In the inset, we report the corresponding thickness profile at $t = 108$. The maximum thickness location is very close to the linear front. The variation of the iso-level of $|\eta|$ well approximating the non-linear front is reported in figure 6.17(b) as a function of $(x/t, y/t)$, for $t = 50$ and $t = 125$. The iso-level well approximates the linear prediction, and at $t = 125$ we observe that the non-linear front has spread downstream in a larger region.

The analysis of the non-linear front shows that, at large times, the perturbation spreads in a larger region than the one predicted by the linear theory. While in the linear regime the advection of perturbation is given by u, in the non-linear regime it is equal to uh^2 (Babchin et al., 1983). As the perturbation grows, regions with thickness $h > 1$ travel faster than the flat film and vice versa. Thus, for large enough times, the linear front is eventually reached (downstream for $h > 1$, upstream for $h < 1$). Our case corresponds to (c,d) in figure 3 of Delbende and Chomaz (1998). For the sake of completeness, we report in Appendix 6.9.4 the results of the non-linear front in the absence of substrate variations. In conclusion, the non-linearities tend to favor streamwise structures and to deform the front in which the perturbation spreads due to the differences in advection.

(a) (b)

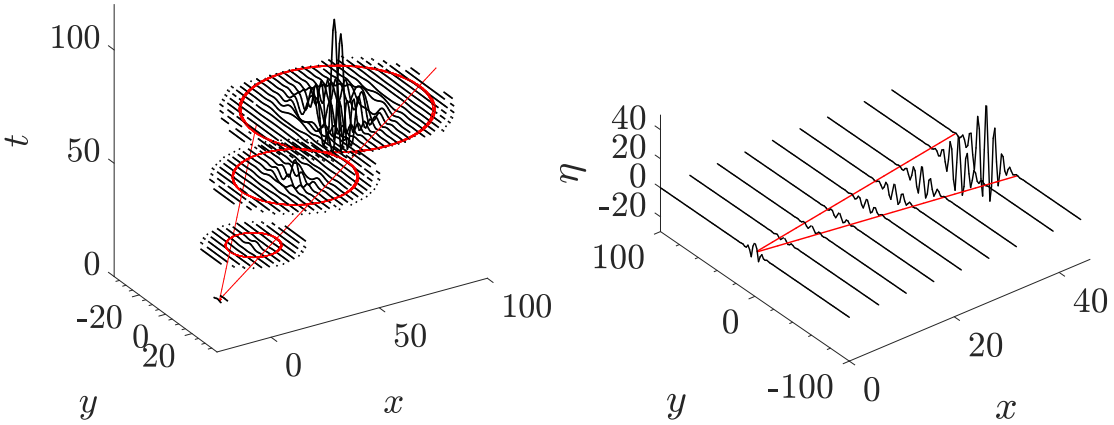

Figure 6.18: Analytical (a) spatio-temporal response to a localized initial perturbation (Section 6.3.2) and (b) spatial response to a localized steady defect (Section 6.6.2), in the absence of the deposition process. The red lines denote the limits in which the perturbation spreads.

6.8 Conclusions and discussion

In this work, we studied the pattern formation of a thin film flowing under an inclined plane, in the presence of material deposition on the substrate, reminiscent of the karst structure formation in limestone caves. We tackled the problem theoretically and numerically studying the linearized dynamics when substrate variations are considered.

The spatio-temporal analysis in the presence of the deposition process was studied in the context of numerical simulations and a novel approach to retrieve the wavepacket properties. The numerical study of the impulse response was generalized to the two-dimensional case with the introduction of the monogenic signal, the two-dimensional analytic continuation of a real signal, based on the Riesz transform. The monogenic signal allows us to reconstruct the amplitude and the phase of the numerical response, and then the asymptotic properties of the wavepacket. This approach, which constitutes the generalization to two propagation directions of the approach introduced in Brancher and Chomaz (1997) and Delbende et al. (1998), can be generally used in flows where the dispersion is not known analytically or when the saddle-point tracking becomes too challenging. Besides, this procedure allows one to proceed to an a posteriori description of the response, without the necessity to a priori define the unstable branches of the dispersion relation, making it suitable for the analysis of complex fluid responses. The numerical procedure aims at deriving the asymptotic behavior for $t \to \infty$ using numerical simulations at finite times, and assumes that the amplitude and the phase of the signal subject to the Riesz transform can be separated (i.e. a separation of scales between the variations of the envelope and the oscillations subsists). We verified the validity of the assumptions in the present case by a comparison with the analytical solution in the absence of substrate variations.

We therefore focused on the study of the linear impulse response in the presence of a deposition law. The temporal analysis of the dispersion relation showed only a slight anisotropy which promotes streamwise aligned structures. Motivated by this, we therefore studied the linear impulse response exploiting the post-processing algorithm. We identified (I) an isotropic region that is advected away (figure 6.18(a)) and (III) a quasi-steady region propagating downstream (figure 6.18(b)) with a front defined by an approximately constant angle, related to the presence of a growing substrate defect at the initial impulse location.

The analysis of the substrate thickness showed that the deposition law selects predominant streamwise structures as the wavepacket is advected away, in (II) the upstream part of the traveling wavepacket. Physically, we related this phenomenon to the fact that, in opposition to rivulets, waves are traveling structures. Perturbations are oscillating at fixed locations, thus having a much smaller effect on the substrate topography.

We thus analyzed the response to a steady defect, for the pure hydrodynamic problem. The region just downstream of the steady obstacle coincides with the quasi-steady region (III) identified in the deposition case, and it is in good agreement with the analytical Green function for a steady defect (figure 6.18(b)). The emergent pattern is characterized by streamwise structures both in the fluid film and on the substrate thickness.

In the non-linear simulations, we exploited the results of the linear analyses and we distinguished the selection mechanisms due to the substrate variations from the non-linear mechanism of rivulets selection in the absence of substrate variations. While in the first case the dominance of streamwise structures is independent of the linear advection velocity, the latter plays a crucial role in the non-linear selection mechanism. The latter promotes the selection of rivulets (in the fluid film) in the downstream part of the traveling wavepacket (I), thus enhancing the deposition of draperies structures. We analyzed the evolution of the fronts between which the perturbation spreads, concluding that the emergence of rivulets modifies the downstream front by nonlinearly increasing the leading edge front velocity.

We conclude that the different selection mechanisms are dominant in different regions of the response. The deposition process couples the hydrodynamic mechanisms of the unsteady response in the absence of substrate variations and the steady response in the presence of localized substrate variations. In common natural environments, the relative importance of the mechanisms may depend on the fluid film and substrate conditions, but always giving rise to predominant draperies structures. The immense diversity of limestone patterns observed in nature may result from secondary instabilities of these predominantly selected primary streamwise-oriented structures.

6.9 Appendix

6.9.1 Numerical method and validation

In this section, we introduce the numerical method to solve equations (6.8) in a rectangular domain, with periodic boundary conditions. We consider the Fourier transforms of the functions (η, η^0):

$$\left[\hat{\eta}, \hat{\eta}^0\right]^T = \iint \left[\eta, \eta^0\right]^T e^{-\mathrm{i}\mathbf{k}\cdot\mathbf{x}} \mathrm{d}\mathbf{x}, \tag{6.45}$$

where $\mathbf{k} = (k_x, k_y)$, are respectively the streamwise and spanwise wavenumbers. Applying the Fourier transform to equation (6.8), the following complex ODE's system is obtained:

$$\frac{d\hat{\eta}}{\mathrm{d}t} = \hat{\eta}(-\mathrm{i}uk_x) + (\hat{\eta} + \hat{\eta}^0)\frac{1}{3}\left(\chi k^2 - k^4\right), \tag{6.46}$$

$$\frac{d\hat{\eta}^0}{\mathrm{d}t} = \check{C}\hat{\eta}, \tag{6.47}$$

where $k = |\mathbf{k}|$. Introducing the vector $\hat{\boldsymbol{\eta}} = [\hat{\eta}, \hat{\eta}^0]^T$, the system of equations reads:

$$\frac{d\hat{\boldsymbol{\eta}}}{\mathrm{d}t} = \begin{bmatrix} \frac{1}{3}\left(\chi k^2 - k^4\right) - \mathrm{i}uk_x & \frac{1}{3}\left(\chi k^2 - k^4\right) \\ \check{C} & 0 \end{bmatrix} \hat{\boldsymbol{\eta}} = A\hat{\boldsymbol{\eta}} \tag{6.48}$$

With the decomposition $\hat{\boldsymbol{\eta}} = \hat{\boldsymbol{\eta}}_r + \mathrm{i}\hat{\boldsymbol{\eta}}_i$, the final system of real ODE's reads:

$$\frac{d\hat{\boldsymbol{y}}}{\mathrm{d}t} = \begin{bmatrix} \frac{d\hat{\boldsymbol{\eta}}_r}{\mathrm{d}t} \\ \frac{d\hat{\boldsymbol{\eta}}_i}{\mathrm{d}t} \end{bmatrix} = \begin{bmatrix} A_r & -A_i \\ A_i & A_r \end{bmatrix} \begin{bmatrix} \hat{\boldsymbol{\eta}}_r \\ \hat{\boldsymbol{\eta}}_i \end{bmatrix} = B\hat{\boldsymbol{y}} \tag{6.49}$$

The solution of this problem can be written as:

$$\hat{\boldsymbol{y}} = \mathrm{expm}[B\,t]\,\hat{\boldsymbol{y}}(0), \tag{6.50}$$

where expm stands for the exponential matrix.

The numerical procedure is implemented in MATLAB. A rectangular domain of size 1000×1000 is considered, with a number of collocation points $N_x = N_y = 1001$. A convergence analysis on (N_x, N_y) has been performed, concluding that convergence is already achieved for 1001 collocation points. No significant changes have been observed increasing the domain size. The initial condition is transformed in the two-dimensional Fourier space using the built-in function for the Fast Fourier Transform *fft2*. Subsequently, the linear system of ODE's is solved using the built-in function for the exponential matrix, and the solution in the space domain is obtained through the Inverse Fast Fourier Transform *ifft2*.

The numerical code is validated against a benchmark case present in the literature for the

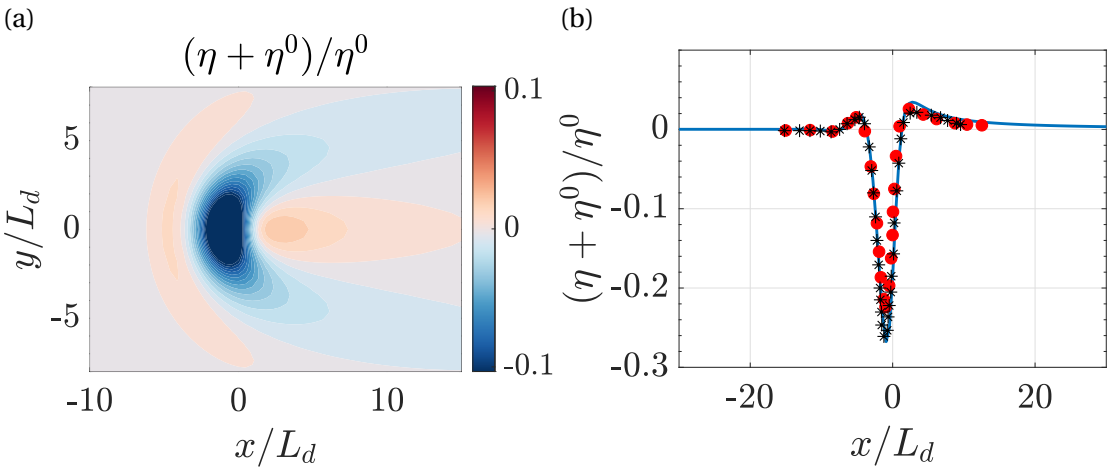

Figure 6.19: Two-dimensional linear response in the presence of a localized steady defect for the flow over an inclined planar substrate, at $y = 0$ as a function of the streamwise coordinate, for $u = 16.75$. Results are rescaled using the non-dimensionalization reported in Decré and Baret (2003) ($L_d = (\gamma h_N/3\rho g cos(\theta))^{1/3}$). (a) Response in the (x, y) plane. (b) Comparison between the experimental (red dots) and numerical (black stars) results of Decré and Baret (2003) and the numerical solution (blue line).

experimental response in the presence of a steady defect for a thin film flowing over an inclined plane, i.e. $\chi = -1$ and $C = 0$. The initial condition is given by $\eta(x, y, 0) = 0$, and $\eta^0(x, y, 0) = -\exp[-(x^2 + y^2)/2\varsigma^2]$, with $\varsigma = 0.17$, which gives the same integral value of the experimental step-down defect used in Decré and Baret (2003) and does not vary with time. In the inertialess case and absence of defects, the flow over an inclined plane is stable and the solution is a film of constant thickness (Kalliadasis et al., 2011). The presence of a localized steady defect creates a region close to the depression characterized by a variation of the free surface elevation $\eta+\eta^0$ (see figure 6.19(a)). In the region just upstream of the depression, there is a small increase in the free surface elevation, followed by a strong decrease. Downstream, there is an overshoot greater than the initial thickness followed by a recovery of the flat film conditions. In figure 6.19(b) we show a comparison of the results of our model with the experimental and theoretical results of Decré and Baret (2003), for the free surface elevation at $y = 0$. Results are rescaled using their non-dimensionalization. The comparison shows a good agreement, thus validating the numerical procedure.

6.9.2 Evaluation of the imaginary part of the spatial wavenumbers from the spatio-temporal growth rate

In this Appendix, we demonstrate equation (6.27,6.28) by generalizing to the two-dimensional case the approach outlined in Delbende et al. (1998). We consider:

$$\omega''\left(v_x, v_y\right) = \omega - k_x v_x - k_y v_y. \tag{6.51}$$

We derive equation (6.51) with respect to the group velocity v_x along the x direction:

$$\frac{\partial \omega''}{\partial v_x} = \frac{\partial \omega}{\partial v_x} - \frac{\partial k_x}{\partial v_x} v_x - k_x - \frac{\partial k_y}{\partial v_x} v_y. \tag{6.52}$$

Since $\omega = \omega(k_x, k_y)$, we evaluate the derivative as follows:

$$\frac{\partial [\omega(k_x, k_y)]}{\partial v_x} = \underbrace{\frac{\partial \omega}{\partial k_x}}_{v_x} \frac{\partial k_x}{\partial v_x} + \underbrace{\frac{\partial \omega}{\partial k_y}}_{v_y} \frac{\partial k_y}{\partial v_x}, \tag{6.53}$$

being v_x and v_y real (Delbende et al., 1998). Substituting in equation (6.52), the imaginary part of the streamwise wavenumber is obtained:

$$\mathrm{Im}\,(k_x) = -\frac{\partial \sigma}{\partial v_x}. \tag{6.54}$$

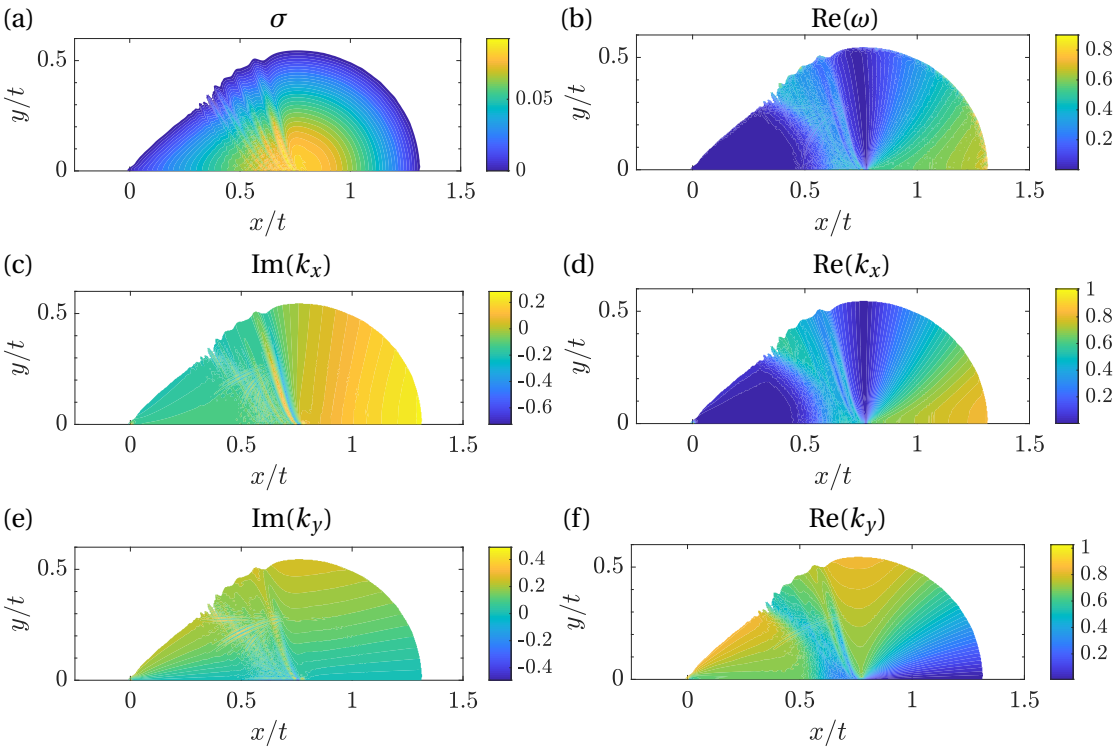

Figure 6.20: Asymptotic properties from the post process algorithm (Section 6.4), for $u = 0.77$ and $C = 10^{-3}$. (a) spatio-temporal growth rate. (b) Real part of the complex frequency. (c) Imaginary part of the streamwise wavenumber. (d) Real part of the streamwise wavenumber. (e) Imaginary part of the spanwise wavenumber. (f) Real part of the spanwise wavenumber.

Deriving ω'' with respect to v_y and following the same procedure, $\mathrm{Im}(k_y)$ reads:

$$\mathrm{Im}\left(k_y\right) = -\frac{\partial \sigma}{\partial v_y}. \tag{6.55}$$

6.9.3 Results of the post-processing algorithm for $C = 10^{-3}$

In this section, for the sake of completeness, we report the results of the post-processing algorithm of Section 6.4 applied for the case in the presence of the deposition process (Section 6.5.3), for $C = 10^{-3}$. The results are similar to those observed in the case $C = 10^{-5}$ (figure 6.8), with a front downstream of the initial position more curved and the region where the two contributions (quasi-steady and spatio-temporal) interact displaced downstream.

6.9.4 Non-linear front in the absence of substrate variations

In this Section, we report the results of the evaluation of the non-linear front for the case in the absence of substrate variations, for $u = 3.85$. The results show a deformation of the front similar to figure 6.17, without the quasi-steady part propagating downstream.

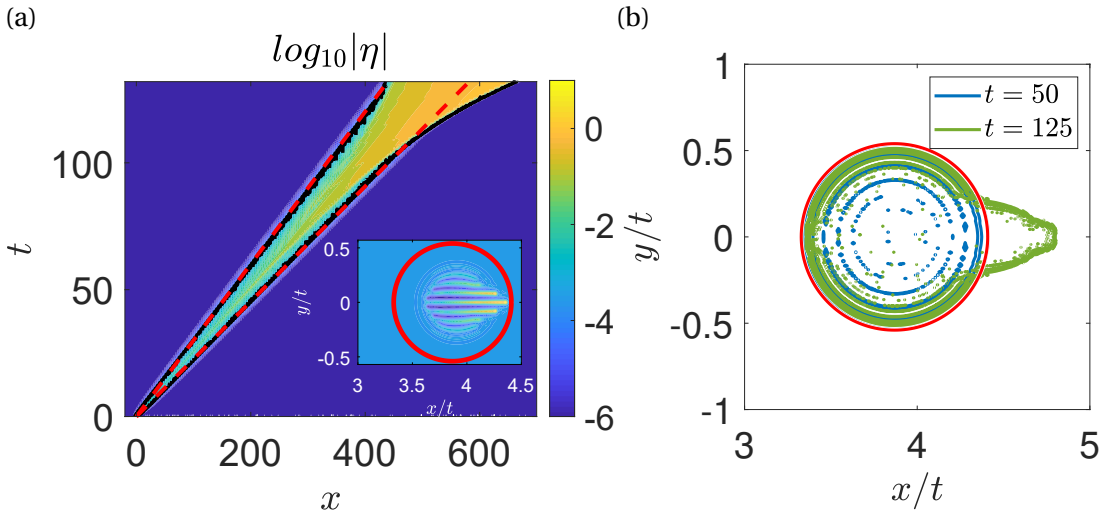

Figure 6.21: $u = 3.85$ and $h_N/\ell_c^* = 1$, no substrate variations. (a) Iso-levels of $|\eta|$ as a function of x and t, for $y = 0$. The read dashed lines denote the linear front, while the black line the iso-level that well approximates the front at small times. In the inset: thickness profile for $t = 108$. (b) Iso-level of $|\eta|$ approximating the non-linear front, for $t = 50$ (blue line) and $t = 125$ (green line). The red line denotes the linear front in absence of substrate variations.

7 Prediction of Self-Assembled Dewetted Nanostructures for Photonics Applications via a Continuum-Mechanics Framework

Remark This chapter is largely inspired by the publication of the same name

L. Martin-Monier[1†], P. G. Ledda[2†], P.L. Pivetau[1], F. Gallaire[2], F. Sorin[1]
[1]Laboratory of Photonic Materials and Fiber Devices , École Polytechnique Fédérale de Lausanne, Lausanne, CH-1015, Switzerland
[2]Laboratory of Fluid Mechanics and Instabilities, École Polytechnique Fédérale de Lausanne, Lausanne, CH-1015, Switzerland
[†] These authors equally contributed to this work

Physical Review Applied **16**, 034025 (2021)

Author contributions P.G.L. developed the model and performed the numerical simulations for the fluid dynamics part, and compared the results with the experiments of L. M-M. P.G.L. wrote the manuscript together with L. M-M, with input from the coauthors.

When a liquid film lies on a nonwettable substrate, the configuration is unstable, and the film spontaneously ruptures to form droplets. This phenomenon, known as dewetting, commonly leads to undesirable morphological changes. Nevertheless, recent works combining spontaneous dewetting triggered by thermal annealing and topographic pattern-directed dewetting demonstrated the possibility to harness dewetting with a degree of precision on par with that of advanced lithographic processes for high-performance nanophotonic applications. Since resonant behavior is highly sensitive to geometrical changes, predicting quantitatively dewetting dynamics is of high interest. We develop a continuum model that predicts the evolution of a thin film on a patterned substrate, from the initial reflow to the nucleation and growth of holes. We provide an operative framework based on macroscopic measurements to model the intermolecular interactions at the origin of the dewetting process, involving length scales that span from sub-nanometer to micrometer. A comparison between experimental and simulated results shows that the model can accurately predict the final distributions, thereby offering predictive tools to tailor the optical response of dewetted nanostructures.

7.1 Introduction

We refer to Section 1.1 for an overview of the dewetting process together with industrial applications, and to Section 1.3.3.2 for a general introduction about dewetting patterns and their stability.

The harnessing of dewetting as a self-assembly process of ordered structures is a relevant topic in nanophotonics, where changes in feature size to as little as 10 nm can strongly impact the resonant behavior and the resulting optical properties. Recent works have also highlighted the possibility of exploiting the resulting dewetted patterns for their tailored scattering properties (Gupta et al., 2019). Resorting to high-index dielectric glasses has relevance in nanophotonics (Gupta et al., 2019), where the control of the nanoresonator geometry allows for wide engineering of scattering and resonant properties. By combining engineered substrates with functional materials, dewetting triggered by thermal annealing has emerged as a viable alternative to induce order through pattern-directed dewetting (Thompson, 2012; Verma and Sharma, 2011; Seemann et al., 2005; Le Bris et al., 2014), as illustrated in figure 7.1. To increase the method's accuracy and further extend its realm of application, the prediction in the most precise manner of the final microstructure based on the exact substrate shape and film-substrate interactions is of paramount importance, which motivates the present study. Several numerical approaches are possible to study the dynamics of a liquid thin film. Since molecular simulations are still too complex numerically, approaches based either on Monte Carlo (Pauliac-Vaujour et al., 2008; Yosef and Rabani, 2006; Ohara and Gelbart, 1998; Rabani et al., 2003) or continuum models, such as the Navier-Stokes equations, may be preferably used (Mahady et al., 2013; Jiang et al., 2012; Hartnett et al., 2015; Afkhami and Kondic, 2015; Mahady et al., 2015). The latter are often based on phase-field or volume-of-fluid approaches (Jiang et al., 2012; Hartnett et al., 2015; Afkhami and Kondic, 2015), so as to simulate the two liquid phases and the solid-phase interactions involved in the dynamics. The interaction with the solid phase leads to a stress singularity to be regularized at the moving contact line, where nanometer-scale interactions become predominant (Bonn et al., 2009). Typical approaches are based on slip-velocity boundary conditions (Mahady et al., 2013; Hartnett et al., 2015; Afkhami and Kondic, 2015) or on the introduction of an intermolecular potential into the flow equations (Mahady et al., 2015, 2016). An alternative to the abovementioned models is the so-called long-wave or lubrication approximation. The latter allows for the reduction of the Navier-Stokes equations to a single equation for fluid thickness (Oron et al., 1997; Kondic et al., 2020). While initially developed for thin films with small slopes, lubrication models also show great potential in the case of large slopes, and thus, for problems with nonzero contact angles (Mahady et al., 2013). The contact line can be modeled through a suitable disjoining pressure, which integrates both attractive long-range van der Waals forces and repulsive short-range intermolecular interactions between solid and fluids (De Gennes et al., 2004; Reiter, 1992).

Intertwining spontaneous dewetting of ultrathin optical glass films by thermal annealing (Reiter, 1992) with topographic pattern-directed dewetting (Bhandaru et al., 2014; Kargupta and Sharma, 2001, 2002) offers some unique yet unexploited opportunities to create nanos-

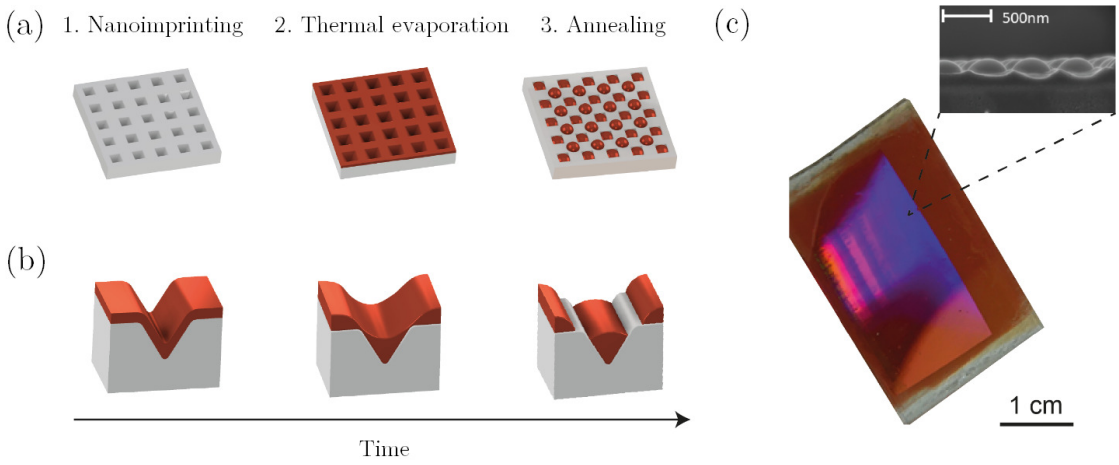

Figure 7.1: Description of dewetting triggered by thermal annealing. (a) Schematic describing the three main process steps: (1) nanoimprinting of a nanoscale texture onto a sol-gel or UV-curable substrate from a silicon master mold, (2) thermal evaporation of a thin (< 100 nm) optical glass layer, and (3) dewetting triggered by thermal annealing above the glass transition temperature. Dewetting process induces an ordered rearrangement of the film, according to the underlying texture. (b) Time evolution of the thin viscous film during dewetting. (c) Optical photograph of a 350 -nm meta-array of selenium nanoparticles.

tructures with tailored optical properties, with a very large set of applications in the realm of nanophotonics. Herein, we propose a continuum model that predicts the evolution of a templated film evolving over prepatterned substrates, based on the modeling of intermolecular interactions occurring on various substrates, for contact angles less than 90°. By comparing experimental and simulated thickness profiles over various patterns, we show that the proposed model is suitable for the accurate prediction of the final morphology and over several length scales (from nm to μm scale). We thereby offer improved control of the dewetting patterns, allowing for the realization of precise architectures relevant to nanophotonics.

7.2 Model description

7.2.1 Dewetting on flat substrates: Validation

An accurate dynamic description of dewetting constitutes a particularly challenging problem. The theoretical framework for the description of fluid flow is based on sider a flat horizontal substrate and introduce a coordinate system, (x, y, z), where the z direction, along which the film thickness is measured, coincides with the vertical one, as sketched in figure 7.2(a). The integration of the Navier- Stokes equations along the z direction, under the classical assumptions of the long-wavelength approximation (Oron et al., 1997; Kondic et al., 2020; Becker et al., 2003), leads to an evolution equation for the thin-film thickness, h, in the (x, y) directions; this is the so-called lubrication or thin-film equation:

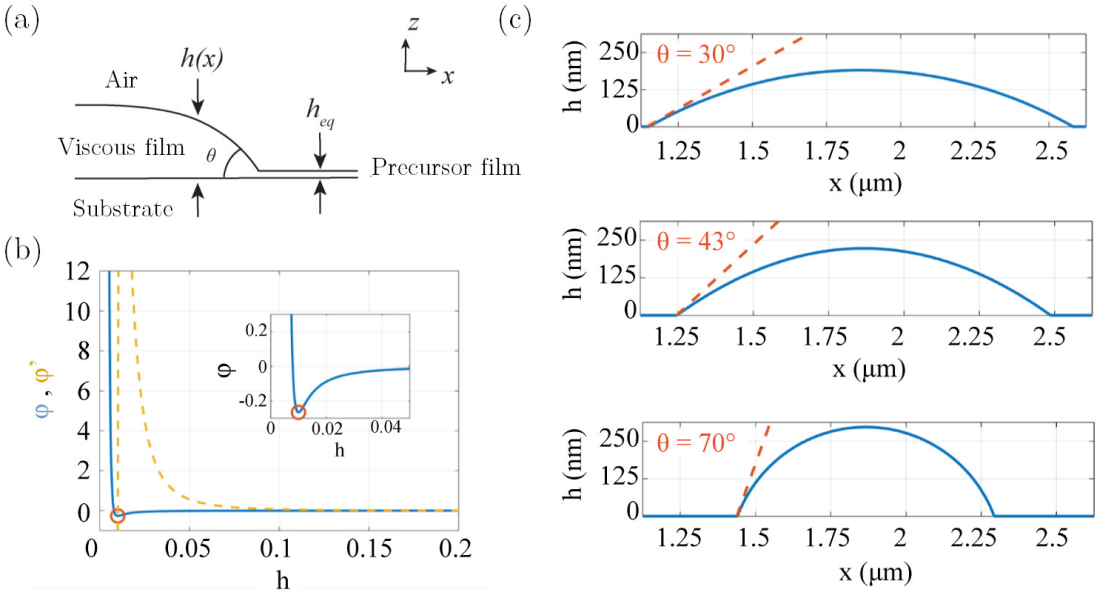

Figure 7.2: Precursor film approach implemented on flat substrates. (a) Schematic describing the components of the system and associated parameters in the precursor-film approach. (b) Lennard-Jones potential associated with the viscous film on a flat substrate. Potential (blue curve) shows a minimum, which is further indicated by its derivative (dashed yellow curve) and by the magnification in the inset. Minimum potential corresponds to a film thickness that coincides with the precursor film thickness, h_{eq}, indicated in (a). (c) Comparison of the results of the two-dimensional thin-film model (blue solid lines) and the prediction (orange dashed lines) given by equation (7.4), for $h_i = 25$ nm and different contact angles reported in the figures. From top to bottom, $A = 5 \times 10^{-20}$ J; 1×10^{-19} J; 2.5×10^{-19} J.

$$\frac{\partial h}{\partial t} = -\frac{1}{3\mu}\nabla \cdot \left\{ h^3 \nabla [\gamma \kappa + \Pi(h)] \right\}, \tag{7.1}$$

where κ is the free-surface curvature, ∇ operates in the (x, y) plane, μ is the fluid dynamic viscosity, γ is the surface-tension coefficient between the fluid and air, and Π is the so-called disjoining pressure. In the classical framework of the long-wavelength approximation, the curvature is implemented with its linearized version, i.e., $\kappa = \nabla^2 h$, which holds for small slopes of the film. As discussed later, we resort here to the complete expression of the curvature to properly account for arbitrary height profiles. Notably, since the thickness is a single-valued function of the position, contact angles greater than 90° cannot be described by this model.

The disjoining pressure term is assumed to stem from a classical Lennard-Jones type potential (Seemann et al., 2001; Mitlin, 1993; Sharma and Khanna, 1998):

$$\varphi(h) = \frac{B}{h^8} - \frac{A}{12\pi h^2}, \tag{7.2}$$

where $A = A_{123}$ is the so-called Hamaker constant of the system substrate (1), film (2), air

(3), and B is the Born coefficient, which are employed to model, respectively, the molecular long-range attractive and short-range repulsive forces. The combination of a repulsive and an attractive term defines a minimum potential for an equilibrium “precursor" film thickness, $h_{eq} = (48\pi B/A)^{1/6}$, which is obtained by imposing $\varphi'(h_{eq}) = 0$ (see figure 7.2(a)). The force derived from the Lennard-Jones potential stems from an imbalance in the interactions between the various constituent molecules. This imbalance is classically embedded in the Hamaker constant, A_{123}, which establishes the influence of constituent materials in long-range interactions, in the presence of multiple bodies, according to Lifschitz theory (Lifshitz et al., 1992; Maldarelli et al., 1980; Ivanov, 1988; Israelachvili, 2015). The previously introduced Lennard-Jones potential is linked to the disjoining pressure, Π, through

$$\Pi = -\frac{\partial \varphi}{\partial h} = \frac{8B}{h^9} - \frac{A}{6\pi h^3}. \tag{7.3}$$

A positive Hamaker constant induces destabilizing pressure gradients for films larger than the equilibrium thickness, h_{eq}. When a region of the film reaches the precursor film thickness, h_{eq}, the local equilibrium at the interface between the precursor film and the thicker regions defines an apparent contact angle, θ (see figure 7.2(a)), given by (Seemann et al., 2001; Sharma, 1993)

$$1 + \tan^2\theta = \left[\frac{\varphi\left(h_{eq}\right)}{\gamma} + 1\right]^{-2}. \tag{7.4}$$

Considering solely angles between 0° to 90°, equation (7.4) provides a bijective relationship between the contact angle and the precursor film h_{eq}.

To validate this approach, we now proceed to simulate the evolution of a thin film and evaluate the resulting contact angle. The thin-film equation is implemented with the full expression of the interface curvature (Wilson, 1982):

$$\kappa = -\nabla \cdot \mathbf{n}, \tag{7.5}$$

$$\mathbf{n} = \frac{1}{\left[1 + (\partial h/\partial x)^2 + (\partial h/\partial y)^2\right]^{1/2}} \begin{pmatrix} -\frac{\partial h}{\partial x} \\ -\frac{\partial h}{\partial y} \end{pmatrix} \tag{7.6}$$

where $\mathbf{n}$ embeds the x and y components of the normal of the fluid-free surface; the problem is completed with the disjoining pressure, $\Pi(h)$, detailed above. The model with the full expression of curvature, despite its simplicity, shows very good agreement with various experimental measurements, even for cases in which the typical assumptions of the long-wave approximation are not respected. To verify the consistency of the relationship between equilibrium thickness and contact angle, we perform numerical simulations with the finite-element solver COMSOL Multiphysics by implementing the weak form of equations (7.1), (7.3), (7.5), and (7.6) in conservative form. We choose three different values of contact angles and three different values of the Hamaker constant and determine the corresponding values of the Born coefficient, B. We then determine the Born coefficient by using equations (7.2)-(7.4). Two-dimensional simulation results (i.e., $\partial h/\partial y = 0$) with an initial thickness of

$h_i = 25$ nm and $\gamma = 3 \times 10^{-2}$ N.m $^{-1}$ are shown in figure 7.2(c), for three different values of $A = 5 \times 10^{-20}, 1 \times 10^{-19}$, and 2.5×10^{-19} J. The numerical values of the contact angle match the predicted ones with an accuracy below 1°, which validates the proposed approach on flat substrates. The implementation of the complete curvature is essential to yield proper results. The linearized curvature, $\kappa = \nabla^2 h$, in the long-wavelength approximation gives contact-angle values with over 10° error compared with the target value. Despite the small size of the final drop states involved, the importance of the complete curvature expression to recover the final static shape is remarkable.

It is also important to note that the presence of a precursor film implies a loss of volume proportional to the precursor-film thickness. The volume error associated with this choice is in all cases presented here inferior to 1%, and thus neglected.

At this stage, an important question arises for the choice of the contact angle. During dewetting, it is common that contact angles evolve dynamically, owing to the elasticity of the triple line (De Gennes et al., 2004). In this framework, it is observed that the final contact angle does not show a strong dispersion in the final stage of dewetting (inferior to 6°, see figure 7.12 within the Supplemental Material). A hysteresis is thus neglected in the rest of this work. Despite this assumption, our model still allows for a relatively accurate prediction of experimental observations, as discussed below.

In previous works that developed a model based on the Lennard-Jones potential (Becker et al., 2003; Seemann et al., 2001; Sharma and Khanna, 1998), the contact angle was inferred from accurate Hamaker constant and Born coefficient data, with good agreement between theoretically derived and experimentally measured contact angles. This approach assumes prior knowledge of the Born coefficient, which is significantly harder to quantify than the Hamaker constant, and thus, constitutes a significant limitation for broader use of such a modeling scheme. Moreover, this requires knowledge of the precursor-film thickness, a challenging quantity to experimentally measure (typically in the angstrom range). Here, we propose to use the Born coefficient, and thus, the equilibrium thickness given by equation (7.4), as an independent parameter to match the experimental and modeled contact angles in analogy to the procedure in figure 7.2(c) (see Appendix 7.4.3). In contrast with previous works, the knowledge of the equilibrium contact angle, Hamaker constant, and surface-tension coefficient is sufficient to effectively model the thin-film dynamics.

7.2.2 Templated dewetting

We now turn to the evolution of a film with fixed contact angle, θ, over a prepatterned (or "templated") substrate, of height profile h_s measured along the z direction, starting from the horizontal reference previously introduced (see figure 7.3(a)). Here, we consider two different types of templates: (i) lines or two-dimensional templates (figure 7.3(b)), characterized by triangular grooves of base W, period P, and spacing $P - W$ along the x direction and invariant along the direction orthogonal to the periodicity one (y direction); and (ii) pyramids or three-

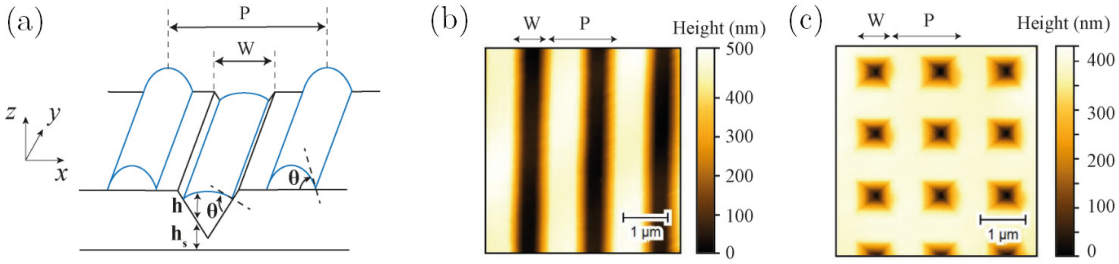

Figure 7.3: Two-dimensional and three-dimensional templates. (a) Schematic introducing the contact angle, θ; the film height profile, h; the substrate height profile, h_s; the inverted pyramid base width, W; and the template period, P. Atomic force microscopy images of textures nanoimprinted on an Ormocomp substrate: (b) triangular grooves (two-dimensional template) and (c) square arrays of inverted pyramids (three-dimensional template).

dimensional templates (figure 7.3(c)), characterized by pyramidal trenches with periodicity P along both x and y directions. We resort to As_2Se_3 thin films thermally evaporated on textured UVcurable polymers or silica substrates (see Appendix 7.4.1 for further details of the materials employed). For the templates shown in figure 7.3(a), the fabrication process (Gupta et al., 2019) leads to dewetted patterns invariant along the y direction.

To accurately predict the thin-film dynamics and the resulting microstructure, the thin-film equation must be adapted to account for the role of the underlying substrate. The total surface curvature, κ, in this new configuration is now given by the curvature of the total elevation of the free surface $(h + h_s)$:

$$\kappa = -\nabla \cdot \mathbf{n_t}, \tag{7.7}$$

$$\mathbf{n}_t = \frac{1}{\left\{1 + \left[(\partial h/\partial x) + (\partial h_s/\partial x)\right]^2 + \left[(\partial h/\partial y) + \left(\partial h_s/\partial y\right)\right]^2\right\}^{1/2}} \begin{bmatrix} \left(-\frac{\partial h}{\partial x} - \frac{\partial h_s}{\partial x}\right) \\ \left(-\frac{\partial h}{\partial y} - \frac{\partial h_s}{\partial y}\right) \end{bmatrix}. \tag{7.8}$$

Another difference from the flat-substrate case lies in the definition of the film thickness in the Lennard-Jones potential. Recalling the definition of potential (7.2), the contact angle depends on the equilibrium thickness. A proper definition of the thickness is therefore crucial to reproduce identical contact angles over the whole substrate. On a flat substrate, thickness is defined straightforwardly as the vertical projection. However, in the case of an underlying inclined substrate, an accurate film thickness is defined as the shortest distance between the film-air interface and the film-substrate, i.e., the projection given by

$$h^* = h\cos\left(\text{atan}\left\{\left[\left(\frac{\partial h_s}{\partial x}\right)^2 + \left(\frac{\partial h_s}{\partial y}\right)^2\right]^{1/2}\right\}\right). \tag{7.9}$$

To validate the proposed scheme, numerical simulations using experimental atomic scanning microscope profiles of nanoimprinted substrates are performed. We take as initial condition a

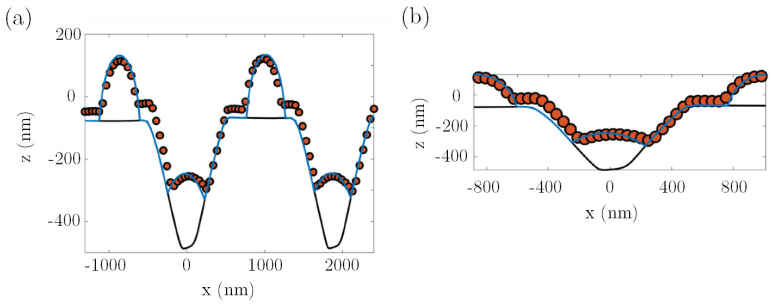

Figure 7.4: Simulated vs experimental dewetted profiles in the 2D case. (a) Simulated dewetted profile (blue) and experimental AFM dewetted profile (orange dots) in the case of a $2-\mu$m-period line pattern with interpyramid spacing 1.1μm and 60 - nm initial film thickness of As_2Se_3. (b) Magnified view of a single period, showing the match between experimental and simulated contact angles.

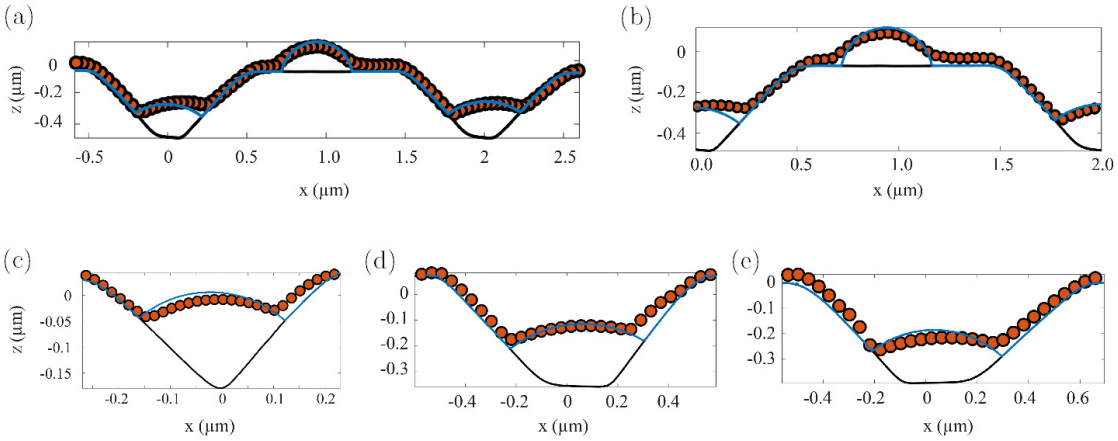

Figure 7.5: Additional comparative analysis between experimental results (orange dots) and simulations (solid blue line) for various 2D templates with varying spacing (see figure 7.3(a)). Experimental data are obtained using As_2Se_3 thin films deposited onto plasma-treated Ormocomp substrates. (a),(b) Final film profile for a substrate with width $W = 850$nm and spacing $P - W = 1\mu$m. (b) represents a zoom over a single unit period of (a), highlighting the reasonable overlap between simulated and experimental height profiles. The initial deposited film thickness is $h_i = 60$nm. (c),(d),(e) Final film profile for different periodic substrates with spacing $P - W = 100$nm. The initial film thicknesses are $h_i = 60$nm for (c) and (e), while $h_i = 80$nm for (d).

constant flat thickness that matches the imposed thicknesses in the experimental campaign (see Appendix 7.4.1). The experimental film profile upon dewetting is then superposed to compare the match between experimental and simulated data. First, investigating the two-dimensional (2D) case, the experimental and simulated dewetted film profiles are compared in figure 7.4 (period 2μm, interpyramid spacing 1.1μm, film thickness 60 nm, contact angle $\theta = 85°$). Additional comparative results in the two-dimensional case are provided in figure 7.5. The numerical scheme is further validated in three dimensions, using a pyramid with largely reduced spacing (interpyramid spacing 150 nm, period 1.1μm, thickness 60 nm, see

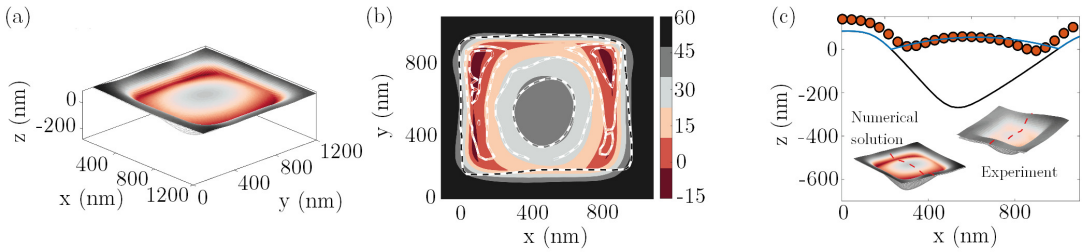

Figure 7.6: Simulated vs experimental dewetted profiles in the three-dimensional case, in the case of a 1.1 - μm-period-inverted pyramid pattern with 850 nm pyramid base. (a) Three-dimensional visualization of the simulated dewetted profile. (b) Comparison of the numerical (colored isocontours) and experimental (dashed isocontours) dewetted profiles. (c) Comparison along one section of the simulated dewetted profile (solid blue line) with the experimental AFM dewetted profile (orange dots).

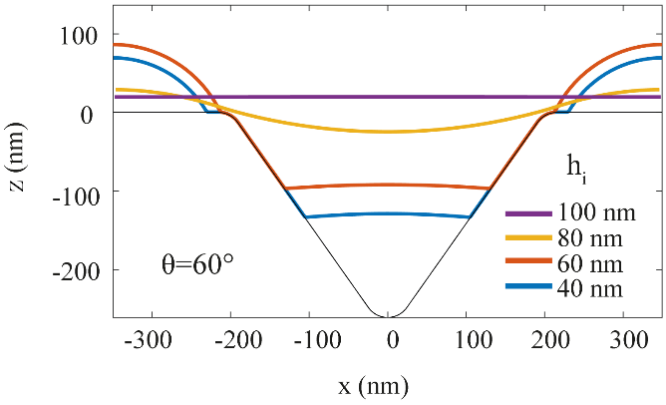

Figure 7.7: Plot representing the final periodic thickness profile at the end of simulation for films of initial increasing thicknesses hi. For h_i = 60nm and h_i = 40nm, the final profile shows two separated droplets. For h_i = 100nm and h_i = 80nm, the final film profile is continuous, indicating that the film will break up according to nucleation and growth of holes at random instead of prescribed locations. The critical thickness hence verifies $60nm < h_{\text{crit}} < 80nm$.

figure 7.6). Remarkably, the model reproduces with accuracy the experimental height profile over the range of thicknesses considered in this work. It is interesting to note that the proposed framework also predicts a thickness threshold, h_{crit} , above which the final film equilibrium, upon simulation, leads to a flat film covering the full substrate, instead of isolated droplets, as shown in figure 7.7 for an initial thickness of h_i = 100 nm. This ultimately leads to dewetting according to nucleation and growth holes with a random location instead of a well prescribed location. The random nucleation and growth of holes are observed experimentally at around 80 nm (contact angle 64.5°), which is well in line with the results of figure 7.7. These results highlight the relevance of continuum-mechanics schemes, even at thicknesses that become comparable with atomistic length scales.

Given that the rearrangement of the material is fundamentally linked to the increase in local curvature, the influence of the radius of curvature of the edges of the underlying substrate

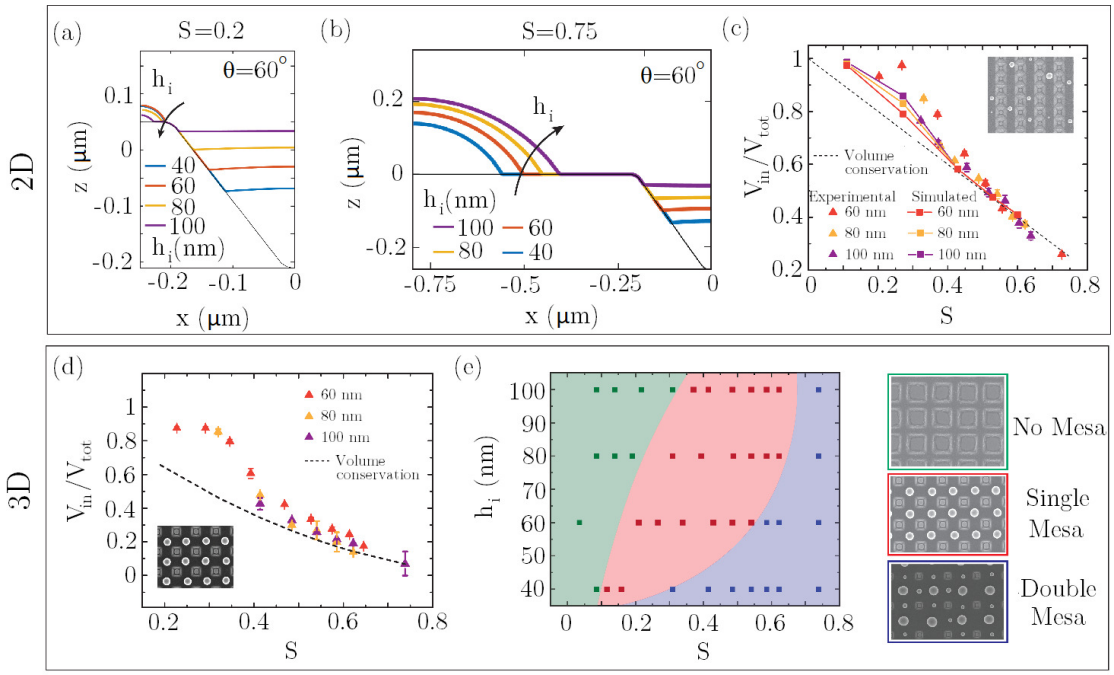

Figure 7.8: Distribution of film material upon dewetting. Simulated two-dimensional final film profiles upon dewetting for spacing-toperiod ratios, S, of $S = 0.2$ (a) and $S = 0.75$ (b). Mesa particle size grows with film thickness for $S = 0.75$; trend is reversed for $S = 0.2$. (c) $V_{\text{in}} / V_{\text{tot}}$ in the case of two-dimensional templates. Colors indicate the initial film thickness. Orange, 60 nm; yellow, 80 nm; purple, 100 nm. (d) Experimental pyramid-volume-to-total-volume ratio in the case of an inverted-pyramid array with increasing spacing. (e) Structure diagram associated with inverted pyramids with varying spacing-to-period ratio and film thickness. Film material is composed of As_2Se_3 on a plasma-treated Ormocomp substrate. Graph's background coloring qualitatively indicates the microstructural stability domains.

on the final structures is further investigated (see figure 7.13 within the Supplemental Material, Section 7.5). Simulated transitory states may differ depending on the pyramid-base edge curvature, giving rise, in some cases, to pinning behavior. Nevertheless, the final dewetted architectures appear to be independent of pyramid edge curvature for sufficiently long simulation times.

A peculiarity of dewetting in such pyramid arrays pertains to the distribution of material in the final microstructure, which widely varies, depending on the spacing-to-period ratio. In figures 7.8(a,c), the final volume inside the pyramid, V_{in}, over the total volume, V_{tot} , is evaluated by simulation in the two-dimensional case. In the case where the final pyramid volume would be solely constituted from the material initially deposited inside the trench, the pyramid volume should be constant with spacing. This would therefore impose a well-defined law, referred to in this work as volume conservation, according to which the initial volume inside and outside the periodic trenches is conserved: $V_{\text{in}} / V_{\text{tot}} = h_i W / h_i P$ and $V_{\text{out}} / V_{\text{tot}} = [h_i (P - W)] / h_i P$. Both the experimental and numerical results show a clear deviation from the volume conservation

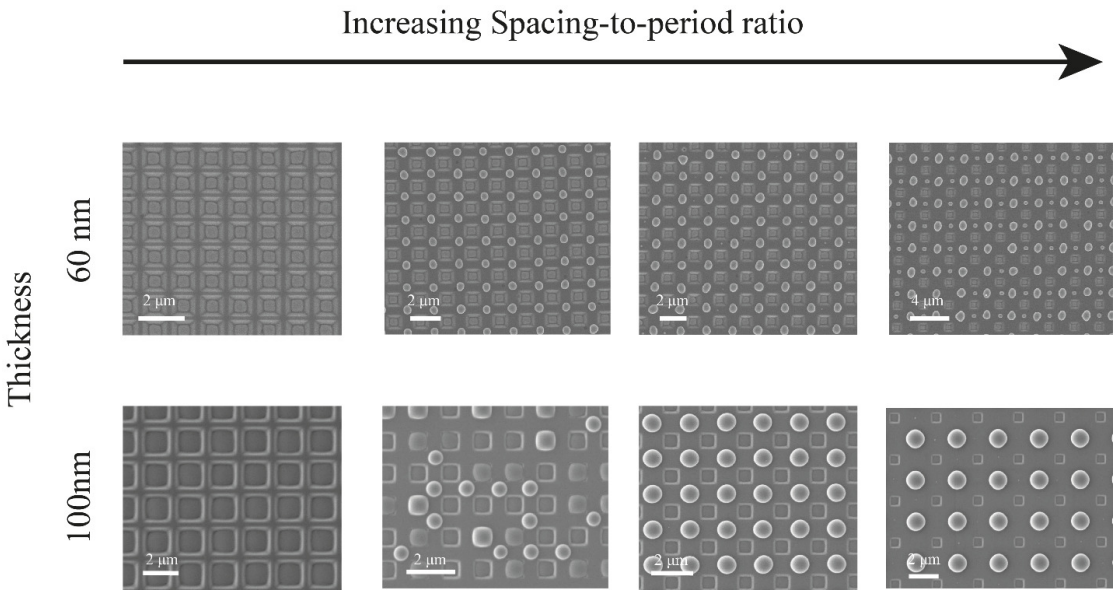

Figure 7.9: Top view scanning electron microscopy (SEM) images of an As_2Se_3 film with increasing thickness deposited on a plasma-treated silica textured sample with increasing spacing-to-period ratio. The structural transition from the absence of mesa (e.g. particle in between pits) to single mesa and then double mesa is visible with an initial film thickness of 60nm. In the 100nm thickness case, the film only shows a single structural transition from the absence of mesa to single mesa.

law at low values of the spacing-to-period ratio, labeled *S*, where the film located at the pyramid edges is preferentially pulled inside the pyramid (see figures 7.8(c,d)). On the contrary, at larger spacing-to-period ratios, the ratio $V_{\text{in}} / V_{\text{tot}}$ follows closely the volume conservation law. While the thickness dependence does not appear in the experimental volume analysis, the deviating trend is observed for all configurations investigated. At reduced spacing, the absence of droplets between pyramids (“mesa") is observed for spacing-to-period ratios up to 0.35, while, at very large spacing, the instability in the top plane gives rises to a double distribution in size, and thus, to a new architecture. To provide the reader with an overview of the architectures as a function of spacing and thickness, a diagram is provided in figure 7.8(e). Additional SEM images, showing the full structural transition with the thickness and spacing-to-period ratio, are provided in figure 7.9. All microstructures observed in the present study are reminiscent of the Wenzel state on textured surfaces (Murakami et al., 2014). This observation can be directly related to the choice of deposition method, which, in the present case, is thermal evaporation under vacuum.

7.2.3 Application in photonics: Phase control

We now turn to exploit this in-depth understanding and control of template dewetting to realize advanced optical metasurfaces. Ordered high-index nanoparticles bear particular importance for metasurfaces or metagratings, which enable the tailoring of the phase, amplitude,

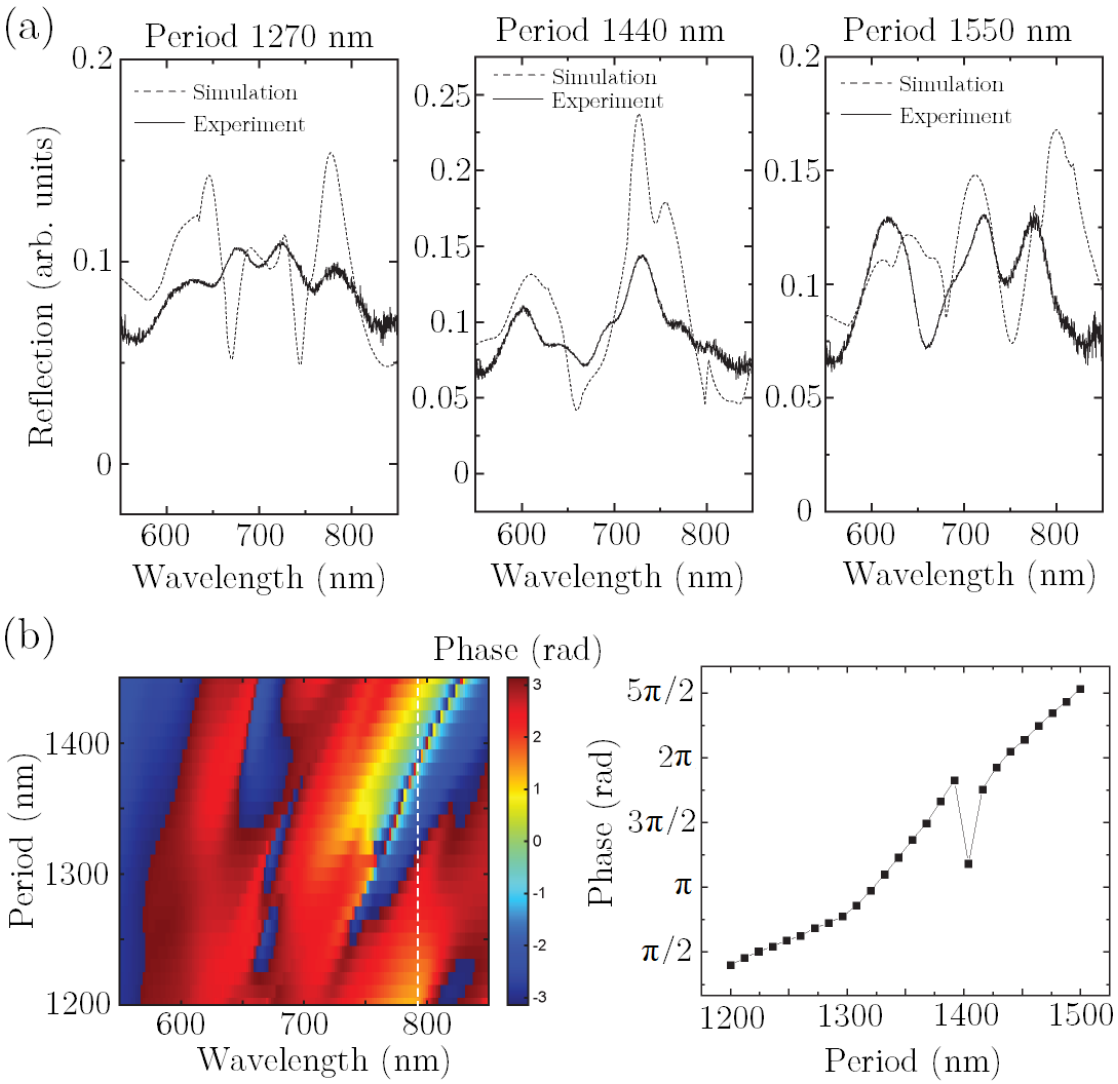

Figure 7.10: Phase control for metagratings. (a) Simulated (dashed line) and experimental (solid line) reflection spectra for three periodicities (P = 1270, 1440, and 1550 nm) and fixed pyramid size of 850 nm. Spectra are not normalized with their own maximum but compared in absolute value. (b) Left, color map representing the phase imparted by the quasi-three-dimensional (3D) resonating structure to the outbound beam, as a function of period and wavelength. Pyramid width, W, is fixed at 850 nm. Right, plot representing phase as a function of period at 784 nm, corresponding to the white dashed line reported in the plot on the left.

and polarization of light over reduced thicknesses, in stark contrast to current bulky optical components (Yu and Capasso, 2014; Li et al., 2017). By engineering the coupling between the various Mie modes through geometry, recent works have demonstrated the ability to tailor the emitted phase. These so-called Huygens meta-atoms provide control over the phase, covering the full $0-2\pi$ range, hence enabling arbitrarily tailored phase profiles (Decker et al., 2015; Leitis et al., 2020; Ra'di et al., 2017). Several demonstrations based on this concept have

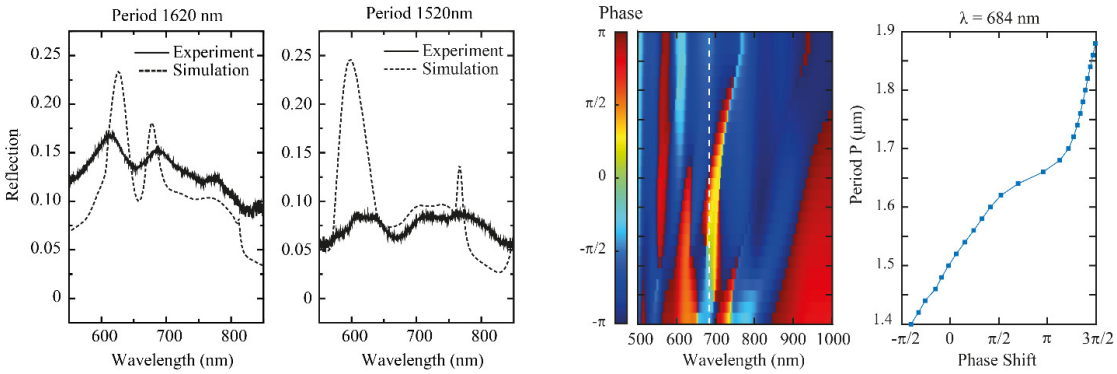

Figure 7.11: All-dielectric Huygens Meta-Gratings for linear features according to the geometry shown in figure 7.3(a). The simulated dash curves are modeled purely enforcing the volume conservation hypothesis, with respective periods of 1620nm and 1520nm and an initial film thickness of 85nm. The experimental data is obtained for a film thickness of 80nm based on microbalance measurements in-situ during evaporation and respective periods of 1600nm and 1500nm. The colormap shows the phase map in reflection, with a sharp transition around 690nm. The phase shift is plotted for $\lambda = 684$nm, showing a clear 2π phase shift for a range of periods spanning from 1400nm to 1900nm.

been implemented, such as lensing. Nevertheless, achieving full control over phase imposes stringent requirements, since geometrical changes of a few tens of nanometers may have a significant impact on the optical response. Given the high accuracy, in terms of both position and spacing in template dewetting, quasi-threedimensional structures present remarkable opportunities, in terms of phase modulation (Gupta et al., 2019; Ra'di et al., 2017).

Let us now focus on the optical properties arising from periodic architectures based on inverted pyramids with increasing spacing along the two principal axes (singlemesa architecture in figure 7.8). We proceed to evaluate the meta-assembly spectrum in reflection for three distinct period values ($P = 1270, 1440, 1550$ nm), keeping the pyramid base constant at 850 nm (see figure 7.10). The experimental spectra of line arrays are further compared with the equivalent simulated shapes. The simulated geometrical shapes rely on both experimental equilibrium contact angles and the volume-conservation criterion, which together define a relationship between evaporated film thickness and line width. Since the system is highly sensitive to slight geometrical changes, as low as 10 nm, experimental and simulated reflection spectra appear relatively well in agreement. We now turn to the evolution in phase for a range of periods from 1200 to 1500 nm. Interestingly, interference between the various individual particle Mie modes cumulate to yield a cumulative phase shift over the complete 2π-phase range at $\lambda = 784$ nm. The phase shift is gradual, spanning from 1200 to 1500 nm, hence allowing for phase control with experimentally attainable accuracies. One can also note a particularly sharp 2π phase shift occurring for periods around 1410 nm, which highlights the sensitivity of imparted phase on geometrical parameters.

A similar study for two-dimensional templates (see figure 7.11) also yields a coherent match

between experimental and simulated spectra. Considering the spacing-to-period ratios studied here, we can resort solely to the volume conservation hypothesis to link thickness with resulting geometrical parameters. This allows for a completely "blind" implementation of geometry in finite-difference time-domain (FDTD) simulation software, which bears significant advantages in terms of design scalability. The phase profile shows extended phase-control possibilities around 684 nm (see figure 7.11), with an extended range of periods to tune the phase, spanning from 1400 to 1900 nm.

7.3 Conclusion

We introduce a modeling framework for the dewetting of films over a templated substrate based on a precursor film approach. By resorting to a Lennard-Jones potential model, solutions to the dewetting problem are identified. Comparisons between final simulated and experimental film profiles show quantitative agreement, thereby providing a predictive model for the fabrication of nanostructures via dewetting on templated substrates. Finally, we demonstrate how this fine understanding of the resulting geometries paves the way for wave-front control in quasi-three-dimensional architectures. Further works to accelerate the convergence of the model in 3D would allow for an end-to-end framework that combines threedimensional dewetting models with photonic simulation tools, enabling the direct simulation of the optical properties of a dewetted pattern based on simple input parameters (mainly initial thickness and pattern profile). This would thereby significantly expand the opportunities for the fabrication of self-assembled nanostructures, with a precision comparable to that of advanced lithographic processes. These considerations find immediate applications in the context of metasurfaces and beyond in the field of nanophotonics.

7.4 Appendix

7.4.1 Sample fabrication

Chalcogenide thin films (Se, As2Se3) are first thermally evaporated (UNIVEX 350, Oerlikon, Germany) onto three types of substrate: two UV-curable polymers (Ormocomp®, Ormostamp®), which are well suited for nanoimprint lithography, and a pure silica texture obtained by a sol-gel process. We evaporate the films on both textured and nontextured regions to later compare these two relative situations. The film thickness is monitored during evaporation using a quartz crystal (Inficon, Switzerland). Film viscosity is dramatically reduced upon annealing above the glass transition temperature, and enhanced chain mobility allows for dewetting to occur. Dewetting is performed by placing the sample for 30 min over a hotplate at 200°C. We verify the steadiness of the patterns by both qualitative and quantitative comparison of the dewetted structures at different times using both scanning electron and atomic force microscopy, observing steady patterns for all studied cases upon 20 min of annealing.

7.4.2 Contact angle measurements

To experimentally determine contact angles, we proceed to dewet evaporated thin films. This is triggered by thermal annealing above the glass transition temperature of the film for extended durations, e.g., twice the time required to observe a stable microstructure based on top-view observations using optical microscopy. To avoid the uncertainty associated with tip shape in atomic force microscopy (AFM), we proceed instead to measure contact angles by cross-section imaging using scanning electron microscopy (SEM). Cross-sections of the obtained samples are then prepared using liquid nitrogen. All SEM samples are coated with a 10 nm carbon film. The SEM images are taken with a Zeiss Merlin field-emission SEM instrument equipped with a GEMINI II column operating at 1.0 kV with a probe current of 70 pA. Contact angles are extracted using image analysis to accurately extract the contact angles (Image J, Contact Angle Module).

7.4.3 Numerical simulations

The numerical implementation of the lubrication equation (7.1) with complete curvature, together with interface-potential expression (7.2), is performed in the finite-element solver COMSOL Multiphysics. The equations are discretized for the variables (h,κ). We consider quadratic Lagrangian elements for spatial discretization, with a triangular nonstructured grid for the two-dimensional case. We exploit the built-in backward differentiation formula algorithm for time marching, setting a tolerance of 10^{-5}. Numerical convergence is achieved by performing several simulations with $h_s = 0$ and verifying the convergence of the contact angle to the desired value.

As outlined above, the approach for the simulation of experimental conditions is based on the choice of the contact angle and the retrieval of the equilibrium thickness and Born coefficient. The Lennard-Jones potential reads

$$\Pi = -\frac{\partial \varphi}{\partial h} = \frac{8B}{h^9} - \frac{A}{6\pi h^3} \tag{7.10}$$

where the Hamaker constant, A, is estimated based on Lifschitz theory. Following Sharma (1993), the macroscopic contact angle at equilibrium is given by

$$1 + \tan^2\theta = \left[\frac{\varphi\left(h_{\mathrm{eq}}\right)}{\gamma} + 1\right]^{-2}, \tag{7.11}$$

where $\varphi\left(h_{\mathrm{eq}}\right)$ is the equilibrium potential, obtained by imposing $\varphi'\left(h_{\mathrm{eq}}\right) = 0$, where h_{eq} is the equilibrium thickness (i.e., precursor-film thickness). Once the contact angle is fixed, the previous relation (7.11) gives a unique value of the equilibrium potential in the range $[0°, 90°]$, with $A > 0$. The value of the equilibrium potential can be used to evaluate the equilibrium thickness. Deriving equation (7.2) with respect to h and evaluating it at equilibrium thickness,

Material	Refractive index	Details	Ref.
SiO_2	1.45	@ 550 nm fused silica	(Malitson, 1965)
As_2Se_3	3.5	@550 nm	Fabricant
Ormocomp (OC)	1.52	@589 nm	Fabricant

Table 7.1: Refractive indices in the visible region of typical materials involved in the present study.

h_{eq}, yields

$$0 = -\frac{8B}{h_{\text{eq}}^9} + \frac{A}{6\pi h_{\text{eq}}^3}, \tag{7.12}$$

$$h_{\text{eq}} = \left(\frac{48\pi B}{A}\right)^{1/6} \rightarrow \frac{B}{A} = \frac{h_{\text{eq}}^6}{48\pi}. \tag{7.13}$$

Substituting B/A in equation (7.2), at the equilibrium thickness, we have

$$\varphi\left(h_{\text{eq}}\right) = \varphi_{\text{eq}} = -\frac{A}{16\pi h_{\text{eq}}^2} \tag{7.14}$$

where $\varphi\left(h_{\text{eq}}\right)$ is associated with a unique contact angle between 0° to 90°, according to equation (7.4). From equations (7.13) and (7.14), we can thus evaluate h_{eq} and $B = (B/A)A$, with the knowledge of φ_{eq} and A.

7.4.4 Evaluation of the Hamaker constant using Lifschitz theory and typical values

The Hamaker constant, A, quantifies the imbalance in van der Waals forces as two interfaces are brought closer to each other. Lifshitz et al. (1992) developed a theory to account for the collective interactive forces between macroscopic particles from quantum-field theory that related the interaction energy with the interparticle distance. The interactions between particles are relative to macroscopic properties: the dielectric constant, ε, and the refractive index, n. The Hamaker constant of a system made of a liquid film (3) placed between a gas or immiscible liquid (2) and a solid (1) can be estimated by considering the overall system energy, which includes (i) permanent polar dipole interactions (Keesom and Debye molecular forces) and (ii) induced dipole interactions (London dispersion forces), which depend on the orbiting electron frequency, ν, and the refractive index, n, of media (Israelachvili, 2015):

$$A \approx \frac{3kT}{4}\left[\frac{\varepsilon_1(0)-\varepsilon_3(0)}{\varepsilon_1(0)+\varepsilon_3(0)}\right]\left[\frac{\varepsilon_2(0)-\varepsilon_3(0)}{\varepsilon_2(0)+\varepsilon_3(0)}\right] + \frac{3h\nu_e}{8\sqrt{2}}\frac{\left(n_1^2-n_3^2\right)\left(n_2^2-n_3^2\right)}{\left(n_1^2+n_3^2\right)^{1/2}\left(n_2^2+n_3^2\right)^{1/2}\left[\left(n_1^2+n_3^2\right)^{1/2}+\left(n_2^2+n_3^2\right)^{1/2}\right]} \tag{7.15}$$

where ν_e is the principal UV-absorption frequency $\left(\sim 3\times10^{15}\text{ Hz}\right)$, n_i refers to the visible real refractive index of species i, and h is the Planck constant. Unless strongly polar molecules are involved, the first term can be safely neglected (Israelachvili, 2015).

Based on Lifschitz theory and the refractive indices provided in Table 7.1, the following values of the Hamaker constant are obtained:

$$\begin{aligned} A_{\mathrm{OC-As_2Se_3-air}} &= 5.7 \times 10^{-19}\ \mathrm{J} \\ A_{\mathrm{SiO_2-As_2Se_3-air}} &= 5.9 \times 10^{-19}\ \mathrm{J} \end{aligned} \tag{7.16}$$

7.4.5 Atomic Force Microscopy measurements

All AFM measurements are performed at room temperature (largely below the glass transition temperature of As_2Se_3, identified at 120°C), which ensures that As_2Se_3 is completely solid during scanning. Atomic force microscopy images are collected in amplitude modulation mode on a commercial Cypher S system (Asylum Research/Oxford Instruments, Santa Barbara, CA). Two kinds of cantilevers were used: the sensitivity of Asyelec cantilevers (Asylum Research) was evaluated from force curves and the spring constant was measured from their thermal spectra, while AC240TS cantilevers (Asylum Research) were calibrated using the built-in GetReal Automated Probe Calibration procedure. The cantilevers were driven acoustically. Using Gwyddion post-processing software, polynomial plane leveling of order 2 was achieved followed by scar removal using the in-built functions. We use the smoothened profiles for an overall comparison of the profiles with numerical simulations. Uncertainties linked to the sharp slope profiles near the triple line are very localized, and do not alter the overall match between the simulated and measured profiles.

7.4.6 Reflection measurements

Reflection spectra are characterized using a Nikon Optiphot 200 inspection microscope (10×, NA = 0.25 objective). A CCD camera (Digital Sight DS-2Mv, Nikon) is used to record the images of the sample, and the images are processed with NIS-Elements F3.2 software. The spectra are characterized with a visible-near-IR spectroscopy system based on an inverted optical microscope (Olympus IX-71) coupled to a spectrometer (Jobin Yvon Horiba Triax 550). The sample is illuminated using a halogen white-light source focused onto the sample using an objective (20×, NA = 0.4). The reflected light is collected through the same objective and recorded using a spectrometer. The reflected intensity is normalized by the spectrum of the lamp obtained by reflection measurements with a silver mirror (Thorlabs PF 10-03-P01). A polarizer (WP25M-UB, Thorlabs) is used to set linear-polarized light illumination for both reflection and transmission measurements.

7.4.7 Optical simulations

The built-in *S*-parameter analyzer from the FDTD solver package (Lumerical) is used to extract complex transmission and reflection coefficients. This analysis script calculates the following quantities: (i) fraction of transmitted and reflected power, using 2D monitors and transmission function; and (ii) complex reflection and transmission coefficients (*S* parameters). The latter

coefficients are calculated from the amplitude and phase of the fields, as measured by the point monitors. This technique assumes that the system is single mode (only one grating order) and that the monitors are far away enough from the structure so that the fields are propagating like a plane wave. A phase correction is also necessary to compensate for the phase that accumulates as fields propagate through the background medium from the source to the metamaterial and from the metamaterial to the monitors. The provided phase, therefore, corresponds to the difference in phase accumulated over the metamaterial layer.

7.5 Supplemental Material

To limit contact angle hysteresis, we proceed in successive steps. The first step consists of a preparation of substrates with low surface roughness. We resort to several substrates, including: (i) sol-gels based on acid-catalyzed Methy (triethoxysilane), followed by a pyrolysis step at 400°C, or (ii) UV curable commercial resins, in particular Ormocomp® and Ormostamp® from Microresist, Germany. The pyrolysis step for sol-gels helps to densify the resulting silica structure while removing residual organic components. To control the resulting surface roughness of silica-based on sol-gel processes as well as the commercial UV resins, we proceed to measure by atomic force microscopy the surface roughness (figure 7.12). All root mean squared (RMS) roughness values are inferior to 1 nm, which, although not competitive with typical Si wafer roughness, compares favorably with most other surfaces. A second step aims at cleaning thoroughly the substrates to remove any chemical inhomogeneities. This is a critical step to ensure a homogeneous substrate surface energy, and consequently homogeneous dewetting patterns. The extensive use of polymers largely restricts the use of commonly-used aggressive solvents to clean wafers such as H2SO4 or HF. Nevertheless, common cleaning procedures help to wash away nano-imprinting residues such as silicone oil traces from the PDMS or other contaminants, All substrates are subsequently washed systematically using isopropanol (degreasing agent), ethanol, and water. The wash cycle is commonly repeated three times, followed by a gentle nitrogen or air gun to dry the substrate surface and blow away eventual debris or particles remaining at the surface. The hysteresis caused by roughness and chemical heterogeneity is further assessed by evaluating the standard deviation of contact angles measurement for a given film/substrate couple. The error bars stem from a combination of imaging analysis-related uncertainties and substrate surface roughness, which induces local triple line pinning and deviation for equilibrium contact angle. As apparent in figure 7.12, limited contact angle hysteresis does occur in all systems studied. Further techniques to decrease the surface roughness of nanoimprinted substrate as well as improve the chemical washing procedure would be of considerable help to reduce contact angle standard deviation and thereby offer better control over templated dewetting.

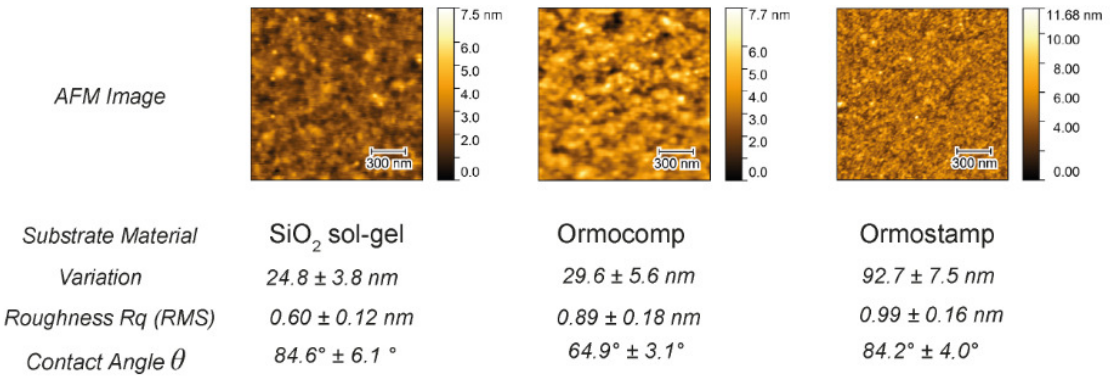

Figure 7.12: Roughness parameters of the substrates used in his work. Root mean square Roughness exhibits values <1 nm. Variation values (i.e. integral of the absolute value associated with the local gradient) show denser features in Ormostamp substrates than in other elements.

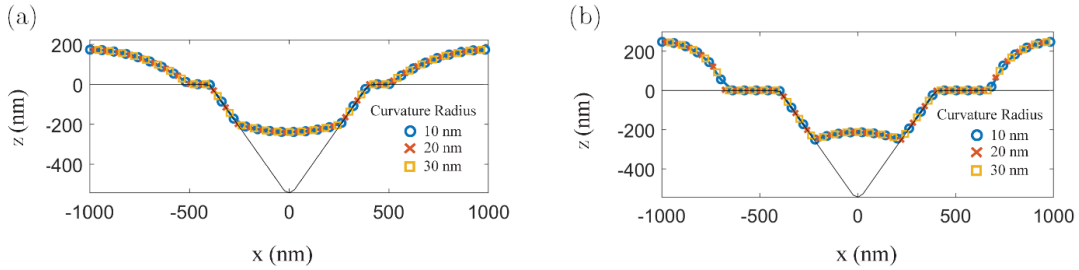

Figure 7.13: Influence of the curvature radius of the dewetted structures in the two-dimensional case. Each plot reproduces the periodic final film profile for three different edge curvatures: 10nm (blue), 20nm (orange), 30nm (yellow). All final profiles overlap closely and are indistinguishable. (a) Contact Angle 40° and (b) Contact angle 80°. The initial film height is 100nm.

8 Gravity-driven coatings on curved substrates: a differential geometry approach

P. G. Ledda[1], M. Pezzulla[2], E, Jambon-Puillet[3], P-T Brun[3], F. Gallaire[1]

[1]Laboratory of Fluid Mechanics and Instabilities, École Polytechnique Fédérale de Lausanne, Lausanne, CH-1015, Switzerland

[2]Slender Structures Lab, Department of Mechanical and Production Engineering, Århus University, Inge Lehmanns Gade 10, 8000 Århus C, Denmark

[3]Department of Chemical and Biological Engineering, Princeton University,Princeton, New-Jersey 08540, USA

Submitted to *Journal of Fluid Mechanics*

Author contributions P.G.L. conceived the project with F.G.. P.G.L. performed the theoretical analyses and numerical simulations, whose results have been discussed with F.G. and compared with the experimental measurements of E. J-P. P.G.L. discussed the results with the coauthors. P.G.L. wrote the manuscript with input from the coauthors.

Although the drainage and spreading processes of thin liquid films on substrates have received growing attention during the last decades, the study of three-dimensional cases is limited to studies on flat and axisymmetric substrates. In this work, we exploit differential geometry to study the drainage and spreading of thin films on generic curved substrates. We initially investigate the drainage and spreading processes on spheroidal and paraboloidal substrates by employing an asymptotic expansion in the vicinity of the pole and a self-similar approach, finding that the thickness distribution is set by the substrate metric and tangential gravity force components. Spheroids with a large ratio between height and equatorial radius are characterized by a growing thickness moving away from the pole, and vice versa. The non-symmetric coating on a toroidal substrate shows that larger thicknesses and a faster spreading are attained on the inner region than on the outer region of the torus. An ellipsoid with three different axes is chosen as a testing ground for three-dimensional drainage and spreading. Modulations in the drainage solution are observed, with a different variation of the thickness along the two axes. By imposing the conservation of mass, an analytical solution for the average spreading front is obtained. The analytical and numerical results are in good agreement. The

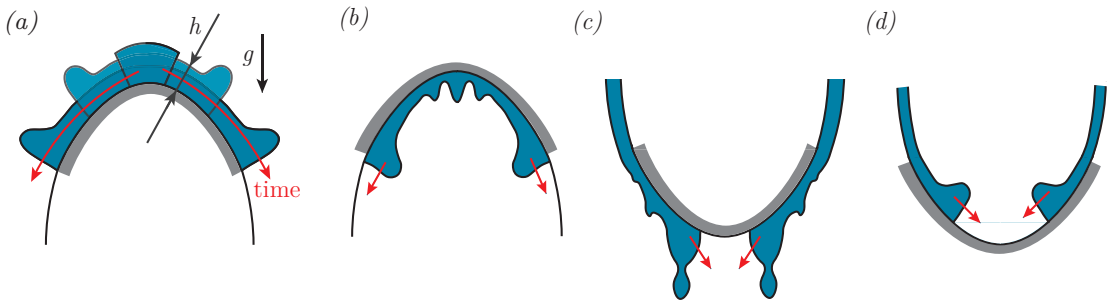

Figure 8.1: Two-dimensional sketches of different types of spreading of an initial mass of fluid on a curved substrates. (a) diverging flow on a substrate (b) diverging flow below a substrate (c) converging flow below a substrate (d) converging flow on a substrate.

resulting drainage solutions show also a good agreement with experimental measurements obtained from the coating of a curing polymer on diverse substrates.

8.1 Introduction

We refer to Sections 1.3.2.3 and 1.3.3.3 for an introduction on the lubrication equation for the flow of a thin film on curved substrates and on gravity currents and spreading patterns, respectively.

Different types of spreading are shown in figure 8.1. The configuration (a) is characterized by a diverging spreading on the curved substrate (Takagi and Huppert, 2010; Lee et al., 2016; Balestra et al., 2019). In this case, the drainage solution fairly reproduces the experimental observations since the hydrostatic pressure gradient due to the gravity component orthogonal to the substrate does not induce any instability of the thin film free surface. If the fluid lies below the curved substrate (configuration (b)), then the Rayleigh-Taylor instability occurs (Balestra et al., 2018a,b), and thus the drainage solution destabilizes with the formation of drops and rivulets. The reverse of these two cases, so-called *converging* flows, are reported in figure 8.1(c,d). While configuration (c) is unstable due to the Rayleigh-Taylor instability, configuration (d) is stable. The axisymmetric converging spreading of configuration (d) was recently analyzed in two different works (Xue and Stone, 2021; Lin et al., 2021), with the study of the position, thickness and velocity of the front and finger formation. In this work, we will focus on the diverging geometry, i.e. case (a).

Despite the abundance of studies on spreading in different conditions, the problem of three-dimensional drainage and spreading has been the object of limited studies on flat and axisymmetric substrates (Lister, 1992; Xue and Stone, 2020), to the best of our knowledge. In this perspective, understanding the drainage and spreading processes on complex curved substrates may open to a deeper understanding of fingering instabilities. Indeed, the lubrication equation in general coordinates offers the yet unexplored opportunity to systematically study the three-dimensional drainage and spreading on complex substrates through analytical

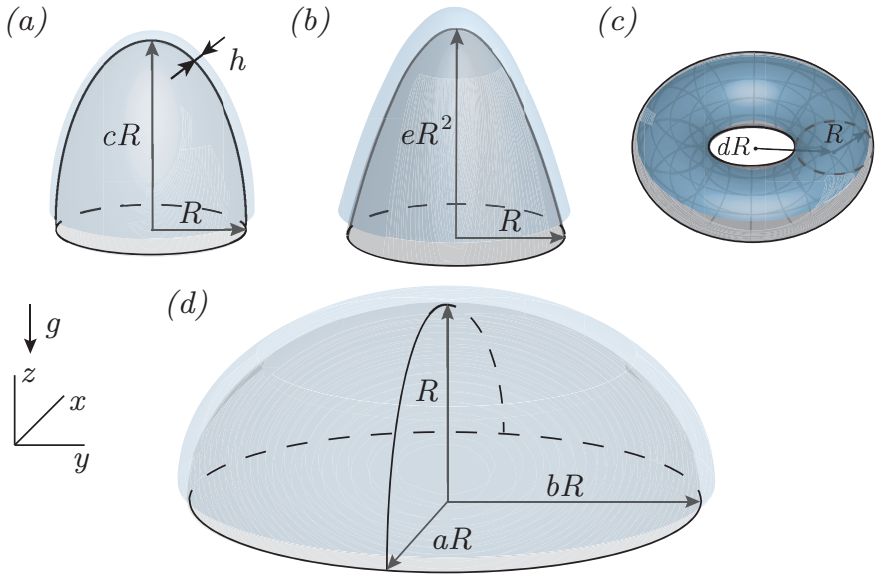

Figure 8.2: Different coated substrates considered in this work: (a) spheroid, (b) paraboloid, (c) torus, (d) ellipsoid.

solutions.

The objective of this Chapter is twofold. We systematically develop analytical solutions and approximations for the drainage and spreading problem on several substrates. We initially recover classical solutions and then focus on axisymmetric substrates whose solution is still unknown. The considered geometries are reported in figure 8.2. As a testing ground for the method, we consider (a) a spheroid (i.e. an ellipsoid with revolution symmetry) of vertical semiaxis (height) cR and equatorial radius R, and (b) a paraboloid of height eR^2 and equatorial radius R. We then study (c) a torus of tube radius R and distance from its rotation axis dR, in which the symmetry of the coating is broken, thus paving the way to the three-dimensional drainage and spreading. In the presence of non-axisymmetric substrates, modulations (*non-uniformities*) of the drainage thickness and the spreading front are expected. The simplest geometry realizing this condition is (d) an ellipsoid with vertical semiaxis R and two different equatorial radii along the x and y directions, respectively, labeled aR and bR. We will consider $b \geq a$, without loss of generality.

The Chapter is organized as follows. In Section 8.2, we introduce the coating problem of a generic substrate and the differential geometry tools necessary to understand the flow configuration. We recover some results for the drainage and spreading on classical substrates by employing different analytical tools. Section 8.3 is devoted to the study of the drainage and spreading on a spheroid and a paraboloid. Subsequently, Section 8.4 studies the problem of non-symmetric drainage and spreading on a torus. We conclude by studying the non-uniform drainage and spreading solution for the ellipsoid, in Section 8.5. Eventually, the analytical and numerical results are compared to experimental measurements.

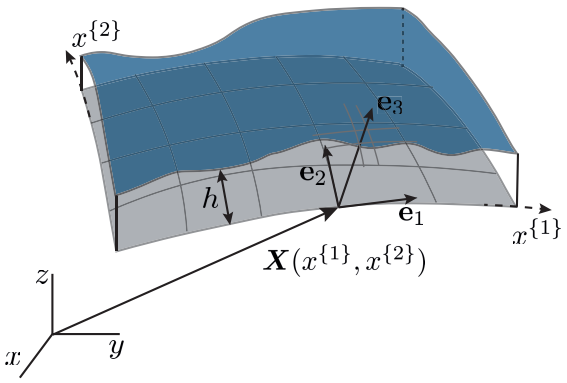

Figure 8.3: Sketch of the coordinates systems employed in this analysis. A global Cartesian reference frame (x, y, z) is considered. At each point, the position of the substrate is identified by the vector $\boldsymbol{X}$, which depends on the chosen parameterization $(x^{\{1\}}, x^{\{2\}})$ of the substrate. The derivatives of the position vector identify the local reference frame on the substrate, on which the lubrication equation is solved.

8.2 The coating problem of a generic substrate

8.2.1 Problem definition and metric terms in general coordinates

In this section, we introduce the essential differential geometry tools to solve the problem of the coating on a generic substrate. Far from being exhaustive, here we define the concept and quantities needed for the lubrication equation. For a complete description of differential geometry and general coordinates, we refer to Deserno (2004). The derivation of the lubrication equation for generic curved substrates can be found in Roy et al. (2002); Thiffeault and Kamhawi (2006) and Wray et al. (2017). We consider a generic substrate $\bar{h}^0$, on which lies a fluid film of thickness $\bar{h}$, and introduce a Cartesian reference frame $(\bar{x}, \bar{y}, \bar{z})$, see figure 8.3. As will become clear afterward, to avoid any confusion between contravariant vectors and powers, the indices indicating contravariant quantities are inside brackets. Since we consider an initial release of fluid of characteristic thickness h_i, we non-dimensionalize the film thickness with the initial one, $\bar{h} = h_i h$. The substrate height and the in-plane directions are instead non-dimensionalized with a characteristic length of the substrate R, e.g. the equatorial radius for solids of revolution: $\bar{h}^0 = R h_0$. Upon non-dimensionalization, the substrate is identified by the position vector $\boldsymbol{X}\left(x^{\{1\}}, x^{\{2\}}\right)$, where $(x^{\{1\}}, x^{\{2\}})$ denote the local coordinates used to parameterize the surface (e.g. the zenith and the azimuth for spherical coordinates, the radial coordinate and the azimuth for a cone). The flow equations are solved in the local and natural reference frame of the substrate. We introduce the local coordinate vectors parallel to the substrate $\mathbf{e}_i = \partial_i \boldsymbol{X}$, $i = 1, 2$ (not necessarily orthonormal), and the normal coordinate vector $\mathbf{e}_3 = \frac{\mathbf{e}_1 \times \mathbf{e}_2}{|\mathbf{e}_1 \times \mathbf{e}_2|}$.

From the knowledge of the local coordinate vectors, we introduce the metric tensor:

$$\mathbb{G}_{ij} = \mathbf{e}_i \cdot \mathbf{e}_j, \tag{8.1}$$

which is symmetric by definition. We introduce the square root of the determinant of the metric on the substrate, which is related to the area element on the surface dA through $dA = w\mathrm{d}x^{\{1\}}\mathrm{d}x^{\{2\}}$ and is defined as:

$$w = \left(\det \mathbb{G}_{ij}\right)^{1/2}. \tag{8.2}$$

The last quantity is also the Jacobian of the transformation that remaps the (x, y, z) coordinates system onto the manifold defined by $\boldsymbol{X}$. We also introduce the second fundamental form and the curvature tensor, which respectively read:

$$\mathbb{S}_{ij} = \partial_i \mathbf{e}_j \cdot \mathbf{e}_3, \quad \mathbb{K}_i^{\{j\}} = \mathbb{S}_{ik}\mathbb{G}^{\{kj\}}, \tag{8.3}$$

where $\mathbb{G}^{\{ij\}}$ is the inverse metric tensor, i.e. $\mathbb{G}^{\{ij\}} = \mathbb{G}_{ij}^{-1}$. The mean $\mathcal{K}$ and the Gaussian $\mathcal{G}$ curvatures are defined from the curvature tensor:

$$\mathcal{K} = \mathrm{tr}\mathbb{K}, \quad \mathcal{G} = \det\mathbb{K}. \tag{8.4}$$

Note that the mean curvature employed here is twice the typical mean curvature defined in differential geometry (Deserno, 2004). Following Einstein's notation for the summation, the generic vector $\mathbf{f}$ can be written in terms of its covariant and contravariant base, i.e. $\mathbf{f} = f^{\{i\}}\mathbf{e}_i = f_i\mathbf{e}^{\{i\}}$, where $\mathbf{e}^{\{i\}}$ is the covector defined as $\mathbf{e}^{\{i\}} \cdot \mathbf{e}_j = \delta_{ij}$. Note that the inverse metric can be evaluated from the contravariant base following the definition $\mathbb{G}^{\{ij\}} = \mathbf{e}^{\{i\}} \cdot \mathbf{e}^{\{j\}}$. The gravity vector reads $\rho g\mathbf{g}$, where g is the acceleration of gravity and $\mathbf{g}$ is the unit vector defining its orientation in the (x, y, z) coordinate system. The two contravariant components parallel to the substrate read $g_t^{\{i\}} = \mathbf{g}\cdot\mathbf{e}^{\{i\}}$, while the normal one reads $g_3 = \mathbf{g}\cdot\mathbf{e}_3$. Starting from the knowledge of the above-defined metric and vector quantities, we now introduce the differential operators along the substrate. The gradient of a scalar function is defined as (Irgens, 2019):

$$\nabla(\cdot) = \partial_i(\cdot)\mathbb{G}^{\{ij\}}\mathbf{e}_j = \partial^{\{i\}}(\cdot)\mathbf{e}_j, \tag{8.5}$$

and the divergence of a generic vector $\mathbf{f} = f^{\{i\}}\mathbf{e}_i$ reads

$$\nabla\cdot(\mathbf{f}) = w^{-1}\partial_i(wf^{\{i\}}). \tag{8.6}$$

The above-defined quantities and differential operators are enough to describe the coating problem on a generic substrate, introduced in the following section.

8.2.2 Lubrication equation and drainage solution

We consider a thin viscous film, flowing on a substrate $\bar{h}^0$, of thickness $\bar{h}$ measured along the direction perpendicular to the substrate itself. The fluid properties are the density ρ, viscosity μ and the surface tension coefficient γ. In the absence of inertia, the lubrication model for a generic curved substrate was first derived by (Roy et al., 2002) via central manifold theory:

$$(1-\bar{\mathcal{K}}\bar{h}+\bar{\mathcal{G}}\bar{h}^2)\frac{\partial \bar{h}}{\partial \bar{t}}+\frac{1}{3}\bar{\nabla}\cdot\bar{\mathbf{q}}=0, \tag{8.7}$$

where $\bar{\mathbf{q}}=\bar{q}^{\{1\}}\mathbf{e}_1+\bar{q}^{\{2\}}\mathbf{e}_2$ is the flux. At order $\mathcal{O}(\epsilon^4)$ for the separation of scales parameters $\epsilon=L_n/L_t$ between the normal L_n and tangential L_t to the substrate characteristic lengths, the dimensional equation in coordinate-free form reads (Roy et al., 2002; Howell, 2003; Roberts and Li, 2006; Thiffeault and Kamhawi, 2006):

$$\begin{aligned}(1-\bar{\mathcal{K}}\bar{h}+\bar{\mathcal{G}}\bar{h}^2)\frac{\partial \bar{h}}{\partial \bar{t}}+\frac{\gamma}{3\mu}\bar{\nabla}\cdot\left[\bar{h}^3\left(\bar{\nabla}\bar{\tilde{\kappa}}-\frac{1}{2}\bar{h}(2\bar{\mathcal{K}}\mathbb{I}-\bar{\mathbb{K}})\cdot\bar{\nabla}\bar{\mathcal{K}}\right)\right]\\ +\frac{\rho g}{3\mu}\bar{\nabla}\cdot\left[\bar{h}^3\left(\bar{\boldsymbol{g}}_t-\bar{h}\left(\bar{\mathcal{K}}\mathbb{I}+\frac{1}{2}\bar{\mathbb{K}}\right)\cdot\bar{\boldsymbol{g}}_t+\bar{\mathrm{g}}_3\bar{\nabla}\bar{h}\right)\right]=0,\end{aligned} \tag{8.8}$$

where $\bar{\boldsymbol{g}}_t$ and $\bar{\mathrm{g}}_3$ identify the unit gravity vector components tangent and normal to the substrate, respectively, and $\bar{\tilde{\kappa}}=\bar{\mathcal{K}}+(\bar{\mathcal{K}}^2-2\bar{\mathcal{G}})\bar{h}+\bar{\nabla}^2\bar{h}$ is the free surface curvature. Beyond the classical physical limitations of the lubrication model (Roy et al., 2002), an important geometrical restriction limits the range of admissible thicknesses depending on the convexity of the substrate. The well-posedness of the problem in the fluid layer relies on the absence of intersection of coordinate lines, which can be formalized by introducing the principal curvatures k_1, k_2 (Thiffeault and Kamhawi, 2006):

$$h<\left(\max\left(k_1,k_2,0^+\right)\right)^{-1},\quad k_{1,2}=\frac{1}{2}\left(\mathcal{K}\pm\left(\mathcal{K}^2-4\mathcal{G}\right)^{1/2}\right) \tag{8.9}$$

The configurations employed in this work are always characterized by negative principal curvatures and thus there is no restriction on the thickness value. We non-dimensionalize the equations by considering $\bar{h}=h_i h$ and$\bar{h}^0=Rh_0$. We introduce the drainage time scale:

$$\tau=\frac{\mu R}{\rho g h_i^2}. \tag{8.10}$$

Upon non-dimensionalization, the thin film equation reads:

$$\begin{aligned}(1-\delta\mathcal{K}h+\delta^2\mathcal{G}h^2)\frac{\partial h}{\partial t}+\frac{1}{3Bo}\nabla\cdot\left[h^3\left(\nabla\tilde{\kappa}-\frac{\delta}{2}h(2\mathcal{K}\mathbb{I}-\mathbb{K})\cdot\nabla\mathcal{K}\right)\right]\\ +\frac{1}{3}\nabla\cdot\left[h^3\left(\boldsymbol{g}_t-\delta h\left(\mathcal{K}\mathbb{I}+\frac{1}{2}\mathbb{K}\right)\cdot\boldsymbol{g}_t+\delta\mathrm{g}_3\nabla h\right)\right]=0,\end{aligned} \tag{8.11}$$

where $\tilde{\kappa}=\mathcal{K}+\delta(\mathcal{K}^2-2\mathcal{G})h+\delta\nabla^2 h$, $Bo=(\rho g R^2)/\gamma$ is the Bond number, and $\delta=h_i/R$.

The so-called drainage solution is identified in the limit $\delta \ll 1$ and when the Bond number is very large $Bo \to \infty$, and results from the following problem:

$$\frac{\partial h}{\partial t} + \frac{1}{3}\nabla \cdot \left[h^3 \boldsymbol{g}_t\right] = 0. \tag{8.12}$$

In this case, the flux per unit length is defined as $\mathbf{q} = q^{\{1\}}\mathbf{e}_1 + q^{\{2\}}\mathbf{e}_2 = h^3 g_t^{\{1\}}\mathbf{e}_1 + h^3 g_t^{\{2\}}\mathbf{e}_2$. In the absence of flux through the boundaries of the domain, the equation states the conservation of the total volume of the fluid. Equation (8.13) can be re-written in components:

$$\frac{\partial h}{\partial t} + \frac{1}{3w}\partial_i \left[w h^3 g_t^{\{i\}} \right] = 0. \tag{8.13}$$

Therefore, the solution of the drainage problem requires only the knowledge of w and the tangential gravity vector components $g_t^{\{i\}}$.

The numerical implementation of the lubrication equation is performed in the finite-element solver COMSOL Multiphysics, in which the lubrication equation is implemented in its conservation form. Quadratic lagrangian elements are exploited for the numerical discretization, while the time-marching is performed with the built-in BDF solver. In the case of equation (8.11), we solve for the variables $(h, \tilde{\kappa})$. We refer to the corresponding sections for more detail about the boundary conditions for the different substrates.

The validation procedure consists of a first mesh size validation. We thus verify the faithfulness of the employed parameterization $\boldsymbol{X}(x^{\{1\}}, x^{\{2\}})$ by a comparison with the parameterization $\boldsymbol{X} = (x, y, h^0(x, y))$, so-called Monge parameterization (Thiffeault and Kamhawi, 2006; Mayo et al., 2015). We also verify the non-dimensionalization by solving the dimensional equation (8.11) and comparing the solution for each substrate with the non-dimensional model. To illustrate and complement the theoretical results, we finally compare in Section 8.6 the drainage problem results to experiments performed following the procedure outlined in Lee et al. (2016) and Jones et al. (2021), for diverse substrates.

In the following, we focus on the drainage solution and derive several analytical expressions for different substrates. We first show the suitability of the model in general coordinates to recover previous literature results and we then study more complex substrates.

8.2.3 Classical drainage and spreading solutions: diverging flow on a sphere, a cylinder and a cone

We initially consider the coating of an initially uniform layer of fluid on a sphere of radius R, recently analyzed by Takagi and Huppert (2010); Lee et al. (2016) and Qin et al. (2021). In non-dimensional form, the parameterization of the spherical surface through the zenith (or colatitude) $x^{\{1\}} = \vartheta$ and azimuth $x^{\{2\}} = \varphi$ reads:

$$\boldsymbol{X}(\vartheta, \varphi) = (\sin\vartheta\cos\varphi, \sin\vartheta\sin\varphi, \cos\vartheta) \tag{8.14}$$

The gravity components tangent to the substrate and w respectively read:

$$g_t^{\{1\}}(\vartheta) = \sin(\vartheta), \quad g_t^{\{2\}} = 0, \quad w(\vartheta) = \sin(\vartheta). \tag{8.15}$$

The drainage problem can be written as follows:

$$\frac{\partial h(\vartheta,t)}{\partial t} + \frac{1}{3w(\vartheta)}\frac{\partial}{\partial \vartheta}\left(g_t^{\{1\}}(\vartheta)w(\vartheta)h(\vartheta,t)^3\right) = 0 \rightarrow \frac{\partial h}{\partial t} + \frac{1}{3\sin(\vartheta)}\frac{\partial}{\partial \vartheta}\left(\sin^2(\vartheta)h^3\right) = 0. \tag{8.16}$$

The problem admits a large-time solution by separation of variables, independent of the initial condition (Couder et al., 2005; Qin et al., 2021):

$$h(z,t) = \eta(z)t^{-1/2}, \quad z = \cos(\vartheta), \tag{8.17}$$

where

$$\eta(z) = \frac{[f(1) - f(z)]^{1/2}}{\left(1-z^2\right)^{1/3}}, \quad f(z) = z\mathrm{Hy}\left(\frac{1}{3}, \frac{1}{2}; \frac{3}{2}; z^2\right), \tag{8.18}$$

where Hy is the hypergeometric function. Takagi and Huppert (2010), with a scaling analysis around the pole, found that $h \approx \sqrt{\frac{3}{4}}t^{-1/2}$. A more formal approach which gives the solution at different orders in ϑ for a generic initial condition, was proposed by Lee et al. (2016) through an asymptotic expansion of equation (8.16) around the pole, i.e. $h(\vartheta,t) = H_0(t) + \vartheta H_1(t) + \vartheta^2 H_2(t) + ...$, leading to the following solution, truncated at $\mathcal{O}(\vartheta^2)$:

$$h(\vartheta,t) \approx \frac{1}{\sqrt{1+\frac{4}{3}t}}\left[1 + \frac{\vartheta^2}{10}\left(1 + C\left(1+\frac{4}{3}t\right)^{-5/2}\right)\right] + \mathcal{O}(\vartheta^4), \tag{8.19}$$

where the constant C depends on the initial condition. Note that the odd terms in the asymptotic expansion are zero because of the symmetry with respect to $\vartheta = 0$. When $t \rightarrow \infty$, the term that multiplies C vanishes, at the leading order. The leading-order large-time solution at order $\mathcal{O}(\vartheta^6)$ reads:

$$h(\vartheta,t) = \sqrt{\frac{3}{4t}}\left(1 + \frac{\vartheta^2}{10} + \frac{41\vartheta^4}{4800} + \frac{1187\vartheta^6}{1584000}\right) + \mathcal{O}(\vartheta^8) + \mathcal{O}\left(\frac{1}{t^{3/2}}\right). \tag{8.20}$$

The large-time solution is thus independent of the initial condition and has a time dependence analogous to the one obtained by Takagi and Huppert (2010) and Qin et al. (2021). The resulting zenith dependence is also an approximation of the hypergeometric function. In figure 8.4(a), the various orders large-time analytical solutions show a good agreement with the numerical solution of equation (8.16). As a consequence, the asymptotic expansion around the pole appears to be suitable to obtain analytical approximations of the exact solution which, in more complicated geometries, may be not straightforward to obtain.

Typical coating applications involve the spreading of an initial volume of fluid located close to the top of the considered geometry (Takagi and Huppert, 2010). Here, following previous works (Huppert, 1982a), we recover some typical relevant quantities such as the position and

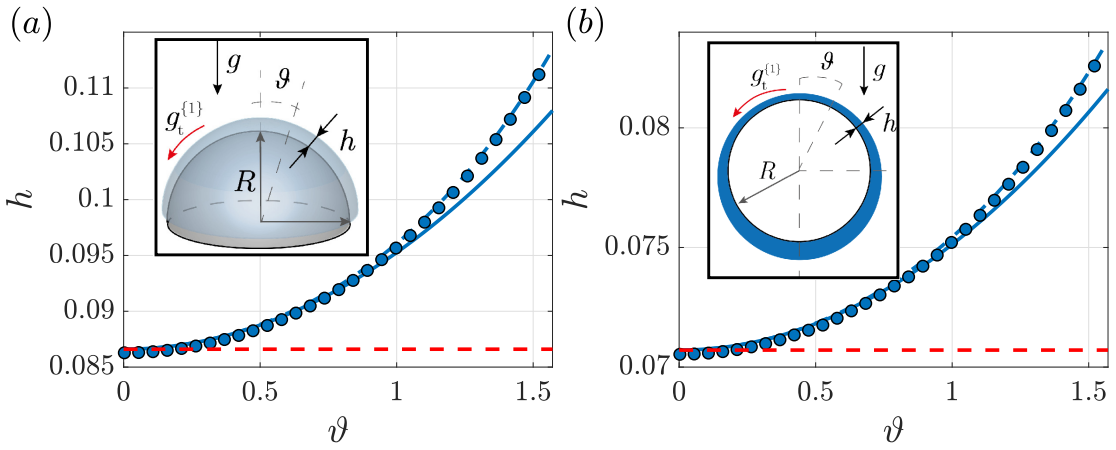

Figure 8.4: (a) Coating on a sphere: film thickness as a function of the zenith ϑ at $t = 100$, numerical simulation (dots), large-time analytical solution at order $\mathcal{O}(1)$ (red dashed line), $\mathcal{O}(\vartheta^2)$ (solid line) and $\mathcal{O}(\vartheta^6)$ (blue dashed line). (b) Coating on a cylinder: film thickness as a function of the zenith ϑ at $t = 300$, numerical simulation (dots), large-time analytical solution at order $\mathcal{O}(1)$ (red dashed line), $\mathcal{O}(\vartheta^2)$ (solid line) and $\mathcal{O}(\vartheta^6)$ (blue dashed line).

thickness of the spreading front. An initial volume of fluid V is released on the substrate. We impose the conservation of mass in general coordinates:

$$\int\int_{\mathbb{S}} h(x^{\{1\}}, x^{\{2\}}, t)\, w \mathrm{d}x^{\{1\}} \mathrm{d}x^{\{2\}} = V, \tag{8.21}$$

where V is the initial volume released on the substrate and $\mathbb{S}$ is the region of the substrate, parameterized with $(x^{\{1\}}, x^{\{2\}})$, in which the volume of fluid is contained, which varies with time because of the moving front. Far from the contact line, the typical drainage solution $h(x^{\{1\}}, x^{\{2\}}, t)$ can be employed, while capillary effects are relevant only in the close vicinity of the front (Huppert, 1982a). For a fixed substrate geometry, w is known, and thus relation (8.21) is an implicit equation with unknown the front position. A typical assumption to simplify the analysis is the employment of the large-time drainage solution. We now consider the case of the spreading on a sphere (of radius R) of an initial mass of fluid of thickness $h_i = 1$, contained in the region $\vartheta < \vartheta_0$, $0 < \varphi < 2\pi$. Substituting the $\mathcal{O}(\vartheta)$ approximation of equation (8.19) and $w \approx \vartheta$ into equation (8.21), one finds the following expressions for the front angle $\vartheta_F(t)$ and the thickness at the front $h_F(\vartheta(t))$:

$$\frac{\vartheta_F}{\vartheta_0} = \left(\frac{4}{3}t\right)^{1/4}, \quad h_F = \left(\frac{\vartheta_0}{\vartheta_F}\right)^{1/2}, \tag{8.22}$$

which is the non-dimensional version of the results reported in Takagi and Huppert (2010).

In the case of the coating on a cylinder of radius R, the non-dimensional parameterization reads:

$$\boldsymbol{X} = (\sin\vartheta, y, \cos\vartheta), \tag{8.23}$$

The tangential gravity component and w read:

$$g_t^{\{1\}} = \sin(\vartheta), \quad g_t^{\{2\}} = 0, \quad w = 1. \tag{8.24}$$

The drainage problem reads:

$$\frac{\partial h}{\partial t} + \frac{1}{3}\frac{\partial}{\partial \vartheta}\left(\sin(\vartheta) h^3\right) = 0. \tag{8.25}$$

Performing an asymptotic expansion around the pole in powers of ϑ, the large-time solution reads (Balestra et al., 2019):

$$h(\vartheta, t) = \sqrt{\frac{3}{2t}}\left(1 + \frac{\vartheta^2}{16} + \frac{43\vartheta^4}{10752} + \frac{109\vartheta^6}{368640}\right) + \mathcal{O}(\vartheta^8) + \mathcal{O}\left(\frac{1}{t^{3/2}}\right), \tag{8.26}$$

whose $\mathcal{O}(1)$ approximation correspond to the result of Takagi and Huppert (2010). Note that the large-time solution is independent of the initial condition, and is in good agreement with the numerical solution of equation (8.25) (see figure 8.4(b)). Takagi and Huppert (2010) also studied the spreading on a cylinder. Following the same steps adopted for the case of the sphere, one obtains the following expressions for the front angle and thickness:

$$\frac{\vartheta_F}{\vartheta_0} = \left(\frac{2t}{3}\right)^{1/2}, \quad h_F = \frac{\vartheta_0}{\vartheta_F}. \tag{8.27}$$

We conclude by considering the classical problem of the coating on a conical substrate, of maximum radius R and height aR. This problem is typically solved by employing a self-similar approach. A large-time solution can be obtained, similar to Qin et al. (2021) for the sphere coating. We consider a parameterization in cylindrical coordinates, which reads, in non-dimensional form:

$$\boldsymbol{X} = (r\cos\varphi, r\sin\varphi, -ar), \tag{8.28}$$

where r is the radius and φ is the azimuth. In this parameterization, the gravity terms and w read:

$$g_t^{\{1\}} = \frac{a}{a^2+1}, \quad g_t^{\{2\}} = 0, \quad w(r) = \sqrt{\left(a^2+1\right)}r \tag{8.29}$$

The lubrication equation reads:

$$\frac{\partial h(r,t)}{\partial t} + \frac{1}{3\sqrt{\left(a^2+1\right)}r}\frac{\partial}{\partial r}\left(\sqrt{\left(a^2+1\right)}r\, g_t^{\{1\}}(r) h(r,t)^3\right) = 0 \tag{8.30}$$

Developing the derivatives, one obtains:

$$\frac{\partial h}{\partial t} + \frac{ah^2}{a^2+1}\frac{\partial h}{\partial r} + \frac{ah^3}{3a^2r+3r} = 0, \tag{8.31}$$

which is completed with the initial condition $h(r,0) = 1$. This problem admits a self-similar solution of the form $h(r,t) = f(\eta)$, where $\eta = t/r$ is the self-similar variable. By substituting the

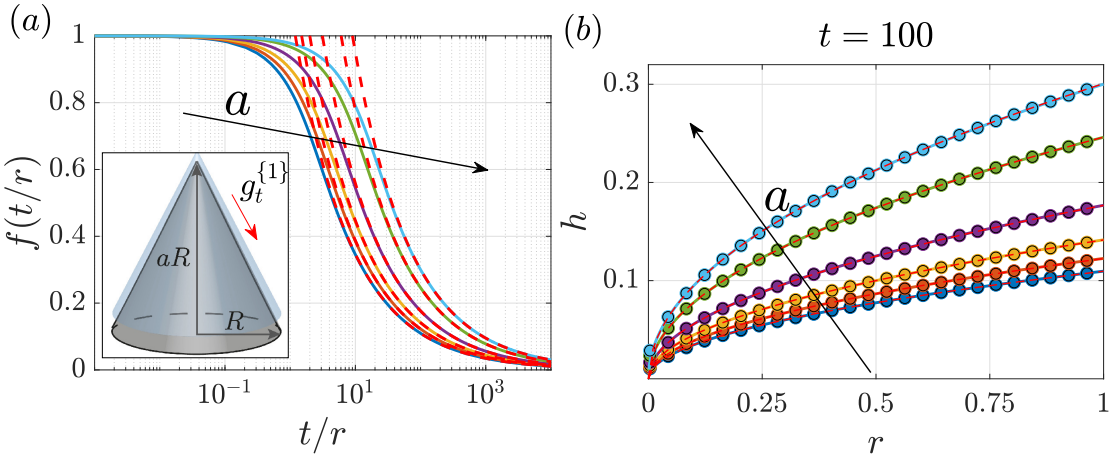

Figure 8.5: (a) Self-similar solution for the coating of a cone $h(r,t) = f(\eta)$ as a function of $\eta = t/r$, for different values of a. The red dashed lines denote the corresponding large-time approximation. (b) Comparison at $t = 100$ between the numerical (colored dots) self-similar (solid lines) and large-time (red dashed lines) solutions. The different colors correspond to $a = 1$ (blue), $a = 2$ (orange), $a = 3$ (yellow), $a = 5$ (purple), $a = 10$ (green), $a = 15$ (cyan).

self-similar ansatz in equation (8.31), one obtains the following ordinary differential equation:

$$f'\left(1 - \frac{a}{1+a^2}\eta f^2\right) + \frac{1}{3}\frac{a}{1+a^2}f^3 = 0, \quad f(0) = 1, \tag{8.32}$$

which can be numerically solved so as to find the solution of the initial value problem. The results are reported in figure 8.5. Moreover,the following expression satisfies equation (8.32):

$$f(\eta) = f_0\eta^{-1/2}, \quad f_0 = \sqrt{\frac{3(a^2+1)}{5a}} \rightarrow h(r,t) = \sqrt{\frac{3(a^2+1)}{5a}}\sqrt{\frac{r}{t}}. \tag{8.33}$$

The latter expression is well known in literature (Acheson, 1990) and well agrees with the numerical self-similar solution as $\eta \rightarrow \infty$, i.e. $t \rightarrow \infty$ or $r \rightarrow 0$ (see figure 8.5). The large-time solution is thus independent of the initial condition.

In analogy to the previous cases, the spreading of an initial mass of fluid of height $h_i = 1$ contained in a region $r < r_0$ can be solved by employing the large-time solution: (8.33):

$$h(r,t) = \sqrt{\frac{3(a^2+1)}{5a}}\sqrt{\frac{r}{t}}, \quad w(r) = \sqrt{\left(a^2+1\right)}r. \tag{8.34}$$

Upon integration in $0 < \varphi < 2\pi$ and $0 < r < r_N$, one obtains the radial position of the front r_N:

$$r_N = \left(\frac{125V^2}{48\pi^2}\frac{a}{(a^2+1)^2}\right)^{1/5} t^{1/5}, \tag{8.35}$$

where $V = \pi r_0^2\sqrt{a^2+1}$ is the initial volume. Noting that $\frac{a}{(a^2+1)^2} = \sin^3(\beta)\cos(\beta)$, where β

is the inclination angle of the cone and the spreading distance from the tip of the cone is $s_N = r_N/\sin(\beta)$, one obtains the classical result for the spreading on a cone (Acheson, 1990):

$$s_N = \left(\frac{125V^2}{48\pi^2}\frac{\cos\beta}{\sin^2\beta}\right)^{1/5} t^{1/5}, \tag{8.36}$$

In this section, we recovered several classical drainage and spreading solutions by employing a systematic approach based on differential geometry and general coordinates, which shows great potential for these kinds of problems. In the following, we systematically study the coating of different geometries by employing the above-described methods. We initially consider the axisymmetric substrates reported in figure 8.2(a,b).

8.3 Drainage and spreading on axisymmetric substrates

8.3.1 Spheroid

8.3.1.1 Drainage problem

In this section, we consider the drainage of a thin film flowing on an spheroidal substrate of equatorial radius R (i.e. $a = b = 1$) and height cR. We non-dimensionalize the in-plane directions and substrate variables with the equatorial radius R. We parameterize the spheroidal surface via the zenith (or colatitude) ϑ and the azimuth φ:

$$\boldsymbol{X}(\vartheta,\varphi) = (\sin\vartheta\cos\varphi, \sin\vartheta\sin\varphi, c\cos\vartheta) \tag{8.37}$$

The gravity term $g_t^{\{1\}}$ and w are:

$$g_t^{\{1\}}(\vartheta) = \frac{c\sin(\vartheta)}{c^2\sin^2(\vartheta)+\cos^2(\vartheta)} \tag{8.38}$$

$$w(\vartheta) = \frac{\sqrt{\sin^2(\vartheta)(-((c^2-1)\cos(2\vartheta)-c^2-1))}}{\sqrt{2}} \tag{8.39}$$

The lubrication equation for the drainage solution reads:

$$\frac{\partial h(\vartheta,t)}{\partial t} + \frac{1}{3w(\vartheta)}\frac{\partial}{\partial\vartheta}\left(g_t^{\{1\}}(\vartheta)\,w(\vartheta)\,h(\vartheta,t)^3\right) = 0 \tag{8.40}$$

We consider as initial condition a constant thickness on the substrate, i.e. $h(\vartheta,0) = 1$. In analogy with the coating problem on a sphere reported in the previous section, the problem is solved through an asymptotic expansion in the vicinity of the pole. We expand the solution at different orders in ϑ:

$$h(\vartheta,t) = H_0(t) + \vartheta^2 H_2(t) + \vartheta^4 H_4(t) + \vartheta^6 H_6(t) + \ldots \tag{8.41}$$

We introduce this ansatz in equation (8.40), and expand in powers of ϑ. At each order $\mathcal{O}(\vartheta^n)$, one obtains an ordinary differential equation for H_n. The problem at order $\mathcal{O}(1)$ reads:

$$\frac{2}{3}cH_0^3 + H_0' = 0, \quad H_0(0) = 1, \tag{8.42}$$

whose associated solution is

$$H_0 = \frac{1}{\sqrt{\frac{4ct}{3}+1}}. \tag{8.43}$$

The equation at order $\mathcal{O}(\vartheta^2)$ reads:

$$(\frac{2c}{3} - c^3)H_0^3 + 4cH_0^2H_2 + H_2' = 0, \quad H_2(0) = 0, \tag{8.44}$$

whose associated solution is

$$H_2 = \frac{(3c^2-2)(64\sqrt{3}c^3t^3 + 144\sqrt{3}c^2t^2 + 108\sqrt{3}ct + 27(\sqrt{3} - \sqrt{4ct+3}))}{10(4ct+3)^{7/2}}. \tag{8.45}$$

The solution up to $\mathcal{O}(\vartheta^2)$ thus reads:

$$h(\vartheta,t) = H_0 + \vartheta^2 H_2 + \mathcal{O}(\vartheta^4) = \frac{1}{\sqrt{\frac{4ct}{3}+1}}\left(1 - \frac{(3c^2-2)(9\sqrt{3} - (4ct+3)^{5/2})}{10(4ct+3)^{5/2}}\vartheta^2\right) + \mathcal{O}(\vartheta^4). \tag{8.46}$$

At large times, the solution simplifies to

$$h(\vartheta,t) = H_0 + \vartheta^2 H_2 + \mathcal{O}(\vartheta^4) = \frac{\left(\sqrt{3}\sqrt{\frac{1}{t}}((3c^2-2)\vartheta^2 + 10)\right)}{20\sqrt{c}} + \mathcal{O}(\vartheta^4) + \mathcal{O}\left(\frac{1}{t^{3/2}}\right) \quad \text{for } t \to \infty \tag{8.47}$$

Applying the same procedure at orders $\mathcal{O}(\vartheta^4)$ and $\mathcal{O}(\vartheta^6)$, the solution up to $\mathcal{O}(\vartheta^6)$, for $t \to \infty$, reads (see Appendix 8.8.1 for further detail):

$$h(\vartheta,t) = \sqrt{\frac{3}{4\mathrm{t}}}\frac{1}{\sqrt{c}}\left(1 + \frac{1}{10}\left(3c^2-2\right)\vartheta^2 - \frac{\left(336c^4 - 408c^2 + 31\right)\vartheta^4}{4800} + \frac{\left(58464c^6 - 115368c^4 + 62667c^2 - 4576\right)\vartheta^6}{1584000}\right) + \mathcal{O}(\vartheta^8) + \mathcal{O}\left(\frac{1}{t^{3/2}}\right) \tag{8.48}$$

Note that the $\mathcal{O}(1)$ large-time solution can be re-written as

$$H_0 = \left(\frac{3}{2\mathcal{K}_p t}\right)^{1/2} + \mathcal{O}\left(\frac{1}{t^{3/2}}\right), \tag{8.49}$$

where $\mathcal{K}_p = 2c$ is the absolute value of the mean curvature at the pole.

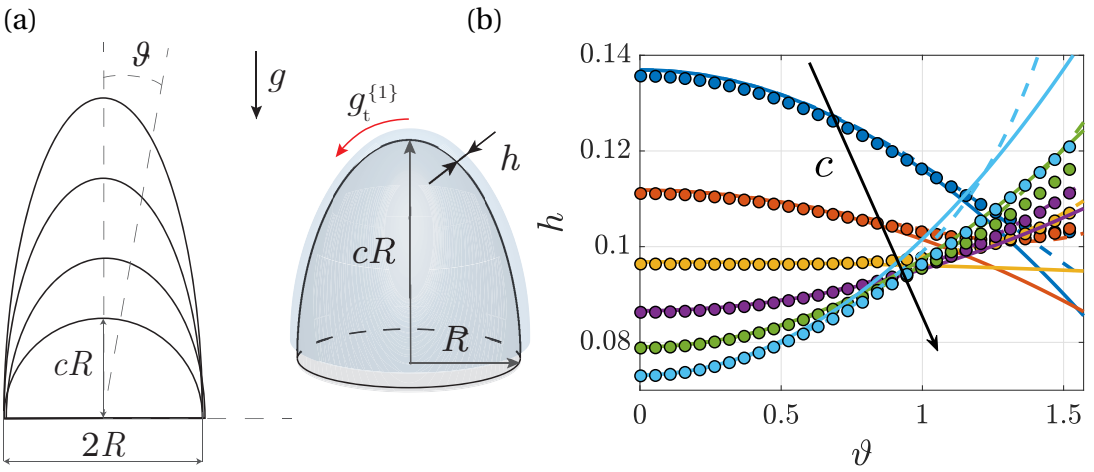

Figure 8.6: (a) Sketch of the spheroidal substrate with varying c. (b) Comparison of the numerical solution at $t = 100$ of equation (8.40) (colored dots) with the analytical ones at order $\mathcal{O}(\vartheta^2)$ (solid lines) and $\mathcal{O}(\vartheta^6)$ (dashed lines). Different colours identify different values of c: $c = 0.4$ (blue), $c = 0.6$ (orange), $c = 0.8$ (yellow), $c = 1$ (purple), $c = 1.2$ (green), $c = 1.4$ (cyan).

We perform numerical simulations of equation (8.40), in the region $0 < \vartheta < \pi/2$. Owing to the hyperbolic nature of the equation, no boundary conditions are necessary at $\vartheta = 0$ and $\vartheta = \pi/2$, and thus we impose only the initial condition $h(\vartheta, 0) = 1$. We verified the faithfulness of the results by a comparison with the same equation solved in the region $0 < \vartheta < (3/4)\pi$ and with the complete model equation (8.11) solved in the domain $0 < \vartheta < \pi$ with a zero flux boundary condition at $\vartheta = \pi$ and parameters $Bo = 10000$ and $\delta = 10^{-4}$. Numerical convergence is achieved with the characteristic element size $\Delta\vartheta = 1°$. Figure 8.6 shows a comparison of the numerical solution of equation (8.40) at $t = 100$ with the analytical ones at order at order $\mathcal{O}(\vartheta^2)$ (solid lines) and $\mathcal{O}(\vartheta^6)$ (dashed lines), which shows an overall good agreement. The solution at order $\mathcal{O}(\vartheta^6)$ gives a better agreement with the numerics in a larger range of ϑ. For $c > 1.2$, the numerical and analytical solutions start to deviate for $\vartheta > 60°$. The agreement with the solution at second order is good in most cases for $\theta < 60°$. The second order term in equation (8.48) simplifies when $c^* = \sqrt{2/3} \approx 0.81$. Under these conditions, the solution at $\mathcal{O}(\vartheta^2)$ is constant along the zenith. The solution at order $\mathcal{O}(\vartheta^6)$ does not admit a constant solution. However, the minimum variation of its integral in the region $0 < \vartheta < \pi/2$, with respect to the constant value given by employing $H_0(t)$, is obtained for $c^* \approx 0.74$. Independently of the considered order of the solution, for smaller (respectively higher) values of c the thickness is lower (respectively higher) than the value at the pole. Moreover, for $c < c^*$, the numerical solution and the analytical one at order $\mathcal{O}(\vartheta^6)$ present a non-monotonous behavior, as shown in figure 8.6 for $c = 0.4, 0.6$. An initial decrease of the thickness with ϑ is followed by a slight increase for $\vartheta > 70°$. The solutions for $c > c^*$ monotonically increase.

The leading order large time analytical solution presents a temporal decay $h \sim t^{-1/2}$. The spherical case is recovered by imposing $c = 1$ (Couder et al., 2005; Lee et al., 2016; Qin et al., 2021), see Section 8.2.3. The large-time solution is independent of the initial thickness h_i.

At the pole, smaller values of c imply a reduction of the gravity component parallel to the substrate. Therefore, it is expected that, at the same time, the thickness decreases with c, in the vicinity of the pole. The drainage solution in spheroids of height much smaller than the equatorial radius is characterized by a decreasing thickness, and vice versa. The different behaviors of the thickness moving away from the pole are explained considering how the flux per unit length perturb the $\mathcal{O}(1)$ solution. The divergence of the flux along the zenith direction reads

$$\frac{1}{w}\partial_1(w g_t^{\{1\}} h^3) \approx \frac{H_0^3}{w}\partial_1(w g_t^{\{1\}}) = \left(\frac{3}{4ct}\right)^{3/2}\left(2c - c\left(3c^2-2\right)\vartheta^2 + \mathcal{O}(\vartheta^4)\right). \tag{8.50}$$

Therefore, for $c < c^*$, the flux increases moving away from the pole, and vice versa for $c > c^*$. An increase (respectively decrease) of the flux thus leads to a decrease (respectively increase) of the thickness (with respect to the $\mathcal{O}(1)$ solution) at larger ϑ since the fluid downstream is transported faster (respectively slower) than the fluid upstream. The non-monotonous behaviors at large ϑ for $c < c^*$ are related to higher order terms.

8.3.1.2 Spreading problem

We now consider an initial volume of fluid of constant height $h_i = 1$ released at $t = 0$ in the region $0 < \varphi < 2\pi$, $0 < \vartheta < \vartheta_0$. Owing to the invariance along the azimuthal direction, the conservation of the initial fluid volume (equation (8.21)) reads:

$$\int_0^{2\pi}\int_0^{\theta_F(t)} h(\vartheta,t)\,w(\vartheta)\mathrm{d}\vartheta\mathrm{d}\varphi = \int_0^{2\pi}\int_0^{\theta_0} 1\,w(\vartheta)\mathrm{d}\vartheta\mathrm{d}\varphi$$
$$\rightarrow \int_0^{\theta_F(t)} h(\vartheta,t)\,w(\vartheta)\mathrm{d}\vartheta = \int_0^{\theta_0} 1\,w(\vartheta)\mathrm{d}\vartheta, \tag{8.51}$$

where $\vartheta_F(t)$ is the front angle; the analytical expression (8.48) for $h(\vartheta,t)$ is employed. Equation (8.51) is numerically solved in Matlab via the built-in function "fsolve". Figure 8.7(a) shows the evolution of the front angle ϑ_F with time, for different values of ϑ_0 and c. An increase in ϑ_0 leads to larger values of ϑ_F, for fixed time. At low times, an increase in c leads to larger ϑ_F; however, at large times, the opposite behavior is observed. In figure 8.7 we report the thickness at the front $h_F = h(\vartheta_F(t),t)$, which presents slight variations with c.

We approximate these analytical results by considering an expansion for $\vartheta \ll 1$:

$$h(\vartheta,t) = \sqrt{\frac{3}{4\mathrm{t}}}\frac{1}{\sqrt{c}} + \mathcal{O}(\vartheta^2) + \mathcal{O}\left(\frac{1}{t^{3/2}}\right), \quad w(\vartheta) = \vartheta + \mathcal{O}(\vartheta^2). \tag{8.52}$$

In this case, keeping at most $\mathcal{O}(\vartheta)$ terms, both the RHS and LHS of equation (8.51) can be analytically integrated and an explicit relation for ϑ_F is found:

$$\sqrt{\frac{3}{4\mathrm{t}}}\frac{1}{\sqrt{c}}\frac{\vartheta_F^2}{2} = \frac{\vartheta_0^2}{2} \rightarrow \vartheta = \vartheta_0\left(\frac{4ct}{3}\right)^{1/4}. \tag{8.53}$$

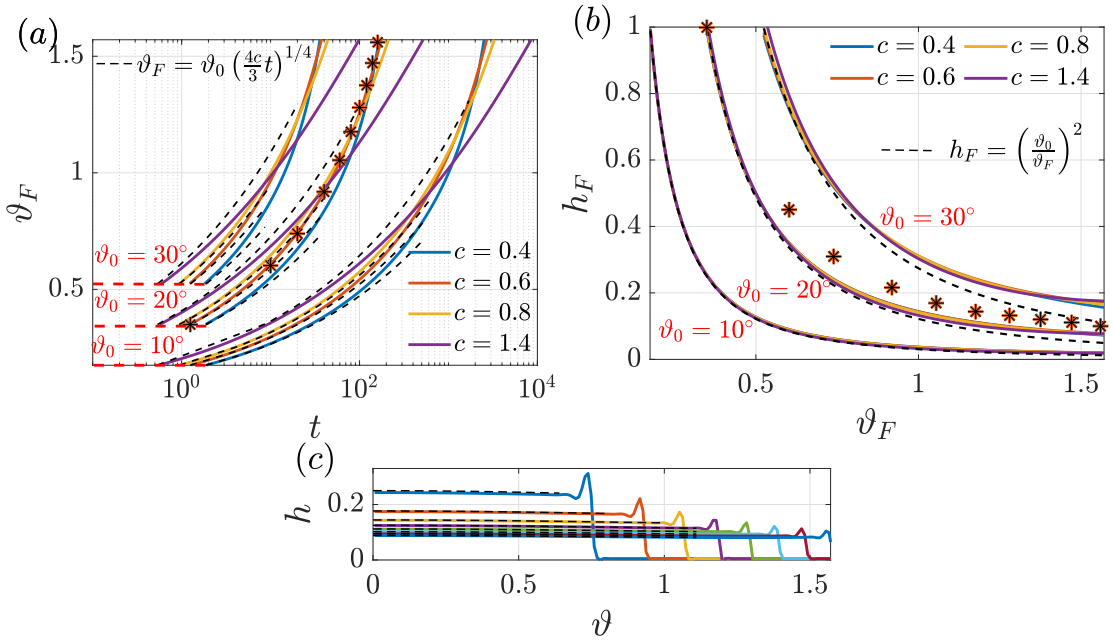

Figure 8.7: Spreading of an initial volume of fluid on an spheroid. (a) Variation of the front angle ϑ_F with time and (b) of the thickness at the front h_F with ϑ_F, for different values of c (coloured lines) and ϑ_0 (different clusters of curves). The black dashed lines correspond to the analytical approximation of the relation $\vartheta_F(t)$ and $h_F(\vartheta_F)$, while the stars are the values recovered by a numerical simulation of the complete model with $c = 0.6$, $Bo = 500$, $\delta = 10^{-3}$. (c) Numerical thickness distribution obtained from the complete model with $c = 0.6$, $Bo = 500$, $\delta = 10^{-3}$ as a function of ϑ at different times: $t = 20$ (blue), $t = 40$ (orange), $t = 60$ (yellow), $t = 80$ (purple), $t = 100$ (green), $t = 120$ (cyan), $t = 140$ (maroon), $t = 160$ (black). The black dashed lines denote the corresponding leading order large time drainage solution.

Note that this expression with $c = 1$ coincides with the solution on a sphere (8.22) found by Takagi and Huppert (2010). We thus find the thickness at the front h_F:

$$h_F = \left(\frac{\vartheta_0}{\vartheta_F}\right)^2. \tag{8.54}$$

These results, reported in black dashed line in figure 8.7(a,b), well agree with the implicit equation for small values of ϑ. The velocity of the front

$$U_F = \mathrm{d}\vartheta_F/\mathrm{d}t = \left(\frac{c}{192}\right)^{1/4} t^{-3/4} \tag{8.55}$$

decreases with time. Therefore, the front slows down as moving downstream toward the equator, for all values of c. Interestingly, the relation $h_F(\vartheta_F)$ is independent of the height of the spheroid.

We verify the faithfulness of this approach by comparing it with the numerical results of the complete model (8.11) with parameters $c = 0.6$, $Bo = 500$ and $\delta = 10^{-3}$ (figure 8.7(c)). To

simulate the spreading on the substrate, we consider a precursor film of size $h_p = 0.005$ (Troian et al., 1989b; Kondic and Diez, 2002) with the following initial condition (Balestra et al., 2019):

$$h(\vartheta,0) = \frac{h_i - h_p}{2}\left(1 - \tanh\left(100\left(\vartheta - \vartheta_0\right)\right)\right) + h_p. \tag{8.56}$$

Figure 8.7(c) shows the evolution with time of the film thickness. In the vicinity of the front, a capillary ridge connects the film to the precursor one. Far from the front, the drainage solution well approximates the thin film evolution. In figure 8.7(a,b), we report also the position and the values of the maximum of the thickness at the ridge, with a good agreement with the analytical approach.

We considered a case in which the substrate can be described by employing two angles, the zenith and the azimuth. In the following, we further explore an axisymmetric substrate by considering the Monge parameterization for surfaces of revolution, similar to the one employed for the conical substrate. For a paraboloid, both the analytical tools introduced for the cone and the sphere can be applied.

8.3.2 Paraboloid

8.3.2.1 Drainage problem

In this section, we consider the coating of a paraboloid of characteristic radial extent R. We parameterize the paraboloidal surface as follows:

$$\boldsymbol{X} = (r\cos\varphi, r\sin\varphi, -er^2) \tag{8.57}$$

The gravity term $g_t^{\{1\}}$ and w now read:

$$g_t^{\{1\}}(r) = \frac{2er}{4e^2r^2+1}, \quad w(r) = r\sqrt{4e^2r^2+1} \tag{8.58}$$

The lubrication equation reads:

$$\frac{\partial h}{\partial t} + \frac{2erh^2}{4e^2r^2+1}\frac{\partial h}{\partial r} + \frac{4\left(2e^3r^2+e\right)h^3}{3\left(4e^2r^2+1\right)^2} = 0. \tag{8.59}$$

In analogy with the sphere case, we expand the solution in series of r:

$$h(r,t) = H_0(t) + r^2H_2(t) + r^4H_4(t) + r^6H_6(t) + \ldots \tag{8.60}$$

Because of symmetry, all the odd terms in r are zero. At order $\mathcal{O}(1)$, one obtains the following problem:

$$\frac{4}{3}eH_0(t)^3 + H_0'(t) = 0, \quad H_0(0) = 1, \tag{8.61}$$

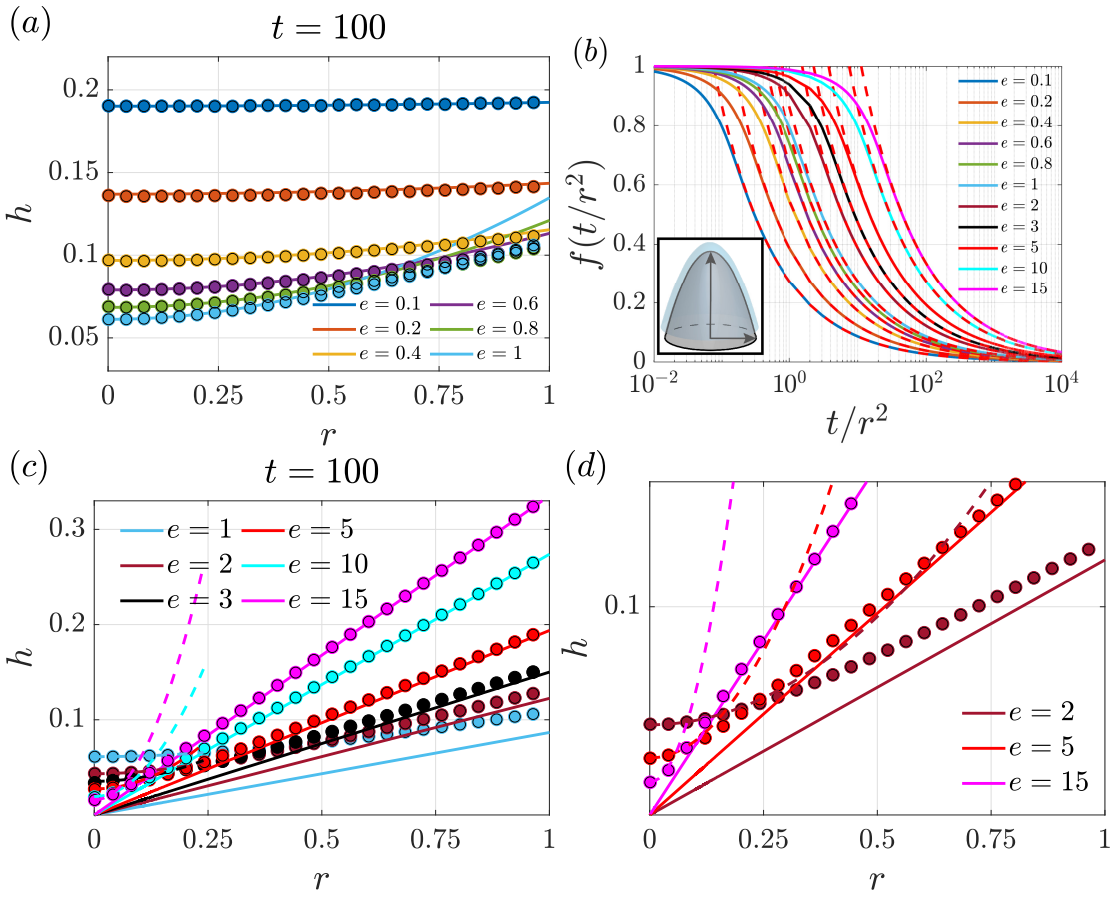

Figure 8.8: (a) Comparison of the analytical solution (equation (8.63), solid lines) against the numerical one (colored dots) for the drainage on a paraboloid. (b) Self-similar solution for the coating on a paraboloid, valid for $er \gg 1$ (colored lines). The red dashed lines are the corresponding large-time approximations (equation (8.67). (c) Comparison of the numerical solution (colored dots) with the self-similar one for $er \gg 1$ (solid lines). The dashed lines denote the $\mathcal{O}(r^6)$ approximation of equation (8.63). (d) Zoom in (c) to highlight the range of validity of the two analytical solutions.

whose solution reads:

$$H_0(t) = \frac{1}{\sqrt{\frac{8et}{3}+1}}. \tag{8.62}$$

In Appendix 8.8.2 we report the analytical developments for higher orders. The solution at order $\mathcal{O}(r^6)$, for $t \to \infty$, reads:

$$h(r,t) = \frac{\sqrt{\frac{3}{2}}\sqrt{\frac{1}{t}}\left(3248e^6r^6 - 1540e^4r^4 + 1650e^2r^2 + 1375\right)}{2750\sqrt{e}} + \mathcal{O}(r^8) + \mathcal{O}\left(\frac{1}{t^{3/2}}\right). \tag{8.63}$$

Also in this case, $H_0 = \left(\frac{3}{2\mathcal{K}_p t}\right)^{1/2}$, where $\mathcal{K}_p = 4e$ is the absolute value of the mean curvature at the top.

In analogy with the spheroid case, equation (8.59) is solved in the domain $0 < r < 1$ with initial condition $h(0,t) = 1$. The faithfulness of the results is verified by numerical simulations of the same equation with $0 < r < 2$ and the complete model (8.11) with parameters $Bo = 10000$ and $\delta = 10^{-4}$. To simulate the outlet condition, we consider the domain $0 < r < 3$ and use a Sponge method to relax the thickness to zero avoiding reflections from the outlet (Högberg and Henningson, 1998). Equation (8.59) is thus modified as follows to impose the Sponge condition:

$$\frac{\partial h}{\partial t} + \frac{2erh^2}{4e^2r^2+1}\frac{\partial h}{\partial r} + \frac{4\left(2e^3r^2+e\right)h^3}{3\left(4e^2r^2+1\right)^2} = -\frac{h}{2}\left(1+\tanh\left(\eta_{sp}\left(r-r_{sp}\right)\right)\right) = -h\mathrm{Sp}(r), \tag{8.64}$$

where $\eta_{sp} = 3$ and $r_{sp} = 2.7$, and initial condition $h(0,t) = 1 - \mathrm{Sp}(r)$. Numerical convergence for all values of e is achieved with a characteristic element size $\Delta r = 0.01$.

The comparison between the analytical and numerical drainage solution is reported in figure 8.8(a). The solution is characterized by mild variations of the thickness with the radius. The comparison shows a good agreement for $e < 1$, while already at $e = 1$ the accuracy of the analytical solution rapidly degrades as $r > 0.5$.

An analytical approximation for larger values of e can be obtained by assuming $er \gg 1$ in equation (8.59):

$$\frac{\partial h}{\partial t} + \frac{h^2}{2er}\frac{\partial h}{\partial r} + \frac{h^3}{6er^2} = 0, \quad h(r,0) = 1. \tag{8.65}$$

The problem admits a self-similar solution of the form $h(r,t) = f(\xi)$, where $\xi = t/r^2$. Following the same procedure of the cone problem, one obtains the following ordinary differential equation:

$$f'\left(1 - \frac{1}{e}\xi f^2\right) + \frac{1}{6e}f^3 = 0, \quad f(0) = 1. \tag{8.66}$$

The resulting equation is formally analogous to the self-similar problem of the cone (8.32), with different coefficients. The numerical solution is reported in figure 8.8(b). We find an approximate solution of the form $f(\xi) = f_0\xi^{-1/2}$, where $f_0 = \sqrt{3e}/2$:

$$h(r,t) = \frac{\sqrt{3e}}{2}\frac{r}{\sqrt{t}}, \tag{8.67}$$

that well agrees with the solution of the self-similar initial value problem for $\xi \to \infty$, i.e. $t \to \infty$ (see red dashed lines in 8.8(b)). The agreement with the numerical solution for $e > 2$, shown in figure 8.8(c) is very good, except in the close vicinity of $r = 0$, in which the expansion of equation (8.63) can be employed.

Also in this case, the thickness increases moving downstream, thus implying a reduction of the flux moving downstream. Interestingly, the drainage problem was approached by employing the asymptotic expansion, the self-similar solution and the large-time scaling arguments.

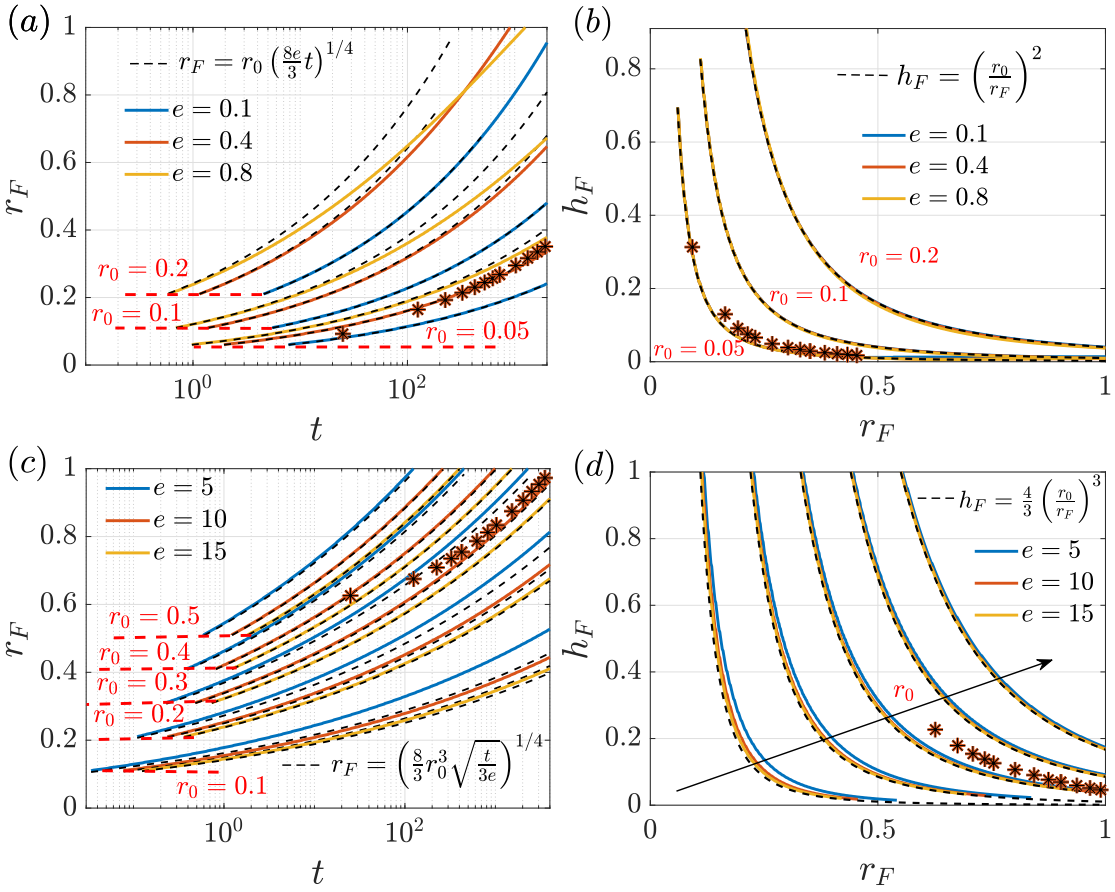

Figure 8.9: Spreading of an initial volume of fluid on an paraboloid. (a,c) Variation of the front angle ϑ_F with time and (b,d) of the thickness at the front h_F with ϑ_F, for different values of the initial angle ϑ_0 and e, for the (a,b) asymptotic and (c,d) self-similar solution. The solid and dot-dashed lines denote the values of ϑ_F and h_F on the outer and inner sides, respectively. The black dashed lines correspond to the analytical approximations of the relation $\vartheta_F(t)$ and $h_F(\vartheta_F)$, respectively, while the stars are the values recovered by a numerical simulation of the complete model with (a,b) $e = 0.8$, $Bo = 5000$, $\delta = 10^{-3}$, $h_p = 0.0025$ and (c,d) $e = 10$, $Bo = 100$, $\delta = 10^{-2}$, $h_p = 0.0025$.

8.3.2.2 Spreading problem

We now focus on the spreading problem of a mass of fluid of initial thickness $h_i = 1$ contained in the region $r < r_0$. The conservation of mass reads:

$$\begin{aligned}\int_0^{2\pi}\int_0^{r_F(t)} h(r,t)\,w(r)\,\mathrm{d}r\,\mathrm{d}\varphi = \int_0^{2\pi}\int_0^{r_0} w(r)\,\mathrm{d}r\,\mathrm{d}\varphi \\ \rightarrow \int_0^{r_F(t)} h(r,t)\,w(r)\,\mathrm{d}r = \int_0^{r_0} w(r)\,\mathrm{d}r,\end{aligned} \tag{8.68}$$

where $w(r)$ is given by equations (8.58). The thickness $h(r,t)$ is given by the two large-time analytical solutions (8.63), valid for small values of e, and (8.67), valid instead when large

values of e are considered, far from the pole. The resulting problems for the front radius r_F and thickness h_F are numerically solved via the built-in function "fsolve" in Matlab, and the results are reported in figure 8.9, for the two different analytical solutions. These results are compared with following two analytical approximations in the vicinity of ($r \ll 1$) and far from the pole ($er \gg 1$). When small values of r and large times are considered, the thickness and w can be approximated as follows:

$$h = \sqrt{\frac{3}{8et}} + \mathcal{O}(r^2) + \mathcal{O}\left(\frac{1}{t^{3/2}}\right), \quad w = r + \mathcal{O}(r^2). \tag{8.69}$$

Substituting in equation (8.68) and keeping at most $\mathcal{O}(r)$ terms, one obtains the front radius and thickness:

$$r_F = r_0 \left(\frac{8et}{3}\right)^{1/4}, \quad h_F = \left(\frac{r_0}{r_F}\right)^2, \tag{8.70}$$

which well compares with the numerical solutions of the implicit relation (8.68) (see figure 8.9(a,b)).

The same analytical developments can be employed for the case $er \gg 1$ and $t \to \infty$:

$$h = \frac{\sqrt{3e}}{2} \frac{r}{\sqrt{t}}, \quad w = r\sqrt{4e^2r^2 + 1} \approx 2er^2, \tag{8.71}$$

which leads to:

$$r_F = \left(\frac{8}{3}\sqrt{\frac{t}{3e}} r_0^3\right)^{1/4}, \quad h_F = \frac{4}{3}\left(\frac{r_0}{r_F}\right)^3. \tag{8.72}$$

Also in this case, a good agreement is observed (see figure 8.9(c,d)). The agreement improves when larger values of e at larger r are considered. We finally compare these theoretical results with two numerical simulations of the complete model, with a good agreement at large times.

Up to now, we considered the drainage and spreading problem on axisymmetric substrates. The analysis was simplified thanks to the absence of odd terms in the asymptotic expansion in ϑ. However, not all geometries are characterized by this symmetry. The symmetry of the spreading process can be broken by different effects, e.g. absence of symmetry with respect to ϑ or non-uniformity due to the presence of a gravity component along the azimuthal direction. We first consider the torus, a substrate in which the symmetry with respect to ϑ is broken, leading to different drainage and spreading along the inner and outer regions.

8.4 Non-symmetric drainage and spreading: coating of a torus

8.4.1 Drainage problem

In this section, we consider the drainage of a thin film flowing on a toroidal substrate of tube radius R and distance dR between the axis of revolution and the center of the tube (see figure 8.10(a)). The torus is thus generated by the rotation along the azimuthal direction

of a circular cross-section whose center is located at a distance d from the axis of rotation. Non-dimensionalizing the in-plane directions and substrate variables with R, the following parameterization based on the zenith ϑ and the azimuth φ is employed:

$$\boldsymbol{X}(\vartheta,\varphi) = ((d+\sin\vartheta)\cos\varphi, (d+\sin\vartheta)\sin\varphi, \cos\vartheta) \tag{8.73}$$

The position along the cylinder, at each azimuthal circular cross-section, is defined through the zenith ϑ. Two limiting cases are identified; the first one occurs for $d \to \infty$, which leads to the cylindrical case. The second case occurs for $d = 1$, in which the points at $\vartheta = -90°$ are in contact, leading to the so-called horn torus. The gravity term $g_t^{\{1\}}$ and w read

$$g_t^{\{1\}}(\vartheta) = \sin(\vartheta) \tag{8.74}$$

$$w(\vartheta) = d + \sin(\vartheta) \tag{8.75}$$

The same procedure employed for the drainage solution of the spheroidal case is adopted. However, in this case we cannot *a priori* neglect the odd terms in the asymptotic expansion:

$$\frac{\partial h(\vartheta,t)}{\partial t} + \frac{1}{3w(\vartheta)}\frac{\partial}{\partial\vartheta}\left(g_t^{\{1\}}(\vartheta)\, w(\vartheta) h(\vartheta,t)^3\right) = 0, \quad h(\vartheta,t) = H_0(t) + \vartheta H_1(t) + \vartheta^2 H_2(t)... \tag{8.76}$$

The resulting problems, at different orders in ϑ, are reported in Appendix 8.8.3. For the sake of brevity, the large time solution at $\mathcal{O}(\vartheta^4)$ reads:

$$h = \sqrt{\frac{3}{2t}}\left(\frac{19377\vartheta^4}{176000d^4} - \frac{1409\vartheta^3}{11000d^3} - \frac{7477\vartheta^4}{147840d^2} + \frac{31\vartheta^2}{200d^2} + \frac{91\vartheta^3}{2640d} - \frac{\vartheta}{5d} + \frac{43\vartheta^4}{10752} + \frac{\vartheta^2}{16} + 1\right) + \mathcal{O}(\vartheta^5) + \mathcal{O}\left(\frac{1}{t^{3/2}}\right) \tag{8.77}$$

The cylinder thickness distribution (8.26) is recovered for $d \to \infty$. The $\mathcal{O}(1)$ solution is analogous to the cylinder case for any value of d. Both substrates are characterized by a unitary non-dimensionalized mean curvature at the pole $\mathcal{K}_p$. Equation (8.76) is solved in the domain $-\pi/2 < \vartheta < \pi/2$ and verified against simulations of the same equation with $-(3/4)\pi/2 < 0 < (3/4)\pi$ and the complete model (8.11) with periodic boundary condition at $\vartheta = \pm\pi$ and parameters $Bo = 10000$ and $\delta = 10^{-4}$. Numerical convergence is achieved with $\Delta\vartheta = 0.5°$. Figure 8.10 shows a comparison between the numerical and large-time analytical solutions of the drainage problem, for different values of d in the range $-\pi/2 < \vartheta < \pi/2$. The distribution is not symmetric with respect to $\vartheta = 0$. In particular, the thickness is larger for negative values of ϑ, i.e. on the inner side of the torus, while for $\vartheta > 0$ the thickness is almost constant. These differences are enhanced as d decreases. The numerical solution well compares with the analytical one at $\mathcal{O}(\vartheta^4)$ while, at $\mathcal{O}(\vartheta^2)$, the agreement is good only in the vicinity of the pole.

The different thickness distributions in the two sides of the circular cross-section of the torus result from the non-symmetric drainage with respect to ϑ. In analogy with the spheroid case,

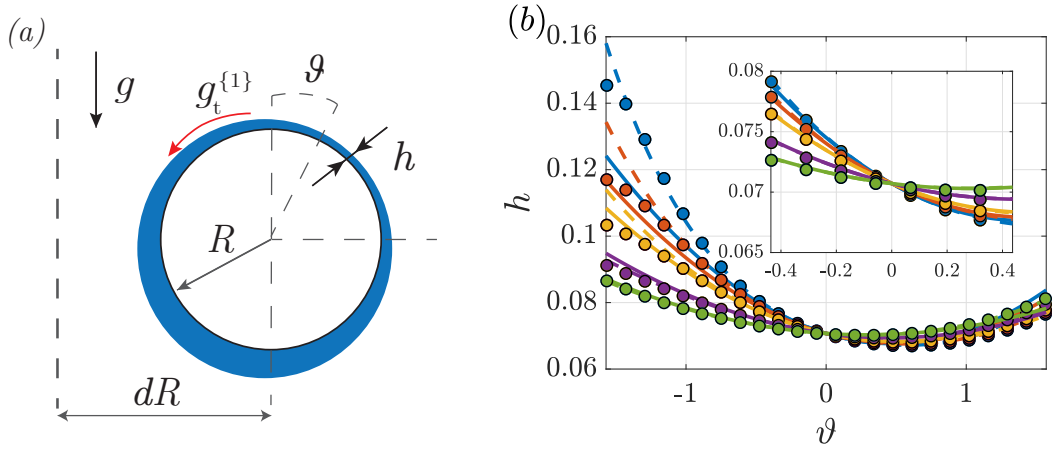

Figure 8.10: (a) Sketch of the axisymmetric flow configuration for a coating of a torus. (b) Drainage solution on a torus at $t = 300$, numerical (colored dots) and analytical solutions at order $\mathcal{O}(\vartheta^2)$ (solid lines) and $\mathcal{O}(\vartheta^4)$ (dashed lines), for $d = 1.1$ (blue),$d = 1.25$ (orange), $d = 1.5$ (yellow), $d = 2.5$ (purple), $d = 5$ (green).

we expect an increase of the thickness when the drainage decreases reaching the bottom part of the torus, and vice versa. In analogy with the previous section, we consider the gravity perturbation of the thickness with respect to the $\mathcal{O}(1)$ solution. The variation of the flux per unit length reads

$$\frac{1}{w}\partial_\vartheta(w g_t^{\{1\}} h^3) \approx \frac{H_0^3}{w}\partial_\vartheta(w g_t^{\{1\}})\left(\frac{3}{2t}\right)^{3/2}\left(\left(-\frac{1}{a^2}-\frac{1}{2}\right)\vartheta^2+\frac{\vartheta}{a}+1\right). \tag{8.78}$$

On the inner part, the variation of the flux is large and negative and thus the tangential gravity component strongly decreases moving downstream, while a milder variation is observed on the outer part. As a consequence, the thickness on the inner part reaches larger values than on the outer part. One would be surprised of these conclusions, since the gravity component $g_t^{\{1\}} = \sin\vartheta$ is symmetric with respect to $\vartheta = 0$. However, one should consider that the metrics on the two sides of the torus are rather different, with faster variations attained on the inner part.

8.4.2 Spreading problem

We now present the results for the spreading of a volume of fluid on a torus. We consider an initial volume of fluid of thickness $h = 1$ in the region $-\vartheta_0 < \vartheta < \vartheta_0$. The breaking of symmetry with respect to $\vartheta = 0$ results in two different spreading fronts for $\vartheta < 0$ (inner side) and $\vartheta > 0$ (outer side). The total volume on each side of the torus is conserved since the flux $q^{\{1\}} = h^3 g_t^{\{1\}} h^3 = 0$ at $\vartheta = 0$.

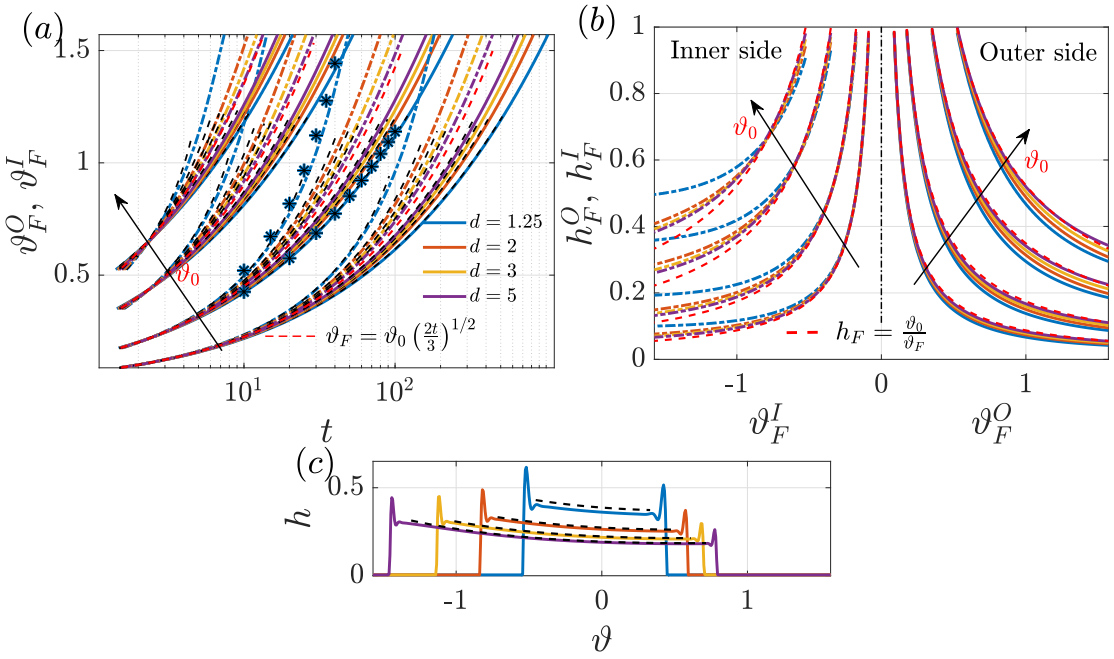

Figure 8.11: Spreading of an initial volume of fluid on a torus. (a) Variation of the front angle ϑ_F with time and (b) of the thickness at the front h_F with ϑ_F, for different values of the initial angle ϑ_0 and d. The solid and dot-dashed lines denote the values of ϑ_F and h_F on the outer and inner sides, respectively. The black and red dashed lines correspond to the $\mathcal{O}(1)$ and $\mathcal{O}(\vartheta)$ analytical approximations of the relation $\vartheta_F(t)$ and $h_F(\vartheta_F)$, respectively, while the stars are the values recovered by a numerical simulation of the complete model with $d = 1.25$, $Bo = 500$, $\delta = 10^{-3}$, precursor film thickness $h_p = 0.005$. (c) Numerical thickness distribution obtained from the complete model with $d = 1.25$, $Bo = 500$, $\delta = 10^{-3}$ as a function of ϑ at different times: $t = 10$ (blue), $t = 20$ (orange), $t = 30$ (yellow), $t = 40$ (purple). The black dashed lines denote the corresponding large-time drainage solutions.

The conservation of mass for the two regions reads:

$$\int_0^{\vartheta_F^O(t)} h(\vartheta,t)\,w(\vartheta)\mathrm{d}\vartheta = \int_0^{\vartheta_0} w(\vartheta)\mathrm{d}\vartheta, \tag{8.79}$$

$$\int_{-\vartheta_F^I(t)}^{0} h(\vartheta,t)\,w(\vartheta)\mathrm{d}\vartheta = \int_{-\vartheta_0}^{0} w(\vartheta)\mathrm{d}\vartheta, \tag{8.80}$$

where $\vartheta_F^O(t)$ and $\vartheta_F^I(t)$ are the front angle on the outer and inner part, respectively, $w(\vartheta) = d + \sin(\vartheta)$, and $h(\vartheta,t)$ is given by equation (8.77). Note that the two integrals on the RHS do not assume the same value, since $w(\vartheta)$ is not symmetric with respect to $\vartheta = 0$. Equations (8.79,8.80) are implicit integrals that are solved in Matlab through the built-in function "fsolve". A first analytical approximation is found by taking the $\mathcal{O}(1)$ approximation, leading to:

$$\int_0^{\vartheta_F^O(t)} \sqrt{\frac{3}{2t}}d\mathrm{d}\vartheta = \int_0^{\vartheta_0} d\,\mathrm{d}\vartheta \rightarrow \frac{\vartheta_F^O}{\vartheta_0} = \sqrt{\frac{2t}{3}}, \tag{8.81}$$

$$\int_{-\vartheta_F^I(t)}^{0}\sqrt{\frac{3}{2t}}d\,\mathrm{d}\vartheta=\int_{-\vartheta_0}^{0}d\,\mathrm{d}\vartheta\rightarrow\frac{\vartheta_F^I}{\vartheta_0}=\sqrt{\frac{2t}{3}},\tag{8.82}$$

i.e. the solution of $\mathcal{O}(1)$ does not depend on d and is analogous to the spreading on a cylinder, presented in Section 8.2.3. The thickness at the front thus reads $h_F=\vartheta_0/\vartheta_F$. A better approximation that includes the curvature of the torus can be obtained by considering the $\mathcal{O}(\vartheta)$ approximation of the integrand:

$$\begin{aligned}\int_0^{\vartheta_F^O(t)}\sqrt{\frac{3}{2t}}(\frac{4}{5}\vartheta+d)\mathrm{d}\vartheta=\int_0^{\vartheta_0}(d+\vartheta)\mathrm{d}\vartheta\rightarrow\vartheta_F^{O2}+\frac{5d}{2}\vartheta_F^O-\left(\frac{5}{2}\left(d\vartheta_0+\vartheta_0^2/2\right)\right)\sqrt{\frac{2t}{3}}=0,\\ \rightarrow\vartheta_F^O(t)=\frac{1}{2}\left(-\frac{5d}{2}+\sqrt{\frac{25d^2}{4}+4(d\vartheta_0+\vartheta_0^2/2)\frac{5}{2}\sqrt{\frac{2t}{3}}}\right)\end{aligned}\tag{8.83}$$

$$\begin{aligned}\int_{-\vartheta_F^I(t)}^{0}\sqrt{\frac{3}{2t}}(\frac{4}{5}\vartheta+d)\mathrm{d}\vartheta=\int_{-\vartheta_0}^{0}(d+\vartheta)\mathrm{d}\vartheta\rightarrow\vartheta_F^{I2}-\frac{5d}{2}\vartheta_F^I+\left(\frac{5}{2}\left(d\vartheta_0-\vartheta_0^2/2\right)\right)\sqrt{\frac{2t}{3}}=0,\\ \rightarrow\vartheta_F^I(t)=\frac{1}{2}\left(\frac{5d}{2}-\sqrt{\frac{25d^2}{4}-4(d\vartheta_0-\vartheta_0^2/2)\frac{5}{2}\sqrt{\frac{2t}{3}}}\right)\end{aligned}\tag{8.84}$$

Figure 8.11(a,b) shows the behaviors of ϑ_F^O, ϑ_F^I and the front thicknesses h_F^O and h_F^I on the inner and outer sides of the torus, respectively, for different values of d and ϑ_0. As concerns panel (a), for a fixed time, the front angle on the inner side is always larger than the one on the outer side. An increase of d leads to a decrease (respectively increase) of ϑ_F on the inner (respectively outer) side. The front thickness does not strongly depend on d, even if some differences can be appreciated on the inner side, for large values of ϑ_F^O. The $\mathcal{O}(1)$ approximation gives a reasonable agreement in the prediction of the front angle and thickness. In particular, it appears to be the lower (respectively upper) limit for the inner (respectively outer) sides, as d increases. The order $\mathcal{O}(\vartheta)$ approximations well follow the implicit relations (8.79) and (8.80). We compare these analytical results with a numerical simulation of the complete model (8.11) with parameters $d=1.25$, $Bo=500$, $\delta=10^{-3}$, $h_p=0.005$, initial condition

$$\begin{aligned}h(\vartheta,0)&=\frac{h_i-h_p}{2}\left(1-\tanh(100(\vartheta-\vartheta_0)\right)+h_p,\quad\text{for }\vartheta>0,\\ h(\vartheta,0)&=\frac{h_i-h_p}{2}\left(1-\tanh(100(-\vartheta-\vartheta_0)\right)+h_p,\quad\text{for }\vartheta<0,\end{aligned}\tag{8.85}$$

and $\vartheta_0=10^\circ$ (see figure 8.11(c)). The agreement between the numerical front angle, given by the maximum thickness location, and the theoretical one is very good, and also the maximum thickness well follows the front thickness predicted by the theory.

The torus case shows non-symmetric drainage and spreading along the zenith direction. However, the presented tools are not necessarily limited to axisymmetric substrates. In the

following, we present how these analyses can be extended to non-axisymmetric substrates which are characterized by a three-dimensional, non-uniform along the azimuthal direction, drainage. We chose as a testing ground an ellipsoid with three different axes.

8.5 Three-dimensional drainage and spreading: coating of an ellipsoid

8.5.1 Numerical drainage solution

In this section, we study the coating of an ellipsoidal substrate of horizontal semiaxes aR, bR and vertical semiaxis R (see figure 8.2); gravity is pointing downward. In non-dimensional form, the following parameterization holds:

$$\boldsymbol{X}(\vartheta,\varphi) = (a\sin\vartheta\cos\varphi, b\sin\vartheta\sin\varphi, \cos\vartheta) \tag{8.86}$$

We identify different limiting cases, depending on the values of a and b. If $a = b = 1$, we recover the spherical case; if $a = b \neq 1$ the resulting substrate is an axisymmetric ellipsoid of unitary height and equatorial radius $a = b$, whose results can be recovered from those of Section 8.3.1. Note that the time scale is different since the in-plane directions and substrate variables are non-dimensionalized with the height and not with the equatorial radius, in the present section. When $a \neq b$ the axisymmetry is broken since the two axes at the equator are different. In the following, we assume that $b \geq a$ and consider the range $0.4 < a, b < 2$. Note that the solutions for $a > b$ can be recovered by simply translating of $\varphi = 90°$ the solution for $b \geq a$ (obtained by swapping the desired values of a and b).

The metric components vary along the φ direction; in particular, the metric tensor is not diagonal. The local coordinates system defined by the parameterization is thus non-orthogonal and a second gravity component parallel to the φ direction, $g_t^{\{2\}}(\vartheta,\varphi)$, appears. The square root of the determinant of the metric and the gravity terms now read:

$$w(\vartheta,\varphi) = \sqrt{\sin^4(\vartheta)\left(a^2\sin^2(\varphi) + b^2\cos^2(\varphi)\right) + a^2b^2\sin^2(\vartheta)\cos^2(\vartheta)} \tag{8.87}$$

$$g_t^{\{1\}}(\vartheta,\varphi) = \frac{\sin(\vartheta)\left(a^2\sin^2(\varphi) + b^2\cos^2(\varphi)\right)}{\sin^2(\vartheta)\left(a^2\sin^2(\varphi) + b^2\cos^2(\varphi)\right) + a^2b^2\cos^2(\vartheta)} \tag{8.88}$$

$$g_t^{\{2\}}(\vartheta,\varphi) = \frac{\sin(\varphi)\cos(\varphi)\left(a^2\cos(\vartheta) - b^2\cos(\vartheta)\right)}{a^2b^2\cos^2(\vartheta)\cos^2(\varphi) + a^2b^2\cos^2(\vartheta)\sin^2(\varphi) + a^2\sin^2(\vartheta)\sin^2(\varphi) + b^2\sin^2(\vartheta)\cos^2(\varphi)} \tag{8.89}$$

The drainage solution $h(\vartheta,\varphi,t)$ satisfies the two-dimensional equation:

$$\frac{\partial h}{\partial t} + \frac{1}{3w}\frac{\partial}{\partial\vartheta}\left(g_t^{\{1\}}wh^3\right) + \frac{1}{3w}\frac{\partial}{\partial\varphi}\left(g_t^{\{2\}}wh^3\right) = 0 \tag{8.90}$$

We solve equation (8.90) by imposing periodic boundary conditions in $0 < \varphi < 2\pi$ and the initial condition $h(\vartheta,\varphi,0) = 1$. We verified that the solution is not influenced by variations

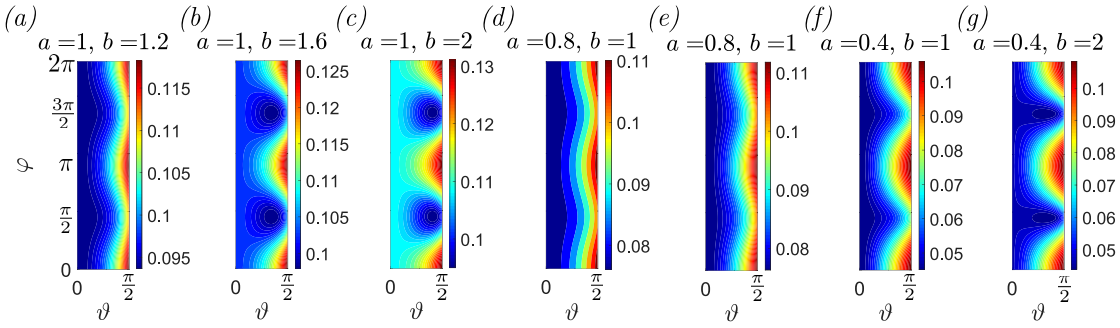

Figure 8.12: Numerical solution of equation (8.90) at $t = 100$ as a function of (ϑ, φ), for different values of the semiaxes a and b, with $a \leq 1$ and $b \geq 1$.

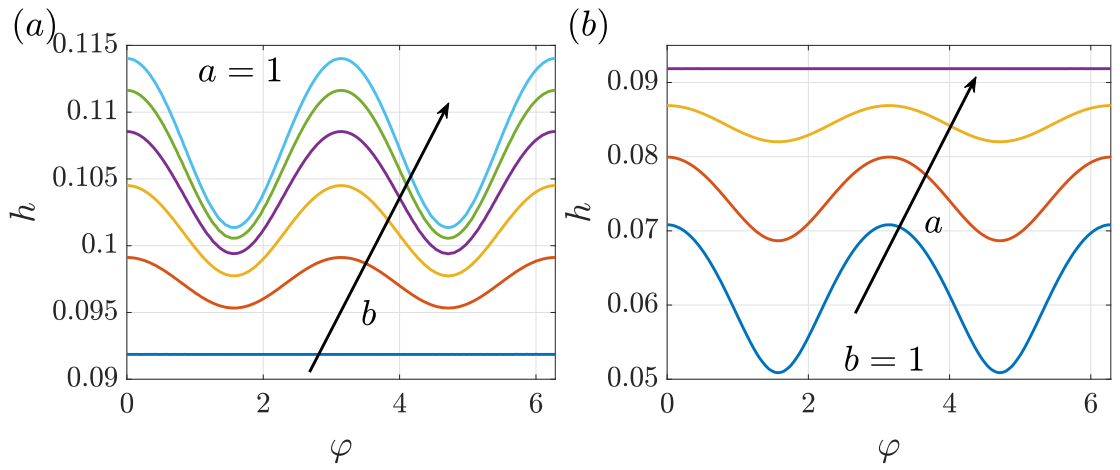

Figure 8.13: Numerical solution of equation (8.90) at $t = 100$ and $\vartheta = \pi/4$ as a function of (φ): (a) $a = 1$ and $b = 1$ (blue), $b = 1.2$ (orange), $b = 1.4$ (yellow), $b = 1.6$ (purple), $b = 1.8$ (green), $b = 2$ (cyan); (b) $b = 1$ and $a = 0.4$ (blue), $a = 0.6$ (orange), $a = 0.8$ (yellow), $a = 1$ (purple).

of the zenith extension of the domain by performing two numerical simulations of (8.90) with different positions of the downstream boundary $\vartheta = \pi/2, (3/4)\pi$, with no appreciable differences in the results. Numerical convergence is achieved with a characteristic mesh size of 0.9°. Figure 8.12 and figure 8.13 respectively show the resulting film distributions and a section at $\vartheta = \pi/4$ for different values of a and b, at $t = 100$. We start by considering a situation in which the height is larger than the semiaxis along the x direction, i.e. $a \leq 1$, and smaller than the semiaxis along the y direction, i.e. $b \geq 1$. The spherical case $a = b = 1$ shows a variation of the thickness only along the zenith ϑ while it is constant along the φ direction, which is consistent with axisymmetry (see Section 8.2.3). We first increase the value of b, with $a = 1$. For $b = 1.2$, the thickness presents modulations along the azimuthal direction, with a maximum thickness localized at $\varphi = k\pi$ $(k = 0, 1, 2)$, i.e. along the direction of the smaller axis a. These modulations are enhanced as b increases, with larger values of the attained thickness. Two regions of low thickness are localized at $\varphi = \pi/2 + k\pi$, along the larger axis b. The same trends are observed further increasing b. When $b = 1$ and a decreases, the thickness presents similar modulations along the azimuthal direction, but the thickness always increases moving

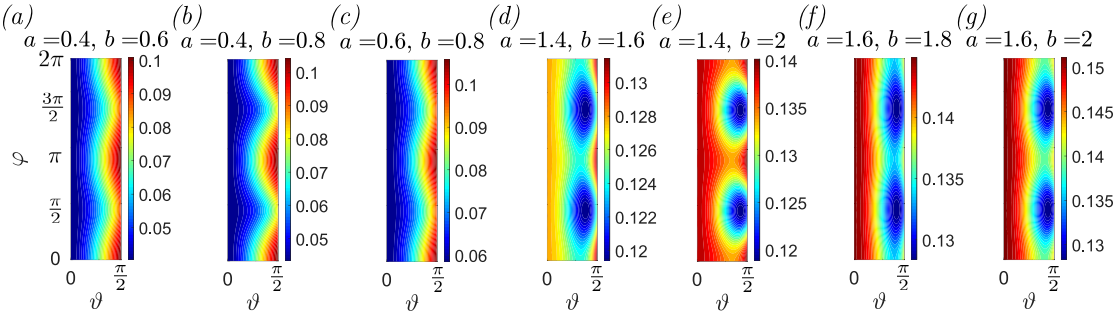

Figure 8.14: Numerical solution of equation (8.90) at $t = 100$ as a function of (ϑ, φ), for different values of the semiaxes a and b, with $a, b < 1$ and $a, b > 1$.

downstream. The thickness decreases as a decreases. Similar patterns are also obtained when small values of a and large values of b are considered.

The numerical solution of equation (8.90) shows the presence of modulations of the thickness along the azimuthal direction. According to Section 8.3.1, an increase (respectively decrease) of the thickness downstream implies a decrease (respectively increase) of the tangential gravity component. In particular, spheroids with small (respectively large) height were characterized by a decrease (respectively increase) of the thickness. We can extend these considerations to an ellipsoid by considering the drainage along the directions defined by (x, y), see figure 8.2(d). We expect to follow these trends along the two semiaxes, depending on a and b. In the axisymmetric case, the thickness increases downstream for height-radius ratios larger than 0.74, which corresponds to $a, b \lessapprox 1.35$. Therefore, when $a, b \lessapprox 1.35$ we always observe an increase of the thickness with ϑ, as observed in figure 8.14(a-c) (see also figure 8.6 for the cases with $c > c^*$). However, the thickness presents clear modulations owing to the non-uniform drainage when $a \neq b$. Similarly, when $a, b \gtrapprox 1.35$ one expects a decrease of the thickness followed by a slight increase at large ϑ, with modulations if $a \neq b$, as shown in figure 8.14(d-g). The intermediate situation occurs when $a \lessapprox 1.35$ and $b \gtrapprox 1.35$, characterized by an increase of the thickness along the x direction and a decrease along the y direction, as observed in figure 8.12(b,c,g).

In the light of this discussion, one may wonder if these patterns persist with time or merely represent a snapshot of a more intricate evolution. In the following, we also aim at clarifying this aspect by deriving an analytical solution for the drainage problem.

8.5.2 Analytical drainage solution

In this section, we derive an analytical solution for the drainage along the ellipsoid, and compare it with the numerical results of the previous section. In analogy with Section 8.3.1, we perform an asymptotic expansion in powers of ϑ, with $\vartheta \ll 1$. The solution at order $\mathcal{O}(1)$ does not depend on φ since at the pole the solution has to be unique. We thus consider the

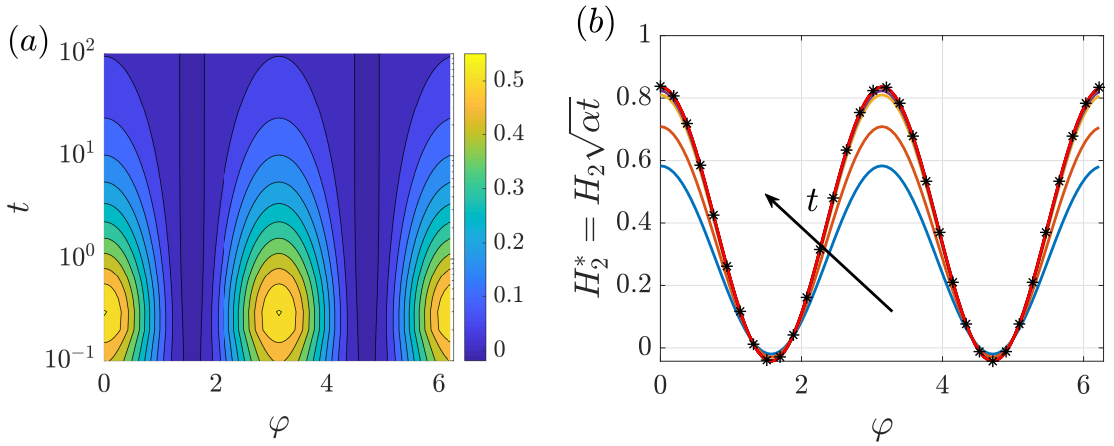

Figure 8.15: Drainage along an ellipsoid with $a = 0.5$ and $b = 1.5$. (a) Spatiotemporal evolution of H_2: iso-contours of H_2 in the (φ, t) plane. (b) Second order correction $H_2^* = H_2/H_0 \approx H_2\sqrt{\alpha t}$ as a function of φ at different times: $t = 0.4$ (blue), $t = 1$ (orange), $t = 5$ (yellow), $t = 10$ (purple) $t = 30$ (green), $t = 50$ (cyan), $t = 70$ (maroon), $t = 90$ (black), $t = 100$ (red). The black stars denote the late-time analytical solution for H_2^* from equation (8.95).

following expansion, in which the odd terms have been removed because of symmetry:

$$h(\vartheta, \varphi, t) = H_0(t) + \vartheta^2 H_2(\varphi, t) + \vartheta^4 H_4(\varphi, t) + \vartheta^6 H_6(\varphi, t) + \ldots \tag{8.91}$$

We expand equation (8.90) at various orders in ϑ. At order $\mathcal{O}(1)$, one obtains the following ODE:

$$\frac{1}{3}\left(\frac{1}{a^2} + \frac{1}{b^2}\right) H_0(t)^3 + H_0'(t) = 0 \rightarrow H_0(t) = \frac{1}{\sqrt{\frac{2}{3}t\left(\frac{1}{a^2} + \frac{1}{b^2}\right) + 1}} = \frac{1}{\sqrt{\alpha t + 1}}, \tag{8.92}$$

where $\alpha = \frac{2}{3}\left(1/a^2 + 1/b^2\right)$. Also in this case, the $\mathcal{O}(1)$ solution reduces to $\left(\frac{3}{2\mathcal{K}_p t}\right)^{1/2}$, $\mathcal{K}_p = \left(1/a^2 + 1/b^2\right)$. The equation at order $\mathcal{O}(\vartheta^2)$ reads:

$$\begin{aligned}\frac{\partial H_2(\varphi, t)}{\partial t} = &\frac{H_0(t)^2\left(\left(b^2 - a^2\right)\sin(2\varphi)\frac{\partial H_2}{\partial \varphi} + 2H_2\left(\left(a^2 - b^2\right)\cos(2y) - 2\left(a^2 + b^2\right)\right)\right)}{2a^2b^2} \\ &+ \frac{H_0(t)^3\left(\left(a^4\left(b^2 - 2\right) - a^2b^4 + 2b^4\right)\cos(2\varphi) + 2\left(a^4\left(-\left(b^2 - 1\right)\right) + a^2\left(b^2 - b^4\right) + b^4\right)\right)}{6a^4b^4},\end{aligned} \tag{8.93}$$

which is a parabolic PDE in $H_2(\varphi, t)$. We numerically solve equation (8.93) with initial condition $H_2(\varphi, 0) = 0$. The periodic boundary conditions at $\varphi = [0, 2\pi]$ are automatically imposed thanks to a Fourier spectral collocation method implemented in Matlab. The time-stepping is performed by employing the built-in function "ode23t", with a tolerance of 10^{-6}. Numerical convergence is achieved with 100 collocation points.

Figure 8.15(a) shows the spatiotemporal evolution of the second order solution $H_2(\varphi, t)$, for $a = 0.5$ and $b = 1.5$. An initial growth in absolute value until $t \approx 0.3$ is followed by a slow decay

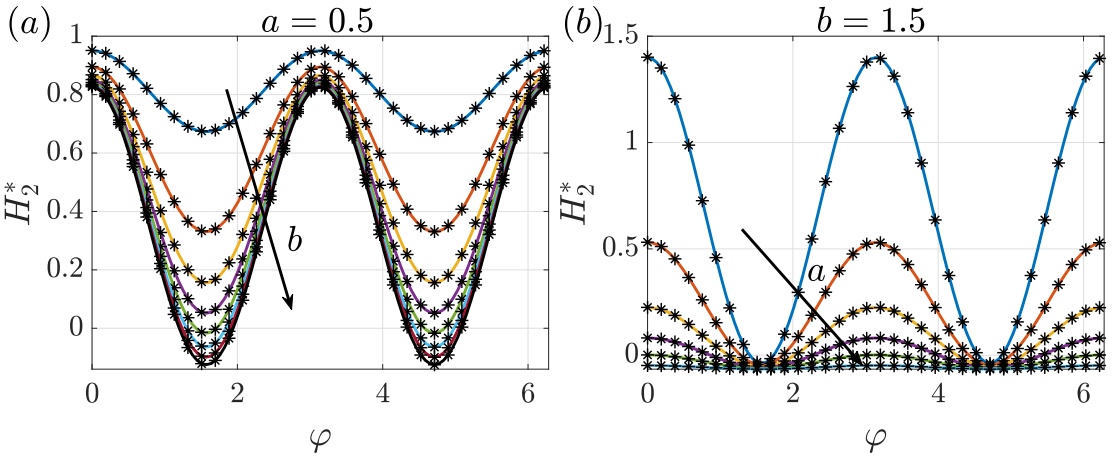

Figure 8.16: (a) Second order correction $H_2^* = H_2/H_0 \approx H_2\sqrt{\alpha t}$ as a function of φ at $t = 100$, for $a = 0.5$ and increasing b: $b = 0.6$ (blue), $b = 0.8$ (orange), $b = 1$ (yellow), $b = 1.2$ (purple), $b = 1.4$ (green), $b = 1.6$ (cyan), $b = 1.8$ (maroon), $b = 2$ (black). (b) H_2^* as a function of φ at $t = 100$, for $b = 1.5$ and increasing a: $a = 0.4$ (blue), $a = 0.6$ (orange), $a = 0.8$ (yellow), $a = 1$ (purple), $a = 1.2$ (green), $a = 1.4$ (cyan). The black stars denote the late-time analytical solution for H_2^* from equation (8.95).

at large times. In figure 8.15(b) we report the H_2 profiles rescaled with H_0, at different times in the slow-decay regime. The second-order solution H_2 is π-periodic and the maximum is attained at $\varphi = k\pi$, i.e. along the smaller axis of the ellipsoid. At $\varphi = k\pi/2$, i.e. along the larger axis of the ellipsoid, the correction reaches much smaller values. As time increases, the profiles collapse on a single curve, suggesting that a large-time solution characterized by a separation of variables is possible, i.e. $H_2(\varphi, t) = H_0(t)H_2^*(\varphi)$.

We introduce this decomposition in equation (8.93). Exploiting equation (8.92), the temporal dependence disappears and the following ODE for $H_2^*(\varphi)$ is obtained:

$$-a^4b^2\cos(2\varphi) + 2a^4b^2 + 2a^4\cos(2\varphi) - 2a^4 + a^2b^4\cos(2\varphi) + 2a^2b^4 + 3a^2b^2\left(a^2-b^2\right)\sin(2\varphi)H_2^{*\prime}(\varphi)$$
$$-2a^2b^2H_2^*(\varphi)\left(3\left(a^2-b^2\right)\cos(2\varphi) - 5\left(a^2+b^2\right)\right) - 2a^2b^2 - 2b^4\cos(2\varphi) - 2b^4 = 0, \quad (8.94)$$

whose solution reads:

$$H_2^*(\varphi) = C_1\sin(2\varphi)\sin^{-\frac{5\left(a^2+b^2\right)}{3\left(a^2-b^2\right)}}(\varphi)\cos^{\frac{5\left(a^2+b^2\right)}{3\left(a^2-b^2\right)}}(\varphi) - \frac{1}{8a^2b^2\left(4a^2+b^2\right)\left(a^2+4b^2\right)}\left(a^6\left(7b^2-4\right)\right.$$
$$\left.+26a^4\left(b^4-b^2\right)+a^2b^4\left(7b^2-26\right)+\left(a^2-b^2\right)\left(a^4\left(b^2+4\right)+a^2b^2\left(b^2+14\right)+4b^4\right)\cos(2\varphi)-4b^6\right), \quad (8.95)$$

where C_1 is a constant to be determined. However, it is observed that $C_1 \neq 0$ implies an unbounded behavior. Therefore, we impose $C_1 = 0$ to prevent non-physical solutions. The analytical result for H_2^* is reported in figure 8.15(b), with an excellent agreement with the numerical solution. Note that imposing $a = b$ leads to $H_2^* = \frac{1}{10}(\frac{3}{b^2} - 2)$, which is formally analogous to the second order solution of the spheroid with $c = 1/b$ (see Section 8.3.1). We then investigate the effect of a and b by considering different cases at $t = 100$, reported in

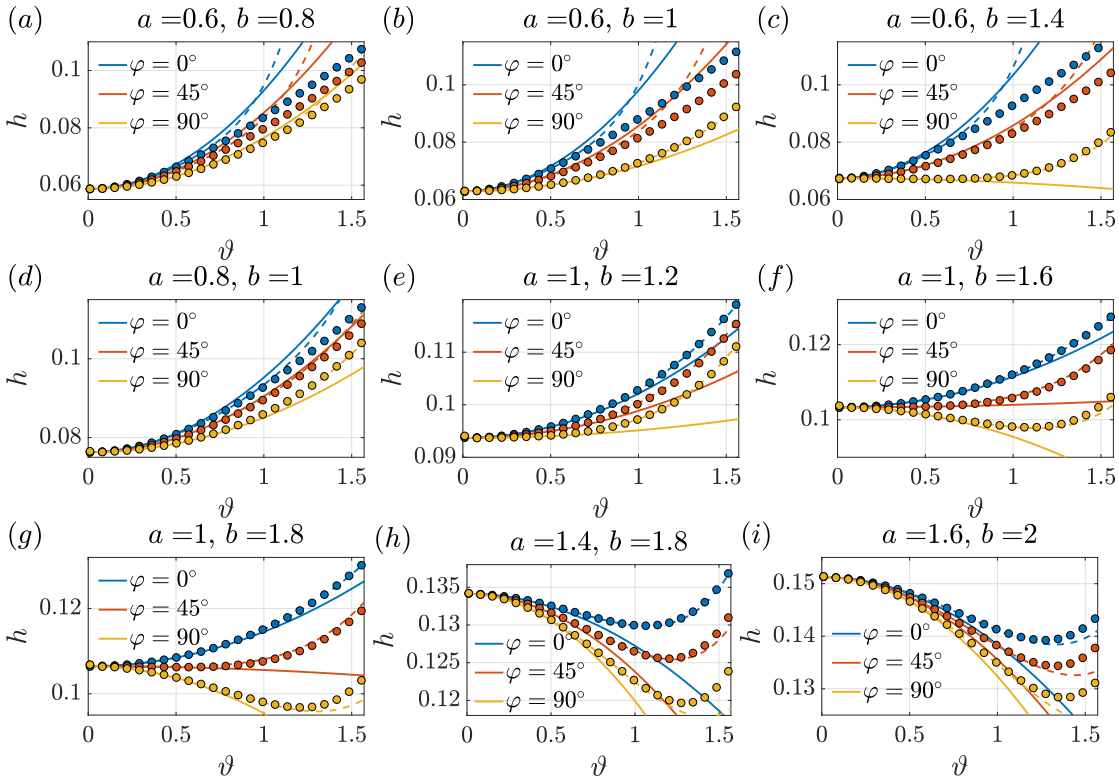

Figure 8.17: Comparison at three different azimuthal sections between the numerical (colored dots) and the quasi-analytical solution for an ellipsoid at $\mathcal{O}(\vartheta^2)$ (solid lines) and $\mathcal{O}(\vartheta^6)$ (dashed lines) at $t = 100$, for different values of a and b.

figure 8.16. An increase of b for fixed $a = 0.5$ (panel (a)) leads to a decrease of H_2^* in the region $\varphi = k\pi/2$, while an increase in a for fixed $b = 1.5$ (panel (b)) shows an overall decrease of H_2^*. Also for these cases, an excellent agreement with the analytical solution is observed.

The faithfulness of the analytical solution is verified against the numerical simulations of Section 8.5.1 in figure 8.17. For the comparison, we consider the solution at orders $\mathcal{O}(\vartheta^2)$ and $\mathcal{O}(\vartheta^6)$. The higher order problems, together with their solutions H_4 and H_6, are reported in Appendix 8.8.4. The same large-time behavior is observed. In general, the analytical solutions at $\mathcal{O}(\vartheta^6)$ compare well with the numerical ones, while those at $\mathcal{O}(\vartheta^2)$ are accurate only in the vicinity of the pole. The analytical solution at $\mathcal{O}(\vartheta^6)$ deviates from the numerical one for $a < 0.8$. The agreement for $a > 0.8$ is satisfactory for any value of b.

8.5.3 Spreading problem

In this section, we consider the spreading of an initial volume of fluid of height $h_i = 1$ contained in the region $0 < \vartheta < \vartheta_0$, $0 < \varphi < 2\pi$. Figure 8.18 shows the evolution of the film thickness with time, for different values of a and b, obtained employing the complete model (8.11) with initial condition formally analogous to equation (8.56), i.e. invariant along the azimuthal

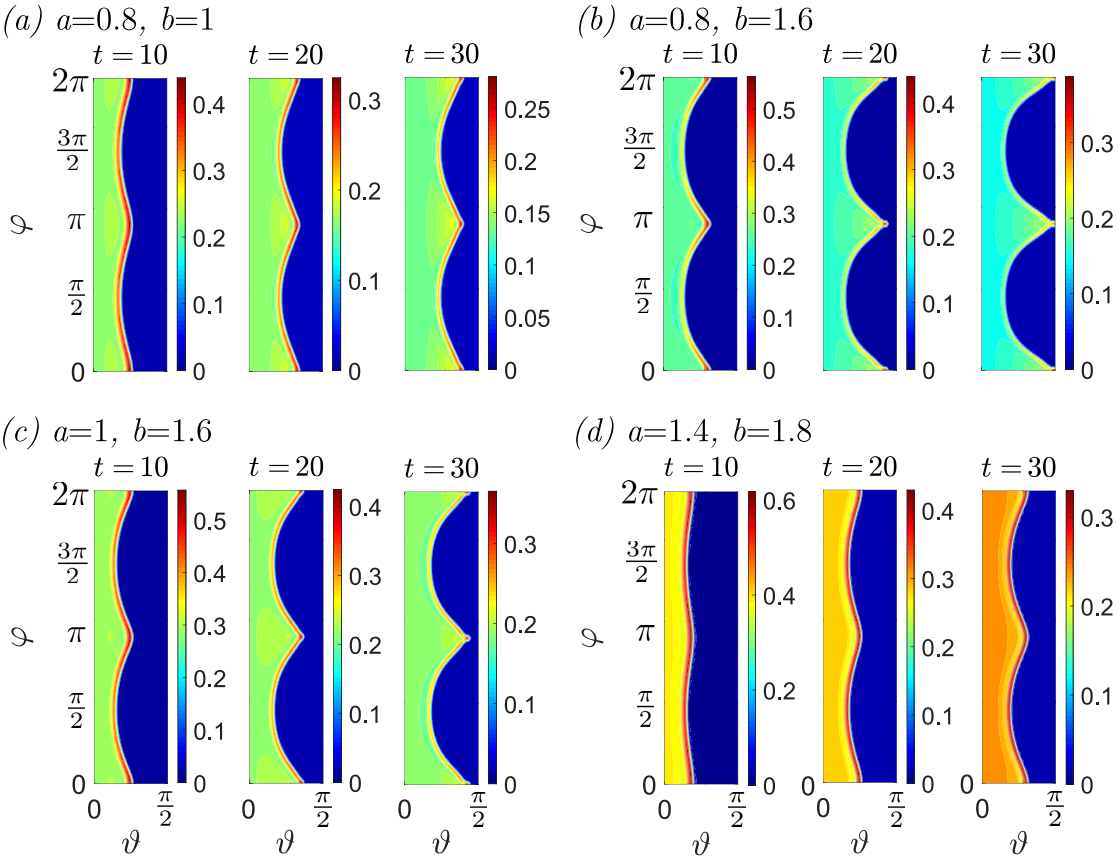

Figure 8.18: Iso-contours of the numerical solution for the spreading of equation (8.11), at different times, for an ellipsoid and $Bo = 100$, $\delta = 10^{-2}$, precursor film $h_p = 0.02$ and $\vartheta_0 = 20°$. (a) $a = 0.8$, $b = 1$, (b) $a = 0.8$, $b = 1.6$, (c) $a = 1$, $b = 1.6$, (d) $a = 1.4$, $b = 1.8$.

direction. For $t = 10$, the maximum thickness position, at which the front is located, is modulated along the azimuthal direction. This modulation accentuates with time and a region of large thickness forms at $\varphi = k\pi$ (along the shorter axis) while the thickness is much lower at $\varphi = k\pi/2$. Therefore, the front presents two peaks of large thickness aligned along the shorter axis. This effect is enhanced when larger (respectively lower) values of b (respectively a) are considered.

In figure 8.19, we report a zoom in the region $0 < \varphi < \pi$ for one simulation of the complete model (8.11) with $Bo = 1000$ and $\delta = 10^{-2}$, together with a three-dimensional rendering of the spreading on the ellipsoid, viewed from the top. The black lines denote the streamlines of the flux $\mathbf{q} = q^{\{1\}}\mathbf{e}_1 + q^{\{2\}}\mathbf{e}_2$. The flux streamlines are almost parallel to the azimuthal direction at low values of ϑ, then bend and align along the zenith direction as ϑ increases. An exception to this behavior is observed at $\varphi = 0, \pi/2$, in which the flow streamlines are always parallel to the zenith direction. The three-dimensional rendering highlights the formation of two, finger-like, front peaks of large thickness along the shorter axis, while the fluid slowly spreads along the larger axis.

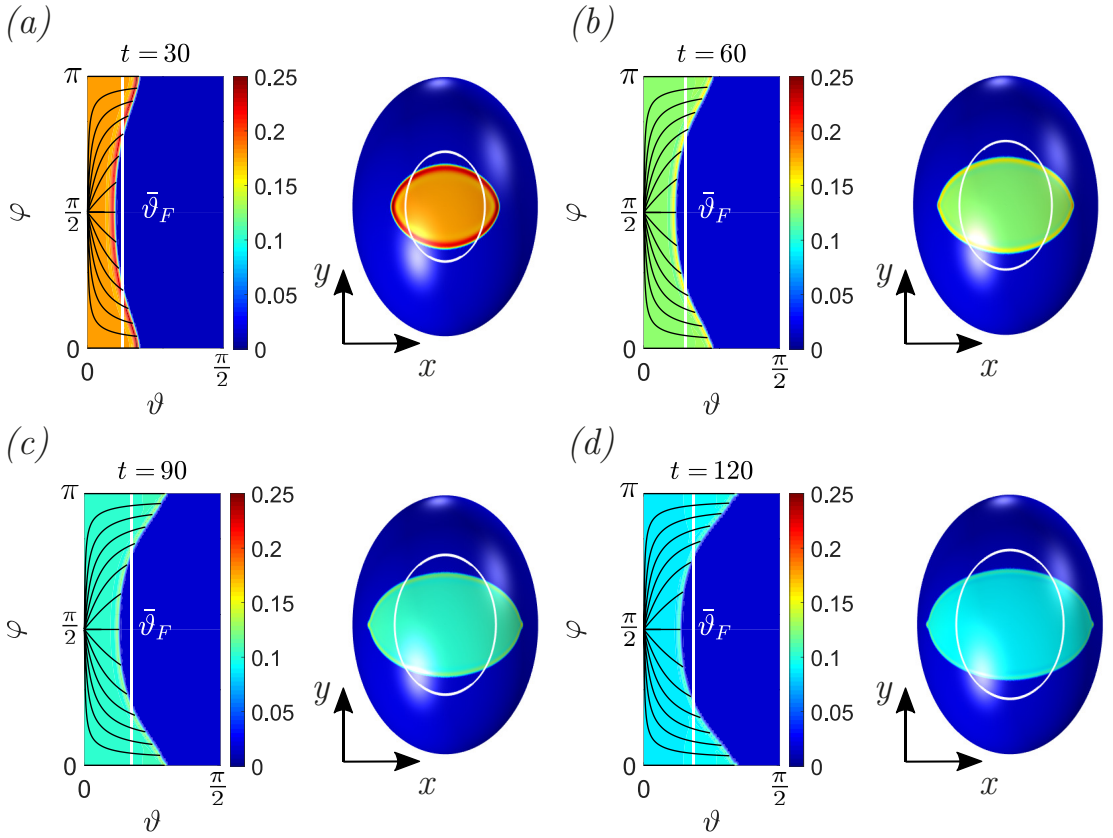

Figure 8.19: Iso-contours of the numerical spreading solution at different times of equation (8.11) for an ellipsoid with $a = 1$, $b = 1.4$, $Bo = 1000$, $\delta = 10^{-2}$, precursor film $h_p = 0.02$ and $\vartheta_0 = 10°$. The black solid lines denote the streamlines of the volume flux per unit length $\mathbf{q}$ and the white line the average front $\bar{\vartheta}_F$.

A scaling law for the spreading front and thickness is obtained by neglecting the modulations of the front, and assuming a constant average value along the azimuth, i.e. $\bar{\vartheta}_F = 1/(2\pi)\int_0^{2\pi}\vartheta_F(\varphi,t)\mathrm{d}\varphi$. The conservation of volume reads:

$$\int_0^{2\pi}\int_0^{\bar{\vartheta}_F(t)} h(\vartheta,t)\,w(\vartheta)\mathrm{d}\vartheta\mathrm{d}\varphi = \int_0^{2\pi}\int_0^{\vartheta_0} w(\vartheta)\mathrm{d}\vartheta\mathrm{d}\varphi$$
$$\rightarrow \int_0^{\bar{\vartheta}_F(t)} h(\vartheta,t)\,w(\vartheta)\mathrm{d}\vartheta = \int_0^{\vartheta_0} w(\vartheta)\mathrm{d}\vartheta, \quad (8.96)$$

where $h = H_0(t) + \vartheta^2 H_2(\varphi,t) + \vartheta^4 H_4(\varphi,t) + \vartheta^6 H_6(\varphi,t)$ is the asymptotic solution obtained in the previous section, and w is given by equation (8.87). Also in this case, an analytical approximation is found by employing the large-time $\mathcal{O}(\vartheta)$ approximation:

$$h = H_0(t) = \frac{1}{\sqrt{\frac{2}{3}t\left(\frac{1}{a^2}+\frac{1}{b^2}\right)}} + \mathcal{O}(\vartheta^2) + \mathcal{O}\left(\frac{1}{t^{3/2}}\right), \quad w = ab\vartheta + \mathcal{O}(\vartheta^2), \quad (8.97)$$

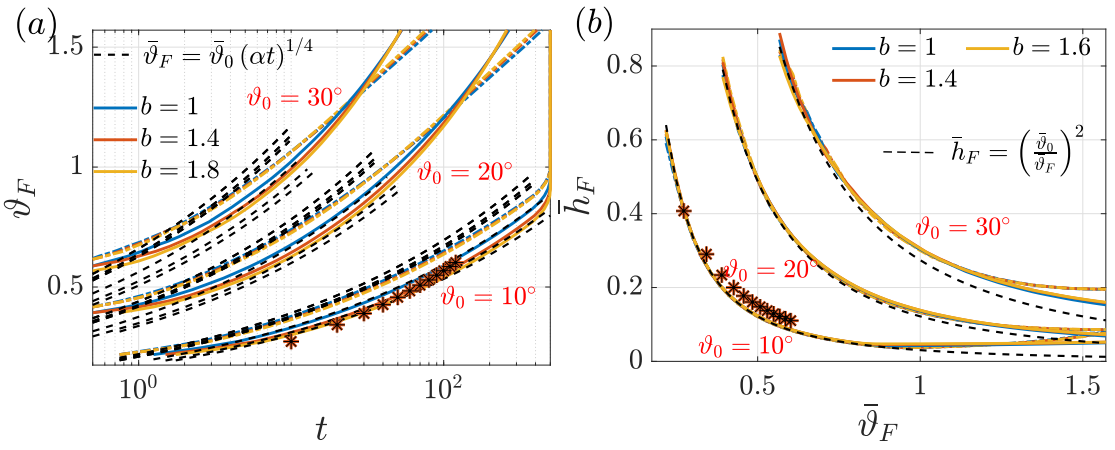

Figure 8.20: Spreading of an initial volume of fluid on an ellipsoid. (a) Variation of the average front angle $\bar{\vartheta}_F$ with time and (b) of the average thickness at the front $\bar{h}_F$ with $\bar{\vartheta}_F$, for $a = 0.6$ (dash-dotted lines), $a = 1$ (solid lines) and different values of the initial angle ϑ_0 and b. The black dashed lines correspond to the analytical approximation of the relation $\bar{\vartheta}_F(t)$ and $\bar{h}_F(\vartheta_F)$, while the stars are the values recovered by a numerical simulation of the complete model with $a = 1$, $b = 1.4$, $Bo = 1000$, $\delta = 10^{-2}$, precursor film $h_p = 0.02$ and $\vartheta_0 = 10°$.

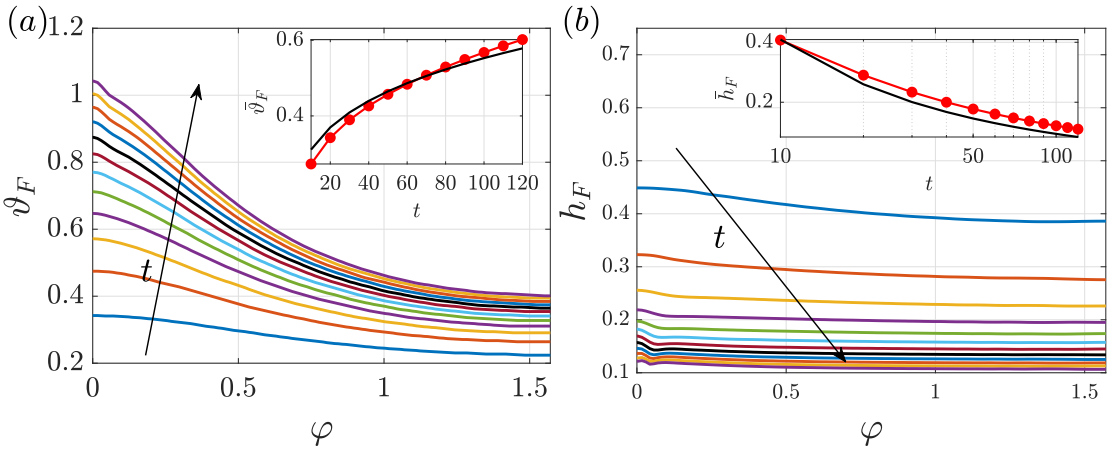

Figure 8.21: Maximum thickness (a) position and (b) value recovered from the numerical spreading simulation with $a = 1$, $b = 1.4$, $Bo = 1000$, $\delta = 10^{-2}$, precursor film $h_p = 0.02$ and $\vartheta_0 = 10°$. Different colours denote different times $10 \le t \le 120$, with step size $\Delta t = 10$. In the insets, we report a comparison between theoretical (black dashed line) and numerical (red dots) (a) average front position and (b) average front thickness.

leading to the following expressions for the average front position and thickness:

$$\bar{\vartheta}_F = \bar{\vartheta}_0 \left(\frac{2}{3} \left(\frac{1}{a^2} + \frac{1}{b^2} \right) t \right)^{1/4}, \quad \bar{h}_F = \left(\frac{\bar{\vartheta}_0}{\bar{\vartheta}_F} \right)^2. \tag{8.98}$$

The azimuth-averaged numerical solution of equation (8.96) and the analytical approximation (8.98) are reported in figure 8.20, displaying a good agreement for low values of ϑ_0 and large

values of a, while the results start to diverge for large ϑ_0 and small a.

Figure 8.21 shows the evolution of the front position and thickness with time, obtained from a numerical simulation of the complete model with $a = 1$, $b = 1.4$, $Bo = 1000$, $\delta = 10^{-2}$, precursor film $h_p = 0.02$ and $\vartheta_0 = 10°$. The values of front position and thickness are averaged and compared with the analytical prediction. The analytical and numerical simulation results show similar trends. However, at large times, the modulations of the front are very large and the front travels much faster along the shorter axis than along the longer one.

The spreading problem on an ellipsoid is characterized by a different front speed along the azimuthal direction, which leads to an accumulation of fluid and a faster spreading along the smaller axis. Peaks of large thickness form together with a modulation of the front, prior to any fingering instability. Therefore, a fingering instability analysis necessarily needs to consider the non-uniform spreading of the fluid along the ellipsoid, which may lead to the preferential formation of fingers. While this analysis focused on the spreading in the absence of surface tension, further studies may involve the formation of fingers resulting from the driven contact line instability.

In this section, we described the drainage and spreading solution for the coating on an ellipsoid. We obtained an analytical solution that well compares with the numerical one. We showed the potential of general coordinates and asymptotic expansions to obtain a two-dimensional analytical solution suitable for a physical interpretation of the drainage and spreading process, in complement to the previous results for axisymmetric geometries. A large-time solution characterized by the separation of temporal and the two spatial dependencies was obtained.

8.6 An experimental comparison

Our work focuses on developing analytical and numerical treatments of the gravity-driven coating on curved substrates. In this section, we compare our predictions to experiments. Rather than measuring the evolution of the film thickness, we use curable elastomers, whose viscosity diverges in a finite time (Lee et al., 2016; Jones et al., 2021). Once cured, the resulting elastic samples can be peeled off the coated surface and measured. The experimental data is compared to the late time drainage solution, here modified to account for the change of viscosity of the elastomer melt over time (Lee et al., 2016; Jones et al., 2021).

The experimental procedure is shown in figure 8.22. We start by 3D printing a mold with the desired geometry (Anycubic i3 Mega). The resulting surface is rough (figure 8.22(a), printer layer height: 0.1mm). We smooth the surface as we apply a first coating using a rapidly curing elastomer (Zhermack VPS-16, see (Jones et al., 2021) for more details on the elastomer mixing procedure). This first layer is sufficiently thin compared to the substrate characteristic size ($\bar{h}/R \sim 10^{-3}$) so that we assume that the substrate curvature remains unchanged after coating. After solidification of the first layer (figure 8.22(b)), we proceed to the experiment and coat the sample with a second layer of elastomer (Zhermack VPS-32, figure 8.22(c)).

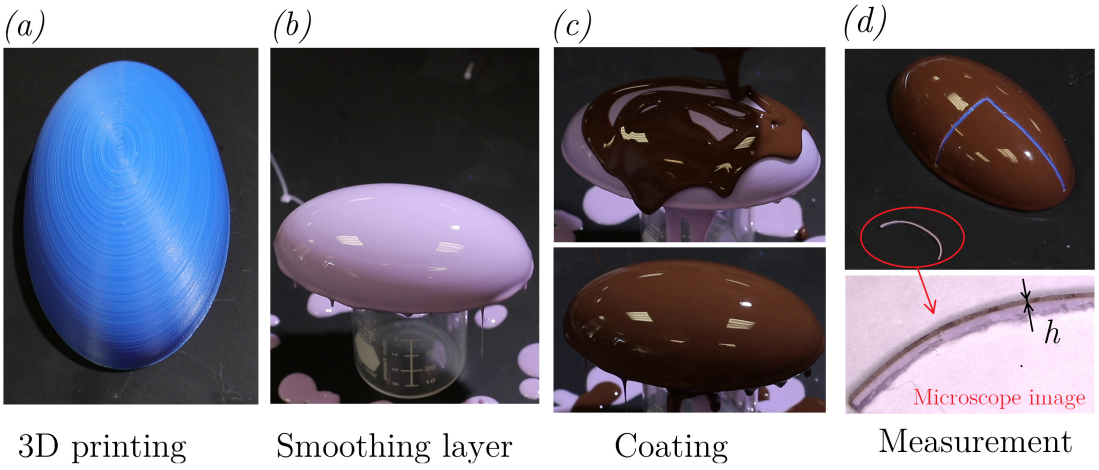

Figure 8.22: Different steps of the experimental procedure. (a) 3D printing of the molds. (b) Smoothing of the mold via a first layer of polymer. (c,d) Coating of the second layer. (e) Peeling of a thin stripe, whose thickness is measured through a microscope. The thickness of the second layer is compared with the analytical and numerical solutions.

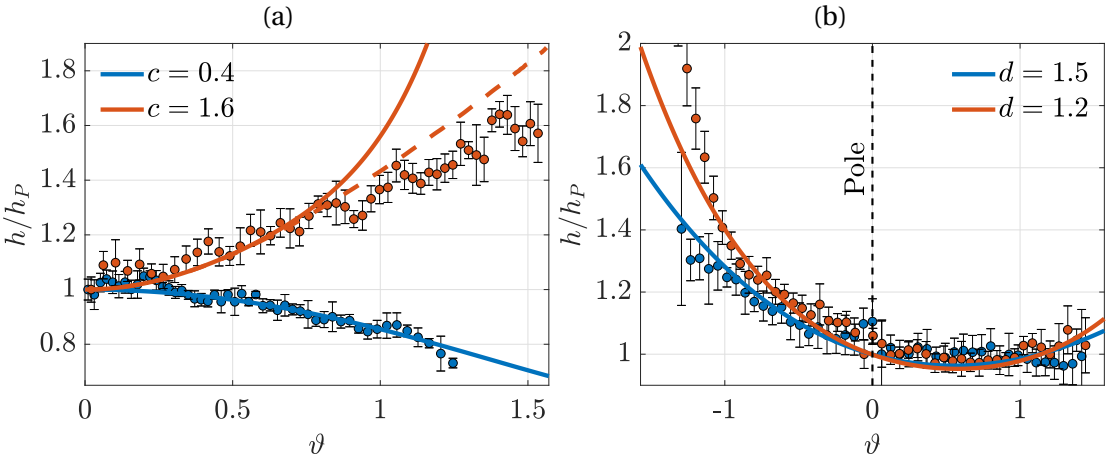

Figure 8.23: Comparison between experimental measurements of h/h_P (colored dots) and the theoretical prediction from (a) Section 8.3.1 for two spheroids with $c = 0.4$ and $R = 30$ mm, $c = 1.6$ and $R = 20$ mm, and (b) Section 8.4 for two tori with $R = 30$ mm, and $d = 1.2, 1.5$. The colored solid thick lines denote the analytical solutions, while the dashed ones the numerical solutions.

After solidification of the second layer, thin strips of the solid shell (containing both layers) are cut, peeled from the substrate and imaged with a microscope (figure 8.22(d)). Dyes are mixed to both elastomers to enhance contrast thereby allowing us to automatically extract the second layer thickness as a function of the arc-length $\bar{h}(\bar{s})$. The errors introduced through the cutting procedure and subsequent image analysis are smoothed by binning the thickness over 50 pixels in the horizontal direction. The standard deviation within each bin defines the experimental uncertainty. Finally, we map the dimensionless arc-length s back to the zenith

angle ϑ with the relation:

$$s(\vartheta) = \int_0^{\vartheta} \sqrt{a^2 \sin^2(\vartheta') \cos^2\varphi + b^2 \sin^2(\vartheta') \sin^2\varphi + c^2 \cos^2\vartheta'} \mathrm{d}\vartheta'. \tag{8.99}$$

In all cases considered, the Bond number is in between $177 < Bo = R^2/\ell_c^2 < 400$, where $\ell_c \approx 1.5$ mm is the capillary length of the polymer, while the final thickness is of order 10^{-1} mm, leading to $\delta \sim 10^{-2} - 10^{-3}$. These values of Bo and δ ensure the accuracy of the drainage solution for the considered cases. Following the results of the asymptotic expansion for $\vartheta \ll 1$, the dimensional large-time thickness can be written as:

$$\bar{h} = h_p f(\text{geometry}), \tag{8.100}$$

where f embeds the spatial distribution and depends only on the geometry, and h_p is the thickness at the pole which depends on the rheology of the polymer melt during the drainage. For a Newtonian fluid, $h_p \sim \sqrt{\mu R/\rho g t}$. For a solidifying polymer, we must account for the change of viscosity of the melt during curing $\mu(t)$ (Lee et al., 2016) and the pole thickness is given by

$$h_p \sim \sqrt{\int_{\tau_w}^{\tau_c} \mu(t) R/\rho g t}, \tag{8.101}$$

where τ_c is the curing time (at which the viscosity diverge) and τ_w the time after mixing at which we start the drainage ($\tau_w \approx 6$ min in our experiments while $\tau_c \approx 18$ min for VPS-32).

In the following, we rescale the measured thickness with the pole thickness so as to have the spatial distribution independent of the fluid rheology $\bar{h}/h_p = f(\text{geometry})$, and compare our data with analytical and numerical results.

Figure 8.23 shows experimental measurements (dots) for two spheroids (a) and two tori (b) compared to the numerical (dashed line) and analytical (solid line) solutions at order $\mathcal{O}(\vartheta^6)$ for the spheroids, and $\mathcal{O}(\vartheta^4)$ for the tori. In all cases, the trend of analytical, numerical and experimental results are similar. For the spheroids, the thickness decreases when moving from the apex to the equator for $c = 0.4$. Instead, for $c = 1.6$ the thickness is found to increase. For the latter case, a favorable agreement for large ϑ is obtained with the numerical solution (dashed line), in agreement with previous discussions. Similar favorable agreements are obtained for tori. In particular, the analytical solution captures the increase in thicknesses observed for $\vartheta < 0$, *i.e.* when the inner part of the torus.

In figure 8.24, we show experimental measurements (dots) for the thickness along the long ($\varphi = \pi/2$) and short ($\varphi = 0$) axis of ellipsoids with various aspect ratios and compare it to the numerical (dashed lines) and analytical (solid lines) solutions. We demonstrate the three possible behaviors previously identified, i.e. (a) thickness increasing both on the short and long axis for $a, b \lessapprox 1.35$, (b,c) thickness increasing along the short axis and decreasing on the long axis for $a \lessapprox 1.35 \lessapprox b$, (d) thickness decreasing along both axes $a, b \gtrapprox 1.35$. In all cases, the

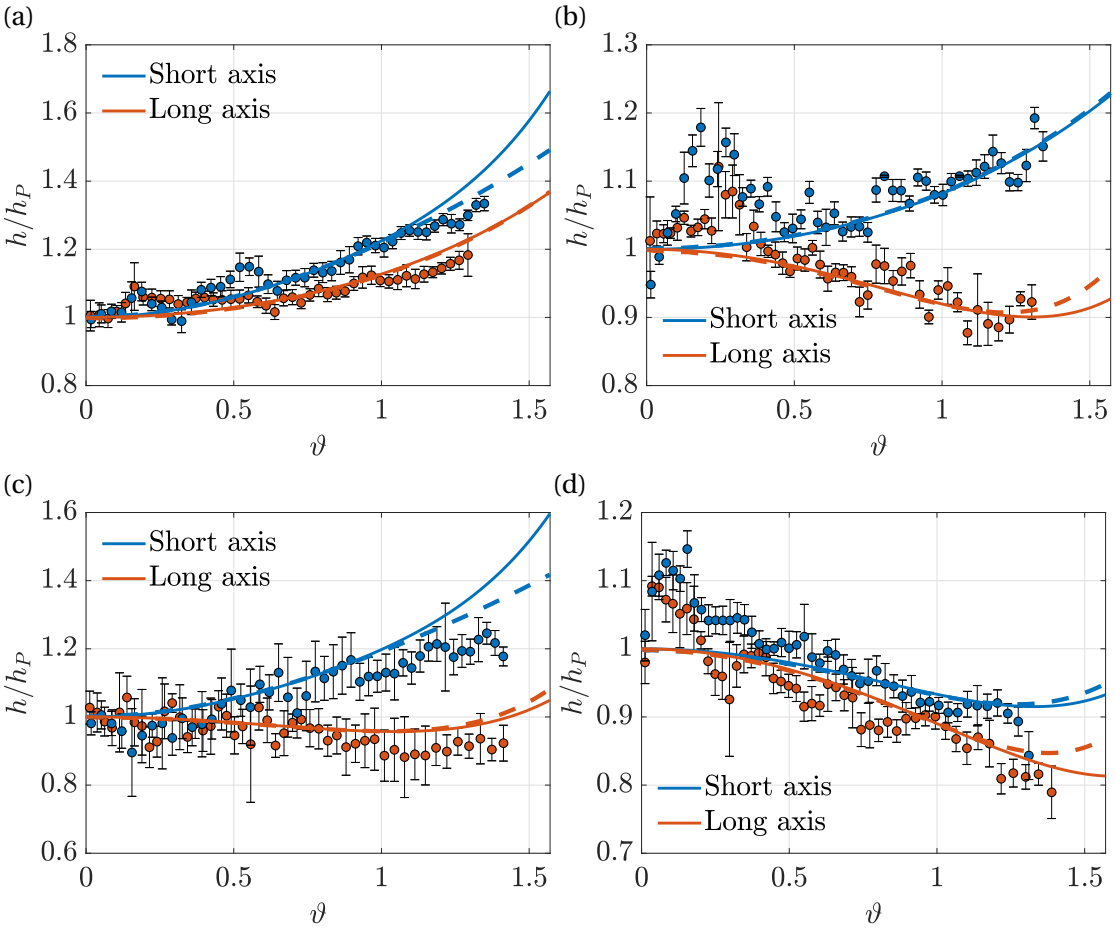

Figure 8.24: Comparison between analytical (solid lines), numerical (dashed lines) solutions and experimental measurements, in analogy with figure 8.24, for ellipsoids with (a) $a = 0.8$, $b = 1$ and $R = 30$ mm, (b) $a = 1$, $b = 1.8$ and $R = 25$ mm, (c) $a = 0.8$, $b = 1.6$ and $R = 30$ mm, (d) $a = 1.6$, $b = 2$ and $R = 20$ mm.

experimental measurements agree favorably with the numerical solutions.

8.7 Conclusion

This work studied the coating problem on a generic substrate with a focus on non-symmetric and three-dimensional drainage and spreading. We analyzed different substrate geometries and derived analytical solutions for the drainage and spreading of an initial volume of fluid, under the assumption of very large Bond number and very thin film compared to the substrate characteristic length. Classical solutions for different substrates were recovered to show the immediacy of the method, subsequently applied to axisymmetric substrates.

An analytical solution for the coating on a spheroid was derived through an asymptotic expansion in the vicinity of the pole. The results show the large-time drainage can be, at the

leading order, described by a temporal decay proportional to $(ct)^{-1/2}$, where c is the ratio between height and equatorial radius. The spatial dependence is a polynomial in ϑ that depends on c. The variation of the thickness was linked to those of the flux per unit length along the substrate: an increase of flux leads to an accumulation of fluid downstream, and vice versa. The drainage solution was then employed to study the spreading of an initial volume of fluid contained in a region close to the pole. The numerical simulations results in terms of thickness and front position were in good agreement with the conservation of volume in general coordinates. The large-time drainage analytical thickness solution was employed. We found simplified analytical expressions which give a good estimate of the spreading process and well agree with numerical simulations.

The paraboloid was chosen as an example in which different analytical solutions of the same problem can co-exist, defining two approximations that work in the vicinity of and far from the pole. Also in this case, both the drainage and spreading results well agreed with numerical simulations.

We then studied the coating of a substrate in which the symmetry of the spreading is broken, i.e. the torus. The coating solution presented much larger values of the thickness on the inner part than on the outer part. As a consequence, the spreading of an initial volume of fluid occurred much faster on the inner region than on the outer region, giving rise to two different spreading fronts.

We concluded the analysis by applying the method to the three-dimensional spreading problem on a non-axisymmetric ellipsoidal substrate, i.e. with three different axes. We first derived a large-time analytical drainage solution which well agrees with the numerical simulations. This solution was characterized by modulations along the azimuthal direction, which are related to the different drainage along the two equatorial axes of the ellipsoid. These modulations reflect in a spreading which does not occur uniformly along the azimuthal direction, but shows an accumulation of fluid and a faster spreading along the shorter axis. These modulations in the front position were interpreted as a primary front destabilization, prior to any fingering instability. We obtained a scaling for the average front which fairly agrees with numerical results. We finally compared the spreading results with experimental measurements and found a good agreement in terms of spatial distributions.

In our analyses, the non-dimensional large-time $\mathcal{O}(1)$ solution obtained through asymptotics has always the same structure, i.e.

$$h = \left(\frac{3}{2\mathcal{K}_p t}\right)^{1/2}, \tag{8.102}$$

where $\mathcal{K}_p$ is the absolute value of the non-dimensional mean curvature at the pole, i.e. $\mathcal{K}_p = 2c$ for a spheroid, $\mathcal{K}_p = 4e$ for a paraboloid, $\mathcal{K}_p = 1$ for a torus, and $\mathcal{K}_p = (1/a^2 + 1/b^2)$ for an ellipsoid. This suggests that a suitable length scale for these substrates is the inverse of the mean curvature at their highest point.

The scope of the present work is to give a coherent and formal framework for the study of

the drainage and coating on generic substrates, which recently gained particular attention, based on the generalization and targeted application of previous analytical developments. These tools are suitable to analyze generic substrates and to study non-uniform spreading fronts. The natural extension of this work is the focus on the destabilization of these spreading fronts. While previous works focused on the fingering instability of two-dimensional fronts (Troian et al., 1989a; Bertozzi and Brenner, 1997; Balestra et al., 2019), similar studies in which the primary front can bend and evolve together with fingering instabilities still need to be pursued. These analyses are not necessarily constrained by the considered configuration, but can be also extended to converging flows (see figure 8.1) and more complex substrates. These findings may find several applications both in environmental studies and thin film technologies.

The interweaving between differential geometry, asymptotic theory and self-similar approach showed great potential in the evaluation of analytical and numerical solutions for the coating on complex geometries, which may find further developments not only in the study of contact line instabilities, but in several coating flow phenomena such as Marangoni, inertia-driven and Rayleigh-Taylor instabilities.

8.8 Appendix

8.8.1 Spheroid: higher order drainage problems

In this section, the higher order drainage problems are described. For the sake of simplicity, we report only the ODE to be solved since their expressions are cumbersome. The ODE at $\mathcal{O}(\vartheta^4)$ reads:

$$H_0^2((\frac{11c}{3}-5c^3)H_2+6cH_4)+\frac{1}{36}c(48c^4-66c^2+19)H_0^3+6cH_0H_2^2+H_4'=0,\quad H_4(0)=0. \tag{8.103}$$

At $\mathcal{O}(\vartheta^6)$, the problem reads:

$$-\frac{1}{3}cH_0H_2((21c^2-16)H_2-48H_4)+H_0^2(-7c^3H_4+(6c^5-\frac{17c^3}{2}+\frac{13c}{5})H_2+\frac{16}{3}cH_4+8cH_6) \tag{8.104}$$

$$+(-\frac{5c^7}{3}+\frac{31c^5}{9}-\frac{257c^3}{120}+\frac{49c}{135})H_0^3+\frac{8}{3}cH_2^3+H_6'=0,\quad H_6(0)=0. \tag{8.105}$$

8.8.2 Paraboloid: higher order drainage solutions

The problem at order $\mathcal{O}(r^2)$ reads:

$$H_2'(t) = -\left(8eH_0(t)^2 H_2(t) - 8e^3 H_0(t)^3\right), \quad H_2(0) = 0, \tag{8.106}$$

whose solution is:

$$H_2(t) = \frac{6e^2\left(512\sqrt{3}e^3t^3 + 576\sqrt{3}e^2t^2 + 216\sqrt{3}et - 27\sqrt{8et+3} + 27\sqrt{3}\right)}{5(8et+3)^{7/2}}. \tag{8.107}$$

The problem at order $\mathcal{O}(r^4)$ reads:

$$H_4'(t) = -\left(\frac{128}{3}e^5 H_0(t)^3 + H_0(t)^2\left(12eH_4(t) - 40e^3 H_2(t)\right) + 12eH_0(t)H_2(t)^2\right), H_4(0) = 0, \tag{8.108}$$

whose solution reads:

$$\begin{aligned} H_4(t) = -\frac{1}{25(8et+3)^{11/2}}(4e^4(&229376\sqrt{3}e^5t^5 + 430080\sqrt{3}e^4t^4 + 322560\sqrt{3}e^3t^3 \\ &+ 120960\sqrt{3}e^2t^2 + 4536et(8et+3)^{3/2} + 1701(8et+3)^{3/2} + 30780\sqrt{3}et - 5103\sqrt{3})). \end{aligned} \tag{8.109}$$

The problem at order $\mathcal{O}(r^6)$ reads:

$$\begin{aligned} H_6'(t) = -(\frac{1}{3}(-640)e^7 H_0(t)^3 - 8eH_0(t)H_2(t)\left(7e^2H_2(t) - 4H_4(t)\right) + 8H_0(t)^2\left(24e^5H_2(t)\right. \\ \left. -7e^3H_4(t) + 2eH_6(t)\right) + \frac{16}{3}eH_2(t)^3), \quad H_6(0) = 0, \end{aligned} \tag{8.110}$$

and the associated solution is:

$$\begin{aligned} H_6(t) = \frac{16e^6}{1375(8et+3)^8}(&425721856\sqrt{3}e^7t^7\sqrt{8et+3} + 1117519872\sqrt{3}e^6t^6\sqrt{8et+3} \\ &- 51093504e^5t^5 + 1257209856\sqrt{3}e^5t^5\sqrt{8et+3} - 95800320e^4t^4 + 785756160\sqrt{3}e^4t^4\sqrt{8et+3} \\ &- 71850240e^3t^3 + 263295360\sqrt{3}e^3t^3\sqrt{8et+3} - 34233840e^2t^2 + 69120864\sqrt{3}e^2t^2\sqrt{8et+3} \\ &+ 32783130et + 23635638\sqrt{3}et\sqrt{8et+3} + 4148739\sqrt{3}\sqrt{8et+3} - 12446217). \end{aligned} \tag{8.111}$$

The final solution is given by $h(r,t) = H_0(t) + r^2H_2(t) + r^4H_4(t) + r^6H_6(t)$. The solution for $t \to \infty$ reads:

$$h(r,t) = \frac{\sqrt{\frac{3}{2}}\sqrt{\frac{1}{t}}\left(3248e^6r^6 - 1540e^4r^4 + 1650e^2r^2 + 1375\right)}{2750\sqrt{e}} + \mathcal{O}(r^8) + \mathcal{O}(t^{-3/2}). \tag{8.112}$$

8.8.3 Torus: drainage solution

Also in this section, we report only the problems when their relative solution is cumbersome. The problems for increasing orders read:

$$H_0{}'(t) = -\frac{1}{3}H_0(t)^3, \quad H_0(0) = 1 \rightarrow H_0(t) = \frac{1}{\sqrt{\frac{2t}{3}+1}}, \tag{8.113}$$

$$H_1'(t) = -\left(\frac{H_0(t)^3}{3d} + 2H_0(t)^2 H_1(t)\right), \quad H_1(0) = 0,$$
$$\rightarrow H_1(t) = \frac{-8\sqrt{3}t^3 - 36\sqrt{3}t^2 - 54\sqrt{3}t + 27\sqrt{2t+3} - 27\sqrt{3}}{5d(2t+3)^{7/2}}, \tag{8.114}$$

$$H_2'(t) = -\left(-\frac{\left(d^2+2\right)H_0(t)^3}{6d^2} + \frac{H_0(t)^2(3dH_2(t)+H_1(t))}{d} + 3H_0(t)H_1(t)^2\right), \quad H_2(0) = 0,$$
$$\rightarrow H_2(t) = \frac{1}{50d^2(2t+3)^{11/2}}\{4\sqrt{3}\left(25d^2+62\right)t^5 + 30\sqrt{3}\left(25d^2+62\right)t^4 + 90\sqrt{3}\left(25d^2+62\right)t^3$$
$$+ 27t^2\left(125\sqrt{3}d^2 + 8\sqrt{2t+3} + 310\sqrt{3}\right) + 81t\left(25\sqrt{3}d^2 + 8\left(\sqrt{2t+3}+5\sqrt{3}\right)\right)$$
$$- 486\left(\sqrt{3}-\sqrt{2t+3}\right)\}, \tag{8.115}$$

$$72d^3H_0(t)H_1H_2 - 6d^3H_0(t)^2H_1 + 36d^3H_0(t)^2H_3(t) + 12d^3H_1^3 + 9d^3H_3'(t) + 9d^2$$
$$H_0(t)H_1^2 + 9d^2H_0(t)^2H_2 - 2d^2H_0(t)^3 - 9dH_0(t)^2H_1 + 3H_0(t)^3 = 0, \quad H_3(0) = 0, \tag{8.116}$$

$$720d^4H_0(t)H_1(t)H_3(t) - 60d^4H_0(t)H_1(t)^2 + 360d^4H_0(t)H_2(t)^2 - 60d^4H_0(t)^2H_2(t)$$
$$+ 360d^4H_0(t)^2H_4(t) + d^4H_0(t)^3 + 360d^4H_1(t)^2H_2(t) + 72d^4H_4'(t) + 144d^3H_0(t)H_1(t)H_2(t)$$
$$- 48d^3H_0(t)^2H_1(t) + 72d^3H_0(t)^2H_3(t) + 24d^3H_1(t)^3 - 72d^2H_0(t)H_1(t)^2 - 72d^2H_0(t)^2H_2(t)$$
$$+ 20d^2H_0(t)^3 + 72dH_0(t)^2H_1(t) - 24H_0(t)^3 = 0, \quad H_4(0) = 0, \tag{8.117}$$

8.8.4 Ellipsoid: higher order drainage solutions

The PDE for $H_4(\varphi, t)$ reads:

$$\begin{aligned}
&\frac{7\cos(2\varphi)H_0^3}{36a^2}+\frac{\cos(2\varphi)H_0^3}{2a^6}+\frac{\cos(2\varphi)H_0^3}{6a^4b^2}+\frac{13\cos(2\varphi)H_0^3}{18b^4}+\frac{\cos(4\varphi)H_0^3}{8a^6}+\frac{\cos(4\varphi)H_0^3}{6a^2b^2}\\
&+\frac{\cos(4\varphi)H_0^3}{8b^6}+\frac{19H_0^3}{72a^2}-\frac{\cos(4\varphi)H_0^3}{12a^4}-\frac{13\cos(2\varphi)H_0^3}{18a^4}-\frac{23H_0^3}{36a^4}+\frac{3H_0^3}{8a^6}-\frac{7\cos(2\varphi)H_0^3}{36b^2}+\frac{19H_0^3}{72b^2}\\
&-\frac{5H_0^3}{9a^2b^2}-\frac{\cos(4\varphi)H_0^3}{8a^4b^2}+\frac{7H_0^3}{24a^4b^2}-\frac{\cos(4\varphi)H_0^3}{12b^4}-\frac{23H_0^3}{36b^4}-\frac{\cos(2\varphi)H_0^3}{6a^2b^4}-\frac{\cos(4\varphi)H_0^3}{8a^2b^4}\\
&+\frac{7H_0^3}{24a^2b^4}-\frac{\cos(2\varphi)H_0^3}{2b^6}+\frac{3H_0^3}{8b^6}+\frac{4\cos(2\varphi)H_2H_0^2}{3a^2}+\frac{2\cos(2\varphi)H_2H_0^2}{b^4}+\frac{\cos(4\varphi)H_2H_0^2}{2a^2b^2}+\frac{11H_2H_0^2}{6a^2}\\
&+\frac{11H_2H_0^2}{6b^2}+\frac{2\cos(2\varphi)H_4H_0^2}{a^2}+\frac{3H_4H_0^2}{a^2}+\frac{3H_4H_0^2}{b^2}+\frac{\cos(2\varphi)\sin(2\varphi)\frac{\partial H_2}{\partial\varphi}H_0^2}{4a^4}\\
&+\frac{\cos(2\varphi)\sin(2\varphi)\frac{\partial H_2}{\partial\varphi}H_0^2}{4b^4}+\frac{\sin(2\varphi)\frac{\partial H_2}{\partial\varphi}H_0^2}{4a^4}+\frac{\sin(2\varphi)\frac{\partial H_2}{\partial\varphi}H_0^2}{4b^2}+\frac{\sin(2\varphi)\frac{\partial H_4}{\partial\varphi}H_0^2}{2b^2}-\frac{\sin(2\varphi)\frac{\partial H_4}{\partial\varphi}H_0^2}{2a^2}\\
&-\frac{\sin(2\varphi)\frac{\partial H_2}{\partial\varphi}H_0^2}{4a^2}-\frac{2\cos(2\varphi)H_2H_0^2}{a^4}-\frac{\cos(4\varphi)H_2H_0^2}{4a^4}-\frac{7H_2H_0^2}{4a^4}-\frac{2\cos(2\varphi)H_4H_0^2}{b^2}-\frac{4\cos(2\varphi)H_2H_0^2}{3b^2}\\
&-\frac{3H_2H_0^2}{2a^2b^2}-\frac{\cos(2\varphi)\sin(2\varphi)\frac{\partial H_2}{\partial\varphi}H_0^2}{2a^2b^2}-\frac{\cos(4\varphi)H_2H_0^2}{4b^4}-\frac{7H_2H_0^2}{4b^4}-\frac{\sin(2\varphi)\frac{\partial H_2}{\partial\varphi}H_0^2}{4b^4}+\frac{2\cos(2\varphi)H_2^2H_0}{a^2}\\
&+\frac{3H_2^2H_0}{a^2}+\frac{3H_2^2H_0}{b^2}+\frac{H_2\sin(2\varphi)\frac{\partial H_2}{\partial\varphi}H_0}{b^2}-\frac{H_2\sin(2\varphi)\frac{\partial H_2}{\partial\varphi}H_0}{a^2}-\frac{2\cos(2\varphi)H_2^2H_0}{b^2}+\frac{\partial H_4}{\partial t}=0
\end{aligned} \tag{8.118}$$

whose numerical solution is reported in figures 8.25 and 8.26. Figure 8.25(b) shows that the values of the rescaled fourth order solution $H_4^* = H_4\sqrt{\alpha t}$ collapse to the same curve as time increase, thus suggesting that also in this case a large-time separation of variables is possible.

Because of its size, we do not write the PDE for H_6 here; however, the solutions are shown in figures 8.27 and 8.28. In analogy with the solutions at order $\mathcal{O}(\vartheta^2)$ and $\mathcal{O}(\vartheta^4)$, the behavior of the large-time solution suggests that a solution $H_n^*(\varphi) = H_n(\varphi, t)/H_0(t)$ satisfies the problem.

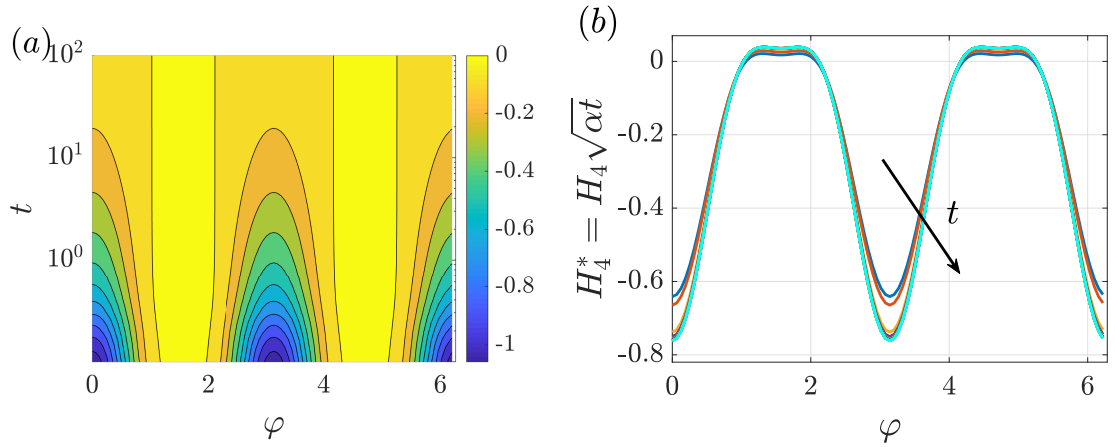

Figure 8.25: Drainage along an ellipsoid with $a = 0.5$ and $b = 1.5$. (a) Spatiotemporal evolution of H_4: iso-contours of H_2 in the (φ, t) plane. (b) Second order correction $H_4^* = H_4/H_0 \approx H_4\sqrt{\alpha t}$ as a function of φ at different times: $t = 0.4$ (blue), $t = 1$ (orange), $t = 5$ (yellow), $t = 10$ (purple) $t = 30$ (green), $t = 50$ (cyan), $t = 70$ (maroon), $t = 90$ (black), $t = 100$ (red).

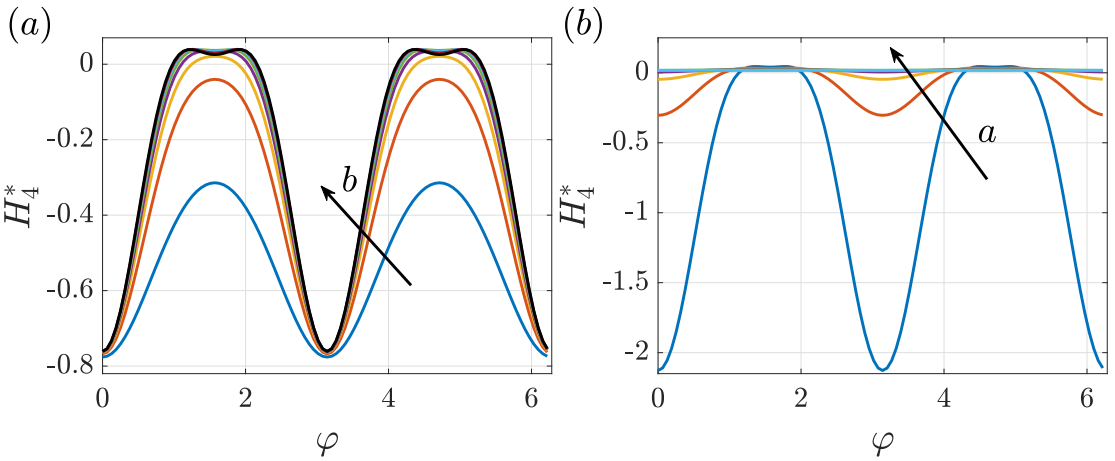

Figure 8.26: (a) Fourth order correction $H_4^* = H_4/H_0 \approx H_4\sqrt{\alpha t}$ as a function of φ at $t = 100$, for $a = 0.5$ and increasing b: $b = 0.6$ (blue), $b = 0.8$ (orange), $b = 1$ (yellow), $b = 1.2$ (purple), $b = 1.4$ (green), $b = 1.6$ (cyan), $b = 1.8$ (maroon), $b = 2$ (black). (b) Second order correction H_4^* as a function of φ at $t = 100$, for $b = 1.5$ and increasing a: $a = 0.4$ (blue), $a = 0.6$ (orange), $a = 0.8$ (yellow), $a = 1$ (purple), $a = 1.2$ (green), $a = 1.4$ (cyan).

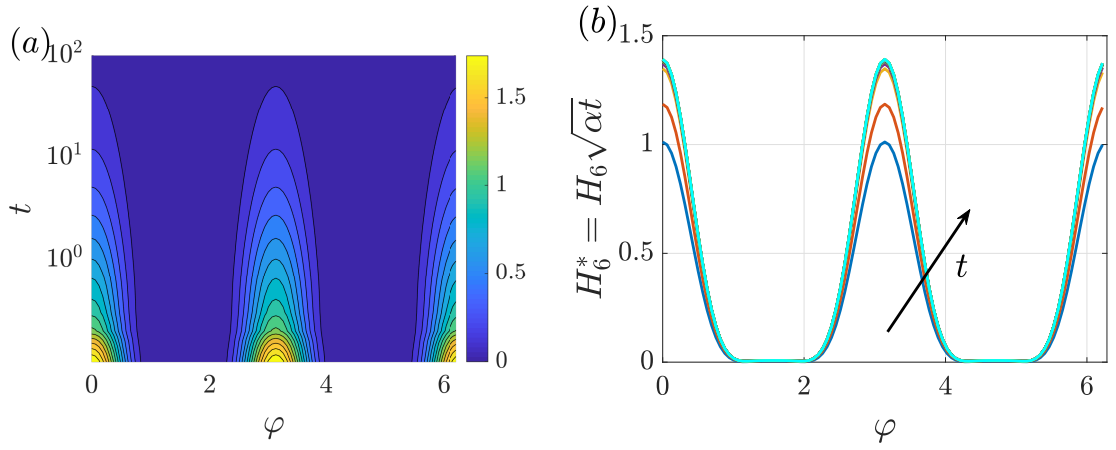

Figure 8.27: Drainage along an ellipsoid with $a = 0.5$ and $b = 1.5$. (a) Spatiotemporal evolution of H_6: iso-contours of H_6 in the (φ, t) plane. (b) Second order correction $H_6^* = H_6/H_0 \approx H_6\sqrt{\alpha t}$ as a function of φ at different times: $t = 0.4$ (blue), $t = 1$ (orange), $t = 5$ (yellow), $t = 10$ (purple) $t = 30$ (green), $t = 50$ (cyan), $t = 70$ (maroon), $t = 90$ (black), $t = 100$ (red).

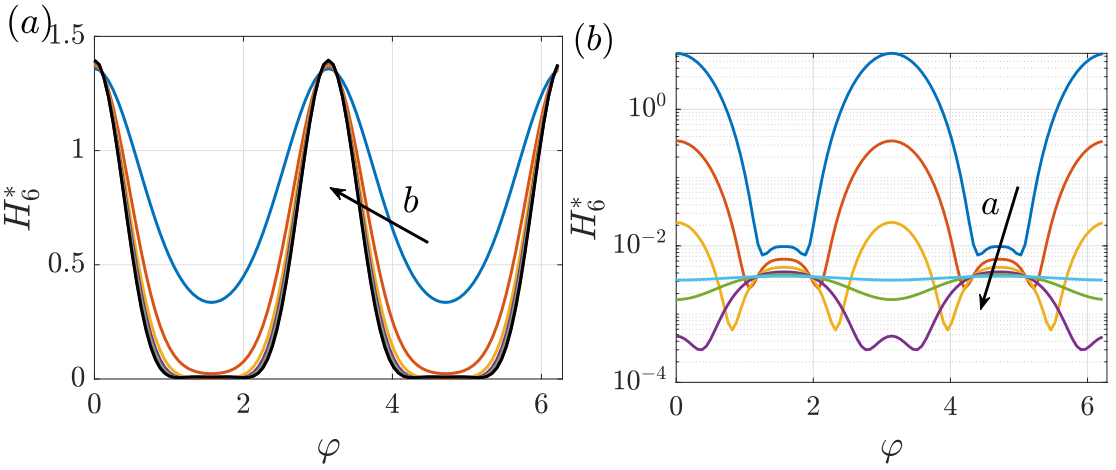

Figure 8.28: (a) Sixth order correction $H_6^* = H_6/H_0 \approx H_6\sqrt{\alpha t}$ as a function of φ at $t = 100$, for $a = 0.5$ and increasing b: $b = 0.6$ (blue), $b = 0.8$ (orange), $b = 1$ (yellow), $b = 1.2$ (purple), $b = 1.4$ (green), $b = 1.6$ (cyan), $b = 1.8$ (maroon), $b = 2$ (black). (b) Second order correction H_6^* as a function of φ at $t = 100$, for $b = 1.5$ and increasing a: $a = 0.4$ (blue), $a = 0.6$ (orange), $a = 0.8$ (yellow), $a = 1$ (purple), $a = 1.2$ (green), $a = 1.4$ (cyan).

Part III

Behavior of permeable bodies invested by a uniform flow or in a falling configuration

9 On the effect of a penetrating recirculation region on the bifurcations of the flow past a permeable sphere

Remark This chapter is largely inspired by the publication of the same name

M. Ciuti[1,2], G. A. Zampogna[1], F. Gallaire[1], S. Camarri[2], P. G. Ledda [1]
[1]Laboratory of Fluid Mechanics and Instabilities, École Polytechnique Fédérale de Lausanne, CH-1015 Lausanne, Switzerland
[2]Dipartimento di Ingegneria Civile e Industriale, Università di Pisa, 56122 Pisa, Italy

Physics of Fluids **33**, 124103 (2021)

Author contributions P.G.L. conceived the project with input from F.G. and G.A.Z.. P.G.L. developed the theoretical framework and the numerical codes. P.G.L. supervised M. C. during his master thesis, performed with the provided tools. P.G.L. wrote the manuscript with input from the coauthors.

We study the flow past a permeable sphere modeled using homogenization theory. The flow through the porous medium is described by the Darcy law, in which the permeability quantifies the resistance for the fluid to pass through the micro-structure. A slip condition on the tangential velocity at the interface between the fluid and porous region is employed to account for the viscous effects in the proximity of the interface. The steady and axisymmetric flow is first characterized under the assumption of a homogenous and isotropic porous medium. In a certain range of permeability, the recirculation region penetrates inside the sphere, resulting in a strong modification of the linear stability properties of the flow and in a decrease of the critical Reynolds numbers for the flow instability. However, for very large permeabilities, a critical permeability value is identified, beyond which the steady and axisymmetric flow remains always linearly stable. The hypothesis of a homogenous porous medium is then relaxed, and the effect of polynomial distributions of permeability inside the body is studied. Interestingly, some macroscopic flow properties do not significantly vary with the permeability distributions, provided that their average is maintained constant. The analysis is concluded by outlining a simplified procedure to retrieve the full-scale structure corresponding to a considered distribution of permeability.

9.1 Introduction

The motivation to study flows around and through porous bodies is exposed in Section 1.1. We refer to Section 1.4 for an overview of the flow past solid and porous bluff bodies.

Owing to the large interest in the flow around permeable spheres, several works often studied the problem in the limit of negligible inertia of the fluid (Levresse et al., 2001; Bhattacharyya, 2010; Josef and Tao, 1964; Neale et al., 1973; Adler, 1981). Yu et al. (2012) investigated the steady and axisymmetric flow around a porous sphere. In this case, the wake can exhibit a penetrating recirculation region. Although the effect of a detached recirculation region on the stability properties of the wake has been widely investigated in the literature, the permeable sphere is identified as the perfect testing ground to study the effect of a penetrating recirculation region. In this work, the steady and axisymmetric flow past a permeable sphere and its bifurcations are studied, with constant and variable permeability properties.

The flow through the permeable sphere can be modeled via different approaches, from the well-known Darcy law (Darcy, 1856), where the velocity is assumed to be proportional to the pressure gradient, to its Brinkman extension (Brinkman, 1949). We refer to Section 1.4.1 for a detailed discussion about the homogenization method, employed here to describe the macroscopic flow inside the sphere. The homogenized model, predominantly validated for simple test cases (Zampogna and Bottaro, 2016; Lācis et al., 2017; Lācis and Bagheri, 2017; Lācis et al., 2020), is exploited to study an actual three-dimensional configuration of interest and highlight the potential of the direct link between micro-structure and homogenized properties through an inverse procedure to retrieve the geometry.

The use of variable permeability distributions, together with a strategy to identify a microscopic geometry that generates such permeability in practice, is a key ingredient for realistic flow control of bluff-body wakes in general and more specifically in this work for the flow past a sphere. The chapter is structured as follows. Section 9.2 presents the mathematical formulation and the numerical implementation. Section 9.3 is devoted to the study of the steady and axisymmetric flow and its bifurcations for a sphere composed by a homogenous porous medium, in which the homogenized properties are taken as parameters. Section 9.4 extends the previous results by considering variable distributions of permeability along the radius. In Section 9.5, a procedure to retrieve the micro-structure of the sphere and verify the faithfulness of the trends observed in the parametric study is outlined.

9.2 Mathematical formulation and numerical implementation

The mathematical formulation and the numerical implementation (whose validation is reported in Appendix 9.7.1) of the problems analyzed in the present work are introduced in this section. We consider the flow of an incompressible Newtonian fluid of density ρ and viscosity μ past a permeable sphere of diameter D. The free-stream velocity is denoted as U_∞ (figure 9.1(a)). A cylindrical reference frame $(\bar{x}_1, \bar{x}_2, \bar{x}_3) = (\bar{x}, \bar{r}, \theta)$ is introduced. The velocity

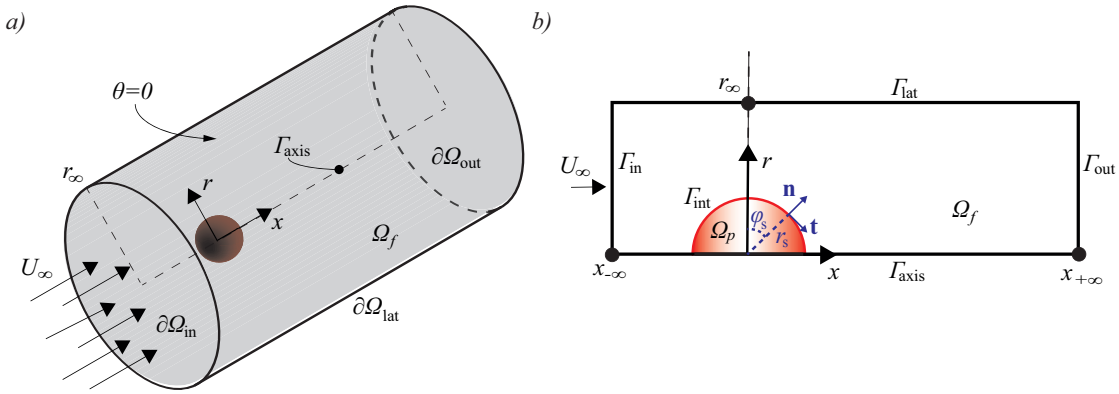

Figure 9.1: (a) Sketch of the three-dimensional flow configuration. (b) Sketch of the computational domain employed for the axisymmetric simulations of this work, together with the global cylindrical and local spherical reference frames. The azimuthal direction is perpendicular to the represented plane.

and pressure fields $(\bar{\boldsymbol{u}}, \bar{p})$, indicated as $\bar{\boldsymbol{u}} = (\bar{u}_1, \bar{u}_2, \bar{u}_3) = (\bar{u}_x, \bar{u}_r, \bar{u}_\theta)$, satisfy the Navier Stokes equations in the fluid region Ω_f:

$$\begin{aligned} &\bar{\nabla} \cdot \bar{\boldsymbol{u}} = 0 \\ &\rho \left(\partial_{\bar{t}} \bar{\boldsymbol{u}} + \bar{\boldsymbol{u}} \cdot \bar{\nabla} \bar{\boldsymbol{u}} \right) + \bar{\nabla} \bar{p} - \mu \bar{\nabla}^2 \bar{\boldsymbol{u}} = \mathbf{0}. \end{aligned} \tag{9.1}$$

The flow through the porous medium Ω_p, characterized by the velocity and pressure fields $(\bar{\boldsymbol{v}}, q)$, is described by employing the homogenized model, formally analogous to the Darcy law (Zampogna and Bottaro, 2016):

$$\bar{\nabla} \bar{q} = -\mu \boldsymbol{\kappa}^{-1} \bar{\boldsymbol{v}}, \tag{9.2}$$

where $\boldsymbol{\kappa}$ is the permeability tensor. Recent homogenization-based developments rigorously defined the conditions at the interface $\partial\Omega_{int}$ between the fluid region and the porous one (Lācis et al., 2017; Bottaro, 2019; Lācis et al., 2020; Naqvi and Bottaro, 2021), which read:

$$\bar{\boldsymbol{u}} - \left(-\frac{\boldsymbol{\kappa}_{\text{int}}}{\mu} \bar{\nabla} \bar{q} \right) = \bar{\boldsymbol{\Lambda}} \left[\bar{\Sigma}(\bar{\boldsymbol{u}}, \bar{p}) \mathbf{n} \right], \quad \bar{q} = -[\bar{\Sigma}(\bar{\boldsymbol{u}}, \bar{p}) \mathbf{n}] \cdot \mathbf{n} \tag{9.3}$$

where $\bar{\Sigma}(\bar{\boldsymbol{u}}, \bar{p}) = -\bar{p}\mathbf{I} + \mu \left(\bar{\nabla} \bar{\boldsymbol{u}} + \bar{\nabla} \bar{\boldsymbol{u}}^T \right)$ and $\boldsymbol{\kappa}_{\text{int}}$ represents the permeability tensor evaluated at the interface (which does not necessarily coincide with the bulk one $\boldsymbol{\kappa}$) and $\bar{\boldsymbol{\Lambda}}$ is the slip tensor. The spherical coordinates radius, colatitude and azimuth $(r_s, \varphi_s, \theta_s = \theta)$ are introduced, whose origin is located at the center of the sphere (see figure 9.1). At the sphere surface, $\mathbf{t}$, $\mathbf{s}$ and $\mathbf{n}$ are the corresponding colatitude, azimuth and radial unit vectors. In this spherical reference

frame, the slip tensor reads:

$$\bar{\mathbf{\Lambda}} = \begin{pmatrix} \bar{\Lambda}_t & 0 & 0 \\ 0 & \bar{\Lambda}_s & 0 \\ 0 & 0 & 0 \end{pmatrix} \tag{9.4}$$

The slip tensor is thus projected onto the cylindrical reference frame employed in this work by introducing the notation $(\mathbf{a}\otimes\mathbf{b})_{ij} = a_i b_j$, obtaining as a result (Zampogna et al., 2019b):

$$\bar{\mathbf{\Lambda}} = \bar{\Lambda}_t \mathbf{t}\otimes\mathbf{t} + \bar{\Lambda}_s \mathbf{s}\otimes\mathbf{s}, \tag{9.5}$$

where $\mathbf{t}$ and $\mathbf{s}$ are expressed in the cylindrical reference frame. The macroscopic quantities, denoted here as permeability, interfacial permeability and slip, actually represent the macroscopic effects of a given microscopic structure on the flow field. In Appendix 9.7.2 the formal problems which link the microscopic structure to these quantities are given, while in sections 9.3 and 9.4 they are treated as free parameters to characterize the flow past a porous sphere. Depending on the values of the homogenized tensors, some limiting cases are identified. The case $\boldsymbol{\kappa} = \boldsymbol{\kappa}_{\text{int}} = \mathbf{0}$ with $\bar{\mathbf{\Lambda}} \neq \mathbf{0}$ is equivalent to a first-order slip condition on a textured surface of a solid sphere (Zampogna et al., 2019b), since no flow occurs inside the body and the velocity normal to the surface is neglected. Another limiting condition occurs when $\boldsymbol{\kappa} \to \infty$ and $\boldsymbol{\kappa}_{\text{int}} \to \infty$. In this case, the porous structure does not induce any resistance to the flow, which is equivalent to the absence of a solid structure. Finally, the condition $\bar{\mathbf{\Lambda}} = \mathbf{0}$ means that the viscous diffusion effects in the proximity of the fluid-porous interface are neglected.

The macroscopic flow problem is completed by the far-field boundary conditions in the fluid domain. At the inlet, a uniform free stream is imposed, i.e. $\bar{\boldsymbol{u}} = U_\infty \mathbf{e}_x$, while on the lateral and outlet boundaries a zero-stress condition is imposed, $\bar{\Sigma}(\bar{\boldsymbol{u}}, \bar{p})\mathbf{n} = \mathbf{0}$. The flow equations are non-dimensionalized by introducing the characteristic length D (the sphere diameter), velocity U_∞, time $\frac{D}{U_\infty}$ and pressure ρU_∞^2, obtaining the following set of non-dimensional equations:

$$\begin{cases} \nabla\cdot\boldsymbol{u} = 0 \\ \partial_t \boldsymbol{u} + \boldsymbol{u}\cdot\nabla\boldsymbol{u} + \nabla p - \frac{1}{Re}\nabla^2\boldsymbol{u} = \mathbf{0} \end{cases} \quad \Omega_f, \tag{9.6}$$

$$\begin{cases} \boldsymbol{v} = -Re\mathbf{Da}\nabla q \\ \nabla\cdot\boldsymbol{v} = 0 \end{cases} \quad \Omega_p, \tag{9.7}$$

together with the non-dimensional interface conditions at $\partial\Omega_{\text{int}}$:

$$\boldsymbol{u} - \left(-Re\mathbf{Da}_{\text{int}}\nabla q\right) = \mathbf{\Lambda}\left[\Sigma(\boldsymbol{u}, p)\mathbf{n}\right], \quad q = -\left[\Sigma(\boldsymbol{u}, p)\mathbf{n}\right]\cdot\mathbf{n}, \tag{9.8}$$

where $\Sigma(\boldsymbol{u}, p) = -p\mathbf{I} + \frac{1}{Re}\left(\nabla\boldsymbol{u} + \nabla\boldsymbol{u}^T\right)$ is the non-dimensional stress tensor, $Re = \frac{U_\infty D}{\nu}$ is the Reynolds number, $\mathbf{Da} = \frac{\boldsymbol{\kappa}}{D^2}$ and $\mathbf{Da}_{\text{int}} = \frac{\boldsymbol{\kappa}_{\text{int}}}{D^2}$ are respectively the Darcy tensor in the bulk and at the interface, and $\mathbf{\Lambda} = \frac{\bar{\mathbf{\Lambda}}}{D}$ is the slip tensor, whose non-zero diagonal components are denoted with Λ_t and Λ_s, respectively along the colatitude and azimuthal directions.

In this work, we focus on the steady and axisymmetric solution (i.e. $\partial_t = 0$ and $\partial_\theta = 0$) of the flow equations (9.6,9.7), so-called baseflow, and its stability with respect to azimuthal disturbances, i.e. the perturbation is expanded in normal modes along the azimuthal direction. Therefore, to compute the baseflow, the flow equations are solved in the azimuthal plane $\theta = 0$, leading to the two-dimensional domain reported in figure 9.1(b). The steady and axisymmetric solution of the equations $(\boldsymbol{U}, P, \boldsymbol{V}, Q)$, with $\boldsymbol{U} = (U_x, U_r)$ and $\boldsymbol{V} = (V_x, V_r)$, satisfies the following set of equations:

$$\begin{cases} \nabla \cdot \boldsymbol{U} = 0 \\ \boldsymbol{U} \cdot \nabla \boldsymbol{U} + \nabla P - \frac{1}{Re} \nabla^2 \boldsymbol{U} = \mathbf{0} \end{cases} \quad \Omega_f, \tag{9.9}$$

$$\begin{cases} \boldsymbol{V} = -Re\mathbf{Da} \nabla Q \\ \nabla \cdot \boldsymbol{V} = 0 \end{cases} \quad \Omega_p, \tag{9.10}$$

together with the non-dimensional interface conditions at Γ_{int}:

$$\boldsymbol{U} - (-Re\mathbf{Da}_{\text{int}} \nabla Q) = \boldsymbol{\Lambda} \left[\Sigma(\boldsymbol{U}, P)\mathbf{n} \right], \quad Q = -\left[\Sigma(\boldsymbol{U}, P)\mathbf{n} \right] \cdot \mathbf{n}. \tag{9.11}$$

The remaining boundary conditions to be imposed are the free-stream condition $\boldsymbol{U} = \mathbf{e}_x = [1,0,0]^T$ at Γ_{inlet}, the free-stress condition $\Sigma(\boldsymbol{U}, P)\mathbf{n} = \mathbf{0}$ at $\Gamma_{\text{lat}} \cup \Gamma_{\text{out}}$, and the boundary condition for the fluid region $\boldsymbol{U} \cdot \mathbf{e}_r = U_r = 0$ on the axis Γ_{axis}.

As mentioned above, the stability properties to perturbations of the baseflow $(\mathbf{U}, P)$ are investigated. To this purpose, a normal mode decomposition of azimuthal wavenumber m and complex frequency σ is considered, whose real and imaginary parts are respectively the growth rate and the frequency. The following ansatz has been introduced

$$\begin{bmatrix} \boldsymbol{u} \\ p \\ \boldsymbol{v} \\ q \end{bmatrix} = \begin{bmatrix} \boldsymbol{U}(x,r) \\ P(x,r) \\ \boldsymbol{V}(x,r) \\ Q(x,r) \end{bmatrix} + \varsigma \begin{bmatrix} \hat{\boldsymbol{u}}(x,r) \\ \hat{p}(x,r) \\ \hat{\boldsymbol{v}}(x,r) \\ \hat{q}(x,r) \end{bmatrix} \exp(\mathrm{i}m\theta + \sigma t), \tag{9.12}$$

$\varsigma \ll 1$. The flow equations (9.6,9.7), with the corresponding boundary conditions, are expanded in powers of ς, using the expression for the flow field given in equation (9.12). At order $\mathcal{O}(1)$, the baseflow equations for $(\boldsymbol{U}, P, \boldsymbol{V}, Q)$ are retrieved, while at order $\mathcal{O}(\varsigma)$ one obtains:

$$\begin{cases} \nabla \cdot \hat{\boldsymbol{u}} = 0 \\ \sigma \hat{\boldsymbol{u}} + \boldsymbol{U} \cdot \nabla_m \hat{\boldsymbol{u}} + \hat{\boldsymbol{u}} \cdot \nabla_0 \boldsymbol{U} + \nabla_m \hat{p} - \frac{1}{Re} \nabla_m^2 \hat{\boldsymbol{u}} = \mathbf{0} \end{cases} \quad \Omega_f, \tag{9.13}$$

$$\begin{cases} \hat{\mathbf{v}} = -Re\mathbf{Da} \nabla_m \hat{q} \\ \nabla_m \cdot \hat{\boldsymbol{v}} = 0 \end{cases} \quad \Omega_p, \tag{9.14}$$

$$\hat{\boldsymbol{u}} - \left(-Re\mathbf{Da}_{\text{int}} \nabla_m \hat{q} \right) = \boldsymbol{\Lambda} \left[\Sigma(\hat{\boldsymbol{u}}, \hat{p})\mathbf{n} \right], \quad \hat{q} = -\left[\Sigma_m(\hat{\boldsymbol{u}}, \hat{p})\mathbf{n} \right] \cdot \mathbf{n}, \tag{9.15}$$

where the following operators are introduced (Meliga et al., 2009):

$$\nabla_m f = \begin{bmatrix} \frac{\partial f}{\partial x} \\ \frac{\partial f}{\partial r} \\ \frac{\mathrm{i}mf}{r} \end{bmatrix}, \tag{9.16}$$

$$\nabla_m \mathbf{g} = \begin{bmatrix} \frac{\partial g_x}{\partial x} & \frac{\partial g_x}{\partial r} & \frac{\mathrm{i}m}{r} g_x \\ \frac{\partial g_r}{\partial x} & \frac{\partial g_r}{\partial r} & \frac{\mathrm{i}m}{r} g_r - \frac{g_\theta}{r} \\ \frac{\partial g_\theta}{\partial x} & \frac{\partial g_\theta}{\partial r} & \frac{\mathrm{i}m}{r} g_\theta + \frac{g_r}{r} \end{bmatrix}, \tag{9.17}$$

$$\nabla_m \cdot \mathbf{g} = \frac{\partial g_x}{\partial x} + \frac{1}{r}\frac{\partial r g_r}{\partial r} + \frac{\mathrm{i}m}{r} g_\theta, \tag{9.18}$$

$$\nabla_m^2 \mathbf{g} = \nabla_m \cdot (\nabla_m \mathbf{g}), \tag{9.19}$$

$$\Sigma_m(\mathbf{g}, f) = -g\mathbf{I} + \frac{1}{Re}\left(\nabla_m \mathbf{g} + \nabla_m \mathbf{g}^T\right). \tag{9.20}$$

The homogenous condition $\hat{\boldsymbol{u}} = \mathbf{0}$ is imposed at the inlet, while on the lateral and outlet boundary the free-stress condition $\Sigma_m(\boldsymbol{u}, p)\mathbf{n} = \mathbf{0}$ is enforced. On the axis, the following regularity conditions have to be imposed (Batchelor and Gill, 1962; Meliga et al., 2009; Viola et al., 2014):

$$u_r = u_\theta = \frac{\partial u_x}{\partial r} = 0 \quad \text{for } m = 0; \tag{9.21}$$

$$\frac{\partial u_r}{\partial r} = u_x = \frac{\partial u_\theta}{\partial r} = 0 \quad \text{for } |m| = 1; \tag{9.22}$$

$$u_r = u_\theta = u_x = 0 \quad \text{for } |m| > 1; \tag{9.23}$$

The outlined set of equations is an eigenvalue problem of complex eigenvalues $\sigma = \mathrm{Re}(\sigma) + \mathrm{i}\mathrm{Im}(\sigma)$, whose real part is the growth rate of the global mode, and the imaginary part is its angular velocity. The flow is asymptotically unstable if at least one eigenvalue has a positive real part; otherwise, the flow is asymptotically stable. Therefore, stable modes are characterized by $\mathrm{Re}(\sigma) < 0$, while unstable ones by $\mathrm{Re}(\sigma) > 0$.

9.2.1 Numerical implementation of the flow equations

The numerical implementation of the flow equations is performed in COMSOL Multiphysics. The steady equations (9.9,9.10) and the eigenvalues problem (9.13,9.14) are implemented through their weak form, employing $P2-P1$ Taylor-Hood elements for the fluid domain. The steady solutions are obtained via the built-in Netwon algorithm, with a relative tolerance of 10^{-6}, while the eigenvalue problem is solved by employing the built-in eigenvalue solver based on the ARPACK library. The numerical implementation of the Darcy law is based on a second-order PDE for q obtained by taking the divergence of equation (9.7):

$$\nabla \cdot \boldsymbol{v} = -Re\nabla \cdot \left(\mathbf{Da}\nabla q\right) = 0 \Rightarrow \nabla \cdot \left(\mathbf{Da}\nabla q\right) = 0. \tag{9.24}$$

The latter formulation holds both for the baseflow and linear stability analysis formulation, substituting q with Q and $\hat{q}$, respectively, for which $P1$ elements are employed. The two problems are numerically coupled via an implementation of the domain decomposition method (Quarteroni, 2017), where the free-fluid and the porous region exchange information thanks to equations (9.15). The interface conditions on the free-fluid velocity and Darcy pressure are imposed via a Dirichlet boundary condition on Γ_{int}. The results of the convergence analysis in terms of domain size and discretization are reported in Appendix 9.7.1.

9.3 Wake flows past spheres of constant permeability

The flow past a sphere of constant permeability is investigated in the present section. A locally isotropic Darcy tensor is considered, i.e. in cylindrical coordinates $\mathbf{Da} = Da\mathbf{I}$, where Da is the Darcy number. Typically, in a homogenous porous medium, the interfacial Darcy number is slightly larger to the bulk one $\mathbf{Da}_{\text{int}} \geq \mathbf{Da}$ owing to the different boundary conditions applied in the proximity of the interface, but of the same order of magnitude (Lācis et al., 2017). Since in this section both $\mathbf{Da}$ and $\mathbf{Da}_{\text{int}}$ are treated as free-parameters, for the sake of simplicity the interface permeability is assumed to be equal to the bulk one, i.e. $\mathbf{Da}_{\text{int}} = \mathbf{Da}$. As concerns the slip tensor $\mathbf{\Lambda}$, the steady and axisymmetric wake is influenced only by Λ_t, since Λ_s appears when the azimuthal direction is considered. However, the latter affects the linear stability analysis results. In the first stage, we impose $\Lambda_t = \Lambda_s = 0$ and the effect of the sole Darcy number is investigated. In the second stage, the effects of positive entries in the slip tensor are studied.

9.3.1 Steady and axisymmetric flow

The steady and axisymmetric flow past a permeable sphere is now described. Previous works showed that the wake past permeable bodies is characterized by a recirculation region that moves downstream and becomes smaller as the permeability increases (cf., for instance, Ledda et al., 2018). However, as already noted by Yu et al. (2012) with a different porous model and for $Re < 200$, the flow past a permeable sphere may present a recirculation region that penetrates inside the body. Figure 9.2 shows the flow streamlines for a fixed Reynolds number $Re = 200$ and for different values of Da. At very low values of Da, the flow is analogous to the solid case. However, already at $Da = 10^{-4}$, the recirculation region penetrates in the rear of the sphere, with non-negligible values of the velocity. A closer look at the frontal part of the sphere shows that the streamlines entering inside the body tend to diverge and the flow leaves the body in the vicinity of the upper region of the sphere, upstream of the point beyond which the streamline that identifies the recirculation region starts. Increasing the permeability, the recirculation region increases its dimensions, as shown for $Da = 10^{-3}$ and $Da = 5 \times 10^{-3}$. At $Da = 7.5 \times 10^{-3}$, the recirculation becomes extremely small and detached from the body, while

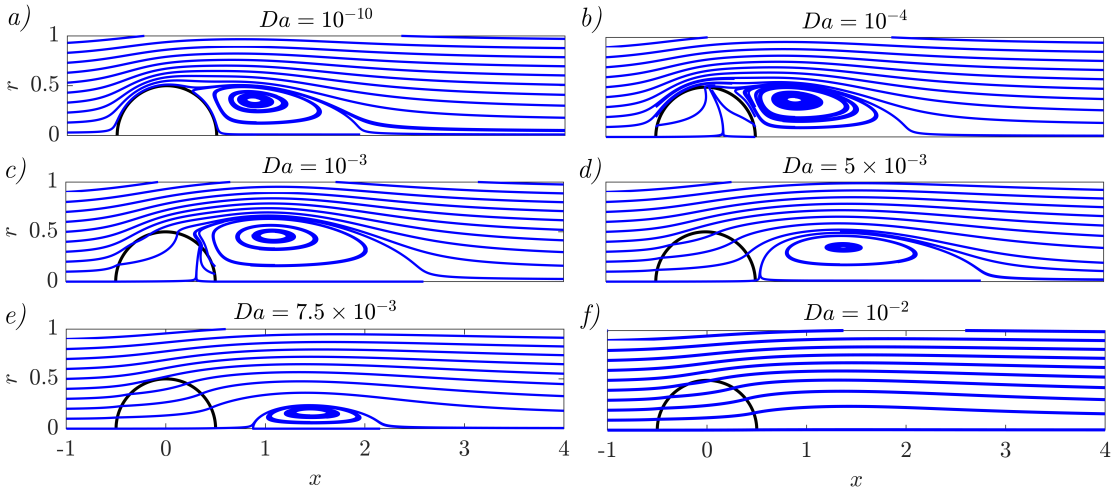

Figure 9.2: Streamlines of the axisymmetric flow past a permeable sphere for $Re = 200$, $\Lambda_t = 0$ and different values of Da.

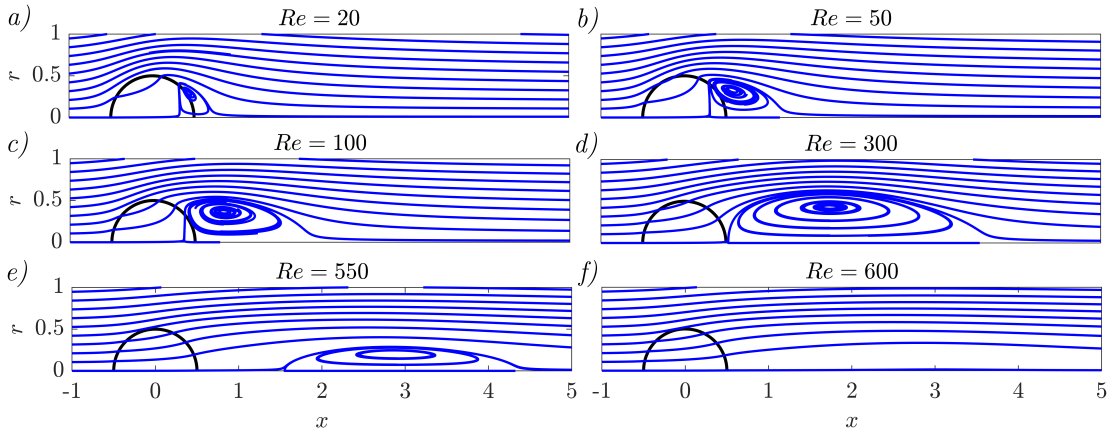

Figure 9.3: Streamlines of the axisymmetric flow past a permeable sphere, for $Da = 3.5 \times 10^{-3}$, $\Lambda_t = 0$ and different values of Re.

at $Da = 10^{-2}$ it eventually disappears.

Figure 9.3 shows the effect of the Reynolds number, for fixed $Da = 3.5 \times 10^{-3}$. At $Re \approx 20$, a penetrating recirculation region develops, whose core is located close to the fluid-porous interface. As the Reynolds number increases, the recirculation region moves downstream, while increasing its dimensions. At $Re = 300$, the recirculation region leaves the body; a further increase in Re leads to smaller recirculations, and eventually their suppression at very large Re.

From a quantitative viewpoint, the recirculation region boundary is defined by the streamline which presents two zeros of the streamwise component of the velocity $u_x = 0$ along $r = 0$. The length of the recirculation region L_r is thus the distance between these two points, measured along the z axis. The distance between the rear of the sphere and the recirculation region X_r is

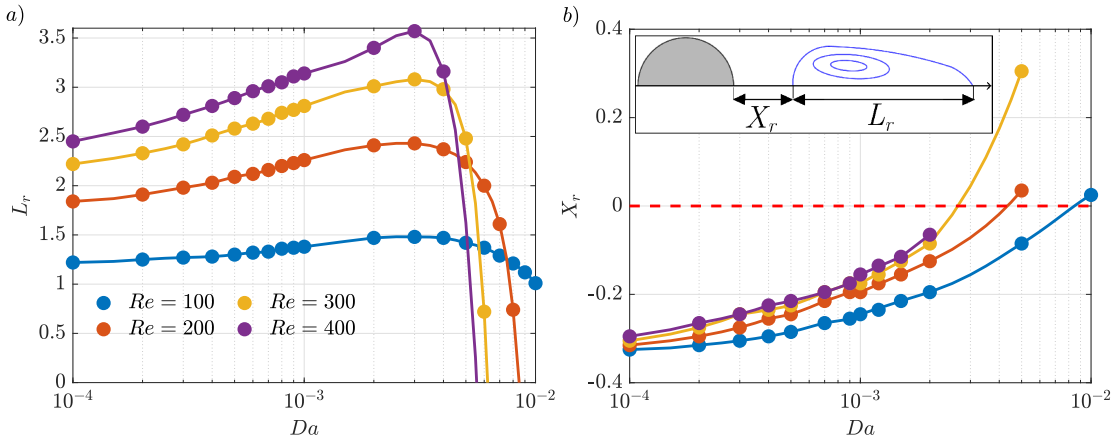

Figure 9.4: Variation of (a) the length of the recirculation region L_r and (b) its distance from the rear of the sphere, X_r, with Da, in case of $\Lambda_t = 0$ and for different values of Re.

instead the streamwise location, from the point $x = 0.5$, of the first zero of the axial velocity. X_r is negative whenever the recirculation region starts inside the body. The results are reported in figure 9.4. For fixed Re, an increase in the Darcy number leads to an increase in the length of the recirculation region. However, at very large permeabilities, a steep decrease of the size of the recirculation is observed, until the recirculation disappears. This effect is observed in the whole range of Re and is enhanced as the latter increases. We finally note that the distance of the recirculation region from the rear is negative (i.e. the recirculation penetrates inside the sphere) in a large range of the considered parameters, and becomes positive only at very large permeabilities and Reynolds numbers.

The initial increase of L_r can be correlated to the streamlines in figure 9.2. While in the solid case there is no flow, in the permeable case the flow passes through the body. Because of the presence of a massive separation, the strong recirculation has enough momentum to overcome the resistance to penetrate inside the rear of the sphere. As Da increases, the velocities inside the body increase while the separation point on the interface does not move appreciably. The presence of larger velocities at the interface enhances the gradients and thus the vorticity, whose effect is an increase of the counterflow generating the recirculation bubble. However, this mechanism enters in competition with the velocity gradients reduction as the body becomes more permeable. As a net effect, the separation point moves downstream until it leaves the body, as the recirculation becomes progressively smaller until it disappears.

The analysis of the steady and axisymmetric wake continues by considering the drag coefficient, defined in non-dimensional form as:

$$C_D = 16 \int_{\Gamma_{\text{int}}} [\Sigma(\boldsymbol{U}, P) \cdot \mathbf{n}] \cdot \mathbf{e}_x \mathrm{d}\Gamma. \tag{9.25}$$

Figure 9.5 shows the variation of C_D with Da, for different values of Re. The drag coefficient increases with Da, reaches a maximum and decreases. However, this decrease is observed

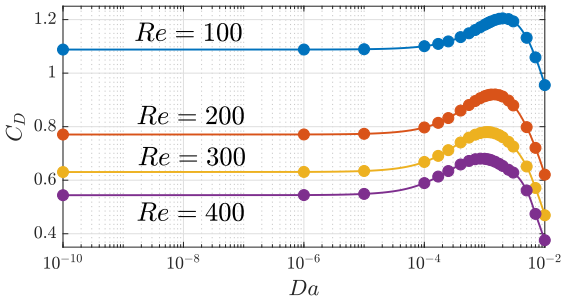

Figure 9.5: Variation of the drag coefficient with Da, in case of $\Lambda_t = 0$ and for different values of Re.

at extremely large permeabilities. This non-monotonous behavior relates to the one of the recirculation region, since both the drag coefficient and the recirculation size are a trace of the vorticity production (Ledda et al., 2018).

The analysis of the steady and axisymmetric wake past a permeable sphere showed results similar to those obtained in Yu et al. (2012), although they are obtained here with a different formulation for the flow through the porous medium. In opposition to permeable rectangles (Ledda et al., 2018), thin disks (Cummins et al., 2017; Ledda et al., 2019) (characterized by detached recirculation regions) and circular (Yu et al., 2011) and square cylinders (Ledda et al., 2018) (characterized by a weak penetration of the recirculation inside the body), the permeable sphere is characterized by the presence of penetration of the recirculation region in a large range of the parameters space. Similar penetrating recirculation regions were observed in a limited parameter range by Tang et al. (2021), for thick disks. The presence of penetration of the recirculation region inside the body is related to (i) the finite extent of the body compared to two-dimensional shapes and (ii) the streamline configuration assumed by the particular axisymmetric shape considered here, i.e. the sphere. The finite size of the body compared to nominally two-dimensional plane shapes imposes a smaller perturbation of the flow, and thus the fluid experiences less resistance to pass through the body. The spherical shape also enhances this behavior because of its streamwise extent, which allows the recirculation region to penetrate and the separation point at the interface to not move significantly while the inner velocities are increasing with Da. However, at some point, the sphere becomes extremely permeable and finally behaves as the other porous bluff-bodies already considered in the literature.

In this section, we described the steady and axisymmetric solution of the flow past a permeable sphere. However, not all the described configurations are likely to be observed. In the next section, we identify, via linear stability analysis, the regions of the parameters space where the steady and axisymmetric solution is linearly stable. Where instead such solutions are unstable, the possible non-steady and non-axisymmetric flow structures are characterized.

9.3.2 Stability analysis of the steady and axisymmetric flow

As introduced in Section 9.2, a perturbation in normal form, of azimuthal wavenumber m, is considered. The wake past a solid sphere presents two bifurcations (Meliga et al., 2009), which occur for $|m| = 1$. The first one occurs at $Re = 212.6$ and it is characterized by $\mathrm{Im}(\sigma) = 0$, i.e. the mode does not oscillate in time. In the non-linear regime, the mode saturates, leading to a steady breaking of the axisymmetry. We thus refer to this mode as the *steady* mode, always considering that, in the linear regime, it presents a pure exponential growth in time. The second bifurcation of the steady and axisymmetric wake occurs at $Re = 280.7$ and is an alternate shedding of vortices, which will be called *unsteady* mode.

Since here we focus on the effect of the permeability on the steady and axisymmetric wake and the eventual suppression of these instabilities, the behavior of these two unstable modes, with azimuthal wavenumber $m = 1$, is studied. The regions in the parameters space in which these two modes present a null growth rate, i.e. the so-called marginal or neutral stability conditions, are first identified.

Figure 9.6 reports the marginal stability curves for the two modes in the $Da - Re$ plane. We initially consider a fixed $Da = 10^{-10}$ with an increase of the Reynolds number. For $Re < 212.6$, all eigenvalues have a negative real part and thus the steady and axisymmetric wake is stable. At $Re = 212.6$, the steady mode is in the neutral stability condition, and beyond it becomes unstable. At $Re = 280.7$, the unsteady mode becomes unstable. In the range $10^{-10} < Da < 10^{-6}$, the critical Reynolds numbers are constant. For larger Da, the critical

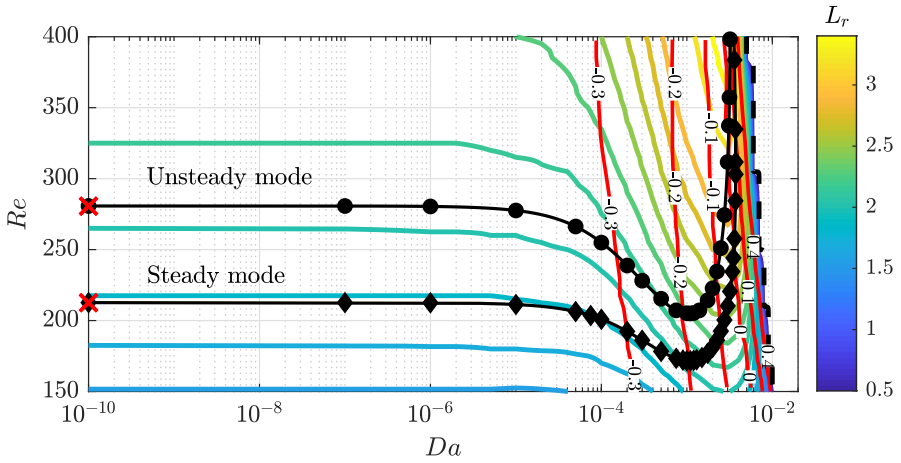

Figure 9.6: Bifurcation diagram in the $Da - Re$ plane, for $\Lambda_t = 0$. The black curve with diamonds denotes the critical Reynolds number for the first bifurcation, beyond which the steady eigenvalue is unstable, while the black one with dots denotes the critical Reynolds number for the second and unsteady bifurcation. The red crosses denote the values of the critical Reynolds numbers for the solid case. The colored and red iso-contours denote the values of the length of the recirculation region L_r and its distance from the rear X_r, respectively. The iso-level $L_r = 0$ is highlighted in black dashed line.

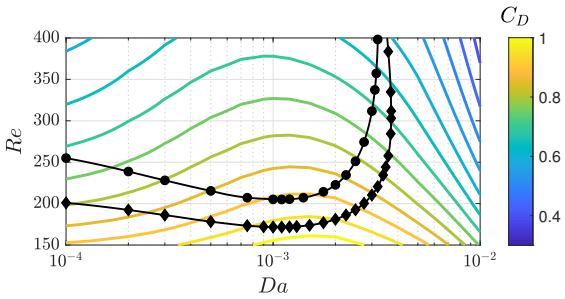

Figure 9.7: Iso-contours of the drag coefficient C_D in the $Da-Re$ plane superimposed onto the bifurcation diagram, for $\Lambda_t = 0$. The black curve with diamonds denotes the critical Reynolds number for the first bifurcation, beyond which the steady eigenvalue is unstable, while the black one with dots denotes the critical Reynolds number for the second and unsteady bifurcation.

Reynolds number decreases more and more quickly until both curves reach a minimum. The marginal stability curves of both the steady and unsteady modes exhibit the minima at $Re = 171.7$ and $Re = 205.1$, respectively, at the same value of $Da = 1.1 \times 10^{-3}$. Below $Re = 171.7$, the steady and axisymmetric wake is thus linearly stable independently of Da. For larger Da, the critical Reynolds numbers drastically increase, with a slight inversion of the curves, i.e. for fixed Da the mode becomes unstable and then stable again as Re increases, similarly to the behavior observed in Ledda et al. (2018, 2019) for different bluff bodies. A critical value of the Darcy number $Da = 3.7 \times 10^{-3}$ is finally obtained, beyond which the steady and axisymmetric wake is linearly stable independently of Re.

Three regions in the parameters space (Re, Da) are identified: one in which the steady and axisymmetric wake is stable, one in which the steady mode is unstable, and one in which both the steady and unsteady modes are unstable. In contrast to other bluff body wakes (Ledda et al., 2018, 2019), the critical Reynolds numbers for the porous sphere drastically decrease as the permeability increases, and the complete stabilization of the flow independently of Re is reached only for very large values of Da, while at intermediate values of Da the flow instability is anticipated by the permeability. This behavior occurs when the recirculation region is penetrating inside the sphere. Therefore, the wake of a permeable sphere is more unstable to perturbations compared to the solid one. This counterintuitive behavior vanishes at very large permeabilities, in which the recirculation region moves downstream of the body and eventually disappears. According to Monkewitz (1988) and the recent analyses of Ledda et al. (2018), the wake instability is correlated to the extent of the recirculation region, which roughly identifies the instability core (Luchini and Bottaro, 2014). Therefore, the iso-levels of the length of the recirculation region follow a trend similar to the marginal stability curves. The iso-levels of L_r indeed follow the same trend, as shown in figure 9.6. In particular, L_r initially increases with Da, while Re_{cr} decreases, and successively L_r decreases rapidly and Re_{cr} increases. The deviations in the proximity of the minimum of Re_{cr} may be related to the change of the velocity profiles composing the wake at each streamwise location (Monkewitz, 1988). The iso-levels of X_r become positive close to the critical Darcy number for unconditional stability. Therefore,

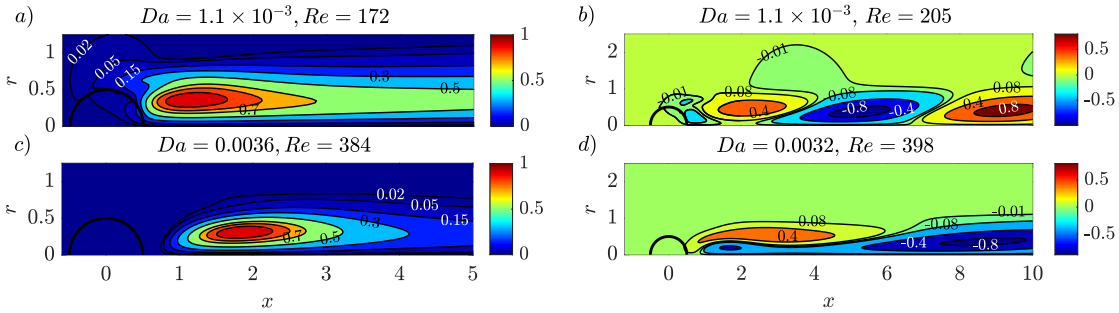

Figure 9.8: Iso-contours of the real part of the streamwise component of the velocity field, rescaled with its maximum absolute value, for the (a, c) steady and (b, d) unsteady modes, at the marginal stability, for $\Lambda_t = 0$.

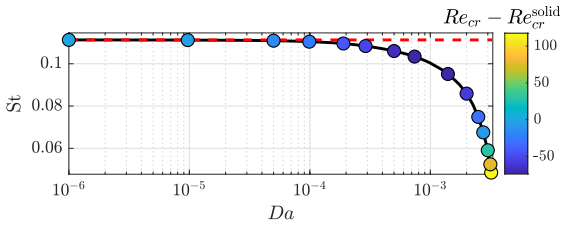

Figure 9.9: Variation of the Strouhal number $\text{St} = \text{Im}(\sigma)/(2\pi)$ of the unsteady mode with Da, following the marginal stability curve for the unsteady instability. The colored dots denote the values of $Re_{cr} - Re_{cr}^{\text{solid}}$, where $Re_{cr}^{\text{solid}} = 280.7$.

the marginal stability curves trend is related to the presence of a penetrating recirculation region.

Figure 9.7 shows the iso-contours of the drag coefficient in the $Da - Re$ plane together with the marginal stability curves. For fixed Re, the maximum of drag is attained at $Da \approx 10^{-3}$, in the vicinity of the minima in the Reynolds numbers of the marginal stability curves. This observation can be explained considering the correlation between the extent of the recirculation region and the critical Reynolds number. The drag increase is predominantly related to the decrease of the pressure in the rear part of the body. Stronger counterflow velocities imply, with a good approximation, smaller pressure values in the rear part and thus a positive drag contribution. At the same time, larger counterflows imply larger recirculation regions (Ledda et al., 2018). Larger values of C_D are thus related to larger values of L_r, and a more unstable wake, as previously discussed (Monkewitz, 1988; Ledda et al., 2018), i.e. the maximum drag is attained in the vicinity of the marginal stability curves minima.

While previous works described the downstream displacement of the mode (Ledda et al., 2018), it is not clear if the latter can move upstream and penetrate inside the body due to the penetrating recirculation region. Figures 9.8a, b) show the unstable modes at the marginal stability conditions corresponding to the minima of the marginal stability curves (see details provided in the figure legend). The instability also develops inside the sphere, even if the associated magnitude is 10^{-2} times lower than the values attained outside, in

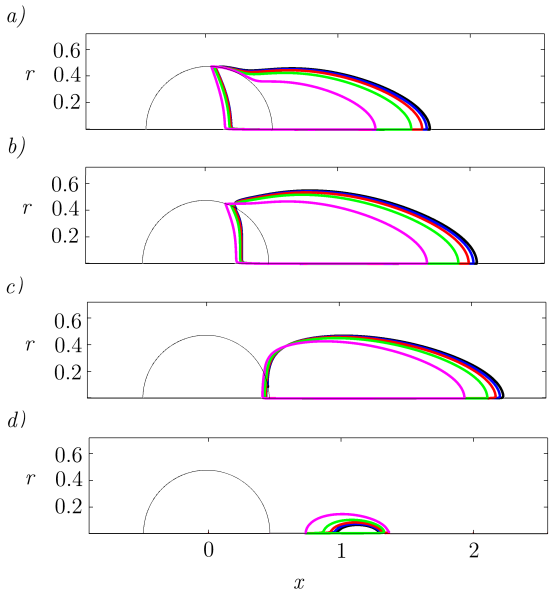

Figure 9.10: Streamline identifying the recirculation region for $Re = 150$, (a) $Da = 10^{-4}$, (b) $Da = 10^{-3}$, (c) $Da = 5 \times 10^{-3}$, (d) $Da = 10^{-2}$. The different colors correspond to $\Lambda_t = 10^{-4}$ (black), $\Lambda_t = 10^{-3}$ (blue), $\Lambda_t = 5 \times 10^{-3}$ (red), $\Lambda_t = 10^{-2}$ (green), $\Lambda_t = 5 \times 10^{-2}$ (magenta).

particular for the unsteady mode. Therefore, an upstream displacement of the mode together with the recirculation region, which penetrates inside the porous sphere, is observed. An increase of the Reynolds number following the marginal stability curve leads to a downstream displacement of the steady mode (figure 9.8(c)), while the unsteady mode (figure 9.8(d)) is characterized by a periodic distribution with larger streamwise wavelength compared to case (b). The resulting unsteady mode is thus characterized by a periodic shedding of vortical structures, whose streamwise wavelength increases with Re, following the marginal stability curve. As a consequence, the shedding frequency of these vortical structures decreases with Da, a conclusion which is quantitatively supported by figure 9.9. The imaginary part of the eigenvalue, which represents the shedding frequency, strongly decreases for $Da > 10^{-3}$.

In this section, we highlighted the peculiarities of the penetrating recirculation region and its consequences on the flow stability. In the following, we consider positive values of the slip tensor components.

9.3.3 Effect of the slip length

The previous sections focused on the permeability effect on the flow past a sphere in the absence of slip. These results are complemented by including the effect of a difference in the velocity at the fluid-porous interface. In the stability analysis, also the azimuthal component of the slip tensor Λ_s has to be considered, owing to the presence of the azimuthal velocity perturbation.

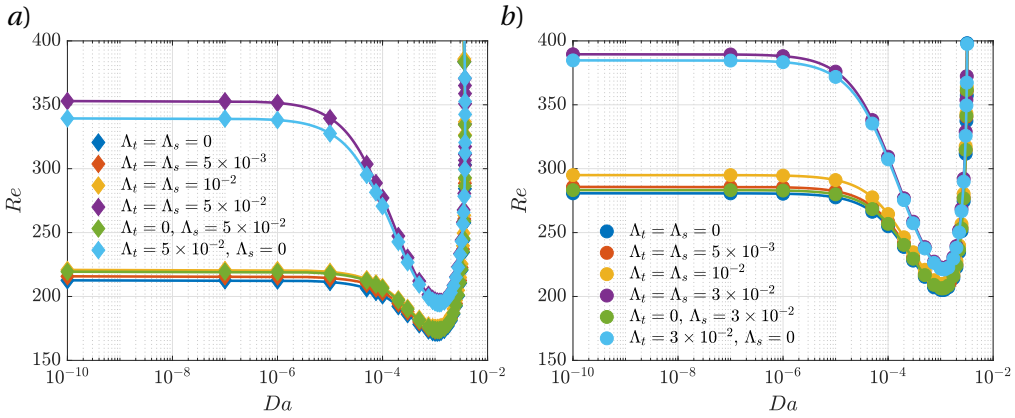

Figure 9.11: Marginal stability curves, for (a) the first and (b) second bifurcation, for different values of Λ_t and Λ_s.

Figure 9.10 shows the streamlines identifying the recirculation region for $Re = 150$. In each frame, Da is fixed and Λ_t varies in the range $10^{-4} < \Lambda_t < 5 \times 10^{-2}$. The introduction of a finite slip length in the problem does not significantly affect the flow morphology, although some differences can be observed. An increase in Λ_t slightly modifies the position of the flow separation points and the recirculation region. At low permeabilities, larger values of slip imply smaller recirculation regions, whose effect becomes significant for $\Lambda_t > 10^{-2}$. These differences become smaller as Da increases. At very large permeabilities, an increase in slip leads to slightly larger recirculations.

These differences in the flow morphologies have a strong effect on the marginal stability curves, as shown in figure 9.11(a) for the steady mode and in figure 9.11(b) for the unsteady mode. Initially, the isotropic case is considered, i.e. $\Lambda_s = \Lambda_t$. The marginal stability curves with varying Λ_t follow the same trend. At low permeabilities, an increase in the slip leads to an increase in the critical Reynolds number, which becomes significant for $\Lambda_t > 10^{-2}$, the minimum values of Re_{cr} slightly increase and the critical permeability for unconditional stability with Re are not significantly influenced by variations of Λ_t. We then investigate the effect of anisotropy in the slip tensor, i.e. $\Lambda_t \neq \Lambda_s$. The results show that the increase in the critical Reynolds number is significant when large values of Λ_t, with $\Lambda_s = 0$, are considered, while a large value of Λ_s with $\Lambda_t = 0$ does not strongly influence the flow morphology. This behavior can be interpreted by considering that Λ_t influences both the baseflow and stability problems, while Λ_s affects only the stability problem. Very large values of Λ_t imply much smaller recirculation regions (for low permeabilities); therefore, the flow is stabilized owing to the reduction of the region in which the instability develops. Higher Reynolds numbers are thus needed to develop the instability, as shown in figure 9.11. These differences become smaller in the proximity of the minima of Re_{cr} and of the critical value of Da for unconditional stability.

The variation of the slip length leads to quantitative differences in the flow morphology and stability properties, with an overall reduction of the size of the recirculation region. However,

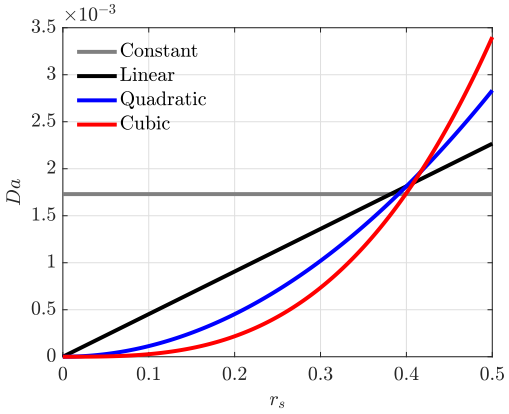

Figure 9.12: Permeability as a function of the radius in spherical coordinates r_s for the distributions employed in the present analysis.

the physics is dominated by the permeability. To deepen the role of the permeability in the flow dynamics and stability, the following section focuses on the effect of variable permeability distributions inside the body, always keeping the hypothesis of an isotropic porous medium.

9.4 Wake flows past spheres of variable permeability

The previous section studied the effect of permeability and slip (kept constant inside the porous medium) on the flow morphology past a permeable sphere. However, typical porous spheres may present variable distributions of permeability rather than a constant one. To give an example, the sea urchin can be seen as a porous structure with a solid core, whose inclusions are needles. Owing to the radial distribution of needles, the permeability increases while reaching the tip of the needles. In addition, many seeds are transported in the air by parachute-like structures, called pappi, composed of filaments that can be arranged in disk or spherical arrays that lead to non-constant permeability distributions.

Despite the increasing interest for these natural structures (Cummins et al., 2018), systematic works on the stability properties in the case of variable permeability are still limited in the literature (Ledda et al., 2019). This section proposes a parametric study in which the permeability varies inside the sphere while always considering an isotropic porous medium, i.e. $\mathbf{Da} = Da(x,r)\mathbf{I}$. We neglect variations of the slip lengths ($\Lambda_t = \Lambda_s = 0$) since they do not qualitatively modify the flow features.

Three polynomial distributions of permeability, linear, quadratic and cubic, are considered. The outlined variations occur along the radius of the spherical reference frame ($r_s, \varphi_s, \theta_s = \theta$) with origin the center of the sphere. A constant average value of the Darcy number, $\overline{Da}$, is imposed for each case:

$$\overline{Da} = \frac{1}{V}\int_V Da(x,r)\ dV = \frac{6}{\pi}\int_0^{2\pi}\int_0^{\pi}\int_0^{0.5} Da(r_s) r_s^2 \sin\vartheta_s \mathrm{d}r_s \mathrm{d}\varphi_s \mathrm{d}\theta_s. \tag{9.26}$$

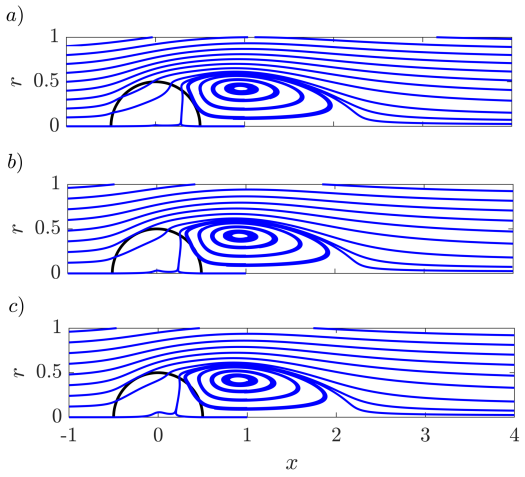

Figure 9.13: Streamlines for $\overline{Da} = 1.7 \times 10^{-3}$, $\Lambda_t = 0$ and $Re = 150$, in the case of (a) linear, (b) quadratic and (c) cubic distributions of permeability along r_s.

The different distributions as a function of $\overline{Da}$ are thus obtained:

- constant: $Da(r_s) = \overline{Da}$,
- linear: $Da(r_s) = \frac{8}{3}\overline{Da} r_s$,
- quadratic: $Da(r_s) = \frac{20}{3}\overline{Da} r_s^2$,
- cubic: $Da(r_s) = 16\overline{Da} r_s^3$.

For the sake of clarity, the notation $Da \propto r_s^\alpha$ is introduced, where $\alpha (= 0,1,2,3)$ is the order of the polynomial distribution. Figure 9.12 shows the different distributions for $\overline{Da} = 1.7 \times 10^{-3}$. An increase in α leads to two effects. First, the permeability decreases close to the sphere center; second, higher values are reached in the proximity of the interface. These considerations will find an application in the following sections, which describe the baseflow and its stability properties.

9.4.1 Steady and axisymmetric flow

This section focuses on the effect of the permeability distribution on the steady and axisymmetric flow. In figure 9.13, a qualitative visualization with the flow streamlines is proposed, for $\overline{Da} = 1.7 \times 10^{-3}$. The flow morphology is not significantly affected, and a slight variation of the size of the recirculation region with α is observed. These slight differences are quantified in figure 9.14(a), which shows the variation of the length of the recirculation region with $\overline{Da}$ and for different values of Re.

In all cases, we observe a behavior similar to the one with constant permeability. An initial increase of L_r is followed by a rapid decay at very large permeabilities. As α increases, the

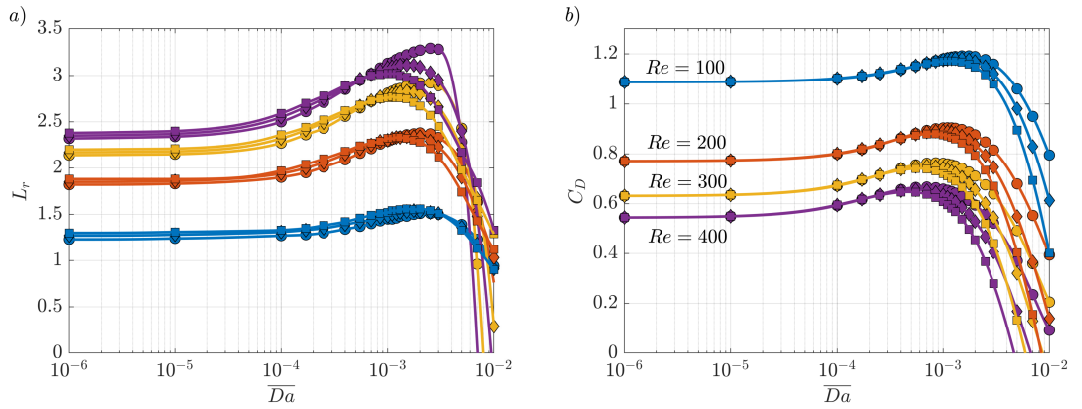

Figure 9.14: (a) Length of the recirculation region L_r and (b) drag coefficient C_D as functions of $\overline{Da}$, in the absence of slip, for the linear (dots), quadratic (diamonds) and cubic (squares) distributions. The different clusters of curves refer to $Re = 100$ (blue), $Re = 200$ (orange), $Re = 300$ (yellow) and $Re = 400$ (purple).

maximum L_r presents slightly larger values attained at smaller values of $\overline{Da}$. At very large permeabilities, the recirculation presents a slower decrease with $\overline{Da}$ as α increases, thus leading again to slightly larger recirculations.

The drag coefficient presents a similar behavior, as reported in figure 9.14(b). Also in this case, the maximum is progressively anticipated as α increases. A slightly smaller maximum is attained for larger values of α.

These observations are explained by an observation of the distributions of permeability outlined in figure 9.12. The initial slightly higher values of L_r for linear, quadratic and cubic distributions are related to the increase of permeability close to the interface, for fixed $\overline{Da}$. In the constant permeability case, an increase of permeability leads to an increase in the size of the recirculation region, for small enough Da. The outlined phenomenon also appears in this case since the permeability close to the interface increases with α. We thus observe a slight increase in the length of the recirculation region and a displacement of the maximum at smaller values of $\overline{Da}$. Beyond the maximum, the slower decrease with α is related to the presence of a core close to the center of small permeability. As a consequence, the fluid is constrained to pass around and through a region of lower permeability. The rapid drop of L_r is thus reduced by the presence of this core of low permeability, which ensures the presence of larger recirculation regions. However, the drag coefficient presents a faster drop with α, at large permeabilities. Despite the presence of the core of low permeability, the pressure and velocity gradients at the interface are largely reduced, and thus the forces acting at the interface decrease.

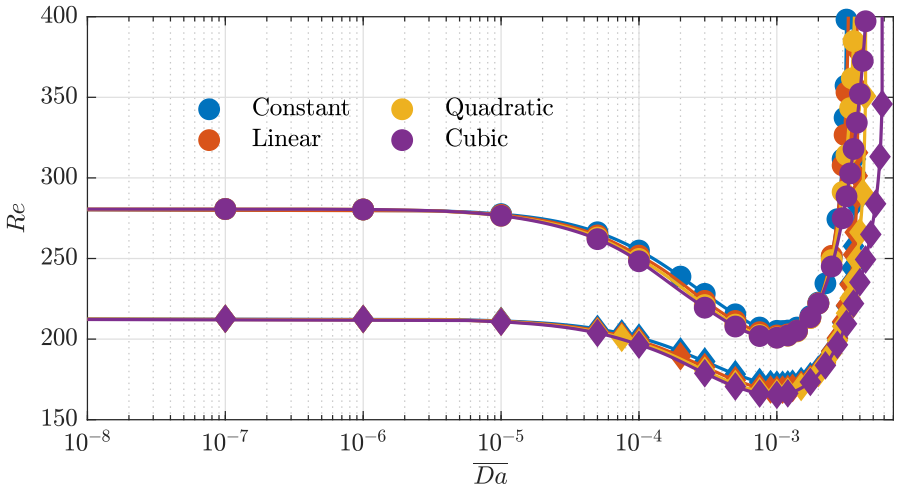

Figure 9.15: Critical Reynolds number as a function of $\overline{Da}$, in the absence of slip, for different distributions of permeability, steady (diamonds) and unsteady (dots) bifurcations.

9.4.2 Stability with respect to azimuthal perturbations

In analogy with the constant permeability case, here we perform a stability analysis of the steady and axisymmetric wake for the different polynomial distributions. The results are reported in terms of marginal stability curves in figure 9.15. The first bifurcation is denoted with diamonds, while the second one with dots. The different colors correspond to the distributions employed in this work. Interestingly, the employment of the average permeability $\overline{Da}$ leads to a collapse of the marginal stability curves for the different distributions. In all cases, a minimum in the critical Reynolds numbers is attained, which slightly decreases employing polynomials of higher order, and a critical value of the permeability beyond which the wake is stable independently of Re is identified, which increases with α. Also these results can be correlated to the different distributions of permeability. The slight decrease in the critical Reynolds number is related to the increase of permeability at the interface which induces larger recirculations as polynomials of higher order are employed, since the stability properties are directly related to the extent of the recirculation regions. The increase in the critical Da with α is instead related to the core of low permeability, which ensures larger recirculations compared to the constant permeability case. Larger recirculations thus imply more unstable configurations, and the instability is moved at larger $\overline{Da}$.

To summarize, the flows and the stability properties are very similar when the same average value of the permeability, $\overline{Da}$, is considered. Moreover, the flow morphologies are weakly dependent on the employed distribution of permeability. The small differences were explained by recalling the constant permeability case and focusing on the (i) decrease of permeability close to the center and (ii) increase of the permeability at the body/fluid interface as α increases. The similarities in the flow morphology result in very similar stability properties at a given $\overline{Da}$.

So far, we have focused on a systematic study in which the permeability and the slip were considered as parameters. However, a remarkable peculiarity of the employed homogenized model is the direct link between the permeability and slip with the structure composing the porous body. While these techniques showed great potential in their employment in the case of simple periodic arrays, applications to more elaborate geometries are still lacking. Henceforth, we aim at retrieving the full-scale structure for a constant permeability in the local spherical reference frame, thus giving an example of how to close the link between porous models and the micro-structure of the porous body itself for a three-dimensional configuration of interest. The inversion of the classical paradigm “from geometry to macroscopic properties" can be of paramount importance in multiple scales structures design, as shown in Schulze and Sesterhenn (2013). Several benefits can be obtained by identifying the desired permeability distribution through the homogenized model and then retrieving the full-scale structure by an inverse design that satisfies the macroscopic properties. There is an infinity of possible geometries with the same macroscopic properties, giving great potential to this inverse paradigm in terms of reduction of computational costs and in the possibility to explore different configurations. In the considered case, different choices for the full-scale structures could be employed, e.g. arrays of cylinders propagating radially from the center or arrays of packed spheres. In this work, we consider a configuration that allows to directly study the full-scale structure with the axisymmetric Navier-Stokes equations, i.e. an array of concentric rings. Using this particular scaffold, we develop a procedure to obtain the geometrical details (the radius and position of the rings) starting from the macroscopic properties of the permeable sphere. However, similar procedures can be developed for different full-scale structures.

9.5 Design of a sphere of constant permeability: concentric rings

9.5.1 Design procedure

The permeable sphere is composed of an array of toroidal fibers with circular cross-sections, oriented such that the rings axes are coincident with the $r = 0$ axis of the cylindrical reference system, see figure 9.16(a). The flow is axisymmetric when the array is invested by a uniform stream along the axial direction and thus solved in one azimuthal cross-section. In the azimuthal cross-section $\theta = 0$, the rings are disposed with polar symmetry and are represented by circular inclusions (see figure 9.16(b), where the fluid region inside the sphere is represented in grey). The procedure consists in the determination of the radius of each ring composing the sphere to obtain the desired distribution of Da. In principle, the radius of each inclusion can be arbitrarily varied to obtain a desired distribution of permeability, as explained next. Since in the previous section we have shown that permeability variations along the radius do not qualitatively change the flow phenomenology and stability properties of the wake, we focus on a constant distribution of permeability. Therefore, the first input parameter of the procedure is the bulk Darcy number Da. A structure composed of N polar repetitions of the element is adopted, sketched in the left frame of figure 9.16(c). Each polar element can be divided in curved elementary cells of characteristic size $\bar{l}_i$ (cf. left frame of figure 9.16(c)). The

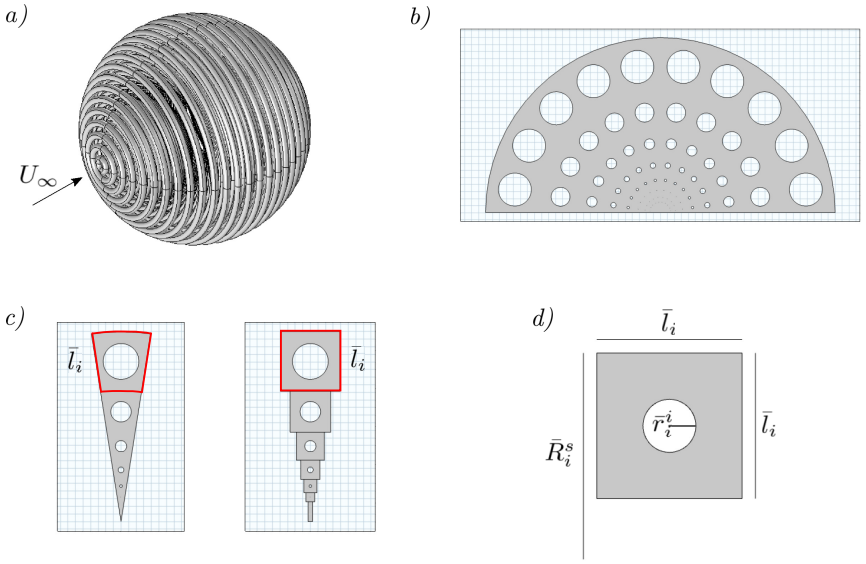

Figure 9.16: (a) Sketch of the three-dimensional structure of the sphere. (b) Fluid domain internal to the sphere and distribution of rings at one azimuthal section. (c) Sketch of the geometrical approximation for each polar repetition which leads to an array of square elementary volumes. (d) Resulting elementary volume for the evaluation of the local permeability, highlighted in red in (c).

procedure to retrieve the full-scale structure is based on the knowledge of the separation of scales parameters of the interface cell of the periodic repetition $\varepsilon = \varepsilon_1$ (cf. the cell highlighted in red in figure 9.16(c)). With the initial definition of ε and Da, the micro-structure is uniquely determined. We now outline the assumptions of the procedure to determine the radii of the rings. We assume $\bar{l}_i \ll \bar{R}_c$, where $\bar{R}_c$ is the local spherical radius. Under this assumption, the curvature of each elementary cell is neglected, implying that the rings can be considered as three-dimensional cylinders. Owing to the azimuthal invariance, we can consider the two-dimensional problem at a fixed azimuthal section and thus each polar repetition can be decomposed in square elementary cells, each containing a single circular inclusion (cf. right frame of figure 9.16(c)). Neglecting the curvature in the azimuthal direction for the same reason, and assessing the invariance of the geometry along the same direction, two-dimensional cells can be finally adopted as microscopic domain. Note that these assumptions are reasonably respected at the interface, while they do not hold close to the center of the sphere. However, the effect on the results of a core of low permeability is weak and manifests itself only at very large permeabilities, as previously shown. The last assumption is equivalent to state that the variations of the micro-structure are sufficiently smooth to consider each cell as a periodic repetition. As will become clear once outlined the procedure, this assumption is respected provided that there is sufficient separation of scales for each cell:

$$\varepsilon_i = \bar{l}_i / D \ll 1. \tag{9.27}$$

The problem is thus simplified by considering two-dimensional elementary cells of different sizes and inclusion radii, whose macroscopic properties (permeability, interface permeability, and slip) are given by simulations with periodic conditions. We now outline the complete procedure, from the determination of the properties of the considered microscopic geometries to the final macro-structure. We can distinguish three different steps, (i) the determination of the properties of the considered micro-structure, i.e. circular inclusions with different radii, (ii) the determination of the distribution and size of the elementary cells composing the porous structure with input ε, and (iii) the determination of the circular inclusions radii with input Da.

The elementary unit-cell characterizing the porous structure is sketched in figure 9.16(d). The method outlined in Naqvi and Bottaro (2021) is exploited to evaluate the permeability, interface permeability, and slip number. The microscopic problems are solved by non-dimensionalizing them with the characteristic microscopic length $\bar{l}_i$. With this precaution, the permeability $\mathbf{K} = K\mathbf{I}$, the interface permeability $\mathbf{K}_{\text{int}} = K_{\text{int}}\mathbf{I}$ and slip λ_t, normalized with respect to the characteristic length of the square elementary cell $\bar{l}_i$, are evaluated by considering a two-dimensional array of inclusions and plotted as a function of the inclusion radius r^i. We refer to Appendix 9.7.2 for further detail about the computations. The results, non-dimensionalized with the microscopic length, are reported in figure 9.17, in the range $10^{-3} < r^i < 0.49$. All quantities diverge as the inclusion radius goes to zero, while they tend to zero as the radius of the solid inclusion reaches $r^i = 0.5$. The cells in figure 9.16(c) are labeled with the index $i = 1, 2, ...$, increasing from the interface to the center. Each i-th cell is characterized by its arc length on the top boundary of the cell, equal to the radial dimension, $\bar{l}_i$, the radius of the solid inclusion $\bar{r}_i^i$, and the local spherical radius at the top boundary of the cell $\bar{R}_i^s$.

The input separation of scales parameter at the interface elementary cell $\varepsilon = \varepsilon_1$ is used to determine the angular distance between two polar repetitions:

$$\Delta\varphi = \frac{2\pi}{N} = \frac{2\bar{l}_1}{\hat{D}} = 2\varepsilon. \tag{9.28}$$

The size ε_{i+1} and radial position R_{i+1}^s of the $(i+1)$th elementary cell of the cross-section are determined via the following recursive relations:

$$R_{i+1}^s = R_i^s - \bar{l}_i/D = R_i^s - \varepsilon_i, \tag{9.29}$$

$$\epsilon_{i+1} = \tfrac{2\pi}{N}\left(R_i^s - \varepsilon_i\right), \tag{9.30}$$

which are non-dimensionalized with the diameter of the sphere. The initial step is given by the external elementary cell ($R_1^s = 0.5$) with the input separation of scales parameter $\varepsilon_1 = \varepsilon$. The recursive algorithm is stopped at the index $i-1$ such that $R_i^s < 0.05$ to avoid extremely small inclusions, i.e. approximately less than 10^{-6} times the sphere radius.

Once the size and position of the elementary cells (each one assumed to be square, cf. left frame of figure 9.16(c)) is determined, one should define the radius of the microscopic inclu-

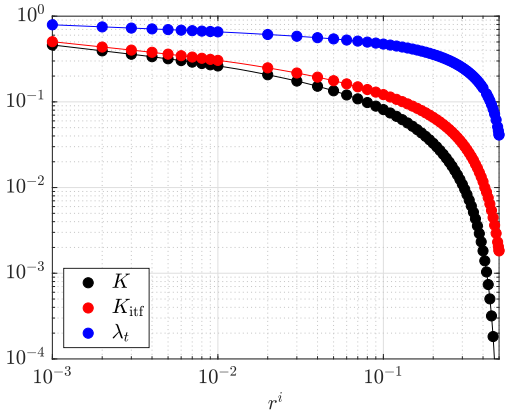

Figure 9.17: Variation of the permeability K, the interface permeability K_{int}, and the slip length λ_t with the radius r^i, for circular inclusions in a square domain.

sions inside each elementary cell. A constant value of Da is thus imposed by exploiting the results of the microscopic simulations shown in figure 9.17, in which the microscopic radius is related to the permeability K. In each cell of size ε_i, the permeability K_i is given by:

$$K_i\left(r_i^i\right) = Da/\varepsilon_i^2. \tag{9.31}$$

Exploiting the bijective relation between r_i^i and K_i (cf. figure 9.17), the radius r_i^i of the inclusions in each elementary cell is thus determined.

For the analysis of the permeable sphere with the homogenized model two additional parameters are needed, i.e. the slip length and the interface Darcy number. At this stage, one could modify the radius of the inclusion close to the interface to obtain the desired values of interface permeability and slip. To avoid further complications in the design procedure, the interface permeability and slip are *a posteriori* evaluated without modifying the microscopic inclusion at the interface:

$$\Lambda_t = \epsilon_1 \lambda_t\left(r_1^i\right), \tag{9.32}$$

$$Da_{\mathrm{int}} = \epsilon_1^2 K_{\mathrm{int}} = \epsilon_1^2 K_{\mathrm{int}}\left(r_1^i\right), \tag{9.33}$$

The geometry of the sphere and its properties are now uniquely determined for a given value of Da and ε. In the following, the results given by the full-scale simulations are compared with the homogenized model where Da, Da_{int} and Λ_t are provided.

9.5.2 Comparison with the homogenized model

We conclude the analysis by comparing some full-scale simulations (FSS) with the homogenized model (HM) for different permeability values. By FSS, we intend simulations that explicitly account for the micro-structure composing the sphere. Such simulations are computationally expensive owing to the scale separation between the macroscopic diameter and

Case	N	ε	Da	Da_{int}	Λ_t
I	14	0.22	1.7×10^{-3}	3.2×10^{-3}	0.079
II	30	0.11	5×10^{-4}	10^{-3}	0.044
III	60	0.05	10^{-5}	4.3×10^{-5}	0.009

Table 9.1: Values of the geometrical parameters and homogenized properties for each case.

	FSS(I)	HM(I)	FSS(II)	HM(II)	FSS(III)	HM(III)
L_r	1.24	1.42	1.36	1.46	1.48	1.5
C_D	0.76	0.80	0.82	0.89	0.86	0.87

Table 9.2: Comparison between the full-scale simulations (FSS) and the homogenized model (HM) for the three outlined cases.

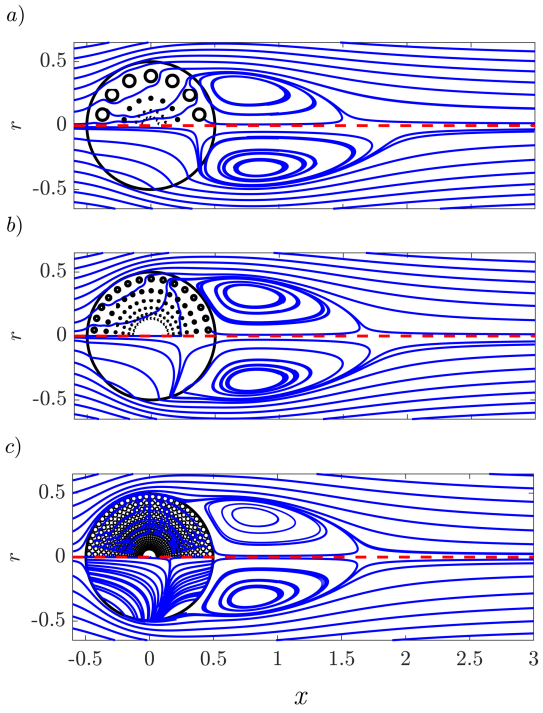

Figure 9.18: Comparison of the flow streamlines between the full-scale simulation (on the top) and homogenized model (on the bottom), (a) Case I, (b) Case II, (c) Case III.

the typical micro-structure size l_i. The purpose of the comparison carried out in the present section is to appraise the accuracy of the much simpler model obtained by homogenization. The following three cases, summarized in table 9.1, are considered:

- Case I, characterized by $N = 14$ polar repetitions and $Da = 1.7\times10^{-3}$.
- Case II, characterized by $N = 30$ polar repetitions and $Da = 5\times10^{-4}$.
- Case III, characterized by $N = 60$ polar repetitions and $Da = 10^{-5}$.

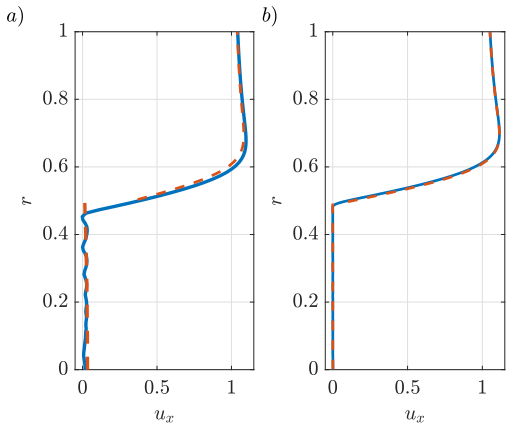

Figure 9.19: Streamwise velocity profile at $x = 0.0175$, homogenized model results (orange dashed lines) and full-scale simulations (blue lines), for Cases (a) II and (b) III.

The FSS results are compared to those of the HM. The Reynolds number is fixed to $Re = 150$, less than the minimum value of Re_{cr} to ensure the linear stability of the FSS and HM solutions. Table 9.2 shows the results in terms of length of the recirculation region and drag coefficient for the three different cases introduced above. The accuracy of the HM is $\mathcal{O}(\varepsilon)$ as predicted by the homogenization theory. In particular, the HM is progressively more accurate as ϵ decreases; at the same time, while the computational cost of the HM is constant with ϵ, the FSS are progressively more CPU-demanding as ϵ decreases.

In figure 9.18 the flow streamlines are qualitatively compared. The flow morphology is well reproduced, in particular when the separation of scales increases. Surprisingly, there is a qualitative agreement even in Case I, for which the separation of scales parameter $\epsilon = 0.22$ is relatively large and thus violates the hypothesis $\epsilon \ll 1$. Figure 9.19 shows a final quantitative comparison, in which the axial velocity profiles at $x = 0.0175$ well agree, for Cases II and III.

Despite the numerous assumptions made to exploit the two-dimensional HM results for the case of a three-dimensional sphere, the FSS well agree with the HM. Therefore, the HM is suitable even for complex flows such as the one outlined in the present work. The flow morphologies outlined in the parametric studies of Sections 9.3 and 9.4 were recovered, thus showing the great potential of the homogenization technique in predicting wake flows via simple equations and boundary conditions, and in reproducing actual wake structures downstream the considered bluff body.

9.6 Conclusions

In this work, we studied the morphology and stability properties of the steady and axisymmetric flow past a permeable sphere. A homogenized model was employed, consisting in the Darcy law inside the porous medium, with a slip condition on the tangential velocity at the interface between the fluid and porous region. The main character in the Darcy model is the

permeability, which quantifies the resistance for the fluid to pass through the micro-structure. The slip length appears in the interface condition as well and accounts for the viscous effects in the proximity of the interface. The initial part of the work was devoted to the steady and axisymmetric flow in the presence of a constant and isotropic permeability and zero slip length. The flow presents a penetration of the recirculation region inside the sphere, which increases its dimensions as the permeability increases, as already observed in Yu et al. (2012), where a different porous model was employed. However, at very large permeabilities, the recirculation region leaves the body, moves downstream, and eventually disappears. The non-monotonous behavior of the recirculation region resulted in a particular behavior of the marginal stability curves for the two bifurcations of the steady and axisymmetric wake. The critical Reynolds numbers for the instability reached a minimum, much lower than the ones of the solid case, and then drastically increased for very large permeabilities. A critical permeability was identified, beyond which the steady and axisymmetric wake is linearly stable independently of the Reynolds number. A consequent analysis showed that the slip length weakly influences the flow morphology. Therefore, the latter is largely affected by the permeability.

We then focused on the effect of various polynomial distributions of permeability along the spherical radial direction r_s, i.e. proportional to r_s^α, still under the assumption of an isotropic porous media. The results showed a similar behavior to the case of constant permeability, with only slight differences. Interestingly, the flow morphologies and stability curves collapse when an average permeability is employed, thus highlighting the secondary role of the spatial distribution of permeability for the considered cases.

While in the previous sections the permeability and slip length were treated as free parameters, in the last section these properties were linked with an actual porous structure. The homogenization theory enabled us to retrieve an actual permeable sphere through some reasonable assumptions. We showed the potential of homogenization theory in the modelization of actual three-dimensional configurations of interest by comparing the homogenized model against the reference cases obtained by full-scale simulations.

This work provides an example of the application of the porous homogenized model with slip to a three-dimensional configuration of interest, together with the characterization of the effect of a penetrating recirculation region on the steady and axisymmetric flow past a permeable sphere, with a focus on its stability properties. In opposition to other bluff body wakes, a remarkable and counterintuitive effect is the decrease of the critical Reynolds number for the marginal stability. The homogenized model was applied to a three-dimensional configuration of interest. Thanks to the direct link with the actual full-scale structure, we showed the potential of the inverse procedure to retrieve the geometry starting from the homogenized parameters. These considerations may find application in the optimization and design of porous structures, not only in aerodynamic flows. The inverse paradigm can significantly decrease the computational effort needed for optimization procedures since (i) the homogenized model contains only a few parameters, which describe the macroscopic effect of the microscopic geometry, that can eventually vary in space, with great advantage

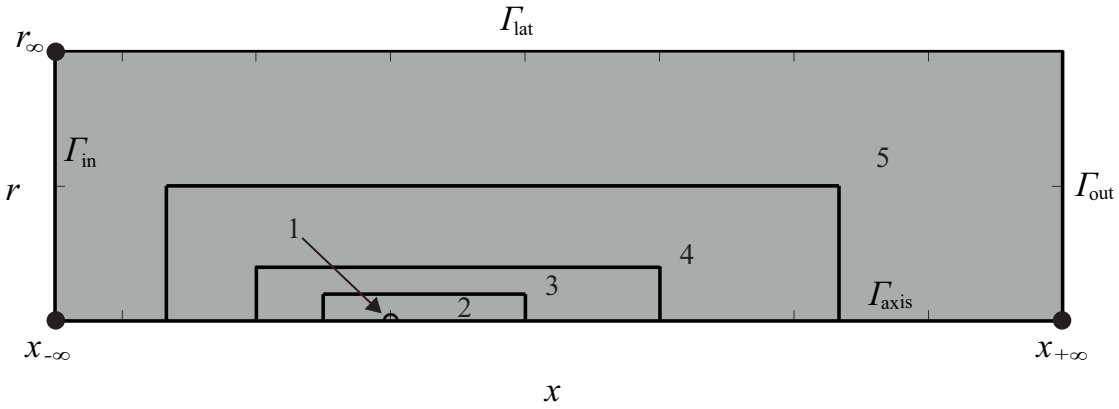

Figure 9.20: Sketch of the refinement regions of the computational domain.

compared to the large numbers of degrees of freedom needed to optimize a micro-structured medium, and (ii) the decoupling between macroscopic effect and microscopic structure design helps in considering different structures without loss of generality. These results can be extended in several ways. While detached recirculation regions are receiving growing attention, further developments may include the analyses of penetrating recirculation regions for different flow configurations. These findings can be applied in classical environmental studies such as porous particle or seed transport (Cummins et al., 2018; Ledda et al., 2019) or in chemical engineering processes which involve the presence and settling of spherical, porous particle clusters (Levresse et al., 2001; Harrison, 1974; Masliyah and Polikar, 1980). In this work, we characterized the two bifurcations of the steady and axisymmetric wake. Further developments may include the non-linear interactions of these two modes varying the permeability and slip length and the secondary instability of the steady non-axisymmetric bifurcated state. Finally, we retrieved the full-scale structure by exploiting the homogenization theory developed for the two-dimensional case. A natural extension of this theory to cylindrical and spherical coordinates would give access to a broader range of geometries and applications.

9.7 Appendix

9.7.1 Numerical validation

In this section, the mesh validation procedure is outlined. The computational domain is sketched in figure 9.20. The extension of the computational domain is from $x = x_{-\infty}$ to $x = x_{+\infty}$ along the x direction and from $r = 0$ (i.e. the symmetry axis) to $r = r_\infty$ along the radial direction. The sphere center is at the origin of the reference system. Five refinement regions are present, labeled with integers from 1 to 5, starting from inside the sphere and moving outward. The mesh is composed of triangular elements. Table 9.3 shows the different meshes considered for the validation.

We consider four different cases, in the vicinity of the marginal stability curves. We verify the

Mesh	$x_{-\infty}$	$x_{+\infty}$	r_∞	n_c	n_2	n_3	n_4	n_5	N_{tot}
M1	−50	100	40	200	15	6.25	2	1.5	334534
M2	−37.5	75	30	200	15	6.25	2	1.5	222393
M3	−30	60	24	200	15	6.25	2	1.5	169039
M4	−25	50	20	200	15	6.25	2	1.5	136696
M5	−25	50	20	220	22.5	7.5	2.5	1.75	158954
M6	−25	50	20	240	27.5	7.5	2.5	1.75	213713
M7	−25	50	20	260	30	7.5	3	2	274383

Table 9.3: Different meshes employed for the validation procedure. The upstream and downstream location of the domain boundaries are denoted $x_{-\infty}$ and $x_{+\infty}$, respectively, the radial size as r_∞, n_c is the number of vertices at the interface, while n_2, n_3, n_4 and n_5 are the vertex densities on the external sides of the corresponding refinement regions; N_{tot} is the total number of elements.

	$Da = 0.0036$		$Da = 0.0032$	
Mesh	σ_1	C_D	σ_2	C_D
M1	−0.0035510	0.6255	−0.0013298 + 0.30833i	0.63275
M2	−0.0035462	0.62558	−0.0013150 + 0.30835i	0.63277
M3	−0.0035322	0.62560	−0.0012567 + 0.30839i	0.63280
M4	−0.0035178	0.62562	−0.0012567 + 0.30839i	0.63282
M5	−0.0034105	0.62594	−0.0011703 + 0.30847i	0.63311
M6	−0.0033208	0.62618	−0.0011307 + 0.30853i	0.63335
M7	−0.0032129	0.62637	−0.0010653 + 0.30860i	0.63354

Table 9.4: Results of the validation procedure for $Re = 390$, with $Da = 0.0036$ (for the steady mode) and $Da = 0.0032$ (for the unsteady mode). We also report the values of the drag coefficient for the corresponding baseflows.

	$Da = 0.0037$		$Da = 0.0031$	
Mesh	σ_1	C_D	σ_2	C_D
M1	8.3077×10^{-4}	0.67046	−0.0042442 + 0.34859i	0.68891
M2	8.3525×10^{-4}	0.67047	−0.0042320 + 0.34860i	0.68893
M3	8.4511×10^{-4}	0.67050	−0.0042127 + 0.34862i	0.68896
M4	8.5985×10^{-4}	0.67053	−0.0041836 + 0.34864i	0.68899
M5	9.0638×10^{-4}	0.67078	−0.0041290 + 0.34867i	0.68921
M6	9.3256×10^{-4}	0.67098	−0.0041154 + 0.34869i	0.68940
M7	9.7854×10^{-4}	0.67113	−0.0040814 + 0.34872i	0.68954

Table 9.5: Results of the validation procedure for $Re = 330$, with $Da = 0.0037$ (for the steady mode) and $Da = 0.0031$ (for the unsteady mode). We also report the values of the drag coefficient for the corresponding baseflows.

convergence of drag coefficient and eigenvalues:

1. Re=390 and:

- (a) $Da = 0.0032$ for the unsteady bifurcation;
- (b) $Da = 0.0036$ for the steady bifurcation;

2. Re=330 and:

- (a) $Da = 0.0031$ for the unsteady bifurcation.
- (b) $Da = 0.0037$ for the steady bifurcation;

To verify the eigenvalues and C_D convergences, we vary (i) the domain size and (ii) the mesh resolution. Starting from Mesh M4 (table 9.3), we progressively increase the domain size (meshes M3,M2 and M1). We then increase the mesh resolution with meshes M5,M6 and M7. The eigenvalues and drag coefficient for the different cases are reported in tables 9.4,9.5. In overall, the relative error on the drag coefficient is always less than 1%. The relative error on the eigenvalues is approximately constant for all cases and ~ 10%. To have a clear picture of the expected accuracy in terms of critical Reynolds number, we evaluate Re_{cr} with meshes M4 and M7 in the vicinity of the considered cases (with fixed Da) :

- for case 1(a), the critical Reynolds numbers for the unsteady bifurcation at $Da = 0.0032$ read $Re_{cr}^{M4} = 398.22$ and $Re_{cr}^{M7} = 396.63$ for meshes M4 and M7, respectively, leading to an error of $\Delta Re_{cr} = 1.58$.
- for case 1(b), the critical Reynolds numbers for the steady bifurcation at $Da = 0.0036$ read $Re_{cr}^{M4} = 383.54$ and $Re_{cr}^{M7} = 384.07$ for meshes M4 and M7, respectively, leading to an error of $\Delta Re_{cr} = 0.53$.
- for case 2(a), the critical Reynolds numbers for the unsteady bifurcation at $Da = 0.0031$ read $Re_{cr}^{M4} = 337.32$ and $Re_{cr}^{M7} = 337.13$ for meshes M4 and M7, respectively, leading to an error of $\Delta Re_{cr} = 0.19$.

For case 2(b), we evaluate the variation of the critical Darcy number in the vicinity of the value for unconditional stability, with fixed $Re = 330$. The critical values read $Da_{cr}^{M4} = 0.003706$ and $Da_{cr}^{M4} = 0.003707$.

The error on the critical Reynolds number increases with Re itself and is, at most, of order $\Delta Re_{cr} \approx 1.6$, and the associated maximum relative error is $\approx 0.4\%$. Also, the precision on the critical Darcy number appears to be satisfactory. Therefore, we conclude that mesh M4 is a good compromise between the accuracy and the computational times for the large parametric study considered, which involves five different parameters (Re,Da, Λ_t, Λ_s, α), with a relative error less than 1% on the critical Reynolds numbers.

9.7.2 Evaluation of permeability and slip via homogenization theory

Several recent works based on multi-scale homogenization aimed at linking the microscopic structure of a porous medium to its macroscopic feedback on the surrounding flow, i.e. the

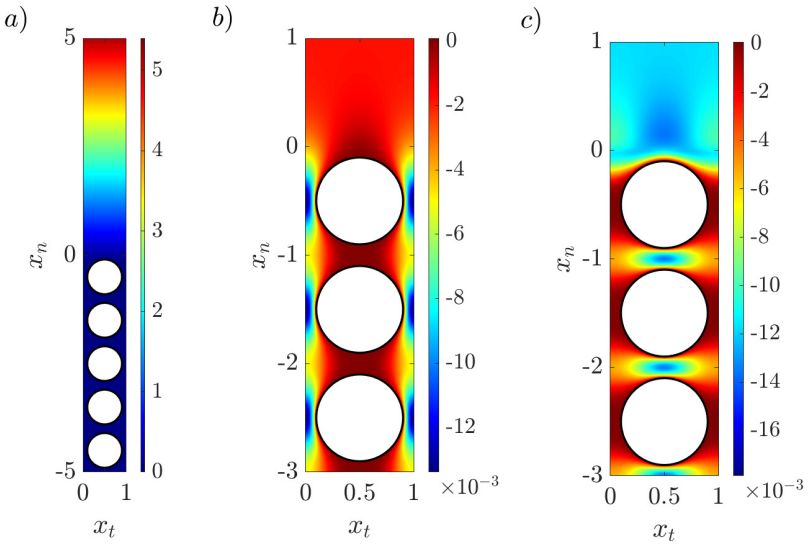

Figure 9.21: Overview of the microscopic solution in the interface cell for a given circular inclusion whose radius is 0.4. (a) $\lambda^{\dagger}_{tt}$ in the whole interface cell. (b),(c) Zoom in on the first three solid inclusions in the interface cell for (b) $\kappa^{\dagger}_{nn}$ and (c) $\kappa^{\dagger}_{tt}$.

bulk permeability and slip interface effects Zampogna and Bottaro (2016); Lācis et al. (2017); Lācis et al. (2020); Bottaro (2019). In these works, the microscopic structure is assumed to be periodic within the porous medium so that the bulk permeability can be calculated once for all in a periodic microscopic elementary cell. Additionally, an interface microscopic cell containing few inclusions across the fluid-porous boundary can be identified where some microscopic problems can be solved to retrieve the interface permeability and slip. In particular, Bottaro Bottaro (2019) and Naqvi and Bottaro Naqvi and Bottaro (2021) have shown that both bulk and interface macroscopic properties can be deduced from a unique interfacial microscopic problem, provided that the normal-to-the-interface size of the microscopic domain is large enough. Adopting this last development, all macroscopic quantities can be retrieved by the solution of the two sets of equations. We introduce the two-dimensional local reference frame (x_n, x_t), where n and t denote the normal and tangent directions to the interface, respectively. The microscopic problems to be solved involve the tensor quantities $\lambda^{\dagger}_{ij}$, $\kappa^{\dagger}_{ij}$ and the vector quantities $\xi^{\dagger}_{j}$ and $\chi^{\dagger}_{j}$, where $i, j = n, t$. The equations, written in components for the sake of clarity, read:

$$\frac{\partial \lambda^{\dagger}_{ij}}{\partial x_i} = 0, \quad -\frac{\partial \xi^{\dagger}_{j}}{\partial x_i} + \frac{\partial^2 \lambda^{\dagger}_{ij}}{\partial x_l^2} = 0, \tag{9.34}$$

$$\lim_{x_n \to +\infty} \frac{\partial \lambda^{\dagger}_{ij}}{\partial x_n} = \delta_{ij}, \quad \lim_{y \to +\infty} \xi^{\dagger}_{j} = 0,$$

and

$$\frac{\partial \kappa_{ij}^{\dagger}}{\partial x_i} = 0, -\frac{\partial \chi_j^{\dagger}}{\partial x_i} + \frac{\partial^2 \kappa_{ij}^{\dagger}}{\partial x_k^2} = \delta_{ij} H(-x_n), \tag{9.35}$$

$$\lim_{x_n \to +\infty} \frac{\partial \kappa_{ij}^{\dagger}}{\partial x_n} = 0, \quad \lim_{x_n \to +\infty} \chi_j^{\dagger} = 0,$$

where H is the Heaviside function centered in $x_n = 0$, corresponding to the starting point of the first interface unit cell. The macroscopic quantities used in the interface conditions (9.15) can be then retrieved by the solutions of problems (9.34,9.35) introducing the following relations

$$\lambda_t = \int_0^1 \lambda_{tt}^{\dagger}(x_n \to +\infty)\, \mathrm{d}t - x_n, \quad K_{\text{int}} = \int_0^1 \kappa_{tt}^{\dagger}(x_n \to +\infty)\, \mathrm{d}t \tag{9.36}$$

and

$$K = \int_0^1 \kappa_{nn}^{\dagger}(x_n \to +\infty)\, \mathrm{d}t. \tag{9.37}$$

The solution for $\lambda_{tt}^{\dagger}$, $\kappa_{nn}^{\dagger}$ and $\kappa_{tt}^{\dagger}$ is represented in the microscopic interface cell in figure 9.21 for a periodic array of cylinders of radius equal to 0.4. Once the average values of the microscopic quantities are evaluated using equations (9.36,9.37), upon rescaling with the macroscopic length, they can be used in equations (9.2) and (9.3) to establish a link between the microscopic structure and the corresponding macroscopic flow field.

10 Homogenization-based design of microstructured membranes: wake flows past permeable shells

Remark This chapter is largely inspired by the publication of the same name

P. G. Ledda[1], E. Boujo[1], S. Camarri[2], F. Gallaire[1], G. A. Zampogna[1]

[1]Laboratory of Fluid Mechanics and Instabilities, École Polytechnique Fédérale de Lausanne, CH-1015 Lausanne, Switzerland,

[2]Dipartimento di Ingegneria Civile e Industriale, Università di Pisa, 56122 Pisa, Italy

Journal of Fluid Mechanics **927**, A31 (2021)

Author contributions P.G.L. conceived the project with input from F.G. and G.A.Z.. P.G.L. performed the theoretical developments, with input from F.G., and numerical simulations, compared with the full-scale simulations performed by G.A.Z.. P.G.L. wrote the manuscript with input from the coauthors.

A formal framework to characterize and control/optimize the flow past permeable membranes by means of a homogenization approach is proposed and applied to the wake flow past a permeable cylindrical shell. From a macroscopic viewpoint, a Navier-like effective stress jump condition is employed to model the presence of the membrane, in which the normal and tangential velocities at the membrane are respectively proportional to the so-called filtrability and slip numbers multiplied by the stresses. Regarding the particular geometry considered here, a characterization of the steady flow for several combinations of constant filtrability and slip numbers shows that the flow morphology is dominantly influenced by the filtrability and exhibits a recirculation region that moves downstream of the body and eventually disappears as this number increases. A linear stability analysis further shows the suppression of vortex shedding as long as large values of the filtrability number are employed. In the control/optimization phase, specific objectives for the macroscopic flow are formulated by adjoint methods. A homogenization-based inverse procedure is proposed to obtain the optimal constrained microscopic geometry from macroscopic objectives, which accounts for fast variations of the filtrability and slip profiles along the membrane. As a test case for the proposed design methodology, the cylindrical membrane is designed to maximize the resulting drag coefficient.

10.1 Introduction

The behavior of wake flows past permeable bodies and membranes is of considerable interest owing to its large range of applications, both in nature and engineering, as exposed in Section 1.1. We refer to Section 1.4 for an overview of the flow past solid and porous bluff bodies.

Therefore, the modification of the permeability of a membrane is a strategy to control and optimize the flow morphology. Lagrangian-based approaches are one category of optimization procedures, which found large interest in the fluid dynamics community, and are based on a variational formulation that allows one to compute gradients at low cost through the use of the so-called adjoint variables (Luchini and Bottaro, 2014). Several studies were developed in a Lagrangian framework, as in the case of the sensitivity to baseflow modifications (Marquet et al., 2008), steady forcing in the bulk (Boujo et al., 2013; Meliga et al., 2014) or at the solid walls by blowing and suction (Meliga et al., 2010; Boujo and Gallaire, 2014, 2015), for different objectives and flow configurations. Adjoint-based sensitivity analysis tools can therefore be used as a building block for optimization procedures, in steady (Camarri and Iollo, 2010) and unsteady (Nemili et al., 2011; Lemke et al., 2014) configurations. In Schulze and Sesterhenn (2013) an adjoint-based optimization procedure to obtain the optimal permeability distribution for trailing-edge noise reduction was proposed, in which the porous medium was modeled via the Darcy law.

Despite the increasing interest for multi-scale structures in fluid mechanics, systematic approaches for the homogenization-based design and optimization of permeable membranes are still lacking. In the present work, we aim to bridge this gap by linking the obtained optimal profile of permeability to a real, realistic, full-scale structure (that can be eventually built). For this purpose, we propose a formal framework for the optimization of permeable membranes, applying it to the particular case of wake flows in the low to moderate Reynolds numbers regime. We exploit the concepts of stability analysis, homogenization theory and gradient-based optimization so as to give a procedure to obtain the full-scale structure satisfying user-defined macroscopic flow objectives. The chapter is structured as follows. In Section 10.2 we introduce the mathematical formulation of the problem and describe the homogenization-based design procedure. We then apply the procedure by first studying, in Section 10.3, the steady solutions of the flow equations and their linear stability with respect to infinitesimal perturbations. Section 10.4 is devoted to the geometric reconstruction of the microscopic geometry for salient cases and to the comparison with the homogenized model. In Section 10.5, we then move to a gradient-based optimization of a membrane with variable properties, and in Section 10.6, using a homogenization-based inverse procedure, we retrieve the full-scale geometry of the considered membrane from the optimal properties found in Section 10.5 and eventually compare the properties of the full-scale structure to those predicted by the homogenized model.

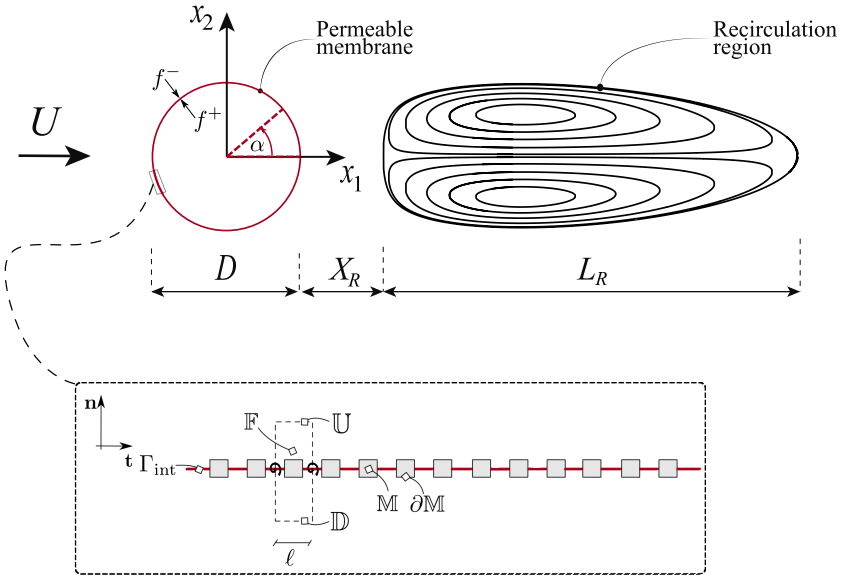

Figure 10.1: Top panel: fluid flow configuration considered in the present work and its typical structure past the cylindrical permeable shell (Γ_{int}, in red) of diameter D, where we denoted the length of the recirculation region L_R and its distance X_R from the rear of the body. The angle α is measured counterclockwise starting from the rear. The superscript $\cdot^-$ indicates that the generic variable f is evaluated in the outer fluid region while the superscript $\cdot^+$ refers to the inner fluid region. Bottom panel: zoom on the shell to highlight its microscopic structure in cylindrical coordinates, made by replication of solid inclusions denoted by $\mathbb{M}$ with boundary $\partial\mathbb{M}$ and sketch of the elementary unit cell in dashed line, whose tangential-to-the-surface size is ℓ. The fluid domain within the unit cell is denoted by $\mathbb{F}$ while its upper and lower boundaries are indicated respectively with $\mathbb{U}$ and $\mathbb{D}$.

10.2 A formal framework to support the design of microstructured permeable surfaces

In this section, we introduce the main physical hypotheses, strategy and tools to aid the design of microstructured membranes in order to tune their aero- and hydro-dynamics properties.

10.2.1 Problem formulation and model description

We consider a two-dimensional permeable cylindrical shell of diameter D subject to an incompressible flow of a Newtonian fluid of constant density ρ and viscosity μ, whose free-stream velocity is U_∞, as depicted in figure 10.1. The cylindrical shell is constituted by a mono-disperse repetition of solid inclusions, whose characteristic length scale is denoted as ℓ. Since $\ell \ll D$ we can introduce a separation of scales parameter defined as the ratio between the two length scales at play:

$$\varepsilon := \frac{\ell}{D} \ll 1. \tag{10.1}$$

Under this assumption, a homogenized model is employed to describe the flow through the membrane (Zampogna and Gallaire, 2020), which is macroscopically represented by a smooth surface with zero thickness. In the outer and inner pure-fluid regions splitted by the permeable shell, the incompressible Navier-Stokes equations hold. The velocity $\bar{\boldsymbol{u}}$ and pressure $\bar{p}$ fields are introduced, where the superscript $\bar{\cdot}$ denotes dimensional variables. In the following, we will employ a notation in components, which is more suitable for the membrane interface boundary condition. Introducing the Cartesian coordinate system $(\bar{x},\bar{y}) = (\bar{x}_1,\bar{x}_2)$ (figure 10.2), these equations read $(i,j=1,2)$:

$$\begin{gathered}\rho\partial_{\bar{t}}\bar{u}_i + \rho\bar{u}_j\partial_j\bar{u}_i = -\partial_i\bar{p} + \mu\partial^2_{jj}\bar{u}_i,\\ \partial_i\bar{u}_i = 0.\end{gathered} \tag{10.2}$$

The flow through the membrane is described by an effective stress jump model, consisting of the discontinuity in the fluid stress and the continuity of velocity across the permeable shell, denoted here with Γ_{int} (red line in figure 10.1). Labelling with the superscript $^-$ and $^+$ variables evaluated respectively in the outer and inner fluid regions, as shown in figure 10.1, the interface conditions at the membrane Γ_{int} read $(i,j,k=1,2)$

$$\begin{gathered}\bar{u}_i = \bar{u}_i^+ = \bar{u}_i^-\\ \bar{u}_i = \frac{\ell}{\mu}M_{ij}\left(\bar{\Sigma}_{jk}\left(\bar{p}^-,\bar{\boldsymbol{u}}^-\right) - \bar{\Sigma}_{jk}\left(\bar{p}^+,\bar{\boldsymbol{u}}^+\right)\right)n_k\end{gathered} \tag{10.3}$$

where $\bar{\Sigma}_{jk}$ is the $jk-$th component of the stress tensor defined as

$$\bar{\Sigma}_{jk}\left(\bar{p},\bar{\boldsymbol{u}}\right) = -\bar{p}\delta_{jk} + \mu(\partial_j\bar{u}_k + \partial_k\bar{u}_j), \tag{10.4}$$

and the components of the tensor M_{ij} (figure 10.1) are

$$M_{ij} = \bar{L}_t t_i t_j - \bar{F}_n n_i n_j, \tag{10.5}$$

where $\bar{L}_t$, $\bar{F}_n$ are evaluated by solving microscopic problems within the elementary unit cell introduced in figure 10.1, in the local reference frame $(\mathbf{t},\mathbf{n}) = ((-\sin(\alpha),\cos(\alpha)),(\cos(\alpha),\sin(\alpha)))$ (cf. Zampogna and Gallaire, 2020, and Section 10.4.2 for a detailed description of these problems and their solution). We note that the generic tensor N_{ij} of the original condition developed in Zampogna and Gallaire (2020) is replaced here by $-M_{ij}$ since, in the present work, we consider only solid inclusions which are symmetric with respect to Γ_{int} and we assume that inertia is negligible within the pores.

By considering D and U_∞ respectively as reference length and velocity scales, we obtain the following system of non-dimensional equations:

$$\begin{gathered}\partial_t u_i + u_j\partial_j u_i = -\partial_i p + \frac{1}{Re}\partial^2_{jj}u_i\\ \partial_i u_i = 0,\end{gathered} \tag{10.6}$$

where we introduced the Reynolds number as $Re = \frac{\rho UD}{\mu}$. The non-dimensional interface condition on Γ_{int} reads:

$$\begin{aligned} u_i &= u_i^+ = u_i^- \\ u_i &= Re\mathcal{M}_{ij}\left(\Sigma_{jk}\left(p^-, \boldsymbol{u}^-\right) - \Sigma_{jk}\left(p^+, \boldsymbol{u}^+\right)\right) n_k, \end{aligned} \tag{10.7}$$

$$\Sigma_{jk}(p, \boldsymbol{u}) = -p\delta_{jk} + \frac{1}{Re}(\partial_j u_k + \partial_k u_j), \tag{10.8}$$

$$\mathcal{M}_{ij} = \mathcal{L} t_i t_j - \mathcal{F} n_i n_j, \tag{10.9}$$

where $\mathcal{L} = \epsilon \bar{L}_t$ and $\mathcal{F} = \epsilon \bar{F}_n$ are respectively labelled as slip and filtrability numbers. The interface condition (10.7) thus states that the velocity at the membrane is proportional to the Reynolds number and to the tensor $\mathcal{M}_{ij}$. According to Zampogna and Gallaire (2020), the tensor $\mathcal{M}_{ij}$ describes the geometry of the microscopic problem with negligible inertial effects within the microscopic domain, in a non-dimensionalization which makes the problem independent of the macroscopic Reynolds number. In the macroscopic perspective, the relative importance between inertial and viscous effects is taken into account by Re in equation (10.7). More specifically, the velocity locally tangential to the interface is proportional to $\mathcal{L}$, while the normal velocity is proportional to $\mathcal{F}$. Therefore, the filtrability and slip numbers denote the capability of the flow to pass through and slip along the membrane, respectively. Different limiting behaviors of the interface condition (10.7) are thus identified. When $\mathcal{F} = 0$, the flow cannot pass through the membrane but it can slip along it. This situation is analogous to the one outlined in Zampogna et al. (2019b) for rough surfaces, and the resulting boundary condition is formally analogous to the so-called Navier-slip condition. When $\mathcal{L} = 0$, a no-slip condition is imposed on the tangential velocity, while the normal one varies in proportion to $\mathcal{F}$. This situation can be interpreted as an averaged Darcy law through the membrane, where the viscous effects and thus the slip at the interface are neglected (Zampogna and Bottaro, 2016). Other limiting cases occur for $\mathcal{F} = 0$ and $\mathcal{L} = 0$, which corresponds to a solid wall condition, and for $\mathcal{F} \to \infty$ and $\mathcal{L} \to \infty$, which corresponds to the imposition of the continuity of stresses across the microscopic elementary volume whose size tends to zero, and thus to the absence of the solid structure. Since the flow configuration is solved numerically, we refer to the caption of figure 10.2 for an explanation of the boundary conditions imposed on the remaining boundaries of the computational domain. These conditions, in non-dimensional form, read $u_1 = 1$, $u_2 = 0$ at the inlet and $(-p\delta_{ij} + \frac{1}{Re}\partial_j u_i)n_j = 0$ on the lateral and outlet boundaries.

10.2.2 Homogenization-based design

In the existing literature, works on permeable bodies and membranes were focused on the evaluation of the macroscopic parameters of the membrane (slip and filtrability) starting from the microscopic geometry. Other works treated the above-mentioned macroscopic quantities as free parameters in order to characterize, modify and optimize the fluid flow surrounding the porous body, without providing an explicit link between these parameters and the microscopic

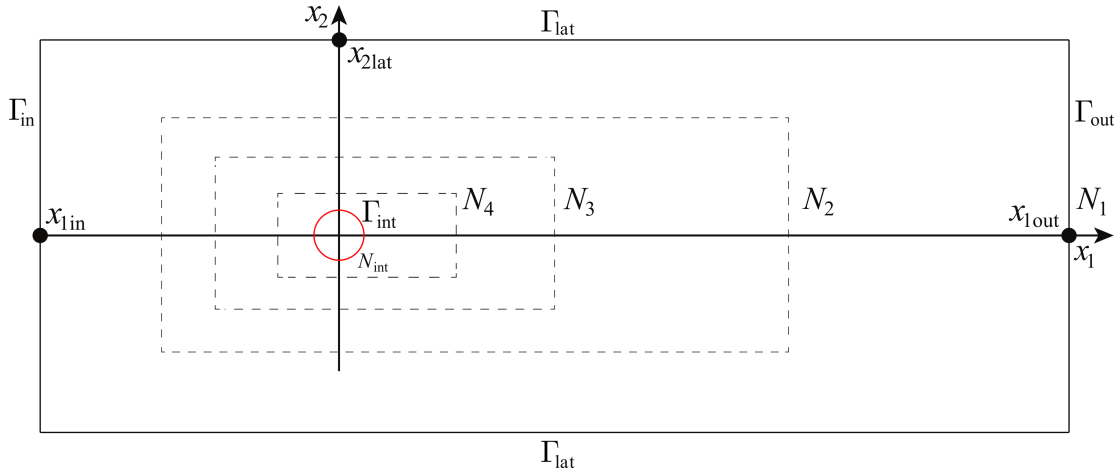

Figure 10.2: Computational domain considered in the present work. The regions denoted with N_j represent the different mesh refinements used when approaching the permeable shell. At the inlet Γ_{in} a free-stream condition with a Dirichlet boundary condition of the form $\bar{u}_1 = U_\infty$ and $\bar{u}_2 = 0$ is imposed, while on the lateral boundaries Γ_{lat} and at the oulet Γ_{out} the stress-free condition $(-\bar{p}\delta_{ij} + \mu\partial_j\bar{u}_i)n_j = 0$ is used. On the interface Γ_{int} conditions (10.3) are imposed.

structure of the membrane. Here, we propose to fill the gap between these two aspects by an *inverse* formulation of the homogenized model that on one hand is extremely efficient for parametric studies and on the other hand allows one to deduce the microscopic geometry which realizes given distributions of $\mathcal{L}$ and $\mathcal{F}$.

The inverse formulation aims at deriving the microscopic characteristics of the membrane based on the macroscopic features of the steady flow. In the present work, an efficient workflow to deduce full-scale structures starting from the homogenized model is adopted (cf. the top frame of figure 10.3). The generic workflow therefore firstly consists of an analysis where the homogenized model is employed. The implementation of the homogenized model implies a decoupling between the microscopic structure and the macroscopic effect on the flow. On the one hand, parametric studies and optimizations are simplified owing to the reduced number of parameters; on the other hand, the retrieval of the full-scale structure is performed in a second step, when the macroscopic feedback embodied in the scalar parameters of the homogenized model is already known.

For illustration purposes, the workflow is specialized to analyze the flow configuration shown in figure 10.1, leading to the following procedure:

- Using the homogenized approach described in the previous section, we perform a parametric study for varying $\mathcal{L}$ and $\mathcal{F}$, by solving the steady version of equations (10.6-10.7) for different values of the Reynolds number.
- We characterize the topological properties of the steady flow (e.g. the characteristic dimensions of the recirculation region) and the aero/hydro-dynamics properties of the

permeable shell as, for instance, its drag coefficient.

- The validity of the performed investigation, carried out assuming that the flow is steady, is verified by linear stability analysis (Chomaz, 2005; Theofilis, 2011). The latter has the advantage to characterize the stability of the steady solution with a computational cost comparable to that needed to compute steady solutions, thus making it suitable for the performed parametric study.

- Once the variety of possible steady solutions is reduced by excluding the unstable configurations, for which the steady analysis would be inappropriate, the objective to be optimized is defined, e.g. the maximum drag coefficient for a fixed Reynolds number. Therefore, the values of $\mathcal{L}$ and $\mathcal{F}$ that maximize the objective function are identified. This can be done by employing adjoint procedures for spatially-homogeneous membrane properties. However, since in this work we perform a parametric study, the values are directly deduced from the latter.

- We then move from the macroscopic perspective to the microscopic one, aiming at identifying the geometry of the membrane that corresponds in macroscopic terms to the optimal configuration previously identified. We therefore perform the microscopic simulations described in Zampogna and Gallaire (2020) for a fixed geometry by varying the fluid-to-solid ratio of the porous shell. We thus define the microscopic geometrical parameters and ε.

- We eventually verify the accuracy of the resulting structure by comparing the full-scale simulations with the homogenized results.

The outlined technique has the great advantage of drastically reducing the complexity of the problem and gives a parametric map of the properties of the flow by varying the microscopic geometry of the membrane. An extension of this technique to treat the case of a microscopic geometry that varies along the membrane is obtained by a gradient-based optimization implemented via a Lagrangian approach, detailed in Section 10.5.2. In particular, we consider as a starting point the configuration, with constant slip and filtrability numbers, that maximizes the drag coefficient. We evaluate the sensitivity of this predefined objective function (drag maximization) with respect to spatial inhomogeneities of the properties of the membrane and perform a gradient-based optimization. The resulting structure is then obtained by following an inverse procedure based on the microscopic calculations of Zampogna and Gallaire (2020), but extended to the case of variable properties along the membrane.

We finally underline that the procedure, illustrated here for the specific case of a wake flow, is of general validity and can thus be applied to a generic flow.

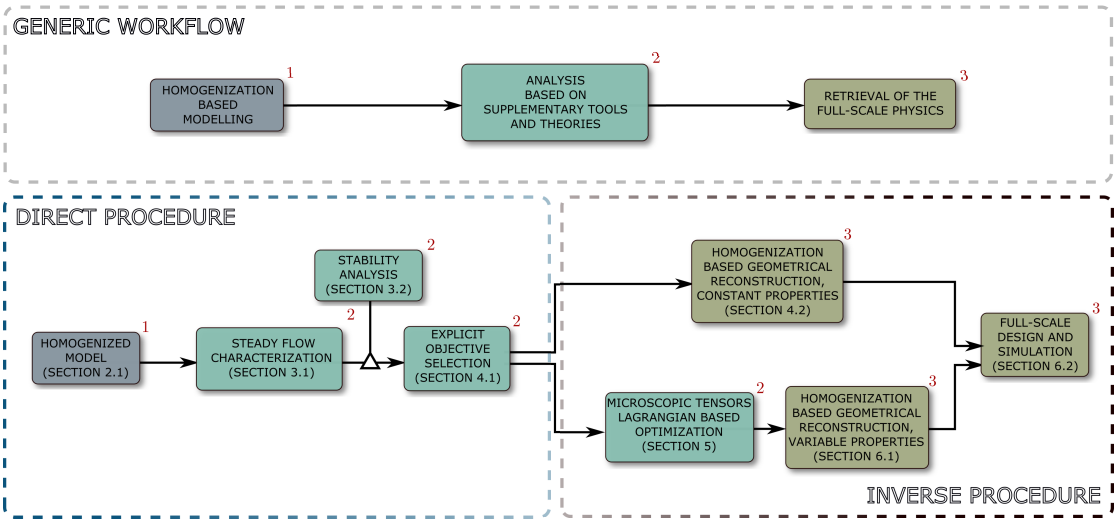

Figure 10.3: Top frame: generic workflow to efficiently analyze a flow configuration via homogenized models integrated in classical analyses like, for instance, parametric studies, stability analysis or adjoint-optimization finalized to identify configurations of interest. The retrieval of the full-scale physics for the identified configurations is done in a last step leading to a substantial reduction of the complexity of the optimization problem. Bottom frames: the generic workflow has been specialized in the present work to design permeable membranes. Colors and red numbers are used to correctly place each step of the procedure adopted in the present work in the generic workflow. A homogenized model is used to characterize a specific flow configuration in a *direct* formulation. This allows one to identify a set of objectives and the corresponding values of the macroscopic parameters realizing these objectives. Homogenization is then used in an *inverse* formulation to associate the values of the macroscopic tensors with a specific microscopic geometry.

10.3 Case study: flow past a cylindrical porous shell

In this section, we report the results of the *direct* part of the procedure sketched in figure 10.3, preparatory to the homogenization-based geometrical reconstruction and Lagrangian optimization, constituting the *inverse* part of the procedure. We characterize the steady flow in terms of the recirculation region and drag coefficient, and then we move to the stability properties of the steady wake and the features of possible unsteady modes.

Equations (10.6) are numerically implemented via their weak formulation in the finite element solver COMSOL Multiphysics, using a domain decomposition method (cf. for instance Quarteroni, 2017) to couple the outer and inner flow. In this framework, the macroscopic model (10.7) acts like an interface condition between two different fluid domains. In order to exchange information from the outer to the inner domain, the stress jump condition is implemented by exploiting the interface integral emerging from the weak formulation, while, to exchange information from the inner to the outer domain, the continuity of velocity is imposed via a Dirichlet boundary condition. We exploit the built-in solver for non-linear systems, based on a Newton algorithm. The spatial discretization is based on the Taylor–Hood (P2-P1)

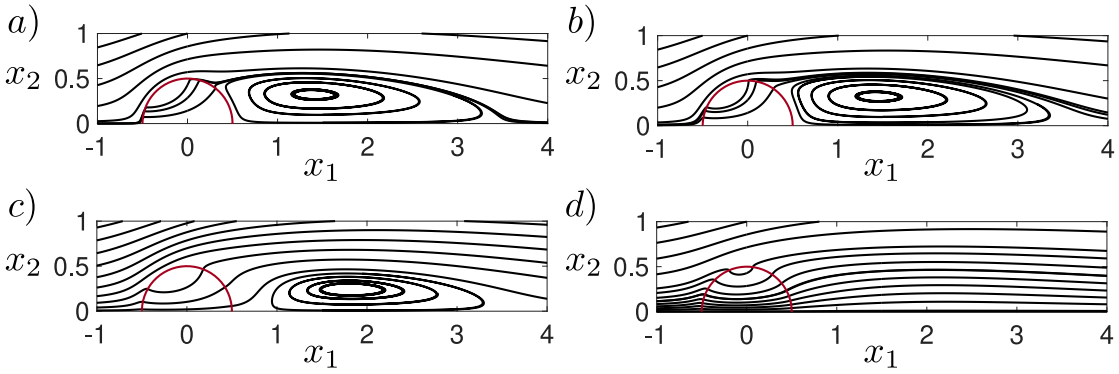

Figure 10.4: Streamlines of the flow past the cylindrical permeable shell at $Re = 50$ for $\mathcal{L} = 10^{-4}$ and four different values of $\mathcal{F}$: (a) $\mathcal{F} = 10^{-4}$, (b) $\mathcal{F} = 10^{-3}$, (c) $\mathcal{F} = 10^{-2}$, (d) $\mathcal{F} = 3 \times 10^{-2}$.

triangular elements. The unstructured grid is made of five different regions of refinement (figure 10.2), whose edge densities have been chosen after a convergence analysis reported in Appendix 10.8.1.

The eigenvalue problems resulting from the linear stability analysis carried out in Section 10.3.2 are solved with the COMSOL Multiphysics built-in eigenvalue solver, based on the ARPACK library; mesh convergence is checked also for this problem and it is reported in Appendix 10.8.1.

10.3.1 Steady flow characterization

The steady wake past a circular solid cylinder is characterized by a recirculation region that is symmetric with respect to the x_1-axis. We denote with $(\boldsymbol{U}, P)$ the steady solution of equations (10.6). Since, by construction, we do not introduce any further asymmetry, also the flow past the permeable cylindrical shell is expected to be x_1-symmetric. For this reason, we only report the flow field in the region $x_2 > 0$. For the present analysis, we introduce the length of the recirculation region L_R and its distance from the rear of the body X_R as defined in figure 10.1. In figure 10.4 we report the flow streamlines for different values of $\mathcal{F}$ when $Re = 50$ and $\mathcal{L} = 10^{-4}$. At low values of $\mathcal{F}$, e.g. $\mathcal{F} = 10^{-4}$, the wake is similar to the solid case, i.e. characterized by a recirculation region attached to the rear of the cylinder ($X_R \approx 0$). As the value of $\mathcal{F}$ increases, the recirculation region detaches from the body and moves downstream. A further increase in $\mathcal{F}$ implies a size reduction of the recirculation region (L_R), and at very large values of $\mathcal{F}$, i.e. $\mathcal{F} = 3 \times 10^{-2}$, the recirculation region eventually disappears ($L_R = 0$).

In figure 10.5 we report the variation of the recirculation region with $\mathcal{F}$, for different slip numbers $\mathcal{L}$ and for $Re = 50$. Independently of the value of the slip number, a behavior similar to the one described in figure 10.4 is observed. For a fixed filtrability number, an increase in $\mathcal{L}$ leads to a slight decrease of L_R, while X_R does not vary noticeably.

A complete characterization of the flow morphology requires also the analysis of the effect

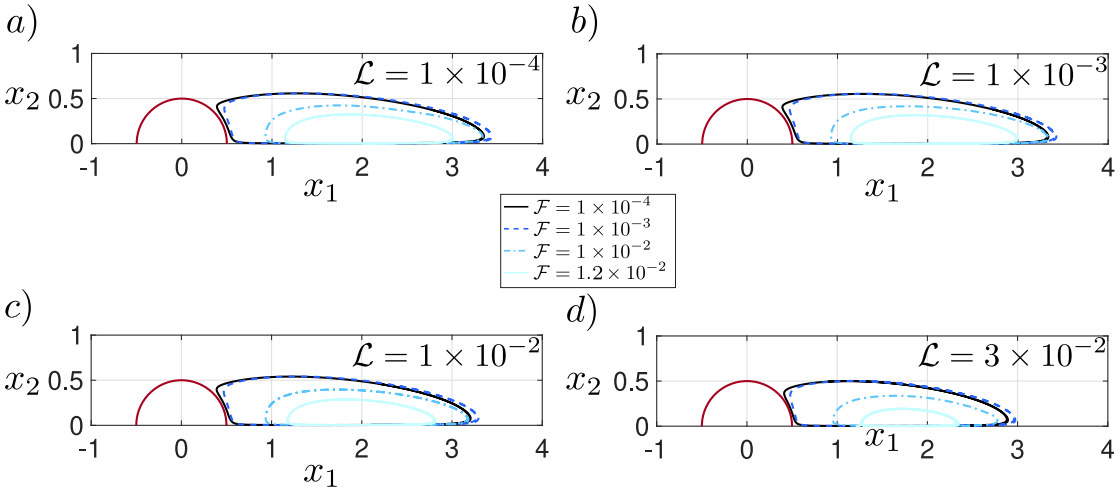

Figure 10.5: Streamlines identifying the recirculation region past the cylindrical permeable shell at $Re = 50$ for different values of $\mathcal{F}$. Each panel corresponds to a single value of $\mathcal{L}$.

of the Reynolds number. In figure 10.6 we show the recirculation regions for fixed filtrability number $\mathcal{F} = 10^{-2}$, for different values of $\mathcal{L}$ and for $Re = 50, 75, 100, 110$. For $Re = 50$, the flow is characterized by a recirculation detached from the body such that $L_R \approx 2$. At $Re = 75$, the recirculation region moves downstream and L_R increases. This effect is enhanced at large values of the slip number. In the last case, $Re = 110$, the recirculation region moves further downstream and L_R decreases, and eventually disappears for large values of $\mathcal{L}$.

The evolution of L_R and X_R with $\mathcal{L}, \mathcal{F}$ and Re is summarized in figure 10.7. The quantities L_R and X_R have been deduced by a Matlab script which evaluates the position of the zeros of the horizontal velocity field sampled on the line $x_2 = 0$. In analogy with the solid case, L_R increases with Re (figure 10.7(a)). The curves are grouped in clusters. Each cluster represents different values of Re, and each curve within the cluster a different value of $\mathcal{L}$. For $Re = 25$, L_R decreases with $\mathcal{F}$ until the recirculation region disappears for $\mathcal{F} \approx 10^{-2}$. A similar trend is observed for $Re = 50$, but in this case the recirculation region disappears for larger values of $\mathcal{F}$. For $Re > 50$, interestingly, the recirculation region grows as the filtrability number increases. L_R reaches a maximum and decreases, until the recirculation region disappears for $\mathcal{F} \approx 1.5 \times 10^{-2}$. For all cases, an increase in $\mathcal{L}$ leads to a slight decrease of L_R, while the trend with $\mathcal{F}$ does not change.

As shown in figure 10.7(b), the distance between the body and the recirculation region, X_R, increases with $\mathcal{F}$, reaching a maximum value approximately equal to 2 for $Re = 100$, while the effect of $\mathcal{L}$ is negligible. An increase in Re leads to an increase in the distance X_R, but the trend with $\mathcal{F}$ remains unchanged.

The morphology analysis of the steady wake shows that L_R and X_R are controlled by the slip and filtrability numbers. Large values of the filtrability number $\mathcal{F}$ strongly influence the flow, implying detached and small recirculation regions, or even the absence of recirculation.

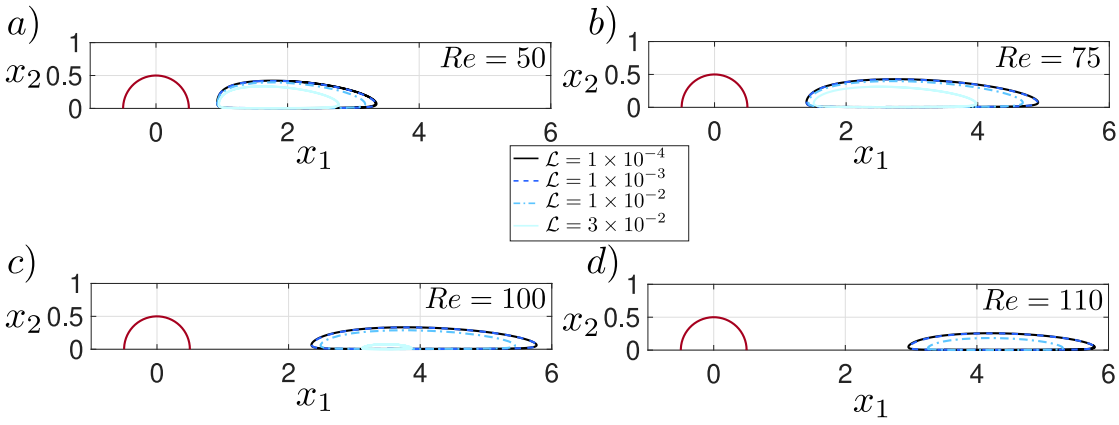

Figure 10.6: Streamlines identifying the recirculation region past the cylindrical permeable shell at $\mathcal{F} = 10^{-2}$ and for different values of Re and $\mathcal{L}$. Note that for $\mathcal{L} = 3 \times 10^{-2}$ and $Re = 110$ recirculation is suppressed.

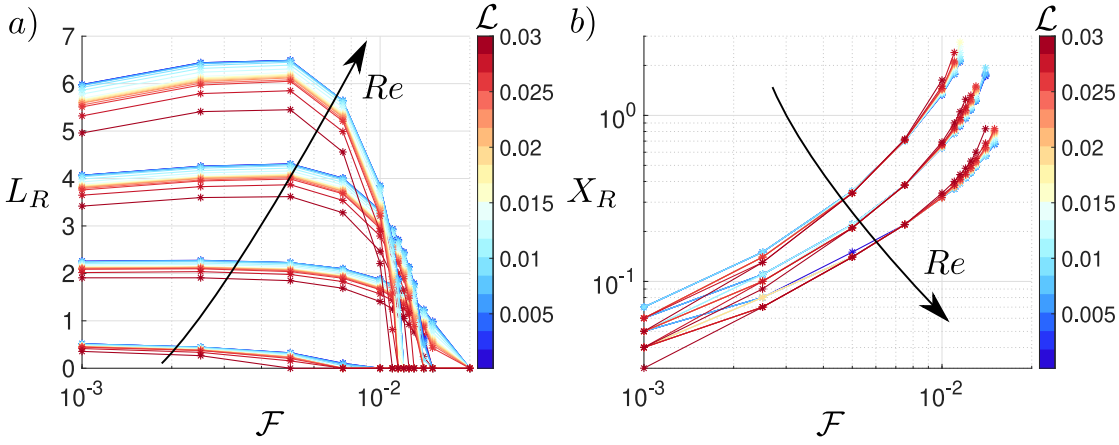

Figure 10.7: Panel (a): length of the recirculation region past the cylindrical permeable shell L_R for $\mathcal{F} \in [10^{-3}, 2 \times 10^{-2}]$ and $\mathcal{L} \in [10^{-3}, 2 \times 10^{-2}]$. Each cluster represents a single value of Re. From the top to the bottom: $Re = 100, 75, 50, 25$. Panel (b): distance of the recirculation region from the rear of the body X_R for the same values of the parameters. From the top to the bottom $Re = 50, 75, 100$.

The slip number $\mathcal{L}$ slightly modifies the shape and distance of the recirculation region, for fixed filtrability number, whilst the qualitative behavior remains unchanged. An increase in the Reynolds number, for large values of $\mathcal{F}$, leads to an initial increase in L_R, followed by a decrease and eventually vanishing, while X_R monotonically increases. The outlined wake morphology strongly resembles the one observed for the wake of porous rectangles (Ledda et al., 2018), where the permeability plays a role similar to the filtrability number.

When the Reynolds number increases, the inertia of the fluid increases and tends to enlarge the recirculation region, whereas the flow can pass through the body more easily, since the velocity at the membrane is proportional to Re (equation (10.7)). The result of this competition is the non-monotonic behavior of the recirculation region size with Re.

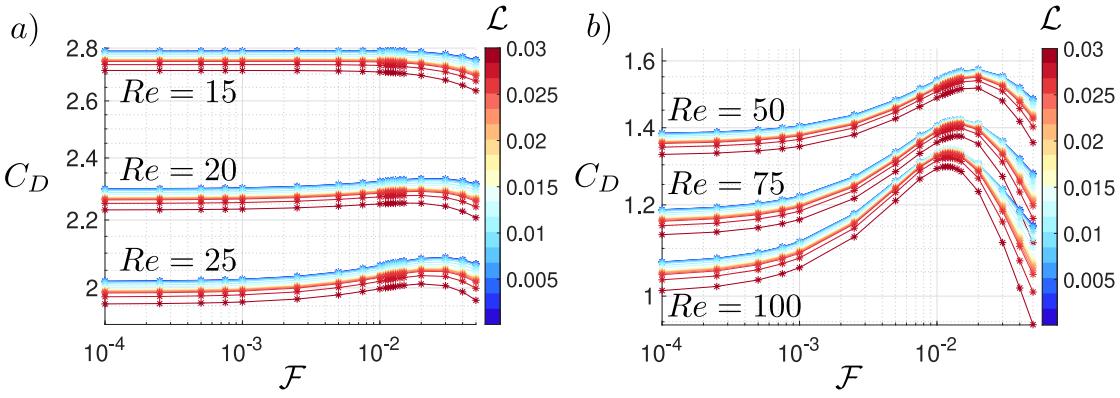

Figure 10.8: Variation of the drag coefficient C_D with $\mathcal{F}$ for different values of $\mathcal{L}$. Each cluster in panel (a) and (b) corresponds to a different value of Re, as denoted in the figure.

We conclude our characterization of the steady wake past a permeable cylindrical shell by considering the drag coefficient

$$C_D = 2 \oint_{\Gamma_{\text{cyl}}} \left(\Sigma_{jk}(P^-, \boldsymbol{U}^-) - \Sigma_{jk}\left(P^+, \boldsymbol{U}^+\right) \right) n_k \delta_{1j} \, \mathrm{d}\Gamma, \tag{10.10}$$

i.e. the drag exerted by the fluid over the outer ($^-$) and inner ($^+$) sides of Γ_{int}, respectively. The drag coefficient of a solid cylinder decreases with Re (Fornberg, 1980). The same behavior is observed in the permeable case (cf. figure 10.8), where, at each value of Re, we observe clusters of curves analogous to figure 10.7. While $\mathcal{L}$ produces slight variations in C_D, the trend in the variation with $\mathcal{F}$ depends on the Reynolds number considered and shows two different types of behavior. Up to $Re = 15$, the drag coefficient decreases with $\mathcal{F}$. From $Re = 20$, C_D slightly increases with $\mathcal{F}$, and this effect is more pronounced as Re further increases. For larger values of Re the curve representing the C_D against $\mathcal{F}$ is no more monotonic and for $Re = 100$, a clear peak is observed, for $\mathcal{F} \approx 1.25 \times 10^{-2}$. Surprisingly, the maximum drag coefficient $C_D \approx 1.34$ is larger than the one for the solid cylinder, $C_D \approx 1.06$ (Fornberg, 1980). Beyond this value of $\mathcal{F}$, the drag coefficient decreases.

In the following, a physical insight on the described drag behavior is provided. Since the maximum is observed by varying the filtrability, while the slip does not have any significant effect on this behavior, we fix $\mathcal{L} = 10^{-4}$ and we focus on the effect of the sole $\mathcal{F}$ in the range $[10^{-4}, 5 \times 10^{-2}]$, for $Re = 100$. Note that the maximum of the drag coefficient in this specific case is obtained for $\mathcal{F} \simeq 1.2 \times 10^{-2}$, which is inside the range considered here. We perform an analysis of the different sources of drag, dividing them in a pressure contribution, i.e. $(\Delta P) n_1 = -(P^- - P^+) n_1$, and in a viscous stress contribution $(\Delta \Sigma^v_{1j}) n_j = (\Sigma^v_{1j}(\boldsymbol{U}^-) - \Sigma^v_{1j}(\boldsymbol{U}^+)) n_j$, where $\Sigma^v_{jk}(\boldsymbol{U}) = \frac{1}{Re}(\partial_j U_k + \partial_k U_j)$. These contributions are reported in figure 10.9(a). The global pressure and viscous contributions to the drag are the integrals of the corresponding curves in figure 10.9(a). Analyzing the integral of the pressure and viscous contributions we observe that (i) the viscous contribution is approximately ten times smaller than the pressure one (except for the case $\mathcal{F} = 5 \times 10^{-2}$) and (ii) the viscous contribution increases with $\mathcal{F}$, while the

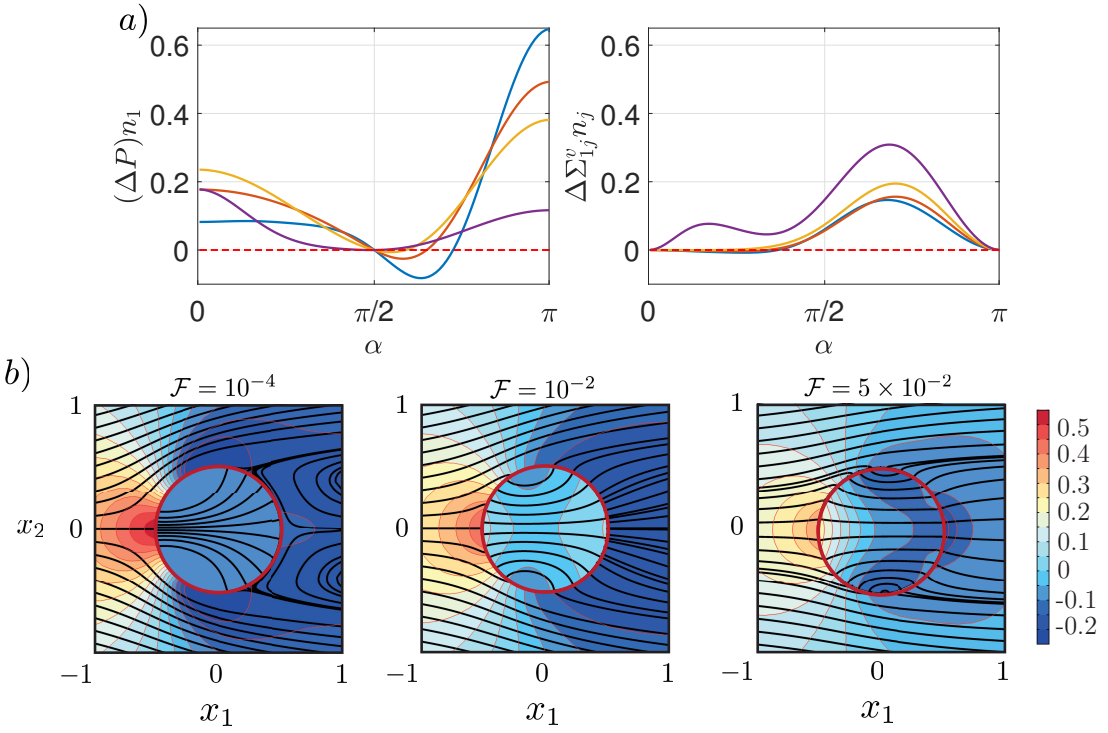

Figure 10.9: Panel (a): pressure (left frame) and viscous stress (right frame) contributions to the drag following the cylinder surface. The angle α is measured counter-clockwise starting from the rear. The colours denote different values of $\mathcal{F} = 10^{-4}$ (blue), $\mathcal{F} = 5 \times 10^{-3}$ (orange), $\mathcal{F} = 10^{-2}$ (yellow), $\mathcal{F} = 5 \times 10^{-2}$ (purple). The slip number is kept fixed to $\mathcal{L} = 10^{-4}$. Panel (b): streamlines (black bold lines) and iso-contours of the pressure for the steady flow around and through the permeable circular membrane, for different values of $\mathcal{F}$ and $\mathcal{L} = 10^{-4}$.

pressure contribution has a maximum at $5 \times 10^{-3} < \mathcal{F} < 10^{-2}$. As a result, the non-monotonous behavior of C_D vs $\mathcal{F}$ can be largely explained by investigating the sole pressure contribution. In the almost-solid case, $\mathcal{F} = 10^{-4}$ (blue line), there is no fluid motion inside the cylinder, and the inner pressure is constant, as shown in the left frame of figure 10.9(b). Therefore, the inner pressure does not contribute to the drag and the distribution of external pressure is the only responsible for integral forces. Focusing on the upper half of the cylinder ($x_2 > 0$), in the front part, for $(3/4)\pi < \alpha < \pi$, the pressure contribution is positive and becomes negative for $\pi/2 < \alpha < (3/4)\pi$. This suction region reduces the total drag since it acts on the front part of the cylinder. In the rear of the cylinder, the pressure contribution is positive with an almost constant negative value, which is the so-called base region. As the filtrability increases, a fluid motion manifests in the inner region of the cylinder, which is associated with a non-uniform distribution of inner pressure (see central frame in figure 10.9(b)). The pressure difference in the upstream part of the cylinder decreases as the filtrability increases since the membrane is progressively more permeable. Thus, an inner flow, oriented towards the downstream face of the cylinder, is generated. As a result of the blockage represented by the downstream cylinder face for the inner flow, the inner pressure increases moving downstream, as indicated by the

concavity of the streamlines (see figures 10.9(b)). At the same time, the external base pressure in the downstream surface of the cylinder is not significantly affected by $\mathcal{F}$ provided that $\mathcal{F} < 10^{-2}$. As a result, the contribution to drag of the pressure difference in the downstream face of the cylinder is larger than for the solid case for $\mathcal{F} < 10^{-2}$. Figure 10.9(a) supports this discussion from a quantitative viewpoint. In particular, comparing cases with $\mathcal{F} < 10^{-2}$ it is possible to see that, as $\mathcal{F}$ increases, (i) the suction at $\alpha \simeq (3/4)\pi$ decreases (thus increasing the drag), (ii) the drag contribution of the upstream face decreases and (iii) the drag contribution of the downstream face increases. At low filtrabilities, (i) and (iii) dominate over (ii), while at larger values of $\mathcal{F}$ the term (ii) becomes predominant. Concerning the viscous contribution, although more modest, figure 10.9(a) shows that it monotonously increases with $\mathcal{F}$.

Conversely, as $\mathcal{F}$ is further increased, see the case $\mathcal{F} = 5 \times 10^{-2}$, the upstream contribution drastically decreases due to the larger filtrability of the membrane. The substantially higher velocities of the inner flow and the larger filtrability cause a very mild increase of the inner pressure when approaching the downstream part of the membrane. This is again shown also by the streamlines (see right frame in figure 10.9(b)) which are almost straight in the inner region. Moreover, the larger flow across the downstream part of the membrane decreases the pressure jump between external and internal flows in that area. As a net result, the pressure contribution to drag, in comparison with the impermeable case (here approximated by $\mathcal{F} = 10^{-4}$) decreases also in the downstream region. Although the viscous contribution to the drag increases, the total drag decreases because it is quantitatively dominated by the pressure, whose contribution rapidly decays.

In this section, we characterized the morphology of the steady flow, describing the effect of the slip and filtrability numbers. However, not all steady solutions previously described can be observed, as some of them may be unstable with respect to perturbations, thus leading to unsteady configurations. Since time-dependent simulations for every studied case (far beyond 1000) are a monumental task, we perform a stability analysis, well-known to give very accurate predictions of the bifurcations for the case at issue in computational times comparable to the ones of the steady analyses (Chomaz, 2005; Theofilis, 2011). Thus, in the following we study the stability of the steady flow solution as $\mathcal{L}$ and $\mathcal{F}$ are varied.

10.3.2 Stability analysis of the steady flow

As mentioned in the previous section, to complete the analysis of the chosen flow configuration, we now establish for which combinations of $(Re, \mathcal{F}, \mathcal{L})$ the solution is linearly stable with respect to perturbations and thus likely to be observed. The occurrence of bifurcations of the flow leading to different configurations is studied in the framework of linear stability analysis (Chomaz, 2005; Theofilis, 2011). We consider the flow solution as the superposition of the steady solution denoted as $[\boldsymbol{U}(x,y), P(x,y)]$, outlined in the previous section, and of an infinitesimal unsteady perturbation. We thus introduce the following normal mode ansatz

$$u_i(x,y,t) = U_i(x,y) + \varsigma \hat{u}_i(x,y)\exp(\sigma t), \quad p(x,y,t) = P(x,y) + \varsigma \hat{p}(x,y)\exp(\sigma t), \qquad (10.11)$$

where $\varsigma \ll 1$. At $\mathcal{O}(1)$ the steady version of the flow equations are obtained, satisfied by $[\boldsymbol{U}, P]$, and at $\mathcal{O}(\varsigma)$ the following system of equations is obtained

$$\begin{gathered} \sigma \hat{u}_i + \hat{u}_j \partial_j U_i + U_j \partial_j \hat{u}_i = -\partial_i \hat{p} + \frac{1}{Re} \partial^2_{jj} \hat{u}_i, \\ \partial_i \hat{u}_i = 0 \end{gathered} \tag{10.12}$$

$$\begin{gathered} \hat{u}_i = \hat{u}_i^+ = \hat{u}_i^- \\ \hat{u}_i = Re \mathcal{M}_{ij} \left(\Sigma_{jk} \left(\hat{\boldsymbol{u}}^-, \hat{p}^- \right) - \Sigma_{jk} \left(\hat{\boldsymbol{u}}^+, \hat{p}^+ \right) \right) n_k, \end{gathered} \tag{10.13}$$

together with the homogeneous Dirichlet boundary condition at the inlet Γ_{in}, $\hat{u}_1 = \hat{u}_2 = 0$, and the stress-free condition on the sides Γ_{lat} and at the outlet Γ_{out}, $(-\hat{p}\delta_{ij} + \frac{1}{Re}\partial_j \hat{u}_i) n_j = 0$.

Equations (10.12, 10.13), together with the boundary conditions on Γ_{in}, Γ_{lat}, Γ_{out}, define an eigenfunction problem with, possibly, complex eigenvalues $\sigma = \text{Re}(\sigma) + \text{i}\,\text{Im}(\sigma)$. The real part of the eigenvalue is the growth rate of the global mode, and the imaginary part its angular velocity. We introduce the associated Strouhal number defined as $\text{St} = \frac{\text{Im}(\sigma)}{2\pi}$. The flow is asymptotically unstable if there exists at least one eigenvalue with positive real part, otherwise it is asymptotically stable. The absence of unstable modes therefore ensures the occurrence of the steady solution, while their presence gives useful information about the emerging unsteady flow configuration.

We turn now to describe the results of the linear stability analysis. The solid case exhibits a Hopf bifurcation at $Re = 46.7$ that drives the flow to a state that is periodic in time, characterized by the alternate shedding of vortices, the so-called von Kármán vortex street (Barkley, 2006). Ledda et al. (2018) showed the suppression of this vortex shedding mode for large enough values of the permeability, in the case of porous rectangular cylinders. A preliminary analysis on the permeable membrane shows that the above-described mode is also the only one that destabilizes the steady wake in the range $10 < Re < 130$. In figure 10.10 we report the marginal stability curves (i.e. the locus of points with $\text{Re}(\sigma) = 0$) in the $(\mathcal{F}, Re)$ plane, for different values of $\mathcal{L}$. The marginal stability curves define a stable and an unstable region in the $(\mathcal{F}, Re)$ plane. At low values of $\mathcal{F}$ and $\mathcal{L}$, the critical Reynolds number Re_{cr} for the marginal stability coincides with the solid one, i.e. $Re_{cr} = 46.7$. An increase in $\mathcal{L}$ leads to a slight increase in Re_{cr} that reaches a maximum approximately equal to 50 for $\mathcal{L} = 0.02$. For $\mathcal{F} > 10^{-3}$ the critical Reynolds number increases. We identify a critical value of $\mathcal{F} = \mathcal{F}_{cr}$ beyond which the steady solution is stable. This value depends on the Reynolds and slip numbers. For fixed $\mathcal{L}$, $\mathcal{F}_{cr}$ initially increases with Re, reaches a maximum and decreases. Among all cases, the maximum value $\mathcal{F}_{cr} \approx 1.08 \times 10^{-2}$ is achieved for $\mathcal{L} \approx 10^{-4}$.

The imaginary part of the eigenvalue well approximates the oscillation frequency of the nonlinear limit cycle in marginal stability conditions (Barkley, 2006). In the inset of figure 10.10, we report the value of the Strouhal number along the marginal stability curve. We do not observe substantial variations in the Strouhal number with respect to the solid case, i.e. $\text{St} \approx 0.116$ (Norberg, 2003).

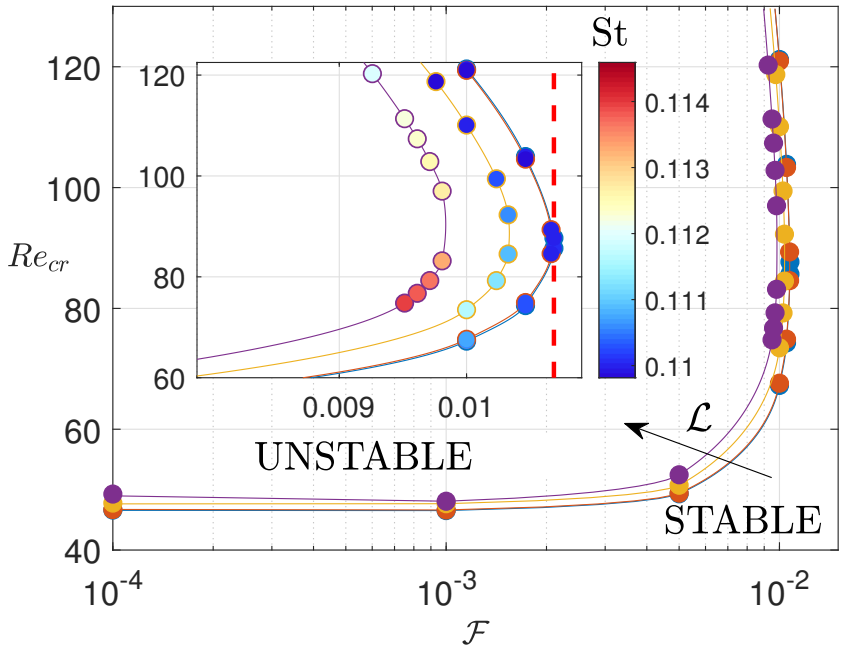

Figure 10.10: Marginal stability curves in the plane $(\mathcal{F}, Re)$. Each curve is associated with a different value of slip number $\mathcal{L} = 10^{-4}$ (blue), $\mathcal{L} = 10^{-3}$ (orange), $\mathcal{L} = 10^{-2}$ (yellow), $\mathcal{L} = 2\times10^{-2}$ (purple). The inset shows a zoom in for large values of $\mathcal{F}$. The colored bullets represent the value of the Strouhal number along the marginal stability curve in the region depicted in the inset.

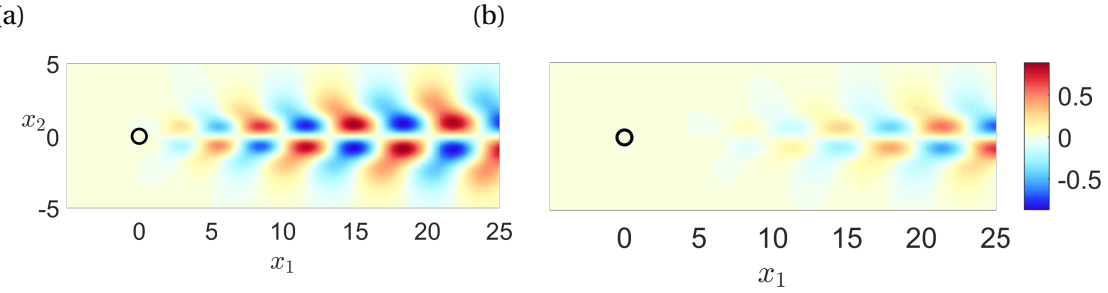

Figure 10.11: Real part of the eigenvector $\hat{u}_1$ associated with the marginally stable eigenvalue for $Re = 46.7$, $\mathcal{L} = 10^{-2}$ and $\mathcal{F} = 10^{-3}$ (panel (a)) and for $Re = 87$, $\mathcal{L} = 10^{-4}$ and $\mathcal{F} = 1.075\times10^{-2}$ (panel (b)). The velocity eigenvectors are normalized by their L_2 norm.

In figure 10.11 we report the spatial distribution of $\mathrm{Re}\,(\hat{u}_1)$ for two different cases, on panel (a) characterized by a recirculation region close to the cylinder, and on panel (b) characterized by a recirculation region far downstream. In both cases, the unstable mode leads to a vortex shedding similar to the solid case one, as already anticipated. As the recirculation region moves downstream, the onset of the vortex shedding is displaced downstream and the flow in proximity of the cylinder is almost steady.

The analysis of the stability properties of the steady wake shows the strong stabilization effect

of the filtrability number. The marginal stability curves strongly resemble those outlined in Ledda et al. (2018, 2019). In particular, the vortex shedding is suppressed for large enough values of the filtrability. This similarity is confirmed by the spatial distribution of the unstable mode, that moves downstream with the recirculation region of the steady flow. Indeed, the stability properties of the wake can be related to the extent of the so-called *absolute region of instability* in a local stability analysis (i.e. performed for the velocity profile at each streamwise location, see Monkewitz, 1988; Giannetti and Luchini, 2007), that roughly corresponds to the recirculation region. As shown in Ledda et al. (2018), there is a critical value of the extent of the recirculation region beyond which the flow becomes unstable. When large values of the filtrability are considered, the recirculation region is small or even absent, and thus the vortex shedding is suppressed. For fixed $\mathcal{F} \approx 10^{-2}$ and $\mathcal{L}$ and increasing Re, the recirculation region initially increases and then decreases its dimensions (cf. figure 10.6). Therefore, the first destabilization and subsequent stabilization for fixed $\mathcal{F}$ and $\mathcal{L}$ is due to the non-monotonic behavior of the length of the recirculation region with Re, which crosses the critical value for the marginal stability twice.

By comparing the marginal stability curve with the drag coefficient, we deduce that the maximum of C_D for the steady flow occurs for a stable configuration for all values of Re. Interestingly, a permeable circular membrane exhibits a larger drag than the equivalent solid one, and this maximum occurs when the steady flow is stable.

In the present section, we performed a parametric study under the framework of bifurcation theory in order to exclude the unstable configurations from the variety of steady solutions obtained in Section 10.3.1. In the next section, we propose a methodology to obtain the full-scale design of the structure by fulfilling some objectives on the macroscopic behavior of the steady flow, under the constraint of stable configuration.

10.4 From objectives to full-scale design

In the previous section, we performed a parametric study on the steady solution of equations (10.6, 10.7) and the stability properties of the resulting wake, considering $\mathcal{L}$ and $\mathcal{F}$ as free parameters. In the present section, we outline a procedure for the objective-based full-scale design of the permeable circular membrane. We first define macroscopic objectives to be fulfilled and, performing microscopic simulations, we identify the geometry which best satisfies the macroscopic requirements. We consider cylindrical permeable shells formed by an array of elliptical inclusions, distributed with a constant angular distance, of axes l_t and l_n (normalized with the microscopic characteristic length) aligned along the tangential and normal directions to the membrane, respectively, in the range $0.02 < l_t, l_n < 0.98$.

10.4.1 Choosing the design objective

An important macroscopic property is the drag exerted on the solid structure by the incoming fluid. Several attempts of controlling this integral quantity, defined by equation (10.10), by permeable surfaces have been carried out, some of them focused on minimizing the drag (Garcia-Mayoral and Jiménez, 2011; Abderrahaman-Elena and García-Mayoral, 2017; Gómez-de Segura and García-Mayoral, 2019), others investigating the conditions for drag maximization (Cummins et al., 2017, 2018).

We fix $Re = 100$ and we study the variation of C_D with $\mathcal{L}$ and $\mathcal{F}$. In figure 10.12 we report the iso-contours of C_D on the $(\mathcal{F},\mathcal{L})$ plane. The bold solid line corresponds to the marginal stability boundary for $Re = 100$. Among all these possible solutions for the drag coefficient, we select the maximum value of the drag coefficient ($C_D = 1.339$), which occurs at $\mathcal{F} = 1.25\times10^{-2}$, $\mathcal{L} = 5\times10^{-3}$ (denoted by $\square$ in figure 10.12) and in the following will be compared with the full-scale simulations. For the sake of completeness, we select other three values of C_D denoted by $\bigcirc, \triangleright, \star$ in figure 10.12, to verify the faithfulness of the homogenized model in the parameters space $(\mathcal{F},\mathcal{L})$ for constant $\mathcal{L} = 10^{-4}$. Note that the case denoted with $\star$ is unstable, but we use it as an additional test case owing to the large recirculation region that this configuration exhibits.

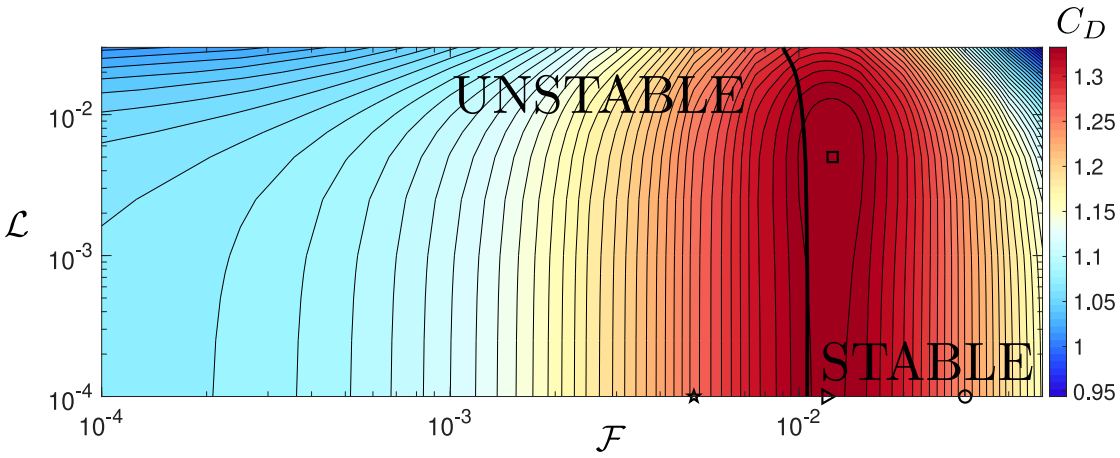

Figure 10.12: Isocontours of C_D for $Re = 100$ in the $(\mathcal{F},\mathcal{L})$ plane. Symbols identify the configurations listed in table 10.1. The marginal stability curve for the value of Re considered is represented by a bold solid line line (all cases on the right side of the curve are stable).

10.4.2 Linking the microscopic geometry to the macroscopic properties: elliptical inclusions

We now turn to describe the procedure for the determination of the microscopic geometry based on the macroscopic flow properties identified in the previous subsection. We first perform microscopic simulations in the domain depicted in figure 10.13(a) (dashed rectangle) whose lengths are non-dimensionalized with the microscopic length ℓ, so that the results do

not depend on the separation of scales parameter $\varepsilon = \frac{\ell}{D}$, according to Zampogna and Gallaire (2020). Within this domain, two different microscopic problems need to be solved to calculate $\bar{F}_n$ and $\bar{L}_t$; they read respectively

$$\begin{aligned} -\partial_i Q + \partial^2_{ll} F_i &= 0 && \text{in } \mathbb{F} \\ \partial_i F_i &= 0 && \text{in } \mathbb{F} \\ F_i &= 0 && \text{on } \partial\mathbb{M} \\ \Sigma_{nn}(Q,\mathbf{F}) &= -1 && \text{on } \mathbb{U} \\ \Sigma_{nn}(Q,\mathbf{F}) &= 0 && \text{on } \mathbb{D} \\ F_i, Q & && \text{periodic along } \mathbf{t} \end{aligned} \tag{10.14}$$

and

$$\begin{aligned} -\partial_i R + \partial^2_{ll} L_i &= 0 && \text{in } \mathbb{F} \\ \partial_i L_i &= 0 && \text{in } \mathbb{F} \\ L_i &= 0 && \text{on } \partial\mathbb{M} \\ \Sigma_{tn}(R,\mathbf{L}) &= -1 && \text{on } \mathbb{U} \\ \Sigma_{tn}(R,\mathbf{L}) &= 0 && \text{on } \mathbb{D} \\ L_i, R & && \text{periodic along } \mathbf{t}, \end{aligned} \tag{10.15}$$

where $i, l = t, n$, i.e. the equations are written in the local frame of reference of the cylinder surface. We refer to figure 10.13(a) for a definition of $\mathbb{F}, \mathbb{M}, \mathbb{U}$ and $\mathbb{D}$. In the microscopic problems (10.14) and (10.15) the scalar fields R and Q appear. They relate the value of the pressure on Γ_{int} to the upward and downward fluid stresses and do not contribute to the determination of the macroscopic flow through the membrane (cf. Zampogna and Gallaire (2020) for a detailed explanation). In the purpose of the present work, we are not directly interested in microscopic fields representing the solution of these problems, but we need only to know the quantities $\bar{F}_n$ and $\bar{L}_t$ which appear in the macroscopic model via equation (10.9), where the symbol $\bar{\cdot}$ denotes the spatial average used in Zampogna and Gallaire (2020), i.e.

$$\bar{\cdot} = \lim_{\mathbb{U}\to\mathbb{D}} \frac{1}{|\mathbb{F}\cup\mathbb{M}|}\int_{\mathbb{F}} \cdot\, d\mathbf{x} = \frac{1}{|\Gamma^{\mathbb{F}}_{\text{int}} \cup \Gamma^{\mathbb{M}}_{\text{int}}|}\int_{\Gamma^{\mathbb{F}}_{\text{int}}} \cdot\, d\mathbf{x}, \tag{10.16}$$

with $\Gamma^{\mathbb{F}}_{\text{int}}$ and $\Gamma^{\mathbb{M}}_{\text{int}}$ the fluid and solid parts of Γ_{int} within the unit cell, as sketched in figure 10.13(a). The linear problems (10.14) and (10.15) are numerically solved for each couple (l_t, l_n), $0.02 < l_t, l_n < 0.98$ (with a step of 0.01), via their weak formulation implemented in the finite-element solver COMSOL Multiphysics. The spatial discretization is based on the Taylor–Hood (P2-P1) triangular elements for **F**-**L** and R-Q, respectively. We refer to Zampogna and Gallaire (2020) for further detail about the solution of the microscopic problems.

After averaging the solution of the microscopic problems, we deduce $\bar{F}_n$ and $\bar{L}_t$, whose isocontours are reported in figure 10.13(b) as functions of the two axes l_n and l_t.

The parameters $\mathcal{F}$ and $\mathcal{L}$ are then calculated by a renormalization of $\bar{F}_n$ and $\bar{L}_t$ with respect to

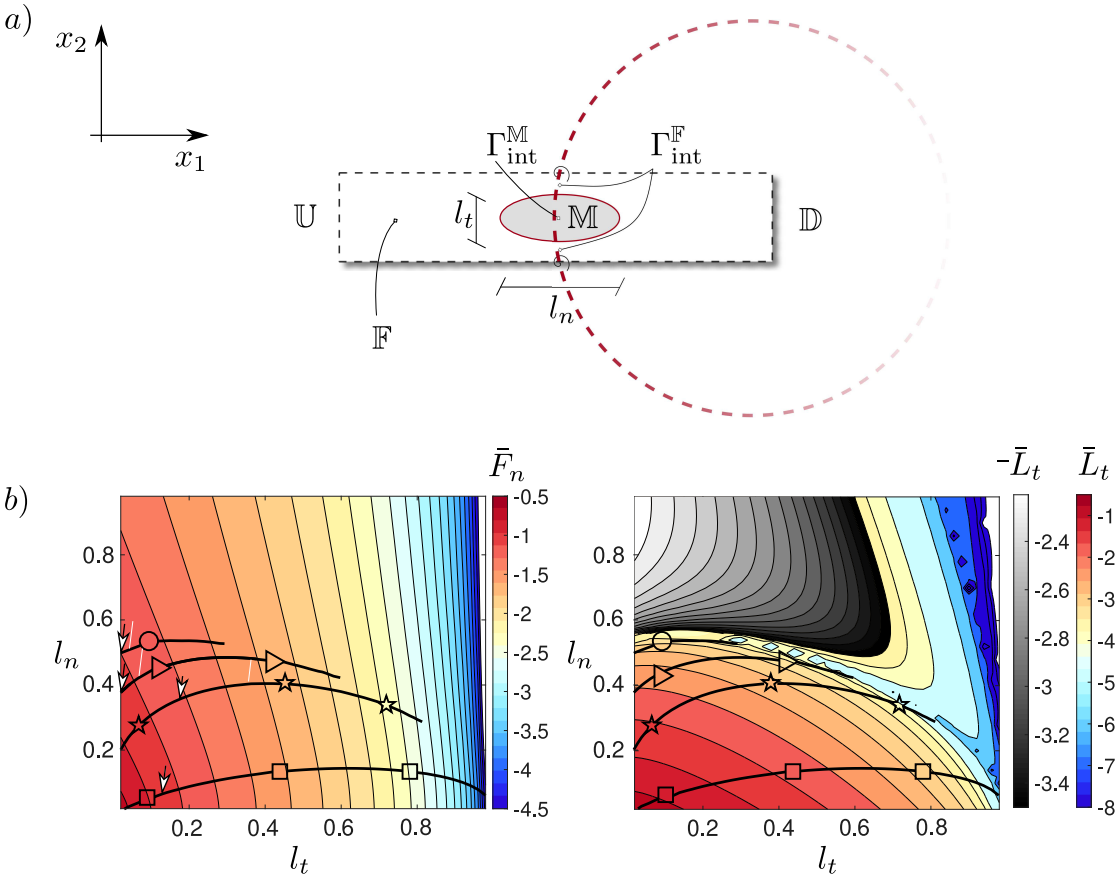

Figure 10.13: Panel (a): Sketch of the membrane (red dashed line) with a zoom on the microscopic elementary cell used to calculate $\bar{L}_t$ and $\bar{F}_n$. The tangential- and normal-to-the-interface axes of the solid inclusion are respectively denoted with l_t and l_n and normalized by ℓ. Panel (b): isocontours of $\bar{F}_n = \frac{\mathcal{F}}{\varepsilon}$ (left) and $\bar{L}_t = \frac{\mathcal{L}}{\varepsilon}$ (right) on the plane (l_t, l_n), in logarithmic scale. Blue-to-red colors indicate positive values of $\bar{F}_n$ and $\bar{L}_t$ while gray-scale refers to negative values of $\bar{L}_t$. The lines identify the isocontours of the possible couples (l_n, l_t) whose symbols correspond to different couples $(\mathcal{F}, \mathcal{L})$ of figure 10.12. Each point on those lines is a good candidate to realize the desired value of $\mathcal{F}$ and $\mathcal{L}$, upon adjustment of the value of ε. The selected values of l_t and l_n are labelled with white arrows for each case.

the macroscopic length scale, i.e.

$$\mathcal{F} = \varepsilon \bar{F}_n \quad \text{and} \quad \mathcal{L} = \varepsilon \bar{L}_t. \tag{10.17}$$

While in a direct approach the parameters defining the full scale geometry l_t, l_n and ε are given and the corresponding filtrability and slip numbers are evaluated, in the inverse procedure they need to be determined based on the choice of a given property that has to be satisfied by the fluid flow. Actually, there is no one-to-one relation linking $\mathcal{F}$ and $\mathcal{L}$ to the microscopic geometry. Once filtrability and slip are chosen, one has potentially full freedom in the choice of the microscopic structure. This choice is essentially related to the geometrical shape of the

microscopic inclusions, in this case ellipsoidal ones with variable axes, and to their relative size with respect to the macroscopic length, as outlined in figure 10.13(b), where several configurations satisfy the desired values of $\mathcal{F}$ and $\mathcal{L}$, each one associated with a value of ε. For the sake of clarity we list the steps to follow in order to determine these geometrical parameters which allow us to define the microscopic geometry of the permeable shell:

- According to the previous subsection, we identify a pair $(\mathcal{F},\mathcal{L}) = (\mathcal{F}^*,\mathcal{L}^*)$ of interest.
- We find in the $l_t - l_n$ plane the possible pairs of (l_t, l_n) that can give the correct set $(\mathcal{F}^*,\mathcal{L}^*)$. These values are found by evaluating the ratio $\mathcal{F}^*/\mathcal{L}^*$, which is not depending on ε (since F_n and L_t are proportional to ε). The potential values of l_n and l_t are those associated with the black solid lines in figure 10.13(b), which realize C_D^* upon renormalization by the proper value of ε that is still undetermined.

  Among the potential candidates, the final value of ε and thus the values of (l_t, l_n) can be chosen based on other constraints (like, for instance, the minimization of microscopic anisotropy, i.e. $l_t \approx l_n$, the minimization of ε or the satisfaction of geometrical properties of the medium like the fluid-to-solid ratio).
- Once the value of ε is selected, there is only one couple (l_t, l_n) that satisfies the macroscopic values of $\mathcal{F}^* = \varepsilon\bar{F}_n$ and $\mathcal{L}^* = \varepsilon\bar{L}_t$. We then deduce $\bar{F}_n$ and $\bar{L}_t$, and eventually l_t and l_n.

The values of ε, l_t and l_n are deduced for each case highlighted by the symbols in figure 10.12. Table 10.1 shows the values found for each case, corresponding to the white pointers in figure 10.13(b). For the cases denoted by $\bigcirc$, $\triangleright$ and $\square$ the values of (l_t, l_n) have been chosen so as to obtain a value of ε of order 10^{-1}, while for the case $\star$ the value of (l_t, l_n) guarantees minimal anisotropy with the constraint $\varepsilon \leq 0.045$.

The final full-scale geometries are thus obtained by distributing the inclusions along the membrane centerline Γ_{int}, with a constant angular distance among them given by $\Delta\phi = 2\pi\lfloor\frac{\varepsilon}{\pi}\rfloor$, with $\lfloor\cdot\rfloor$ the integer part in order to have an integer number of inclusions along the cylindrical shell. Two examples of microscopic geometries obtained are depicted in figure 10.14, where 69 and 32 inclusions are employed. Once the full-scale geometry is built the reliability of the inverse procedure is verified as explained in the next section.

10.4.3 Comparison between the homogenized and the full-scale results

We verify the faithfulness of the homogenization approach and the subsequent retrieval of the microscopic geometry by comparing the results obtained using the equivalent model with the feature-resolved flow past the full-scale permeable shell. To deduce the full-scale flow, the Navier-Stokes equations are solved in the full-scale domain, where each solid inclusion forming the membrane is explicitly taken into account in the fluid domain and thus in the

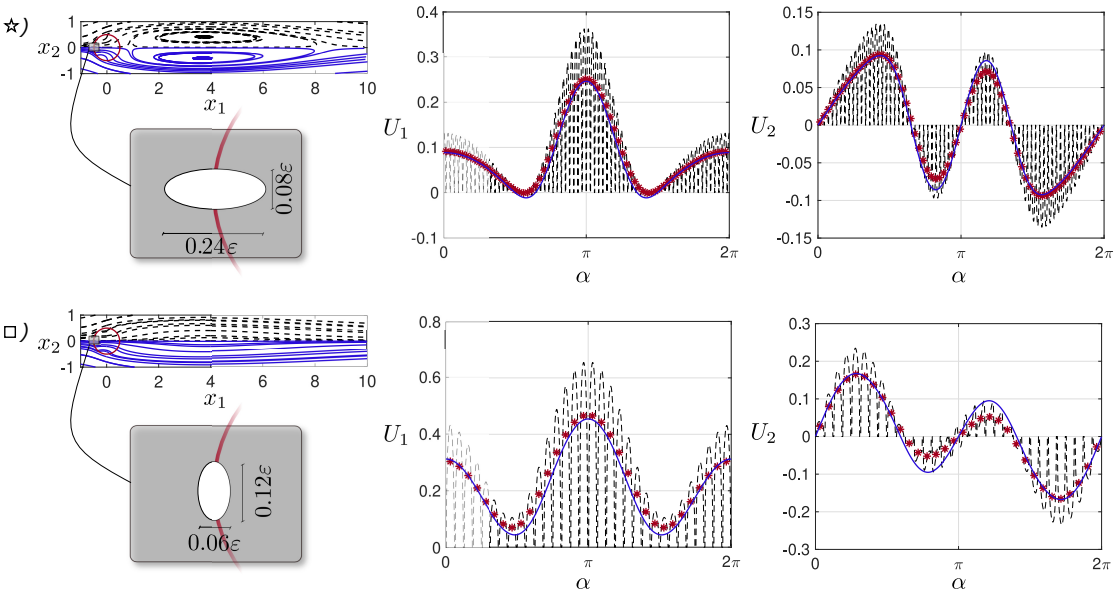

Figure 10.14: Comparison between full-scale and equivalent model for case ⋆ and □ identified in figure 10.12. The microscopic geometry forming the cylindrical shell, sketched for each case in the grey insets on the left, is the result of the inverse procedure explained in Section 10.4.2. Left column: flow streamlines for the full scale case (black dashed lines) and for the macroscopic model (blue solid lines). Central and right column: horizontal and vertical velocities, U_1 and U_2 sampled on the cylindrical shell using the angle α measured counterclockwise starting from the rear. Dashed lines represent the full-scale model, blue lines the macroscopic model and red stars the average of the full-scale model, calculated applying a discrete version of the integral in equation (10.16), based on a 1-point Gaussian rule, to the velocity profile in each microscopic elementary cell forming the membrane. Numerical values of ε, $\mathcal{F}$, $\mathcal{L}$ and other representative values of the fluid flow (C_D, X_R, L_R) are listed in table 10.1 for each case.

mesh. The full-scale problem is solved by the finite-element solver COMSOL Multiphysics, using the same numerical setup as for the macroscopic flow solution. In order to have spatially converged results, mesh M1 (cf. table 10.2) has been modified in the vicinity of the full scale structure. A circular refinement region of diameter $1.1L$ has been added with a resolution chosen in order to guarantee at least 10^2 cells between two adjacent solid inclusions whose boundary has been discretized using at least 50 segments. The boundary conditions on $\Gamma_{in}, \Gamma_{out}$ and Γ_{lat} are the same as in the case of the macroscopic model (10.7), while we impose a no-slip condition on the walls of each microscopic inclusion, i.e. $u_i|_{\Gamma_{\partial\mathbb{M}}} = 0$.

In figure 10.14 we report two sample comparisons of the flow fields obtained with the homogenized model and with the full-scale simulations (cases ⋆ and □ identified in figure 10.12), together with the velocities at the membrane. In both cases, we observe a good agreement between the two approaches, with an error on the velocities along the membrane of the order of ε, as expected.

In table 10.1 we report the reference values (C_D, L_R, X_R) for all cases identified in figure

	N	ε	l_t	l_n	$\mathcal{F}$	$\mathcal{L}$	C_D	C_D^{EQ}	L_R	L_R^{EQ}	X_R	X_R^{EQ}
⋆	69	4.49×10^{-2}	0.08	0.24	5.0×10^{-3}	1×10^{-4}	1.264	1.259	7.386	7.358	0.431	0.421
□	32	9.82×10^{-2}	0.12	0.06	1.25×10^{-2}	5×10^{-3}	1.338	1.339	–	–	–	–
▷	31	1.01×10^{-1}	0.02	0.38	1.2×10^{-2}	1×10^{-4}	1.350	1.334	–	–	–	–
◯	10	3.14×10^{-1}	0.02	0.50	3.0×10^{-2}	1×10^{-4}	1.365	1.239	–	–	–	–

Table 10.1: Relevant geometrical and physical parameters for the cases chosen in figure 10.12; N indicates the number of inclusions forming the membrane, the superscript ^{EQ} denotes quantities calculated using model (10.7) on Γ_{int} while the absence of superscript denotes quantities evaluated from the full-scale solution.

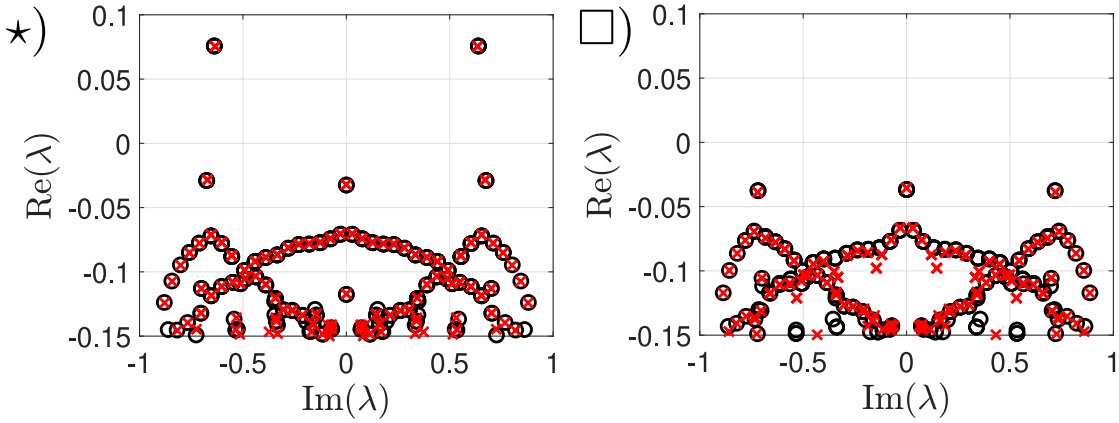

Figure 10.15: Comparison between the homogenized and full-scale results of the stability analysis. The crosses and the circles denote the eigenvalues obtained from the full-scale structure and from the homogenized model, respectively, for the two reported cases.

10.12. Also in this case, we observe an overall good agreement, even for extremely large values of ε, which are far beyond the rigorous domain of validity of the theory. Only for the case denoted by ◯ the differences in the C_D are non-negligible, suggesting that a maximum value of ε beyond which macroscopic model (10.7) is no more applicable lies between 10^{-1} and 3.5×10^{-1}. A complete validation also requires the comparison of the stability properties of the flow between homogenized model and full-scale simulations, reported in figure 10.15. We observe a good agreement between the spectra, and in particular the leading eigenvalues are well described by the homogenized model. Considering the one with largest real part, the relative errors on the absolute value are 0.25% for the case ⋆ ($\sigma = 0.076 + 0.64$i), and 0.6% for the case □ ($\sigma = -0.039 + 0.72$i). We finally stress the importance of the validation described above, since it constitutes a strong proof of the faithfulness of the model developed in Zampogna and Gallaire (2020) in the case of flows with non-negligible macroscopic inertia.

In this section, we outlined a method for the geometrical reconstruction of the microscopic geometry based on the macroscopic properties of the membrane, thus concluding the first branch of the scheme described by figure 10.3. We note that the homogenized model, combined with the stability analysis technique, allows us to perform a parametric study spanning

a massive range of possible geometries with extremely fast outputs. The flow through the resulting microscopic structure shows a good agreement with the homogenized model, thus giving confidence to the parametric study carried out in Section 10.3. We verified the validity of the homogenized model through permeable membranes for Reynolds numbers of the order of 10^2. The error on the final solution is of order ε, thus degrading the solution when extremely large values of ε are considered. Nevertheless, the homogenized model gives also in these cases fairly reasonable results that can be used as guidelines in a first parametric study, before optimizing the resulting microscopic structure.

The previous analysis was focused on membranes with monodisperse and identical microscopic inclusions along the centerline of the membrane. In the following, we analyze the opportunity to exploit membranes of variable permeability by employing a Lagrangian-based optimization, i.e. we focus on the second branch of the diagram of figure 10.3, in the inverse procedure part.

10.5 Adjoint-based optimization of membranes of variable properties

The purpose of the present section consists of finding profiles of $\mathcal{F}$ and $\mathcal{L}$ which are *optimal* with respect to a given objective, here specifically the maximization of the drag coefficient. To accomplish this task, a variational approach is used.

10.5.1 Sensitivity with respect to variations of the slip and filtrability numbers

In this section, we introduce the theoretical framework for the adjoint-based optimization of the structure of the membrane. We recall that, at the interface, we denote with the superscript $\cdot^+$ the variables evaluated in the inner part of the cylinder and with $\cdot^-$ those evaluated in the outer part. Any small modification $\delta\mathcal{M}_{ij}$ of the tensor component $\mathcal{M}_{ij}$ (i.e. variations of $\mathcal{F}$ or $\mathcal{L}$) induces a perturbation $(\delta\boldsymbol{u}, \delta p)$ on the flow field such that $(\boldsymbol{u}, p) = (\boldsymbol{U} + \delta\boldsymbol{u}, P + \delta p)$. The drag coefficient, i.e. the objective in the Lagrangian framework, is written as follows:

$$C_D = 2 \oint_{\Gamma_{\text{cyl}}} \left(\Sigma_{jk}\left(p^-, \boldsymbol{u}^-\right) - \Sigma_{jk}\left(p^+, \boldsymbol{u}^+\right) \right) n_k \delta_{1j} \, \mathrm{d}\Gamma. \tag{10.18}$$

The modification $\delta\mathcal{M}_{ij}$ thus perturbs the drag by δC_D according to

$$\delta C_D = 2 \oint_{\Gamma_{\text{cyl}}} \left(\Sigma_{jk}\left(\delta p^-, \delta\boldsymbol{u}^-\right) - \Sigma_{jk}\left(\delta p^+, \delta\boldsymbol{u}^+\right) \right) n_k \delta_{1j} \, \mathrm{d}\Gamma = \oint_{\Gamma_{cyl}} \nabla_{\mathcal{M}_{ij}} C_D \delta\mathcal{M}_{ij} \, \mathrm{d}\Gamma, \tag{10.19}$$

The quantities $\left(\delta\boldsymbol{u}^\pm, \delta p^\pm\right)$ are the solution of equation (10.28) reported in Appendix 10.8.2, where a formal derivation of the sensitivity functions (i.e. the functions describing the variations of the objective C_D with respect to the control variable $\mathcal{F}$ and $\mathcal{L}$) is carried out. In the Lagrangian framework, the sensitivities of the drag coefficient with respect to variations of $\mathcal{L}$

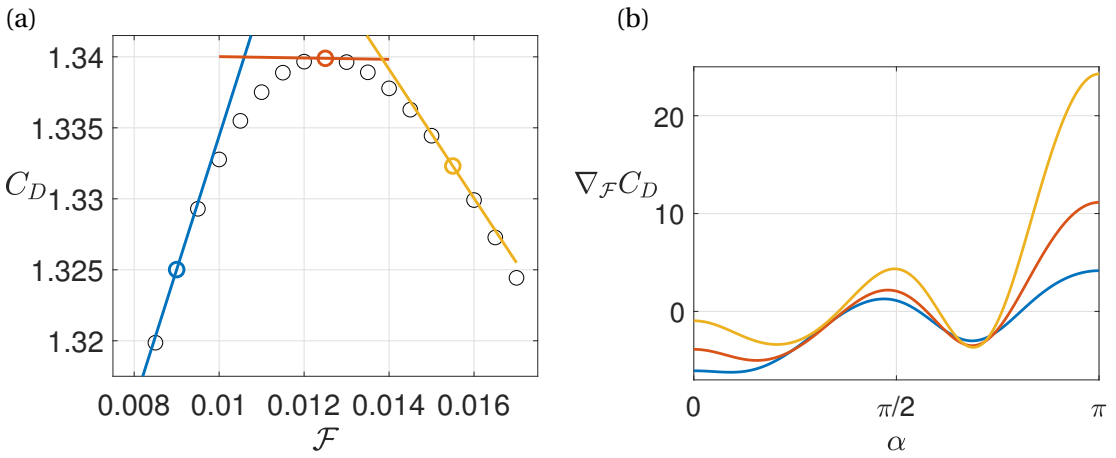

Figure 10.16: Panel (a): variation of the drag coefficient with $\mathcal{F}$, for $\mathcal{L} = 5 \times 10^{-3}$, directly evaluated from macroscopic model (10.6, 10.7) (black circles) and predictions of the gradient via the sensitivity approach (coloured lines) carried out around the configurations identified by coloured circles. Panel (b): distribution of sensitivity with respect to $\mathcal{F}$ along the $y > 0$ part of the cylinder, i.e. $0 < \alpha < \pi$, for the configurations denoted with colors in panel (a).

and $\mathcal{F}$ are

$$\nabla_{\mathcal{F}} C_D = -Re u_i^{\dagger\dagger} \left(\Sigma_{jk}(P^-, \boldsymbol{U}^-) - \Sigma_{jk}\left(P^+, \boldsymbol{U}^+\right) \right) n_i n_j n_k \tag{10.20}$$

and

$$\nabla_{\mathcal{L}} C_D = Re u_i^{\dagger\dagger} \left(\Sigma_{jk}(P^-, \boldsymbol{U}^-) - \Sigma_{jk}\left(P^+, \boldsymbol{U}^+\right) \right) t_i t_j n_k, \tag{10.21}$$

where the Lagrange multipliers $(\boldsymbol{u}^\dagger, p^\dagger, \boldsymbol{u}^{\dagger\dagger})$, also called adjoint variables, are the solution of the following linear problem

$$\begin{aligned} \partial_i u_i^\dagger = 0, \quad u_j^\dagger \partial_i U_j - U_j \partial_j u_i^\dagger = \partial_i p^\dagger + \tfrac{1}{Re} \partial_{jj}^2 u_i^\dagger \quad & \text{in } \Omega \\ \left(\Sigma_{ik}\left(-p^{\dagger-}, \boldsymbol{u}^{\dagger-}\right) - \Sigma_{ik}\left(-p^{\dagger+}, \boldsymbol{u}^{\dagger+}\right) \right) n_k - u_i^{\dagger\dagger} = 0 \quad & \text{on } \Gamma_{\text{int}} \\ u_i^{\dagger+} = u_i^{\dagger-} \quad & \text{on } \Gamma_{\text{int}} \end{aligned} \tag{10.22}$$

and

$$u_i^{\dagger\dagger} = Re^{-1} \mathcal{M}_{ji}^{-1} \left(u_j^{\dagger-} - 2\delta_{1j} \right) \quad \text{on } \Gamma_{\text{int}}, \tag{10.23}$$

together with the adjoint boundary conditions $u_i^\dagger = 0$ at the inflow, $\partial_2 u_1^\dagger = u_2^\dagger = 0$ at the transverse boundaries and $\Sigma_{ik}\left(-p^\dagger, \boldsymbol{u}^\dagger\right) n_k + u_k n_k u_i^\dagger = 0$ at the outflow. At this point, it is clear that in order to understand how the control variables $\mathcal{F}$ and $\mathcal{L}$ influence the objective function C_D via equations (10.20, 10.21), the linear problem (10.22) has to be solved, without the necessity to explicitly evaluate the perturbed state $(\boldsymbol{u}, p) = (\boldsymbol{U} + \delta\boldsymbol{u}, P + \delta p)$. The linear adjoint problem presents an advantage in terms of computational time with respect to the non-linear problem for $(\boldsymbol{u}, p)$, and is suitable for a gradient-based optimization with a progressive update of the distribution of the membrane properties.

In figure 10.16(a) we report the variation of the drag coefficient with $\mathcal{F}$, for fixed $\mathcal{L} = 5 \times 10^{-3}$ (black dots), together with the prediction given by the sensitivity analysis (solid lines), close

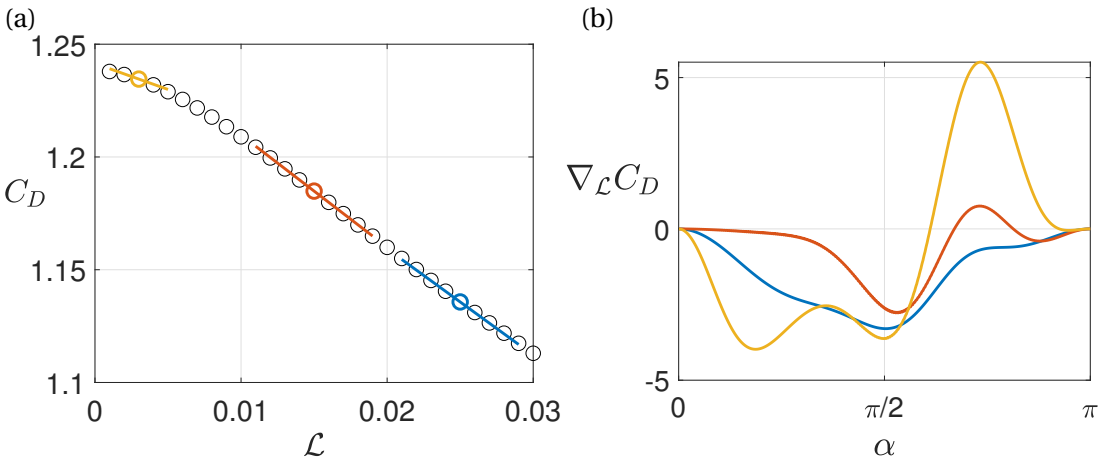

Figure 10.17: Panel (a): variation of the drag coefficient with $\mathcal{L}$, for $\mathcal{F} = 0.03$, directly evaluated from macroscopic model (10.6, 10.7) (black circles) and predictions of the gradient via the sensitivity approach (coloured lines) carried out around the corresponding coloured circles. Panel (b): distribution of sensitivity with respect to $\mathcal{L}$ along the $y > 0$ part of the cylinder, $0 < \alpha < \pi$.

to the configuration of maximum C_D identified by the □ symbol in figure 10.12. Note that, at this stage, we keep $\mathcal{F}$ uniform along the membrane. A good agreement is observed, in the vicinity of the points where the sensitivity is evaluated, i.e. $\delta\mathcal{F} \approx 0.01\mathcal{F}$. The deviation becomes more important for variations larger than $\delta\mathcal{F} \approx 0.01\mathcal{F}$, showing a rather strong effect of non-linearities close to the point of the maximum drag coefficient. In figure 10.16(b) we show the distribution of sensitivity along the upper part of the cylinder, for three cases. The distribution exhibits a non-monotonic behavior, with positive values in the front and in the middle of the membrane, and negative values close to the rear of the cylinder.

The same analysis is performed for uniform variations of $\mathcal{L}$ (figure 10.17). In this case, we observe a monotonic behavior, and the variations of the drag coefficient with $\mathcal{L}$ are considerably smaller than those observed when varying $\mathcal{F}$. The distribution, at low values of $\mathcal{L} \approx 5 \times 10^{-3}$ shows a peak at $\alpha \approx 130°$, that decreases with $\mathcal{L}$, and is negative in the other regions of the membrane.

In this section, we derived the sensitivity of the drag coefficient with respect to variations of $\mathcal{F}$ and $\mathcal{L}$. In the following, we exploit the sensitivity analysis to introduce a gradient-based optimization for the geometry of the membrane, when both the filtrability and slip numbers are varied together, so as to find the optimal distribution of $\mathcal{F}$ and $\mathcal{L}$ to maximize the drag coefficient.

10.5.2 Optimal distribution of the properties of the membrane

The sensitivity functions found in the previous section are used here to obtain the optimal distributions of $\mathcal{F}$ and $\mathcal{L}$ that maximize the drag coefficient. The starting profiles of $\mathcal{F}$ and $\mathcal{L}$

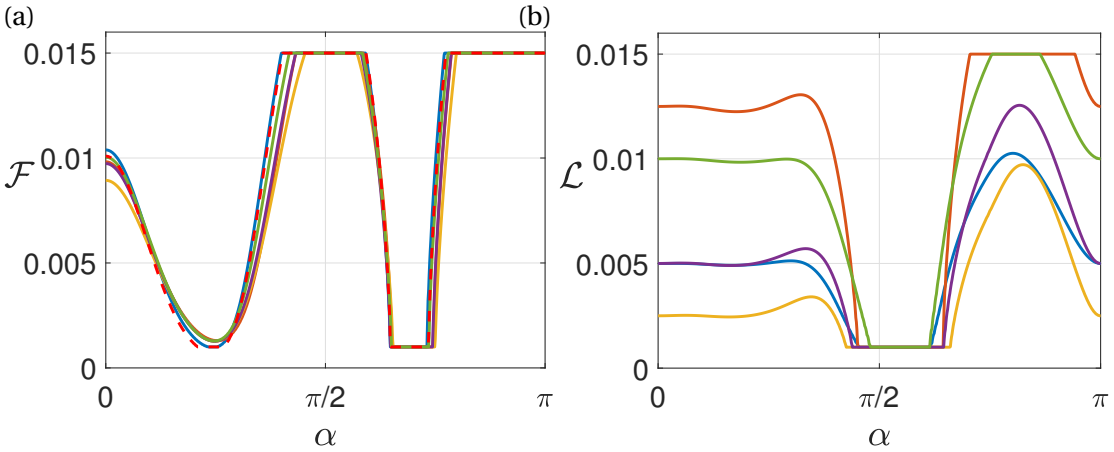

Figure 10.18: Results from the gradient-based optimization. Final distribution of (a) $\mathcal{F}$ and (b) $\mathcal{L}$, when both $\mathcal{F}$ and $\mathcal{L}$ are optimized for different initial guesses (coloured lines) and when only variations of $\mathcal{F}$ are considered with initial guess $\mathcal{F}^{(0)} = 0.0125$ and $\mathcal{L}^{(0)} = 0.005$ (red dashed line). The various initial guesses are $\mathcal{F}^{(0)} = 0.0125$ and $\mathcal{L} = 0.005$ (blue), $\mathcal{F}^{(0)} = 0.005$ and $\mathcal{L}^{(0)} = 0.0125$ (orange), $\mathcal{F}^{(0)} = 0.0025$ and $\mathcal{L}^{(0)} = 0.0025$ (yellow), $\mathcal{F}^{(0)} = 0.005$ and $\mathcal{L}^{(0)} = 0.005$ (purple), $\mathcal{F}^{(0)} = 0.01$, $\mathcal{L}^{(0)} = 0.01$ (green).

for the gradient-based optimization are uniform. We chose different values of the initial guess, among which $\mathcal{F}^{(0)} = 1.25 \times 10^{-2}$ and $\mathcal{L}^{(0)} = 5 \times 10^{-3}$, i.e. the values that maximize C_D when the permeable membrane is formed by a repetition of a single microscopic inclusion (case denoted by the $\square$ symbol in figure 10.12). We implement gradient-ascent iterative procedure, using as initial guess $\mathcal{F}^{(0)}$ and $\mathcal{L}^{(0)}$. At each iteration (i), the value of the gradients $\nabla^{(i)}_{\mathcal{F}} C_D$ and $\nabla^{(i)}_{\mathcal{L}} C_D$ are evaluated by the adjoint analysis proposed above. We thus update the distribution of $\mathcal{F}$ and $\mathcal{L}$ in the direction of the gradient as follows

$$\mathcal{F}^{(i+1)} = \mathcal{F}^{(i)} + \nabla^{(i)}_{\mathcal{F}} C_D \delta\mathcal{F} \quad \text{and} \quad \mathcal{L}^{(i+1)} = \mathcal{L}^{(i)} + \nabla^{(i)}_{\mathcal{L}} C_D \delta\mathcal{L}, \tag{10.24}$$

with fixed step sizes $\delta\mathcal{F} = 10^{-2}\mathcal{F}^{(0)}$ and $\delta\mathcal{L} = 10^{-2}\mathcal{L}^{(0)}$. During the optimization procedure, the values of $\mathcal{F}$ and $\mathcal{L}$ have to remain strictly positive, to avoid non-physical values. Besides, too small or too large values jeopardize the inverse procedure, since large differences in the dimensions of the microscopic inclusions are difficult to handle without considering large values of the parameter ε, which degrade the accuracy of the homogenized model. Typical procedures to regularize the problem are based on the introduction of auxiliary variables to transform the inequality conditions into equality ones (Schulze and Sesterhenn, 2013), or on the truncation of the gradient when the threshold values are reached (Lin, 2007). In this work, for the sake of simplicity, we apply the latter procedure and we restrict the research of the optimal profiles to the intervals $10^{-3} < \mathcal{F}, \mathcal{L} < 1.5 \times 10^{-2}$. At each iteration, values of $\mathcal{F}$ or $\mathcal{L}$ larger (resp. lower) than the threshold value, due to an increase (resp. decrease) along the gradient direction, are imposed to be equal to the threshold value. The iterative procedure is stopped when the relative difference between two successive evaluations of the drag coefficient is less than 10^{-4}.

In figure 10.18 we report the optimal distribution of $\mathcal{F}$ and $\mathcal{L}$ along the semi-cylinder found via the iterative algorithm, for the optimization with both $\mathcal{F}$ and $\mathcal{L}$, with different initial guesses. Note that, depending on the initial value, a different number of iterations is needed to achieve convergence. While the final distribution of $\mathcal{F}$ does not show significant variations with the initial guess, the profiles of $\mathcal{L}$ are different. In the rear part, $0 < \alpha < \pi/2$, $\mathcal{L}$ remains constant and equal to the initial value. For $\alpha \approx \pi/2$, all distributions collapse to the lower threshold value, and in the front part they assume different values. However, the effect of the slip number on the final value of the drag coefficient (figure 10.19(a)) is small and the differences are below 0.5%. Therefore, the effect of the filtrability is predominant and the optimal distribution of $\mathcal{F}$ is weakly influenced by $\mathcal{L}$. We thus consider the case in which the slip number is kept fixed, while the optimization is performed only on $\mathcal{F}$. The resulting distribution (red dashed line in figure 10.18(a)) is very similar to the other ones optimized both with respect to $\mathcal{F}$ and $\mathcal{L}$. Both approaches converge to a similar value of C_D (figure 10.19(b)), which is $\approx 6\%$ larger than the maximum drag obtained with uniform membrane properties. We therefore conclude that the optimization procedure leads to significantly larger values of C_D, in which the effect of the filtrability is predominant, with a weak dependence on the initial guess.

The increase of drag in the optimal configuration can be related to the previous observations in the case of constant filtrability. The optimization procedure tends to increase the filtrability in the front part ($\alpha \approx \pi$) of the cylinder and at $\alpha \approx \pi/2$, while it tends to decrease it at $\alpha \approx \pi/4$ and $\alpha \approx (3/4)\pi$. Compared to the constant filtrability case, the curvature of the streamlines is enhanced, thus leading to a more marked recompression in the inner part of the downstream portion of the membrane. This effect, leading to an increase of global drag, is enhanced in the optimal configuration since the flow is more constrained to pass through the front and the streamlines leave the cylinder through a narrower region, at $\alpha \approx \pi/2$, owing to the large values of filtrability in these regions. This constraint further magnifies the effects of the inner pressure gradients presented in the constant properties case. The analysis of the distributions of slip number shows that the drag is not influenced by variations of slip in the rear part of the cylinder.

In this section, we performed an adjoint-based optimization of the flow with respect to the drag. The typical computational time for one step of the optimization is equivalent to the one of a steady calculation of the non-linear Navier-Stokes equations, i.e. around one minute for a common laptop computer. Since on average 30-60 iterations were needed to achieve convergence, with the presented simple algorithm, one optimization lasts for 30-60 minutes. The decoupling between microscopic properties and macroscopic effects on the flow allows one to move from a generic shape optimization problem to an optimization problem for the two scalar distributions $\mathcal{F}(\alpha)$ and $\mathcal{L}(\alpha)$, making the optimization procedure straightforward to implement compared to a full-scale case. Once the distribution of membrane properties is known, the inverse procedure has to be applied to choose the microscopic structure. In the following, we aim at retrieving an optimal full-scale structure of the membrane starting from the optimal profile of $\mathcal{F}$ found in the present section.

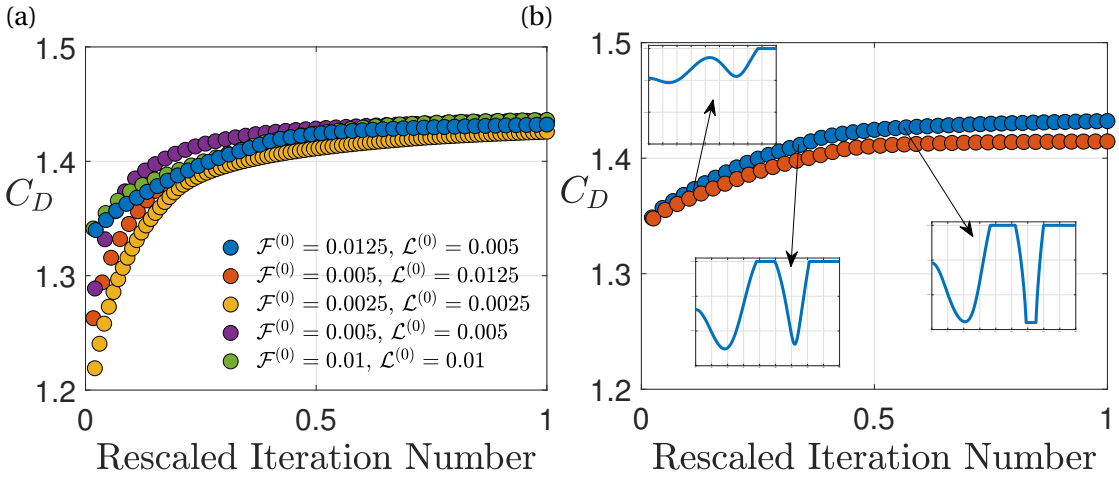

Figure 10.19: (a)Variation of the drag coefficient during the optimization procedure, for different initial guesses, as a function of the iteration number rescaled by the total number of iterations required to reach convergence. (b) Variation of the drag coefficient during the iterative procedure of the gradient-based optimization, when both $\mathcal{F}$ and $\mathcal{L}$ (blue dots) and only $\mathcal{F}$ (orange dots) are varied, with initial guess $\mathcal{F}^{(0)} = 0.0125$ and $\mathcal{L}^{(0)} = 0.005$. In the insets, we report the distributions of $\mathcal{F}$ for different iterations, the horizontal and vertical axes of the insets correspond to $0 < \alpha < \pi$ and $0 < \mathcal{F} < 1.55 \times 10^{-2}$, respectively.

10.6 Full-scale design of membranes of variable properties

In order to fulfill the inverse procedure introduced in figure 10.3, we link the optimal distribution of filtrability and slip found in Section 10.5.2 to a real full-scale structure of the permeable shell where the microscopic solid inclusions vary in shape and/or size. Since the effective stress jump condition developed by Zampogna and Gallaire (2020) has not been initially thought for membranes formed by solid inclusions of variable shape along the membrane, the first step to reach our objective is to modify and prove the validity of the macroscopic model for this case.

10.6.1 Application of the effective stress jump model to the case of membranes with fast-varying microscopic geometry

The easiest way to compute the microscopic tensors within the homogenization framework consists of assuming that the solid structure consists of a periodic repetition of a given unit cell (cf. for a review Hornung, 1997). To relax this assumption one may assume that the variations of the microscopic structure are slow (cf., for instance, Dalwadi et al., 2016) and hence solve the microscopic periodic problems (10.14) and (10.15) over each periodic unit cell and then compute the effective macroscopic tensors by averaging the microscopic solution over each cell. In the context of the present work, since fast variations of $\mathcal{F}$ and $\mathcal{L}$ can be noticed in the optimal distributions of figure 10.18, we need a model to link the effective properties to the microscopic geometry, without any assumption about the nature of the variations of the

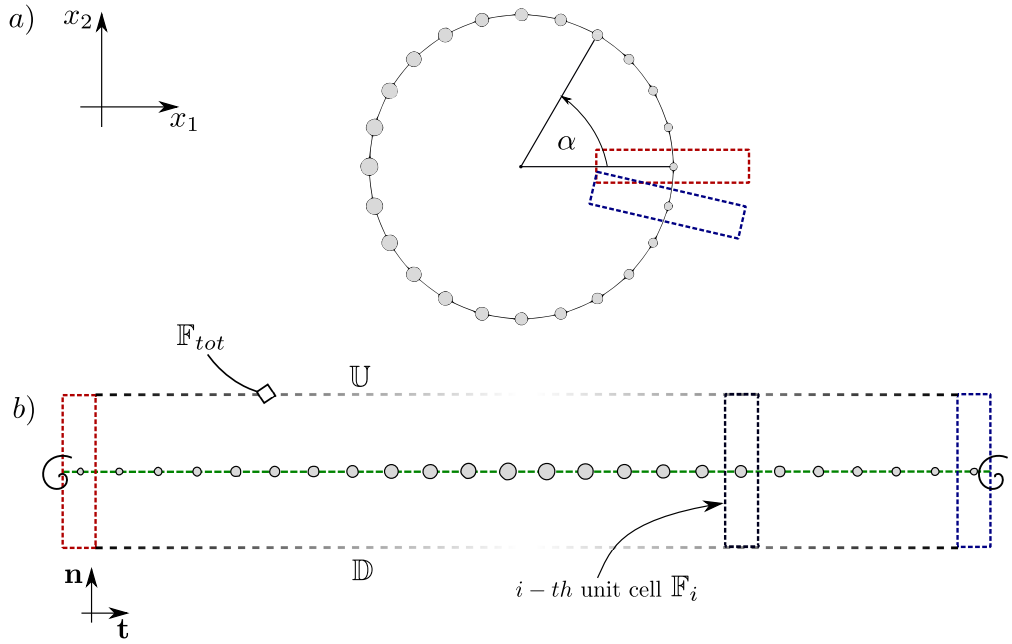

Figure 10.20: Panel (a): example of a cylindrical shell formed by variable microscopic inclusions, corresponding to distribution D1 in table 10.3. Panel (b): sketch of the microscopic domain, $\mathbb{F}_{tot}$, built by "unrolling" the cylindrical shell (red and blue unit cells correspond to their "rolled" counterpart in panel (a)). In order to deduce averaged profiles of F_n and L_t the solution is averaged within each cell over the green dashed line.

inclusions along the membrane. The macroscopic model of Zampogna and Gallaire (2020) is adapted here so as to describe this case when the following hypotheses are valid:

- the permeable shell is the surface of a rotational body, whose radius is R;
- the constraint $\ell/D \ll 1$ is still valid.

Under such assumptions, the macroscopic curvature is neglected in the microscopic domain as also done in Zampogna and Gallaire (2020) and the microscopic problems (10.14) and (10.15) are solved in the entire cylindrical shell, $\mathbb{F}_{tot}$, sketched in figure 10.20(b), defined as

$$\mathbb{F}_{tot} = \cup_{i=1}^{N} \mathbb{F}_i, \tag{10.25}$$

where $\mathbb{F}_i$ is the fluid domain within the $i-th$ unit cell sketched in figure 10.20(b) and N the total number of solid inclusions on the shell. On the left and right sides of $\mathbb{F}_{tot}$, we impose periodic boundary conditions as we are dealing with the surface of a rotational body. With these modifications, i.e. solving the microscopic problems (10.14) and (10.15) over $\mathbb{F}_{tot}$ instead of over each $\mathbb{F}_i$, the assumption of slow variations of the microscopic geometry is superfluous and a fast-varying microscopic geometry can be studied and associated with the optimal profile of $\mathcal{F}$ found in the previous subsection.

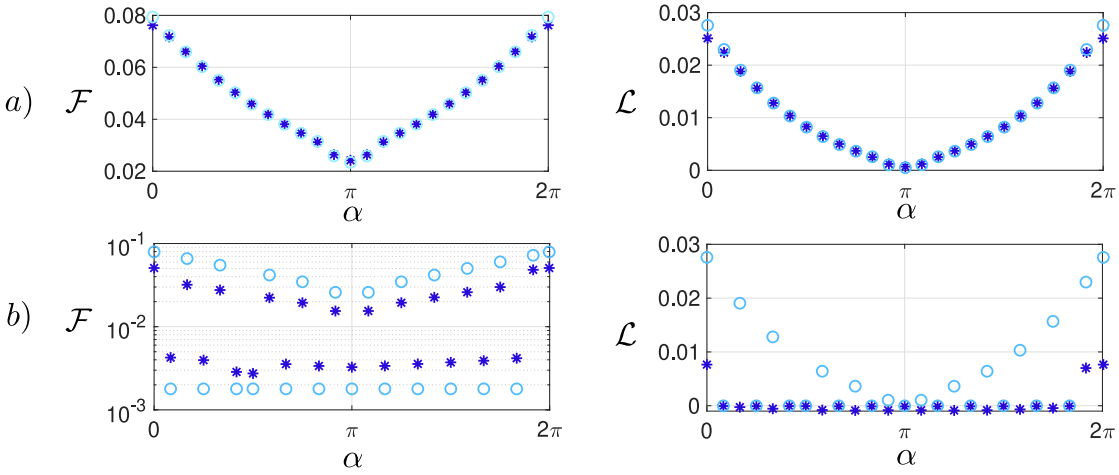

Figure 10.21: Values of $\mathcal{F}$ and $\mathcal{L}$ along $\mathbb{F}_{tot}$ (blue stars) and corresponding values computed within each cell $\mathbb{F}_i$ (light-blue circles) for distributions D1 (panel(a)) and D2 (panel (b)) described in table 10.3.

To validate the model, we first calculate the microscopic quantities associated with two different distributions of solid inclusions along the membrane, D1 and D2. They represent an example of slow- (D1) and fast-varying (D2) microscopic geometries (cf. table 10.3). The distribution D1 is represented in the Cartesian frame of reference in figure 10.20(a) and in the local frame of reference of the cylinder in figure 10.20(b). The values of $\mathcal{F}$ and $\mathcal{L}$ for distributions D1 and D2 are shown in figures 10.21(a) and 10.21(b), respectively. While blue stars represent the values extracted from the solutions computed within $\mathbb{F}_{tot}$ by averaging over each unit cell, the light-blue circles represent the values of $\mathcal{F}$ and $\mathcal{L}$ deduced by classical calculations over each periodic unit cell $\mathbb{F}_i$. In the case of slow variations of the microscopic structure, the periodic problems (10.14) and (10.15) over the unit cell provide acceptable results for the effective tensors. Conversely, the important discrepancies between the blue and light-blue profiles represented in panel (b) show that fast-variations of the microscopic geometries affect in a relevant way the values of the effective quantities $\mathcal{F}$ and $\mathcal{L}$ and microscopic problems (10.14) and (10.15) have to be computed over the entire microscopic domain $\mathbb{F}_{tot}$.

The last statement is supported by the comparison between the full-scale and the equivalent model that can be done once the effective values of $\mathcal{F}$ and $\mathcal{L}$ have been found. As shown in figure 10.22, the macroscopic velocities evaluated over the membrane are in perfect agreement with the full-scale profile for the case D1 of slow-varying geometries. The drag coefficient computed from the equivalent solution, C_D^{EQ}, is equal to 1.225, with a relative error with respect to the full-scale solution of $\approx 1.5\%$, in the order of the approximation. No substantial differences are noticed using the values of the effective tensor extracted from $\mathbb{F}_{tot}$ or from each periodic unit cell $\mathbb{F}_i$. On the contrary, when distribution D2 is considered (figure 10.22(b)), the use of the effective tensor calculated within $\mathbb{F}_{tot}$ allows us to drastically reduce the error between the full-scale simulation and the macroscopic model.

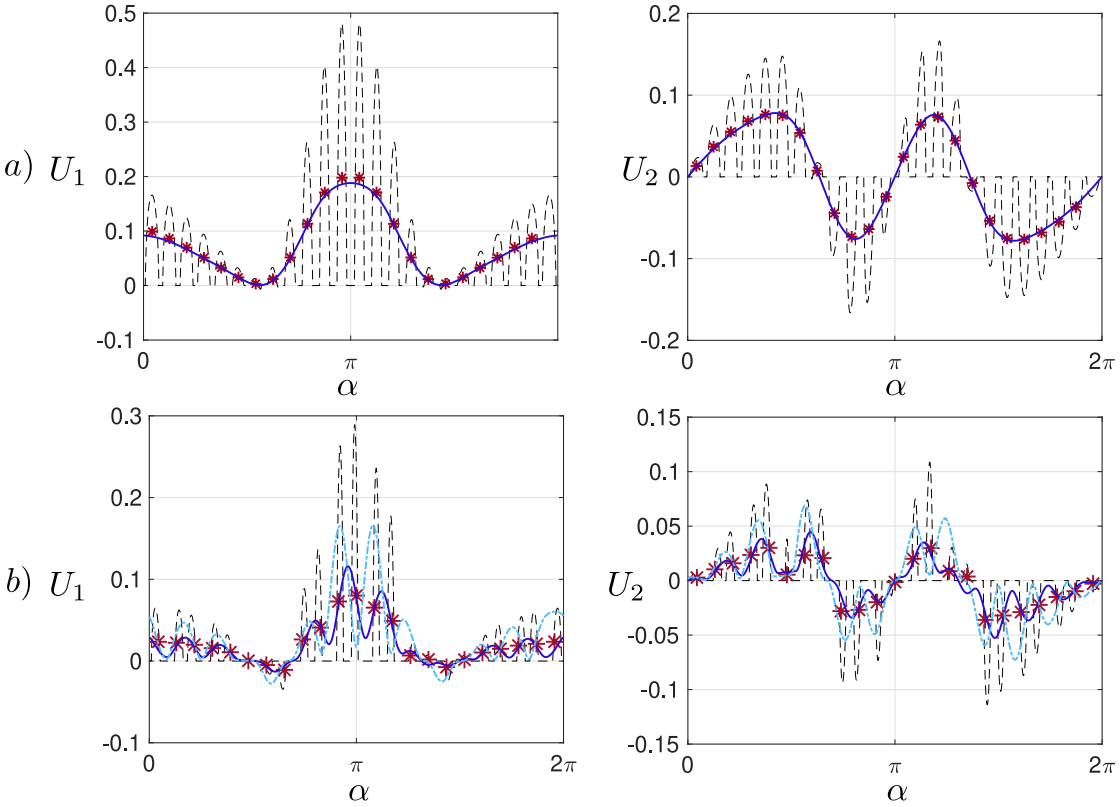

Figure 10.22: Comparison between the full-scale solution and the macroscopic model for distribution D1 and D2 (panels *a* and *b* respectively). All quantities are evaluated over the equivalent membrane Γ_{int}. Dashed lines represent the full-scale model, blue lines the macroscopic model where the values of the effective tensors have been calculated in $\mathbb{F}_{tot}$, light-blue dot-dashed lines correspond to the macroscopic model where the values of the effective tensors have been calculated in each periodic unit cell $\mathbb{F}_i$ and red stars are the average of the full-scale model.

10.6.2 Retrieving the full-scale microscopic geometry from the optimal $\mathcal{F}$-$\mathcal{L}$-profiles

In the previous paragraph we showed that the effective stress jump condition of Zampogna and Gallaire (2020) is reliable also in the case of fast-varying microscopic geometries when the adequate precautions described above are taken into account to formulate the microscopic problems (10.14, 10.15). We thus apply it to link the optimal distributions of effective filtrability and slip profiles found in Section 10.5.2 to a distribution of microscopic solid inclusions in order to design an optimal cylindrical membrane for drag maximization. For the sake of simplicity, we consider the case in which the optimization procedure is performed only on the value of $\mathcal{F}$, letting $\mathcal{L}$ vary accordingly to the microscopic calculations. This allows us to focus our attention only on circular (rather than elliptical) inclusions of variable radius. As a consequence, the profile of $\mathcal{L}$ is unequivocally defined once the $\mathcal{F}$ profile is retrieved. This simplifying assumption has a marginal effect on the resulting optimal drag since the latter

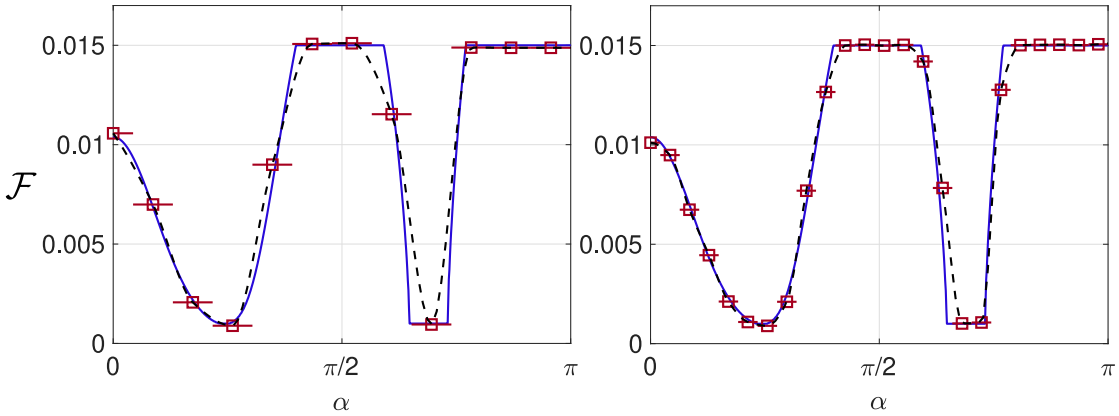

Figure 10.23: Variation of the optimal $\mathcal{F}$-profile with α. Blue lines correspond to the values of $\mathcal{F}$ found in Section 10.5.2 while red squares to the values of $\mathcal{F}$ reconstructed from the microscopic problems in $\mathbb{F}_{tot}$. Black dashed lines correspond to the profiles reconstructed via a piecewise cubic interpolation of the red square-profile. In the left panel 23 inclusions have been placed on the cylindrical shell ($\varepsilon = 0.1369$) while on the right one 47 inclusions have been used ($\varepsilon = 0.0667$). A larger number of inclusions allows us to better reconstruct the $\mathcal{F}$ profile.

is only weakly affected by $\mathcal{L}$. Nevertheless, the following procedure can be straightforwardly generalized to variable distributions of both $\mathcal{F}$ and $\mathcal{L}$, by considering for instance elliptical inclusions as in Section 10.4.2. The numerical implementation is based on a bisection method, where at each iteration the value of the radius of each inclusion is adjusted so as to reach the aimed values of $\mathcal{F}$ up to a relative tolerance of 1%. For the iterative procedure to be well defined, an initial guess has to be taken. A good candidate is the value of $\mathcal{F}$ given by the case of perfectly periodic microstructures. The separation of scales parameter ε is a free parameter and has to be chosen to unequivocally define the radius of the solid inclusions. The resulting distributions are sketched in figure 10.23 for two different values of $\varepsilon = 0.1369, 0.0667$, corresponding to 23 and 47 solid inclusions over the cylinder, respectively. We reconstruct the continuous $\mathcal{F}$ and $\mathcal{L}$ profiles via a piecewise-cubic interpolation (black dashed lines in figure 10.23) of the piecewise constant values obtained from the solution of the microscopic problems averaged in each unit cell (red squares); however, we verified that the following results were not affected by a different choice of the interpolation. As last check, we perform macroscopic and full-scale simulations in order to i) confirm the validity of the model in this case and ii) check that the full-scale geometry actually maximizes the drag coefficient, as predicted in the Lagrangian-based optimization procedure. Figures 10.24 and 10.25 provide qualitative and quantitative information about the flow past the two retrieved full-scale optimal structures. According to panel (a) of those figures, for both values of ε the full-scale solution reproduces well the behavior and properties of the macroscopic flow calculated using the optimal profile of $\mathcal{F}$. The drag coefficients calculated over the two full-scale structures are $C_D^{\varepsilon=0.1369} = 1.427$ and $C_D^{\varepsilon=0.0667} = 1.412$, while the corresponding one estimated by the macroscopic model is equal to 1.414, exhibiting an error of about 1% in the worst case. The variability of the microscopic inclusions is shown in panel (b) of figures 10.24 and 10.25, where

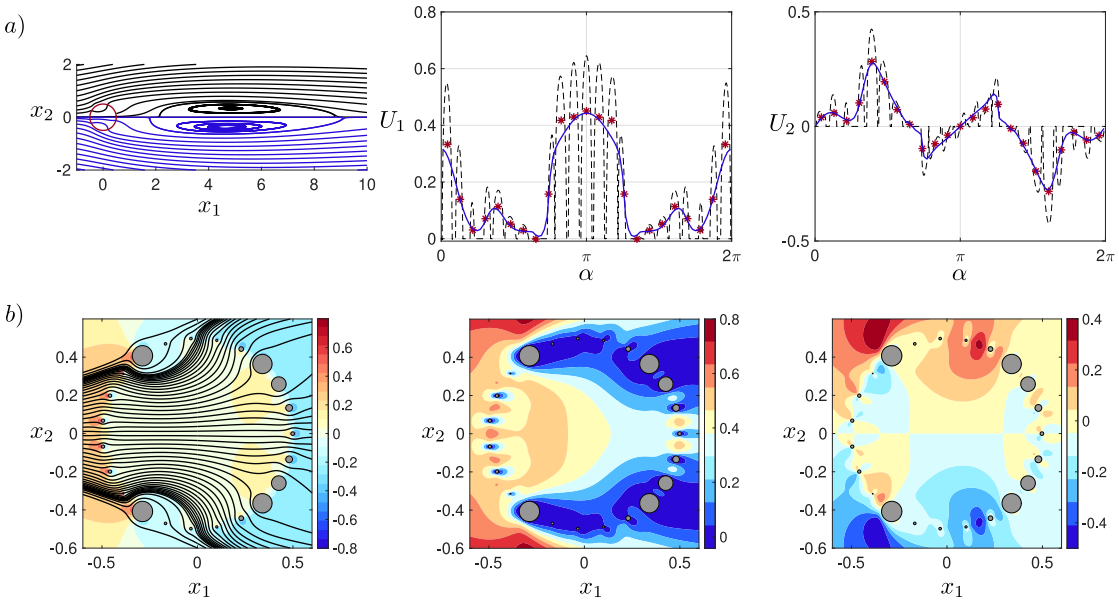

Figure 10.24: Flow past the optimal cylindrical structure deduced from the profile of $\mathcal{F}$ computed in Section 10.5.2. A total number of 23 solid inclusions (sketched in dark gray in panel (b)) have been placed on the cylinder leading to a value of ε equal to 0.137. Top row: comparison between full-scale and macroscopic solution. In the left panel the flow streamlines for the full-scale simulation (black lines) and for the macroscopic model (blue lines). In the central and right panels the horizontal and vertical velocities are represented over Γ_{int}. Black dashed lines represent the full-scale solution, blue lines the macroscopic model, where $\mathcal{F}$ and $\mathcal{L}$ are evaluated using the reconstructed profiles (cf. figure 10.23), and red stars the averaged full-scale profile. Bottom row: isocontours of pressure (left panel), horizontal (center panel) and vertical velocity (right panel) around the cylindrical shell. In the left panel also flow streamlines within the shell have been represented to better appreciate the flow behavior.

a focus on the pressure and velocity fields across the cylindrical shell reveals the presence of local microscopic flow structures that become less and less important as ε decreases. We refer to table 10.3 for the geometrical data used to build each full scale structure and to figure 10.28 for their visualization.

These last findings accomplish the procedure sketched in figure 10.3. As previously shown, the inverse procedure admits multiple solutions, whose number can be further reduced by imposing other kinds of geometrical or functional constraints to the problem considered.

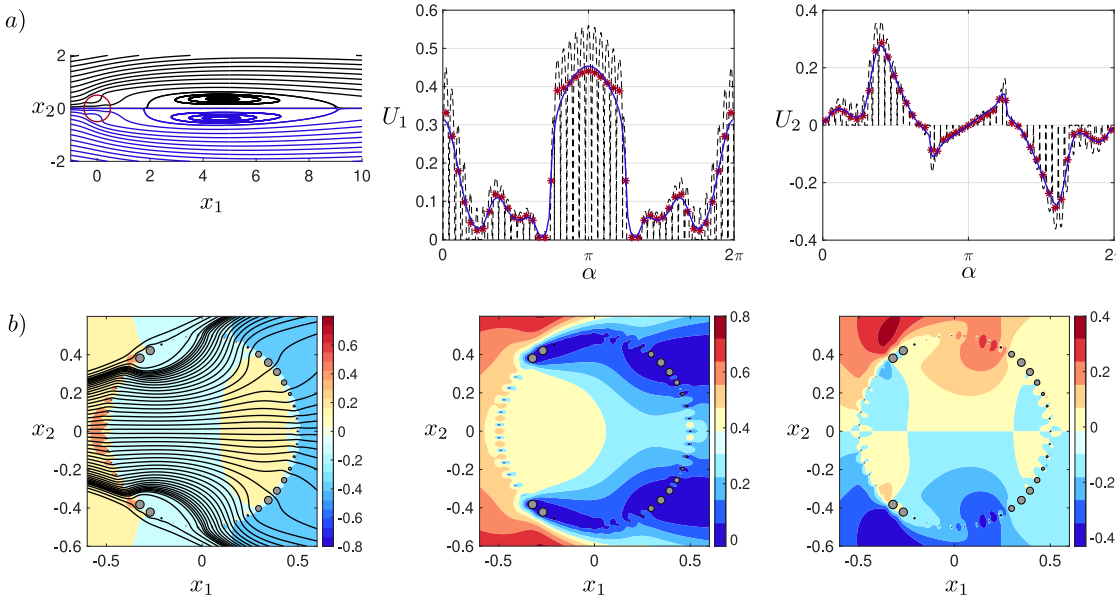

Figure 10.25: Same as figure 10.24 for a total number of 47 solid inclusions on the cylinder, leading to $\varepsilon = 0.066$.

10.7 Conclusions and perspectives

In this work, we proposed an approach for the *homogenization-based optimization of permeable membranes*. We considered as a test case the wake flow past a permeable circular cylinder. The first part of the procedure was a parametric study of the steady flow configurations and their stability with respect to perturbations. In this framework, the membrane was modeled by the effective stress jump interface condition developed in Zampogna and Gallaire (2020), for symmetric configurations with respect to the centerline of the membrane. Under these conditions, the membrane properties are described by two scalars, the filtrability and the slip numbers, the former representing the ability of the fluid to pass through the membrane while the latter its ability to flow along the tangential-to-the-membrane direction. The flow morphology strongly resembles the one outlined in Ledda et al. (2018). The recirculation region past the cylinder detaches from the body and moves downstream, becomes smaller and disappears, as the filtrability number was increased. An increase in the slip number showed a decrease in the dimensions of the recirculation region. Interestingly, for large values of the filtrability number, the drag coefficient presents a maximum that is substantially larger than the drag coefficient of an impermeable cylinder. A bifurcation diagram was identified via the stability analysis, which unraveled the stabilization of the steady wake for large values of filtrability, a situation similar to the one outlined in Ledda et al. (2018). The unstable mode leads to a vortex shedding whose onset region moves downstream as the filtrability is increased.

Once the unstable configurations were excluded from the analysis, the second part of the work was focused on the reconstruction of the membrane based on the values of filtrability and slip numbers, identified to obtain proper macroscopic characteristics of the flow. We considered

different test cases, among which the conditions that maximize the drag coefficient. We also outlined a procedure to recover the microscopic geometry that satisfies the constraints of filtrability and slip numbers, for elliptical inclusions. The agreement between the homogenized model and the full-scale simulations was very good, proving not only the faithfulness of the inverse procedure, but also the accuracy of the effective stress jump condition which was initially tested in Zampogna and Gallaire (2020) only in the Stokes flow regime.

The third part of the work was devoted to the optimization of a membrane whose filtrability and slip numbers were allowed to vary along the cylinder and to the reconstruction of the corresponding microscopic structure. As a test case, we considered as optimal objective the maximization of the drag coefficient. We first evaluated the sensitivity with respect to variations of the filtrability and slip numbers and thus performed a gradient-ascent optimization, using as initial guess the values of filtrability and slip numbers that maximize the drag in the case of constant membrane properties. In this test case, we obtained an increase in the drag coefficient of 6% with respect to the case with constant membrane properties, and thus of 34% with respect to the solid case. We then introduced a procedure to recover the microscopic structure that satisfies an optimal filtrability distribution, focusing on circular inclusions. The introduction of a new modified domain of validity of the microscopic problems associated with filtrability and slip numbers allowed us to correctly link these quantities to a full-scale geometry. Also in this case the agreement was fully satisfactory, thus validating the proposed approach both for constant and variable distributions of filtrability and slip numbers along the membrane.

This work aims at giving a rationale to the application of homogenized models to design membranes in the context of flow control, providing fast and accurate predictions and the opportunity to directly link macroscopic characteristics of the membrane to microscopic geometries. Thanks to the generality of the macroscopic model, real three-dimensional permeable shells can be handled at the cost of adding only one more parameter, representing the ability of the fluid to flow along the second tangent-to-the-membrane direction, much lower than the cost of adding approximately $1/\varepsilon$ degrees of freedom due to the meshing of a real full-scale three-dimensional membrane. The potential of the method stems from the decoupling between microscopic properties and macroscopic effects on the flow, which allows one to have a plethora of possible microscopic configurations giving the same macroscopic flow. This decoupling drastically simplifies the adjoint-based optimization procedure, allowing to obtain a single distribution of membrane properties which can be satisfied by an infinite number of possible microscopic geometries; the number of corresponding microscopic geometries can be further reduced by imposing other constraints. Despite the theoretical and analytical complexity of the homogenization technique, the final result consists of a simple boundary condition for the macroscopic flow model that enables to explore a vast range of geometrical configurations, with the great advantage of a drastic reduction of the complexity and computational times needed to carry out the solution.

This work may be extended in several ways. The procedure explained here is a first step

Mesh	$x_{1\text{in}}$	$x_{1\text{out}}$	$x_{2\text{lat}}$	N_1	N_2	N_3	N_4	N_{int}	No. Elements	C_D	Re(σ)	Im(σ)
$M1$	-30	90	25	1	1.25	5	13.3	31.9	144008	1.3398	-0.0368	0.7198
$M2$	-30	90	25	1.25	1.55	6.3	16.7	39.8	161896	1.3398	-0.0368	0.7198
$M3$	-30	90	25	1.5	1.9	7.5	20	47.8	187498	1.3398	-0.0367	0.7198
$M4$	-30	90	25	2	2.5	10	26.7	63.7	241094	1.3398	0.0367	0.7199
$M1B$	-45	120	37.5	1	1.25	5	13.3	31.9	164918	1.3338	-0.0383	0.7186
$M1C$	-60	180	50	1	1.25	5	13.3	31.9	193202	1.3340	-0.0384	0.7187

Table 10.2: Results of the mesh convergence. The edge densities are denoted with N, for different regions as depicted in figure 10.2.

towards a rational design of membranes; if integrated with a model describing the equivalent transport of diluted substances across a permeable wall it represents a potential answer to the necessity identified in Park et al. (2017) to find the right balance of filtrability between a fluid and a diluted substance. The comparisons considered in the present work show that the homogenized model well reproduces the flow behavior in the case of inertial flows. The differences with respect to the full-scale solution are larger for cases in which the microscopic Reynolds number, $Re_{micro} = U\ell/\nu$, is large (cf. for instance the case denoted by ◯ in table 10.1 where $Re_{micro} \approx 25$). This pushes us to proceed toward an extension of the model for high-Re flows, where the inertia of the flow within the membrane cannot be neglected (Zampogna and Bottaro, 2016).

We conclude by observing that the interweaving of homogenization theory, bifurcation analysis and adjoint optimization methods showed great potential, opening up the path to a rational design of complex structures that can find a wide and varied range of applications in fluid dynamics.

10.8 Appendix

10.8.1 Mesh convergence

In this section, we report the results of the mesh convergence. We considered the case $Re = 100$, $\mathcal{F} = 1.25 \times 10^{-2}$ and $\mathcal{L} = 5 \times 10^{-3}$. We verified both the convergence with respect to the size of the domain and with respect to the number of elements. The results are reported in Table 10.2, for the drag coefficient and for the unstable eigenvalue studied in Section 10.3.2. We initially increased the number of elements for the mesh $M1$, verifying the convergence. We therefore increased the domain size to verify its effect. We conclude that the number of elements and the size of the domain have a small impact on the baseflow and global stability results, two significant digits remaining constant for every measured quantity. The mesh $M1$ (shown in figure 10.26) is suitable for the study and it has been used throughout the work.

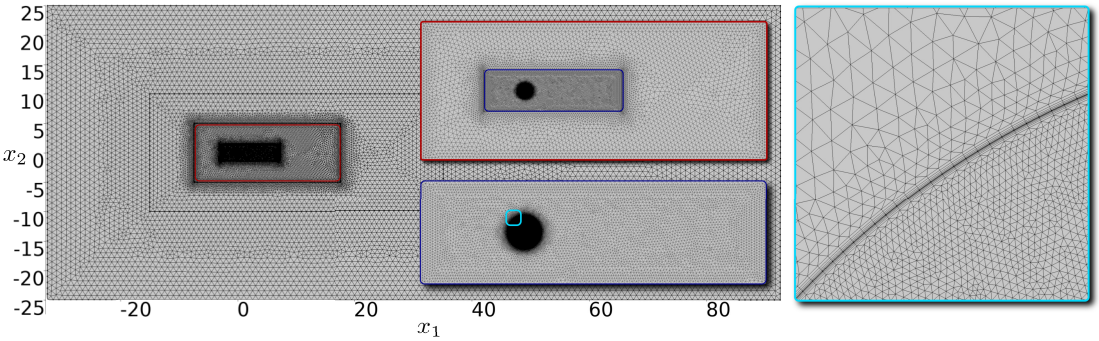

Figure 10.26: Overview of the mesh denoted by $M1$ in table 10.2 used for the macroscopic computations. In each colored inset recursive magnifications approaching the cylinder are shown. In the light-blue inset prismatic layers adjacent to the fictitious interface Γ_{int} can be noticed; they have been added in order to well evaluate the normal-to-the-membrane fluid stress and integral quantities like the drag force acting on the cylinder.

10.8.2 Derivation of the sensitivity of the drag coefficient with respect to variations of the membrane properties

We propose here an extensive derivation of the sensitivity functions briefly introduced in Section 10.5.2. For the sake of clarity, we recall that, at the interface, we denote with the superscripts $\cdot^+$ and $\cdot^-$ the following limits

$$f^- = \lim_{x_i \to \Gamma^-_{\text{int}}} f \quad \text{and} \quad f^+ = \lim_{x_i \to \Gamma^+_{\text{int}}} f, \tag{10.26}$$

with Γ^-_{int} and Γ^+_{int} the outer and inner sides of Γ_{int}. The drag coefficient, i.e. the objective in the Lagrangian framework, is defined in equation (10.18). According to this equation, any small modification of the tensor component $\mathcal{M}_{ij}$ modifies the drag by δC_D according to

$$\delta C_D = 2 \oint_{\Gamma_{\text{cyl}}} \left(\Sigma_{jk}\left(\delta p^-, \delta \boldsymbol{u}^-\right) - \Sigma_{jk}\left(\delta p^+, \delta \boldsymbol{u}^+\right) \right) n_k \delta_{1j} \, \mathrm{d}\Gamma = \oint_{\Gamma_{cyl}} \nabla_{\mathcal{M}_{ij}} C_D \delta \mathcal{M}_{ij} \, \mathrm{d}\Gamma, \tag{10.27}$$

where $\left(\delta \boldsymbol{u}^{\pm}, \delta p^{\pm}\right)$ is the linear perturbation to the base solution induced by the variation of the membrane tensor, whose governing equations can be deduced by substituting the perturbed variables $\left(\boldsymbol{u} = \boldsymbol{U} + \delta \boldsymbol{u}, p = P + \delta p\right)$ in equations (10.6, 10.7) and read

$$\begin{aligned} \partial_i \delta u_i = 0, \quad \delta u_j \partial_j U_i + U_j \partial_j \delta u_i = -\partial_i \delta p + \tfrac{1}{Re} \partial^2_{jj} \delta u_i \quad & \text{in } \Omega \\ \delta u_i^+ = \delta u_i^- = \delta u_i \quad & \text{on } \Gamma_{\text{int}} \\ \delta u_i = Re \mathcal{M}_{ij} \left(\Sigma_{jk}\left(\delta p^-, \delta \boldsymbol{u}^-\right) - \Sigma_{jk}\left(\delta p^+, \delta \boldsymbol{u}^+\right) \right) n_k + & \\ + Re \delta \mathcal{M}_{ij} \left(\Sigma_{jk}\left(p^-, \boldsymbol{u}^-\right) - \Sigma_{jk}\left(p^+, \boldsymbol{u}^+\right) \right) n_k \quad & \text{on } \Gamma_{\text{int}}, \end{aligned} \tag{10.28}$$

together with boundary conditions $\delta u_i = 0$ at the inlet and $\Sigma_{jk}\left(\delta p, \delta \boldsymbol{u}\right) n_k = 0$ at the outflow.

We introduce the Lagrange multipliers $(\boldsymbol{u}^\dagger, p^\dagger, \boldsymbol{u}^{\dagger\dagger})$ referred to as the adjoint solution, and

define the functional

$$\begin{aligned}\mathcal{J}\left(\boldsymbol{u},p,\boldsymbol{u}^{\dagger},p^{\dagger},\boldsymbol{u}^{\dagger\dagger},\mathcal{M}\right) = C_D \\ &- \int_{\Omega} p^{\dagger}\partial_i u_i \mathrm{d}\Omega \\ &- \int_{\Omega} u_i^{\dagger}\left(u_j\partial_j u_i - \partial_j \Sigma_{ij}\left(p,\boldsymbol{u}\right)\right)\mathrm{d}\Omega \\ &- \oint_{\Gamma_{\mathrm{int}}} u_i^{\dagger\dagger}\left[u_i - Re\mathcal{M}_{ij}\left(\Sigma_{jk}\left(p^{-},\boldsymbol{u}^{-}\right) - \Sigma_{jk}\left(p^{+},\boldsymbol{u}^{+}\right)\right)n_k\right]\mathrm{d}\Gamma,\end{aligned} \tag{10.29}$$

whose gradient with respect to any variable f is

$$\frac{\partial \mathcal{J}}{\partial f}\delta f = \lim_{\epsilon\to 0}\frac{\mathcal{J}(f+\epsilon\delta f)-\mathcal{J}(f)}{\epsilon}. \tag{10.30}$$

The variation of the drag coefficient thus reads:

$$\delta C_D = \frac{\partial \mathcal{J}}{\partial\left(\boldsymbol{u},p\right)}\delta\left(\boldsymbol{u},p\right) + \frac{\partial \mathcal{J}}{\partial \mathcal{M}_{ij}}\delta\mathcal{M}_{ij}, \tag{10.31}$$

since the gradient of the functional with respect to the adjoint variable is zero as long as the state equation is satisfied. The gradient with respect to $\left(\boldsymbol{u},p\right)$ is

$$\begin{aligned}\frac{\partial \mathcal{J}}{\partial\left(\boldsymbol{u},p\right)}\delta\left(\boldsymbol{u},p\right) = 2\oint_{\Gamma_{\mathrm{int}}} &\left(\Sigma_{ij}\left(\delta p^{-},\delta\boldsymbol{u}^{-}\right) - \Sigma_{ij}\left(\delta p^{+},\delta\boldsymbol{u}^{+}\right)\right)n_j\delta_{1i}\,\mathrm{d}\Gamma \\ &- \int_{\Omega} p^{\dagger}\partial_i\delta u_i \mathrm{d}\Omega \\ &- \int_{\Omega} u_i^{\dagger}\left(U_j\partial_j\delta u_i + \delta u_j\partial_j U_i - \partial_j\Sigma_{ij}\left(\delta p,\delta\boldsymbol{u}\right)\right)\mathrm{d}\Omega \\ &- \oint_{\Gamma_{\mathrm{int}}} u_i^{\dagger\dagger}\left[\delta u_i^{-} - Re\mathcal{M}_{ij}\left(\Sigma_{jk}(\delta p^{-},\delta\boldsymbol{u}^{-}) - \Sigma_{jk}(\delta p^{+},\delta\boldsymbol{u}^{+})\right)n_k\right]\mathrm{d}\Gamma\end{aligned} \tag{10.32}$$

Integrating by parts and using the divergence theorem, we obtain analogous boundary terms

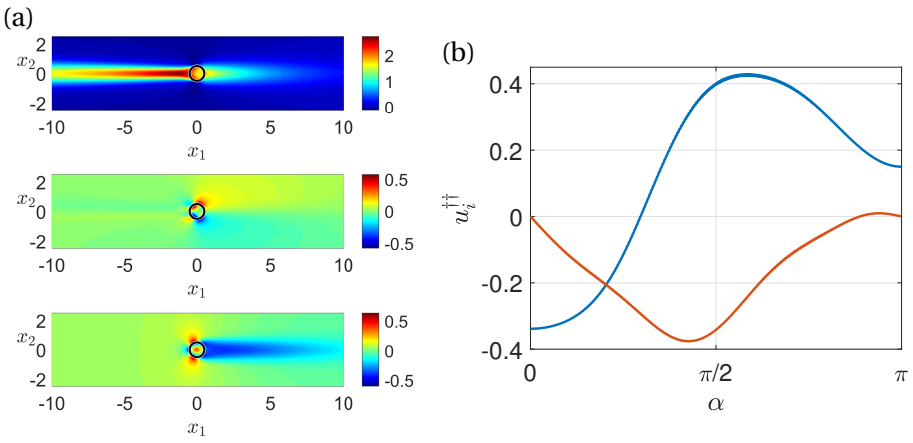

Figure 10.27: Adjoint field for $Re = 100$, $\mathcal{F} = 1.25 \times 10^{-2}$, $\mathcal{L} = 5 \times 10^{-3}$. Panel (a): from top to bottom, $u_1^\dagger$, $u_2^\dagger$, $p^\dagger$. Panel (b): $u_1^{\dagger\dagger}$ (blue curve) and $u_2^{\dagger\dagger}$ (orange curve) evaluated over Γ_{int} for $\alpha \in [0, \pi]$.

at Γ_{int} for the inner and outer problems, to which we add those of the interface condition:

$$
\begin{aligned}
\frac{\partial \mathcal{J}}{\partial (\boldsymbol{u}, p)} \delta(\boldsymbol{u}, p) = \\
&\oint_{\Gamma_{\text{int}}} \Sigma_{ij}(\delta p^-, \delta \boldsymbol{u}^-)\, n_j \left(2\delta_{i1} - u_i^{\dagger -} + u_k^{\dagger\dagger} Re \mathcal{M}_{ki}\right) \\
&+ \left(\Sigma_{ij}(-p^{\dagger -}, \boldsymbol{u}^{\dagger -}) n_j + U_k n_k u_i^{\dagger -} - u_i^{\dagger\dagger}\right) \delta u_i^- \, \mathrm{d}\Gamma \\
-&\oint_{\Gamma_{\text{int}}} \Sigma_{ij}(\delta p^+, \delta \boldsymbol{u}^+)\, n_j \left(2\delta_{i1} - u_i^{\dagger +} + u_k^{\dagger\dagger} Re \mathcal{M}_{ki}\right) \\
&+ \left(\Sigma_{ij}(-p^{\dagger +}, \boldsymbol{u}^{\dagger +}) n_j + (U_k n_k)\, u_i^{\dagger +}\right) \delta u_i^+ \, \mathrm{d}\Gamma \\
&+ \oint_{\partial\Omega} -\Sigma_{ij}(\delta p, \delta \boldsymbol{u})\, n_j u_i^\dagger + \left(\Sigma_{ij}(-p^\dagger, \boldsymbol{u}^\dagger) n_j + U_k n_k u_i^\dagger\right) \delta u_i \mathrm{d}\Gamma \\
&+ \int_\Omega \partial_i u_i^\dagger \delta p \, \mathrm{d}\Omega \\
&- \int_\Omega u_j^\dagger \partial_i U_j - U_j \partial_j u_i^\dagger - \partial_i p^\dagger - \frac{1}{Re} \partial_{jj}^2 u_i^\dagger \delta u_i \, \mathrm{d}\Omega
\end{aligned}
\tag{10.33}
$$

Exploiting the relation $\delta \boldsymbol{u} = \delta \boldsymbol{u}^+ = \delta \boldsymbol{u}^-$, canceling the surface term on Ω and the boundary terms on Γ_{int} and $\partial\Omega$, we define $(\boldsymbol{u}^\dagger, p^\dagger)$ as the solution to the adjoint linear equations

$$
\begin{aligned}
\partial_i u_i^\dagger = 0, \quad u_j^\dagger \partial_i U_j - U_j \partial_j u_i^\dagger = \partial_i p^\dagger + \tfrac{1}{Re} \partial_{jj}^2 u_i^\dagger \quad &\text{in } \Omega \\
\left(\Sigma_{ik}(-p^{\dagger -}, \boldsymbol{u}^{\dagger -}) - \Sigma_{ik}(-p^{\dagger +}, \boldsymbol{u}^{\dagger +})\right) n_k - u_i^{\dagger\dagger} = 0 \quad &\text{on } \Gamma_{\text{int}} \\
u_i^{\dagger +} = u_i^{\dagger -} \quad &\text{on } \Gamma_{\text{int}}
\end{aligned}
\tag{10.34}
$$

with

$$
u_i^{\dagger\dagger} = Re^{-1} \mathcal{M}_{ji}^{-1} \left(u_j^{\dagger -} - 2\delta_{1j}\right) \quad \text{on } \Gamma_{\text{int}}, \tag{10.35}
$$

together with adjoint boundary conditions $\boldsymbol{u}^{\dagger}=0$ at the inflow and $\Sigma_{ik}\left(-p^{\dagger},\boldsymbol{u}^{\dagger}\right)n_k+U_k n_k u_i^{\dagger}=0$ at the outflow and lateral boundaries of the domain Γ_{lat}. We thus have:

$$\delta C_D=\frac{\partial\mathcal{J}}{\partial\mathcal{M}_{ij}}\delta\mathcal{M}_{ij}=\oint_{\Gamma_{\text{int}}}u_i^{\dagger\dagger}Re\delta\mathcal{M}_{ij}\left(\Sigma_{jk}(P^-,\boldsymbol{U}^-)-\Sigma_{jk}\left(P^+,\boldsymbol{U}^+\right)\right)n_k\,\mathrm{d}\Gamma. \tag{10.36}$$

Since $\mathcal{M}_{ij}=\mathcal{L}t_i t_j-\mathcal{F}n_i n_j$, we are able to evaluate the sensitivities with respect to $\mathcal{F}$ and $\mathcal{L}$ separately. Specializing equation (10.36) for $\mathcal{F}$ we obtain

$$\delta C_D=\frac{\partial\mathcal{J}}{\partial\mathcal{F}}\delta\mathcal{F}=-\oint_{\Gamma_{\text{int}}}u_i^{\dagger\dagger}Re\delta\mathcal{F}n_i n_j\left(\Sigma_{jk}(P^-,\boldsymbol{U}^-)-\Sigma_{jk}\left(P^+,\boldsymbol{U}^+\right)\right)n_k\,\mathrm{d}\Gamma. \tag{10.37}$$

The sensitivity with respect to $\mathcal{F}$ thus reads

$$\nabla_{\mathcal{F}}C_D=-Reu_i^{\dagger\dagger}n_i n_j\left(\Sigma_{jk}(P^-,\boldsymbol{U}^-)-\Sigma_{jk}\left(P^+,\boldsymbol{U}^+\right)\right)n_k, \tag{10.38}$$

while, applying the same procedure with respect to $\mathcal{L}$, we obtain

$$\nabla_{\mathcal{L}}C_D=Reu_i^{\dagger\dagger}t_i t_j\left(\Sigma_{jk}(P^-,\boldsymbol{U}^-)-\Sigma_{jk}\left(P^+,\boldsymbol{U}^+\right)\right)n_k. \tag{10.39}$$

It is finally clear that the gradients of C_D can be evaluated only if the solution of the adjoint problem 10.34 is known. As a matter of example, in figure 10.27 we report the adjoint fields $(\boldsymbol{u}^{\dagger},p^{\dagger},\boldsymbol{u}^{\dagger\dagger})$ for $Re=100$, $\mathcal{F}=1.25\times10^{-2}$ and $\mathcal{L}=5\times10^{-3}$.

10.8.3 Geometrical data associated with the full-scale structures analyzed in Section 10.6

In Section 10.6 different full-scale geometries with arbitrary varying solid inclusions have been proposed. Table 10.3 lists the parameter needed to build the cylidrincal shell for each case. Distributions D1 and D2 correspond to test cases 1 and 2 that leads to the profiles of $\mathcal{F}$ and $\mathcal{L}$ depicted in panels (b) and (c) of figure 10.22, while distributions D3 and D4 correspond to the optimal full-scale structures found in Section 10.6.2 with ϵ equal to 0.1369 and 0.0667, respectively. Each entry of the table contains the value of the radius of the $i-th$ circular solid inclusion, normalized by ℓ. The $i-$th inclusion is positioned at an angle $\alpha=\frac{2\pi}{N}(i-1)$ where $N=23$ for distributions D1, D2, D3 and $N=47$ for distribution D4. To have a visual idea of which kind of structures we are dealing with, in figure 10.28 a visualization of the corresponding full-scale membrane geometries is represented for the distributions listed in table 10.3.

i	D1	D2	D3	D4
1	0.10	0.10	0.070	0.0300
2	0.11	0.40	0.130	0.0320
3	0.12	0.12	0.280	0.0750
4	0.13	0.40	0.370	0.1170
5	0.14	0.14	0.090	0.2100
6	0.15	0.40	0.043	0.2750
7	0.16	0.40	0.050	0.3000
8	0.17	0.17	0.050	0.2300
9	0.19	0.40	0.390	0.0550
10	0.20	0.19	0.015	0.0150
11	0.22	0.40	0.063	0.0090
12	0.23	0.22	0.062	0.0135
13	0.22	0.40	0.062	0.0140
14	0.20	0.22	0.063	0.0110
15	0.19	0.40	0.015	0.0060
16	0.18	0.19	0.390	0.0500
17	0.17	0.40	0.050	0.3200
18	0.16	0.17	0.050	0.3300
19	0.15	0.40	0.043	0.0008
20	0.14	0.15	0.090	0.0085
21	0.13	0.40	0.370	0.0132
22	0.12	0.13	0.280	0.0149
23	0.11	0.40	0.130	0.0160
24	–	–	–	0.0160

Table 10.3: Values of the radius of the $i-$th solid inclusion, non-dimensionalized with the microscopic length, for $i = 1,...,24$ for distributions D1, D2, D3 and D4. Please notice that, in distribution D4, 47 solid inclusions are present and the radius of the $j-th$ inclusion for $j = 25,...,47$ is equal to the radius of the $i-th$ inclusion, satisfying the formula $j = 47-i+1$.

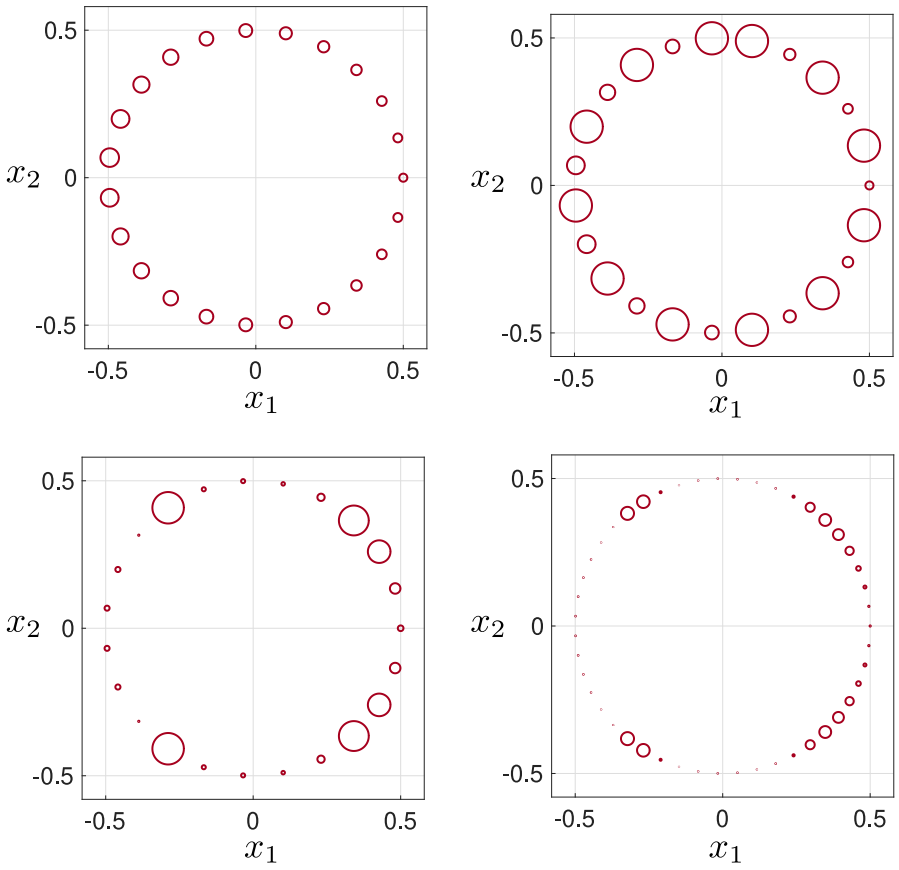

Figure 10.28: Visualization of the whole full-scale membrane geometry for configurations D1, D2, D3 and D4 in lexicographic order.

11 Wakes and paths of buoyancy-driven permeable disks: a linear stability approach

G. Vagnoli[1,2], G. A. Zampogna[1], S. Camarri[2], F. Gallaire[1], P. G. Ledda[1]
[1]Laboratory of Fluid Mechanics and Instabilities, École Polytechnique Fédérale de Lausanne, Lausanne, CH-1015, Switzerland,
[2]Dipartimento di Ingegneria Civile e Industriale, Università di Pisa, 56122 Pisa, Italy

In preparation

Author contributions P.G.L. conceived the project with input from F.G. and G.A.Z.. P.G.L. developed the theoretical framework and the numerical codes. P.G.L. supervised G. V. during his master thesis, performed with the provided tools. P.G.L. wrote the chapter with input from the coauthors.

The prediction of trajectories of falling or rising objects immersed in a viscous fluid is a key problem in fluid dynamics. Here, we perform a stability analysis with respect to azimuthal perturbations of the steady vertical path of a homogenous and isotropic permeable disk, modeled through homogenization theory. The flow across the disk is defined by two scalars, the filtrability and the slip number, which respectively represent the ability of the flow to pass through or slip tangentially to the disk. The relative velocity of the steady and axisymmetric flow associated with the vertical steady path presents a recirculation region detached from the body, which becomes smaller and disappears as the disk becomes more permeable. In analogy with the solid disk, one steady and three oscillatory unstable modes are identified, for low values of the filtrability. The neutral stability curves are modified by the filtrability, with frequent interactions between these modes. For large filtrability, the steady mode remains unstable in a certain range of Reynolds numbers, for all values of the disk inertia, but a further increase of filtrability reduces this range until quenching of the instability. An analysis of the spatial distribution of the eigenvectors reveals flow structures similar to the solid case, with an increase of the wake oscillations as the critical Reynolds numbers for the instabilities increase with the filtrability.

11.1 Introduction

We refer to Section 1.4 for a general introduction about instabilities of wake flows past bluff bodies, fluid-structure interaction of falling bodies, the flow modifications induced by porous structures and the modelization of the flow through a permeable membrane.

The instability of a falling solid disk was studied in Tchoufag et al. (2014). The authors expanded the flow equations by considering a steady and axisymmetric baseflow describing the vertical falling or rising trajectory, perturbed along the azimuthal direction with a normal mode expansion. The resulting linear stability problem is composed of the linearized Navier–Stokes equations coupled with Newton's equations for the rigid body motion. One stationary and three oscillatory unstable modes with azimuthal wavenumber $m = \pm 1$ were identified, for three different disk thicknesses. The variation of the body inertia results in a variety of behaviors, with marginal stability curves that often intersect, frequency jumps, and stabilization-destabilization sequences for fixed inertia and increasing Reynolds number, or vice versa.

While Chapters 9 and 10 investigated the modifications induced by the introduction of permeability on wake flows past fixed bodies, in this Chapter we employ the membrane model to study the bifurcations of the steady and axisymmetric flow of the vertical falling or rising path of a permeable disk. The Chapter is organized as follows. In Section 11.2, we describe the theoretical framework and the numerical implementation. Section 11.3 introduces the steady and axisymmetric flow of a falling/rising disk in vertical trajectory, which will serve as a baseflow for the stability analysis of Section 11.4. We investigate the role of filtrability and slip in modifying the neutral stability conditions in the parameters space and present the spatial distribution of the unstable modes.

11.2 Problem formulation

In this section, we introduce the configuration and the equations for the fluid-solid coupled problem. We consider a thin permeable disk composed of a periodic microstructure of characteristic length ℓ. We introduce the separation of scales parameter:

$$\varepsilon = \frac{\ell}{D}, \tag{11.1}$$

where D is the disk diameter (see figure 11.1). We assume that the thickness of the disk is of the same order as the microscopic characteristic length, i.e. $t/D = \alpha\varepsilon$, $\alpha = \mathcal{O}(1)$. Also, the disk is composed of a material of density ρ_b and we denote with $\mathcal{V}$ its volume. The disk is immersed in a viscous fluid of density ρ and viscosity μ. We denote with $\bar{\boldsymbol{v}}(\bar{t})$ and $\bar{\boldsymbol{\Omega}}(\bar{t})$ the translational and rotational velocities of the body during its trajectory, respectively. We introduce a cartesian reference frame $(\bar{x}, \bar{y}, \bar{z})$ for Newton's equations, while we employ cylindrical coordinates $(\bar{x}, \bar{r}, \bar{\theta})$ for the incompressible Navier-Stokes equations for the flow

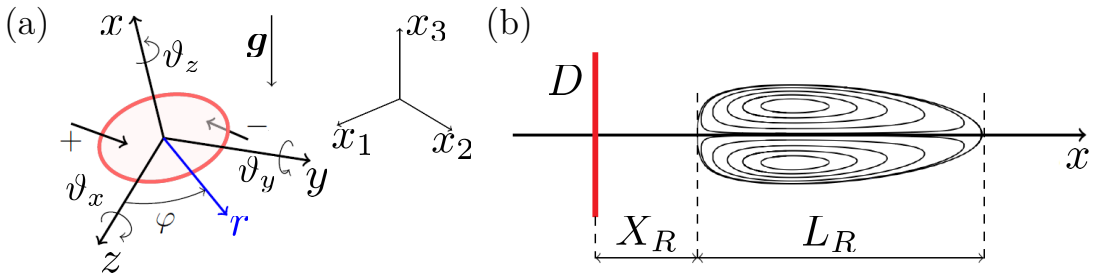

Figure 11.1: (a) Sketch of the falling disk, together with relevant quantities and the two employed reference frames. (b) Sketch of the relative velocity recirculation region past the permeable disk.

dynamics (see figure 11.1). Following Tchoufag et al. (2014), the flow equations are written in terms of absolute velocity, but with the above-defined coordinate systems rotating with the disk. The $\bar{x}$-direction, common to both coordinate systems, is aligned along the disk axis. The set of equations reads (Tchoufag et al., 2014):

$$\begin{aligned}
\nabla\cdot\bar{\boldsymbol{u}} &= 0,\\
\frac{\partial\bar{\boldsymbol{u}}}{\partial\bar{t}} + (\bar{\boldsymbol{u}}-\bar{\boldsymbol{w}})\cdot\nabla\bar{\boldsymbol{u}} + \bar{\boldsymbol{\Omega}}\times\bar{\boldsymbol{u}} &= -\frac{1}{\rho}\boldsymbol{\nabla}\bar{p} + \nu\nabla^2\bar{\boldsymbol{u}},\\
M\frac{\mathrm{d}\bar{\boldsymbol{v}}}{\mathrm{d}\bar{t}} + M\bar{\boldsymbol{\Omega}}\times\bar{\boldsymbol{v}} &= (M-\rho\mathcal{V})\boldsymbol{g} + \int_{\Gamma_d}\bar{\Sigma}\boldsymbol{n}\mathrm{d}\Gamma,\\
\bar{\boldsymbol{\mathcal{I}}}\cdot\frac{\mathrm{d}\bar{\boldsymbol{\Omega}}}{\mathrm{d}\bar{t}} + \bar{\boldsymbol{\Omega}}\times(\bar{\boldsymbol{\mathcal{I}}}\bar{\boldsymbol{\Omega}}) &= \int_{\Gamma_d}\bar{\boldsymbol{r}}\times(\bar{\Sigma}\boldsymbol{n})\mathrm{d}\Gamma,\\
\frac{\mathrm{d}\boldsymbol{\Xi}}{\mathrm{d}t} &= \bar{\boldsymbol{\Omega}},
\end{aligned} \tag{11.2}$$

where $\boldsymbol{w} = \boldsymbol{v} + \boldsymbol{\Omega}\times\mathbf{r}$, $\boldsymbol{\Xi}$ is the vector of the three Euler angles $(\vartheta_x, \vartheta_y, \vartheta_z)$, $M = \rho_b\mathcal{V}$ is the mass of the disk and $\boldsymbol{\mathcal{I}}$ is the inertia tensor. The problem is closed with the far field condition $\bar{\boldsymbol{u}} = \mathbf{0}$ and with the membrane condition at the disk interface, which is expressed in terms of the relative velocity $\boldsymbol{u}^r = \boldsymbol{u} - \boldsymbol{w}$, continuous across the interface:

$$\bar{\boldsymbol{u}}^r = \frac{\ell}{\mu}\bar{\mathcal{M}}\left[\bar{\Sigma}\left(\bar{\boldsymbol{u}}^{r-}, \bar{p}^-\right)\boldsymbol{n} - \bar{\Sigma}\left(\bar{\boldsymbol{u}}^{r+}, \bar{p}^+\right)\boldsymbol{n}\right] \quad \text{on } \Gamma_d, \tag{11.3}$$

where $\bar{\mathcal{M}}$ is a tensor whose components read:

$$\bar{\mathcal{M}}_{ij} = \bar{L}_t t_i t_j - \bar{F}_n n_i n_j, \tag{11.4}$$

and $\bar{L}_t$, $\bar{F}_n$ are evaluated by solving microscopic problems within the elementary unit cell, as described in Zampogna and Gallaire (2020) and in the previous chapter. Upon substitution of $\boldsymbol{u}^r = \boldsymbol{u} - \boldsymbol{w}$ and noting that $\bar{\boldsymbol{w}}^+ = \bar{\boldsymbol{w}}^-$ since the interface has no thickness at the macroscopic level, in the employed model, one obtains

$$\bar{\boldsymbol{u}} - \bar{\boldsymbol{w}} = \frac{\ell}{\mu}\bar{\mathcal{M}}\left[\bar{\Sigma}\left(\bar{\boldsymbol{u}}^-, \bar{p}^-\right)\boldsymbol{n} - \bar{\Sigma}\left(\bar{\boldsymbol{u}}^+, \bar{p}^+\right)\boldsymbol{n}\right] \quad \text{on } \Gamma_d \tag{11.5}$$

The proposed equation is formally analogous to the one in (Zampogna and Gallaire, 2020) and is valid as long as the inertia within the pores is negligible. In the impermeable case, the interface condition reduces to $\bar{\boldsymbol{u}} - \bar{\boldsymbol{w}} = \boldsymbol{0}$, i.e. zero relative velocity (no-slip condition). The equations for the fluid-structure coupled problem are non-dimensionalized with a characteristic falling or rising velocity U and the disk diameter D, leading to:

$$\begin{aligned}
&\boldsymbol{\nabla}\cdot\boldsymbol{u} = 0\\
&\frac{\partial \boldsymbol{u}}{\partial t} + (\boldsymbol{u}-\boldsymbol{w})\cdot\boldsymbol{\nabla}\boldsymbol{u} + \boldsymbol{\Omega}\times\boldsymbol{u} = -\boldsymbol{\nabla}p + \frac{1}{Re}\nabla^2\boldsymbol{u},\\
&\boldsymbol{w} = \boldsymbol{v} + \boldsymbol{\Omega}\times\boldsymbol{r},\\
&M^*\left(\frac{\mathrm{d}\boldsymbol{v}}{\mathrm{d}t} + \boldsymbol{\Omega}\times\boldsymbol{v}\right) - \frac{M-\rho\mathcal{V}}{\rho D^2U^2}\boldsymbol{g} = \int_{\Gamma_d}\Sigma(\boldsymbol{u},p)\boldsymbol{n}\mathrm{d}\Gamma,\\
&\boldsymbol{\mathcal{I}}\frac{\mathrm{d}\boldsymbol{\Omega}}{\mathrm{d}t} + \boldsymbol{\Omega}\times(\boldsymbol{\mathcal{I}}\boldsymbol{\Omega}) = \int_{\Gamma_d}\boldsymbol{r}\times[\Sigma(\boldsymbol{u},p)\boldsymbol{n}]\mathrm{d}\Gamma,\\
&\frac{\mathrm{d}\boldsymbol{\Xi}}{\mathrm{d}t} = \boldsymbol{\Omega},\\
&\lim_{\|\boldsymbol{r}\|\to\infty}\boldsymbol{u} = 0,\\
&\boldsymbol{u}-\boldsymbol{w} = \mathrm{Re}\,\mathcal{M}\left[\Sigma\left(\boldsymbol{u}^-,p^-\right)\boldsymbol{n} - \Sigma\left(\boldsymbol{u}^+,p^+\right)\boldsymbol{n}\right] \quad \text{on } \Gamma_d,
\end{aligned} \tag{11.6}$$

where $Re = \frac{\rho UD}{\mu}$ is the Reynolds number, M^* is the non-dimensional mass and $\boldsymbol{\mathcal{I}}$ is the dimensionless inertia tensor, whose non-zero components read $\boldsymbol{\mathcal{I}}_{yy} = \boldsymbol{\mathcal{I}}_{zz} = \mathcal{I}^* = I_{yy}/(\rho D^5)$, $\boldsymbol{\mathcal{I}}_{xx} = I_{xx}/(\rho D^5)$. The above-defined tensor $\mathcal{M}$, specialized to the considered reference frame and in non-dimensional form, reads:

$$\mathcal{M} = \begin{pmatrix} -\mathcal{F} & 0 & 0\\ 0 & \mathcal{L} & 0\\ 0 & 0 & \mathcal{L}, \end{pmatrix} \tag{11.7}$$

under the assumption of homogenous and isotropic microscopic structure. We introduce the filtrability and the slip numbers, $\mathcal{F}$ and $\mathcal{L}$, which respectively quantify the ability of the flow to pass through or slip on the interface. As already mentioned, the flow through the membrane is modeled under the assumption of negligible thickness, i.e. $\varepsilon \ll 1$. We thus neglect the $\mathcal{O}(\varepsilon^2)$ terms and the integral contributions along the thickness in Newton's equations by setting $\varepsilon = 0$ in equations (11.6).

We study the linear stability of the steady and axisymmetric flow resulting from a steady vertical falling or rising path of the permeable disk. The following decomposition is introduced ($\varsigma \ll 1$):

$$\begin{aligned}
[\boldsymbol{u},p] &= [\boldsymbol{U}(x,r),P(x,r)] + \varsigma[\boldsymbol{u}'(x,r,\theta),p'(x,r,\theta)],\\
\boldsymbol{v}(t) &= -\mathbf{e}_x + \varsigma\boldsymbol{v}'(t), \quad \boldsymbol{\Omega}(t) = \varsigma\boldsymbol{\omega}'(t), \quad \boldsymbol{\Xi}(t) = \varsigma\boldsymbol{\xi}'(t).
\end{aligned} \tag{11.8}$$

For small angles, $\boldsymbol{g} = -g\mathbf{e}_x + \varsigma g\left(\vartheta_y \mathbf{e}_z - \vartheta_z \mathbf{e}_y\right)$. Upon substitution in equation (11.6), the flow equations at order $\mathcal{O}(1)$ read:

$$\begin{aligned}
&\boldsymbol{\nabla}\cdot\boldsymbol{U} = 0\\
&(\boldsymbol{U}+\mathbf{e}_x)\cdot\nabla\boldsymbol{U} + \nabla P - \frac{1}{\mathrm{Re}}\nabla^2\boldsymbol{U} = \mathbf{0}\\
&\lim_{\|\mathbf{r}\|\to\infty}\boldsymbol{U} = \mathbf{0}\\
&\boldsymbol{U}+\mathbf{e}_x = \mathrm{Re}\,\mathcal{M}\left[\Sigma\left(\boldsymbol{U}^-, P^-\right)\mathbf{n} - \Sigma\left(\boldsymbol{U}^+, P^+\right)\mathbf{n}\right] \quad \text{on } \Gamma_d,
\end{aligned} \tag{11.9}$$

which are the steady and axisymmetric Navier-Stokes equations for the baseflow associated with the vertical falling of the disk. In the case of vertical and steady motion, the flow equations are analogous to the fixed body case, if the relative velocity $\boldsymbol{U}^r = \boldsymbol{U} + \mathbf{e}_x$ is considered. Newton's equations at $\mathcal{O}(1)$ relate the drag coefficient C_D with the non-dimensionalized gravity term:

$$\frac{\pi}{8}C_D = \frac{M-\rho\mathcal{V}}{\rho D^2 U^2}g. \tag{11.10}$$

From this result, we also distinguish between the falling and rising cases, which depend on $M-\rho\mathcal{V}$. Since $M=\rho_b\mathcal{V}$, the gravity term depends on the sign of $\rho_b/\rho - 1 = \mathcal{R}-1$, which gives a falling vertical path for $\mathcal{R}>1$, and vice versa. From the point of view of the study of instabilities, there is no difference between the two cases, since they correspond to an inversion of the considered reference frames.

At order $\mathcal{O}(\varsigma)$, one obtains the linearized Navier Stokes and Newton's equations:

$$\begin{aligned}
&\nabla\cdot\boldsymbol{u}' = 0\\
&\frac{\partial\boldsymbol{u}'}{\partial t} + (\boldsymbol{U}+\boldsymbol{e}_x)\cdot\nabla\boldsymbol{u}' + (\boldsymbol{u}'-\boldsymbol{w}')\cdot\nabla\boldsymbol{U} + \boldsymbol{\omega}'\times\boldsymbol{U} = -\nabla p' + \frac{1}{Re}\nabla^2\boldsymbol{u}'\\
&\boldsymbol{w}' = \boldsymbol{u}' + \boldsymbol{\omega}'\times\boldsymbol{r}\\
&M^*\left(\frac{\mathrm{d}\boldsymbol{v}'}{\mathrm{d}t} - \boldsymbol{\omega}'\times\boldsymbol{e}_x\right) - \frac{\pi C_D}{8}\left(\theta_y'\boldsymbol{e}_z - \theta_z'\boldsymbol{e}_y\right) = \int_{\Gamma_d}\Sigma(\boldsymbol{u}', p')\boldsymbol{n}\mathrm{d}\Gamma\\
&\boldsymbol{\mathcal{I}}\frac{\mathrm{d}\boldsymbol{\omega}'}{\mathrm{d}t} = \int_{\Gamma_d}\boldsymbol{r}\times[\Sigma(\boldsymbol{u}', p')\boldsymbol{n}]\mathrm{d}\Gamma\\
&\frac{\mathrm{d}\boldsymbol{\xi}'}{\mathrm{d}t} = \boldsymbol{\omega}'\\
&\lim_{\|\boldsymbol{r}\|\to\infty}\boldsymbol{u}' = 0, \quad \boldsymbol{u}'-\boldsymbol{w}' = Re\mathcal{M}\left[\Sigma\left(\boldsymbol{u}'^-, p'^-\right)\boldsymbol{n} - \Sigma\left(\boldsymbol{u}'^+, p'^+\right)\boldsymbol{n}\right] \quad \text{on } \Gamma_d
\end{aligned} \tag{11.11}$$

We consider a normal mode expansion of the perturbation of azimuthal wavenumber m and complex growth rate $\sigma\in\mathbb{C}$:

$$\begin{aligned}
\boldsymbol{u}'(x,\boldsymbol{r},t) = \hat{\boldsymbol{u}}(x,r)\mathrm{e}^{\mathrm{i}m\varphi+\sigma t}, \quad p'(x,\boldsymbol{r},t) = \hat{p}(x,r)\mathrm{e}^{\mathrm{i}m\varphi+\sigma t}\\
\boldsymbol{v}'(t) = \hat{\boldsymbol{v}}\mathrm{e}^{\sigma t}, \quad \boldsymbol{\omega}'(t) = \hat{\boldsymbol{\omega}}\mathrm{e}^{\sigma t}, \quad \boldsymbol{\xi}'(t) = \hat{\boldsymbol{\xi}}\mathrm{e}^{\sigma t}.
\end{aligned} \tag{11.12}$$

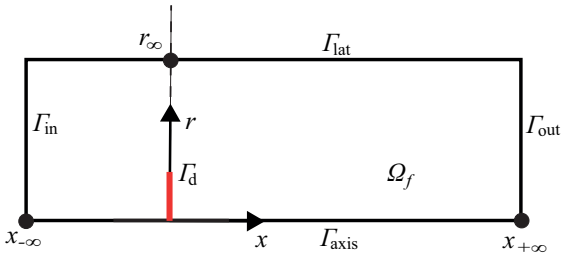

Figure 11.2: Sketch of the computational domain.

In the solid case, (Tchoufag et al., 2014), modes with $m = 0$ are stable. Besides, modes with $|m| > 2$ modes do not influence the path linear instability since the integral contribution in Newton's equations is zero, and thus the wake dynamics is decoupled from the disk's one. In the following, we focus on the modifications of the bifurcations with wavenumber $m = \pm 1$ induced by the membrane filtrability and slip. We exploit the azimuthal symmetry in the wavenumber $m = \pm 1$ and reduce the number of unknowns. The assumption $m = \pm 1$ implies, by symmetry, $\hat{v}_x = \hat{\vartheta}_x = 0$, and thus $\boldsymbol{\mathcal{I}}_{xx}$ is not involved in the dynamics. The projections of the linearized Newton's equations along y and z are combined, and a single equation is obtained. This is achieved by introducing the variables (Jenny et al., 2004):

$$\hat{v}_\pm = \hat{v}_y \mp \mathrm{i}\,\hat{v}_z, \quad \hat{\omega}_\pm = \hat{\omega}_z \pm \mathrm{i}\hat{\omega}_y, \quad \hat{\vartheta}_\pm = \hat{\vartheta}_z \pm \mathrm{i}\hat{\vartheta}_y, \tag{11.13}$$

depending on the chosen sign for $m = \pm 1$. The developments are formally analogous to the ones reported in Tchoufag et al. (2014), to which we refer for the general form of the linearized eigenvalue problem, except for the interface boundary condition at the disk interface, which reads:

$$\hat{\boldsymbol{u}} - \frac{\hat{v}_\pm}{2}\left(\boldsymbol{e}_r \pm i\boldsymbol{e}_\varphi\right) + \frac{r\hat{\omega}_\pm}{2}\boldsymbol{e}_x = \mathrm{Re}\,\mathcal{M}\left[\Sigma_\pm\left(\hat{\boldsymbol{u}}^-, \hat{p}^-\right)\boldsymbol{n} - \Sigma_\pm\left(\hat{\boldsymbol{u}}^+, \hat{p}^+\right)\boldsymbol{n}\right] \quad \text{on } \Gamma_d, \tag{11.14}$$

where

$$\Sigma_\pm(\hat{\boldsymbol{u}}, \hat{p}) = -\hat{p}\boldsymbol{I} + \mathrm{Re}\left(\nabla_\pm \hat{\boldsymbol{u}} + \nabla_\pm \hat{\boldsymbol{u}}^T\right), \quad \nabla_\pm \boldsymbol{F} = \begin{bmatrix} \frac{\partial F_r}{\partial r} & \frac{\partial F_\varphi}{\partial r} & \frac{\partial F_z}{\partial r} \\ \frac{\pm F_r}{r} - \frac{F_\varphi}{r} & \frac{\pm \mathrm{i}F_\varphi}{r} + \frac{F_r}{r} & \frac{\pm \mathrm{i}F_z}{r} \\ \frac{\partial F_r}{\partial z} & \frac{\partial F_\varphi}{\partial z} & \frac{\partial F_z}{\partial z} \end{bmatrix} \tag{11.15}$$

The result is an eigenvalue problem in the form

$$\sigma \mathbf{B}\hat{\mathbf{q}} + \mathbf{L}\left(m = \pm 1, Re, M^*, \mathcal{I}^*, \mathcal{F}, \mathcal{L}, \mathbf{Q}\right)\hat{\mathbf{q}} = \mathbf{0}, \quad \mathbf{Q} = [\boldsymbol{U}, P], \quad \hat{\mathbf{q}} = \left[\hat{\boldsymbol{u}}, \hat{p}, \hat{v}_\pm, \hat{\omega}_\pm, \hat{\vartheta}_\pm\right] \tag{11.16}$$

The baseflow equations are governed by three parameters $(Re, \mathcal{F}, \mathcal{L})$ while the stability problem, upon choice of $m = \pm 1$, depends also on the parameters M^* and $\mathcal{I}^*$.

The baseflow and linear stability equations are solved in a rectangular domain corresponding to a section φ =const, for the variables (x, r) (see figure 11.2). We impose zero velocity at the

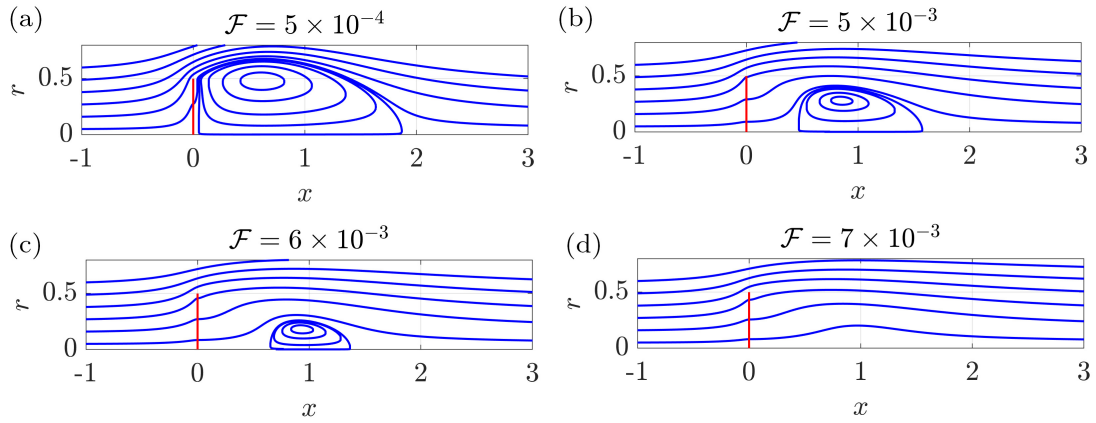

Figure 11.3: Streamlines of the baseflow relative velocity $\boldsymbol{U} + \mathbf{e}_x$ for $Re = 85$, $\mathcal{L} = 10^{-4}$, and different values of $\mathcal{F}$.

boundary located at $x = x_{-\infty}$ and $r = r_{\infty}$, and the free-stress condition at $x = x_{+\infty}$, together with the membrane interface condition at $(x = 0, r < 0.5)$. The numerical implementation of the weak form of the various equations is performed in COMSOL Multiphysics, with Taylor-Hood elements for the velocity and pressure fields. The coupled Newton's equations are implemented as ODE problems. The integrals at the disk surface are evaluated through a fourth-order Gaussian quadrature rule. We employ a domain decomposition method for the flow upstream and downstream of the disk, and at $x = 0$ we impose the continuity of stresses and velocity for $r > 0.5$. We validated the algorithm against the stability results for a solid disk with thickness 10^{-4} by including a solid region in $0 < x < 10^{-4}$ and $r < 0.5$, and performed a mesh convergence analysis for the permeable and infinitely thin disk for large values of the Reynolds number and filtrability. The results are reported in Appendix 11.6.1.

11.3 Baseflow

We begin our analysis by describing the baseflow results. Figure 11.3 shows the streamlines of the relative velocity $\boldsymbol{U} + \mathbf{e}_x$ for $Re = 85$, $\mathcal{L} = 10^{-4}$ and different values of $\mathcal{F}$. In general, the flow is characterized by a toroidal recirculation region, reminiscent of the one of the fixed solid disk. The flow at low filtrabilities (subfigure (a)) is characterized by a recirculation region very similar to the solid case, with a slight detachment from the rear of the body. An increase in $\mathcal{F}$ (subfigures (b,c)) leads to a slight downstream displacement of the recirculation region, which decreases its dimensions, until it disappears (subfigure (d)).

These observations are quantitatively confirmed by figure 11.4(a), which presents the iso-contours of the length of the recirculation region L_R as a function of Re and $\mathcal{F}$, for different values of $\mathcal{L}$. An increase of the filtrability, with fixed Re, leads to a decrease of L_R. The length of the recirculation region instead presents a non-monotonous behavior with Re, in the vicinity of the iso-level $L_R = 0$. For $\mathcal{F} = 7 \times 10^{-4}$, and $Re < 25$, the flow does not present a recirculation

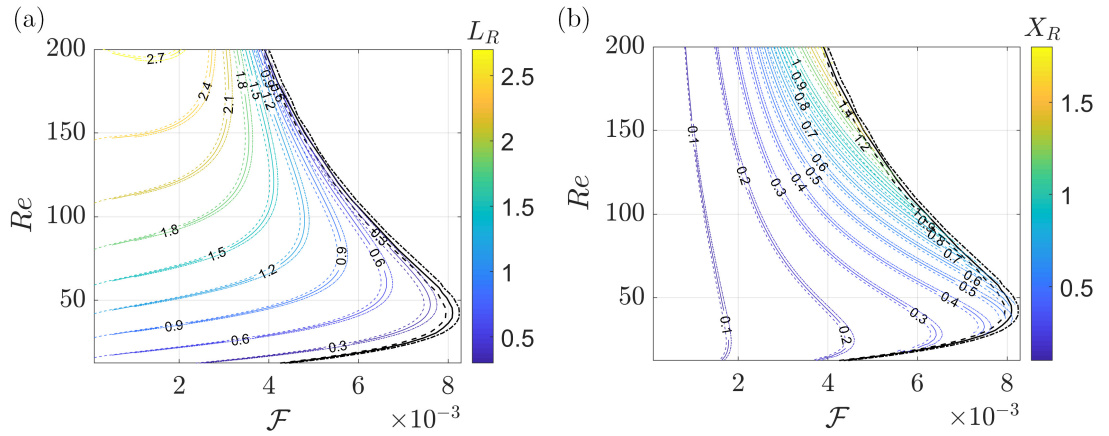

Figure 11.4: Iso-contours of (a) the length of the recirculation region L_R and (b) of the distance X_R between the disk and the recirculation region, as functions of Re and $\mathcal{F}$, for different values of $\mathcal{L}$: $\mathcal{L} = 10^{-4}$ (dashed), $\mathcal{L} = 5 \times 10^{-4}$ (solid), $\mathcal{L} = 10^{-3}$ (dot-dashed). The black lines denote the iso-levels $L_R = 0$, for the corresponding cases.

region. In the range $25 < Re < 75$, L_R increases, reaches a maximum and decreases until $L_R = 0$, at $Re \approx 75$. The recirculation region becomes slightly larger as $\mathcal{L}$ increases, for fixed $\mathcal{F}$ and Re. As a consequence, the iso-contour $L_R = 0$ slightly moves toward larger filtrabilities, together with the critical values of $\mathcal{F}$ beyond which $L_R = 0$, independent of Re. Figure 11.4(b) shows the iso-contours of the distance X_R between the disk and the recirculation region. While X_R monotonically increases with $\mathcal{F}$, an analogous non-monotonous behavior with Re is observed, with an initial decrease followed by an increase. The downstream displacement is always of the order of the diameter of the disk, and it does not exceed $X_R \sim 1.5$. We conclude our characterization of the baseflow with the parameters by reporting, in figure 11.5, the iso-levels of the drag coefficient C_D. An increase of the Reynolds number leads to a monotonous decrease of C_D. At low values of the Reynolds number, C_D monotonically decreases with $\mathcal{F}$. However, for $Re \sim 80$, a slight increase of the drag coefficient with $\mathcal{F}$ is observed. At larger Reynolds numbers, a peak in the iso-contours is visible, highlighting a non-monotonous behavior of C_D with $\mathcal{F}$. At very large filtrabilities, beyond the iso-level $L_R = 0$, the drag coefficient monotonically decreases and goes asymptotically to zero. Variations of $\mathcal{L}$ do not qualitatively influence the observed trends.

The baseflow presents a detached recirculation region which becomes smaller and moves downstream as the filtrability increases; an increase in $\mathcal{L}$ leads to a counter-intuitive slight increase of the length of the recirculation region. This behavior can be qualitatively explained in the light of the considered geometry. An increase in $\mathcal{F}$ implies a larger attainable streamwise velocity. As a consequence, the flow streamlines are less constrained to pass around the body and the flow becomes more parallel. This leads to a reduction of the vertical velocity and thus of the counterflow generated by the separation at the disk edge. An increase in $\mathcal{L}$ with fixed $\mathcal{F}$ leads to the opposite behavior. While the ability of the flow to pass through the body is not

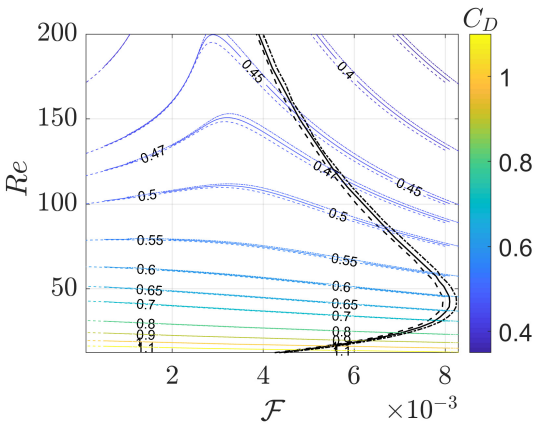

Figure 11.5: Iso-contours of the drag coefficient C_D as a function of Re and $\mathcal{F}$, for different values of $\mathcal{L}$: $\mathcal{L} = 10^{-4}$ (dashed), $\mathcal{L} = 5 \times 10^{-4}$ (solid), $\mathcal{L} = 10^{-3}$ (dot-dashed). The black lines denote the iso-levels $L_R = 0$, for the corresponding cases.

modified, larger transversal velocities can be attained at the disk surface because of the slip condition. This leads to an increase in the size of the recirculation region since the separation is stronger. However, the effect of $\mathcal{L}$ is mild and does not strongly modify the qualitative behaviors.

Variations of filtrability and slip induce a re-organization of the solid and void fractions of the disk, thus modifying the values of M^* and $\mathcal{I}^*$. These variations are strongly related to the considered microscopic structure. Since the microscopic geometry is not specified, M^* and $\mathcal{I}^*$ are considered as independent parameters. In the following, we fix $M^* = 16\mathcal{I}^*$, as in the solid case. Also, we consider $\mathcal{L} = 10^{-4}$ and investigate the role of $\mathcal{F}$ in modifying the marginal stability curves of the freely-falling disk. Some relevant results for varying $\mathcal{L}$ and M^* are reported in Appendix 11.6.2.

11.4 Stability analysis

11.4.1 Marginal stability curves in the $(\mathcal{I}^*, Re)$ plane

11.4.1.1 The modes of the impervious case

We begin our analysis by presenting the neutral curves, i.e. the values of $(\mathcal{I}^*, Re)$ associated with zero growth rate of an eigenvalue, for different values of $\mathcal{F}$. Following the results and notation of Tchoufag et al. (2014), figure 11.6 shows (a) the neutral curves of the various modes which become unstable in the $(\mathcal{I}^*, Re)$ plane, for $\mathcal{F} = 10^{-4}$, (b) the associated Strouhal numbers $St = \mathrm{Im}(\sigma)/(2\pi)$ at the marginal stability and (c) the real part of the streamwise component of the velocity field, rescaled with $\hat{\vartheta}_{\pm}$. In analogy with the solid case, at very low filtrability, three oscillating (black, red and blue) and one non-oscillating (*steady*, green) unstable global modes are observed. Modes with label F are also called "fluid" modes and

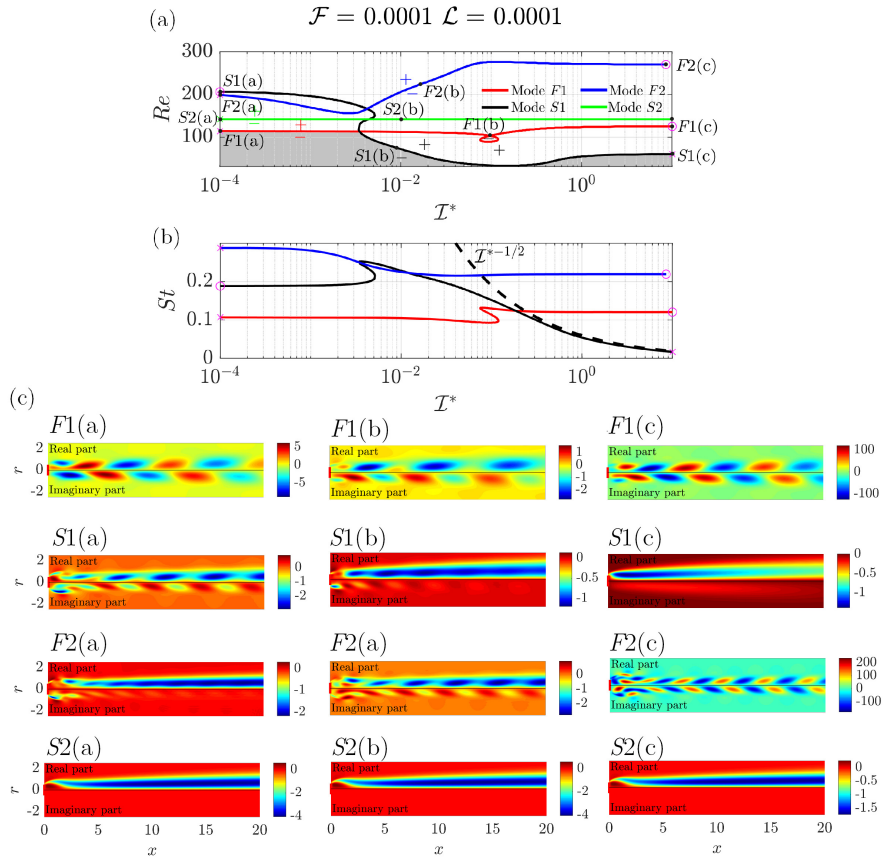

Figure 11.6: (a) Neutral curves in the $(\mathcal{I}^*, Re)$ plane, for $\mathcal{F} = 10^{-4}$, $\mathcal{L} = 10^{-4}$ and $M^* = 16\mathcal{I}^*$. (b) Strouhal number $St = \mathrm{Im}(\sigma)/(2\pi)$ following the neutral curves in the $(\mathcal{I}^*, Re)$ plane. The symbols "+" and "-" denote, respectively, unstable and stable regions for the corresponding eigenvalue. (c) Real part of the streamwise component of the velocity field $\hat{\boldsymbol{u}}$, rescaled with $\hat{\vartheta}_{\pm}$, for different cases reported in the subfigure (a).

coincide with the ones given by the stability analysis of the wake past a fixed disk, for $\mathcal{I}^* \to \infty$, in opposition to the "solid" modes, labeled with S, which are present only in the coupled problem. We denote with "+" and "-" unstable and stable regions for the corresponding eigenvalues. At these low values of $\mathcal{F}$ and $\mathcal{L}$, the stability map and the modes' structure are in line with the impermeable disk case of Tchoufag et al. (2014).

The strength of the fluid-structure interaction, for oscillatory instabilities, can be qualitatively assessed by considering the wake re-organization between the real and imaginary parts of the fluid velocity field, rescaled with $\hat{\vartheta}_{\pm}$. This re-scaling allows identifying in the real and imaginary parts two different instants in the linear dynamics of the wake, i.e. the ones with maximum $\hat{\vartheta}_y$ and $\hat{\vartheta}_z$. When the interaction is strong, a re-organization of the wake between real and imaginary parts is observed. In particular, one can identify so-called "SPT" (sign preserving type) and "SAT" (sign alternating type) disturbances. The first is an elongated wake of constant sign moving downstream, reminiscent of the steady instability of a fixed disk,

while the second shows the alternation of positive and negative structures which reduce their amplitude downstream. SPT structures can be related to the variation of the disk orientation, with a weak effect on the wake, while SAT disturbances can be seen as a footprint of the wake instability (Tchoufag et al., 2014). The dominance of one of these structures on the other, or their coexistence, can be seen as a manifestation of the segregation or interaction between disk free-fall (or rise) and wake dynamics. This picture helps to give a rationale for the instability. A second comparison between the various modes to assess the relative importance of the fluid-structure interaction can be made by considering the amplitude of the wake oscillations rescaled with $\hat{\vartheta}_{\pm}$: larger values imply a stronger effect on the wake than on the dynamics of the object.

Mode $F1$ (red lines) is an oscillatory mode whose neutral curve is almost independent of the inertia $\mathcal{I}^*$. Also the Strouhal number shows mild variations with $\mathcal{I}^*$. Cases $F1$(a)-(c) report the spatial distribution of mode $F1$ for different values of inertia. The eigenvectors are similar to the ones associated with the unsteady bifurcation of the steady and axisymmetric wake past a fixed disk (Meliga et al., 2009). Mode $F1$ indeed is identified as the first unsteady bifurcation of the fixed disk in the limit $\mathcal{I}^* \to \infty$. In all cases, the real and imaginary parts of the eigenmode present decaying structures of alternating sign moving downstream. The increase of inertia does not strongly modify the spatial distribution, but an increase of the intensity of the rescaled eigenvector for the fluid streamwise velocity is observed. However, while at low and large inertia the mode presents almost symmetric structures of alternating sign both in the real and imaginary parts, at intermediate inertia this symmetry is less pronounced, with a re-organization of the wake past the disk.

Mode $S1$ instead shows strong variations with $\mathcal{I}^*$ of the critical Reynolds number for the instability. The neutral curve is initially decreasing, reaches a minimum in the Reynolds number and increases again toward an asymptotic value. For $\mathcal{I}^* \to \infty$, mode $S1$ frequency asymptotically follows the law $St \sim \mathcal{I}^{*-1/2}$. The eigenvectors (cases $S1$(a,b)) show strong differences between the real and imaginary parts. While the real part is predominantly characterized by an elongated wake of constant sign moving downstream, the imaginary part presents structures of alternating sign of lower amplitude. In case $S1$(c), the imaginary part is almost absent.

The blue line is the neutral curve of another oscillating mode labeled $F2$. According to Tchoufag et al. (2014), this mode is retrieved also in the fixed disk case. At large inertia (case $F1$(c)), mode $F2$ strongly resembles mode $F1$, but with a larger frequency and thus oscillation of lower spatial wavelength in the wake.

The green line represents the marginal stability curve of the steady mode $S2$, which is independent of M^* and $\mathcal{I}^*$ (Tchoufag et al., 2014). The eigenvector presents a wake with zero imaginary part.

For case $F1$(b), we observe a slight fluid-structure coupling for mode $F1$, while cases $F1$(a,c) show a much lower coupling, since the wake distributions of the real and imaginary parts are very similar SAT disturbances. In case $F1$(c), the amplitude of the fluid streamwise velocity is

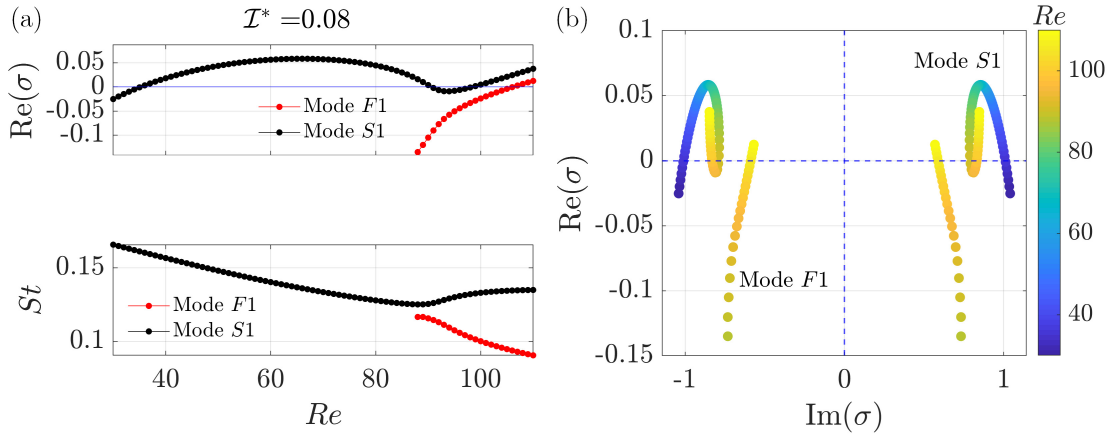

Figure 11.7: Evolution of the modes $F1$ and $S1$ with Re, for fixed $\mathcal{F} = 10^{-4}$, $\mathcal{L} = 10^{-4}$, $\mathcal{I}^* = 0.08$ and $M^* = 16\mathcal{I}^*$. (a) Variation of the real part (top) and of the Strouhal number $St = \mathrm{Im}(\sigma)/(2\pi)$ (bottom). (b) Eigenvalues of the modes $F1$ and $S1$ in the complex plane, for different values of Re.

also very large, thus suggesting a dominance of the wake instability, with small perturbations on the disk dynamics. For mode $S1$ (cases $S1$(a,b)), the real and imaginary parts are, with a good approximation, SPT and SAT disturbances, respectively. This implies a re-organization of the wake and thus a strong fluid-structure coupling. However, observing the amplitude of the real and imaginary parts, the dynamics seems dominated by the disk falling rather than the wake instability, in particular at large $\mathcal{I}^*$. Mode $F2$ shows, at low and intermediate inertia, a dominance of the SPT disturbances and thus of the disk path instability. At large inertia, SAT patterns dominate, highlighting the predominance of the wake instability. This analysis does not apply to the stationary mode, since its imaginary part is identically zero. Following Tchoufag et al. (2014), a zero imaginary part, rescaled with $\hat{\vartheta}_\pm$, implies $\hat{\vartheta}_z = 0$ and thus an exponentially growing tilting of the body, whose wake is merely a consequence of the disk inclination.

We note the presence of a destabilization-stabilization sequence with Re for mode $S1$, at $\mathcal{I}^* \approx 4 \times 10^{-3}$. An interesting feature is the apparent loop in the red marginal stability curve. The mode inside the region defined by the loop is stable, and is associated with a restabilization of the $S1$ mode, see figure 11.7 for the evolution of the modes $S1$ and $F1$ with Re, for fixed inertia $\mathcal{I}^* = 0.08$. These phenomena are characterized by sudden changes in the Strouhal number, as reported in the bottom plot of figure 11.6. We prefer to keep the red color for the loop following Tchoufag et al. (2014), but the symbols "+" and "-" denoting unstable and stable regions are colored in black, i.e. the color of mode $S1$.

The collective marginal stability curve, for all modes, is defined by the region lying below the lower limit defined by these curves. In this case, for $\mathcal{I}^* < 3.5 \times 10^{-3}$, the collective marginal stability curve is given by mode $F1$ (red). The black and red curves intersect and the collective marginal stability is given by the mode $S1$ (black curve), for larger $\mathcal{I}^*$. The collective stable

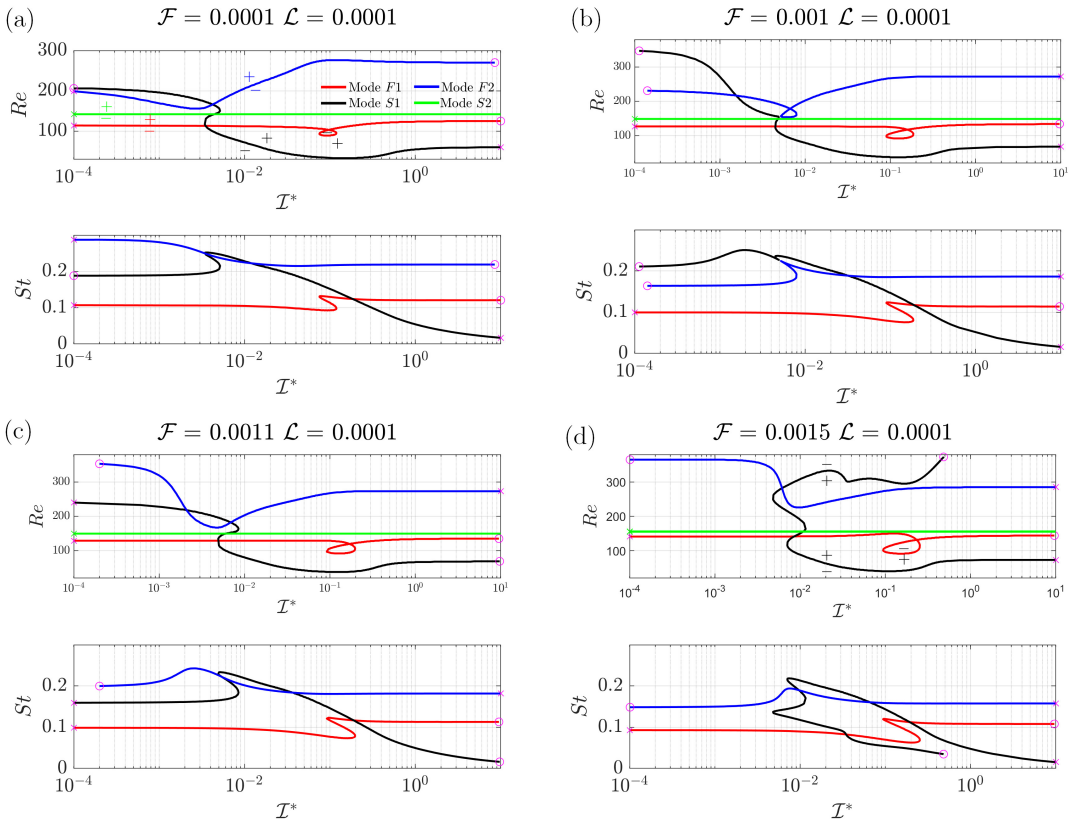

Figure 11.8: Marginal stability curves for an permeable disk as a function of $\mathcal{I}^*$ for different values of $\mathcal{F}$, $\mathcal{L} = 10^{-4}$ and $M^* = 16\mathcal{I}^*$. Critical Reynolds number (on the top) and Strouhal number (on the bottom). The magenta symbols help to identify the values of Strouhal number associated with the marginal stability curves.

region is thus the grey area highlighted in figure 11.6(a).

11.4.1.2 The effect of the filtrability

Variations of the filtrability $\mathcal{F}$ induce profound changes in the marginal stability curves. The three figures 11.8-11.10 show the evolution of the neutral curves in the $(\mathcal{I}^*, Re)$ plane, for different values of $\mathcal{F}$, $\mathcal{L} = 10^{-4}$ and $M^* = 16\mathcal{I}^*$. Since the neutral curves intersect, interact and exchange branches, with very similar spatial distributions of the eigenvectors in these regions, we keep the nomenclature as clear as possible labeling with continuity the behavior at large inertia, which appears to be more regular. We now present some of the behaviors of the neutral curves as filtrability increases. Figure 11.8(b) shows the neutral curves for $\mathcal{F} = 10^{-3}$. While modes $F1$ and $S2$ are not qualitatively influenced in comparison with case $\mathcal{F} = 10^{-4}$, modes $S1$ and $F2$ interact in the region of the destabilization-stabilization sequence. The two curves present the same value of the critical Reynolds number for the instability and Strouhal number, and thus the eigenvalues coincide. At (c) $\mathcal{F} = 1.1 \times 10^{-3}$, the modes exchange the branches

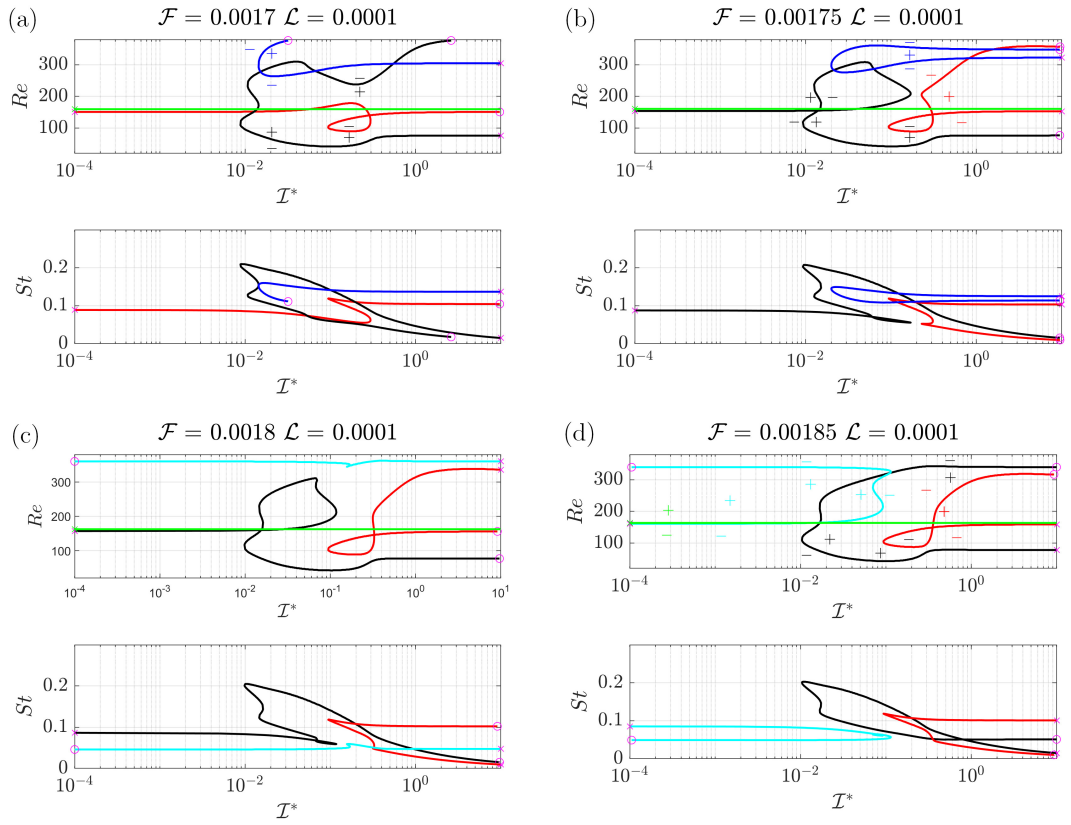

Figure 11.9: Same as figure 11.8 for different values of $\mathcal{F}$.

located at low inertia. At the same time, we observe an increase in the size of the stable region identified by the loop. The neutral curves are again modified with filtrability, as shown in (c,d). Interestingly, in 11.8(d), Mode $S1$ is stable independently of Re, for $\mathcal{I}^* < 5 \times 10^{-3}$. For larger values of inertia, intricate destabilization-stabilization sequences can be observed; the mode also appears to be stable for large Re and $\mathcal{I}^* < 5 \times 10^{-1}$.

Increasing again the filtrability, several exchanges between branches are observed, see figure 11.9. As reported in figure 11.9(b) for $\mathcal{F} = 1.75 \times 10^{-3}$, Mode $S1$ now shows a second stable loop region in the range $10^{-2} < \mathcal{I}^* < 10^{-1}$ and destabilizes again for all values of inertia. We observe several destabilization-stabilization sequences, increasing Re with fixed $\mathcal{I}^* = 1.5 \times 10^{-2}$. Besides, the stable loop region highlighted in red is still present in the parameters space. As a result of these interactions, Mode $F1$ is unstable only at large values of inertia, and exhibits a destabilization-stabilization sequence with Re. Similarly, Mode $F2$ is characterized by a narrow band of instability, which is present only for $\mathcal{I}^* > 2 \times 10^{-2}$. For lower values of $\mathcal{I}^*$, the instability related to mode $F2$ is absent. In this case, the primary destabilization is due to Mode $S1$, independently of $\mathcal{I}^*$.

An increase in the filtrability number $\mathcal{F}$ leads to shrinking of this band of instability, and for $\mathcal{F} = 0.0018$ the neutral curve of mode $F2$ disappears from our range of parameters. However,

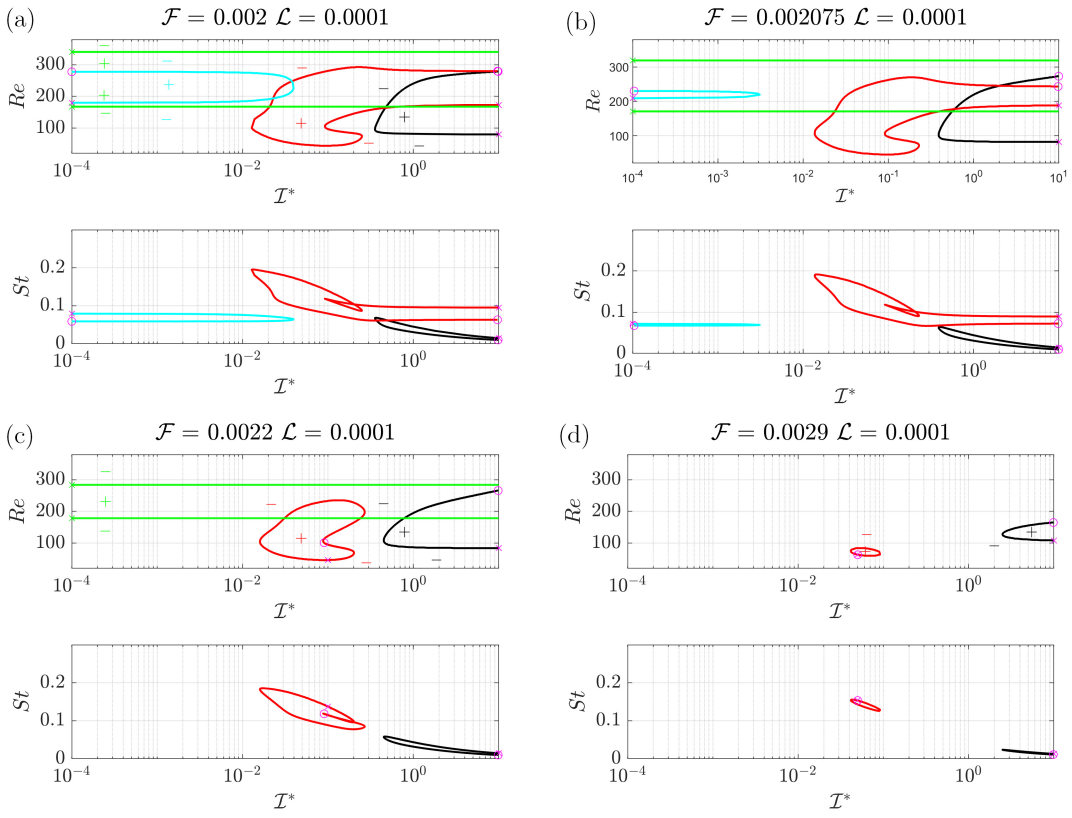

Figure 11.10: Same as figure 11.8 for different values of $\mathcal{F}$.

another mode becomes unstable in the considered parameter range, reported in cyan (see figure 11.9(c)). We performed a linear stability analysis of the fixed permeable disk with $\mathcal{F} = 1.8 \times 10^{-3}$ and $Re = 360$, retrieving this bifurcation. Therefore, we label this mode as mode $F3$. Modes $S1$ and $F3$ interact with mode $F1$ and, at $\mathcal{F} = 1.85 \times 10^{-3}$ (11.9(d)), a new configuration of the neutral curves is reached. In particular, the second stable loop of Mode $S1$ disappears. Mode $F3$ is unstable for values $\mathcal{I}^*$ smaller than approximately 0.1, with the already highlighted destabilization-stabilization sequence for increasing Re. for $\mathcal{I}^* \approx 0.1$, the sequence is characterized by two alternating destabilizations and stabilizations. Mode $S1$ and $F1$ show unstable regions for $\mathcal{I}^* > 10^{-2}$ and $\mathcal{I}^* > 3 \times 10^{-1}$, respectively. The stable loop region highlighted in red is still present in the parameters space. Still focusing on the case of figure 11.9(d), the primary destabilization is due to modes $S2$ and $S1$ at low and large values of $\mathcal{I}^*$, respectively.

Interestingly, for $\mathcal{F} = 1.925 \times 10^{-3}$ (figure 11.10(a)), also Mode $S2$ is stable at large values of Re and thus all modes exhibit the same destabilization-stabilization behavior. The loop in the marginal stability curve disappears, while we observe a large stable region for $\mathcal{I}^* \approx 0.3$. The unstable regions related to the three oscillating modes progressively shrink increasing filtrability, as shown in figure 11.10(b).

Increasing again filtrability, mode $F3$ is always stable and its neutral curve disappears from the $(Re,\mathcal{I}^*)$ plane (figure 11.10(c)). Figure 11.10(d) shows very small unstable regions associated with modes $F1$ and $S1$, for $\mathcal{F} = 0.0029$. Eventually, for $\mathcal{F} \sim 3 \times 10^{-3}$ all modes are damped, at least in the range of the considered parameters.

Therefore, a common behavior of the neutral curves associated with the unsteady bifurcations is the formation of a stable region at low (modes $F1$, $F2$ and $S1$) or at large (mode $F3$) inertia. Neutral branches thus present an overall turning point which defines one, or more, destabilization-stabilization sequences with Re. The destabilization and stabilization branches of the neutral curves approach until the disappearance of the unstable region of the related mode. The "longest surviving" mode, for large $\mathcal{F}$ and large $\mathcal{I}^*$, is mode $S1$. A linear stability analysis for the fixed disk (Appendix 11.6.3) shows that the unsteady mode presents the inversion point of the marginal stability curve for $\mathcal{F} \approx 2.2 \times 10^{-3}$. This is confirmed by figure 11.10(c,d), in which mode $F1$ is stable at large inertia.

11.4.2 The collective marginal stability curves

The bifurcations highlighted here are obtained in a linear framework. Linear stability analysis is accurate in predicting the threshold at the first bifurcation encountered by the baseflow, e.g. increasing the Reynolds number. In figure 11.11(a), we report the collective marginal stability curves which define the first bifurcation. At low values of $\mathcal{I}^*$, the critical Reynolds numbers are almost constant, until intersection with mode $S1$. For $\mathcal{F} > 0.0019$, the marginal stability is given by the steady mode $S2$. As $\mathcal{I}^*$ increases, the critical value of Re decreases, reaches a minimum and slowly increases again. We notice the presence of a stable region given by the above-mentioned loop. This region becomes larger as the filtrability increases and, for $\mathcal{F} = 2.075 \times 10^{-3}$, merges with the lower, stable, part of the $(\mathcal{I}^*, Re)$ plane. For large $\mathcal{F}$ (red curves), the marginal stability curves are closed and only small portions of the parameters space are unstable.

The emerging mode at the marginal stability depends on the considered values of $\mathcal{I}^*$ and $\mathcal{F}$. In the solid case, for $\mathcal{I}^* < 4 \times 10^{-3}$, the first destabilization is due to mode $F1$ while for larger values to mode $S1$. An increase in the filtrability modifies this picture. We consider the almost horizontal part of the curves for small $\mathcal{I}^*$ in figure 11.11(a). For $\mathcal{F} < 1.85 \times 10^{-3}$, the destabilization is due to an oscillatory mode. However, for larger values of $\mathcal{F}$ (as also shown in figure 11.9(d)), the primary instability is due to mode $S2$ (green lines). This behavior is reminiscent of the solid disk with a diameter-thickness ratio of 10, observed in Tchoufag et al. (2014), where the steady mode dominates the dynamics at low values of inertia. The unstable range in terms of Reynolds number progressively shrinks, until the mode is stable, for $\mathcal{F} > 2.2 \times 10^{-3}$.

Therefore, permeable disks may primarily destabilize due to a non-oscillatory instability, for small inertia, and eventually present a stable vertical falling path. For $\mathcal{F} \sim 3 \times 10^{-3}$, all instabilities are quenched, at least in the considered parameters range. The destabilization-

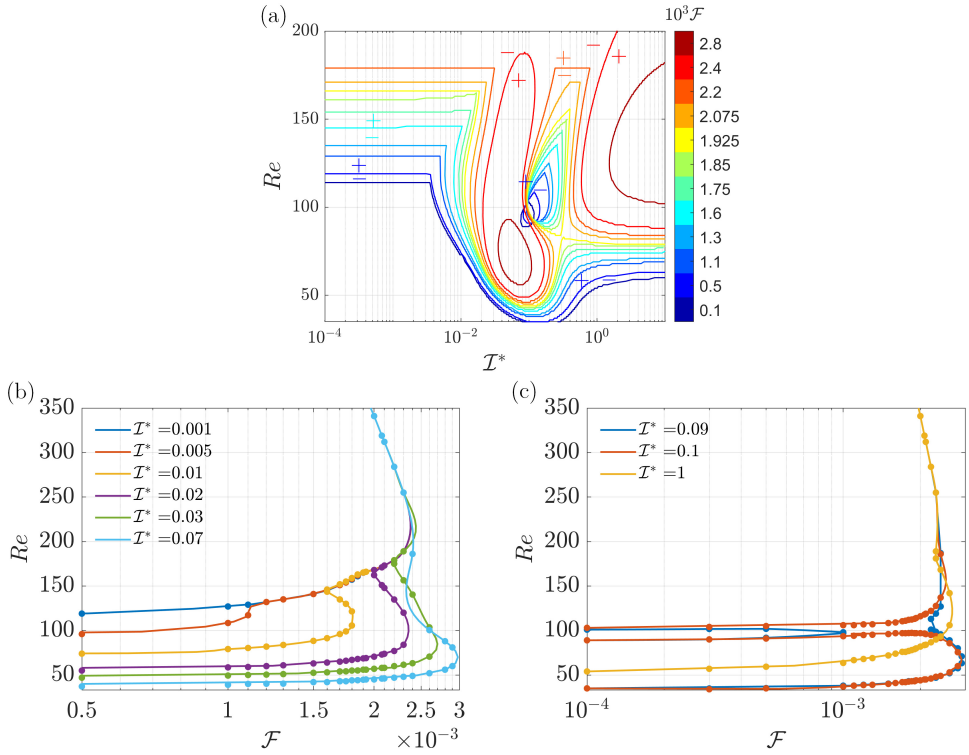

Figure 11.11: Collective marginal stability curves for $\mathcal{L} = 10^{-4}$, $M^* = 16\mathcal{I}^*$, and (a) for different values of $\mathcal{F}$ (coloured lines), in the $(\mathcal{I}^*, Re)$ plane, and (b,c) for different values of $\mathcal{I}^*$ (colored lines) in the $(\mathcal{F}, Re)$ plane.

stabilization sequence with the Reynolds number is similar to the one observed with the Reynolds number in the previous chapters, and related to the presence of the term $Re\mathcal{M}$ in equation (11.14). As the Reynolds number increases, the increase of the flow inertia, which tends to destabilize the trajectory, is counteracted by the increase of the flow velocity through the disk, since the bleeding velocity is proportional to the Reynolds number. For large filtrabilities, the classical non-monotonous behavior with the Reynolds number is thus recovered.

To have a better insight into the non-monotonous behavior of the marginal stability curves and how the bifurcations behave in the parameters space, we report in figure 11.11(b,c) the collective marginal stability curves in the $(\mathcal{F}, Re)$ plane, for different values of $\mathcal{I}^*$. Figure 11.11(b) shows the results for $\mathcal{I}^* < 0.07$. Case $\mathcal{I}^* = 0.001$ shows a monotonous increase and an inversion of the marginal stability curve, in analogy with the results of Chapter 10. For larger values of the inertia, the marginal stability curves present a "jump" due to the change in the mode that gives the marginal stability. In some cases, we observe a first inversion of the curve, followed by a change in the marginally stable mode and a second inversion in the curve. However, for large Reynolds numbers, all curves collapse to the same one, which is the one given by the steady mode $S2$ (green line in the previous plots). The stable region due to the loop in the $(\mathcal{I}^*, Re)$ plane can be observed also in the $(\mathcal{F}, Re)$ plane, as shown in figure 11.11(c). For $\mathcal{I}^* = 0.09$, there is a narrow range of Reynolds numbers in the vicinity of $Re = 100$,

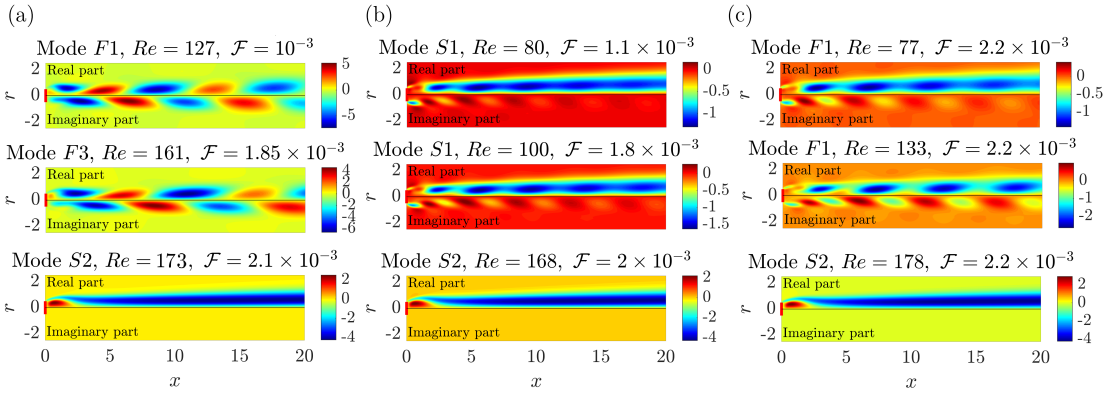

Figure 11.12: Real part of the streamwise component of the velocity field $\hat{\boldsymbol{u}}$, rescaled with $\hat{\vartheta}_{\pm}$, for different values reported in the top figure, (a) $\mathcal{I}^* = 10^{-3}$, (b) $\mathcal{I}^* = 10^{-2}$, (c) $\mathcal{I}^* = 3 \times 10^{-2}$.

whose interior is stable. Increasing $\mathcal{I}^*$, the two branches merge, leading to the situation of case $\mathcal{I}^* = 0.01$. The narrow region in the vicinity of $Re \approx 100$ is now stable regardless of the filtrability. Increasing $\mathcal{I}^*$, we leave the loop region and the marginal stability curve is reminiscent of the one of a fixed body (e.g. Chapter 10).

11.4.3 Spatial distribution of the eigenvectors and trajectories

Figure 11.12 shows the spatial distribution of the eigenmodes which define the primary bifurcation, for different values of inertia and increasing $\mathcal{F}$. We begin by considering (a) $\mathcal{I}^* = 10^{-3}$. For $\mathcal{F} = 10^{-3}$, the first bifurcation is defined by mode $F1$. In analogy with the case $\mathcal{F} = 10^{-4}$ (figure 11.6), the eigenvector shows similar real and imaginary parts, characterized by sign alternating type disturbances. A larger filtrability, $\mathcal{F} = 1.85 \times 10^{-3}$, leads to a primary bifurcation given by mode $F3$. The spatial structure of the eigenvector is reminiscent of mode $F1$, with slightly more elongated structures of alternating sign, both for the real and imaginary parts. A further increase in filtrability, $\mathcal{F} = 2.1 \times 10^{-3}$, leads to a switch of the primary destabilization to the steady mode $S2$. The eigenvector is characterized by a spatial distribution very similar to the case $\mathcal{F} = 10^{-4}$, with a sign change between the region close to and downstream of the disk.

For (b) $\mathcal{I}^* = 10^{-2}$, the primary destabilization at $\mathcal{F} = 1.1 \times 10^{-3}$ is given by mode $S1$. The mode shows real and imaginary parts characterized by large amplitude SPT and low amplitude SAT disturbances, respectively. An increase of the filtrability ($\mathcal{F} = 1.8 \times 10^{-3}$) does not appreciably modify the eigenvector. However, in analogy with case (a), for $\mathcal{F} = 2 \times 10^{-3}$, the marginal stability is given by the steady mode $S2$, with the same spatial distribution of case $\mathcal{I}^* = 10^{-3}$, $\mathcal{F} = 2.1 \times 10^{-3}$.

When large values of $\mathcal{F}$ are considered, frequent destabilization-stabilization sequences and successive destabilizations are observed, as Re increases. Case (c) $\mathcal{I}^* = 3 \times 10^{-2}$ shows three eigenvectors at the marginal stability, for $\mathcal{F} = 2.2 \times 10^{-3}$ and for increasing Re (see also figure

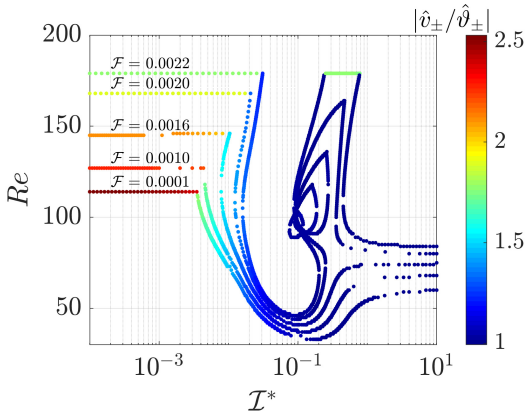

Figure 11.13: Absolute value of the ratio $\hat{v}_\pm/\hat{\theta}_\pm$ following the collective marginal stability curves.

11.10(c)). The primary destabilization occurs at $Re = 77$, with mode $F1$. The real part shows an SPT structure, while the imaginary part SAT structures of much lower amplitude. Increasing the Reynolds number, mode $F1$ returns marginally stable at $Re = 133$. The spatial distribution has changed, with the presence of SAT structures of larger amplitude, in the imaginary part. At $Re = 178$, the steady bifurcation occurs, with a spatial distribution analogous to the previously described cases.

We conclude our presentation of the eigenvectors by reporting, in figure 11.13, the values of the ratio $|\hat{v}_\pm/\hat{\vartheta}_\pm|$ in the $(\mathcal{I}^*, Re)$ plane, for the primary bifurcation. At low values of $\mathcal{I}^*$, a progressive increase in $\mathcal{F}$ leads to a decrease of $|\hat{v}_\pm/\hat{\vartheta}_\pm|$. The ratio is constant increasing the inertia. Increasing $\mathcal{I}^*$, the primary bifurcation switches, and $|\hat{v}_\pm/\hat{\vartheta}_\pm|$ decreases as inertia increases, following the marginal stability curves. At large values of inertia, the ratio is very low and weakly influenced by the parameters. A particular behavior occurs at $\mathcal{F} = 2.2 \times 10^{-3}$ and $\mathcal{I}^* \sim 4 \times 10^{-1}$, in which the primary bifurcation is given by mode $S2$ and the values of $|\hat{v}_\pm/\hat{\vartheta}_\pm|$ are much larger, compared to the ones resulting from the other modes.

The analysis of the eigenvectors showed the modifications induced by variations of the filtrability on the primary bifurcation. For low inertia values, a common behavior is the transition from an oscillatory mode to a steady mode for the primary bifurcation. An increase of $\mathcal{F}$ leads to an increase of the critical Reynolds number and to sign alternating structures of larger streamwise wavelength for mode $F1$, at $\mathcal{I}^* = 10^{-3}$. The stretching of the mode is related to the decrease of the Strouhal number, as explained in Chapter 9. Lower values of St imply vortical structures with a larger streamwise extent. Mode $S1$ instead shows an increase of the amplitude of the imaginary part, characterized by SAT structures, as $\mathcal{F}$ and Re increase. Therefore, the fluid-structure coupling in this case is stronger, with larger oscillations in the near wake. A similar effect is observed in figure 11.12(c): an increase in the Reynolds number leads to larger oscillations in the wake. Therefore, the predominant effect of the filtrability is the variation of the instability thresholds. An increase in the Reynolds number is associated with

the increase of amplitude of the SAT structures, and thus of the wake oscillations. However, the competition between the increase of the flow inertia is counteracted by the increase of bleeding flow, which eventually dampens the instabilities. The steady mode *S*2, responsible for a steady oblique path, appears to be ubiquitous as the filtrability increases, and does not show strong variations with $\mathcal{F}$ and Re.

11.5 Conclusion and discussion

In this Chapter, we studied the linear stability of the steady falling or rising trajectory of a thin permeable disk. We initially focused on the steady and axisymmetric flow associated with the steady vertical path as the filtrability and slip number vary. The flow presents a recirculation region detached from the body, which becomes smaller and disappears as the filtrability increases. An increase in the slip number leads to a slight increase in the size of the recirculation region. We related this behavior to the increase of the transversal velocity, for fixed filtrability, which leads to a stronger separation downstream of the disk and thus to larger recirculation regions. The non-monotonous behavior of the length and distance from the body of the recirculation region with the Reynolds number is present also in this case, in analogy with previous Chapters 9 and 10. The drag coefficient shows a maximum with the filtrability, for large Reynolds numbers. These results suggest that wake flows past permeable bodies with streamwise extent less or comparable to the transversal one behave similarly, with a detached recirculation region and the eventual disappearance of the counterflow.

Subsequently, we focused on the stability of the steady vertical trajectory with respect to azimuthal perturbations. For low filtrability, a behavior analogous to the solid case was observed, with the presence of one non-oscillatory and three oscillatory modes. An increase in the filtrability led to complex interactions between the neutral curves, with sudden changes in the branches which define the primary destabilization of the steady and axisymmetric vertical path. For large filtrability, the neutral curves show a destabilization-stabilization sequence with the Reynolds number already observed for other permeable bluff bodies (Ledda et al., 2018, 2019). The collective marginal stability curves which define the primary destabilization of the baseflow show a progressive shift toward larger Reynolds numbers as $\mathcal{F}$ increases. At the same time, the restabilization branch of the neutral curves progressively moves toward smaller Reynolds numbers, until the instability is quenched. The stable loop region highlighted in Tchoufag et al. (2014) becomes larger as the filtrability increases and, for $\mathcal{F} \approx 1.925 \times 10^{-3}$, it merges with the stable region of the parameters space below the neutral curves. The linear stability shows the existence of a stable region regardless of $\mathcal{F}$ that coincides with the above-mentioned loop region. One or multiple destabilization-stabilization sequences can be observed, depending on the value of inertia. We identified a critical filtrability $\mathcal{F} \sim 3 \times 10^{-3}$, beyond which the linear instability is prevented, at least in the considered range of parameters. A qualitative analysis of the fluid-structure coupling has been performed in analogy with Tchoufag et al. (2014). While all oscillatory modes always present a fluid-structure coupling, which depends on the relative amplitude of sign preserving and sign alternating structures in

the wake, and the amplitude of SAT oscillations increases with the filtrability. We related this behavior to the increase in the critical Reynolds number related to the increase in filtrability, which induces stronger wake oscillations because of the increase in the flow inertia.

This Chapter aims at giving a theoretical basis for the study of the path instabilities of falling or rising permeable objects. While we showed the potential of introducing permeability in quenching the linear instability of falling or rising objects, several extensions of this work may be performed. A first natural extension is related to the study of the path instability related to modes $m = 0$. While following the results of Tchoufag et al. (2014) we focused only on modes with $m = \pm 1$, an investigation of the behavior of the axisymmetric modes with filtrability and slip would give further insight into the understanding of the falling path of porous thin disks. A second extension is the analysis of thicker disks, described with a porous model such as the one reported in Chapter 9. Moreover, all these analyses have been performed in a linear framework. A fully non-linear campaign of direct numerical simulations, following Auguste et al. (2013), still needs to be pursued. This analysis would help in understanding (i) if the linear stability analysis well predicts the non-linear behaviors (as already confirmed in the solid case) and (ii) the different non-linear trajectories. From this point of view, an interesting problem is the interaction between the non-oscillatory and oscillatory modes which occurs at low inertia and for $\mathcal{F} = 0.001925$. A weakly non-linear analysis would be suitable in this case and could help to determine the super- or sub-critical nature of the transitions. Besides, a transient investigation from initial zero velocity would shed light on the linear destabilization-stabilization sequence increasing the Reynolds number.

Further developments include the validation of these results by comparison with linear stability analysis and non-linear trajectories of permeable disks composed of an actual microscopic structure. With the aim of controlling the falling or rising trajectory, the optimization tools described in Chapter 10 would be suitable to extend these analyses, both in the passive case (i.e. fixed values of $\mathcal{F}$ and $\mathcal{L}$) or in the active control of filtrability and slip to adjust the non-linear trajectory in real-time. The direct link between the microstructure and its macroscopic effect given by homogenization gives the opportunity to realize actual microscopic structures satisfying the desired flow features.

11.6 Appendix

11.6.1 Validation of the numerical method and convergence

In this section, we report the validation of the numerical method and the mesh convergence analysis. In figure 11.14 we compare the implemented numerical algorithm against the results of Tchoufag et al. (2014) for a solid disk of thickness $\varepsilon = 10^{-4}$, for fixed $\mathcal{I}^* = 4 \times 10^{-3}$. The results show a very good agreement against the literature results. Subsequently, we perform a mesh convergence study on the eigenvalues for the infinitely thin disk at large Reynolds numbers and filtrability, for modes $S1$ and $F1$. The convergence is performed by increasing the

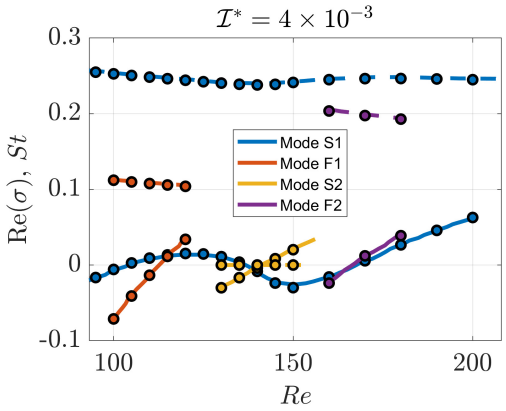

Figure 11.14: Validation of the neutral curves (solid lines) and Strouhal number (dashed lines) against the results of Tchoufag et al. (2014), for a thin solid disk of thickness $\varepsilon = 10^{-4}$ and $\mathcal{I}^* = 4 \times 10^{-3}$.

domain size and by refining the mesh discretization. The convergence analysis for mode $F1$, at $\mathcal{I}^* = 10^{-3}$, $Re = 180$, $\mathcal{F} = 2 \times 10^{-3}$, $\mathcal{L} = 10^{-4}$ and $M^* = 16\mathcal{I}^*$ is reported in table 11.1. Table 11.2 instead shows the mesh convergence results for mode $S1$, at $\mathcal{I}^* = 100$, $Re = 130$, $\mathcal{F} = 2 \times 10^{-3}$ and $\mathcal{L} = 10^{-4}$. In both cases, the mesh $M0$ is a good compromise between resolution and computational times, in the investigation of this large parameters space.

11.6.2 The effect of slip length and disk mass

The effect of the slip length on the marginal stability curves is reported in figure 11.15. In all cases, we observe marginal stability curves similar to the ones of case $\mathcal{L} = 10^{-4}$. An increase of the slip number leads to a slightly more unstable configuration, for the same $\mathcal{F}$.

Figure 11.16 instead shows the neutral curves for $\mathcal{F} = 0.002$, $\mathcal{L} = 10^{-4}$ and different values of M^*. Even if the neutral curves are modified, the picture is qualitatively unchanged, with a primary destabilization induced by the non-oscillatory mode at low inertia and by oscillatory modes at larger inertia. In particular, an increase in M^* leads to a stabilization of the oscillatory modes at small Reynolds numbers.

11.6.3 Stability analysis of the wake flow past a fixed membranal disk

In figure 11.17 we report the neutral curves for the steady and axisymmetric wake past a fixed permeable disk. The neutral curves strongly resemble those reported in Chapters 9 and 10, with a critical value of the filtrability beyond which the wake is stable and with the destabilization-stabilization sequence increasing Re, at large $\mathcal{F}$.

Mesh	$x_{-\infty}$	x_{∞}	r_{∞}	N_{el}	C_D	Re(σ)	Im(σ)
M0	25	50	25	24718	0.4388	-1.435×10^{-3}	0.4956
M1-A	30	50	25	25777	0.4388	-1.442×10^{-3}	0.4956
M1-B	35	50	25	26705	0.4388	-1.438×10^{-3}	0.4956
M1-C	40	50	25	27657	0.4388	-1.470×10^{-3}	0.4956
M2-A	25	70	25	28534	0.4388	-1.436×10^{-3}	0.4956
M2-B	25	90	25	32317	0.4388	-1.431×10^{-3}	0.4956
M2-C	25	100	25	34437	0.4388	-1.438×10^{-3}	0.4956
M3-A	25	50	30	27926	0.4388	-1.458×10^{-3}	0.4956
M3-B	25	50	35	31188	0.4388	-1.474×10^{-3}	0.4956
M3-C	25	50	40	34370	0.4388	-1.486×10^{-3}	0.4956
M4-A	25	50	25	29065	0.4389	-1.453×10^{-3}	0.4956
M4-B	25	50	25	35027	0.4389	-1.443×10^{-3}	0.4956
M4-C	25	50	25	43456	0.4390	-1.447×10^{-3}	0.4957

Table 11.1: Mesh convergence analysis for mode $F1$, at $\mathcal{I}^* = 10^{-3}$, $Re = 180$, $\mathcal{F} = 2 \times 10^{-3}$, $\mathcal{L} = 10^{-4}$ and $M^* = 16\mathcal{I}^*$. N_{el} denotes the number of elements.

Mesh	$x_{-\infty}$	x_{∞}	r_{∞}	N_{el}	C_D	Re(σ)	Im(σ)
M0	25	50	25	24718	0.4736	1.820×10^{-3}	0.02886
M1-A	30	50	25	25777	0.4736	1.820×10^{-3}	0.02886
M1-B	35	50	25	26705	0.4736	1.820×10^{-3}	0.02886
M1-C	40	50	25	27657	0.4736	1.820×10^{-3}	0.02886
M2-A	25	70	25	28534	0.4736	1.820×10^{-3}	0.02886
M2-B	25	90	25	32317	0.4736	1.821×10^{-3}	0.02886
M2-C	25	100	25	34437	0.4736	1.821×10^{-3}	0.02886
M3-A	25	50	30	27926	0.4736	1.820×10^{-3}	0.02886
M3-B	25	50	35	31188	0.4736	1820×10^{-3}	0.02886
M3-C	25	50	40	34370	0.4736	1.819×10^{-3}	0.02886
M4-A	25	50	25	29065	0.4737	1.821×10^{-3}	0.02886
M4-B	25	50	25	35027	0.4738	1.821×10^{-3}	0.02886
M4-C	25	50	25	43456	0.4739	1.822×10^{-3}	0.02886

Table 11.2: Mesh convergence analysis for mode $S1$, at $\mathcal{I}^* = 100$, $Re = 130$, $\mathcal{F} = 2 \times 10^{-3}$, $\mathcal{L} = 10^{-4}$ and $M^* = 16\mathcal{I}^*$. N_{el} denotes the number of elements.

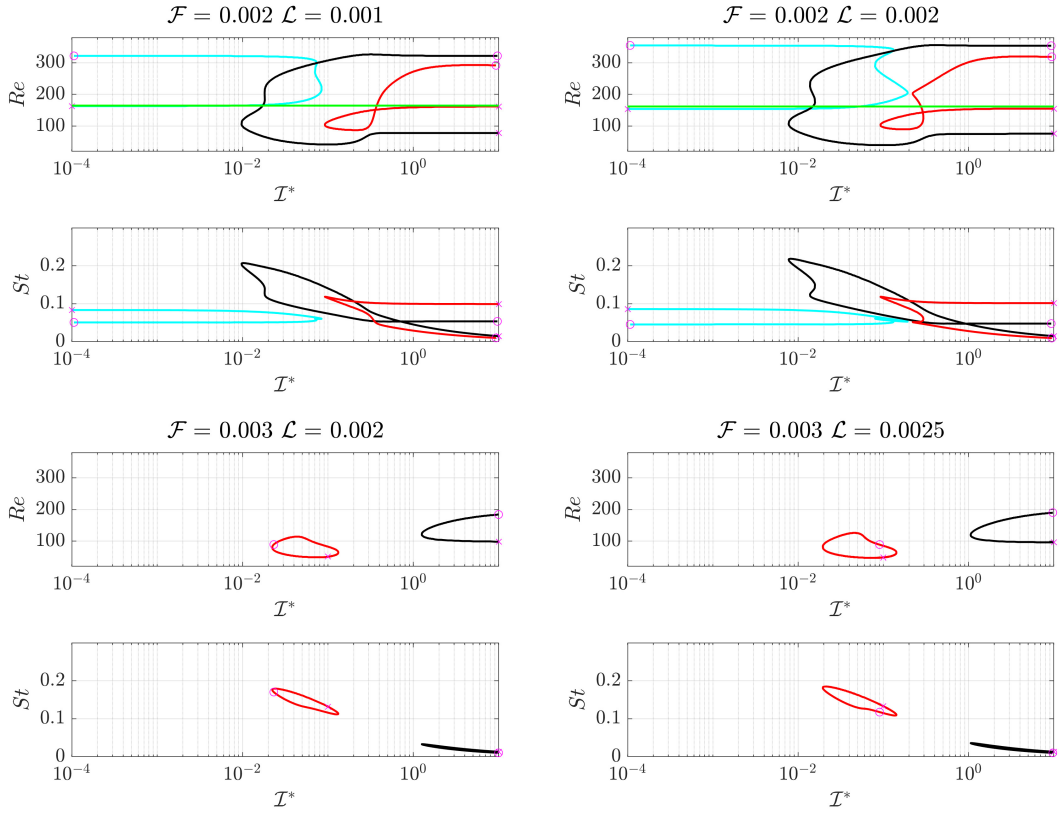

Figure 11.15: Marginal stability curves for an permeable disk as a function of $\mathcal{I}^*$ for different values of $\mathcal{F}$ and $\mathcal{L}$, with $M^* = 16\mathcal{I}^*$, critical Reynolds number (on the top) and Strouhal number (on the bottom). The different colors correspond to mode $F1$ (red), $S1$ (black), $F3$ (cyan), and $S2$ (green). The magenta symbols help to identify the values of Strouhal number associated with the marginal stability curves.

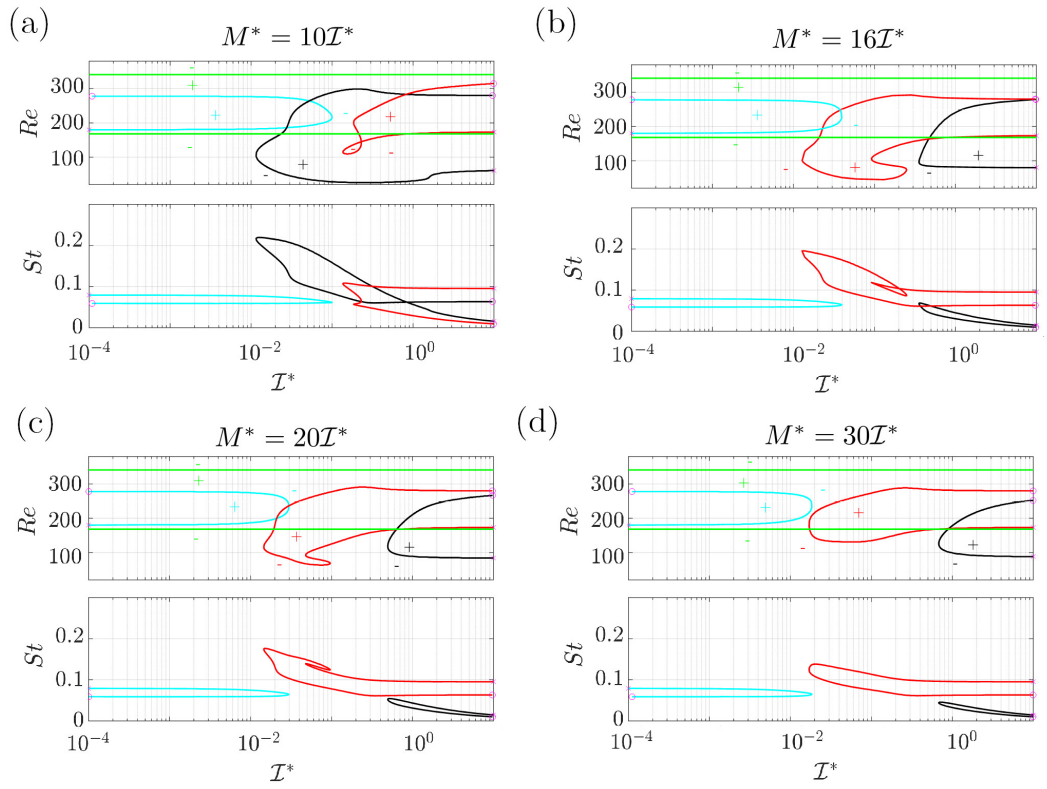

Figure 11.16: Marginal stability curves for an permeable disk as a function of $\mathcal{I}^*$ for different values of $\mathcal{F}$ and M^*, with $\mathcal{L} = 10^{-4}$, critical Reynolds number (on the top) and Strouhal number (on the bottom). The different colors correspond to mode $F1$ (red), $S1$ (black), $F3$ (cyan), and $S2$ (green). The magenta symbols help to identify the values of Strouhal number associated with the marginal stability curves.

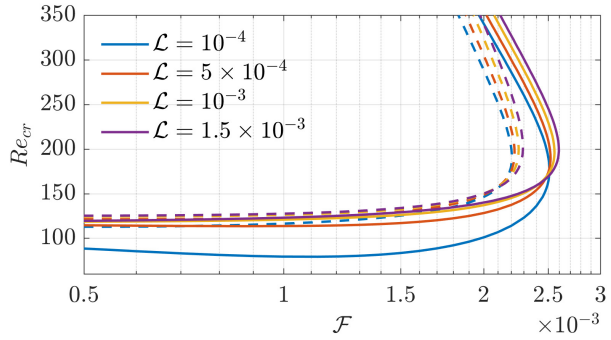

Figure 11.17: Marginal stability curves for the steady and axisymmetric flow past a permeable disk, for different values of $\mathcal{L}$ and for the steady (solid lines) and unsteady (dashed lines) bifurcations.

12 Conclusion and perspectives

This thesis exploited multiscale approaches to systematically study the macroscopic behavior of different flows, from coating patterns to the onset of instabilities of wakes past permeable bluff bodies. **Part I** studied the pattern formation of the flow of a thin film under an inclined planar substrate through a lubrication model. The effect of modulations or large variations of the substrate for different coating patterns, i.e. substrate growth due to a deposition law, dewetting at the nanoscale and spreading on almost arbitrarily curved substrates, was analyzed in **Part II**. **Part III** investigated the wake flow modifications due to the introduction of permeability in rigid bodies. Since major conclusions were drawn at the end of each chapter, we present here a brief overview of the different parts and chapters, with possible extensions and future perspectives.

12.1 Part I

12.1.1 Overview

Inspired by the experimental patterns observed in Brun et al. (2015), **Part I** studied the two-dimensional pattern formation of a thin film flowing under an inclined planar substrate. In **Chapter 2**, we studied the steady free-surface patterns emerging from a flat film condition. We observed the predominance of steady structures aligned along the streamwise direction, called rivulets, and characterized their growth and propagation through linear theory. When forced by a stationary localized perturbation, a front develops, predicted with the group velocity of the unstable wave packet. The response to a sinusoidal forcing at the inlet showed the possibility to force rivulets with different profiles and spacing. The streamwise-invariance was exploited to derive a one-dimensional model which reproduces these structures, in the case of the most amplified wavelength. We recovered the rivulet shape through a pure equilibrium between capillarity and gravity forces, i.e. the profile is a two-dimensional pendent drop with an imposed flow rate in the transversal direction.

In **Chapter 3**, the emergence of rivulet structures was numerically and experimentally ra-

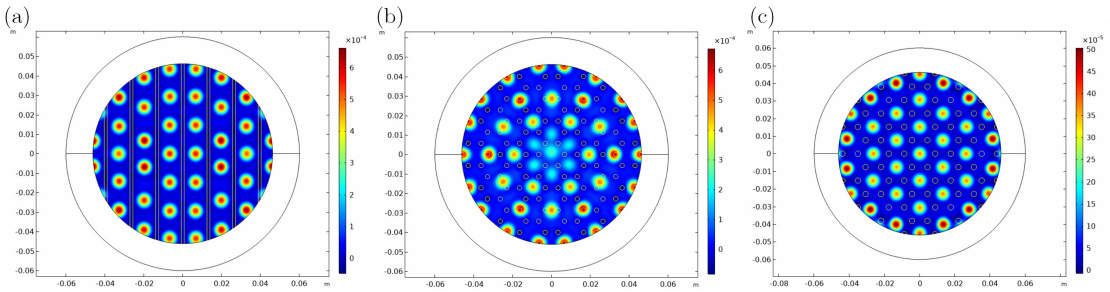

Figure 12.1: Numerical long-time pendent drop patterns resulting from the destabilization of a thin film of initial thickness $h_i = 300\mu m$ in the presence of (a) trenches and (b,c) pits, under the action of centrifugal forces because of the rotation of the circular plate, kept constant. Courtesy of E. Jambon-Puillet.

tionalized via the weakly non-linear impulse response of a flat film. We imposed as initial condition an impulse, experimentally obtained by blowing air with a syringe. The perturbation was advected away with the linear advection velocity and rivulets were nonlinearly selected downstream of the traveling impulse. A secondary stability analysis of one-dimensional and steady rivulets revealed a strong stabilization mechanism for large inclinations or very thin films. We obtained a general stability threshold below which rivulets are stable. The theoretical results were compared with experimental measurements of the streamwise oscillations of the rivulet profile, with a good agreement.

Chapter 4 deepened, with a numerical approach, the emergence of lenses on the rivulet profile, when the latter is forced with a small harmonic oscillation at the inlet. The linearized dynamics in the presence of a time-harmonic inlet forcing reproduces the formation of small-amplitude lenses that travel on the rivulet and grow moving downstream, rationalized with a weakly non-parallel stability analysis. The occurrence of the lenses, their spacing and thickness profile, is controlled by the inclination angle, flow rate, and the frequency and amplitude of the time-harmonic inlet forcing. The results of the linear simulations with inlet forcing were combined with the computations of nonlinear traveling lenses solutions in a double-periodic domain to obtain an estimate of the dripping length, for a large range of conditions.

Chapter 5 was instead focused on the dripping problem of a single droplet traveling on a very thin film. Through these simplified configurations, we were able to highlight the fundamental physical mechanisms leading to dripping when a slightly inclined plane is considered. Drops shrink over the course of their motion, resulting in an increase of thickness in their wake, reminiscent of rivulet formation. Combining experiments and numerical simulations, we rationalized the transition between the conventional growth regime and the previously unknown decay regime. Using an analytical treatment of the Landau-Levich meniscus that connects the drop to the film, we quantitatively predicted the drop dynamics in the two flow regimes and the value of the critical inclination angle for the transition.

The results of **Part I** may find application in the context of the design of soft material through self-assembly processes (Marthelot et al., 2018), e.g. to produce textured surfaces. By tuning the inclination angle and initial deposited thickness, via a small sinusoidal substrate perturbation one can obtain rivulets with spacing $\sqrt{5}\pi\ell_c^* < L_y < 2\sqrt{5}\pi\ell_c^*$ (see **Chapter 2**). Note that, for thin enough films, the resulting rivulets do not differ significantly from sinusoidal profiles invariant along the streamwise direction. The critical angle below which lenses are not observed as a function of the characteristic thickness can be deduced from figure 3.10 in **Chapter 3**. A good approximation is given by the linear relation

$$\theta_{cr} \approx \frac{\pi}{2} - 0.93\frac{h_N}{\ell_c}. \tag{12.1}$$

For larger angles, rivulets do not stay intact, but lenses form on the rivulets, leading to more intricate patterns. The results of **Chapter 5**, which identified a critical transition between dripping and rivulet formation in the wake of a single drop at

$$\theta_{dr} \approx \frac{\pi}{2} - 0.67\frac{h_N}{\ell_c}, \tag{12.2}$$

may find application in dripping prevention for drops directly deposited on substrates in coating and printing technologies (Kumar, 2015), and in the control and transport of pendent drops via crafted substrate topography. As shown in figure 12.1, the combined action of centrifugal and gravity forces combined with substrate topography may lead to different drop patterns. The presence of trenches (figure 12.1(a)) leads to aligned droplets whose size appears to be quite uniform. The presence of pits (figure 12.1(b,c)) organized in hexagonal arrays leads to smaller drops in the vicinity of the center, in particular when small spacings compared to the most amplified wavelength ($\lambda_{RT} = 2\pi\sqrt{2}\ell_c$) are considered (subfigure (b)).

The intrinsic three-dimensionality of the problem would lead to other dripping routes still to be determined. However, rivulets seem to be a ubiquitous pattern for a thin film flowing under an inclined plane. Also in the case of a single drop sliding on a very thin film, a sufficiently strong advection is enough to lead to a rivulet formation in the wake of a shrinking drop.

12.1.2 Future developments

In **Chapters 2,3,4** we mainly focused on the properties and stability of the rivulet profile whose spanwise wavelength was the most amplified one from the flat film linear stability analysis. However, as observed in **Chapter 2**, there is a range of unstable wavelengths which can be forced, in the range $\sqrt{5}\pi\ell_c^* < L_y < 2\sqrt{5}\pi\ell_c^*$. **It is not clear how the results are modified when different, non-dominant, spanwise wavelengths are forced. Indeed, the change in spanwise wavelength modifies the rivulet profile (see figure 12.2), thus leading to different stability properties. Further investigations may thus include the role of the forcing spanwise wavelength in the secondary instability of rivulets.**

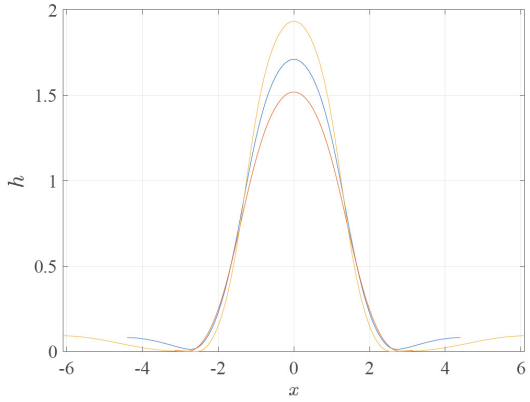

Figure 12.2: Two-dimensional rivulet profiles with different wavelengths.

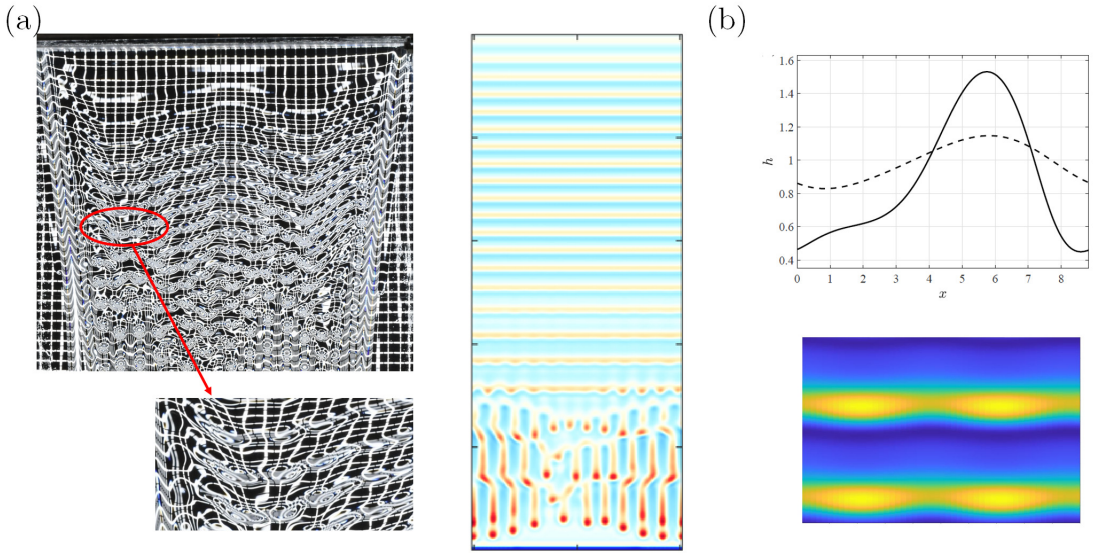

Figure 12.3: Route to dripping from a strong temporal forcing at the inlet. (a) Experimental (left) and numerical (right) visualization of the film thickness, which shows an initial pattern characterized by spanwise invariant waves, which destabilize and form drop-like structures. Further downstream, these drop-like structures stretch along the streamwise direction and strongly resemble rivulets. (b) Stability analysis of the two-dimensional traveling wave profile (with two examples shown on the top) with respect to spanwise perturbations. On the bottom: most amplified mode from the dispersion relation, superposed to the baseflow profile. The resulting pattern is reminiscent of the one observed in (a).

The initial flat film destabilization followed by a secondary instability of rivulets is a possible route to dripping. We experimentally observed a different route, which occurs when a strong temporal forcing is imposed at the inlet, see figure 12.3(a). Downstream of the inlet, traveling structures purely modulated along the streamwise direction emerge, so-called **waves**. In the experimental picture, the spanwise modulations from the inlet are amplified, and drop-like

structures form at the waves fronts. A similar pattern is observed in the numerical simulation. These drop-like structures stretch along the streamwise directions and rivulet structures form. **The wave destabilization can be studied in the context of a secondary linear stability analysis (figure 12.3(b)).** The first step consists in the evaluation of the streamwise-periodic and spanwise-invariant waves which ensure the correct inlet flow rate (Kalliadasis et al., 2011). The lubrication equation reads:

$$\partial_t h + u h^2 \partial_x h + \frac{1}{3}\partial_x \left[h^3 \left(\partial_x \kappa + \partial_x h \right) \right] = \sigma(t) h, \tag{12.3}$$

where $\sigma(t)$ is a parameter which, at each time iteration, ensures the correct flow rate. The flow rate $q(x,t)$, after integration of the Nusselt velocity profile at each streamwise location (Kalliadasis et al., 2011) and considering invariance in the spanwise direction, reads:

$$q(x,t) = \frac{1}{3} h^3 \left[u + \partial_x h + \partial_x \kappa \right] \tag{12.4}$$

In the case of a traveling wave in a periodic domain the temporal and spatial means coincide, and therefore the spatial mean is constant and equal to its initial value. We therefore obtain a transient problem which leads to a traveling wave solution $H_w(x,t)$. In the moving reference frame at the velocity of the wave c, i.e. $\xi = x - ct$, the traveling wave solution is steady, $H_w(\xi)$. One can therefore expand with a linear mode expansion in time and along the spanwise direction to derive the dispersion relation in the moving reference frame. A representative superposition of the baseflow with the most unstable temporal mode, with an arbitrary amplitude, is reported in figure 12.3(b). The resulting pattern is characterized by drop-like structures similar to the ones observed in experiments and numerical simulations. **A complete analysis of the wave destabilization would lead to a better understanding of this alternative route to dripping. To understand the role of weak non-parallelism in the wave evolution from the inlet and the region of propagation of rivulets, the analysis can be complemented with a Floquet analysis of the time-periodic and spatially varying two-dimensional baseflow with respect to spanwise perturbations (Barkley and Henderson, 1996).**

While **Chapter 5** was focused on a single drop on a thin film, **further developments may be focused on the dripping problem of a lens from a rivulet**. As observed, the complete curvature is essential to predict the correct lens growth from a rivulet. **A preliminary analysis, similar to Chapter 5, would be to deposit a large drop on a rivulet and determine the dripping and shrinking regimes.** In opposition to the case of a thin film, one should consider the matching problem between the drop profile and the overhanging rivulet. **A successive analysis can be focused on the determination of three-dimensional traveling lenses on a steady rivulet profile.**

However, droplets may also interact and merge. In figure 12.4 we report the process at different stages. The typical configuration is characterized by a large lens that travels faster than a smaller one downstream. The larger lens then absorbs the smaller one. The result is a large lens which eventually drips, if the final volume is large enough. **Further studies may**

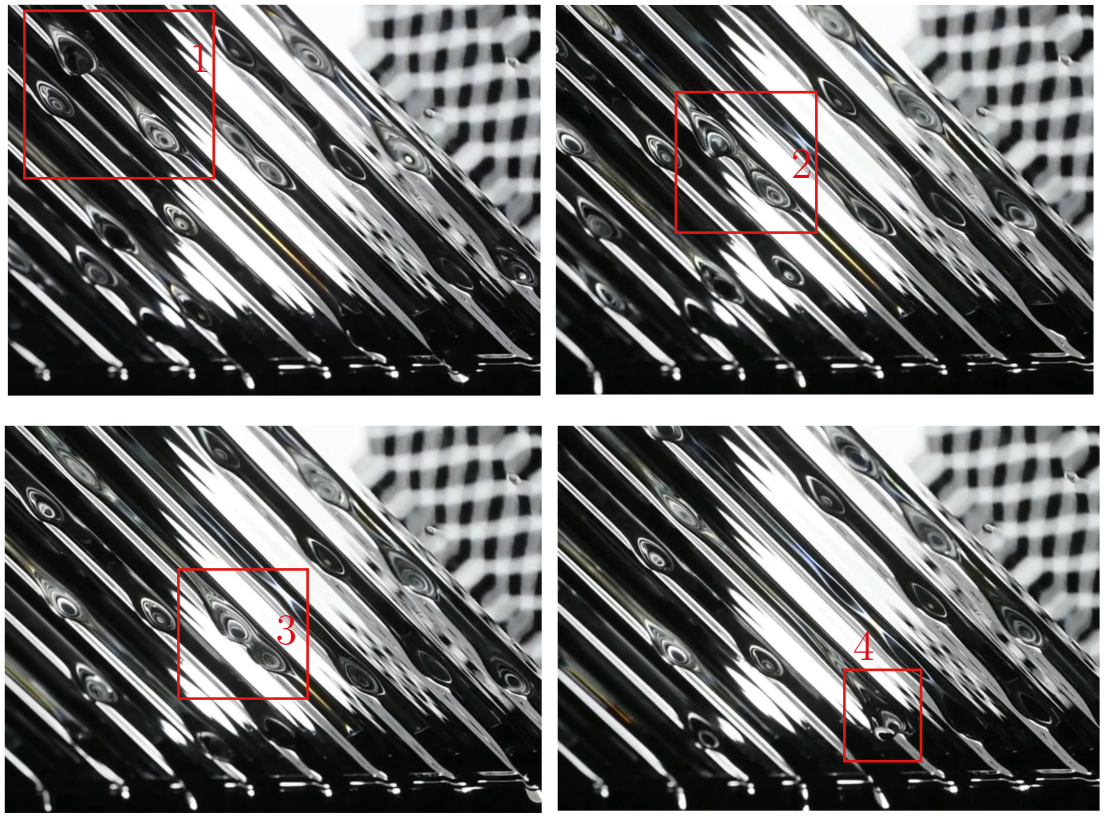

Figure 12.4: Experimental pictures of merging of two lenses: (1,2) the largest lens is faster than the smaller one, and in (3) the two lenses merge. The resulting lens travels downstream (4) and drips.

investigate how lenses merge and develop a criterion to determine the final volume and lens shape, together with a dripping prediction.

We point out that all results in **Part I** were obtained in the case of negligible inertia. When the inertia of the flow is considered, falling films over inclined substrates are well-known to destabilize and form Kapitza waves (Kalliadasis et al., 2011). The inertia-driven destabilization has to be combined with the gravity effects, when the film is suspended underneath the inclined substrate. Some results of this competition obtained by Charogiannis et al. (2018) are reported in figure 12.5. When the inertia of the fluid is very low, i.e. $Re < 1$, we observe the formation of rivulets structures, in analogy with this work. In cases (b,c), with $Re < 10$, the flow pattern is characterized by rivulets with lenses, in analogy with the secondary instability of rivulets. For $Re > 10$ (d,e), the pattern is intricate and reminiscent of Kapitza waves observed for a thin film over an inclined substrate. If the substrate is more inclined (f), a more ordered pattern with elongated rivulets is recovered, combined with streamwise steep modulations. Rietz et al. (2021) performed a numerical investigation through non-linear simulations in a periodic domain, studying the deviation from the spacing predicted by the classical Rayleigh-Taylor instability. **Further studies may deepen the problem of pattern formation when the**

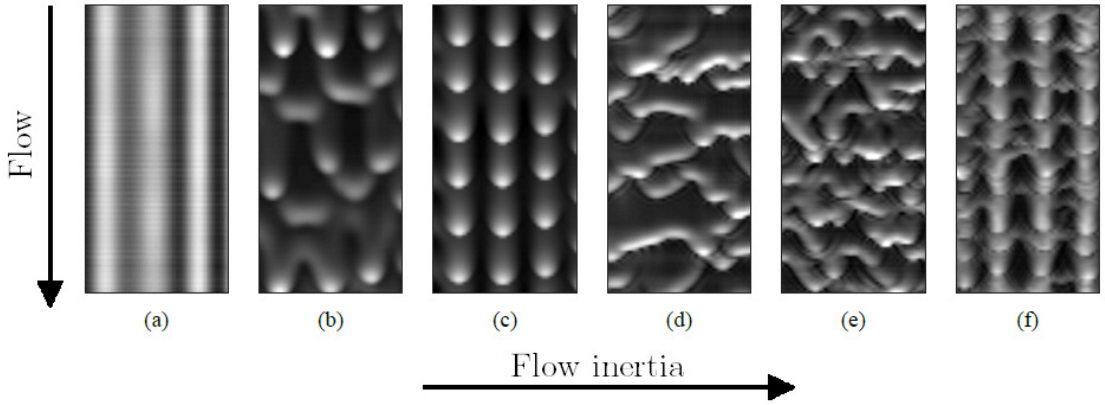

Figure 12.5: Experimental patterns, reproduced with permission from Charogiannis et al. (2018) (https://doi.org/10.1103/PhysRevFluids.3.114002), for different values of the Kapitza number $Ka = \frac{\gamma}{\rho \nu^{4/3} g^{1/3}}$, Reynolds number $Re = \Gamma/\nu$ and inclination angles: (a) Re = 0.6, Ka = 13.1 and $\theta = 30°$, (b) Re = 3.5, Ka = 13.1 and $\theta = 30°$, (c) Re = 7.4, Ka = 13.1 and $\theta = 30°$, (d) Re = 19, Ka = 330 and $\theta = 15°$, (e) Re = 36, Ka = 330 and $\theta = 30°$, and (f) Re = 118, Ka = 330 and $\theta = 45°$.

inertia of the flow is not negligible. In this perspective, the lubrication model should be abandoned in favor of the more reliable WRIBL models (Kofman et al., 2018). An initial study may concern the role of inertia in modifying the flow patterns observed in Part I when the inertia is progressively increased, by increasing the Reynolds number or further inclining the substrate. A parallel study may instead study the reversed problem, i.e. how the inertia-driven instability is modified by a slight hydrostatic gravity component. **In this context, the linear and weakly non-linear impulse responses may give further insight into the understanding of the different physical mechanisms involved in this competition.** When one effect dominates over the other, it would be reasonable to consider a simplified two-dimensional baseflow which retains most of the dominant physical effect (e.g. rivulet when gravity dominates, waves when inertia-driven instability is predominant) and understand how the flow reacts to three-dimensional perturbations. This aspect is important also in the context of pattern formation when the hydrodynamic problem is coupled with dissolution and erosion processes of the substrate, e.g. karren patterns (Bertagni and Camporeale, 2021). These ideas will be outlined in the following.

12.2 Part II

12.2.1 Overview

Modifications of the substrate topography induce effects on the classical hydrodynamic problem. Inspired by the draperies formation in limestone caves, the feedback mechanism between the hydrodynamic problem and the growth of the substrate due to a deposition law

was studied in **Chapter 6**. We proposed a novel approach for the spatio-temporal analysis of two-dimensional fields resulting from linear simulations via the Riesz transform and monogenic signal, the multidimensional complex continuation of a real signal. This method allowed us to rationalize the two-dimensional pattern formation. The deposition linearly selects substrate structures aligned along the streamwise direction, as the spatio-temporal response is advected away. Furthermore, the growth of the initial defect produces a quasi-steady region also characterized by streamwise structures both on the substrate and the fluid film, which is in good agreement with the Green function for a steady defect on the substrate, in the absence of deposition. The non-linear simulations highlighted the selection of streamwise structures and the bending of the non-linear front in which the simulation spreads. All these mechanisms contribute to the predominance of streamwise structures both in the fluid film and on the substrate. A second result, which may be of interest in coating and fabrication processes, comes from the study of the steady response. The presence of defects on a planar substrate induces the formation of a wake behind the perturbation, in which rivulets spread within a front and grow downstream. Third, the two-dimensional post-processing method revealed itself as a suitable tool to understand complex fluid responses. This procedure is particularly suitable when the dispersion is not known analytically or the saddle-point tracking becomes too challenging. This procedure allows one to proceed to an a posteriori description of the response, without the necessity to a priori define the unstable branches of the dispersion relation.

However, the underlying substrate can be employed as a forcing to induce desired patterns (figure 12.1). **Chapter 7** showed how substrates can be tailored so as to obtain ordered dewetting patterns, which find several applications in nanophotonics. Through a lubrication model based on capillarity and the Lennard-Jones intermolecular potential, we were able to reconstruct the observed experimental patterns and understand the role of the underlying substrate in the definition of the final configuration. As a preliminary guideline for fabrication of ordered dewetted nanostructures, there is a critical value of the spacing-to-period-ratio $S \approx 0.4$ beyond which the initial volume of fluid deposited inside and outside the pits is conserved. The resulting ordered structures are drops with a certain contact angle that fill the underlying volume, and can be recovered through a lubrication model, when the contact angle is less than 90°.

In **Chapter 8**, we showed how drainage and spreading solutions are modified by the underlying substrate, investigating different configurations. We observed how the drainage flow is modified between the inner and outer region of a torus because of the different metrics, and how the breaking of axisymmetry leads to preferential directions in the drainage and spreading on an ellipsoid. These findings may find application in coating processes of intricate shapes such as gloves fabrication (Akabane, 2016), and applications in which the thickness of the resulting shells may be relevant, e.g. buckling of these thin structures (Reis, 2015).

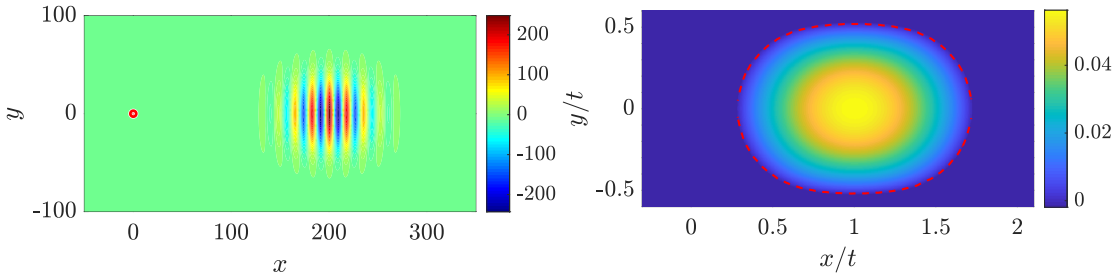

Figure 12.6: Flow of a thin film on an inclined substrate modeled through the Benney equation (Kalliadasis et al., 2011) for $\beta = 45°$, $We = 10$, $Re = 3$. On the left: numerical solution at $t = 200$. On the right: spatiotemporal growth rate obtained from the post-processing algorithm.

12.2.2 Future developments

Chapter 6 investigated the two-dimensional patterns which stem from the coupling between hydrodynamics and growth of the substrate due to deposition. A first extension is the **application of the post-processing algorithm based on the Riesz transform to other relevant cases in which the two-dimensional pattern formation, in the linear regime, is not well understood. The already mentioned karren patterns are worth to be investigated.** Bertagni and Camporeale (2021) performed a linear stability analysis with respect to spanwise perturbations of the two-dimensional solution with a flat interface, resulting from the Navier-Stokes equations, concentration transport and interface conditions at the water-air interface. The authors showed that the instability of this solution can be related to the longitudinal parallel channels observed on rocks and is due to positive feedback between the hydrodynamics and the enhanced dissolution. **The problems of understanding pattern formation in 2D or 3D problems, not only limited to dissolution on rocks but to a great variety of patterns observed in geophysical flows (Meakin and Jamtveit, 2010) and beyond, with or without lubrication approximation, are the perfect testing ground for the post-processing algorithm.** Inspiring examples are *chevron* patterns (e.g. those in Saint-Brevin, France), ripples and barkhan dunes in sandy deserts. These patterns are encountered all around our Solar System, such as the *Sputnik Planitia* and *Tartarus Dorsa* in Pluton, induced by the interaction between wind and sublimation of ices of different compositions (Bordiec, 2020).

To show the immediacy of the method, the flow of a thin film on an inclined substrate is governed by the non-dimensional Benney equation (Kalliadasis et al., 2011):

$$\partial_t h + h^2 \partial_x h + Re \frac{2}{5} \partial_x \left(h^6 \partial_x h \right) + \nabla \cdot \left[-Ct \frac{h^3}{3} \nabla h + We \frac{h^3}{3} \nabla \nabla^2 h \right] = 0, \tag{12.5}$$

where $Ct = \cot\beta$, $Re = g \sin\beta h_N^3 / (3\nu^2)$ is the Reynolds number, $We = \ell_c^2 / (h_N^2 \sin\beta)$, and β is the angle with respect to the horizontal. Once linearized around the flat film solution $h = 1$, the problem reads:

$$\partial_t \eta + \partial_x \eta + \frac{2}{5} Re \partial_{xx} \eta - \frac{1}{3} Ct \nabla^2 \eta + \frac{1}{3} We \nabla^4 \eta = 0. \tag{12.6}$$

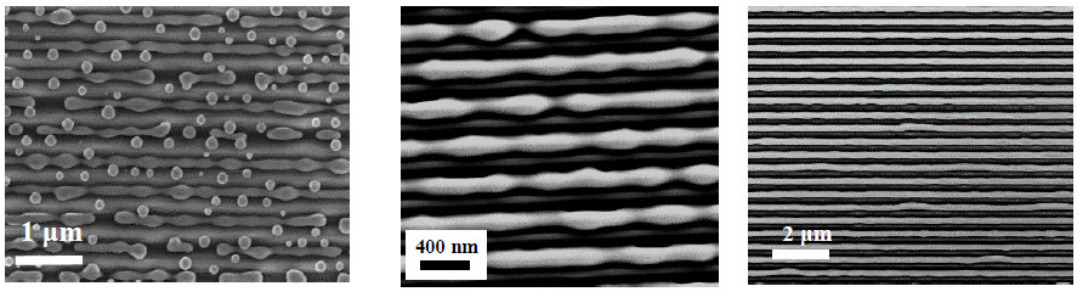

Figure 12.7: Experimental patterns, reproduced with permission from Gupta et al. (2019), As_2Se_3 film on a periodic 350 nm line silica lattice. From left to right: $h_i = 25$ nm, $h_i = 33$ nm, $h_i = 42$ nm.

Figure 12.6 shows the linear response and the spatiotemporal growth rate for $\beta = 45°$, $We = 10$, $Re = 3$. The numerical solution shows the emergence of streamwise-modulated structures traveling downstream; the front in which the perturbation spreads is elliptical. **The ease of implementation and interpretation of the post-processing method makes it suitable also for an extension to the three-dimensional case, via the three-dimensional Riesz transform.**

Linear stability analysis may be also employed to understand the competition between the template reflow and dewetting on a patterned substrate (Chapter 7) when the substrate is shaped with triangular grooves, see figure 12.7. Depending on the thickness of the deposited film, the competition between the reflow induced by the substrate and the spinoidal decomposition would lead to different patterns prior to the solidification of the deposited material. The destabilization of the two-dimensional patterns has been related to the different time scales at play (Gupta et al., 2019). **A stability-oriented approach would be to consider the steady baseflow obtained from two-dimensional simulations and then perturb along the transversal direction.** For each template, one would obtain a different dispersion relation as a function of the transverse wavenumber, which can be used to predict the most amplified wavelength and growth rate.

At the macroscale, the effect of the substrate on another instability, i.e. fingering, still needs to be explored. The spreading on an ellipsoid is characterized by π-periodic modulations induced by the absence of symmetries on the substrate. In the case of flat, cylindrical and spherical substrates one can assume the invariance of the time-dependent baseflow to exploit a normal mode expansion along the transversal or the azimuthal direction for a transient-growth approach (Balestra et al., 2019). However, when the substrate does not present these symmetries, a normal mode expansion cannot be employed, since the transient baseflow varies both along the azimuthal and zenith directions. **It would be interesting to understand how modulations of the front modify the classical picture of the fingering instability due to the interaction with the reflow induced by the substrate.**

The design of crafted substrates, both with large and small substrate variations, is a problem

of interest in fabrication techniques. **In this context, optimization techniques would be suitable to optimize the substrate shape to control the film thickness, e.g. quenching the fingering instability, also in the presence of other effects such as centrifugal forces or other physical phenomena, e.g. the Rayleigh-Taylor instability, Marangoni effects or dewetting.** As concerns dewetting, the optimization of superhydrophobic surfaces would be of great interest. If the microstructure composing the substrate is much smaller than the thin film, one could think of the employment of a slip boundary condition to modify the film thickness. Homogenization technique offers a suitable solution in connecting the microstructure with the macroscopic effect on the flow, as explained in the following.

12.3 Part III

12.3.1 Overview

Permeability strongly modifies the flow past bluff bodies. In the case of thin permeable bodies, an increase in permeability induces a downstream displacement and shrinking of the recirculation region and, for large permeabilities, the suppression of flow instabilities. For thicker bodies, the flow may show non-trivial features which deserved further investigation. **Chapter 9** studied the flow past a permeable sphere modeled using homogenization theory. The steady and axisymmetric flow was first characterized under the assumption of a homogenous and isotropic porous medium. In a certain range of permeability, the recirculation region penetrates inside the sphere, resulting in a strong modification of the linear stability properties of the flow and in a decrease in the critical Reynolds numbers for the flow instability. However, for very large permeabilities, a critical permeability value is identified, beyond which the steady and axisymmetric flow remains always linearly stable. The hypothesis of a homogenous porous medium was then relaxed, and the effect of polynomial distributions of permeability inside the body was studied. Some macroscopic flow properties do not significantly vary with the permeability distributions, provided that their average is maintained constant. The analysis is concluded by outlining a simplified procedure to retrieve the full-scale structure corresponding to a considered distribution of permeability.

The retrieval procedure was then included in a larger context in **Chapter 10**. A formal framework to characterize and control/optimize the flow past permeable membranes by means of a homogenization approach was proposed and applied to the wake flow past a permeable cylindrical shell. A characterization of the steady flow for several combinations of constant filtrability and slip numbers showed that the flow morphology is dominantly influenced by the filtrability and exhibits a recirculation region that moves downstream of the body and eventually disappears as filtrability increases. A linear stability analysis showed the suppression of vortex shedding as long as large values of the filtrability number are employed. In the control/optimization phase, specific objectives for the macroscopic flow were formulated via adjoint methods. A homogenization-based inverse procedure was proposed to obtain the optimal constrained microscopic geometry from macroscopic objectives, which accounts for

fast variations of the filtrability and slip profiles along the membrane.

Chapter 11 extended these analyses to the fluid-structure interaction, by considering the azimuthal instabilities of the wake past a disk falling on a vertical path. The disk was modeled with the membrane model obtained through homogenization. The sequence of bifurcations varying the macroscopic properties and the inertia of the membrane is non-trivial and shows several interactions of modes, which modify the marginal stability threshold of the vertical path. These modes exhibit a destabilization-stabilization mechanism with the Reynolds number, a behavior already encountered for other permeable bluff bodies. As the filtrability increases, the unstable region progressively shrinks and, for very large filtrabilities, the vertical path is linearly stable.

These considerations aim at giving a formal framework in the study of wake flows past permeable bodies and optimization procedures. The homogenized model allowed us to perform parametric studies, whose results faithfully reproduce full-scale simulations, for different configurations. A result of practical interest is the linear stability of the wake, which occurs for a threshold value of the permeability (in other words the filtrability). Typically, the instability occurs far downstream of the body. The decoupling between the microstructure and its macroscopic effect on the flow allowed to develop an inverse procedure for optimizations, which showed great potential and immediacy of application. This procedure is not limited to wake flows, it can be extended to other configurations.

12.3.2 Future developments

Part III showed how homogenized models can be suitable to understand flow bifurcations and implemented in optimization procedures, applied to flows with $Re = \mathcal{O}(10^2)$. **The advantage of decoupling the microstructure from its macroscopic effect is not limited only to wake flows but in all cases in which a separation of scales in the solid structure is present**, e.g. the flow in a channel with rough walls. **A natural extension is the study of the role of the microstructure in modifying the flow features at higher Reynolds numbers. To this extent, the employed models are based on the assumption of Stokes flow inside the pores. A necessary extension to make these models suitable at $Re = \mathcal{O}(10^3)$ is the introduction of inertia in the pores.** While such extension already exists for the flow through bulk porous media (Zampogna and Bottaro, 2016), similar developments for the porous-fluid interface condition and for microstructured membranes are missing.

Chapter 11 just started to investigate the fluid-structure interaction of flows past porous bodies. The modifications in the bifurcations induced by the porosity may find several developments. **The first extension needed is the understanding of the fluid inertia within the pores when the rigid porous body presents motion degrees of freedom. A subsequent study may be focused on the fluid-structure interaction of a porous object, e.g. in falling trajectory or in the context of Vortex Induced Vibrations.**

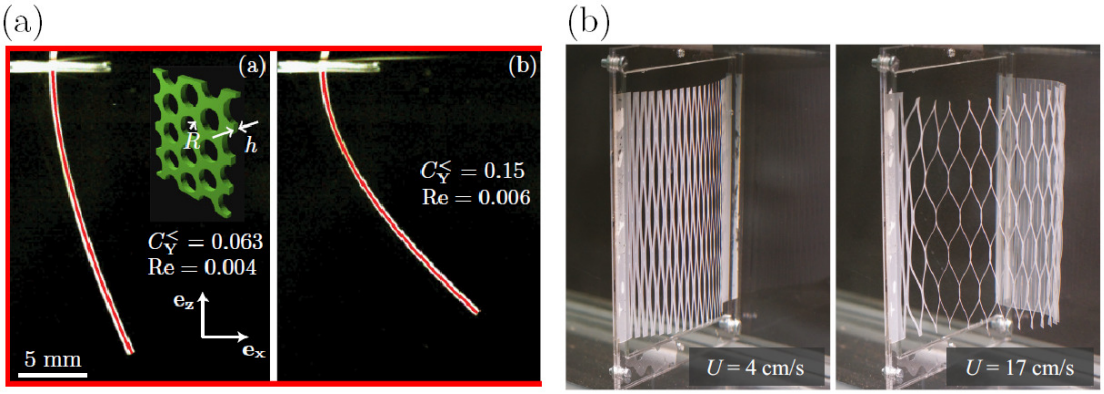

Figure 12.8: (a) Deformation of a porous flexible strip, clamped at one end, towed through a viscous fluid, reproduced with permission from Pezzulla et al. (2020) (https://doi.org/10.1103/PhysRevFluids.5.084103). (b) Deformation of a kirigami sheet invested by a water stream, reproduced with permission from Marzin et al. (2022) (https://doi.org/10.1103/PhysRevFluids.7.023906).

Fluid-structure interactions also include the deformation of the microstructure. A typical example is the deformation of a canopy induced by a fluid stream (Nepf, 2012). Homogenized models with faithfully describe the deformations of porous beds have been developed in Zampogna et al. (2019a) and Lācis et al. (2017). Two examples of fluid-structure interaction of a porous membrane are reported in figure 12.8, extracted from Pezzulla et al. (2020) and Marzin et al. (2022). In figure 12.8(a), a porous strip, clamped at one end, is towed through a viscous fluid. At very low Reynolds numbers, the drag coefficient is almost constant in a large range of permeability and thus the deformations predominantly depend on the porosity, which sets the bending stiffness of the flexible strip. At larger Reynolds numbers, the flow has enough energy to pass through the holes and thus the deformations are set by the competition between porosity and permeability. In figure 12.8(b), a kirigami sheet is subject to a water stream. Depending on the free-stream velocity, different deformations of the sheet are induced. These deformations result from the competition between the fluid forces and the stretching of the kirigami sheet, both influenced by the geometry. **The small and large deformations of a porous membrane subject to fluid forces still need to be modeled within the homogenization framework.**

12.4 Final remarks

Multiscale models showed great potential in the understanding of pattern formation. The separation between “fast” and “slow” variations allowed us to retain the essential physics needed to understand the large-scale behavior of the considered flows and to develop analytical and semi-analytical tools in the context of asymptotic analysis, bifurcation theory, and optimization. The rivulet formation is the perfect example which explains this concept. While retaining a simplified physics with semi-parabolic velocity and linear pressure profiles inside

the thin film, the resulting model shed light on the emergence and stability of these non-trivial and intricate free-surface patterns. The lubrication model allowed us to exploit several stability methods (local, weakly non-parallel and global stability analysis) and simplified models to describe the rivulet profile (one-dimensional model with imposed flow rate and elastica analogy).

Far from being exhaustive, we focused on two different flows, i.e. thin films and wake flows around and through porous bodies. Countless problems are characterized by a separation of scales and by the interplay of different physics. An example which combines the two main directions of this thesis is mucociliary clearance, i.e. the removal of mucus from the lung. The lung walls present a dense canopy of cilia oscillating from upstream to downstream (so-called *metachronal* waves) and transport the mucus film attached to the walls out of the lung, thus removing foreign particles (Fulford and Blake, 1986). At the large scale, mangroves are groups of shrubs and trees encountered in coastal intertidal zones. Mangroves protect nearby areas from tsunamis and extreme weather events, are effective in carbon sequestration and storage and impede climate change (van Zelst et al., 2021). In these examples, the interaction between free-surface deformations, the flow through the porous structure and the deformations of the structure itself may play a role. Multiscale models combined with linear stability tools may be suitable to understand these flow patterns characterized by intrinsic multiphysics.

Bibliography

Abdelall, F., Abdel-Khalik, S., Sadowski, D., Shin, S., and Yoda, M. (2006). On the rayleigh–taylor instability for confined liquid films with injection through the bounding surfaces. *International journal of heat and mass transfer*, 49(7-8):1529–1546.

Abderrahaman-Elena, N. and García-Mayoral, R. (2017). Analysis of anisotropically permeable surfaces for turbulent drag reduction. *Physical Review Fluids*, 2(11):114609.

Acheson, D. J. (1990). *Elementary fluid dynamics*. Oxford: Clarendon Press.

Adler, P. (1981). Streamlines in and around porous particles. *Journal of Colloid and Interface Science*, 81(2):531–535.

Afkhami, S. and Kondic, L. (2015). On the dewetting of liquefied metal nanostructures. *Journal of Engineering Mathematics*, 94(1):5–18.

Akabane, T. (2016). Production method & market trend of rubber gloves. *International Polymer Science and Technology*, 43(5):45–50.

Alexeev, A. and Oron, A. (2007). Suppression of the Rayleigh-Taylor instability of thin liquid films by the Marangoni effect. *Physics of Fluids*, 19(8):082101.

Ancey, C. (2007). Plasticity and geophysical flows: a review. *Journal of Non-Newtonian Fluid Mechanics*, 142(1-3):4–35.

Andersen, A., Pesavento, U., and Wang, Z. J. (2005). Analysis of transitions between fluttering, tumbling and steady descent of falling cards. *Journal of Fluid Mechanics*, 541:91–104.

Arratia, C., Mowlavi, S., and Gallaire, F. (2018). Absolute/convective secondary instabilities and the role of confinement in free shear layers. *Physical Review Fluids*, 3(5):053901.

Assemat, P., Fabre, D., and Magnaudet, J. (2012). The onset of unsteadiness of two-dimensional bodies falling or rising freely in a viscous fluid: a linear study. *Journal of fluid mechanics*, 690:173–202.

Auguste, F., Magnaudet, J., and Fabre, D. (2013). Falling styles of disks. *Journal of Fluid Mechanics*, 719:388–405.

Aussillous, P. and Quéré, D. (2002). Bubbles creeping in a viscous liquid along a slightly inclined plane. *EPL (Europhysics Letters)*, 59(3):370.

Babchin, A., Frenkel, A., Levich, B., and Sivashinsky, G. (1983). Nonlinear saturation of Rayleigh–Taylor instability in thin films. *The Physics of fluids*, 26(11):3159–3161.

Balestra, G., Badaoui, M., Ducimetière, Y.-M., and Gallaire, F. (2019). Fingering instability on curved substrates: optimal initial film and substrate perturbations. *Journal of Fluid Mechanics*, 868:726–761.

Balestra, G., Kofman, N., Brun, P.-T., Scheid, B., and Gallaire, F. (2018a). Three-dimensional Rayleigh-Taylor instability under a unidirectional curved substrate. *Journal of Fluid Mechanics*, 837:19–47.

Balestra, G., Nguyen, D. M.-P., and Gallaire, F. (2018b). Rayleigh-Taylor instability under a spherical substrate. *Physical Review Fluids*, 3(8):084005.

Balestra, G. M. N. (2018). Pattern formation in thin liquid films: from coating-flow instabilities to microfluidic droplets. Technical report, EPFL.

Balmforth, N. J., Burbidge, A. S., Craster, R. V., Salzig, J., and Shen, A. (2000). Visco-plastic models of isothermal lava domes. *Journal of Fluid Mechanics*, 403:37–65.

Balmforth, N. J. and Kerswell, R. R. (2005). Granular collapse in two dimensions. *Journal of Fluid Mechanics*, 538:399–428.

Barannyk, L., Papageorgiou, D., and Petropoulos, P. (2012). Suppression of Rayleigh–Taylor instability using electric fields. *Mathematics and Computers in Simulation*, 82(6):1008–1016.

Barkley, D. (2006). Linear analysis of the cylinder wake mean flow. *Europhysics Letters*, 75(5):750–756.

Barkley, D. and Henderson, R. (1996). Three-dimensional floquet stability analysis of the wake of a circular cylinder. *Journal of Fluid Mechanics*, 322:215–241.

Barlow, N., Helenbrook, B., and Weinstein, S. (2017). Algorithm for spatio-temporal analysis of the signalling problem. *IMA Journal of Applied Mathematics*, 82(1):1–32.

Batchelor, G. K. and Gill, A. E. (1962). Analysis of the stability of axisymmetric jets. *Journal of Fluid Mechanics*, 14(4):529–551.

Battiato, I. and Rubol, S. (2014). Single-parameter model of vegetated aquatic flows. *Water Resources Research*, 50(8):6358–6369.

Beavers, G. S. and Joseph, D. D. (1967). Boundary conditions at a natural permeable wall. *Journal of Fluid Mechanics*, 30:197–207.

Becker, J., Grün, G., Seemann, R., Mantz, H., Jacobs, K., Mecke, K. R., and Blossey, R. (2003). Complex dewetting scenarios captured by thin-film models. *Nature materials*, 2(1):59–63.

Belmonte, A., Eisenberg, H., and Moses, E. (1998). From flutter to tumble: inertial drag and froude similarity in falling paper. *Physical Review Letters*, 81(2):345.

Benjamin, T. B. (1968). Gravity currents and related phenomena. *Journal of Fluid Mechanics*, 31(2):209–248.

Benney, D. J. (1966). Long waves on liquid films. *Journal of Mathematics and Physics*, 45(1-4):150–155.

Bers, A. (1975). Linear waves and instabilities. In *Plasma physics–les houches 1972*.

Bertagni, M. and Camporeale, C. (2021). The hydrodynamic genesis of linear karren patterns. *Journal of Fluid Mechanics*, 913.

Bertagni, M. B. and Camporeale, C. (2017). Nonlinear and subharmonic stability analysis in film-driven morphological patterns. *Physical Review E*, 96(5):053115.

Bertozzi, A. L. and Brenner, M. P. (1997). Linear stability and transient growth in driven contact lines. *Physics of Fluids*, 9(3):530–539.

Bestehorn, M. and Merkt, D. (2006). Regular surface patterns on Rayleigh-Taylor unstable evaporating films heated from below. *Physical review letters*, 97(12):127802.

Bhandaru, N., Das, A., Salunke, N., and Mukherjee, R. (2014). Ordered alternating binary polymer nanodroplet array by sequential spin dewetting. *Nano letters*, 14(12):7009–7016.

Bhandaru, N., Kaur, G., Panjla, A., and Verma, S. (2021). Spin coating mediated morphology modulation in self assembly of peptides. *Nanoscale*, 13(19):8884–8892.

Bhattacharyya, A. (2010). Effect of momentum transfer condition at the interface of a model of creeping flow past a spherical permeable aggregate. *European Journal of Mechanics-B/Fluids*, 29(4):285–294.

Bico, J. and Quéré, D. (2002). Self-propelling slugs. *Journal of Fluid Mechanics*, 467:101–127.

Bischof, J., Scherer, D., Herminghaus, S., and Leiderer, P. (1996). Dewetting modes of thin metallic films: nucleation of holes and spinodal dewetting. *Physical review letters*, 77(8):1536.

Bongarzone, A., Bertsch, A., Renaud, P., and Gallaire, F. (2021). Impinging planar jets: hysteretic behaviour and origin of the self-sustained oscillations. *Journal of Fluid Mechanics*, 913:A51.

Bonn, D., Eggers, J., Indekeu, J., Meunier, J., and Rolley, E. (2009). Wetting and spreading. *Reviews of modern physics*, 81(2):739.

Boos, W. and Thess, A. (1999). Cascade of structures in long-wavelength Marangoni instability. *Physics of Fluids*, 11(6):1484–1494.

Bordiec, M. (2020). *Formation d'ondes topographiques par transfert de masse et diffusion dans un écoulement turbulent : analyse d'exemples naturels terrestres et planétaires et modélisations*. PhD thesis. Thèse de doctorat dirigée par Bourgeois, Olivier Sciences de la Terre et des planètes Nantes 2020.

Bottaro, A. (2019). Flow over natural or engineered surfaces: an adjoint homogenization perspective. *Journal of Fluid Mechanics*, 877:P1.

Boujo, E., Ehrenstein, U., and Gallaire, F. (2013). Open-loop control of noise amplification in a separated boundary layer flow. *Physics of Fluids*, 25(12):124106.

Boujo, E. and Gallaire, F. (2014). Controlled reattachment in separated flows: a variational approach to recirculation length reduction. *Journal of Fluid Mechanics*, 742:618–635.

Boujo, E. and Gallaire, F. (2015). Sensitivity and open-loop control of stochastic response in a noise amplifier flow: the backward-facing step. *Journal of Fluid Mechanics*, 762:361–392.

Brancher, P. and Chomaz, J.-M. (1997). Absolute and convective secondary instabilities in spatially periodic shear flows. *Physical review letters*, 78(4):658.

Breugem, W. P. (2004). The influence of wall permeability on laminar and turbulent flows, Theory and simulations. *Doctoral dissertation, TU Delft, Delft University of Technology*.

Brevdo, L. (1991). Three-dimensional absolute and convective instabilities, and spatially amplifying waves in parallel shear flows. *Zeitschrift für angewandte Mathematik und Physik ZAMP*, 42(6):911–942.

Briggs, R. J. (1964). Electron stream interaction with plasmas. In *Handbook of Plasma Physics*. MIT Press.

Brinkman, H. C. (1949). A calculation of the viscous force exerted by a flowing fluid on a dense swarm of particles. *Flow, Turbulence and Combustion*, 1(1):27.

Brochard-Wyart, F. and De Gennes, P. (1992). Dynamics of partial wetting. *Advances in colloid and interface science*, 39:1–11.

Brun, P.-T., Damiano, A., Rieu, P., Balestra, G., and Gallaire, F. (2015). Rayleigh-Taylor instability under an inclined plane. *Physics of Fluids*, 27(8):084107.

Brunet, P., Flesselles, J. M., and Limat, L. (2007). Dynamics of a circular array of liquid columns. *EUROPEAN PHYSICAL JOURNAL B*, 55(3):297–322.

Brunet, Y. (2020). Turbulent flow in plant canopies: historical perspective and overview. *Boundary-Layer Meteorology*, 177(2):315–364.

Buhmann, D. and Dreybrodt, W. (1985). The kinetics of calcite dissolution and precipitation in geologically relevant situations of karst areas: 1. open system. *Chemical geology*, 48(1-4):189–211.

Bulow, T. and Sommer, G. (2001). Hypercomplex signals-a novel extension of the analytic signal to the multidimensional case. *IEEE Transactions on signal processing*, 49(11):2844–2852.

Burgess, J., Juel, A., McCormick, W., Swift, J., and Swinney, H. L. (2001). Suppression of dripping from a ceiling. *Physical review letters*, 86(7):1203.

Camarri, S. and Iollo, A. (2010). Feedback control of the vortex-shedding instability based on sensitivity analysis. *Physics of Fluids*, 22(9):094102.

Camporeale, C. (2015). Hydrodynamically locked morphogenesis in karst and ice flutings. *Journal of Fluid Mechanics*, 778:89–119.

Camporeale, C. and Ridolfi, L. (2012). Hydrodynamic-driven stability analysis of morphological patterns on stalactites and implications for cave paleoflow reconstructions. *Phys. Rev. Lett.*, 108:238501.

Cantat, I. (2013). Liquid meniscus friction on a wet plate: Bubbles, lamellae, and foams. *Physics of Fluids*, 25(3):031303.

Carriere, P. and Monkewitz, P. (1999). Convective versus absolute instability in mixed rayleigh–bénard–poiseuille convection. *Journal of Fluid Mechanics*, 384:243–262.

Casseau, V., Croon, G., Izzo, D., and Pandolfi, C. (2015). Morphologic and aerodynamic considerations regarding the plumed seeds of tragopogon pratensis and their implications for seed dispersal. *PLOS ONE*.

Castro, I. P. (1971). Wake characteristics of two-dimensional perforated plates normal to an air-stream. *Journal of Fluid Mechanics*, 46(3):599–609.

Chakrabarty, P., Ghorai, A., Ray, S. K., and Mukherjee, R. (2020). Polymer thin-film dewetting-mediated growth of wettability-controlled titania nanorod arrays for highly responsive, water-stable self-powered uv photodetectors. *ACS Applied Electronic Materials*, 2(9):2895–2905.

Chandrasekhar, S. (2013). *Hydrodynamic and hydromagnetic stability*. Courier Corporation.

Chang, H. (1994). Wave evolution on a falling film. *Annual review of fluid mechanics*, 26(1):103–136.

Charogiannis, A., Denner, F., van Wachem, B. G. M., Kalliadasis, S., Scheid, B., and Markides, C. N. (2018). Experimental investigations of liquid falling films flowing under an inclined planar substrate. *Physical Review Fluids*, 3(11):114002.

Chomaz, J.-M. (2005). Global instabilities in spatially developing flows: Non-normality and nonlinearity. *Annual Review of Fluid Mechanics*, 37(1):357–392.

Cimpeanu, R., Papageorgiou, D., and Petropoulos, P. (2014). On the control and suppression of the Rayleigh-Taylor instability using electric fields. *Physics of Fluids*, 26(2):022105.

Citro, V., Siconolfi, L., Fabre, D., Giannetti, F., and Luchini, P. (2017). Stability and sensitivity analysis of the secondary instability in the sphere wake. *AIAA Journal*, 55(11):3661–3668.

Couder, Y., Fort, E., Gautier, C.-H., and Boudaoud, A. (2005). From bouncing to floating: Noncoalescence of drops on a fluid bath. *Phys. Rev. Lett.*, 94:177801.

Craster, R. V. and Matar, O. K. (2009). Dynamics and stability of thin liquid films. *Reviews of modern physics*, 81(3):1131.

Crighton, D. and Gaster, M. (1976). Stability of slowly diverging jet flow. *Journal of Fluid Mechanics*, 77(2):397–413.

Cummins, C., Seale, M., Macente, A., Certini, D., Mastropaolo, E., Viola, I., and Nakayama, N. (2018). A separated vortex ring underlies the flight of the dandelion. *Nature*, 562(7727):414–418.

Cummins, C., Viola, I. M., Mastropaolo, E., and Nakayama, N. (2017). The effect of permeability on the flow past permeable disks at low reynolds numbers. *Physics of Fluids*, 29(9):097103.

D'Alessio, S., Pascal, J., Jasmine, H., and Ogden, K. (2010). Film flow over heated wavy inclined surfaces. *Journal of Fluid Mechanics*, 665:418–456.

Dalwadi, M. P., Bruna, M., and Griffiths, I. M. (2016). A multiscale method to calculate filter blockage. *Journal of Fluid Mechanics*, 809:264–289.

Darcy, H. (1856). *Les Fontaines publiques de la ville de Dijon*. V. Dalmont.

De Gennes, P.-G., Brochard-Wyart, F., Quéré, D., et al. (2004). *Capillarity and wetting phenomena: drops, bubbles, pearls, waves*, volume 336. Springer.

de Langre, E. (2008). Effects of wind on plants. *Annual Review of Fluid Mechanics*, 40(1):141–168.

Decker, M., Staude, I., Falkner, M., Dominguez, J., Neshev, D. N., Brener, I., Pertsch, T., and Kivshar, Y. S. (2015). High-efficiency dielectric huygens' surfaces. *Advanced Optical Materials*, 3(6):813–820.

Decré, M. M. J. and Baret, J.-C. (2003). Gravity-driven flows of viscous liquids over two-dimensional topographies. *Journal of Fluid Mechanics*, 487:147–166.

Delbende, I. and Chomaz, J.-M. (1998). Nonlinear convective/absolute instabilities in parallel two-dimensional wakes. *Physics of Fluids*, 10(11):2724–2736.

Delbende, I., Chomaz, J.-M., and Huerre, P. (1998). Absolute/convective instabilities in the batchelor vortex: a numerical study of the linear impulse response. *Journal of Fluid Mechanics*, 355:229–254.

Derjaguin, B. and Churaev, N. (1974). Structural component of disjoining pressure. *Journal of Colloid and Interface Science*, 49(2):249–255.

Deserno, M. (2004). Notes on differential geometry. Available at http://www.cmu.edu/biolphys/deserno/pdf/diff_geom.pdf.

Didden, N. and Maxworthy, T. (1982). The viscous spreading of plane and axisymmetric gravity currents. *Journal of Fluid Mechanics*, 121:27–42.

Dietze, G., Picardo, J., and Narayanan, R. (2018). Sliding instability of draining fluid films. *Journal of Fluid Mechanics*, 857:111–141.

Diez, J. A. and Kondic, L. (2001). Contact line instabilities of thin liquid films. *Phys. Rev. Lett.*, 86:632–635.

Dreybrodt, W. (1999). Chemical kinetics, speleothem growth and climate. *Boreas*, 28(3):347–356.

Duprat, C., Ruyer-Quil, C., Kalliadasis, S., and Giorgiutti-Dauphiné, F. (2007). Absolute and convective instabilities of a viscous film flowing down a vertical fiber. *Physical review letters*, 98(24):244502.

Duprat, C. and Stone, H. A. (2015). *Fluid-Structure Interactions in Low-Reynolds-Number Flows*. Royal Society of Chemistry.

Elimelech, M. and Phillip, W. (2011). The future of seawater desalination: Energy, technology, and the environment. *Science*, 333:712–717.

Endrikat, S., Modesti, D., García-Mayoral, R., Hutchins, N., and Chung, D. (2021). Influence of riblet shapes on the occurrence of kelvin–helmholtz rollers. *Journal of Fluid Mechanics*, 913.

Ergun, S. (1952). Fluid flow through packed columns. *Chem. Eng. Progr*, 48:88–94.

Ern, P., Risso, F., Fabre, D., and Magnaudet, J. (2012). Wake-induced oscillatory paths of bodies freely rising or falling in fluids. *Annual Review of Fluid Mechanics*, 44:97–121.

Fabre, D., Assemat, P., and Magnaudet, J. (2011). A quasi-static approach to the stability of the path of heavy bodies falling within a viscous fluid. *Journal of fluids and structures*, 27(5-6):758–767.

Fabre, D., Auguste, F., and Magnaudet, J. (2008). Bifurcations and symmetry breaking in the wake of axisymmetric bodies. *Physics of Fluids*, 20(5):051702.

Felsberg, M. and Sommer, G. (2001). The monogenic signal. *IEEE transactions on signal processing*, 49(12):3136–3144.

Fermigier, M., Limat, L., Wesfreid, J., Boudinet, P., and Quilliet, C. (1992). Two-dimensional patterns in rayleigh-taylor instability of a thin layer. *Journal of Fluid Mechanics*, 236:349–383.

Fernandes, P. C., Risso, F., Ern, P., and Magnaudet, J. (2007). Oscillatory motion and wake instability of freely rising axisymmetric bodies. *Journal of Fluid Mechanics*, 573:479–502.

Field, S. B., Klaus, M., Moore, M., and Nori, F. (1997). Chaotic dynamics of falling disks. *Nature*, 388(6639):252–254.

Finnigan, J. (2000). Turbulence in plant canopies. *Annual Review of Fluid Mechanics*, 32(1):519–571.

Flato, G., Marotzke, J., Abiodun, B., Braconnot, P., Chou, S. C., Collins, W., Cox, P., Driouech, F., Emori, S., Eyring, V., et al. (2014). Evaluation of climate models. In *Climate change 2013: the physical science basis. Contribution of Working Group I to the Fifth Assessment Report of the Intergovernmental Panel on Climate Change*, pages 741–866. Cambridge University Press.

Forchheimer, P. (1901). Wasserbewegung durch boden. *Z. Ver. Deutsch. Ing.*, 45:1782–1788.

Fornberg, B. (1980). A numerical study of steady viscous flow past a circular cylinder. *Journal of Fluid Mechanics*, 98(4):819–855.

Fritzmann, C., L owenberg, J., Wintgens, T., and Melin, T. (2007). State-of-the-art of reverse osmosis desalination. *Desalin.*, 216:1–76.

Fulford, G. R. and Blake, J. R. (1986). Muco-ciliary transport in the lung. *Journal of theoretical Biology*, 121(4):381–402.

Gallaire, F. and Brun, P.-T. (2017). Fluid dynamic instabilities: theory and application to pattern forming in complex media. *Philosophical Transactions of the Royal Society A: Mathematical, Physical and Engineering Sciences*, 375(2093):20160155.

Gallaire, F. and Chomaz, J.-M. (2003). Mode selection in swirling jet experiments: a linear stability analysis. *Journal of Fluid Mechanics*, 494:223–253.

Garcia-Mayoral, R. and Jiménez, J. (2011). Drag reduction by riblets. *Philosophical transactions of the Royal society A: Mathematical, physical and engineering Sciences*, 369(1940):1412–1427.

Garnaud, X., Lesshafft, L., Schmid, P., and Huerre, P. (2013). The preferred mode of incompressible jets: linear frequency response analysis. *Journal of Fluid Mechanics*, 716:189–202.

Gaster, M. (1962). A note on the relation between temporally-increasing and spatially-increasing disturbances in hydrodynamic stability. *Journal of Fluid Mechanics*, 14(2):222–224.

Gaster, M., Kit, E., and Wygnanski, I. (1985). Large-scale structures in a forced turbulent mixing layer. *Journal of Fluid Mechanics*, 150:23–39.

Giannetti, F. and Luchini, P. (2007). Structural sensitivity of the first instability of the cylinder wake. *Journal of Fluid Mechanics*, 581:167–197.

Glasner, K. (2007). The dynamics of pendant droplets on a one-dimensional surface. *Physics of Fluids*, 19(10):102104.

Gómez-de Segura, G. and García-Mayoral, R. (2019). Turbulent drag reduction by anisotropic permeable substrates – analysis and direct numerical simulations. *Journal of Fluid Mechanics*, 875:124–172.

Gumowski, K., Miedzik, J., Goujon-Durand, S., Jenffer, P., and Wesfreid, J. (2008). Transition to a time-dependent state of fluid flow in the wake of a sphere. *Physical Review E*, 77(5):055308.

Gupta, T. D., Martin-Monier, L., Yan, W., Le Bris, A., Nguyen-Dang, T., Page, A. G., Ho, K.-T., Yesilköy, F., Altug, H., Qu, Y., et al. (2019). Self-assembly of nanostructured glass metasurfaces via templated fluid instabilities. *Nature nanotechnology*, 14(4):320–327.

Hahn, S. (2003). Complex signals with single-orthant spectra as boundary distributions of multidimensional analytic functions. *Bull. Pol. Ac.: Tech*, 2(2):155–161.

Hamed, A. M., Peterlein, A. M., and Speck, I. (2020). Characteristics of the turbulent flow within short canopy gaps. *Physical Review Fluids*, 5(12):123801.

Harrison, D. (1974). Fluidization. *Science Progress (1933-)*, 61(242):191–217.

Hartnett, C. A., Mahady, K., Fowlkes, J. D., Afkhami, S., Kondic, L., and Rack, P. (2015). Instability of nano-and microscale liquid metal filaments: transition from single droplet collapse to multidroplet breakup. *Langmuir*, 31(50):13609–13617.

Hayes, M., O'Brien, S. B. G., and Lammers, J. H. (2000). Green's function for steady flow over a small two-dimensional topography. *Physics of Fluids*, 12(11):2845–2858.

Heining, C. and Aksel, N. (2009). Bottom reconstruction in thin-film flow over topography: Steady solution and linear stability. *Physics of Fluids*, 21(8):083605.

Herminghaus, S., Jacobs, K., Mecke, K., Bischof, J., Fery, A., Ibn-Elhaj, M., and Schlagowski, S. (1998). Spinodal dewetting in liquid crystal and liquid metal films. *Science*, 282(5390):916–919.

Hill, C., Forti, P., and Shaw, T. (1997). *Cave minerals of the world*, volume 238. National speleological society Huntsville.

Högberg, M. and Henningson, D. (1998). Secondary instability of cross-flow vortices in falkner–skan–cooke boundary layers. *Journal of Fluid Mechanics*, 368:339–357.

Hornung, U. (1997). *Homogenization and Porous Media*. Springer, New York.

Hosoi, A. E. and Bush, J. W. M. (2001). Evaporative instabilities in climbing films. *Journal of fluid Mechanics*, 442:217.

Hoult, D. P. (1972). Oil spreading on the sea. *Annual Review of Fluid Mechanics*, 4(1):341–368.

Howell, P. (2003). Surface-tension-driven flow on a moving curved surface. *Journal of engineering mathematics*, 45(3):283–308.

Huerre, P. and Monkewitz, P. (1990). Local and global instabilities in spatially developing flows. *Annual review of fluid mechanics*, 22(1):473–537.

Huerre, P. and Rossi, M. (1998). *Hydrodynamic instabilities in open flows*, page 81–294. Collection Alea-Saclay: Monographs and Texts in Statistical Physics. Cambridge University Press.

Huppert, H. E. (1982a). Flow and instability of a viscous current down a slope. *Nature*, 300(5891):427–429.

Huppert, H. E. (1982b). The propagation of two-dimensional and axisymmetric viscous gravity currents over a rigid horizontal surface. *Journal of Fluid Mechanics*, 121:43–58.

Huppert, H. E. (1986). The intrusion of fluid mechanics into geology. *Journal of fluid mechanics*, 173:557–594.

Huppert, H. E. (2006). Gravity currents: a personal perspective. *Journal of Fluid Mechanics*, 554:299–322.

Huppert, H. E. and Simpson, J. E. (1980). The slumping of gravity currents. *Journal of Fluid Mechanics*, 99(4):785–799.

Indeikina, A., Veretennikov, I., and Chang, H.-C. (1997). Drop fall-off from pendent rivulets. *Journal of Fluid Mechanics*, 338:173–201.

Irgens, F. (2019). *Tensor Analysis*. Springer.

Israelachvili, J. N. (2015). *Intermolecular and surface forces*. Academic press.

Iungo, G., Viola, F., Camarri, S., Porté-Agel, F., and Gallaire, F. (2013). Linear stability analysis of wind turbine wakes performed on wind tunnel measurements. *Journal of Fluid Mechanics*, 737:499–526.

Ivanov, I. (1988). *Thin liquid films*. CRC Press.

Jackson, C. (1987). A finite-element study of the onset of vortex shedding in flow past variously shaped bodies. *Journal of fluid Mechanics*, 182:23–45.

Jaworski, J. and Peake, N. (2020). Aeroacoustics of silent owl flight. *Annual Review of Fluid Mechanics*, 52(1):395–420.

Jeffreys, H. (1930). The draining of a vertical plate. *Mathematical Proceedings of the Cambridge Philosophical Society*, 26(2):204–205.

Jenny, M., Dušek, J., and Bouchet, G. (2004). Instabilities and transition of a sphere falling or ascending freely in a newtonian fluid. *Journal of Fluid Mechanics*, 508:201–239.

Jensen, K. H., Berg-Sørensen, K., Bruus, H., Holbrook, N., Liesche, J., Schulz, A., Zwieniecki, M., and Bohr, T. (2016). Sap flow and sugar transport in plants. *Rev. Mod. Phys.*, 88(035007).

Jiang, W., Bao, W., Thompson, C. V., and Srolovitz, D. J. (2012). Phase field approach for simulating solid-state dewetting problems. *Acta materialia*, 60(15):5578–5592.

Johnson, T. and Patel, V. (1999). Flow past a sphere up to a reynolds number of 300. *Journal of Fluid Mechanics*, 378:19–70.

Jones, T. J., Jambon-Puillet, E., Marthelot, J., and Brun, P.-T. (2021). Bubble casting soft robotics. *Nature*, 599(7884):229–233.

Josef, D. and Tao, L. (1964). The effect of permeability on the slow motion of a porous sphere in a viscous liquid. *Zamm*, 44(8/9):361–364.

Juniper, M. P. (2007). The full impulse response of two-dimensional jet/wake flows and implications for confinement. *Journal of Fluid Mechanics*, 590:163–185.

Kalliadasis, S., Bielarz, C., and Homsy, G. (2000). Steady free-surface thin film flows over topography. *Physics of Fluids*, 12(8):1889–1898.

Kalliadasis, S., Ruyer-Quil, C., Scheid, B., Velarde, M., and García, M. (2011). *Falling liquid films*, volume 176. Springer Science & Business Media.

Kapitza, P. L. (1948). Wave flow of thin layers of viscous liquid. *Zh. Eksper. Teoret. Fiz.*, 18:3–28.

Kapitza, P. L. and Kapitza, S. P. (1965). Wave flow of thin layers of a viscous fluid: Experimental study of undulatory flow conditions. *Collected Papers of PL Kapitza (ed. D. Ter Haar)*, 2.

Kargupta, K. and Sharma, A. (2001). Templating of thin films induced by dewetting on patterned surfaces. *Physical Review Letters*, 86(20):4536.

Kargupta, K. and Sharma, A. (2002). Dewetting of thin films on periodic physically and chemically patterned surfaces. *Langmuir*, 18(5):1893–1903.

Kaufmann, G. (2003). Stalagmite growth and palaeo-climate: the numerical perspective. *Earth and Planetary Science Letters*, 214(1-2):251–266.

Kaufmann, G. and Dreybrodt, W. (2007). Calcite dissolution kinetics in the system caco3–h2o–co2 at high undersaturation. *Geochimica et Cosmochimica Acta*, 71(6):1398–1410.

Keulegan, G. H. (1957). An experimental study of the motion of saline water from locks into fresh water channels. *Nat. Bur. Stand. Rept. Technical Report*, 5168.

Kheshgi, H., Kistler, S., and Scriven, L. (1992). Rising and falling film flows: viewed from a first-order approximation. *Chemical engineering science*, 47(3):683–694.

Kim, H. I., Mate, C. M., Hannibal, K. A., and Perry, S. S. (1999). How disjoining pressure drives the dewetting of a polymer film on a silicon surface. *Physical review letters*, 82(17):3496.

King, K., Weinstein, S., Zaretzky, P., Cromer, M., and Barlow, N. (2016). Stability of algebraically unstable dispersive flows. *Phys. Rev. Fluids*, 1:073604.

Kofman, N., Rohlfs, W., Gallaire, F., Scheid, B., and Ruyer-Quil, C. (2018). Prediction of two-dimensional dripping onset of a liquid film under an inclined plane. *International Journal of Multiphase Flow*, 104:286–293.

Kondic, L. and Diez, J. (2001). Pattern formation in the flow of thin films down an incline: Constant flux configuration. *Physics of Fluids*, 13(11):3168–3184.

Kondic, L. and Diez, J. (2002). Flow of thin films on patterned surfaces: Controlling the instability. *Physical review. E, Statistical, nonlinear, and soft matter physics*, 65:045301.

Kondic, L., González, A. G., Diez, J. A., Fowlkes, J. D., and Rack, P. (2020). Liquid-state dewetting of pulsed-laser-heated nanoscale metal films and other geometries. *Annual Review of Fluid Mechanics*, 52(1):235–262.

Krechetnikov, R. (2010). On application of lubrication approximations to nonunidirectional coating flows with clean and surfactant interfaces. *Physics of Fluids*, 22(9):092102.

Kumar, S. (2015). Liquid transfer in printing processes: liquid bridges with moving contact lines. *Annual Review of Fluid Mechanics*, 47:67–94.

Labbé, R. and Duprat, C. (2019). Capturing aerosol droplets with fibers. *Soft Matter*, 15(35):6946–6951.

Lācis, U. and Bagheri, S. (2017). A framework for computing effective boundary conditions at the interface between free fluid and a porous medium. *J. Fluid Mech.*, 812:866–889.

Lācis, U., Zampogna, G., and Bagheri, S. (2017). A computational continuum model of poroelastic beds. *Proceedings of the Royal Society A: Mathematical, Physical and Engineering Sciences*, 473(2199):20160932.

Landau, L. D. and Levich, B. (1942). Dragging of a liquid by a moving plate. *Acta Physicochem. URSS*, 17.

Lapuerta, V., Mancebo, F., and Vega, J. (2001). Control of Rayleigh-Taylor instability by vertical vibration in large aspect ratio containers. *Physical Review E*, 64(1):016318.

Lācis, U., Sudhakar, Y., Pasche, S., and Bagheri, S. (2020). Transfer of mass and momentum at rough and porous surfaces. *Journal of Fluid Mechanics*, 884:A21.

Le Bris, A., Maloum, F., Teisseire, J., and Sorin, F. (2014). Self-organized ordered silver nanoparticle arrays obtained by solid state dewetting. *Applied Physics Letters*, 105(20):203102.

Ledda, P. G., Siconolfi, L., Viola, F., Camarri, S., and Gallaire, F. (2019). Flow dynamics of a dandelion pappus: A linear stability approach. *Phys. Rev. Fluids*, 4:071901.

Ledda, P. G., Siconolfi, L., Viola, F., Gallaire, F., and Camarri, S. (2018). Suppression of von kármán vortex streets past porous rectangular cylinders. *Phys. Rev. Fluids*, 3:103901.

Lee, A., Brun, P.-T., Marthelot, J., Balestra, G., Gallaire, F., and Reis, P. M. (2016). Fabrication of slender elastic shells by the coating of curved surfaces. *Nature communications*, 7(1):1–7.

Leitis, A., Heßler, A., Wahl, S., Wuttig, M., Taubner, T., Tittl, A., and Altug, H. (2020). All-dielectric programmable huygens' metasurfaces. *Advanced Functional Materials*, 30(19):1910259.

Lemke, M., Reiss, J., and Sesterhenn, J. (2014). Adjoint based optimisation of reactive compressible flows. *Combustion and Flame*, 161(10):2552–2564.

Lerisson, G. (2017). *Stabilité d'une onde de gravité interne, analyse locale, globale et croissance transitoire.* PhD thesis. Thèse de doctorat dirigée par Chomaz, Jean-Marc et Ortiz Clerc, Sabine Mécanique des fluides Paris Saclay 2017.

Lerisson, G., Ledda, P., Balestra, G., and Gallaire, F. (2019). Dripping down the rivulet. *Physical Review Fluids*, 4(10):100504.

Levresse, P., Manas-Zloczower, I., and Feke, D. (2001). Hydrodynamic analysis of porous spheres with infiltrated peripheral shells in linear flow fields. *Chemical engineering science*, 56(10):3211–3220.

Li, G., Zhang, S., and Zentgraf, T. (2017). Nonlinear photonic metasurfaces. *Nature Reviews Materials*, 2(5):1–14.

Lifshitz, E. M., Hamermesh, M., et al. (1992). The theory of molecular attractive forces between solids. In *Perspectives in Theoretical Physics*, pages 329–349. Elsevier.

Limat, L., Jenffer, P., Dagens, B., Touron, E., Fermigier, M., and Wesfreid, J. (1992). Gravitational instabilities of thin liquid layers: dynamics of pattern selection. *Physica D: Nonlinear Phenomena*, 61(1-4):166–182.

Lin, C.-J. (2007). Projected gradient methods for nonnegative matrix factorization. *Neural computation*, 19(10):2756–2779.

Lin, T.-S., Dijksman, J., and Kondic, L. (2021). Thin liquid films in a funnel. *Journal of Fluid Mechanics*, 924.

Lin, T.-S., Kondic, L., and Filippov, A. (2012). Thin films flowing down inverted substrates: Three-dimensional flow. *Physics of Fluids*, 24(2):022105.

Lister, J., Rallison, J., and Rees, S. (2010). The nonlinear dynamics of pendent drops on a thin film coating the underside of a ceiling. *Journal of Fluid Mechanics*, 647:239–264.

Lister, J. R. (1992). Viscous flows down an inclined plane from point and line sources. *Journal of Fluid Mechanics*, 242:631–653.

Liu, M., Huai, W., and Ji, B. (2021). Characteristics of the flow structures through and around a submerged canopy patch. *Physics of Fluids*, 33(3):035144.

Lu, G., Li, W., Yao, J., Zhang, G., Yang, B., and Shen, J. (2002). Fabricating ordered two-dimensional arrays of polymer rings with submicrometer-sized features on patterned self-assembled monolayers by dewetting. *Advanced Materials*, 14(15):1049–1053.

Luchini, P. and Bottaro, A. (2014). Adjoint equations in stability analysis. *Annual Review of Fluid Mechanics*, 46(1):493–517.

Macdonald, I. F., El-Sayed, M. S., Mow, K., and Dullien, F. A. (1979). Flow through Porous Media - the Ergun Equation Revisited. *Industrial and Engineering Chemistry Fundamentals*, 18(3):199–208.

Mahady, K., Afkhami, S., Diez, J., and Kondic, L. (2013). Comparison of navier-stokes simulations with long-wave theory: Study of wetting and dewetting. *Physics of Fluids*, 25(11):112103.

Mahady, K., Afkhami, S., and Kondic, L. (2015). A volume of fluid method for simulating fluid/fluid interfaces in contact with solid boundaries. *Journal of Computational Physics*, 294:243–257.

Mahady, K., Afkhami, S., and Kondic, L. (2016). A numerical approach for the direct computation of flows including fluid-solid interaction: Modeling contact angle, film rupture, and dewetting. *Physics of Fluids*, 28(6):062002.

Maldarelli, C., Jain, R. K., Ivanov, I. B., and Ruckenstein, E. (1980). Stability of symmetric and unsymmetric thin liquid films to short and long wavelength perturbations. *Journal of Colloid and Interface Science*, 78(1):118–143.

Malitson, I. H. (1965). Interspecimen comparison of the refractive index of fused silica. *Josa*, 55(10):1205–1209.

Marquet, O., Sipp, D., and Jacquin, L. (2008). Sensitivity analysis and passive control of cylinder flow. *Journal of Fluid Mechanics*, 615:221.

Marthelot, J., Strong, E. F., Reis, P. M., and Brun, P.-T. (2018). Designing soft materials with interfacial instabilities in liquid films. *Nature communications*, 9(1):4477.

Marzin, T., Le Hay, K., de Langre, E., and Ramananarivo, S. (2022). Flow-induced deformation of kirigami sheets. *Physical Review Fluids*, 7(2):023906.

Masliyah, J. H. and Polikar, M. (1980). Terminal velocity of porous spheres. *The Canadian Journal of Chemical Engineering*, 58(3):299–302.

Matin, A., Khan, Z., Zaidia, S. M. J., and Boyce, M. C. (2011). Biofouling in reverse osmosis membranes for seawater desalination: Phenomena and prevention. *Desalin.*, 281:1–16.

Maxwell, J. (1875). Capillary action. *Encyclopaedia Britannica*, 9th Edn.

Mayo, L. C., McCue, S. W., Moroney, T. J., Forster, W. A., Kempthorne, D. M., Belward, J. A., and Turner, I. W. (2015). Simulating droplet motion on virtual leaf surfaces. *Royal Society open science*, 2(5):140528.

Meakin, P. and Jamtveit, B. (2010). Geological pattern formation by growth and dissolution in aqueous systems. *Proceedings of the Royal Society A: Mathematical, Physical and Engineering Sciences*, 466(2115):659–694.

Mei, C. C. and Vernescu, B. (2010). *Homogenization methods for multiscale mechanics*. World scientific.

Meliga, P., Boujo, E., Pujals, G., and Gallaire, F. (2014). Sensitivity of aerodynamic forces in laminar and turbulent flow past a square cylinder. *Physics of Fluids*, 26(10):104101.

Meliga, P., Chomaz, J.-M., and Sipp, D. (2009). Unsteadiness in the wake of disks and spheres: instability, receptivity and control using direct and adjoint global stability analyses. *Journal of Fluids and Structures*, 25(4):601–616.

Meliga, P., Sipp, D., and Chomaz, J.-M. (2010). Open-loop control of compressible afterbody flows using adjoint methods. *Physics of Fluids*, 22(5):054109.

Melville, W. (1983). Wave modulation and breakdown. *Journal of Fluid Mechanics*, 128:489–506.

Meyer, E. and Braun, H.-G. (2000). Controlled dewetting processes on microstructured surfaces–a new procedure for thin film microstructuring. *Macromolecular Materials and Engineering*, 276(1):44–50.

Mitlin, V. S. (1993). Dewetting of solid surface: Analogy with spinodal decomposition. *Journal of colloid and interface science*, 156(2):491–497.

Monkewitz, P. A. (1988). The absolute and convective nature of instability in two dimensional wakes at low Reynolds numbers. *The Physics of Fluids*, 31(5):999–1006.

Monkewitz, P. A., Huerre, P., and Chomaz, J.-M. (1993). Global linear stability analysis of weakly non-parallel shear flows. *Journal of Fluid Mechanics*, 251:1–20.

Monkewitz, P. A. and Sohn, K. (1988). Absolute instability in hot jets. *AIAA journal*, 26(8):911–916.

Morariu, M. D., Voicu, N. E., Schäffer, E., Lin, Z., Russell, T. P., and Steiner, U. (2003). Hierarchical structure formation and pattern replication induced by an electric field. *Nature materials*, 2(1):48–52.

Mowlavi, S., Arratia, C., and Gallaire, F. (2016). Spatio-temporal stability of the kármán vortex street and the effect of confinement. *Journal of Fluid Mechanics*, 795:187–209.

Murakami, D., Jinnai, H., and Takahara, A. (2014). Wetting transition from the cassie–baxter state to the wenzel state on textured polymer surfaces. *Langmuir*, 30(8):2061–2067.

Naqvi, S. B. and Bottaro, A. (2021). Interfacial conditions between a free-fluid region and a porous medium. *International Journal of Multiphase Flow*, 141:103585.

Natarajan, R. and Acrivos, A. (1993). The instability of the steady flow past spheres and disks. *Journal of Fluid Mechanics*, 254:323–344.

Neale, G., Epstein, N., and Nader, W. (1973). Creeping flow relative to permeable spheres. *Chemical Engineering Science*, 28(10):1865–1874.

Neale, G. and Nader, W. (1974). Practical significance of brinkman's extension of darcy's law: Coupled parallel flows within a channel and a bounding porous medium. *The Canadian Journal of Chemical Engineering*, 52(4):475–478.

Nemili, A., Özkaya, E., Gauger, N., Thiele, F., and Carnarius, A. (2011). Optimal control of unsteady flows using discrete adjoints. In *41st AIAA Fluid Dynamics conference and exhibit*, page 3720.

Nepf, H. M. (1999). Drag, turbulence, and diffusion in flow through emergent vegetation. *Water Resources Research*, 35(2):479–489.

Nepf, H. M. (2012). Flow and transport in regions with aquatic vegetation. *Annual Review of Fluid Mechanics*, 44(1):123–142.

Norberg, C. (2003). Fluctuating lift on a circular cylinder: review and new measurements. *Journal of Fluids and Structures*, 17(1):57–96.

Ochoa-Tapia, J. A. and Whitaker, S. (1995). Momentum transfer at the boundary between a porous medium and a homogeneous fluid-I. Theoretical development. *International Journal of Heat and Mass Transfer*, 38(14):2635–2646.

Ohara, P. C. and Gelbart, W. M. (1998). Interplay between hole instability and nanoparticle array formation in ultrathin liquid films. *Langmuir*, 14(12):3418–3424.

Olivier, J. (2004). Fog harvesting: An alternative source of water supply on the west coast of south africa. *GeoJournal*, 61(2):203–214.

Oron, A. (2000). Nonlinear dynamics of three-dimensional long-wave marangoni instability in thin liquid films. *Physics of Fluids*, 12(7):1633–1645.

Oron, A., Davis, S. H., and Bankoff, S. G. (1997). Long-scale evolution of thin liquid films. *Reviews of modern physics*, 69(3):931.

Park, H. B., Kamcev, J., Robeson, L. M., Elimelech, M., and Freeman, B. D. (2017). Maximizing the right stuff: the trade-off between membrane permeability and selectivity. *Science*, 356(6343).

Park, K.-C., Chhatre, S., Srinivasan, S., Cohen, R., and McKinley, G. (2013). Optimal design of permeable fiber network structures for fog harvesting. *Langmuir*, 29(43):13269–13277.

Pasche, S., Avellan, F., and Gallaire, F. (2017). Part load vortex rope as a global unstable mode. *Journal of Fluids Engineering*, 139(5).

Pauliac-Vaujour, E., Stannard, A., Martin, C., Blunt, M. O., Notingher, I., Moriarty, P., Vancea, I., and Thiele, U. (2008). Fingering instabilities in dewetting nanofluids. *Physical review letters*, 100(17):176102.

Pesavento, U. and Wang, Z. J. (2004). Falling paper: Navier-stokes solutions, model of fluid forces, and center of mass elevation. *Physical review letters*, 93(14):144501.

Peschka, D., Haefner, S., Marquant, L., Jacobs, K., Münch, A., and Wagner, B. (2019). Signatures of slip in dewetting polymer films. *Proceedings of the National Academy of Sciences*, 116(19):9275–9284.

Pezzulla, M., Strong, E. F., Gallaire, F., and Reis, P. M. (2020). Deformation of porous flexible strip in low and moderate reynolds number flows. *Phys. Rev. Fluids*, 5:084103.

Pier, B. (2003a). Finite-amplitude crossflow vortices, secondary instability and transition in the rotating-disk boundary layer. *Journal of Fluid Mechanics*, 487:315–343.

Pier, B. (2003b). Open-loop control of absolutely unstable domains. *Proceedings of the Royal Society of London. Series A: Mathematical, Physical and Engineering Sciences*, 459(2033):1105–1115.

Pier, B. (2008). Local and global instabilities in the wake of a sphere. *Journal of Fluid Mechanics*, 603:39–61.

Pier, B. (2011). Signalling problem in absolutely unstable systems. *Theoretical and Computational Fluid Dynamics*, 25(1):7–17.

Pier, B., Huerre, P., and Chomaz, J.-M. (2001). Bifurcation to fully nonlinear synchronized structures in slowly varying media. *Physica D: Nonlinear Phenomena*, 148(1-2):49–96.

Pirat, C., Mathis, C., Maissa, P., and Gil, L. (2004). Structures of a continuously fed two-dimensional viscous film under a destabilizing gravitational force. *PHYSICAL REVIEW LETTERS*, 92(10).

Pitts, E. (1973). The stability of pendent liquid drops. part 1. drops formed in a narrow gap. *Journal of Fluid Mechanics*, 59(4):753–767.

Prandtl, L. (1904). Verhandlungen des dritten internationalen mathematiker-kongresses. *Heidelberg, Leipeizig*, pages 484–491.

Provansal, M., Mathis, C., and Boyer, L. (1987). Bénard-von kármán instability: transient and forced regimes. *Journal of Fluid Mechanics*, 182:1–22.

Pumir, A., Manneville, P., and Pomeau, Y. (1983). On solitary waves running down an inclined plane. *Journal of fluid mechanics*, 135:27–50.

Qin, J., Xia, Y.-T., and Gao, P. (2021). Axisymmetric evolution of gravity-driven thin films on a small sphere. *Journal of Fluid Mechanics*, 907.

Quarteroni, A. (2017). *Domain decomposition methods*, pages 555–612. Springer International Publishing, Cham.

Rabani, E., Reichman, D. R., Geissler, P. L., and Brus, L. E. (2003). Drying-mediated self-assembly of nanoparticles. *Nature*, 426(6964):271–274.

Ra'di, Y., Sounas, D. L., and Alù, A. (2017). Metagratings: Beyond the limits of graded metasurfaces for wave front control. *Physical review letters*, 119(6):067404.

Rahardianto, A., McCool, B. C., and Cohen, Y. (2010). Accelerated desupersaturation of reverse osmosis concentrate by chemically-enhanced seeded precipitation. *Desalin.*, 264:256–267.

Rayleigh (1882). Investigation of the character of the equilibrium of an incompressible heavy fluid of variable density. *Proceedings of the London Mathematical Society*, s1-14(1):170–177.

Redon, C., Brochard-Wyart, F., and Rondelez, F. (1991). Dynamics of dewetting. *Physical review letters*, 66(6):715.

Reis, P. M. (2015). A perspective on the revival of structural (in) stability with novel opportunities for function: from buckliphobia to buckliphilia. *Journal of Applied Mechanics*, 82(11):111001.

Reiter, G. (1992). Dewetting of thin polymer films. *Physical review letters*, 68(1):75.

Reyssat, E. (2014). Drops and bubbles in wedges. *Journal of fluid mechanics*, 748:641–662.

Rietz, M., Kneer, R., Scheid, B., and Rohlfs, W. (2021). Spanwise structuring and rivulet formation in suspended falling liquid films. *Physical Review Fluids*, 6(8):084805.

Rietz, M., Scheid, B., Gallaire, F., Kofman, N., Kneer, R., and Rohlfs, W. (2017). Dynamics of falling films on the outside of a vertical rotating cylinder: waves, rivulets and dripping transitions. *Journal of Fluid Mechanics*, 832:189–211.

Roberts, A. J. and Li, Z. (2006). An accurate and comprehensive model of thin fluid flows with inertia on curved substrates. *Journal of Fluid Mechanics*, 553:33–73.

Rohlfs, W., Pischke, P., and Scheid, B. (2017). Hydrodynamic waves in films flowing under an inclined plane. *Physical Review Fluids*, 2(4):044003.

Roman, B., Gay, C., and Clanet, C. (2020). Pendulums, drops and rods: a physical analogy.

Romanov, D., Kaufmann, G., and Dreybrodt, W. (2008). Modeling stalagmite growth by first principles of chemistry and physics of calcite precipitation. *Geochimica et Cosmochimica Acta*, 72(2):423–437.

Roy, R. V., Roberts, A. J., and Simpson, M. E. (2002). A lubrication model of coating flows over a curved substrate in space. *Journal of Fluid Mechanics*, 454:235–261.

Roy, S. and Mukherjee, R. (2012). Ordered to isotropic morphology transition in pattern-directed dewetting of polymer thin films on substrates with different feature heights. *ACS applied materials & interfaces*, 4(10):5375–5385.

Rubio, R. G., Ryazantsev, Y. S., Starov, V. M., Huang, G.-X., Chetverikov, A. P., Arena, P., Nepomnyashchy, A. A., Ferrus, A., and Morozov, E. G. (2013). *Without Bounds: A Scientific Canvas of Nonlinearity and Complex Dynamics*. Springer.

Ruschak, K. (1978). Flow of a falling film into a pool. *AIChE Journal*, 24(4):705–709.

Ruyer-Quil, C. and Manneville, P. (2000). Improved modeling of flows down inclined planes. *The European Physical Journal B-Condensed Matter and Complex Systems*, 15(2):357–369.

Schaeffer, E., Thurn-Albrecht, T., Russell, T. P., and Steiner, U. (2000). Electrically induced structure formation and pattern transfer. *Nature*, 403(6772):874–877.

Scheid, B. (2013). Rivulet structures in falling liquid films. In *Without Bounds: A Scientific Canvas of Nonlinearity and Complex Dynamics*, pages 435–441. Springer.

Scheid, B., Kofman, N., and Rohlfs, W. (2016). Critical inclination for absolute/convective instability transition in inverted falling films. *Physics of Fluids*, 28(4):044107.

Scheid, B., Ruyer-Quil, C., Thiele, U., Kabov, O. A., Legros, J. C., and Colinet, P. (2005). Validity domain of the benney equation including the marangoni effect for closed and open flows. *Journal of Fluid Mechanics*, 527:303–335.

Schlichting, H. and Kestin, J. (1961). *Boundary layer theory*, volume 121. Springer.

Schmid, P. J., Henningson, D. S., and Jankowski, D. (2002). Stability and transition in shear flows. applied mathematical sciences, vol. 142. *Appl. Mech. Rev.*, 55(3):B57–B59.

Schulze, J. and Sesterhenn, J. (2013). Optimal distribution of porous media to reduce trailing edge noise. *Computers & Fluids*, 78:41–53. LES of turbulence aeroacoustics and combustion.

Schwartz, L. W. and Roy, R. V. (2004). Theoretical and numerical results for spin coating of viscous liquids. *Physics of fluids*, 16(3):569–584.

Scriven, L. E. (1988). Physics and applications of dip coating and spin coating. *MRS Online Proceedings Library (OPL)*, 121.

Seemann, R., Brinkmann, M., Kramer, E. J., Lange, F. F., and Lipowsky, R. (2005). Wetting morphologies at microstructured surfaces. *Proceedings of the National Academy of Sciences*, 102(6):1848–1852.

Seemann, R., Herminghaus, S., and Jacobs, K. (2001). Dewetting patterns and molecular forces: A reconciliation. *Physical Review Letters*, 86(24):5534.

Sferrazza, M., Heppenstall-Butler, M., Cubitt, R., Bucknall, D., Webster, J., and Jones, R. A. L. (1998). Interfacial instability driven by dispersive forces: The early stages of spinodal dewetting of a thin polymer film on a polymer substrate. *Physical Review Letters*, 81(23):5173.

Shannon, M. A., Bohn, P. W., Elimelech, M., Georgiadis, J. G., Mariñas, B. J., and Mayes, A. M. (2008). Science and technology for water purification in the coming decades. *Nature*, 452:301–310.

Sharma, A. (1993). Equilibrium contact angles and film thicknesses in the apolar and polar systems: Role of intermolecular interactions in coexistence of drops with thin films. *Langmuir*, 9(12):3580–3586.

Sharma, A. and García-Mayoral, R. (2020). Turbulent flows over dense filament canopies. *Journal of Fluid Mechanics*, 888.

Sharma, A. and Khanna, R. (1998). Pattern formation in unstable thin liquid films. *Physical Review Letters*, 81(16):3463.

Shenoy, A. and Kleinstreuer, C. (2008). Flow over a thin circular disk at low to moderate reynolds numbers. *Journal of Fluid Mechanics*, 605:253–262.

Shi, W., Anderson, M., Tulkoff, J., Kennedy, B., and Boreyko, J. (2018). Fog harvesting with harps. *ACS applied materials & interfaces*, 10(14):11979–11986.

Short, M., Baygents, J., Beck, J., Stone, D., Toomey, R., and Goldstein, R. (2005a). Stalactite growth as a free-boundary problem: A geometric law and its platonic ideal. *Phys. Rev. Lett.*, 94:018501.

Short, M., Baygents, J., and Goldstein, R. (2005b). Stalactite growth as a free-boundary problem. *Physics of fluids*, 17(8):083101.

Shukla, I. and Gallaire, F. (2020). Frequency selection in a gravitationally stretched capillary jet in the jetting regime. *Journal of Fluid Mechanics*, 894:A6.

Silvi, N. and Dussan, E. B. (1985). The rewetting of an inclined solid surface by a liquid. *The Physics of fluids*, 28(1):5–7.

Simpson, J. E. (1982). Gravity currents in the laboratory, atmosphere, and ocean. *Annual Review of Fluid Mechanics*, 14(1):213–234.

Smith, S. H. (1969). On initial value problems for the flow in a thin sheet of viscous liquid. *Zeitschrift für angewandte Mathematik und Physik ZAMP*, 20(4):556–560.

Spaid, M. and Homsy, G. (1996). Stability of newtonian and viscoelastic dynamic contact lines. *Physics of Fluids*, 8(2):460–478.

Stammer, D., Bracco, A., Braconnot, P., Brasseur, G. P., Griffies, S., and Hawkins, E. (2018). Science directions in a post cop21 world of transient climate change: Enabling regional to local predictions in support of reliable climate information. *Earth's Future*, 6(11):1498–1507.

Stein, E. and Weiss, G. (2016). *Introduction to Fourier analysis on Euclidean spaces*, volume 32. Princeton university press.

Sterman-Cohen, E., Bestehorn, M., and Oron, A. (2017). Rayleigh-Taylor instability in thin liquid films subjected to harmonic vibration. *Physics of Fluids*, 29(5):052105.

Sterman-Cohen, E. and Oron, A. (2020). Dynamics of nonisothermal two-thin-fluid-layer systems subjected to harmonic tangential forcing under rayleigh–taylor instability conditions. *Physics of Fluids*, 32(8):082113.

Strong, E. F., Pezzulla, M., Gallaire, F., Reis, P., and Siconolfi, L. (2019). Hydrodynamic loading of perforated disks in creeping flows. *Phys. Rev. Fluids*, 4:084101.

Sunada, S., Takashima, H., Hattori, T., Yasuda, K., and Kawachi, K. (2002). Fluid-dynamic characteristics of a bristled wing. *Journal of experimental biology*, 205(17):2737–2744.

Takagi, D. and Huppert, H. E. (2010). Flow and instability of thin films on a cylinder and sphere. *Journal of Fluid Mechanics*, 647:221–238.

Taneda, S. (1956). Experimental investigation of the wake behind a sphere at low reynolds numbers. *Journal of the Physical Society of Japan*, 11(10):1104–1108.

Tang, T., Xie, J., Yu, S., Li, J., and Yu, P. (2021). Effect of aspect ratio on flow through and around a porous disk. *Phys. Rev. Fluids*, 6:074101.

Taylor, G. I. (1950). The instability of liquid surfaces when accelerated in a direction perpendicular to their planes. i. *Proceedings of the Royal Society of London. Series A. Mathematical and Physical Sciences*, 201(1065):192–196.

Tchoufag, J., Fabre, D., and Magnaudet, J. (2014). Global linear stability analysis of the wake and path of buoyancy-driven disks and thin cylinders. *Journal of fluid mechanics*, 740:278–311.

Theofilis, V. (2011). Global linear instability. *Annual Review of Fluid Mechanics*, 43(1):319–352.

Thickett, S. C., Neto, C., and Harris, A. T. (2011). Biomimetic surface coatings for atmospheric water capture prepared by dewetting of polymer films. *Advanced Materials*, 23(32):3718–3722.

Thiffeault, J.-L. and Kamhawi, K. (2006). Transport in thin gravity-driven flow over a curved substrate. *arXiv preprint nlin/0607075*.

Thompson, C. V. (2012). Solid-state dewetting of thin films. *Annual Review of Materials Research*, 42:399–434.

Thompson, D. W. (1942). *On growth and form*, volume 2. Cambridge university press Cambridge.

Thompson, M. C., Radi, A., Rao, A., Sheridan, J., and Hourigan, K. (2014). Low-Reynolds-number wakes of elliptical cylinders: From the circular cylinder to the normal flat plate. *Journal of Fluid Mechanics*, 751:570–600.

Trefethen, L. and Bau III, D. (1997). *Numerical linear algebra*, volume 50. Siam.

Troian, S. M., Herbolzheimer, E., Safran, S. A., and Joanny, J. F. (1989a). Fingering instabilities of driven spreading films. *EPL (Europhysics Letters)*, 10(1):25.

Troian, S. M., Wu, X. L., and Safran, S. A. (1989b). Fingering instability in thin wetting films. *Physical Review Letters*, 62(13):1496.

Tseluiko, D., Blyth, M., and Papageorgiou, D. (2013). Stability of film flow over inclined topography based on a long-wave nonlinear model. *Journal of Fluid Mechanics*, 729:638–671.

Turing, A. M. (1952). The chemical basis of morphogenesis. *Philosophical Transactions of the Royal Society of London. Series B, Biological Sciences*, 237(641):37–72.

Unser, M., Sage, D., and Van De Ville, D. (2009). Multiresolution monogenic signal analysis using the riesz–laplace wavelet transform. *IEEE Transactions on Image Processing*, 18(11):2402–2418.

Van Dyke, M. (1975). Perturbation methods in fluid mechanics/annotated edition. *NASA STI/Recon Technical Report A*, 75.

Van Saarloos, W. (2003). Front propagation into unstable states. *Physics reports*, 386(2-6):29–222.

van Zelst, V., Dijkstra, J. T., van Wesenbeeck, B. K., Eilander, D., Morris, E. P., Winsemius, H. C., Ward, P. J., and de Vries, M. B. (2021). Cutting the costs of coastal protection by integrating vegetation in flood defences. *Nature communications*, 12(1):1–11.

Verma, A. and Sharma, A. (2011). Self-organized nano-lens arrays by intensified dewetting of electron beam modified polymer thin-films. *Soft Matter*, 7(23):11119–11124.

Vesipa, R., Camporeale, C., and Ridolfi, L. (2015). Thin-film-induced morphological instabilities over calcite surfaces. *Proceedings of the Royal Society A: Mathematical, Physical and Engineering Sciences*, 471(2176):20150031.

Viola, F., Arratia, C., and Gallaire, F. (2016). Mode selection in trailing vortices: harmonic response of the non-parallel batchelor vortex. *Journal of Fluid Mechanics*, 790:523–552.

Viola, F., Iungo, G. V., Camarri, S., Porté-Agel, F., and Gallaire, F. (2014). Prediction of the hub vortex instability in a wind turbine wake: stability analysis with eddy-viscosity models calibrated on wind tunnel data. *Journal of Fluid Mechanics*, 750:R1.

Volodin, P. and Kondyurin, A. (2008a). Dewetting of thin polymer film on rough substrate: I. theory. *Journal of Physics D: Applied Physics*, 41(6):065306.

Volodin, P. and Kondyurin, A. (2008b). Dewetting of thin polymer film on rough substrate: Ii. experiment. *Journal of Physics D: Applied Physics*, 41(6):065307.

Vreugdenhil, C. B. (1994). *Numerical methods for shallow-water flow*, volume 13. Springer Science & Business Media.

Wagner, H., Weger, M., Klaas, M., and Schröder, W. (2017). Features of owl wings that promote silent flight. *Interface Focus*, 7(1):20160078.

Weidner, D., Schwartz, L., and Eres, M. (2007). Suppression and reversal of drop formation in a model paint film. *Chemical Product and Process Modeling*, 2(3).

Weinstein, S. and Ruschak, K. (2004). Coating flows. *Annu. Rev. Fluid Mech.*, 36:29–53.

Whitaker, S. (1986). Flow in porous media i: A theoretical derivation of darcy's law. *Transport in porous media*, 1(1):3–25.

Williamson, C. H. K. (1996). Vortex dynamics in the cylinder wake. *Annual Review of Fluid Mechanics*, 28(1):477–539.

Willmarth, W. W., Hawk, N. E., and Harvey, R. L. (1964). Steady and unsteady motions and wakes of freely falling disks. *The physics of Fluids*, 7(2):197–208.

Wilson, S. (1982). The drag-out problem in film coating theory. *Journal of Engineering Mathematics*, 16(3):209–221.

Wong, C. Y., Trinh, P. H., and Chapman, S. J. (2020). Shear-induced instabilities of flows through submerged vegetation. *Journal of Fluid Mechanics*, 891.

Wray, A. W., Papageorgiou, D. T., and Matar, O. K. (2017). Reduced models for thick liquid layers with inertia on highly curved substrates. *SIAM Journal on Applied Mathematics*, 77(3):881–904.

Wu, T., J. Brokaw, C., and Brennen, C. (1975). *Swimming and Flying in Nature: Volume 2*.

Wyart, F. B. and Daillant, J. (1990). Drying of solids wetted by thin liquid films. *Canadian Journal of Physics*, 68(9):1084–1088.

Xie, R., Karim, A., Douglas, J. F., Han, C. C., and Weiss, R. A. (1998). Spinodal dewetting of thin polymer films. *Physical Review Letters*, 81(6):1251.

Xu, H., Cantwell, C. D., Monteserin, C., Eskilsson, C., Engsig-Karup, A. P., and Sherwin, S. J. (2018). Spectral/hp element methods: Recent developments, applications, and perspectives. *Journal of Hydrodynamics*, 30(1):1–22.

Xue, N. and Stone, H. A. (2020). Self-similar draining near a vertical edge. *Physical review letters*, 125(6):064502.

Xue, N. and Stone, H. A. (2021). Draining and spreading along geometries that cause converging flows: Viscous gravity currents on a downward-pointing cone and a bowl-shaped hemisphere. *Physical Review Fluids*, 6(4):043801.

Yiantsios, S. G. and Higgins, B. G. (1989). Rayleigh-Taylor instability in thin viscous films. *Physics of Fluids A: Fluid Dynamics*, 1(9):1484–1501.

Yosef, G. and Rabani, E. (2006). Self-assembly of nanoparticles into rings: A lattice-gas model. *The Journal of Physical Chemistry B*, 110(42):20965–20972.

Yoshikawa, H. N., Mathis, C., Satoh, S., and Tasaka, Y. (2019). Inwardly rotating spirals in a nonoscillatory medium. *Physical review letters*, 122(1):014502.

Yu, N. and Capasso, F. (2014). Flat optics with designer metasurfaces. *Nature materials*, 13(2):139–150.

Yu, P., Zeng, Y., Lee, T. S., Chen, X. B., and Low, H. T. (2011). Steady flow around and through a permeable circular cylinder. *Computers & Fluids*, 42(1):1–12.

Yu, P., Zeng, Y., Lee, T. S., Chen, X. B., and Low, H. T. (2012). Numerical simulation on steady flow around and through a porous sphere. *International Journal of Heat and Fluid Flow*, 36:142–152.

Zaccaria, D., Bigoni, D., Noselli, G., and Misseroni, D. (2011). Structures buckling under tensile dead load. *Proceedings of the Royal Society A: Mathematical, Physical and Engineering Sciences*, 467(2130):1686–1700.

Zampogna, G. and Gallaire, F. (2020). Effective stress jump across membranes. *Journal of Fluid Mechanics*, 892:A9.

Zampogna, G., Lācis, U., Bagheri, S., and Bottaro, A. (2019a). Modeling waves in fluids flowing over and through poroelastic media. *International Journal of Multiphase Flow*, 110:148 – 164.

Zampogna, G., Pluvinage, F., Kourta, A., and Bottaro, A. (2016). Instability of canopy flows. *Water Resources Research*, 52(7):5421–5432.

Zampogna, G. A. and Bottaro, A. (2016). Fluid flow over and through a regular bundle of rigid fibres. *Journal of Fluid Mechanics*, 792:5–35.

Zampogna, G. A., Magnaudet, J., and Bottaro, A. (2019b). Generalized slip condition over rough surfaces. *Journal of Fluid Mechanics*, 858:407–436.

Zong, L. and Nepf, H. (2012). Vortex development behind a finite porous obstruction in a channel. *Journal of Fluid Mechanics*, 691:368–391.

Pier Giuseppe Ledda

Contact Information École Polytechnique Fédérale de Lausanne, EPFL
STI IGM LFMI MED 2 2526
Station 9 CH-1015 Lausanne, Switzerland
E-mail: pier.ledda@epfl.ch

Personal data

Birth date	17.04.1993
Birth place	Bosa, Sardinia, Italy
Citizenship	Italian
Languages	Italian (mother tongue), Sardinian (mother tongue), English (fluent), French (fluent)

Education

08.2018-05.2022 PhD in Mechanical Engineering, EPFL, Lausanne, Switzerland
Laboratory of Fluid Mechanics and Instabilities
Thesis title: *From coating flow patterns to porous body wake dynamics via multiscale models*, under the supervision of Prof. François Gallaire

09.2015-05.2018 Master's Degree in Aerospace Engineering - Aerodynamics, University of Pisa, Italy
Thesis title: *Behavior of wake flows past porous bluff bodies*
Final Mark: 110/110 e Lode

09.2012-09.2015 Bachelor's Degree in Aerospace Engineering, University of Pisa, Italy
Final Mark: 110/110 e Lode

09.2007-06.2012 Diploma di Liceo Scientifico, I.I.S. G.A. Pischedda, Bosa, Italy
Final Mark: 100/100 e Lode

Teaching experience

Teaching Assistant

Hydrodynamics (EPFL Master 2019,2020,2021), Prof. F. Gallaire (62 hours)

Two-phase Flows and Heat Transfer (EPFL Master 2019,2020,2021), Prof. F. Gallaire (61 hours)

Information, Calcul, Communication (EPFL Bachelor 2019), Prof. M. Rajman (9 hours)

Students supervisor

Wake flow past a permeable sphere: characterization, stability and design (EPFL and University of Pisa Master 2021)

Three-dimensional instability of the von Karman vortex street past a porous cylinder (EPFL and University of Pisa Master 2022)

Wakes and paths of buoyancy-driven permeable disks: a linear stability approach (EPFL and University of Pisa Master 2022)

List of publications

G. Vagnoli, G.A. Zampogna, S. Camarri, F. Gallaire, P.G. Ledda
Wakes and paths of buoyancy-driven permeable disks: a linear stability approach.
In preparation

P.G. Ledda, M. Pezzulla, E. Jambon-Puillet, P-T Brun, F.Gallaire
Gravity-driven coatings on generic substrates: a differential geometry approach.
Submitted to Journal of Fluid Mechanics

G.A. Zampogna, P.G. Ledda, F. Gallaire
Transport across thin membranes: effective solute flux jump.
Under revision in Proceedings of the Royal Society A

M. Ciuti, G.A. Zampogna, F. Gallaire, S. Camarri, P.G. Ledda
On the effect of a penetrating recirculation region on the bifurcations of the flow past a permeable sphere.
Physics of Fluids 33, 124103 (2021) (doi:10.1063/5.0075244)

P.G. Ledda, E. Boujo, S. Camarri, F. Gallaire, G.A. Zampogna
Homogenization based design of microstructured membranes: wake flows past permeable shells.
Journal of Fluid Mechanics 927, A31 (2021) (doi:10.1017/jfm.2021.756)

L. Martin-Monier, P.G. Ledda, P.L. Piveteau, F. Gallaire, F. Sorin
Prediction of Self-Assembled Dewetted Nanostructures for Photonics Applications via a Continuum-Mechanics Framework.
Physical Review Applied 16, 034025 (2021) (doi:10.1103/PhysRevApplied.16.034025)

E. Jambon-Puillet, P.G. Ledda, F. Gallaire, P-T Brun
Drops on the Underside of a Slightly Inclined Wet Substrate Move Too Fast to Grow.
Physical Review Letters 127, 044503 (2021) (doi:10.1103/PhysRevLett.127.044503)

P.G. Ledda, F. Gallaire
Secondary instability in thin film flows under an inclined plane: growth of lenses on spatially developing rivulets.
Proceedings of the Royal Society A 477:20210291 (2021) (doi:10.1098/rspa.2021.0291)

P.G. Ledda, G. Balestra, G. Lerisson, B. Scheid, M. Wyart, F. Gallaire
Hydrodynamic-driven morphogenesis of karst draperies: Spatio-temporal analysis of the two-dimensional impulse response.
Journal of Fluid Mechanics, 910, A53 (2021) (doi:10.1017/jfm.2020.1010)

P.G. Ledda, G. Lerisson, G. Balestra, F. Gallaire
Instability of a thin viscous film flowing under an inclined substrate: the emergence and stability of rivulets.
Journal of Fluid Mechanics, 904, A23 (2020) (doi:10.1017/jfm.2020.673)

G. Lerisson, P.G. Ledda, G. Balestra, F. Gallaire
Instability of a thin viscous film flowing under an inclined substrate: steady patterns.
Journal of Fluid Mechanics, 828, A6 (2020) (doi:10.1017/jfm.2020.396)

G. Lerisson, P.G. Ledda, G. Balestra, F. Gallaire
Dripping down the rivulet. Paper associated with a video winner of the 2018 APS/DFD Milton van Dyke Award,
Physical Review Fluids 4, 100504 (2019) (doi:10.1103/PhysRevFluids.4.100504)

P.G. Ledda, L. Siconolfi, F. Viola, S. Camarri, F. Gallaire
Flow dynamics of a dandelion pappus: a linear stability approach.
Physical Review Fluids, 4, 071901(R) (2019) (doi:10.1103/PhysRevFluids.4.071901).

P.G. Ledda, L. Siconolfi, F. Viola, F. Gallaire, S. Camarri
Suppression of von Karman vortex streets past porous rectangular cylinders.
Physical Review Fluids, 3, 103901 (2018) (doi:10.1103/PhysRevFluids.3.103901).

Conferences and seminars

11.2021 **P.G. Ledda, E. Boujo, S. Camarri, F. Gallaire, G.A. Zampogna**
Homogenization-based optimization and design of microstructured membranes: flow past a circular cylindrical shell
74th Annual Meeting of the APS Division of Fluid Dynamics , Phoenix, USA.

09.2021 **P.G. Ledda, G. Lerisson, G.Balestra, F. Gallaire**
To drip or not to drip: pattern formation of a thin film flowing under an inclined plane
European Coating Symposium, Bruxelles, Belgium,

08.2021 **P.G. Ledda, G. Lerisson, G.Balestra, F. Gallaire**
Instability of a thin film flowing under an inclined plane
25th International Congress of Theoretical and Applied Mechanics (ICTAM 2020+1), Milan (held online), Italy

11.2020 **P.G. Ledda, G.Balestra, G. Lerisson, B. Scheid, M. Wyart, F. Gallaire**
On the origin of draperies structures in limestone caves: two-dimensional analysis of the impulse response
73rd Annual Meeting of the APS Division of Fluid Dynamics , Chicago (held online), USA.

09.2020 **P.G. Ledda, G. Lerisson, G.Balestra, F. Gallaire**
Rivulet formation in a thin film flowing under an inclined plane
Virtual Technical Meeting of the Society of Engineering Science

11.2019 **P.G. Ledda, G. Lerisson, G.Balestra, F. Gallaire**
Pattern formation of a thin film flowing under an inclined plane
72nd Annual Meeting of the APS Division of Fluid Dynamics , Seattle, USA

Summer schools

07.2019 Fluid Dynamics for Sustainability and the Environment Summer School, Ecole Polytechnique, Palaiseau, France

04.2018 ERCOFTAC Montestigliano Spring School, "Lattice-Boltzmann methods for fluid dynamics", Brenna, Italy

Awards

2018 APS/DFD Milton van Dyke Award at the DFD Gallery of Fluid Motion. Original video available online at the Gallery of Fluid Motion https://doi.org/10.1103/APS.DFD.2018.GFM.V0070